

Jimson Mathew  
Lenin Gopal  
Filbert H. Juwono *Editors*

# Artificial Intelligence for Sustainable Energy

Select Proceedings of the International  
Conference, GEn-CITy 2023

# Lecture Notes in Electrical Engineering

## Volume 1142

### Series Editors

- Leopoldo Angrisani, Department of Electrical and Information Technologies Engineering, University of Napoli Federico II, Napoli, Italy
- Marco Artega, Departamento de Control y Robótica, Universidad Nacional Autónoma de México, Coyoacán, Mexico
- Samarjit Chakraborty, Fakultät für Elektrotechnik und Informationstechnik, TU München, München, Germany
- Jiming Chen, Zhejiang University, Hangzhou, Zhejiang, China
- Shanben Chen, School of Materials Science and Engineering, Shanghai Jiao Tong University, Shanghai, China
- Tan Kay Chen, Department of Electrical and Computer Engineering, National University of Singapore, Singapore, Singapore
- Rüdiger Dillmann, University of Karlsruhe (TH) IAIM, Karlsruhe, Baden-Württemberg, Germany
- Haibin Duan, Beijing University of Aeronautics and Astronautics, Beijing, China
- Gianluigi Ferrari, Dipartimento di Ingegneria dell'Informazione, Sede Scientifica Università degli Studi di Parma, Parma, Italy
- Manuel Ferre, Centre for Automation and Robotics CAR (UPM-CSIC), Universidad Politécnica de Madrid, Madrid, Spain
- Faryar Jabbari, Department of Mechanical and Aerospace Engineering, University of California, Irvine, CA, USA
- Limin Jia, State Key Laboratory of Rail Traffic Control and Safety, Beijing Jiaotong University, Beijing, China
- Janusz Kacprzyk, Intelligent Systems Laboratory, Systems Research Institute, Polish Academy of Sciences, Warsaw, Poland
- Alaa Khamis, Department of Mechatronics Engineering, German University in Egypt El Tagamoa El Khames, New Cairo City, Egypt
- Torsten Kroeger, Intrinsic Innovation, Mountain View, CA, USA
- Yong Li, College of Electrical and Information Engineering, Hunan University, Changsha, Hunan, China
- Qilian Liang, Department of Electrical Engineering, University of Texas at Arlington, Arlington, TX, USA
- Ferran Martín, Departament d'Enginyeria Electrònica, Universitat Autònoma de Barcelona, Bellaterra, Barcelona, Spain
- Tan Cher Ming, College of Engineering, Nanyang Technological University, Singapore, Singapore
- Wolfgang Minker, Institute of Information Technology, University of Ulm, Ulm, Germany
- Pradeep Misra, Department of Electrical Engineering, Wright State University, Dayton, OH, USA
- Subhas Mukhopadhyay, School of Engineering, Macquarie University, Sydney, NSW, Australia
- Cun-Zheng Ning, Department of Electrical Engineering, Arizona State University, Tempe, AZ, USA
- Toyoaki Nishida, Department of Intelligence Science and Technology, Kyoto University, Kyoto, Japan
- Luca Oneto, Department of Informatics, Bioengineering, Robotics and Systems Engineering, University of Genova, Genova, Italy
- Bijaya Ketan Panigrahi, Department of Electrical Engineering, Indian Institute of Technology Delhi, New Delhi, Delhi, India
- Federica Pascucci, Department di Ingegneria, Università degli Studi Roma Tre, Roma, Italy
- Yong Qin, State Key Laboratory of Rail Traffic Control and Safety, Beijing Jiaotong University, Beijing, China
- Gan Woon Seng, School of Electrical and Electronic Engineering, Nanyang Technological University, Singapore, Singapore
- Joachim Speidel, Institute of Telecommunications, University of Stuttgart, Stuttgart, Germany
- Germano Veiga, FEUP Campus, INESC Porto, Porto, Portugal
- Haitao Wu, Academy of Opto-electronics, Chinese Academy of Sciences, Haidian District Beijing, China
- Walter Zamboni, Department of Computer Engineering, Electrical Engineering and Applied Mathematics, DIEM—Università degli studi di Salerno, Fisciano, Salerno, Italy
- Junjie James Zhang, Charlotte, NC, USA
- Kay Chen Tan, Department of Computing, Hong Kong Polytechnic University, Kowloon Tong, Hong Kong

The book series *Lecture Notes in Electrical Engineering* (LNEE) publishes the latest developments in Electrical Engineering—quickly, informally and in high quality. While original research reported in proceedings and monographs has traditionally formed the core of LNEE, we also encourage authors to submit books devoted to supporting student education and professional training in the various fields and applications areas of electrical engineering. The series cover classical and emerging topics concerning:

- Communication Engineering, Information Theory and Networks
- Electronics Engineering and Microelectronics
- Signal, Image and Speech Processing
- Wireless and Mobile Communication
- Circuits and Systems
- Energy Systems, Power Electronics and Electrical Machines
- Electro-optical Engineering
- Instrumentation Engineering
- Avionics Engineering
- Control Systems
- Internet-of-Things and Cybersecurity
- Biomedical Devices, MEMS and NEMS

For general information about this book series, comments or suggestions, please contact [leontina.dicecco@springer.com](mailto:leontina.dicecco@springer.com).

To submit a proposal or request further information, please contact the Publishing Editor in your country:

#### **China**

Jasmine Dou, Editor ([jasmine.dou@springer.com](mailto:jasmine.dou@springer.com))

#### **India, Japan, Rest of Asia**

Swati Meherishi, Editorial Director ([Swati.Meherishi@springer.com](mailto:Swati.Meherishi@springer.com))

#### **Southeast Asia, Australia, New Zealand**

Ramesh Nath Premnath, Editor ([ramesh.premnath@springernature.com](mailto:ramesh.premnath@springernature.com))

#### **USA, Canada**

Michael Luby, Senior Editor ([michael.luby@springer.com](mailto:michael.luby@springer.com))

#### **All other Countries**

Leontina Di Cecco, Senior Editor ([leontina.dicecco@springer.com](mailto:leontina.dicecco@springer.com))

**\*\* This series is indexed by EI Compendex and Scopus databases. \*\***

Jimson Mathew · Lenin Gopal · Filbert H. Juwono  
Editors

# Artificial Intelligence for Sustainable Energy

Select Proceedings of the International  
Conference, GEn-CITy 2023



Springer

*Editors*

Jimson Mathew  
Department of Computer Science  
and Engineering  
Indian Institute of Technology Patna  
Patna, Bihar, India

Lenin Gopal  
Department of Electrical and Electronic  
Engineering  
University of Southampton Malaysia  
Iskandar Puteri, Johor, Malaysia

Filbert H. Juwono  
Department of Electrical and Electronic  
Engineering  
Xi'an Jiaotong-Liverpool University  
Suzhou, Jiangsu, China

ISSN 1876-1100                   ISSN 1876-1119 (electronic)  
Lecture Notes in Electrical Engineering  
ISBN 978-981-99-9832-6       ISBN 978-981-99-9833-3 (eBook)  
<https://doi.org/10.1007/978-981-99-9833-3>

© The Editor(s) (if applicable) and The Author(s), under exclusive license to Springer Nature  
Singapore Pte Ltd. 2024

This work is subject to copyright. All rights are solely and exclusively licensed by the Publisher, whether the whole or part of the material is concerned, specifically the rights of translation, reprinting, reuse of illustrations, recitation, broadcasting, reproduction on microfilms or in any other physical way, and transmission or information storage and retrieval, electronic adaptation, computer software, or by similar or dissimilar methodology now known or hereafter developed.

The use of general descriptive names, registered names, trademarks, service marks, etc. in this publication does not imply, even in the absence of a specific statement, that such names are exempt from the relevant protective laws and regulations and therefore free for general use.

The publisher, the authors, and the editors are safe to assume that the advice and information in this book are believed to be true and accurate at the date of publication. Neither the publisher nor the authors or the editors give a warranty, expressed or implied, with respect to the material contained herein or for any errors or omissions that may have been made. The publisher remains neutral with regard to jurisdictional claims in published maps and institutional affiliations.

This Springer imprint is published by the registered company Springer Nature Singapore Pte Ltd.  
The registered company address is: 152 Beach Road, #21-01/04 Gateway East, Singapore 189721,  
Singapore

Paper in this product is recyclable.

# Preface

Intelligence of machines is quickly transforming every perspective of our life, from managing a business, decision making and risk management, interactive information retrieval, information gathering systems, personalization systems, recommendation systems, and energy management. AI has improved our productivity and influenced our preferences. AI systems have now become very pervasive and an integral part of human life. They make decisions every minute, invisible to the users and, interestingly, incomprehensible even to the creators. The opaqueness of these systems is becoming a significant cause of worry, and solutions require an interdisciplinary approach. Another concern is whether data-driven learning inherently has a capability to internalize, propagate or exacerbate biases and engender discriminatory behavior, and how we can address such considerations through developing a new breed of algorithms. AI makes an important contribution to various fields of engineering. This book comprises select proceedings of the International Conference on Green Energy, Computing and Intelligent Technology (GEn-CITy 2023). The contents of this book focus on artificial intelligence for sustainable energy. This volume tries to integrate research across diverse topics related to data science, such as green computing, communication and networks, green energy and power system, smart grid, intelligent systems and sensors, aerospace and automation technologies, AI implementation in manufacturing and green technologies and sustainability. The chapters in this volume will represent research from different perspectives that offer novel theoretical implications that span multiple disciplines.

Patna, India  
Iskandar Puteri, Malaysia  
Suzhou, China

Jimson Mathew  
Lenin Gopal  
Filbert H. Juwono

# Contents

<b>Miniaturized Thin Flexible Fractal-Slot-Based Artificial Magnetic Conductor for Radio Frequency Identification Applications .....</b>	1
Man Seng Sim, Raimi Dewan, Faishal Adilah Suryanata, and Kok Yeow You	
<b>Effect of Nacelle Shape on the Flow Fields of Upwind and Downwind Wind Turbines .....</b>	13
Jay Prakash Goit and Takatsugu Kameda	
<b>Automated Transformer Health Prediction: Evaluation of Complexity and Linearity of Models for Prediction .....</b>	21
Andrea Wong Saen Er, W. K. Wong, Filbert H. Juwono, I. M. Chew, Saaveethya Sivakumar, and Arul Paruvachi Gurusamy	
<b>Design, Development and Experiment Analysis of Solar Panel Cleaning System .....</b>	35
Laurence Gerry John, Goh Thing Thing, J. Ragupathy, H. S. Chua, and Fu Pang Han	
<b>Modeling of Controller for Motor-Controlled Prosthetic Hand Based on Machine Learning Strategy in Classifying Two-Channel Surface EMG Signals .....</b>	51
Salina Mohmad and Abdalrahman Khaled Elnagar	
<b>Iterative Hard Thresholding Algorithm Using Norm Exponent .....</b>	73
Bamrung Tausiesakul and Krissada Asavaskulkiet	
<b>Unveiling the Root Cause of EV Charging Irregularities: A Statistical Approach .....</b>	87
Ankit Bajaj, Dinesh Gopalani, Rachit Mathur, Hemanjaneya Reddy, Swapna Satyanarayan, and Ansuman Chand	

<b>Performance Analysis of Wireless Power Charging and Future Enhancement Techniques for Drones .....</b>	101
Ahmed. O. MohamedZain, Jiehan Teoh, Kianmeng Yap, and Huangshen Chua	
<b>IIUM Gombak Driving Cycle for Motorcycle .....</b>	123
Hafizi Malik and Ahmad Syahrin Idris	
<b>Securing Wireless Communications in IoT: A Study of One-Step Majority Logic Decodable Codes for Physical Layer Security .....</b>	141
Otmane El Mouaatamid, Mohamed Lahmer, Mostafa Belkasmi, and Karim Rkizat	
<b>IRS-Aided Cyclostationary Spectrum Sensing in Dynamic Spectrum Access Networks .....</b>	153
Sanjeev Raghooonath and Sean Rocke	
<b>Prediction of Electricity Consumption Demand Based on Long-Short Term Memory Network .....</b>	165
Amanullah Khan, Siti Marwangi Mohamad Maharum, Faezah Harun, and Jawad Ali Shah	
<b>A New Quantum-Resistant Electronic Voting Based on Fully Homomorphic Encryption .....</b>	179
Meryem Cherkaoui Semmouni, Mostafa Belkasmi, Abderrahmane Nitaj, and Ali Azougaghe	
<b>Mitigation of Electromagnetic Interference from DC-DC Converters for Electric Vehicle Application .....</b>	195
Satabda Chaudhuri, Ishan Mukherjee, and S. Hemamalini	
<b>Deep Learning-Based Bioimpedance Spectroscopy Using Start of Frame Delimiter in Human Body Communications .....</b>	209
Aaron Roopnarine and Sean Rocke	
<b>Reliability-Based Single Bit-Flipping Decoding Algorithm for LDPC Codes .....</b>	221
Soufian Addi, Mostafa Belkasmi, Ahlam Berkani, and Ahmed Azouaoui	
<b>Design of an Automated System for Door Set Measurement Using IoT Technologies: A Manufacturer's Perspective .....</b>	239
Takahiro Usuzuki, Sivajothi Paramasivam, Tamil Moli Loganathan, and Hari Krishnan Munisamy	
<b>Classification of Helpful and Unhelpful Online Customer Reviews Using XLNet and BERT Variants .....</b>	255
Muhammad Bilal, Muhammad Haseeb Arshad, and Muhammad Ramzan	

<b>Characterization and Absorption Test of Cellulose from Oil Palm Empty Fruit Bunch for Potential Use in Oil Spill Clean-Up .....</b>	271
N. F. Afandi, Adrian Wei-Yee Tan, Pravin Mariappan, Savisha Mahalingam, and Abreeza Manap	
<b>Comparative Study of Various Deep Learning Models for Structural Anomaly Detection .....</b>	281
Nitin Mohariya, Rushikesh Gade, and Jimson Mathew	
<b>Cutting Temperature in Machining of Ti-6Al-4V Alloy and Its Predictive Model .....</b>	297
Elango Natarajan, Manickam Ramasamy, S. Ramesh, Chun Kit Ang, and V. Kaviarasan	
<b>Tools for Automated Structural Health Monitoring Using Deep Learning and Computer Vision Techniques .....</b>	307
Rushikesh Gade, Surbhi Raj, and Jimson Mathew	
<b>Public Blockchain-Based Data Integrity Protection for Federated Learning in UAV Networks Using MAVLink Protocol .....</b>	321
Jing Huey Khor, Michail Sidorov, Shaw Zuan Law, Sui Yuan Tan, and Peh Yee Woon	
<b>Improving Production Rate by Analyzing Wire-Electrical Discharge Machining Parameters and Developing a Prediction Model .....</b>	335
S. Suresh, S. Ramesh, Elango Natarajan, Chun Kit Ang, Kanesan Muthusamy, and D. Velmurugan	
<b>Computer-Aided Potato Disease Detection by Using Deep Learning Techniques .....</b>	349
Fareeha Razaq, Muhammad Bilal, Muhammad Ramzan, Muhammad Naveed, and Samreen Razzaq	
<b>An Investigation into the Technical Feasibility of Incorporating Wind Energy for Electric Vehicle Charging Systems .....</b>	363
Belal Aldabagh, Nur Hasalli Binti Ibrahim, and Azizul Rahman Bin Abd Aziz	
<b>Surface-Modified PDMS-Aluminum Triboelectric Generator .....</b>	381
Emaediong Sylvanus Udofia, Anas A. Ahmed, Yusri Md Yunos, and Mohamed Sultan Mohamed Ali	

<b>Investigating the Performance of Control Strategies for Voltage and Frequency Regulation in Decentralized Power Generation System .....</b>	<b>391</b>
P. G. Arul, Lenin Gopal, Filbert H. Juwono, and Vun Jack Chin	
<b>Exploring the Feasibility of Recycled Carbon Fiber for Damage Sensing in Composite Materials .....</b>	<b>407</b>
Ting Yang Ling, Fan Zhang, and Khong Wui Gan	

## About the Editors

**Jimson Mathew** is currently a Professor in the Department of Computer Science and Engineering at the Indian Institute of Technology, Patna, India. He received a Master's in computer engineering from Nanyang Technological University, Singapore, and a Ph.D. degree in computer engineering from the University of Bristol, Bristol, UK. He has held positions with the Center for Wireless Communications, National University of Singapore, Bell Laboratories Research Lucent Technologies North Ryde, Australia, Royal Institute of Technology KTH, Stockholm, Sweden, and Department of Computer Science, University of Bristol, UK. He is a senior member of IEEE. He has previously served as a Guest Editor for ACM TECS. He also regularly serves on the program committee of top international conferences and holds multiple patents. His research interests include fault-tolerant computing, computer vision, machine learning, and IoT systems.

**Lenin Gopal** (Member, IEEE) received the B.Eng. degree in Electrical and Electronics Engineering from Madurai Kamaraj University, Madurai, India, in 1996, the M.Eng. degree in telecommunications engineering from Multimedia University, Cyberjaya Malaysia, in 2006, and the Ph.D. degree from Curtin University, Bentley, WA, Australia, in 2015. He was an Associate Professor with the Department of Electrical and Computer Engineering, Curtin University Malaysia, Miri, Sarawak, Malaysia, from February 2008 to December 2021. He is currently an Associate Professor at the University of Southampton Malaysia (UoSM), Iskandar Puteri Johor Malaysia. He is a member of IEEE. He served as a Guest Editor for the *Journal of Information Science and Engineering* in the years 2019–2020 and 2021–2022, and he is currently serving as a Guest Editor for the special issue on Green Sustainable Technologies for Creating a Better World in the *Journal of Information Science and Engineering*. He also regularly serves on the program committee of top international conferences. His research interests include signal processing for communications, power-line communications, and the Internet of things (IoT).

**Filbert H. Juwono** received the B.Eng. degree in electrical engineering and the M.Eng. degree in telecommunication engineering from the University of Indonesia,

Depok, Indonesia, in 2007 and 2009, respectively, and the Ph.D. degree in electrical and electronic engineering from The University of Western Australia, Perth, WA, Australia, in 2017. He is currently an Assistant Professor with Xi'an Jiaotong–Liverpool University, China. His research interests include signal processing for communications, wireless communications, power-line communications, machine learning applications, and biomedical engineering. He was a recipient of the prestigious Australian Awards Scholarship, in 2012. He serves as an Associate Editor for *IEEE Access*, a Review Editor for *Frontiers in Signal Processing* and the Editor-in-Chief for a newly established journal *Green Intelligent Systems and Applications*. He is a Senior Member of the IEEE and a Fellow of the Higher Education Academy.

# Miniaturized Thin Flexible Fractal-Slot-Based Artificial Magnetic Conductor for Radio Frequency Identification Applications



Man Seng Sim , Raimi Dewan , Faishal Adilah Suryanata , and Kok Yeow You

**Abstract** This paper designs a miniaturized flexible artificial magnetic conductor (AMC) based on a  $T$ -square fractal structure with slot operating at 920 MHz. The main advantage of the proposed AMC is the compact size, simplicity in design, and flexibility. This is achieved by optimization of the fractal-slot-based AMC structure on a thin polycarbonate substrate using computer simulation technology (CST) microwave studio simulator software. The results show that the proposed AMC is smaller in size compared to the conventional square-based AMC. In particular, unit cell size reduction of 22.4% is achieved, in which the unit cell size of the proposed AMC is 76 mm, which is only 23.3% of the operating wavelength. The proposed AMC can be applied in radio frequency identification (RFID) applications for performance enhancement.

**Keywords** Flexible · Metamaterials · Miniaturization · RFID

## 1 Introduction

Artificial magnetic conductors (AMCs) are metamaterial structures which behave as perfect magnetic conductors (PMCs) [1]. Ideally, at the operating frequency, AMCs reflect the incident electromagnetic wave with reflection magnitude and phase of +1 and 0°, respectively [2]. The operation bandwidth of an AMC is the range of frequency

---

R. Dewan · F. A. Suryanata

Advanced RF and Microwave Research Group, Faculty of Electrical Engineering, Universiti Teknologi Malaysia, UTM Johor Bahru, 81310 Johor, Malaysia  
e-mail: [raimi.dar@utm.my](mailto:raimi.dar@utm.my)

IJN-UTM Cardiovascular Engineering Centre, Institute of Human Centered Engineering, Universiti Teknologi Malaysia, UTM Johor Bahru, 81310 Johor, Malaysia

M. S. Sim · K. Y. You  
Department of Communication Engineering, Faculty of Electrical Engineering, Universiti Teknologi Malaysia, UTM Johor Bahru, 81310 Johor, Malaysia

within the reflection phase from  $+90^\circ$  to  $-90^\circ$  [3]. At this range of reflection phase, the destructive interference between the incident and reflection waves would not occur. This allows the AMCs to act as a reflector with in-phase reflection and have applications in microwave and antenna applications [4, 5].

AMCs are normally designed on a two-dimensional array of metallic structures on a conductor-backed dielectric substrate. Different geometrical structures such as slotted patch [3], staircase pattern [6], meandered line [7], square and symmetric slots [8], and square patches with via holes [9] have been proposed. However, some of the state-of-the-art AMC designs are complicated, rigid, and not suitable for body-worn radio frequency identification (RFID) applications [10].

In this paper, a miniaturized flexible planar AMC design using *T*-square fractal structure with slot is designed and investigated. The operating frequency,  $f$  is designed at 920 MHz, which is the frequency allocated for the RFID applications. The dielectric substrate is flexible, which is suitable for body-worn RFID applications. Miniaturization of the AMC leads to less chance of fracture and damage, easier to be incorporated into wearable antenna applications, and cheaper fabrication cost due to the smaller substrate and metallic sheet. The proposed AMC is simple to fabricate as it does not involve overly small dimensions of metallic structures or gaps between them. Moreover, the AMC design involves only straight outlines without any curvatures and therefore it can be fabricated by manually cutting by hand and removing unwanted shapes from adhesive metallic sheet without sophisticated machine. The conventional printed circuit board (PCB) fabrication procedure is not needed. Additionally, the proposed design also does not require via holes as the shorting pins and lumped elements.

## 2 Methodology

The AMC unit cell is simulated using computer simulation technology (CST) Microwave Studio. Based on Fig. 1a, the boundary conditions of the  $X_{\min}$ ,  $X_{\max}$ ,  $Y_{\min}$ , and  $Y_{\max}$  planes are set as ‘unit cell’ to represent the periodic arrangement of the unit cell. The ‘open’ boundary is set at  $Z_{\max}$ , and a Floquet mode waveguide port excites plane waves from this open boundary. The number of Floquet modes is set as ‘2’ for the two fundamental modes TE (0, 0) and TM (0, 0). With reference to Fig. 1b, the excitation port is placed at a distance of a wavelength ( $\lambda = 326$  mm at  $f = 920$  MHz) from the AMC surface. The reference plane of the port is exactly placed on the AMC surface to ensure a correct monitoring of the phase of the reflection signals.

Based on Fig. 2a, the conventional AMC unit cell using square patch is simulated using polycarbonate substrate (dielectric constant,  $\epsilon_r = 2.9$ , loss tangent,  $\tan \delta = 0.01$ , thickness,  $t = 0.5$  mm). With reference to Fig. 2b, the AMC is a three-layered metal-dielectric-metal structure. The initial unit cell size  $p$  is approximated as half the value of effective operating wavelength,  $\lambda$  [4]. The dimensions are then optimized to shift the operating frequency to the desired frequency. The optimized dimensions

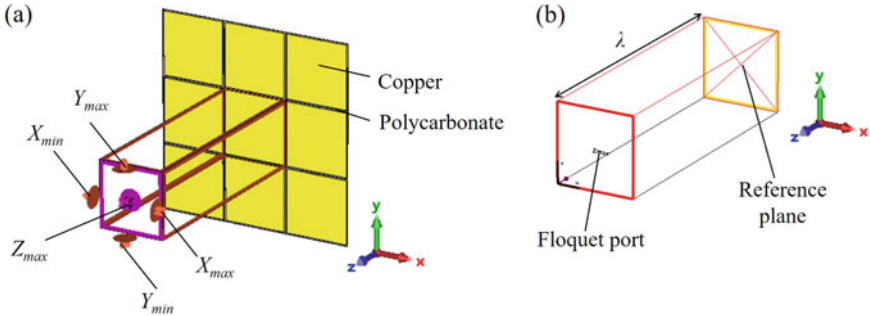


**Fig. 1** Simulation settings in CST: **a** boundary conditions, **b** excitation port

of the square-patch AMC are: unit cell size,  $p = 98$  mm and side length,  $l = 94$  mm. The simulated reflection phase is shown in Fig. 2c, in which the AMC operates at 920 MHz for reflection phase of 0°.

Using the same simulation setting, the square-patch structure is changed to a  $T$ -square fractal structure with slot by removing several rectangular structures from the square patch to realize miniaturization. This structural change affects the inductance of the patch as well as the mutual couplings or capacitive value between the adjacent AMC unit cells to achieve the desired electrical properties of the equivalent RLC circuit. The resonant frequency  $f$  of the circuit can be expressed as follows:

$$f = \frac{1}{2\pi\sqrt{LC}} \quad (1)$$

where  $L$  and  $C$  represent inductance and capacitance, respectively [7]. The design evolution of the proposed AMC structure is illustrated in Fig. 3.

### 3 Results and Discussion

AMC based on  $T$ -square fractal with and without slots is designed and investigated. Parametric analyses are performed to study the relationship between the geometrical dimensions of the AMC and the operating frequency. In this section, the results are presented and discussed.

#### 3.1 T-Square Fractal

A  $T$ -square fractal structure in its first iteration are optimized to operate at 920 MHz. It is worth mentioning that higher-order iterations are not considered in this work to avoid complexity and difficulty in fabrication. With reference to Fig. 4a, the metallic

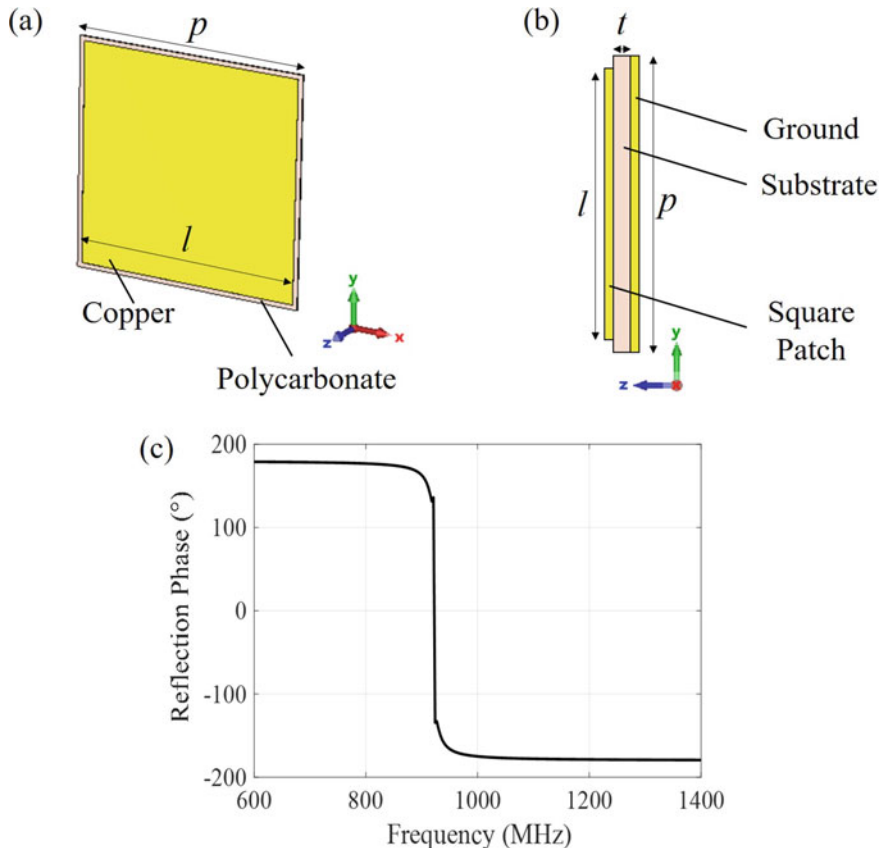


**Fig. 2** **a** Perspective view, **b** side view of conventional AMC based on metallic square patch, **c** reflection phases as a function of frequency for AMC with  $p = 98$  mm,  $l = 94$  mm

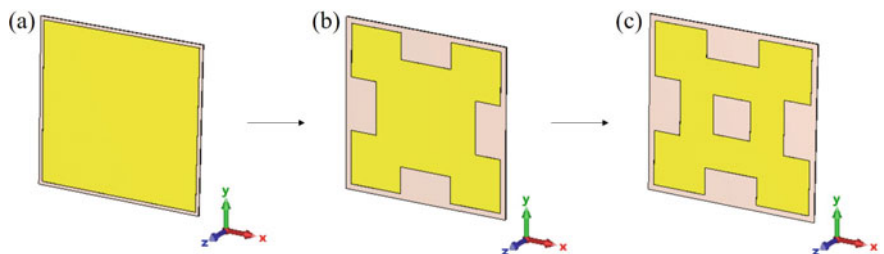


**Fig. 3** Design evolution, **a** conventional square patch, **b** T-square fractal, **c** T-square fractal with slot

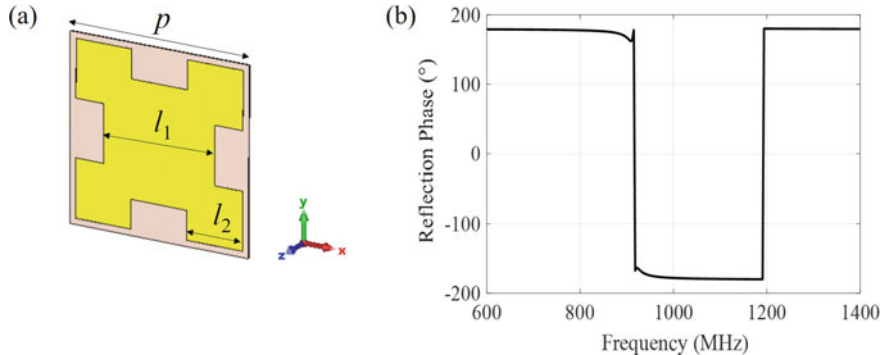


**Fig. 4** **a** AMC based on *T*-square fractal structure, **b** reflection phases as a function of frequency for AMC with  $p = 90$  mm,  $l_1 = 56$  mm, and  $l_2 = 28$  mm

fractal structure consists of a bigger square with side length of  $l_1$  and four smaller squares with side length of  $l_2$ . The smaller squares are placed and centered at each convex corner of the bigger square, with condition  $l_2 = l_1/2$ . The finalized dimensions are  $p = 90$  mm,  $l_1 = 56$  mm, and  $l_2 = 28$  mm. The reflection phase is shown in Fig. 4b. The required size of  $p$  for *T*-square fractal structure ( $p = 90$  mm) is less than that of conventional square-patch structure ( $p = 98$  mm).

In the proposed fractal design,  $l_1$  is the main parameter that affects the overall size of the fractal structure when  $l_2$  is always set as half the value of  $l_1$ . Therefore, the parametric analyses for  $l_1$  are carried out to investigate the effect toward the operation frequency. Figure 5a shows the variation of reflection phases for different  $l_1$  while other parameters related to the substrate and ground structures are kept constant. The result shows that the smaller the size of the fractal structure, the higher the operating frequency. Figure 5b shows the required size of  $l_1$  for the AMC to operate at other frequencies.

### 3.2 T-Square Fractal with Slot

With reference to Fig. 6a, a slot structure is then added to the proposed AMC structure by removing a square with side length,  $s$  from the center of the fractal structure. According to the parametric analyses in Fig. 7, slot structure with larger value of  $s$  will shift the operating frequency of the AMC to lower frequency. This is a good approach to realize miniaturization as unit cell size increment is normally required for an AMC to operate at lower frequency. In this case, the introduction of slot to the fractal structure does not affect the overall unit cell size but manages to lower the operating frequency. The finalized optimized fractal with slot structure is  $p = 76$  mm,  $l_1 = 46$  mm,  $l_2 = 23$  mm, and  $s = 23$  mm, and the reflection phase is shown in Fig. 6b.

**Fig. 5** **a** Variation of reflection phase for different  $l_1$ ; **b** operating frequency as a function of  $l_1$  for AMC based on  $T$ -square fractal structure

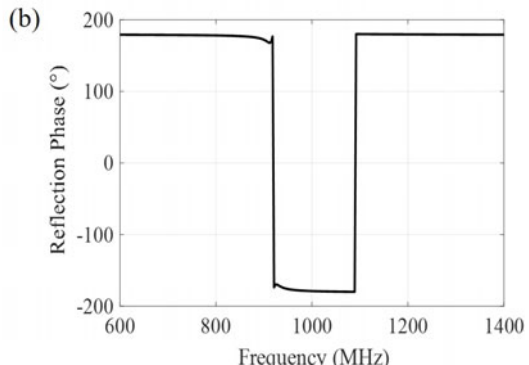
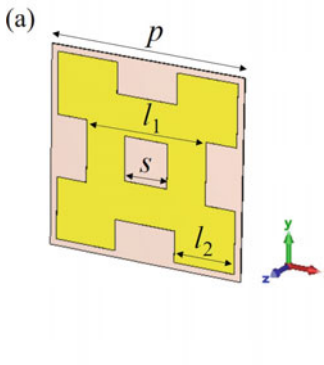
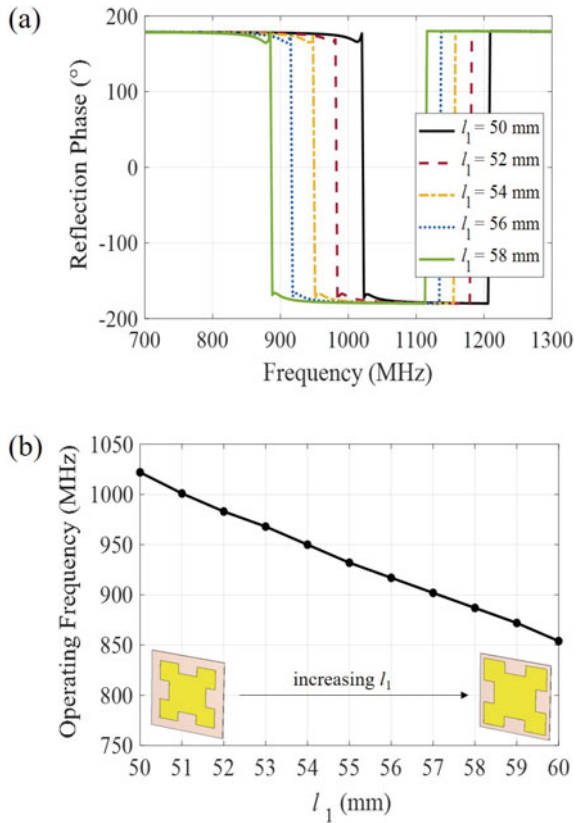
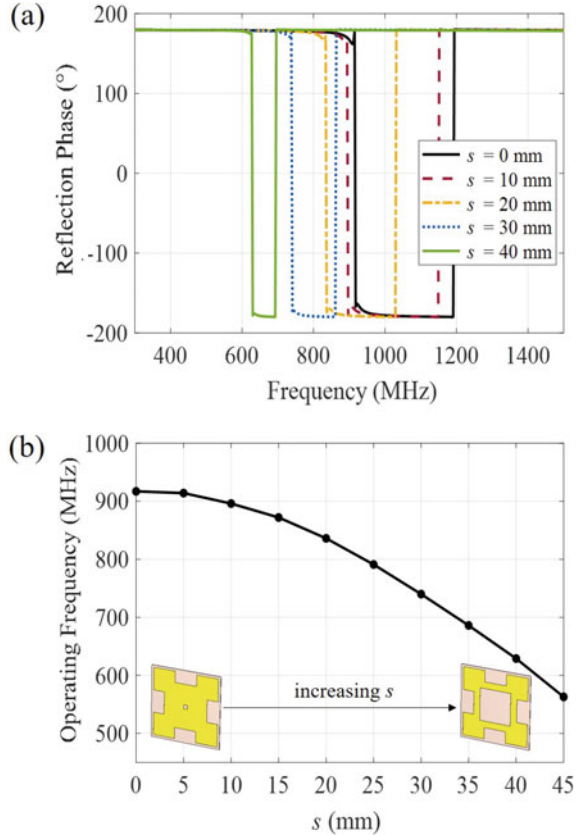


**Fig. 6** **a** AMC based on  $T$ -square fractal structure with slot, **b** reflection phase as a function of frequency for AMC with  $p = 76\text{ mm}$ ,  $l_1 = 46\text{ mm}$ ,  $l_2 = 23\text{ mm}$ , and  $s = 23\text{ mm}$

**Fig. 7** **a** Variation of reflection phase for different  $s$ , **b** operating frequency as a function of  $s$ , for AMC based on  $T$ -square fractal with slot structure



The unit cell size of the proposed fractal-slot-based AMC ( $p = 76$  mm) has been reduced compared to the conventional square-patch AMC ( $p = 98$  mm) and  $T$ -square fractal without slot structure ( $p = 90$  mm). The detailed unit cell size comparison can be referred in Table 1. The fractal-slot-based AMC achieves a unit cell size reduction of 22.4% compared to conventional square-patch-based AMC.

The electric and magnetic field distributions have been simulated at 920 MHz to have a better understanding of the working mechanism of the fractal-slot-based AMC. With reference to the field distribution plots in Fig. 8, it can be seen that the slot structure acts as a significant structure in response to the incoming electromagnetic waves. Based on Fig. 8a, the electric field mainly concentrates vertically around the smaller squares and slot structures. Based on Fig. 8b, the magnetic field concentrates horizontally at the region near the sides of the bigger square and slot structures.

One of the drawbacks of the proposed AMC is narrow operation bandwidth, which is a common limitation for metamaterials. However, the bandwidth can be improved by increasing the thickness of the substrate. The proposed AMC structure is simulated with different thicknesses of the substrate while other geometrical parameters are

**Table 1** Comparison of the state of the art and proposed AMC unit cell

References	Topology	Substrate			$f$ (GHz)	$\lambda$ (mm)	$p$ (mm)
		$t$ (mm)	$\varepsilon_r$	$\tan \delta$			
[11]	Square with slots	0.762	3.0	0.0013	6	50	12 (0.240 $\lambda$ )
[12]	Square	3.0	10.2	0.0035	0.915	328	29.3 (0.089 $\lambda$ )
[13]	Rectangle	1.6	4.4	0.0025	0.98	306	$p_x = 34.5$ (0.113 $\lambda$ ) $p_y = 1.1875$ (0.004 $\lambda$ )
[14]	Meander line	5.08	10.2	0.0023	0.868	345	10 (0.029 $\lambda$ )
[15]	Zig-zag	6.35	3.2	0.003	0.92	326	$p_x = 74.5$ (0.229 $\lambda$ ) $p_y = 16$ (0.049 $\lambda$ )
[16]	Ring and strips	1.52	4.2	0.02	0.915	328	100 (0.305 $\lambda$ )
This work	Square	0.5	2.9	0.01	0.92	326	98 (0.301 $\lambda$ )
	Fractal without slot	0.5	2.9	0.01	0.92	326	90 (0.276 $\lambda$ )
	Fractal with slot	0.5	2.9	0.01	0.92	326	76 (0.233 $\lambda$ )

$t$ —substrate thickness;  $\varepsilon_r$ —substrate dielectric constant;  $\tan \delta$ —loss tangent of substrate;  $f$ —zero-degree ( $0^\circ$ ) phase operating frequency;  $\lambda$ —free-space wavelength at  $f$ ;  $p$ —unit cell size of AMC

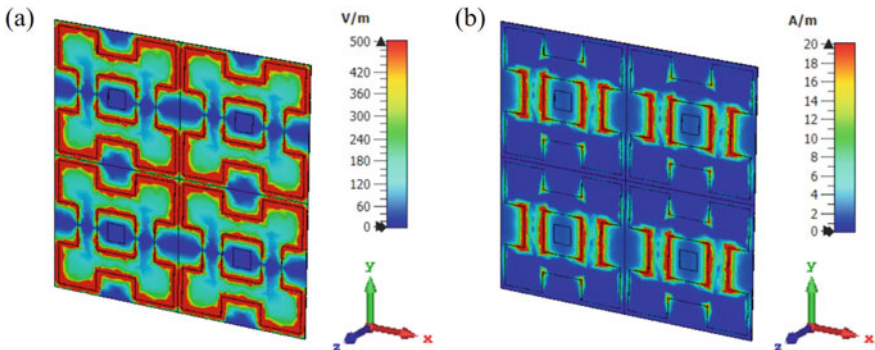


**Fig. 8** **a** Electric field distribution plot, **b** Magnetic field distribution plot, for  $T$ -square fractal AMC with slot, at operating frequency of 920 MHz

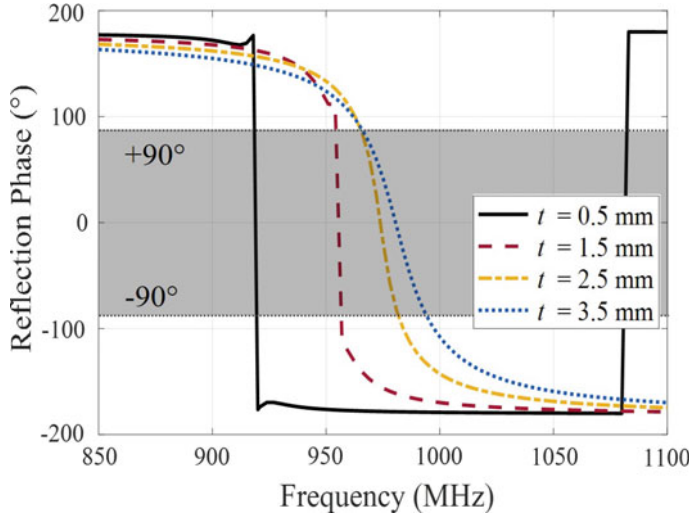


**Fig. 9** Variation of reflection phase for different thickness,  $t$  of substrate. The gray area indicates the operating region of the AMC within the reflection phases of  $+90^\circ$  to  $-90^\circ$

kept constant. The results as shown in Fig. 9 show that the larger the thickness of the substrate, the larger the bandwidth. The bandwidth of the AMC is 2 MHz, 18 MHz, and 30 MHz for 1.5 mm, 2.5 mm, and 3.5 mm, respectively.

The thickness of the substrate is mainly affected by the substrate material, operation frequency, and desired bandwidth. The substrate material used for the proposed AMC is polycarbonate, which is durable and not easily fractured when bent due to its high mechanical and tensile strength. Therefore, the minimum thickness of the substrate for the proposed AMC is suggested to be 0.5 mm for narrow-band operation at 920 MHz, considering the commercially available substrate thickness. Moreover, the AMC might deform if a lower thickness is used in wearable RFID applications. Besides the aforementioned mechanical concern, the desired operation bandwidth is a significant factor when selecting the appropriate thickness for RFID applications. It is suggested to have a thickness that is just adequate to cover the entire desired operation bandwidth. This is because excessive thickness would lead to more reflection signal loss due to dielectric loss in the substrate and also increase the weight, which limits its wearable applications.

Based on Table 1, the proposed AMC is compared with some AMCs in recent published works. The unit cell size  $p$  of the proposed AMC is comparable with some of the AMCs. However, some of the state-of-the-art AMCs have smaller  $p$  due to their substrate having high dielectric constant,  $\epsilon_r$ . This is because higher  $\epsilon_r$  will shift the resonance frequency,  $f$ , to lower frequency [11]. The proposed AMC uses thinner flexible substrate and simpler design topology.

## 4 Conclusion

This paper proposed an AMC based on  $T$ -square fractal with slot structure. The fractal-based structure achieves the operating frequency of 920 MHz with smaller unit cell size compared to the conventional square-patch-based AMC structure. The parametric analyses show that increasing the length of the slot would shift the operating frequency to lower frequency. This is a useful strategy to realize miniaturization by introducing the slot structure to reduce the overall unit cell size of the AMC. Moreover, the increment of substrate thickness can improve the operation bandwidth. The proposed AMC is compact, simple, and flexible. It is envisaged for the AMC to be applied as an in-phase reflector in wearable RFID devices for communication range improvement.

**Acknowledgements** The authors would like to acknowledge the Ministry of Higher Education, Universiti Teknologi Malaysia, and Research Management Centre for the support of this work under the UTM Encouragement Research Grant with grant number Q.J130000.3851.20J74 and Fundamental Research Grant Scheme with grant number R.J130000.7823.5F678.

## References

1. Ripin, N., Lim, E.H., Bong, F.L., Chung, B.K.: Miniature folded dipolar patch with embedded AMC for metal mountable tag design. *IEEE Trans. Antennas Propag.* **68**(5), 3525–3533 (2020)
2. Belabbas, K., Khedrouche, D., Hocini, A.: Artificial magnetic conductor-based millimeter wave microstrip patch antenna for gain enhancement. *J. Telecommun. Inf. Technol.* **1**, 56–63 (2021)
3. Hazarika, B., Basu, B., Nandi, A.: An artificial magnetic conductor-backed monopole antenna to obtain high gain, conformability, and lower specific absorption rate for WBAN applications. *Int. J. RF Microw. Comput. Aided Eng.* **30**(12), e22441 (2020)
4. Dewan, R., Rahim, M.K.A., Hamid, M.R., Yusoff, M.F.M., Samsuri, N.A., Murad, N.A., Kamardin, K.: Artificial magnetic conductor for various antenna applications: an overview. *Int. J. RF Microw. Comput. Aided Eng.* **27**(6), e21105 (2017)
5. Shahzad, M.A., Paracha, K.N., Naseer, S., Ahmad, S., Malik, M., Farhan, M., Ghaffar, A., Hussien, M., Sharif, A.B.: An artificial magnetic conductor-backed compact wearable antenna for smart watch IoT applications. *Electronics* **10**(23), 2908 (2021)
6. Hazarika, B., Basu, B., Nandi, A.: A wideband, compact, high gain, low-profile, monopole antenna using wideband artificial magnetic conductor for off-body communications. *Int. J. Microw. Wirel. Technol.* **14**(2), 194–203 (2022)
7. Ramos, W.T., Mesquita, R.C., Silva, E.J.: Design of the artificial magnetic conductors with meander line elements: reduction in the first and second resonant frequencies. *Mater. Res. Exp.* **4**(7), 075801 (2017)
8. Ashyap, A.Y., Dahlan, S.H., Abidin, Z.Z., Kamarudin, M.R., Majid, H.A., Alduais, N.A.M., Hashim Dahri, M., Alhandi, S.A.: C-shaped antenna based artificial magnetic conductor structure for wearable IoT healthcare devices. *Wireless Netw.* **27**(7), 4967–4985 (2021)
9. Khan, S., Ali, H., Khalily, M., Shah, S.U.A., Kazim, J.U.R., Ali, H., Tanougast, C.: Miniaturization of dielectric resonator antenna by using artificial magnetic conductor surface. *IEEE Access* **8**, 68548–68558 (2020)
10. Alemaryeen, A., Noghanian, S.: On-body low-profile textile antenna with artificial magnetic conductor. *IEEE Trans. Antennas Propag.* **67**(6), 3649–3656 (2019)

11. De Cos, M.E., Las-Heras, F.: Novel flexible artificial magnetic conductor. *Int. J. Antennas Propag.* **2012**, 1–7 (2012)
12. Xu, R., Liu, J., Wei, K., Hu, W., Xing, Z.J., Li, J.Y., Gao, S.S.: Dual-band circularly polarized antenna with two pairs of crossed-dipoles for RFID reader. *IEEE Trans. Antennas Propag.* **69**(12), 8194–8203 (2021)
13. Bansal, A., Sharma, S., Khanna, R.: Platform tolerant dual-band UHF-RFID tag antenna with enhanced read range using artificial magnetic conductor structures. *Int. J. RF Microw. Comput. Aided Eng.* **30**(2), e22065 (2020)
14. Elzuwawi, H.H., Tahseen, M.M., Elzwawi, G.H., Denidni, T.A.: A new RFID monopole antenna using a compact AMC structure. *Microw. Opt. Technol. Lett.* **61**(7), 1835–1840 (2019)
15. Rahim, M.K.A., Hamid, M.R., Samsuri, N.A., Murad, N.A., Zubir, F., Ayop, O., Yusof, M.F.M., Majid, H.A.: Antenna with artificial magnetic conductor for wireless application. In: 2019 IEEE Asia-Pacific Conference on Applied Electromagnetics (APACE), pp. 1–5. IEEE (2019)
16. Sarkar, S., Gupta, B.: A dual-band circularly polarized antenna with a dual-band AMC reflector for RFID readers. *IEEE Antennas Wirel. Propag. Lett.* **19**(5), 796–800 (2020)

# Effect of Nacelle Shape on the Flow Fields of Upwind and Downwind Wind Turbines



Jay Prakash Goit and Takatsugu Kameda

**Abstract** This work compares aerodynamic loads, power outputs and wake fields of upwind and downwind wind turbines. To that end, wind tunnel experiments are performed with model wind turbines with cylindrical and ellipsoidal nacelles, to investigate whether the nacelle shape changes the performance or flow characteristics of the turbine configurations. The thrust and the power coefficients of both upwind and downwind turbines show similar trends with no significant difference between peak power coefficients of the two configurations. For the laminar and uniform inflow conditions, wind speed is slightly higher around the rotor centre in the wake of the downwind turbine. However, the effect of nacelle shape to the wake field is not significant. Turbulence intensity profiles for upwind and downwind configurations do not show significant differences and peak values of turbulence intensities can be observed around the rotor tip region. Differences between turbulence profiles for experiments with cylindrical and ellipsoidal nacelles are negligible. The study shows that downwind turbines with both types of nacelles showed comparable performance and wake characteristics to their upwind counterparts. Therefore, they can be scaled up with flexible and cheaper blades, without having to compromise in terms of turbine performance.

**Keywords** Upwind wind turbine · Downwind wind turbine · Wind turbine wake

## 1 Introduction

Utility-scale wind turbines have increased significantly in size and some of the largest turbines have rotor diameters of more than 200 m and rated power higher than 10 MW. In addition to the obvious advantage of increased power output, such turbines also have potential to reduce the cost of wind energy, since fewer units are required to reach the nameplate capacity of the wind farm thus reducing the development as well as operation and maintenance costs. Such utility-scale wind turbines are predominantly

---

J. P. Goit (✉) · T. Kameda

Department of Mechanical Engineering, Kindai University, Hiroshima 739-2116, Japan  
e-mail: [jay.goit@hiro.kindai.ac.jp](mailto:jay.goit@hiro.kindai.ac.jp)

horizontal axis, three bladed and have rotors installed upwind of towers, i.e., upwind configuration. However, current upwind configurations pose an important constraint in terms of scaling up the designs. In order to avoid tower strike, blades of large upwind turbines have to be designed with higher stiffness, thus increasing the cost of blade manufacturing. Downwind turbines, which have rotors installed downwind of towers, can potentially have cheaper flexible blades since the axial wind loads will bend them away from the tower. Consequently, downwind rotors can have smaller tower clearance, and thus, they do not require larger tilt and cone angles. Based on these factors, downwind configurations can be expected to operate close to optimum design condition [1].

Two additional advantages of downwind turbines related to their aerodynamic characteristics are often discussed in the literature. Nacelles, which are upstream from the rotor in downwind configurations, deflect the wind towards the outer region [2]. Since wind turbine blades are designed such that the outer region contributes more to the power production, nacelle-induced flow deflection is expected to improve the output in downwind configuration. Another advantage of downwind turbines is that they have tendency to align with the incoming wind, thus reducing the yaw misalignment. However, downwind configuration experiences strong tower shadow effect resulting from the wind speed deficit in the wake of towers [3]. As a result, blades of downwind turbines experience cyclic impulsive loading and induce vibration to the turbine structure at blade-passing frequency (BP). Tower shadow can also become the source of higher power fluctuation [4].

Even though the advantages and disadvantages of downwind turbines are stated in the literatures, direct comparisons between the two configurations in terms of power output and flow fields have not received sufficient attention. The aim of this work is to compare aerodynamic loads, power outputs and wake fields of upwind and downwind wind turbines. To that end, we perform wind tunnel experiments for two different types of nacelles—cylindrical and ellipsoidal—and investigate whether nacelle-induced blockage and flow deflection really improve the performance of downwind turbines.

## 2 Measurement Setup

The model wind turbine (KDWT25) used in the experiments has both rotor diameter ( $D$ ) and hub height ( $y_h$ ) of 0.25 m. The rotor of KDWT25 was optimized using BEMTurbine [5], an in-house open-source tool. The turbine was designed to perform optimally at the tip speed ratio of 4. Tip speed ratio is given by

$$\lambda = \frac{\Omega D}{2U}, \quad (1)$$

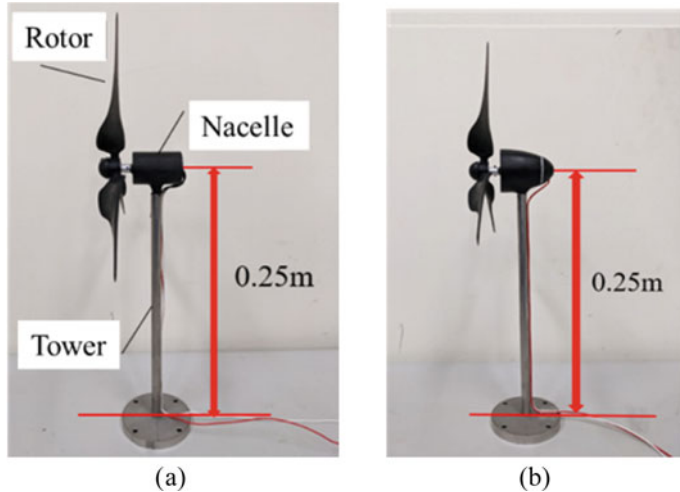


**Fig. 1** Model wind turbines with **a** cylindrical, and **b** ellipsoidal nacelles

where  $\Omega$  is the angular velocity of the rotor,  $D$  is the rotor diameter and  $U$  is inflow velocity. It should be noted that utility-scale turbines and reference research turbines (e.g., NREL-5 MW, DTU 10 MW, etc.) are designed for the optimum tip speed ratio of around 7. Therefore, to obtain aerodynamic characteristics similar to those turbines, model turbines should also have  $\lambda$  value around 7. However, this will result in very high rotational speed, which in turn will increase the friction losses from the moving components inside the generator. For example, at inflow wind speed of 5 m/s and  $\lambda = 7$ , model turbine used in this study will rotate at the speed of 2600 rpm. It is not practical to operate a turbine at such high rotational speeds and thus model turbine is designed at the lower optimum tip speed ratio of 4. Readers can refer to Goit [6] for the description of KDWT25 designs and BEMTurbine. Figure 1 shows the model wind turbines with cylindrical and ellipsoidal nacelles used in this study.

All measurements were conducted in a closed-circuit type wind tunnel at the School of Engineering, Kindai University. The tunnel test section has a square cross-section of  $0.59 \times 0.59 \text{ m}^2$  and the streamwise length of 1.38 m. The blockage ratio which is defined as  $\beta = A_t / A_{WT}$  ( $A_t$ : rotor area,  $A_{WT}$ : wind tunnel cross-section) is 14%. Although  $\beta$  is slightly higher than what is suggested for wind tunnel experiments, the effect of blockage is not discussed in this work. Figure 2 shows the schematic of the test section. The average free stream velocity ( $u_0$ ) was set to 5 m/s. Both free stream and turbine wake wind speeds were measured using hot wire anemometry with  $I$ -type hot wire probe (Kanomax 0248R-T5). Calibration of hot wire anemometers was done using pitot tube and differential manometer (Okano Seisakusho DMP-202N12). At each measurement point, wind speed data was collected for the period of 10 s and at the sampling rate of 5 kHz. Optical tachometer was used to measure rotational speed. Rotational speed and torque of the

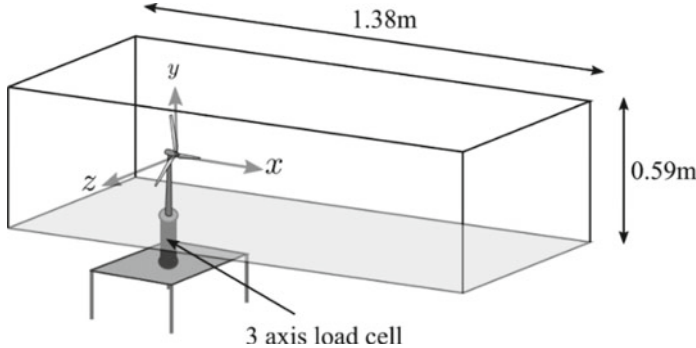


**Fig. 2** Schematic of the wind tunnel test section

turbines were controlled using variable resistor. Power outputs were computed from the voltage and current readings on the multimeters.

### 3 Results and Discussions

Experiments were performed at the inflow wind speed of 5 m/s, and average inflow turbulence intensity was 0.72%. Note that large utility-scale wind turbines almost always experience atmospheric turbulence. For the height between 100 and 200 m, which is the hub-height range of large wind turbines, turbulence intensity is around 5% at offshore sites, while it can be higher than 10% at onshore sites. However, for the accurate comparison of upwind and downwind turbines, experiments should be performed in ideal condition of uniform and laminar inflow conditions as done in this study.

First of all, the performance of the two turbine configurations is compared in Fig. 3. Its shows thrust coefficient ( $C_T$ ) and power coefficient ( $C_P$ ) as a function of tip speed ratio ( $\lambda$ ). Here,  $C_T$  and  $C_P$  are defined as

$$C_T = \frac{T}{\frac{1}{2}\rho U^2 A_t} \quad (2)$$

$$C_P = \frac{P}{\frac{1}{2}\rho U^3 A_t}, \quad (3)$$

where  $T$  is the axial thrust force measured using a load cell,  $P$  is aerodynamic power of rotor,  $\rho$  is air density and  $A_t = \pi/4D^2$  is the rotor area. Thrust coefficients for the two configurations almost overlap for the tip speed ratio range considered in this study.  $C_T$  values at the design tip speed ratio, i.e.,  $\lambda = 4$ , are 0.78 for upwind and 0.76 for the downwind turbine, indicating slightly higher thrust coefficient for the upwind configuration. The values are comparable to those of actual utility-scale

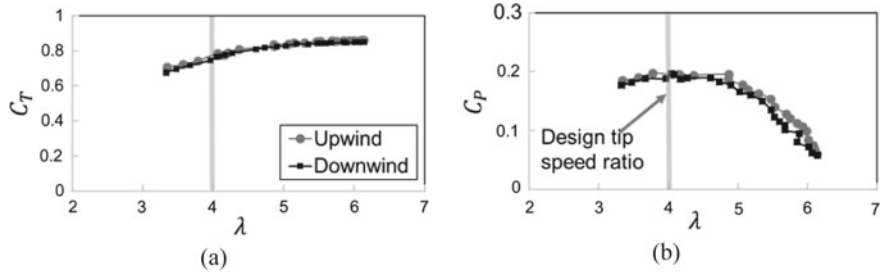


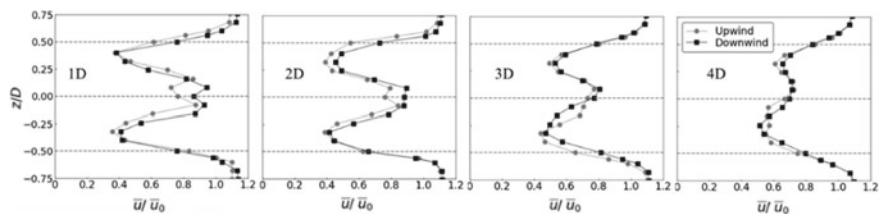
**Fig. 3** Wind turbine performance as a function of tip speed ratio ( $\lambda$ ), **a** thrust coefficient, **b** power coefficient

wind turbines whose  $C_T$  values are in the range 0.7–0.8. Power coefficients also show similar trend for the two turbine configurations. The peak  $C_P$  values for both configurations are around the design tip speed ratio. This peak  $C_P$  for upwind turbine is 0.195 while that of downwind turbine is 0.196, later being slightly higher, but the difference is not significant.

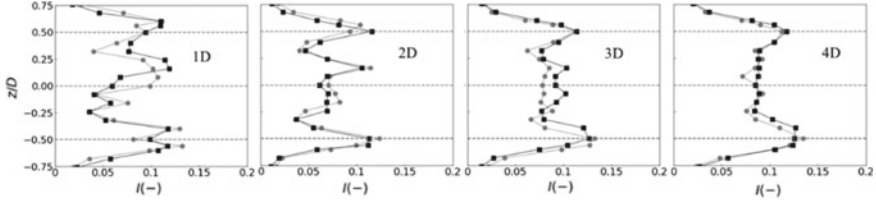
As discussed earlier, nacelle of the downwind configuration should induce blockage and deflect the incoming wind radially outward. Since the airfoils used in the outer region of the blades are more efficient, nacelle-induced blockage may be responsible for higher efficiency of the downwind turbine. However, it can be observed that the difference between  $C_P$  values of the two configurations is not very significant. Future work should include more detailed experiments to discretely quantify the difference in the performance of upwind and downwind turbines.

Figure 4 through 7 compares mean velocity and turbulence intensity profiles in the wake of the upwind and downwind turbines. Figures 4 and 5 show profiles for the cylindrical nacelle, while Figs. 6 and 7 show the profiles for the ellipsoidal nacelle. Measurements were conducted along the spanwise direction at the hub-height level, i.e.,  $y_h = 0.25$  m. Spanwise interval of measurement points was set to 20 mm. Furthermore, data was collected in the near wake region, i.e., from 1D through 4D downstream from the rotor position.

Both upwind and downwind configurations have similar velocity profiles with the largest velocity drop occurring close to the outer region of the rotors. Gradual



**Fig. 4** Comparison of mean streamwise velocity profiles at the hub-height plane in the wake of the upwind and downwind turbines with cylindrical nacelle. Dashed-horizonal lines indicate position of centre and edges of the rotor



**Fig. 5** Comparison of turbulence intensity profiles at the hub-height plane in the wake of the upwind and downwind turbines with cylindrical nacelle

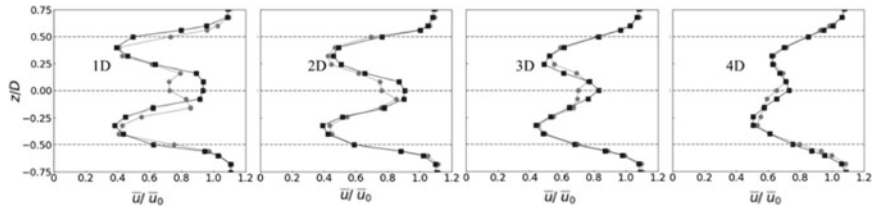


**Fig. 6** Comparison of mean streamwise velocity profiles at the hub-height plane in the wake of the upwind and downwind turbines with ellipsoidal nacelle

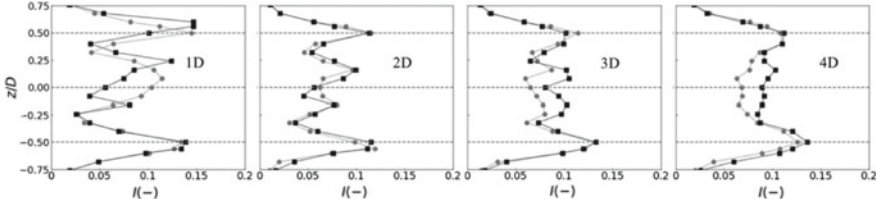


**Fig. 7** Comparison of turbulence intensity profiles at the hub-height plane in the wake of the upwind and downwind turbines with ellipsoidal nacelle

increase in velocity magnitudes can be observed in the nacelle region. Dual peaks of lower wind speeds are observed at all four streamwise positions, though the shape is gradually distorted downstream. The mean wind speed is higher in the wake of downstream turbine at  $x = 1D$  and  $2D$ , around the rotor centre. No conspicuous difference between the wake for turbines with cylindrical and ellipsoidal nacelle is observed. In the experiments with the ellipsoidal nacelle, wind speed at the rotor centre is higher for downwind turbine at  $1D$ , compared to the profile of upwind turbine (with ellipsoidal nacelle) as well as the profile of downwind turbine with cylindrical nacelle. Ellipsoidal nacelle with its aerodynamic shape was expected to deflect flow towards the outer region of the rotor for downstream turbine. However, this was not particularly observed in the current experiments. We also compared the power outputs of turbines with ellipsoidal nacelle (not shown here), but no big difference between the two configurations was observed. This shows that both upwind and downwind

turbines will display comparable aerodynamic performance. And, because the size of nacelle is small compared to the rotor size, improved performance with flow deflection towards the outer region of the rotor expected with ellipsoidal nacelle in the downwind configuration is negligible.

Turbulence intensity profiles in Figs. 5 and 7 for upwind and downwind configurations do not show significant differences. Peak values of turbulence intensities can be observed at the rotor tip. This can probably be attributed to the tip vortices. The study shows that with laminar and uniform inflow conditions, added turbulence intensities due to wind turbines can be between 10 and 15% at the rotor tip. The largest turbulence intensity values were observed at 1D for all cases, while for the remaining three downstream positions turbulence level did not reduce significantly. This may be due to the fact that wind turbine wakes are able to sustain its characteristics for longer downstream distance in the laminar or low turbulent ambient flow. Difference between turbulence profiles for experiments with cylindrical and ellipsoidal nacelles is negligible.

Even though downwind configuration or ellipsoidal nacelle does not improve the performance of turbine in terms of power output, they do not have negative impact on the efficiency either. One important advantage of downwind configuration is that it can be scaled up and can still have comparatively flexible blades. This will help to maintain the lower cost of extremely large downwind turbines. If the cheaper turbines can be installed without having to compromise in terms of turbine performance, then this would reduce the overall cost of wind energy. Furthermore, comparable wake characteristics of upwind and downwind configuration means both turbines may perform in a similar manner when installed in wind farms. However, since the current study only conducted experiments with a single turbine, performances and aerodynamics of upwind and downwind turbines cannot be predicted in the context of wind farms. Detail experiments or simulations of wind farm and boundary layer interactions with upwind and downwind turbines are required to compare the dynamics of two configurations when installed in wind farms.

## 4 Conclusions

In this study, we have compared the aerodynamic characteristics and power performances of upwind and downwind wind turbines. To that end, we performed wind tunnel experiments with cylindrical and ellipsoidal nacelles, to investigate whether the nacelle shape changes the performance or flow characteristics of the two turbine configurations. The findings of the study can be summarized as follows:

- (1) The thrust and the power coefficients of both upwind and downwind turbines showed similar trend. The difference between peak power coefficients of the two configurations was not significant.

- (2) For the laminar and uniform inflow conditions, wind speed was slightly higher around the rotor centre in the wake of downwind turbine. However, the effect of nacelle shape to the wake field was not significant.
- (3) Turbulence intensity profiles for upwind and downwind configurations did not show significant differences and peak values of turbulence intensities could be observed around the rotor tip region. Furthermore, for downstream positions from 2D through 4D, turbulence level did not reduce significantly. Difference between turbulence profiles for experiments with cylindrical and ellipsoidal nacelles was negligible.

**Acknowledgements** The authors acknowledge Takahashi Industrial and Economic Research Foundation for supporting this work. The authors would like to thank Mr. Satoshi Goi of Kindai University for his assistance during the experiments. The authors are extremely grateful to Mr. Koji Umenishi of Kindai University for helping with the manufacturing of tower, base, rotor shaft, and several other components necessary for the experiments.

## References

1. Larwood, S.M., Chow, R.: Comparison of upwind and downwind operation of the NREL phase VI experiment. *J. Phys. Conf. Ser.* **753**(2) (2016)
2. Bortolotti, P., Kapila, A., Bottasso, C.L.: Comparison between upwind and downwind designs of a 10 MW wind turbine rotor. *Wind Energy Sci.* **4**, 115–125 (2019)
3. Yoshida, S.: Combined blade-element momentum—lifting line model for variable loads on downwind turbine towers. *Energies* **11**, 2521 (2018)
4. Wang, Z., Tian, W., Hu, H.: A Comparative study on the aeromechanic performances of upwind and downwind horizontal-axis wind turbines. *Energy Convers. Manag.* **163**(February), 100–110 (2018)
5. BEMTurbine. [Online]. Available: <https://github.com/goitjay/BEMTurbine>
6. Goit, J.P.: A method for the design of a scaled wind turbine for wind tunnel experiments. *Kindai Univ. Fundam. Technol. Next Gener. Res. Inst. Annu. Rep.* **11**(April), 75–79 (2020)

# Automated Transformer Health Prediction: Evaluation of Complexity and Linearity of Models for Prediction



Andrea Wong Saen Er, W. K. Wong<sup>✉</sup>, Filbert H. Juwono<sup>✉</sup>, I. M. Chew<sup>✉</sup>, Saaveethya Sivakumar<sup>✉</sup>, and Arul Paruvachi Gurusamy<sup>✉</sup>

**Abstract** Transformer failure is a significant concern in electrical power systems as it can result in costly damages and endanger human lives. Early detection of defects can minimize damage before it becomes dangerous to work with. Predicting transformer health is essential for ensuring continuous quality of service to consumers through a predictive maintenance approach. Maintenance records of transformers often include temperature, oil quality, and vibration. The challenge lies in developing models that enable the prediction of the transformer health index (HI) from these maintenance records. Several research studies have formally reported various implementations of machine learning algorithms to predict transformer health index (HI). In this research report, authors introduce a machine learning algorithm and classification on transformer health detection approach using a support vector machine (SVM) and an artificial neural network (ANN). The direction of this study is to evaluate the complexity of this prediction domain using both machine learning models. Both SVM/ANN are commonly deployed machine learning models in most application domains. The authors investigate this problem from both regression and classification perspectives, implementing various kernel functions associated with the SVM such as radial basis function (RBF) and artificial neural network (ANN). Despite the good separation between classes and good regression on the training set using more nonlinear models, it is observed that overfitting occurs when evaluating

---

A. W. S. Er (✉) · W. K. Wong · I. M. Chew · S. Sivakumar  
Sensor Research Group, Curtin University Malaysia, Miri, Sarawak, Malaysia  
e-mail: [700037223@student.curtin.edu.my](mailto:700037223@student.curtin.edu.my)

W. K. Wong  
e-mail: [weikit.w@curtin.edu.my](mailto:weikit.w@curtin.edu.my)

I. M. Chew  
e-mail: [chewim@curtin.edu.my](mailto:chewim@curtin.edu.my)

F. H. Juwono  
Department of Electrical and Electronic Engineering, Xi'an Jiaotong-Liverpool University,  
Suzhou, Jiangsu, China  
e-mail: [Filbert.Juwono@xjtlu.edu.cn](mailto:Filbert.Juwono@xjtlu.edu.cn)

A. P. Gurusamy  
Connected Intelligence Research Group, University of Southampton Malaysia, Johor, Malaysia  
e-mail: [a.p.gurusamy@soton.ac.uk](mailto:a.p.gurusamy@soton.ac.uk)

on independent test sets for both regression and classification (especially in cases involving SVM). The authors found that more nonlinear kernels (SVM) yielded better performance thereby indicating that future research may benefit from more linear models. The study postulates that machine learning models should be chosen based on the general suitability, data linearity, and complexity to achieve accurate predictions of transformer health index (HI). The results of this study may provide insights for future research in developing models that can accurately predict transformer health.

**Keywords** Support vector machine (SVM) · Radial basis function (RBF) · Artificial neural network (ANN) · Classification · Transformer health index (HI)

## 1 Introduction

Predicting transformer health using machine learning is a useful application in the field of electrical engineering. In general, transformers play a crucial role in electrical power systems, and their failure can result in significant downtime and costly repairs. By predicting the health of transformers, maintenance can be performed proactively, preventing failure and reducing downtime [12]. However, transformer is prone to many technical failures if one of its assembly parts is a defect or not maintained well. Therefore, specific maintenance schedule is planned to have lower risk of transformer failure. With automation, transformer health can be assessed easily to detect any defects at early stages. Automated transformer health classification could contribute to the smart grid technology, hence reducing long-term cost and investment in new electrical equipment, specifically transformers. There are several approaches to predict transformer health using machine learning. One approach is to use historical data on transformer performance and failure, along with data on environmental factors such as temperature and humidity, to train a model to predict future failures. Another approach is to use sensors installed on the transformer to collect real-time data on its performance and use that data to train a model to predict future failures. Some of the factors that can be used to predict transformer health using machine learning include temperature, maintenance oil quality, humidity, and partial discharge.

It was observed that most of the research work relating to this research domain is executed from the regression point of view. As most of the existing work implements some form of machine learning and unbalanced dataset, this may be less ideal as unbalanced dataset is known to skew recognition toward majority dataset. As such, this research fills in the gap of investigating this research area from the perspective of classification. Additionally, this research report aims to evaluate the effectiveness of different kernel functions for gauge linearity in transformer health classification using maintenance features. We investigate its complexity of the classification process using support vector machine (SVM) and compare the accuracy of different kernel functions. Similarly, ANN will also be deployed to evaluate the

linearity and complexity of model required for classification. Changing the kernel types and processing layer gives an indication of the complexity /linearity required by the machine learning model. The complexity and linearity would be useful to guide future researchers in this domain application. By convention, the least linear and least complex configuration of machine learning models are implemented in line with the “Occam’s razor” principle in computational machine learning implementation. The principle states that the least complex model should selected in the case where both “complex” and “simpler” models yielded similar results ([10]). The public domain dataset used for this research was documented in [11] and available at [3]. The power transformer health condition is determined by various conditions such as hydrogen, oxygen, nitrogen, methane, CO, CO<sub>2</sub>, ethylene, ethane, acetylene, dibenzyl disulfide (DBDS), power factor, dielectric rigidity, and water content. These are common maintenance features that are used to predict health index (HI) which ranges from 0 to 100%.

## 2 Literature Review

In this section, some of the relevant literature reviews will be investigated to establish the existing findings in this area.

Among the various methods proposed, dissolved gas has often been used for predicting health index (HI). In [12], it was presented that RF model provides the best performance in predicting power transformer health index with accuracy of 97.3%. However, RF model causes overfitted model. The dissolved gas analysis (DGA), oil quality, and paper condition are used in the suggested HI technique to evaluate the power transformer insulation system. In this context, the proposed AI models are established using data gathered from 504, 150-kV transformers. authors study seven artificial intelligence (AI) algorithms: k-nearest neighbor (kNN), support vector machine (SVM), random forest (RF), naive Bayes (NB), artificial neural network (ANN), adaptive boosting (AdaBoost), and decision tree. The scoring-weighting-based HI approach is used as the benchmark for comparing the performance of the proposed AI-based HI models. Findings indicate that the random forest model, with an accuracy of 97.3%, performs the best in forecasting power transformer HI.

Dissolved gas analysis (DGA) is commonly used technique to diagnose and decide maintenance of a transformer. In [1], data-driven DGA classification approaches were implemented. In light of this, this research provides a novel DGA-based health index formulation that integrates data-driven models and subject-matter expertise. The proposed method’s effectiveness in classifying transformer faults and spotting emerging abnormal patterns is supported by the results. DGA test is able to trace various failures such as arcing, partial discharge (PD), overheating, aging of oil caused by thermal condition as reported in [9].

Similarly, in [5], a new model is proposed to compute the power transformer health index (PTHI) using data from 631 samples in Malaysia and 730 samples from the Gulf region. The proposed model adopts various intelligent classification methods such

as decision tree, support vector machine, k-nearest neighbor, and ensemble methods to predict the PTHI state. The model is built in two stages with feature reductions that minimize testing time, effort, and costs. The effectiveness of the adopted feature reduction technique is demonstrated by the reduced-feature models. The proposed model is validated against uncertain noise in features of up to  $\pm 20\%$  and shows superior classification accuracy compared to recent work.

The authors in [7] propose a method for estimating the apparent age of power transformers based on a probabilistic health index. Unlike the traditional method, the probabilistic health index is calculated using a Bayesian belief network that combines various types of monitoring data. This index is then used to estimate the apparent age of the transformer. The apparent age reflects the overall health of the transformer and allows for easy comparison and sorting of transformer fleets. Power utilities can use the estimated apparent age to prioritize transformers and plan replacements. The method is validated through case studies with different transformers and has proven to be advantageous over traditional methods.

With regard to machine learning models, the literature survey does not seem to show a dominant model that shows much better results. Various models including  $K_{th}$  nearest neighbor (KNN), artificial neural network (ANN), support vector machines (SVM) were among those commonly implemented. In [13], the authors implemented support vector machine classifier show better results around 81.4% and multilayer artificial neural network (MLANN) with prediction result accuracy of about 76% .

According to [2], the authors use machine learning (ML) to predict the insulation health of medium voltage distribution transformers based on oil test results. The approach was validated using two databases of over 1000 transformer oil samples from different utility companies in the Gulf region. The study was conducted in two steps: the first step involved classifying the transformer health condition using several pattern recognition tools based on the full set of input test features. In the second step, the same pattern recognition tools were used for a reduced number of test features, and a previously developed model was used to reduce the number of tests required for health index calculations. The study found that reducing the number of tests did not affect the accuracy of the ML prediction models, which can reduce the cost of transformer asset management. The general regression neural network (GRNN) developed was reported with a 83% when predicting the transformer health.

In [6], a fuzzy logic-based HI transformer prediction was implemented. Diagnostic tests performed on the transformer insulation are typically used to directly evaluate the health of the transformer. The results of these tests are then utilized to assess the transformer's condition and determine how much longer it has to live. The health index displays the transformer's insulation degradation by utilizing several transformer parameters. Evaluation of the transformer's health index is highly challenging since these transformer factors frequently function simultaneously. In this study, many factors are used to build fuzzy submodels (such as DGA, oil dielectric strength, loading information, insulation resistance, and CDF) for the evaluation of transformer critical circumstances.

In Mengrong [8], transformer health prediction by implementing dynamic analysis on the temperature alone. Only the transformer's present temperature and historical

temperature trend can be accurately reflected by the conventional subway condition monitoring system. By relying on the temperature threshold, the equipment's current operational state can be assessed. However, the technology is unable to foresee how the transformer's temperature would fluctuate in the future. Transformer winding temperature is a crucial indicator of the equipment's operational status. A dependable foundation for the creation of an operation and maintenance plan for operation and maintenance employees can be provided by accurate winding temperature forecast, which can also help in assessing the operational state of equipment. Many variables, including operational power and ambient temperature, which frequently exhibit nonlinear fluctuations, have an impact on the winding temperature.

Similarly in Chantola [4], authors have also implemented a form of fuzzy logic prediction for prediction health index. Diagnostic tests carried out in the transformer's insulation are used to determine the general state of a transformer. The findings of these tests are then utilized to estimate remaining life and evaluate health in a timely manner. Using various transformer parameters, this illustrates insulation degradation in a transformer. It would be challenging to evaluate the transformer health index because most of these parameters work simultaneously. This study uses a variety of parameters, including DGA, SFRA, water content, IFT, UV spectrophotometry, and transformer hot spot temperature, to build fuzzy submodels for evaluating the various critical states of the transformer.

From the existing literature, it was observed that various researchers have attempted to implement various machine learning models for predicting the health status of the transformer. Most notably, authors have resorted to some form of maintenance record for prediction. However, it is also notable that none of the existing research has attempted to investigate the linearity of model required to classify and predict the health of the transformer and perform an "apple to apple" comparison. In view of this apparent gap, it is therefore an established objective to perform the study in the spoken direction. The research question arises: What level of model linearity will be required for adequate regression/classification to predict health index (HI)? Considering the full feature set, how does the model perform generalize to independent dataset. These questions are important to give more insights that may affect the direction of future research. For this research report, two baseline machine learning models will be deployed to answer the research question. This will be achieved by varying the kernels of SVM and the processing layer for ANN.

### 3 Methodology

From the literature conducted, most predictions of transformer health rely on the maintenance record of transformer. Alternatively, some have implemented dissolved gas content for prediction purposes. The dissolved gasses in transformer oil allow for indepth diagnostics of transformer condition and subsequently the HI. As discussed in the previous section, the objective of the research is to evaluate the model complexity required to predict the health of transformer. In particular, this research will focus

**Table 1** Feature list

Index	Features parameter	Unit
1	Hydrogen	H
2	Oxygen	O <sub>2</sub>
3	Nitrogen	N
4	Methane	CH <sub>4</sub>
5	Carbon monoxide	CO
6	Carbon dioxide	CO <sub>2</sub>
7	Ethylene	C <sub>2</sub> H <sub>4</sub>
8	Ethane	C <sub>2</sub> H <sub>6</sub>
9	Acetylene	C <sub>2</sub> H <sub>2</sub>
10	Dibenzyl disulfide (DBDS)	C <sub>2</sub> H <sub>6</sub> S <sub>2</sub>
11	Power factor (PF)	N/A
12	Interfacial voltage	V
13	Dielectric rigidity	V/m
14	Water content	H <sub>2</sub> O
15	Health index (HI)	N/A

on two common machine learning models namely ANN and SVM. Despite varying datasets being implemented, this report may act as a comparative result to the existing results acquired. In addition, the results in this report will reveal more insights into the effects of changing the kernels and processing parameters, ergo the complexity, linearity, and overfitting associated. The data is available publicly and is documented in [3, 11]. In order to evaluate complexity, dataset with 15 features was applied to predict HI as shown in Table 1. Generally, when the output is a continuous value, regression approach is the preferred machine learning approach. However, authors posit that there is an opportunity to treat this as a classification problem, hence to gauge the complexity of models/nonlinearity/generalization of the transformer data.

### 3.1 Machine Learning Models

The technical aspects of acquiring the data are documented in [3, 11]. In the spectrum of model complexity, machine learning models vary from linear to highly nonlinear. Among the various machine learning models, support vector machines (SVM) enable a flexibility of using various kernels, thereby enabling a good observation on the suitability of model linearity or complexity. In this research exploration, authors attempt to correlate models complexity/Linearity of models as an attempt to study the relationship between HI and the dissolved gas, maintenance features.

For classification, the HI values were classified into various bins as the dataset was found to be skewed toward low value HI. The arrangement is shown in Table 2.

**Table 2** Classes of health index (%) and description

HI/%	Condition	Class
85–100	Very good	3
70–85	Good	3
50–70	Fair	3
30–50	Poor	2
0–30	Very poor	1

**Table 3** Results of implementation on various SVM kernel and ML models (regression)

Kernel/model	Training sets ( $R^2$ )	Independent test sets ( $R^2$ )
Linear kernel	0.5139	0.3165
Rbf kernel ( $\lambda = 0.1$ )	0.8802	-0.0231
Rbf kernel ( $\lambda = 0.01$ )	0.8802	-0.0285
Rbf kernel ( $\lambda = 0.001$ )	0.8865	-0.0260
ANN (hidden layer = 1)	0.5792	0.5020
ANN (hidden layer = 2)	0.6252	0.5069
ANN (hidden layer = 3)	0.6600	0.7440

**Table 4** Results of implementation on various SVM kernel and ML models (classification for three class)

Kernel/model	Training sets (Accuracy)	Independent test (Accuracy)
Linear kernel	0.7702	0.7426
Rbf kernel ( $\lambda = 0.1$ )	0.5988	0.6241
Rbf kernel ( $\lambda = 0.01$ )	0.6106	0.6201
Rbf kernel ( $\lambda = 0.001$ )	0.6094	0.5993
ANN (hidden layer = 1)	0.713	0.690
ANN (hidden layer = 2)	0.7260	0.634
ANN (hidden layer = 3)	0.729	0.6006

Data is split 80%–20% (training-testing) for SVM and 70%–15% -15% (training-validation–testing) for ANN. Referring to Tables 3 and 4, ten trials were performed and mean results were reported.

The individual binary SVM uses a kernel projection and plane to separate two target/outlier classes. The problem of classification is given by  $(x_i, y_i)$ , where  $x_i$  is the feature set,  $y_i$  is the respective label values,  $y_i \in [-1, +1]$ ,  $i = 1, 2, \dots, n$ , and  $n$  is the number of instances. We denote  $f(\mathbf{x}) = \mathbf{w}\mathbf{x} - b$ , where  $b$  is a constant, as the boundary that separates the data vectors  $\mathbf{x} \in \Re^n$  into the label of  $-1$  or  $+1$ . We may consider a hyperplane vector,  $\mathbf{w}$  which separates the multi-dimensional data into their respective label. In particular,  $f(\mathbf{x}) > 0$  will be labeled as  $+1$  and  $f(\mathbf{x}) < 0$  as  $-1$ . The objective of the plane optimization is to minimize  $\|\mathbf{w}\|$  s.t.  $y_i(f(\mathbf{x})) \geq 1$ .

This effectively maximizes the margin. Please keep in mind that the margin refers to the maximum width of the slab parallel to the hyperplane that has no interior data points. The points surrounding the hyperplane are known as support vectors. The support vector points are defined by  $x_i$  on the plane such that  $y_i(f(x_i)) = 1$ .

The minimization of  $\|\mathbf{w}\|$  creates a hard margin to separate the points. We further denote the points (slack variables) near the plane region which are misclassified during training as  $\zeta_d$ , where  $d = 1, 2, \dots, D$ . We also introduce a weight  $c$  to make trade-off between maximizing the distance between +1 and -1 label group and minimizing the number of slack variables. The final objective function considering the slack variables is given by

$$\begin{aligned} \min_{\mathbf{w}, b} \quad & (\|\mathbf{w}\| + c \sum_d \zeta_d) \\ \text{s.t.} \quad & y_i(f(\mathbf{x})) \geq 1, \end{aligned} \quad (1)$$

where  $c = 0.1$ .

We can further maximize nonlinear separation between classes by introducing a kernel that projects the original data into higher dimension, i.e.,  $\Re^n \rightarrow \Re^{n+1}$ . Higher dimension can be obtained using various transforms. In this paper, we implemented the radial basis function (RBF),  $G$  to obtain the additional dimension for projection (kernel). Assume that  $\mathbf{x}$  and  $\bar{\mathbf{x}}$  are two feature vectors (2-D), a higher dimension can be generated using

$$G(\mathbf{x}, \bar{\mathbf{x}}) = \exp(-(\gamma \|\mathbf{x} - \bar{\mathbf{x}}\|)^2), \quad (2)$$

where  $\gamma = 1$  is the parameter for adjusting the kernel.

Neural networks work by a series of cascaded interconnected nodes vaguely resembling their biological counterpart. The resulting structure is capable of approximating any nonlinear function. The output of an ANN node can be written as multiple regression model plus bias, i.e.,  $\beta \mathbf{x}^T + \epsilon$ , where  $\beta$  is the weight vector depicted by the edges and  $\epsilon$  is the bias value. To accommodate the nonlinearity, a transfer function (or also known as activation function) is introduced. The expression for the output of the transfer function in each node is given by

$$S\left(\sum \beta \mathbf{x}^T + \epsilon\right) = \frac{1}{1 + e^{-\sum \beta \mathbf{x}^T + \epsilon}}, \quad (3)$$

where  $S(\cdot)$  is the sigmoid transfer function. For simplicity, from now on, the vector  $\beta$  denotes a solution of  $1 \times (n + 1)$ , where  $n$  is the number of variables ( $\beta$  includes the bias term  $\epsilon$ ).

Neural networks have been used in many modeling tasks. In general, there are a variety of approaches for optimizing the weights, such as gradient descent or stochastic methods. The following approach is used in this paper. With each subsequent iteration,  $\beta$  is adjusted with the first order Jacobian. Given in each iteration  $(\beta + \delta)$ ,  $\delta$  can be calculated such that  $f(x_i, \beta + \delta) \approx f(x_i, \beta + J_i \delta_i)$  for the  $i$ th instance (row), where  $J_i = \partial f(x_i, \beta_i) / \partial \beta$  is the Jacobian matrix.

The sum of the squared error,  $S(\boldsymbol{\beta} + \boldsymbol{\delta})$ , is given by

$$S(\boldsymbol{\beta} + \boldsymbol{\delta}) \approx \sum_{i=1}^m [y_i - f(x_i, \boldsymbol{\beta}) - J_i \boldsymbol{\delta}]^2, \quad (4)$$

where  $\mathbf{y}$  is the target vector. Derivation of  $S(\boldsymbol{\beta} + \boldsymbol{\delta})$  w.r.t.  $\boldsymbol{\delta}$  gives

$$(J^T J) \boldsymbol{\delta} = J^T (\mathbf{y} - f(\boldsymbol{\beta})). \quad (5)$$

Adding a damping factor,  $\lambda$  to adjust the  $\boldsymbol{\delta}$  yields

$$(J^T J + \lambda I) \boldsymbol{\delta} = J^T (\mathbf{y} - f(\boldsymbol{\beta})). \quad (6)$$

Note that  $\lambda$  can be considered as a form of learning rate.

## 4 Results and Analysis

In this section, the results from evaluating with the various machine learning models are presented. As explained, this investigation can be viewed from two perspectives: regression and classification problem. In the original paper in which the authors have acquired and analyzed the results, online regression was considered. It is noteworthy that the dataset is highly imbalanced. SVM generally has high robustness to filter out noisy feature from the dataset from the selection of hyperplane.

### 4.1 Analysis on Regression Models

The original authors implement optimized decision trees and evaluated using a correlation  $R$  (refer to [11]) (Based on the report, a correlation coefficient,  $R$  is 0.9836 with the mean absolute error of 0.2276.) The equivalent is  $R^2 = 0.967$ . In our current approach, the best  $R^2$  acquired is 0.6877 (testing) and 0.6800 (training) using ANN. Since decision trees were implemented in the original research paper, it is expected that model has automatically implemented an “embedded” feature selection. It must be noted that our goal of this current research report remains to evaluate the linearity/complexity of the mapping from features to the health index on more common machine learning models, namely ANN/SVM on regression/classification perspective. Average results were acquired across 10 trials. The average results are shown in Tables 3 and 4. From the results acquired from Tables 3 and 4, in contrast, a decision border that has a high value of sigma takes data points that are further away into account. The  $C$  coefficient is fixed at 0.1 for all the configurations.

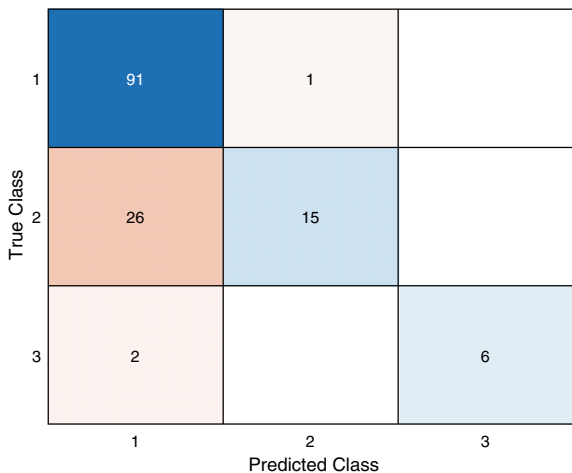
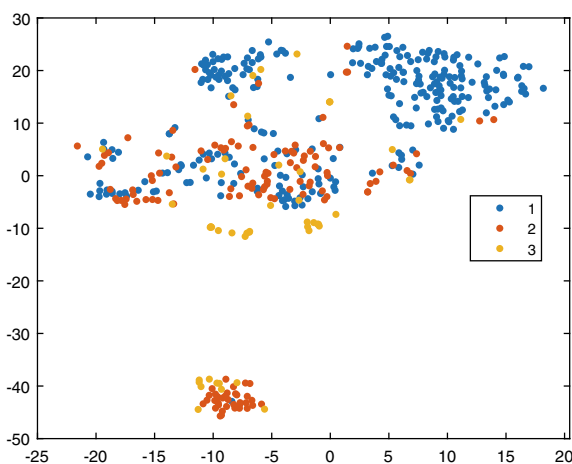
## 4.2 Analysis on Classification Models

SVM works by projection of existing data to higher dimension. Technically this is known as “Kernel Trick” among researchers in this domain. Generally, linear kernels are observed to be less overfitting (better generalization) as compared to their nonlinear counterparts. The confusion matrix for the linear kernel SVM on classification approach is shown in Fig. 1. The confusion matrix was acquired from the evaluation of the best “linear” kernel trained SVM. It is noteworthy that random selection of training and test partition data may affect the test and train results. As such, the mean performance may be more suitable criteria. As stated, only three classes were considered due to the highly imbalanced dataset. Even so, the confusion matrix showed relatively well-categorized classes. the dataset is skewed toward low HI transformer readings. Corresponding to the confusion matrix, T-SNE analysis was also performed. T-SNE is a visualization approach to gauge nonlinearity of feature sets. As shown in Fig. 2, the three classes are highly no separable with virtually not able to be separated with a linear line. The RBF kernels are able to have better mapping results but ultimately result in overfitting when tested with independent test datasets. In a support vector machine (SVM), the kernel scale refers to a parameter used to control the width of the kernel function. The kernel function is a crucial component of the SVM algorithm, as it maps the input data into a higher-dimensional feature space where a linear separation of classes may be possible.

The kernel function calculates the similarity or distance between pairs of data points. One commonly used kernel function is the radial basis function (RBF) or Gaussian kernel, which is defined as:

$$K(x_i, x_j) = \exp(-\lambda ||x_i - x_j||^2) \quad (7)$$

In this equation,  $\lambda$  is the kernel scale parameter,  $||x_i - x_j||^2$  represents the squared Euclidean distance between the two input vectors  $x_i$  and  $x_j$ . The kernel scale parameter  $\lambda$  determines the influence of each training example on the classification decision boundary. It controls the flexibility of the decision boundary and the smoothness of the resulting classification. A small value of  $\lambda$  will result in a broader kernel and a smoother decision boundary. It will consider more training examples for classification, potentially leading to overfitting if the dataset is noisy or contains outliers. On the other hand, a large value of  $\lambda$  will result in a narrower kernel and a more complex decision boundary. It will consider only nearby training examples for classification, potentially leading to overfitting if the dataset is sparse or there is a large variation in the data. The optimal value of the kernel scale parameter depends on the specific dataset and problem at hand. It is typically determined through cross-validation or grid search techniques, where different values of  $\lambda$  are evaluated, and the one that yields the best performance is selected.

**Fig. 1** Confusion matrix**Fig. 2** tsne-plot of features and visualization of embeddings

## 5 Conclusion and Future Work

In this research, authors have attempted to evaluate the complexity and nonlinearity required to perform regression to predict health index (HI) of transformer. In comparison with SVM, the various neural networks have been shown to be more effective in mapping input to output. Neural networks are known to be efficient for task of this nature but lack transparency in model. From the results acquired for SVM, it was shown that nonlinear models have better mapping (both regression and classification models) on training sets. However, it was shown that the models overfitted when tested with independent test feature sets. The best-performing kernel was noted to be linear kernel (refer to Tables 3 and 4). However, it is also noteworthy that the publically available dataset used [3, 11] has limitations. Firstly, the dataset is

highly unbalanced. The dataset is skewed toward  $\text{HI} < 0.3$ . In fact, there lacks publicly available dataset. Hence, considerations were made in view of such limitations. Nevertheless, it is sufficient to achieve the objective.

In view of the results, it is apparent that models that lean toward more linear kernels, tend to perform better in terms of preventing over fitting. Variances in the dataset are relatively high in the current dataset. For future directions, it is imperative to further investigate the contributions of the various features. Possibly a weighted feature set with LASSO restriction can be considered. The take-home message from the research report is this: The publically available dataset was evaluated for prediction of HI using dissolved gas contents and other maintenance features. It was found that nonlinear kernels and more hidden layers adequately separate the classes. However, when further tested with independent test sets (for the case of SVM), the model trained is shown to be inadequate in mapping the features to respective HI. Neural networks are shown to generalize well (at least in the case of the current dataset applied). This scenario implies the high variances in the dataset and the limitation of SVM to generalize. Thus, this somehow gives an indication that more work can be performed to mitigate this. This may be due to high variances in the dataset or the inability for model to generalize.

Overall, this is the finding of the research to investigate nonlinearity of model required for this task and generalization issues. It is noteworthy that this dataset has some limitations, and thus, the results should be taken with this consideration.

- Neural network performs better in the both models. More processing layers produced better mapping without sacrificing generalization.
- SVM approach shows lack of generalization when tested with independent data.
- Linear kernels performed better on SVM (generalization). This may suggest similar geometrical classifiers and may yield better generalization when more linear models are considered.

## References

1. Aizpurua, J.I., Stewart, B.G., McArthur, S.D.J., Lambert, B., Cross, J.G.: Towards a comprehensive DGA health index. In: IEEE 2nd International Conference on Dielectrics (ICD), pp. 1–4 (2018). <https://doi.org/10.1109/ICD.2018.8514697>
2. Alqudsi, A., El-Hag, A.: Application of machine learning in transformer health index prediction. *Energies* **12**, 2694 (2019). <https://doi.org/10.3390/en12142694>
3. Arias Velásquez, R.M., Mejía Lara, J.V.: Data for: root cause analysis improved with machine learning for failure analysis in power transformers. <https://www.kaggle.com/datasets/shashwatwork/failure-analysis-in-power-transformers-dataset>
4. Chantola, A., Sharma, M., Saini, A.: Integrated fuzzy logic approach for calculation of health index of power transformer. In: 2018 Second International Conference on Inventive Communication and Computational Technologies (ICICCT), pp. 1045–1050 (2018). <https://doi.org/10.1109/ICICCT.2018.8473316>
5. Ghoneim, S.S.M., Taha, I.B.M.: Comparative study of full and reduced feature scenarios for health index computation of power transformers. *IEEE Access* **8**, 181326–181339 (2020). <https://doi.org/10.1109/ACCESS.2020.3028689>

6. Idrees, M., Riaz, M.T., Waleed, A., Paracha, Z.J., Raza, H.A., Khan, M.A., Hashmi, W.S.: Fuzzy logic based calculation and analysis of health index for power transformer installed in grid stations. In: 2019 International Symposium on Recent Advances in Electrical Engineering (RAEE). vol. 4, pp. 1–6 (2019). <https://doi.org/10.1109/RAEE.2019.8887016>
7. Li, S., Wu, G., Dong, H., Yang, L., Zhen, X.: Probabilistic health index-based apparent age estimation for power transformers. IEEE Access **8**, 9692–9701 (2020). <https://doi.org/10.1109/ACCESS.2020.2963963>
8. Mengrong, G., Hongjian, L.: Research on temperature prediction of subway transformer based on LSTM. In: IEEE International Conference on Artificial Intelligence and Computer Applications (ICAICA). pp. 555–558 (2022). <https://doi.org/10.1109/ICAICA54878.2022.9844506>
9. Murugan, R., Ramasamy, R.: Understanding the power transformer component failures for health index-based maintenance planning in electric utilities. Eng. Failure Anal. **96**, 274–288 (2019). <https://doi.org/10.1016/j.engfailanal.2018.10.011>
10. Nisbet, B.: Tutorial e—feature selection in knime. In: Nisbet, R., Miner, G., Yale, K. (eds.) Handbook of Statistical Analysis and Data Mining Applications, 2d edn., pp. 377–391. Academic Press, Boston (2018). <https://doi.org/10.1016/B978-0-12-416632-5.00027-X>
11. Radiansyah, D., Prasojo, R.A., Suwarno, Abu-Siada, A.: Root cause analysis improved with machine learning for failure analysis in power transformers. Eng. Failure Anal. **115**, 104684 (2020). <https://doi.org/10.1016/j.engfailanal.2020.104684>
12. Radiansyah, D., Prasojo, R.A., Suwarno, Abu-Siada, A.: Artificial intelligence-based power transformer health index for handling data uncertainty. IEEE Access **9**, 150637–150648 (2021). <https://doi.org/10.1109/ACCESS.2021.3125379>
13. Saravanan, D., Hasan, A., Singh, A., Mansoor, H., Shaw, R.N.: Fault prediction of transformer using machine learning and DGA. In: IEEE International Conference on Computing, Power and Communication Technologies (GUCON). pp. 1–5 (2020). <https://doi.org/10.1109/GUCON48875.2020.9231086>

# Design, Development and Experiment Analysis of Solar Panel Cleaning System



Laurence Gerry John, Goh Thing Thing, J. Ragupathy, H. S. Chua, and Fu Pang Han

**Abstract** As the world moves towards a greener future, adoption of renewable energy sources has become very popular and solar power has become one of the most desirable sources of energy. The performance and efficiency of solar panel modules are very much affected by environmental parameters such as temperature, irradiance and dust. Many studies found that the accumulation of dust on the surface of solar panels has seriously reduced the output power of a solar panel. Dust that has accumulated on the panels may reflect or refract the photons thus preventing them from reaching the surface of the panel. Thus, it has reduced the efficiency of solar panels by 3–25%. This study aims to design and fabricate a solar panel cleaning system. The system will be placed atop the solar panels. It consists of an on-board cleaning brush, water tank and control electronics. After the fabrication of the design, testing is done using an acrylic panel embedded with LDR sensors. The intensity of the light passing through the panel is measured before and after multiple cleaning passes. Based on the results, the cleanliness of the surface had significantly improved the efficiency of the panel from 60 to 98% after 3 cleaning passes using water jet.

**Keywords** Renewable energy · Solar panel · Cleaning robot · Arduino ESP32 · Real case study

---

L. G. John · G. T. Thing (✉) · H. S. Chua · F. P. Han

School of Engineering, University of Wollongong Malaysia, Utropolis, Glenmarie, 40150 Shah Alam, Selangor, Malaysia  
e-mail: [ttgoh@uow.edu.my](mailto:ttgoh@uow.edu.my)

G. T. Thing · H. S. Chua · F. P. Han  
UOW Malaysia KDU Penang University College, Jalan Anson, 10400 George Town, Pulau Pinang, Malaysia

J. Ragupathy  
Galactic Advance Engineering (M) Sdn Bhd, Petaling Jaya, Selangor, Malaysia

## 1 Introduction

Energy production has recently been focused on adapting renewable sources of energy. The use of solar power has taken focus due to its abundance around the world and its ability to generate energy with limited impact to the environment [1–3]. A photovoltaic system uses solar panels to convert solar radiation into electrical energy. The simulation results [4] show that maximum power point tracking (MPPT), which is a technique used to optimize the power output of a photovoltaic (PV) system by continuously tracking and adjusting the electrical load to ensure that the system operates at its maximum power point. However, environmental factors such as temperature, sunlight intensity, weather condition and dust on the surface of solar panels are heavily affecting the efficiency of the solar panels.

Many studies were done on the effects of dust accumulation on photovoltaic cells in relation to performance [3, 5]. Dust and dirt accumulation on the solar panel over time has a significant impact on reducing the output power of the panel. Pollutants deposited on the solar panel have reduced the amount of incident light hitting the panel and increased the panel's temperature out of its optimal working range, thus reducing the panel's efficiency. Kazem et al. [3] and Hussain et al. [6] concluded that the power drops due to pollutants being deposited on the panel vary from 3–25% depending on the quantity and type of pollutant.

Additional studies focusing on the means and methods proposed for a solar panel cleaning solution. This project aimed to develop a solar panel cleaning system to reduce the impact of dust and dirt on the solar panel to improve the efficiency of the solar panels. The system will be installed at the solar panel, and it will be enabled when the solar panel cleaning is required. An additional GUI is developed for the monitoring and control of the cleaning system.

## 2 Effects of Dust on the Performance of Solar Panel

According to Hussain et al. [6], Gupta et al. [7] and Mani and Pillai [8], it is very important to study the effects of the accumulation of dust on the surface of the solar panel. The deposition of  $4 \text{ g/m}^2$  of dust with particle diameters ranging between 0.5 and 10 mm can cause the efficiency of the solar panel to drop by 40%, especially if the solar panels are placed in countries around the solar belt zone (predominantly desert countries).

The efficiency of solar systems is mainly affected by the weather, shady/dark environments and dust accumulation [9]. Dust accumulation occurs due to pollen, sand, bird droppings and other similar pollutants being deposited on the surface of the photovoltaic panel. Such pollutants prevent incident light from hitting the PV cells. An analysis was done on the negative effects of dust accumulation on the output power of PV cells in Saudi Arabia, where a 50% reduction in output power could happen due to not cleaning the PV cells for six months [2].

Varying the amount of dust on a PV panel caused a drop in output power compared to a baseline clean PV cell. The output power decreased by 2.3, 7.5, 17 and 27% for dust depositions of  $0.63 \text{ g/m}^2$ ,  $1.89 \text{ g/m}^2$ ,  $3.15 \text{ g/m}^2$  and  $3.78 \text{ g/m}^2$ , respectively.

### 3 Solar Panel Cleaning System

PV cells are usually installed outdoors and easily get polluted. Thus, the solar panel cleaning system is essential to ensure the efficiency of the output power is maintained at the optimum level. Kazem et al. [3] compared a few solar panel cleaning methods in his research. Frequency and cost of cleaning per method were put into consideration in the study. According to researchers, natural cleaning using rain and wind is unreliable due to insufficient amounts of rainfall. The use of special surfaces preventing accumulation of pollutants may increase the cost of building PV panels. High pressure water cleaning can remove dust more effectively. However, heat shocks might occur during the cleaning process. Electrodynamic display and superhydrophobic aircraft on PV can clean the accumulated dry dust in a short period without using water. However, it was found that this method is unable to remove wet mud particles that stick to the PV cells.

Altıntaş and Arslan [1] studied two types of cleaning systems which are wet cleaning and dry cleaning. Wet cleaning systems using ionized distilled water performed better as compared to dry cleaning systems in which the dust particles often scratched the surface of the panel. Particularly in rainy dusty areas, PV cells are covered with multiple layers of mud which require excessive cleaning. Autonomous cleaning systems are developed to clean the PV panels frequently and efficiently while reducing the amount of water used. In this study, electrostatic cleaning was discussed too. However, the cost of retrofitting electrostatic cleaning panels is relatively high.

The objective of this project is to develop an effective and cost-efficient solution for cleaning solar panels. This will be achieved by utilizing a moving robot equipped with a water pump to enhance the cleaning process.

### 4 Overall System Description

Photovoltaic panels are commonly placed in an open space environment. Three methods of PV panels arrangement are rows of arrays (on solar farms and large industrial building), tightly packed together in a grid system (on house roofs and some industrial buildings) and individual panels (for small buildings and houses), and these are the most common layouts, refer to Fig. 1.

Based on the suggestion given by Kazem [3] and Altıntaş [1], the design of the solar panel cleaning system focused on a wheel-based system built with a cylindrical cleaning brush and a water tank. The system was controlled over a local Wi-Fi

**Fig. 1** Automatic cleaned PV [8]



network using a GUI on a computer. The system has four drive wheels, and each can rotate and steer independently.

Figure 2 shows the system's functionality. Three microcontrollers (ESP32) were used to control the system. The master ESP32 was connected to the local network and received commands from the GUI at the workstation. User Datagram Protocol (UDP) in conjunction with Json objects was used to send and receive information between the cleaning system and the GUI. Two ESP32 slave devices were used to control the steering, speed and read sensor data. Four BLDC motor drivers were used to control the speed and direction of the BLDC motors. The BLDC motors used were hub motors with a built-in gearbox, and this allows for high torque at low speeds. The secondary slave ESP32 will be used to control the DC motors (steering) through the dc motor driver. Additional current sensors will be read using this microcontroller.

#### 4.1 3D Design and Fabrication

The design of the model focused on a ground vehicle with swerve drives. This allowed each wheel to steer independently from one another, providing a high degree of control and versatility. The vehicle has a component case which contains all electrical components. Water tank was located underneath the vehicle.

The cleaning solution in Fig. 3 contained all the necessary components for operation. It was powered by two 12 v 4.5 Ah lead acid batteries connected in series. The BLDC motors have an operating voltage of 24 v with the DC motors operating at 12 v. The electronic components operated at either 3.3 or 5 v. A built-in water jet allowed the system to coat the panel with water before cleaning. The cleaning is done using a cylindrical brush attached at the front of the vehicle (see Fig. 4). The entire system weighs 45.2 kg with no water and 50 kg with water, having a 4.8 L water tank fitted underneath the cleaning system.

The system uses 0.5 L/min of water when paired with a HVV 11,001 water jet; thus, a full tank will last ~ 9 min 36 s. The vehicle is set to move at 2.5 cm/s with a

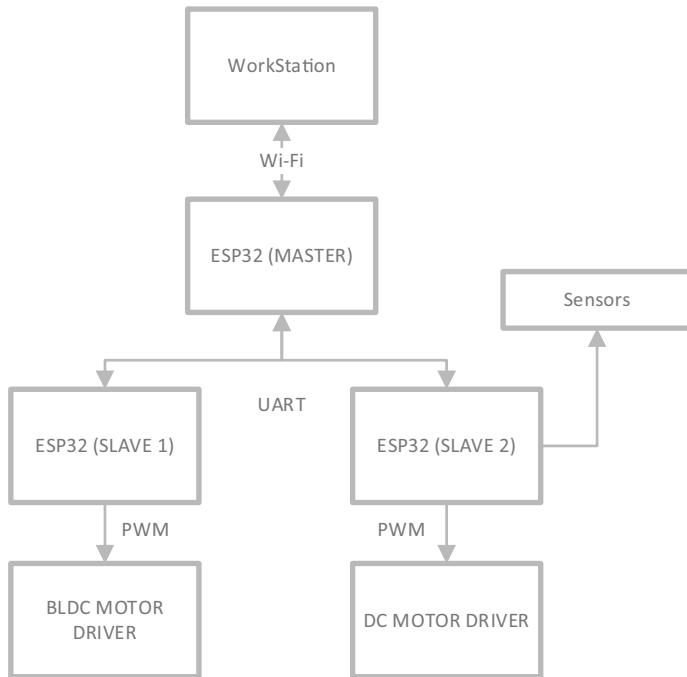


**Fig. 2** System functionality

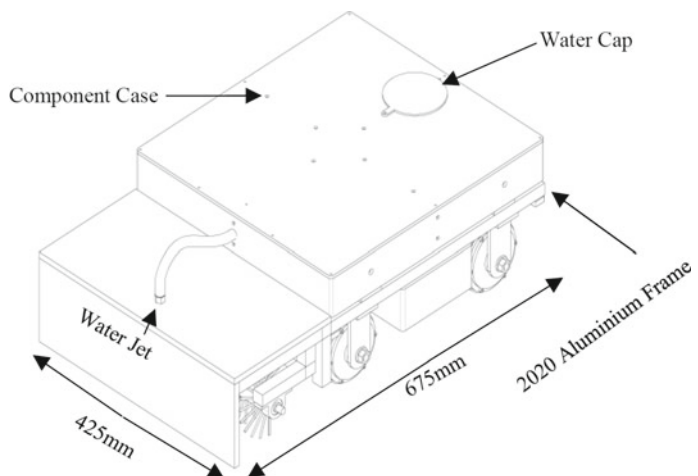


**Fig. 3** Solar cleaning solution isometric view 1

**Fig. 4** Solar cleaning solution isometric view 2

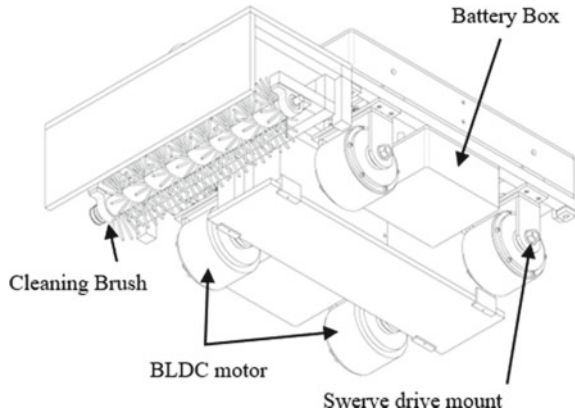


**Fig. 5** Solar cleaning solution rear view



cleaning brush width of 360 mm, thus covering an area of  $0.54 \text{ m}^2/\text{min}$ . The cleaning brush is a PVC brush with 0.2 mm nylon threads, refer to Fig. 5.

The swerve modules were mechanically coupled to the DC motors located inside the component case. Pilot lights were included to indicate the status of the cleaning system.

The implementation of the circuitry and component connection was illustrated in Fig. 8. Two 12 v lead acid batteries were connected in series to power the system. The voltage was split into three voltage levels (5, 12 and 24 v). 24 v was used to power the BLDC motors, BLDC motor drivers and pilot lights. On the other hand, 12 v was used to power the DC motors (steering), DC motor drivers and cleaning brush motor.

Information such as speed of the BLDC motors, angle of the DC motors and the status of the cleaning brush and water pump was sent via master ESP32 controller over a local network using UDP datagrams to display on GUI. It is to enable user to monitor the condition of the cleaning system.

The microcontroller acts as both a workstation and an access point. A workstation can send datagrams to the ESP32 if both devices are connected to the same network

or if the workstation is connected to the ESP32 access point. The UDP datagrams were embedded with Json objects. When a datagram is received, the Json object is parsed, and functions are carried out by the master ESP32 using the key of the Json object. Any data required to be relayed to the slave ESP32 was done using UART. The relevant Json objects are forwarded to the slave ESP32, decoded and the changes applied. Data is streamed from the ESP32 (Master) to the workstation every 100 ms. This data provides feedback for the user at the workstation on the status of the vehicle. Streamed data includes, speed (rpm), angle of wheels, water pump status, cleaning brush status and current values for relevant components. The workstation can send movement commands (if any) within 100 ms, and all other data sent asynchronously.

## 4.2 GUI Implementation

The GUI, created using QT5 framework designed for Windows 10, is used to monitor and send commands to the cleaning system. GUI must be configured to broadcast mode, and the parameters set must match the configuration set in the cleaning system so that the monitoring and control can be executed.

Once the setup and connection were done, real-time monitoring data which streamed from the ESP32 can be displayed on GUI. Figure 6 shows the data of the BLDC motor at a given timestamp. Additional streamed data for the steering angle of the DC motors is shown in Fig. 7. Streamed data also includes the cleaning brush state (on/off), water pump state (on/off), while cleaning brush current and water pump current were also displayed in the GUI. All relevant data pertaining to the cleaning system is streamed to the GUI in 100 ms intervals (Fig. 8).

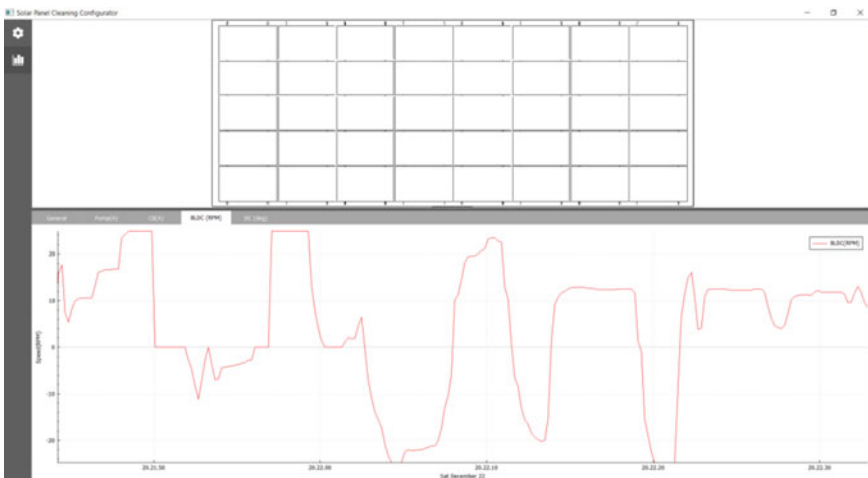


**Fig. 6** GUI monitoring interface BLDC motor

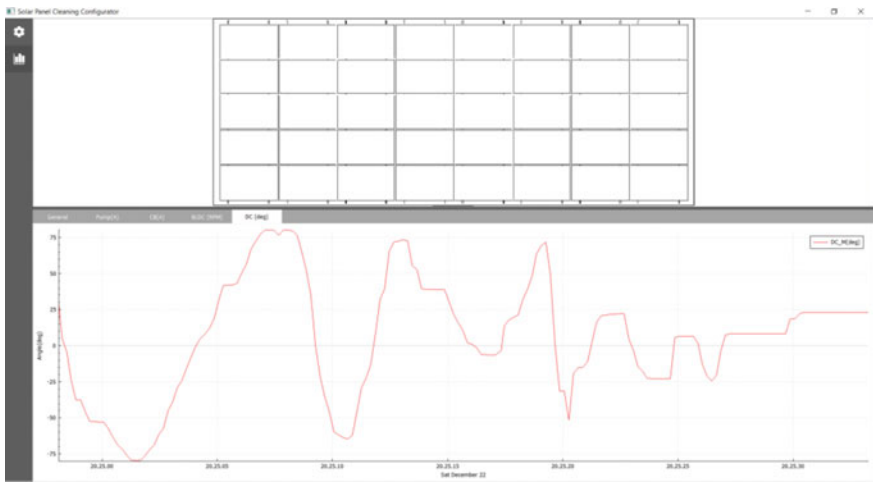


**Fig. 7** GUI monitoring interface DC motor ( $\theta$ )

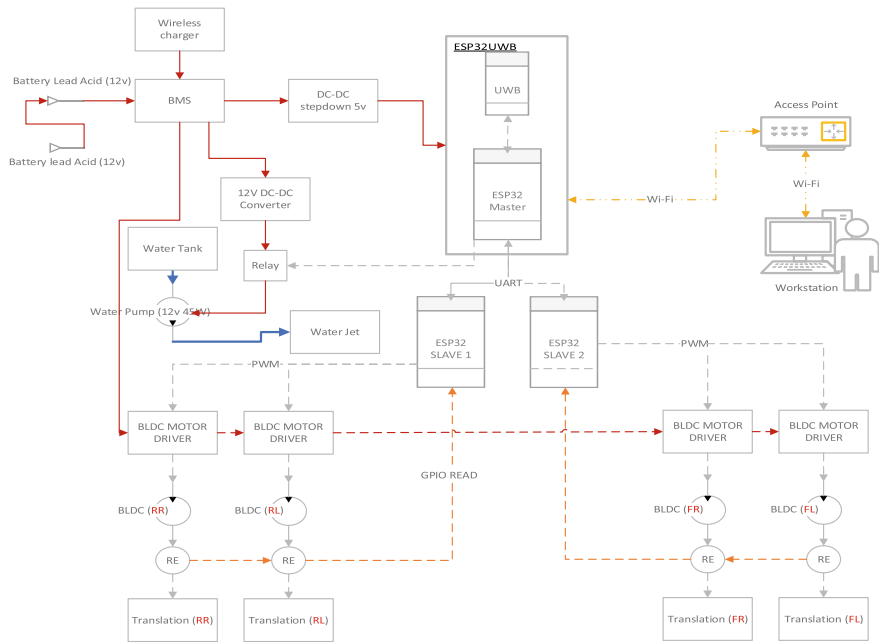


**Fig. 8** Circuitry and system functionality

## 5 Results and Discussion

A clear acrylic panel embedded with LDR sensors is used to simulate the surface of a solar panel as shown in Fig. 9. The panel is deposited with dirt to simulate a dirty solar panel. The cleanliness of the panel is calculated by measuring the amount of light passing through the panel using the LDR sensors. The measured voltage varying from 0 to 3.3 v is representation of the amount of light passing through the panel, with 3.3 v indicating the maximum measured incident light. The voltage of the new and clean panel was initially measured and recorded as a baseline reference. 10 g/section (0.036 g/cm<sup>2</sup>) of dry soil is deposited on the panel. The system cleans the panel 3 times (*n*th Pass), each of which the results were recorded as shown in Tables 1 and 2.

$V_{\text{avg}}$  is the average voltage across all LDR sensors and is used as a baseline in calculating the panel's relative cleanliness. (Note: *n* is the LDR sensor number, *V* is the voltage.)

**Fig. 9** Acrylic panel

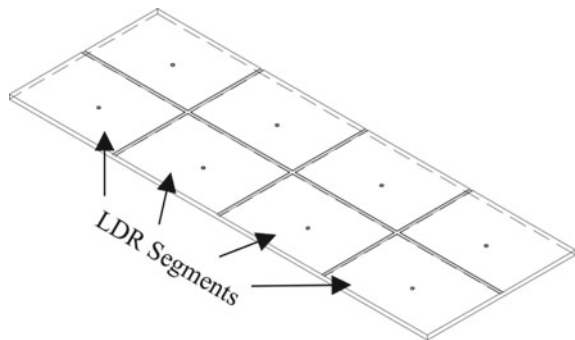


**Table 1** Surface cleaning without water pump

LDR	Voltage before cleaning (V)	Voltage after 1st pass (V)	Voltage after 2nd pass (V)	Voltage after 3rd pass (V)
1	0.973	1.471	1.523	1.692
2	0.701	1.296	1.512	1.743
3	0.982	1.432	1.487	1.539
4	0.793	1.304	1.530	1.747
5	0.748	1.362	1.465	1.620
6	0.822	1.418	1.515	1.534
7	0.890	1.339	1.357	1.716
8	0.815	1.231	1.441	1.492

**Table 2** Surface cleaning with water pump

LDR	Voltage before cleaning (V)	Voltage after 1st pass (V)	Voltage after 2nd pass (V)	Voltage after 3rd pass (V)
1	0.718	1.688	2.558	2.8944
2	0.831	1.965	2.429	2.9436
3	0.689	1.798	2.664	2.9552
4	0.850	1.965	2.429	2.8400
5	0.848	1.754	2.676	2.9077
6	0.853	1.812	2.620	3.0678
7	0.922	1.734	2.583	3.0319
8	0.902	1.519	2.687	3.0526

$$V_{\text{avg}} = \frac{\left( \sum_{n=1}^8 V_n \right)}{8} \quad (1)$$

$V_{\text{r, avg}}$  is the average voltage measured across all LDR sensors relative to each cleaning pass. A higher measured voltage indicates less dirt on the surface of the panel.

$$V_{r, \text{avg}} = \frac{\left( \sum_{n=1}^8 V_n \right)}{8} \quad (2)$$

Cr is the relative cleanliness of the panel. Thus, if Cr = 60%, the panel is 60% clean or there is 40% dirt reaming on the panel ( $100 - 60 = 40\%$ ).

$$C_R = V_{r, \text{avg}} / V_{\text{avg}} \quad (3)$$

Table 1 shows the results of the panel's cleanliness after it was cleaned by cleaning robot without using its water pump. The panel was deposited with 10 g/section of dirt. The deposited dirt was mixed with water using a 4:1 ratio; thus, for 80 g of dirt deposited, 20 ml of water was used. The deposits were left to dry prior to the testing process.

Figure 10 shows the result of the uncleaned panel. The panel has a relative cleanliness of 25.509% with a standard deviation of 0.095. The standard deviation measures how evenly the dirt is spread throughout the surface of the panel, with red accents indicating higher deposits of dirt and blue accents indicating lower deposits of dirt. For the uncleaned panel in Fig. 10, the variation of dirt deposited in each section is between 71 and 80%.

The cleaning vehicle was then set to clean the panel surface and the results are shown in Fig. 11. After the first cleaning pass, the amount of dirt remaining on the surface decreases to 58.814% with a standard deviation of 0.075, resulting in an

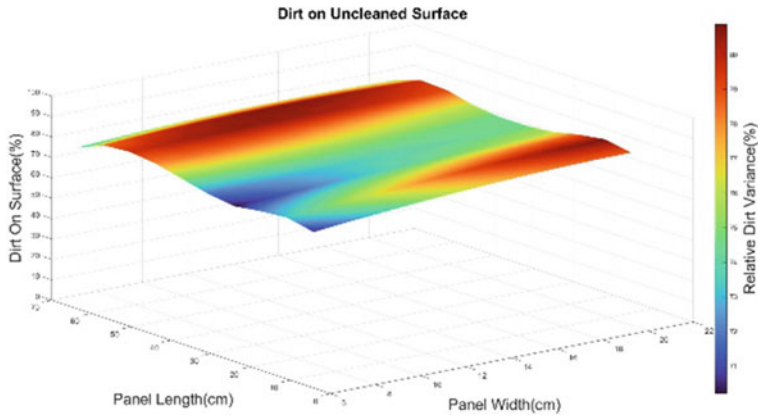


**Fig. 10** Dirt on surface, uncleaned panel

improved cleanliness of 15.677%. The variation of dirt across the surface is between 56 and 63%.

The vehicle was initiated to do a second cleaning pass. After the cleaning pass, the amount of dirt remaining on the surface is 55.107% ( $\Delta 3.707$ ) with a standard deviation of 0.054. The variation of dirt across the surface is 54–60%. The results are shown in Fig. 12.

The third cleaning pass was initiated, and the dirt remaining on the surface of the panel is 50.355% ( $\Delta 4.752\%$ ). The amount of dirt remaining on the surface varies between 47 and 57% (Fig. 13).

After each cleaning pass, there was a drop in the amount of dirt measured across the surface of the panel, the standard deviation for each pass is  $< 0.096$  ( $\Delta 10\%$ ). However,

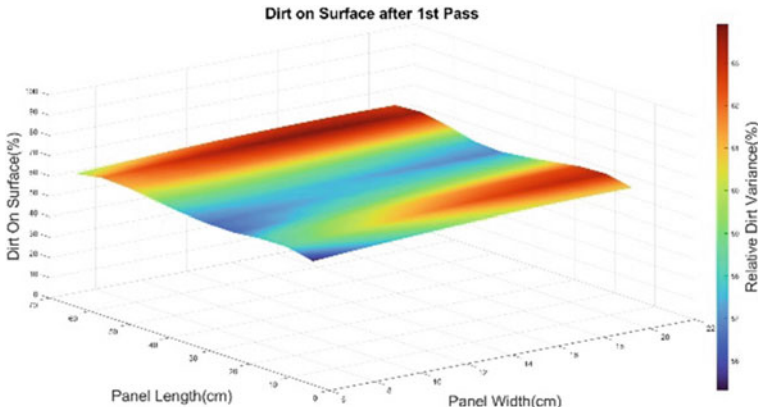


**Fig. 11** Dirt on surface, first pass

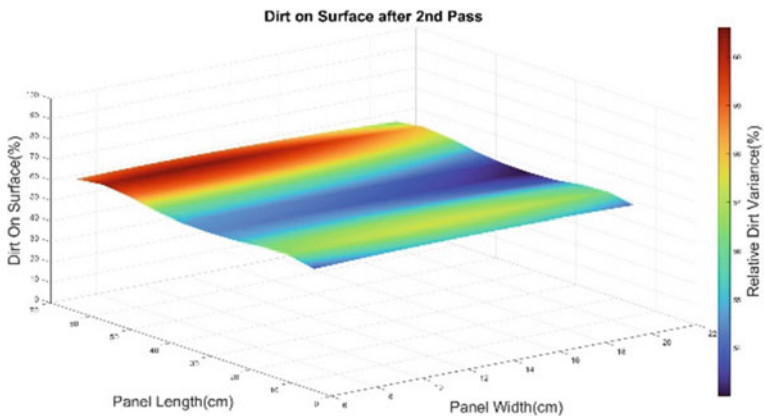


**Fig. 12** Dirt on surface, second pass

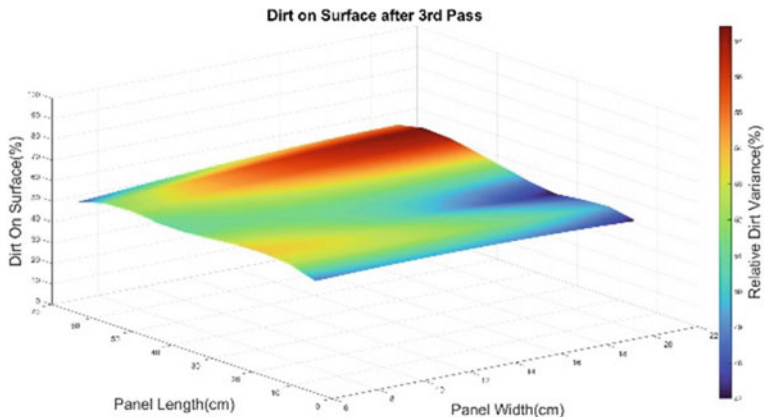


**Fig. 13** Dirt on surface third pass

the delta between each cleaning pass did not exceed 15.577%; thus, multiple passes would be required to achieve near 100% cleanliness.

Table 2 contains the data of the panel's cleanliness with the usage of the systems water pump. In this test, the panel was also cleaned three times using the vehicles cleaning brush in conjunction with its water pump. Water is sprayed upon the panel's surface as the vehicle drives along it, while the cleaning brush simultaneously scrubs the surface of the panel. Deposited with 10 g of water/dirt mixture per section (ratio 1:4), the panel was left to dry before the tests were launched. The results collected are shown in Fig. 14. The initial amount of dirt on the surface was 74.907% with a standard deviation of 0.077, resulting in a variation of dirt across the surface between 72 and 82%.

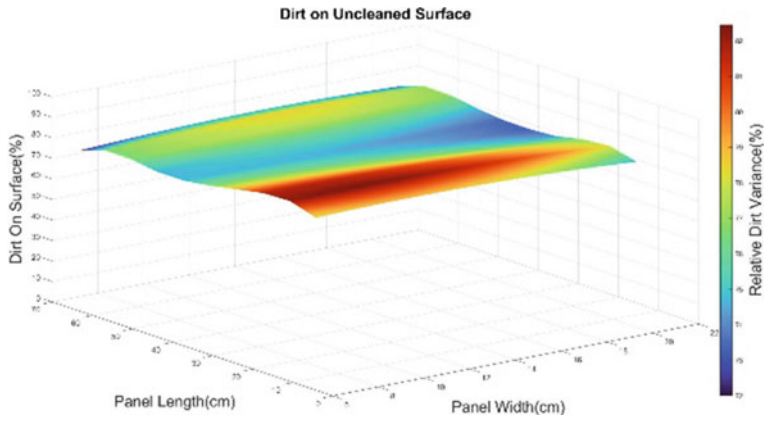


**Fig. 14** Dirt on surface, uncleaned panel

The water pump and cleaning brush were activated before moving atop the panel. After the first pass of cleaning, the results show that the dirt remaining on the surface is 45.985%, having a standard deviation of 0.137, resulting in the dirt on the surface varying between 42 and 52% (see Fig. 15).

After the second pass was initiated, the amount of dirt on the panel was reduced to 21.648%. A standard deviation of 0.097 shows a variation of the dirt on surface between 19 and 27% (Fig. 16).

The panel was cleaned for a third time, reducing the dirt remaining on the surface to 10.096%. The standard deviation of 0.077 indicates a fluctuation of dirt on the panel between 7 and 13% (Fig. 17).

With the usage of water pump in conjunction with the cleaning brush, the system achieved a final surface cleanliness of 89.904%. After the first pass, the standard

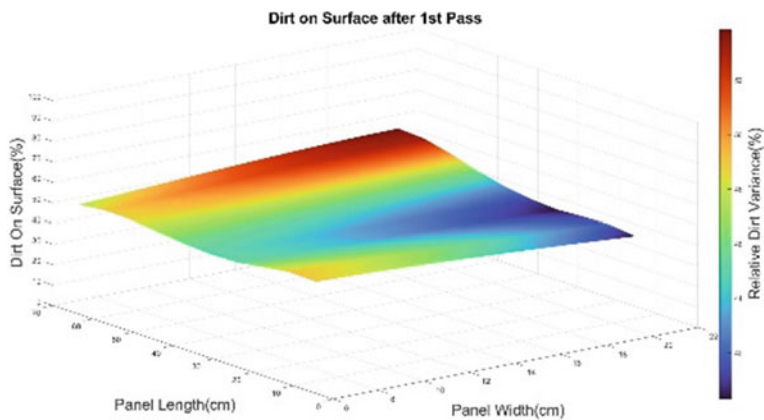


**Fig. 15** Dirt on surface, first pass

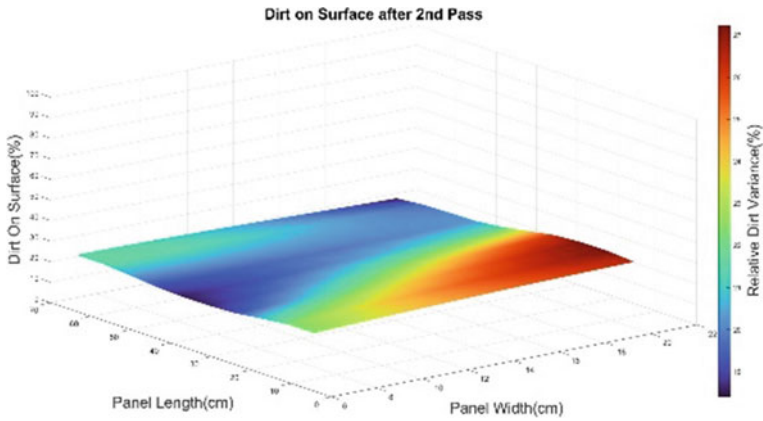


**Fig. 16** Dirt on surface, second pass

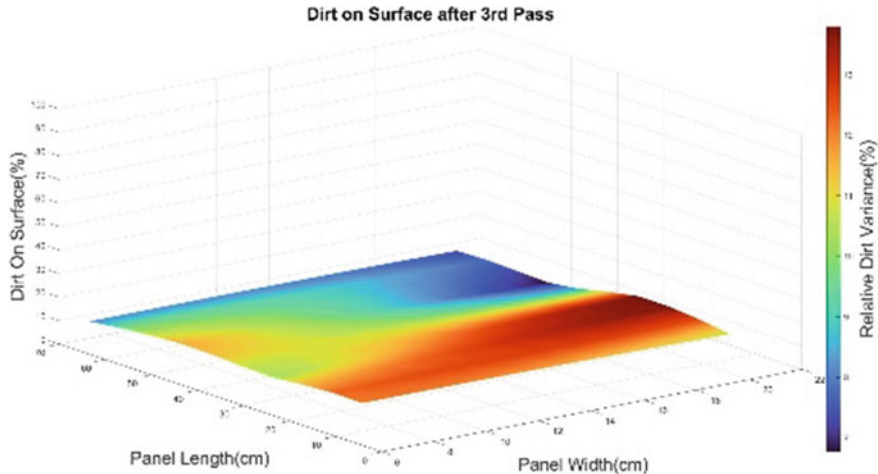
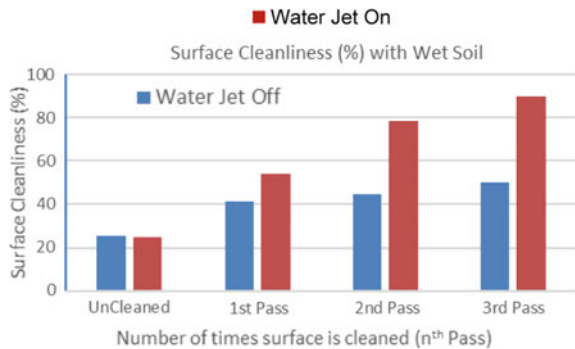


**Fig. 17** Dirt on surface, third pass

deviation increased from 0.077 to 0.137. This happens as the soil was not damp enough to be removed uniformly. After the second pass, the soil was dampened further and this resulted in a smaller standard deviation of 0.097. The standard deviation was further reduced to 0.077 after the third pass.

The first pass with water pump has a cleanliness delta of  $\Delta 28.922\%$  which is much greater than the  $\Delta 15.677\%$  of the first pass without using the water pump (Fig. 11). In the second and third passes with water pump, the cleaning system improved the surface cleanliness by 24.337% and 11.552%, respectively. A comparison of surface cleanliness with and without using the water pump is presented in Fig. 18. The huge

**Fig. 18** Surface cleanliness (%) water jet vs no water jet



difference in the chart clearly implies that the system can clean effectively when both the water pump and cleaning brush are employed.

## 6 Conclusion

The effects of dirt/pollutants on solar panels are profound. Different types of pollutants will affect the performance of the solar panel differently, and the effects of pollutants that an individual experiences are highly dependent on their environment and geological condition. The day-to-day effects of pollutants on the solar panel do not seem evident; however, once the effects compound over time, there is a noticeable drop in efficiency. Thus, certain industries and more importantly location will require solar cleaning solutions.

The proposed cleaning solution was designed in AutoCAD, fabricated using additive and subtractive manufacturing techniques, having a dedicated GUI and circuitry, which establishes a reasonable baseline for further development.

The results showed the system's ability to clean the surface of solar panel with and without water. A maximum surface cleanliness of 89.9% was achieved, with a variance of dirt remaining on the surface between 7 and 13%. The system has some limitations such as multiple passes are required to clean the surface effectively, and the assembly in certain areas of the design is tedious due to poor mechanical foresight. Improvements can be made by integrating a DC motor with a higher torque for the cylindrical cleaning brush, as this will improve the cleaning results where the brush can maintain a high coefficient of friction between the bristles and the panel surface without a drop in angular velocity. A redesign of certain mechanical parts is required to make the assembly process easier. The consideration of adding certain chemical compounds into the water to improve cleaning results may also be explored.

**Acknowledgements** The authors would like to thank Galactic Advance Engineering (M) Sdn. Bhd. and UOW Malaysia University College, Postgraduate and Research Centre (PGRC) for sponsoring and providing materials and resources for the project.

## References

1. Altıntaş, M., Arslan, S.: The study of dust removal using electrostatic cleaning system for solar panels. *Sustainability* **13**(16), 9454 (2021)
2. Akyazi, Ö., Şahin, E., Özsoy, T., Algül, M.: A solar panel cleaning robot design and application. *Avrupa Bilim ve Teknoloji Dergisi* 343–34 (2019)
3. Kazem, H.A., Chaichan, M.T., Al-Waeli, A.H., Sopian, K.: A review of dust accumulation and cleaning methods for solar photovoltaic systems. *J. Clean. Prod.* **V**(276), 123187 (2020)
4. Mohamed Zain, A.O., Huang Shen, C., Govinda, S., Albert, F.Y.C., Al-Talib, A.A.M.: Matlab design and power analysis of MPPT controller for solar PV using Perturb and observation algorithm. *J. Mech. Cont. Math. Sci. Special Issue-1*, 259–270 (2019)
5. Maghami, M.R., Hizam, H., Gomes, C., Radzi, M.A., Rezadad, M.I., Hajighorbani, S.: Power loss due to soiling on solar panel: a review. *Renew. Sustain. Energy Rev.* **59**, 1307–1316 (2016)
6. Hussain, A., Batra, A., Pachauri, R.: An experimental study on effect of dust on power loss in solar photovoltaic module. *Renew. Wind, Water, Solar* **4**(9) (2017)
7. Gupta, V., Sharma, M., Pachauri, R.K., Babu, K.D.: Comprehensive review on effect of dust on solar photovoltaic system and mitigation techniques. *Solar Energy* **V**(191), 596–622 (2019)
8. Mani, M., Pillai, R.: Impact of dust on solar photovoltaic (PV) performance: research status, challenges and recommendations. *Renew. Sustain. Energy* **14**(9), 3124–3131 (2010)
9. Myyas, R.E.N., Al-Dabbasa, M., Tostado-Véliz, M., Jurado, F.: A novel solar panel cleaning mechanism to improve performance and harvesting rainwater. *Sol. Energy* **237**, 19–28 (2022)

# Modeling of Controller for Motor-Controlled Prosthetic Hand Based on Machine Learning Strategy in Classifying Two-Channel Surface EMG Signals



Salina Mohmad and Abdalrahman Khaled Elnagar

**Abstract** This research study presents a computationally improved system using a pattern recognition (PR) algorithm to classify fingers movement based on data acquired by a surface EMG (sEMG) sensor when muscle is contracting. Ten subjects were involved in this investigation where the forearm's muscle activities were acquired using two-channel sEMG placed at the flexor digitorum superficialis and extensor digitorum muscles. The focus of this study is to integrate the sensor with servo motors to control the movement of artificial limbs or prosthetics based on which muscle is at work. The work involved signal processing on raw sEMG signals, followed by multiple time domain feature extraction (TD). sEMG signal is then segmented using an overlapping window of size 250 ms and increments of 50 ms. The feature extraction was used to build up the convolutional neural network (CNN) which is used to train the classes of fingers movement. The dataset was split into 80% for training and 20% for testing the classifier. The CNN model was able to incorporate most of the data's variability while maintaining an average classification accuracy of 98%.

**Keywords** Surface EMG · Convolutional neural network

## 1 Background

The human body is a complex piece of biological machinery in terms of performing daily activity tasks [1]. Prosthesis limbs are physiologically used extremely to perform complex usual daily tasks such as gripping, pushing, catching, and lifting. Human arms are used to engage with the environment interaction via sensing the object by touching, carrying weight, and determining the temperature, and pressure. A prosthesis is an artificial device that is comparable in shape and size to a missing

---

S. Mohmad (✉) · A. K. Elnagar

School of Engineering, University of Wollongong, Malaysia, Selangor, Malaysia  
e-mail: [msalina@uow.edu.my](mailto:msalina@uow.edu.my)

body part and is meant to augment or enable the portion of the body to regain usage or function as a cosmetic substitute [2]. When compared to other organ prostheses, limb prostheses are the most prevalent. They are classified into several categories based on the intended use and the section of the limb to be replaced. This includes cosmetic prosthetic limb, which is designed especially for appearance instead of functionality and efficiency. Types of amputations include the transfemoral; amputation above the elbow, a transtibial; amputation below the elbow, trans-radial; amputation below the elbow, and trans-humeral; amputation above the elbow [3].

The myoelectric approach is more advanced in the means of controlling a prosthetic limb that employs electromyography (EMG) signals produced by the user to accomplish control of the prosthetic hand. This is acquired from muscle motion contraction which produces an electrical signal when the electrodes are attached to the surface of the skin that can detect the muscle movements to control the prosthetic limb [4, 5]. The most popular are on/off, proportional, and pattern recognition control. The pattern recognition algorithm control will be one of the controls covered and implemented in this study. The concept of pattern recognition (PR) has been proven for improving the quality of controlling the upper prosthetic where the first generation has been built in the 1960s [6]. The pattern recognition algorithm method, with the EMG signal, is primarily according to the corresponding of a certain class of the prosthetic limb movement which is typically redundant with trials from the EMG signal patterns from the other classes.

The electromyogram (EMG) is a biological signal characterized by an electrical potential generated by muscle cells. The amplitude of EMG signals varies from (0–10 mV) and the frequency is low (0–500 Hz). The electromyogram signal has a prominent energy range of 50–150 Hz. EMG signals include a variety of data about the neurological system, as well as physical and psychological muscle qualities. Pre-processing is used to eliminate undesirable signal components from raw electromyograms (EMGs), such as motion artifacts or power line interference. The EMG signals are then windowed, and signal features are computed over each window. Signal features are classified into three types: time domain (TD), frequency domain (FD), and time–frequency domain (TFD), with each describing a distinct aspect of the signal [7].

This paper aims to develop an algorithm to detect the electromyography (EMG) signal using a convolutional neural network (CNN) and build a 3D-printed prosthetic arm controlled by the low-cost MyoWare muscle sensor using two-channel surface electrodes (sEMG). The motivation to carry out this project is to write a new computationally improved system using a pattern recognition (PR) algorithm to classify the fingers movement through the EMG signals taken on skin's surface when muscles are contracting, using low-cost sensor. The work also focuses on low number of electrodes/channels, which are only two in this work. Signals coming from only two channels are usually hard to classify due to the lack of information in categorizing the signal's behavior.

## 2 Literature Review

A study approach has been developed in accordance with the objectives that were outlined for this project. To accomplish the goal of the research, this will be put into action. The pattern recognition process that is based on sEMG control is comprised of several processes that are reliant on the collection of data, the conditioning of the signal, the window segmentation, the feature extraction, the classification, and finally the controlling in real time (refer Fig. 1). Signal acquisition noise, electromagnetic disturbances, signal instability, and motion artifacts induced by electrodes and connections are only some of the interferences that may be found in recorded EMG signals.

### 2.1 Pre-processing

In pattern recognition algorithms, the initial step taken on the raw signals is called pre-processing. Its purpose is to improve signal analysis by removing interferences that are intrinsic to the signal. Since the pre-processed EMG signal outputs have a random quality, they cannot be used as valid input for the pattern detection method. Therefore, to extract the descriptive properties, the window (segmentation) of the pre-processed data is required.

Different pre-processing techniques are used on the raw EMG data. Different types of filtering are usually used at this stage: the band-pass filter (BPF) cut-off frequency between 5 and 500 Hz, low-pass filter (LPF) cutting at 500 Hz, and high-pass filter (HPF). These sorts of filters have been employed in sEMG signals, starting from 5 Hz or sometimes higher. Additionally, the notch filter can also be applied at frequency between 50 and 60 Hz to suppress the power line interference (PLI). The filtered signals are then converted via analog-to-digital conversion into its digital form.

Table 1 shows the comparison of different combinations of filter type used, filter range in Hz, and sampling frequency in Hz from previous work carried out by other authors in pre-processing of sEMG signals. It can be seen from the table, that the

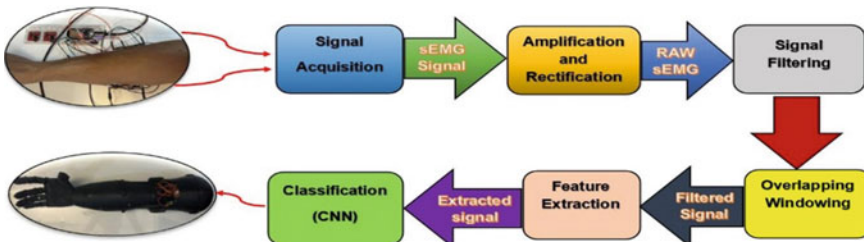


**Fig. 1** Sequence of pattern recognition process based on sEMG signals

**Table 1** Summary of filter type, range, and sampling frequency used by other authors

Authors	Filter typed	Filter range (Hz)	Sampling frequency (Hz)	Remarks
Wang [8]	Amplifier	5–1000	2400	AR coefficients
Paul [9]	BPF + Butterworth	15–500	500	Notch filter at 50 Hz
Al-Muifraje [10]	BPF + Butterworth	5–500	2000	Butterworth to remove PLI
Li [11]	BPF	10–500	1024	–
Shi [12]	BPF + Butterworth	20–500	2000	Fourth-order Butterworth/notch filter at 50 Hz
Qi [13]	LPF–HPF	950/750	2000	Third-order filter
Zhang [14]	BPF	20–500	1500	Notch filter at 50 Hz
Adewuyi [15]	BPF	30–350	1000	Eight-order Chebyshev filter
Geng [16]	HPF	60	1024	Five-order Butterworth
Nagashwathi [17]	BPF	20–450	1000	Notch filter at 50 Hz
Young [18]	HPF	20	1000	Third-order Butterworth
Bao [19]	HPF	20	1024	Third-order Butterworth

\* BPF=band-pass filter, HPF=high-pass filter, LPF=low-pass filter

frequency range for BPF is ranging from 5 to 500 Hz while HPF has cut-off frequency between 20 and 60 Hz. Sampling frequency varies from 500 to 2400 Hz with the majority of works recorded either having 1000 or 2000 Hz. In the remark's column, it can be observed that many authors are adding notch filter to their pre-processing of the sEMG signal due to the reason stated earlier.

### 2.1.1 Windowing

Processed EMG signals are divided into multiple segments or windows. Gesture detection figures out when a hand gesture starts and stops, based on the EMG signal's changes when muscles contract. Thus, the lengths of the segments change depending on how long the hand gestures are. The length of the window must be selected appropriately in real time to obtain a latency that is considered acceptable.

There are essentially two different methods of windowing, overlapping and non-overlapping (adjacent) windows. The sliding windowing techniques will divide the EMG signals into fixed segments that are either next to each other (adjacent sliding windowing) or overlap (overlapping sliding windowing) as shown in Fig. 2.

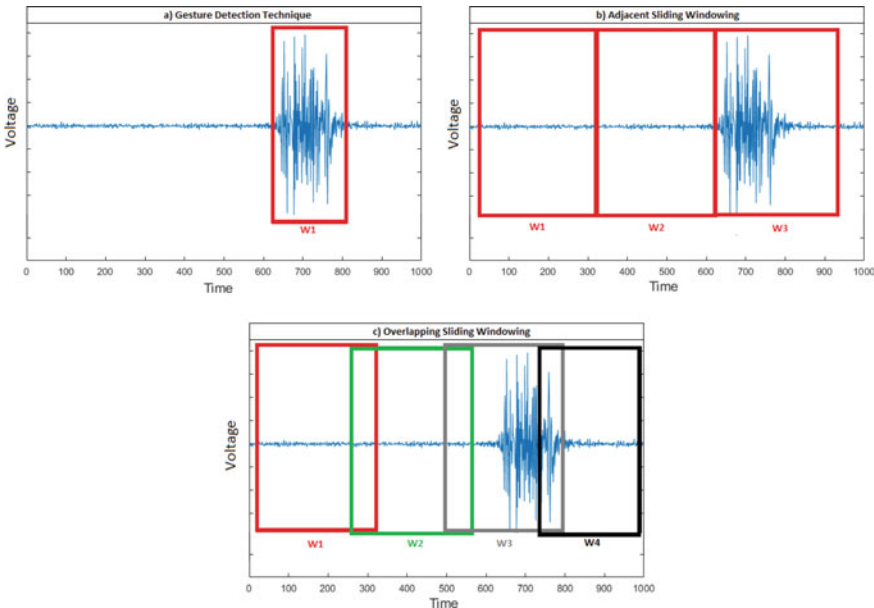


**Fig. 2** Segmentation of the EMG of a gesture using the three techniques: **a** gesture detection, **b** adjacent sliding windowing, and **c** overlapping sliding windowing [20]

For analysis and feature extraction, the former approach employs custom-length consecutive segments. Because of high-speed processors, the processing time is frequently shorter than the length of the time segment, causing the processor to be idle for a period of time. Overlapping windowing takes advantage of idle time to acquire extra data to process. The overlapping window technique is more suited in sEMG control systems because it yields better classification accuracy, a more consistent controller delay, and reduces the duration of the latency [21]. Overlapping between two successive segments often falls within the range of 0% (non-overlapping or neighboring windowing) to almost 100%. Adjusting this parameter allows one to make the most efficient use of available computational resources by determining the pace at which classes classifying are made.

The segment length (in terms of time samples) sets the relative importance of speed of reaction versus accuracy of classification. The accuracy of the classification would improve if the window length was increased, but this would result in a delay in reaching a decision. According to Englehart and Hudgins [22], a longer window length allows for more features to be extracted, resulting in higher classification accuracy, but a slower response time for the prosthetic controller. Whereas a shorter window length results in lower classification performance but a faster controller response.

Given that the windowing parameters used will have an impact on the extracted feature properties, it is critical to identify the best windowing settings that will result

**Table 2** Common window size and increments used by sample authors

Study	Analysis window length (ms)	Window increments (ms)	Window overlap (%)
Young [18]	250	50	80
Englehart [22]	256	32	87.5
Nahid [24]	250	50	80
Amsuss [25]	128	50	61
Shen [26]	200	100	50

in the extraction of an accurately robust feature set for multi-class limb movement intent decoding [23]. Despite this, several combinations of windowing settings have been published in earlier research with little or no explanation in their selection. Table 2 shows examples of window sizing, increments, and overlapping percentage used by other authors in their work in related studies.

## 2.2 Feature Extraction and Classification

Data will undergo signal processing and data normalization to achieve the desired level of consistency. After that comes the step-by-step process of feature extraction, in which each step is accompanied by an equation that defines the approach, and experimental data are provided so that a straightforward comparison can be made. In the end, the data will be fed into the algorithm to appropriately classify the movement.

Feature extraction is an essential part of signal processing analysis for improving classification performance in motion pattern recognition. The raw EMG signals are converted into a feature vector. Time domain (TD) features, frequency domain (FD) features, and time–frequency domain (TFD) features are the three primary types of features used in EMG signal analysis. Power spectrum density (PSD) information from the signals is included in FD features, which are derived using parametric techniques or a periodogram rather than TD features. In 1993, five TD features were introduced: mean absolute value (MAV), mean absolute value slope (MAV slope), slope sign changes (SSC), zero crossing (ZC), and waveform length (WL). Later, other approaches using root mean square (RMS), variance (VAR), and standard deviation (SD) were used to extract EMG signals for identification of hand movements.

There are numerous classifiers, including simple logistic regression (SLR), artificial neural networks (ANN), linear discriminant analysis (LDA), naive Bayes (NB), K-nearest neighbor (KNN), nonlinear logistic regression (NLR), multi-layer perceptron (MLP), and support vector machines (SVMs), among others. In EMG signals classification, the number of electrode channels (NCh) does influence the precision of classification process. It was determined that the accuracy rises with increasing number of channels [27].

**Table 3** Summary of EMG classes/channel, features, classifier, and accuracy by selected authors

Authors	Classes/Channels	Features	Classifier	Accuracy (%)
Zhang [28]	3/4	MAV, ZC, WL, SSC	LDA	95.4
Matsubara [29]	5/4	RMS	SVM	73 ± 13
Al-Timemy et al. [27]	15/6	6AR, RMS, WL, ZC, IAV, SSC	LDA	98.0
Liu [30]	7/57	TD, 6AR, RMS	LDA, KNN	97–98
Li [31]	7/6	MAV, ZC, SSC, WL	Boosted Random forests rejection	92
Pan [32]	7/7	MAV, ZC, WL, SSC	LDA	95.64

\*MAV—Mean absolute value, SSC—Slope sign changes, ZC—Zero crossing, WL—Waveform length, RMS—Root mean square, IAV—Integrated absolute value, TD—Time domain, AR—Augmented reality, LDA—Linear discriminant analysis, KNN— $K$ -nearest neighbor, SVM—Support vector machines

Table 3 shows the comparison of number of classes and channels used, type of features, and classifiers as well as the classification accuracy of some works done in the past by respective authors.

### 3 Methodology

The pattern recognition process based on sEMG control consists of a series of steps dependent on data collecting, signal conditioning, window segmentation, feature extraction, classification, and ultimately controlling in real time. Many interferences were present in the process of recording the EMG signals, including signal acquisition noise, electromagnetic disturbances, signal instability, and motion artifacts caused by electrodes and connections. Pre-processing is the first stage in pattern recognition algorithms for effective signal analysis and eliminating inherent interferences. Pre-processed EMG signal outputs are of a random character and are not considered a viable input for the pattern identification approach. Thus, the window (segmentation) of the pre-processed data is necessary to extract the descriptive characteristics.

Principally, there are two distinct windowing techniques: overlapping window and non-overlapping (adjacent) window. However, the overlapping windowing approach has been proposed to be implemented, and the window length must be chosen correctly in real time to achieve an acceptable latency. A longer window length would increase classification accuracy but would delay the classifier's performance. Then the data will be proceeded with a signal processing and data normalization to standardize the data. Following that, is the sequence of the feature extraction in which each procedure is defined by an equation, and experimental data are supplied for simple comparison. Finally, the data will be inputted into the algorithm to classify

the movement; accordingly, the analysis will be carried out in Python software using script files with the same sample size and segment length. Python was chosen due to its simplicity as well as the compatibility with a well-established library supported by other major deep learning frameworks, such as Theano and TensorFlow.

### 3.1 Data Acquisition Protocols

Initially, surface electrodes are placed on the individual's forearm to collect electromyographic data. The MyoWare muscle sensor with two channels and three electrodes was used to acquire the electromyographic data. Using the Nyquist theorem and a 12-bit analog-to-digital converter, the ESP32 microcontroller was used to gather EMG signals at a sampling frequency of 1000 Hz. The Nyquist theorem was used to determine the sampling frequency.

EMG channel-1 signals are largely taken from the extensor carpi ulnaris and extensor digitorum muscles, while channel-2 signals are mostly received from the flexor digitorum superficialis and palmaris longus muscles. While the common reference electrode was placed into the bone region, participants were instructed to sit on a comfortable chair with their forearm resting on a table as in Fig. 3.

The data was collected from ten individuals who did not undergo limb amputations. The subjects' age varies from 20 to 25 years old, with nine of them being male and one female. Each participant performs five distinct classes of unique finger motions in succession. These comprise the index (*I*), ring (*R*), little (*L*), hand close (HC), and middle classes (*M*) as shown in Fig. 4. Each participant was required to do six trials for each class, with each trial lasting for five seconds. The participants were given five minutes to rest their muscles between testing sessions. Following digitization, each channel has a total of 5000 sample points.

**Fig. 3** Sensor placement on the forearm of Subject A





**Fig. 4** Classes of individual finger movements

### 3.2 Data Pre-processing

It is necessary to apply the data structure to be able to use the most effective machine learning algorithms to classify the data that has been collected. Python programming was used to acquire the data, which was afterward saved in CSV file formats. There were ten folders containing all the subjects' data, with each folder including one of the five separate classes and six CSV file format trials. There are thus a total of thirty CSV files for each topic. Therefore, it was necessary to combine all the files containing the collected data into a single file as a first step. Since this technique needed Python code, it could only be implemented using the said programming language. The CSV file with the findings comprises around one million sample points across all classes. The data were collected in raw format as indicated in Fig. 5, which demonstrates that the signal contains noise and distortion. To mitigate these difficulties and analyze the signal, several filtering algorithms have been used.

Typically, the frequency of raw EMG signals spans from 10 to 500 Hz, with the major energy between lied between 50 and 150 Hz. Figure 6 demonstrates that within the signal frequency band, undesirable electrical noise may cause the emergence of certain rapid oscillations. In addition, movement artifacts or electrical networks may be the cause of slow oscillations, which have the potential to corrupt EMG data. It is feasible to eliminate these unwanted signals from the original EMG signal by using a fourth-order Butterworth and band-pass filter with cut-off frequencies between 20 and 450 Hz. Next, further analysis, such as calculating the mean values of the absolute EMG signal or obtaining other features, will not result in the negative and positive values of the EMG signals cancelling out due to their interaction [33]. In order to conclude the second step, the envelope of the filtered EMG signal was obtained. This was done because the resulting output gives a more realistic representation of the muscle-generated forces. Filtering removes the signal's inherent noise. Using

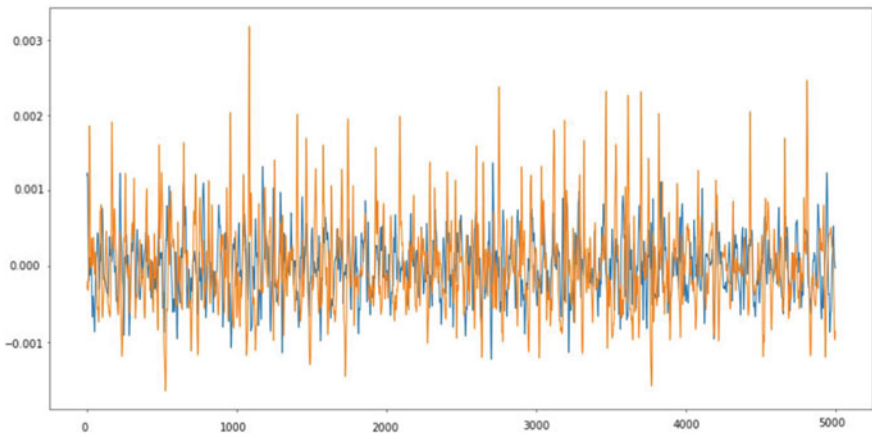


**Fig. 5** Raw EMG signal for two channels

a notch filter with cut-off frequencies of 49 and 52 Hz, more noise reduction was accomplished as shown in Fig. 6.

Table 4 shows the value of the cut-off frequency used in filtering the EMG signal in Fig. 6 with respect to the type of filter used. The remark column indicates the purpose of each filter.

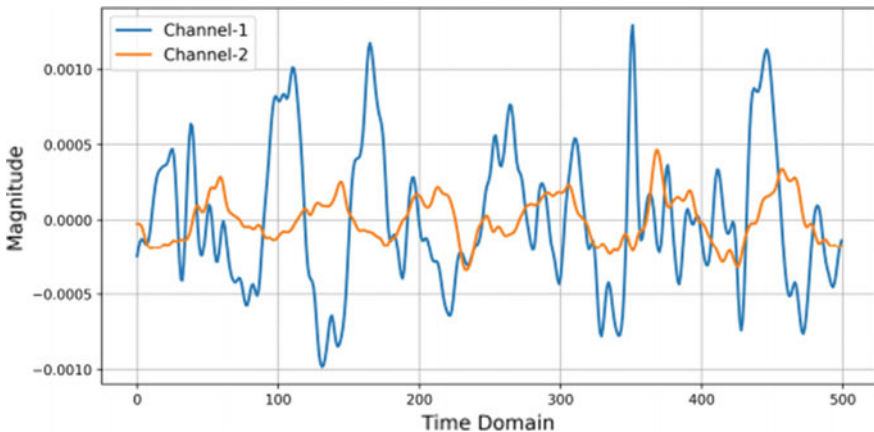


**Fig. 6** Filtered EMG signal from two channels sensor

**Table 4** Cut-off frequency of the filter used

Type of filter	Cut-off value (Reference)	Remarks
Notch filter	49 and 52 Hz	Remove the power line interface
Fourth-order Butterworth bandpass filter	20–450 Hz	Reduce the noise and motion artifact

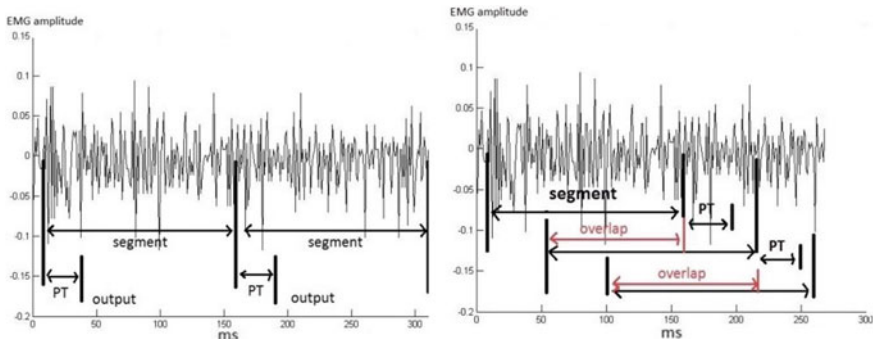
### 3.3 Data Segmentation and Windowing

Since the goal of the project is to achieve real-time control of the prosthetic limb, the size of the window should be reduced to make it possible to achieve an adequate response during real-time classification.

When considering both the window size and the amount of processing time needed to generate classified control instructions, the window size should be less than 300 ms. Data augmentation is required because the amount of dataset used by deep learning algorithms must be increased.

The overlapping windows technique (Fig. 7), which was proposed by most of the authors, is used in the dataset since it is the enhancement method that has shown to be most successful when it comes to EMG classification.

In addition, the overlapping windows result in strides that are shorter than the size of the window, rather than the motions being broken down into distinct periods of 250 ms (in this case 50 ms). When using a window that is 250 ms long with a stride length of 50 ms, which is equivalent to 250 samples per window with ten samples increment, the overlap that occurs between two successive windows is 250 ms, which is about 80% overlapped. When used inside a real-time classification system, this strategy results in more accurate prediction of the classes as well as more accurate control.

**Fig. 7** Two different windowing approaches: adjacent and overlapping

### 3.4 Feature Extraction

#### Time Domain (TD)

To effectively identify various classes, it is essential to choose the EMG signal's features accurately. To achieve this, features from the time and frequency domains must be extracted. However, because of the greater power discrimination and computational effectiveness of the extraction strategies, time domain characteristics are selected. Python was used to generate time domain characteristics for signal classification, such as mean absolute value (MAV), root mean square (RMS), variance (VAR), standard deviation (STD), and zero cross (ZC).

#### Data Normalization

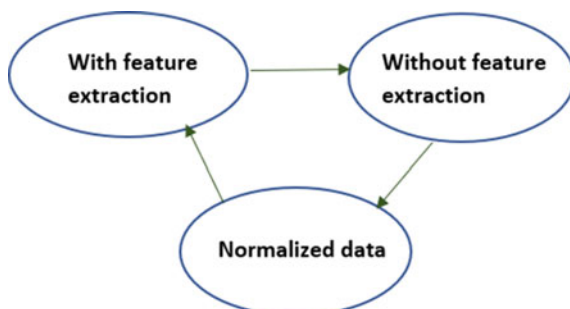
Normalization is a pre-processing technique used to standardize data. After extracting the useful information from the dataset by using the time domain approach, it is crucial to normalize and scale the data from 0 to 1 before training to reduce the computational time and learning speed.

$$x_{\text{normalization}} = \frac{x - m}{x_{\max} - x_{\min}}$$

$x$  is representing data point to normalize,  $m$  is the mean of the dataset,  $x_{\max}$  is the highest value, and  $x_{\min}$  the lowest value in the dataset. This technique is generally used in the inputs of data. The non-normalized data points with wide ranges can cause instability in convolutional neural networks. To compare the effectiveness of feature extraction approach for classifier, the normalized data were processed further into three categories as shown in Fig. 8.

- (i) normalized data with feature extraction, in which the different features described earlier are extracted from the normalized data;
- (ii) normalized data without feature extraction, in which the normalized data are used as inputs; and

**Fig. 8** Three types of inputs used for comparing the impacts of feature extraction methods on classification performance



- (iii) windowing data with feature extraction, a window of the size 250 ms with the increment of the size 50 ms is sliding over the normalized data and creating the overlapped “windowing data” before feature extraction is performed.

### 3.5 Classification Algorithm

The deep learning algorithms are completely implemented in Python. “TensorFlow” and “Keras” libraries are employed for developing networks. These libraries are well-known, powerful, and open-source software libraries for developing neural networks and machine learning methods. The training data and the testing data are separated 80% for the training dataset and 20% for the testing dataset. The CNN is constructed from three major layers: convolutional layers, pooling layers, and fully connected (FC) layers. However, the deep learning architectures of this project comprise of eight main layers, four convolutional layers, two pooling layers, one dropout layer, and one dense layer. Moreover, the first layer of the CNN model takes (250,2) as the input shape size which represents the window size and the number of EMG channels. Following with two convolutional layers with a kernel filter size of 8 and stride length is 1 with rectified linear unit (ReLU) activation function. Passing the layer with max pooling layer which takes the max pooling value with a pool size of 8 and stride of 8 resulting in a window size of  $8 * 8$  matrix and adding another two convolutional layers with the same value of kernel size window as the previous convolutional layer.

Finally, the output features of the previous layer are taken and applied to a fully connected layer. Drop out layer is used to reduce overfitting with a drop rate of 0.5. The last layer is the dense layer which contains the number of classes to train the network, which stand at four classes and the activation function that is applied in SoftMax which act as the classifier to map the non-normalized output. Figure 9 illustrates the overall architecture of the convolutional neural network (CNN). Table 5 on the other hand shows the hyperparameters value for the CNN used in the project.

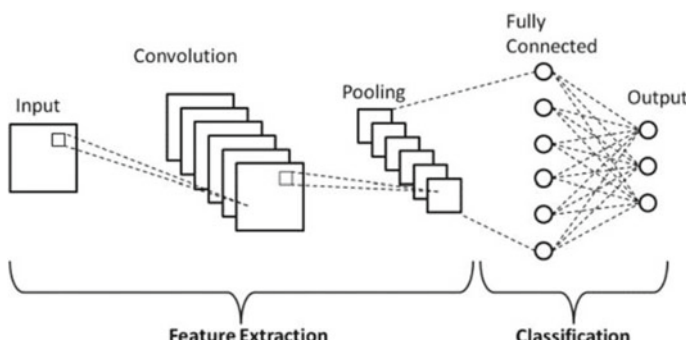


**Fig. 9** Architectures of the convolutional neural network (CNN) [34]

**Table 5** CNN selected hyperparameters

Batch size	32
Training epoch	100
Activation function	ReLU
Classifier	SoftMax
Optimizer	Adam
Loss function	Cross-entropy

### 3.6 Hardware Design

#### Electrical Circuit

Figure 10 shows the overall electrical control for the system which was implemented using a combination of microcontroller-microcomputer Raspberry Pi, servo motors motor driver, and ESP32 microcontroller. This technique enables the combination of the Raspberry Pi's processing power with the more flexible input/output of the specialized ESP32. The focus of the controller is to control to movement of a motorized arm prosthetic. Signals from the sEMG will be classified with respect to the finger's movement based on respective muscle contraction. The output from this will be sent to the motor controller to move the correct servo motor based on which finger should be moving.

The entire system was powered by a 7.4 V, 1500 mAh rechargeable lithium-polymer battery for the prosthetic arm to be portable. The ESP32 microcontroller is supplied by the Raspberry Pi's USB connection. The ESP32's 3.3 V output is then used to power the MyoWare EMG sensor. Servo motors can sustain a voltage of up to 6 V; however, the Raspberry Pi's maximum input voltage is only 5 V. As a result, it was determined that servo motors would run at 5 V to avoid extra complication

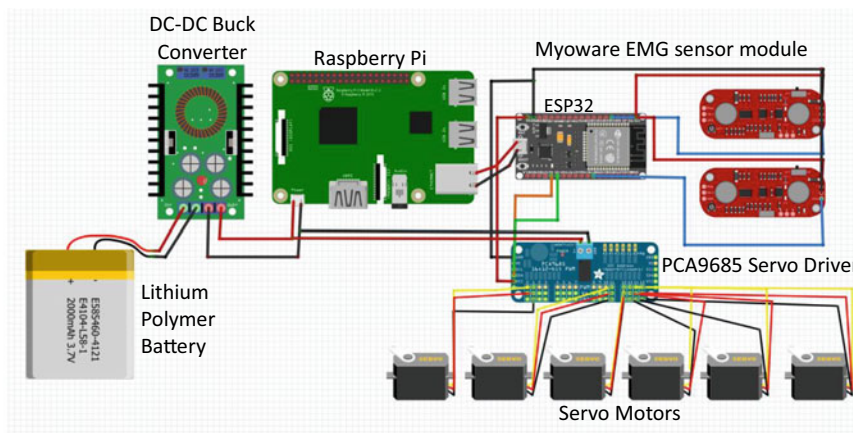


**Fig. 10** Electrical system architecture

on power converters. Thus, a high-power (300 W) DC-DC adjustable buck converter was used to lower the battery voltage to 5 V. Buck converters provide accurate voltage regulation, which is needed by sensitive electrical components in the system.

The intelligence component's pre-processing and classification process will be hosted by the Raspberry Pi while the sensor's signal collection and motor control will be controlled by the ESP32. ESP32 and Raspberry Pi will be connected to each other through ESP32's USB port and Raspberry Pi's USART serial communication protocol for the purpose of exchanging information (EMG signal control commands).

## Mechanical Design

A well-designed mechanical system that accurately reflects the functioning of the human arm is essential for developing a practical myoelectric prosthesis. Mechanical design considers a wide range of factors, including the sorts of forces acting on the system and how the joints are activated. The prosthetic arm was designed and fabricated using 3D printer and some commonplace equipment. Tendons may be made from any high-strength line that doesn't give when tightly pulled. Tension is applied to these lines, which leads to the fingers' movement, through servo motors located in the forearm by gently pulling on the tendons. These servo motors should be located as near to the fingers as feasible yet their bulk feature prevented them from stowing in the palm area. The motors are then hidden inside the forearm instead.

SolidWorks is used for 3D modeling of the mechanical assemblies and parts of the prosthetic arm. There are three printed pieces that make up each finger, and they're held together using polypropylene pins. The synthetic tendon is looped around the finger's inner tip to provide a locking point for the tendons. This tendon forms a closed loop inside the finger by following passageways within the tissue. All the joints of the finger are subjected to rotational stresses, and the finger curls upwards when the tendon is pulled.

The tendon locking point is crucial so that when the tendon is tense, it pulls the tip of the finger and forces all joints to spin. When the finger is closed, tension is applied to the opposite end of the tendon to open it. To achieve this tension, a high-quality braided fishing line was employed, since it stretches very little. Nylon fishing line would stretch over time resulting in a loss of tension which would severely influence finger motions. Tendons in the biological human hand operate in a similar way, but there are significantly more biological tendons connecting to distinct bones, allowing for more exact control of the fingers.

Figure 11 illustrates the 3D-printed model of an index finger of the prosthetic arm with its joint and artificial tendon location. It shows the tendon line with its respective movement at the joint whenever the respective servo motor controlling the finger receives a triggered signal from the ESP32 microcontroller.

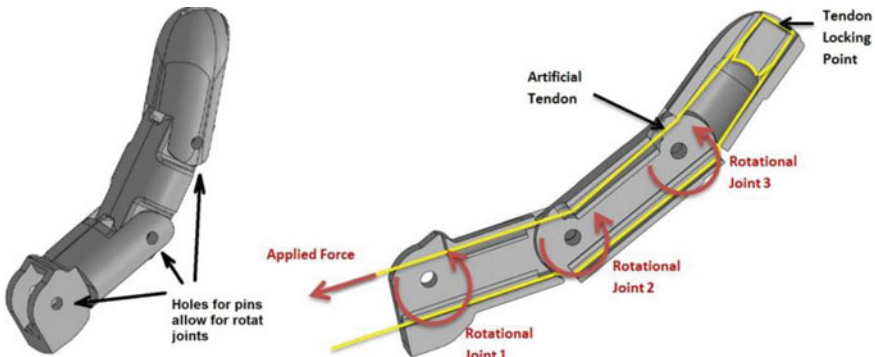


**Fig. 11** Index finger model with the tendon line movement mechanism

## 4 Results and Discussion

The selection of features is one of the most important factors in getting strong classifier performance. The CNN classifier's performance is dependent on time domain features, which are computationally less costly than frequency domain features. Because the signal's causal nature is being employed, selecting the proper characteristic is much more important. Thus, different combinations of time domain feature extraction have been investigated to compare the accuracy of the classes.

According to most of the literature, the combination of MAV, STD, ZC, VAR, and RMS usually produce excellent performance in sEMG-based movement classification. Therefore, the study had been carried out to observe the performance of the best possible combinations of the time domain applied. Table 6 summarizes some of the best results of feature combinations done through this work.

Different combinations of feature extraction are used to compare the accuracy of the algorithm. It can be observed from Table 6 according to the findings of the research on features, a combination of features specifically the MVA + RMS + VAR + STD + ZC combination produced a higher classification accuracy compared with results obtained using three features. This is because more data information can be fed to the algorithm. The performance was obtained for the deep learning

**Table 6** Summary of TD investigated in the study

Feature combinations	Classification accuracy (%)
RMS + MAV + SSC	95.42
RMS + MAV + WL	96.02
RMS + MAV + VAR + WL	96.68
RMS + MAV + VAR	95.62
MAV + WL + SSC	95.5
MAV + RMS + VAR + STD + ZC	98.46

network (CNN) trained on six distinct overlapping window lengths (150, 200, 250, 256, 300 and 350 ms) for each subject. For making a comparison regarding the two increment strides, the maximum accuracy of each of the methods was investigated on each overlapping window length (25 and 50 ms). It was decided not to consider any windows with a duration of more than 350 ms since anything lasting longer than that, in addition to the classification time, would influence the real-time performance of the assistive solutions.

This may be attributable to the decreased number of classes, as well as the narrower activity of interest and the optimization of the hyperparameters. Choosing the window's length for real-time predictions should be based on several factors such as accuracy level, post-processing technique, and processing delay. The CNN algorithm's inherent nature causes it to scan the complete training set for each prediction. This might lead to increased delays and memory limitations during real-time predictions. These reasons combined with low classification accuracy cause it to be unsuitable for real-time predictions.

As shown in Fig. 12, the larger the window size is, the higher the performance gain is achieved by the model and vice versa. However, response time is a crucial component of the prosthetic hand. Longer reaction time may lead to worse output. Nevertheless, numerous instantaneous reactions accompanied by imprecise motions may result in annoyance or even rejection of the prosthesis. For the development of the prosthetic hand, establishing a balance between response speed and reliability or accuracy of classification is vital.

For this project, the window size and stride are the primary characteristics that contribute to a model's computational complexity. Large window sizes need more processing power and memory and can increase response time. Stride, on the other hand, represents the frequency with which the model makes choices; consequently, a lower stride would increase the processor's activity rate, as well as calculation cost and power use. For real-time judgments, majority voting is often seen as an efficient tactic that may improve overall dependability. The outcome of scattering feature extraction. The distribution of data shown in Fig. 13 is extremely obvious and does

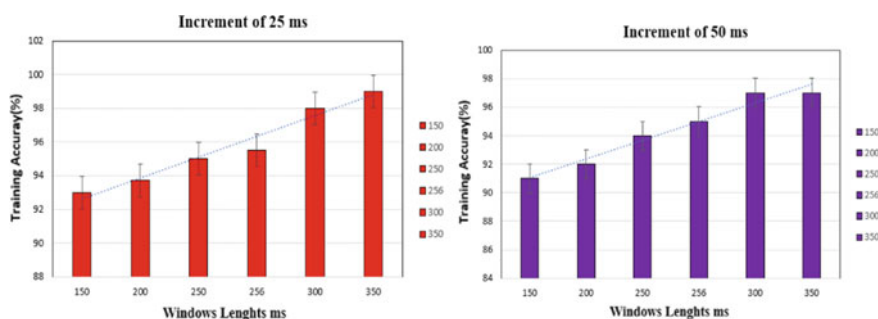
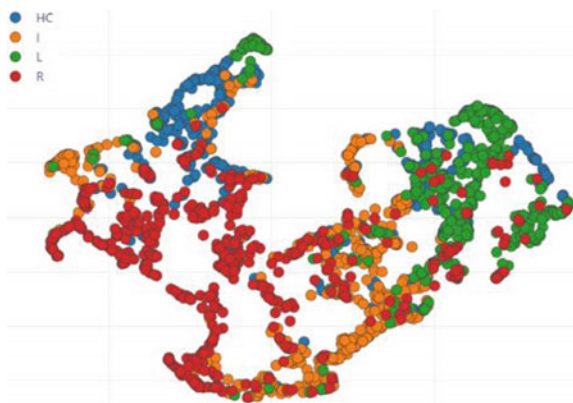


**Fig. 12** Different window sizes and accuracy with and incitement of 25 and 50 ms

**Fig. 13** Scatter plot of the feature extraction



not correspond with the data. Evidently, it shows that there are certain data points that overlap or are combined in other regions of movement.

Due to the large quantity of data, the Euclidean distance value for the feature is affected. The number of high-value data is bigger than the number of coincidence data. The class separability perspective is important for determining the effectiveness of the EMG characteristics. If quality in class separability can be established, the rate of misclassification will be minimal. To put it another way, the intended outcome is to have the least amount of similarity or variance among features of the same class while having the greatest amount of distance across groups.

The performance of classification is evaluated via the use of scatter graphs showing the relationships between characteristics retrieved from the muscle channel and the various movements. Figure 14 depicts the accuracy and loss curve based on the number of epochs. The precision plot simply represents the guesses properly identified by CNN. The training is parameterized at 100 epochs with a learning rate of 0.01, such that the network fine-tunes its weights in the final 50 training epochs. With these settings, the network exhibits behavior that achieves an accuracy of around 90% before the 20th epoch, with a little dip from the 50th to the 55th epoch. Finally, in training, it reaches 98% accuracy. Validation drops reaching 97% in the final period. The model's performance shows a good fit with no overfitting or underfitting.

The confusion matrix derived from the research is shown in Fig. 15 which represents the predicted classes and the errors. Moreover, when it comes to the performance of EMG-based activity classification accuracy, it often leads to an error known as the accuracy trap. The model's overall accuracy does not communicate the overall generalization across all the classes, which is essential for accurate classification. Besides accuracy, the most important parameters for selecting the best model are prediction delay and model size. It was also desired for the scope of this project to design a robotic hand that is smaller, lighter, and more realistic than the robotic hand designs that can be found online.

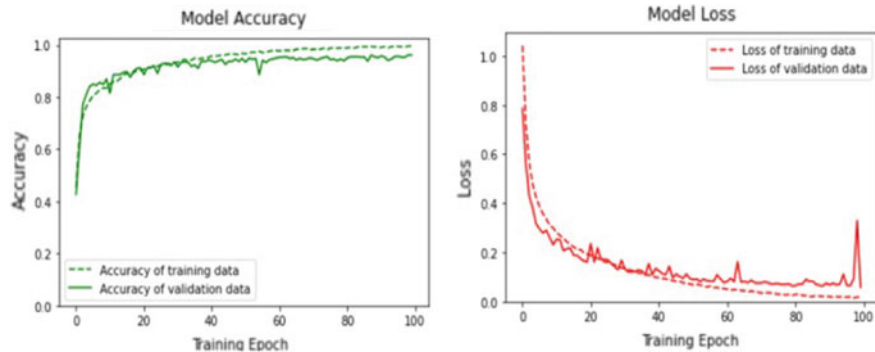
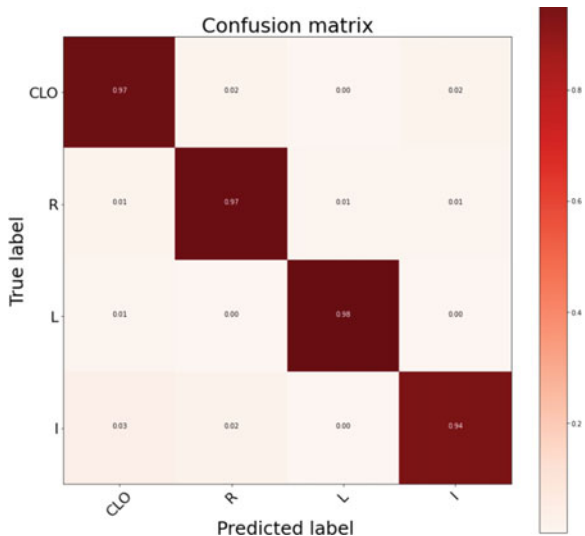


**Fig. 14** Model training accuracy and loss accuracy from the collected dataset

**Fig. 15** Confusion matrix



## 5 Conclusion

In this paper, a machine learning strategy to classify EMG signals using two channels of a low-cost sEMG MyoWare is presented. This method, which trains and recognizes finger motions using sEMG data, is showing promising output while using lesser channels than previous studies and employing convolutional layer neural network approach. The dataset was collected from ten participants who did not have amputated limbs. Each participant completed six exercises for one class, with a five-second time limit on each exercise. The training for each finger movement only requires four trials, while the verification only requires two trials; this corresponds to an accuracy rate of eighty percent and twenty percent, respectively. There were several different combinations of time domains that were investigated and evaluated for

feature extraction and output to feed into the network for training and verification purposes. This method achieved a level of accuracy of more than or equal to 98% when it was tested on different people using the five-finger movement classification.

**Acknowledgements** Part of this work was supported by the UOW Malaysia KDU Research Grant 2022 (UOWMKDURG/2020/1/004).

## References

1. Xu, K., et al.: A prosthetic arm based on EMG pattern recognition. In: International Conference on Robotics and Biomimetics IEEE, Qingdao, China, pp. 1179–1184 (2016)
2. Mark, M.: Sensory feedback system for prosthetic arms. MSc Thesis, University of Salford Manchester (2015)
3. Bennett Wilson, A.: History of Amputation Surgery and Prosthetics (Digital Resource Foundation), p. 3
4. Adhikari, S.: EMG controlled Prosthetic-Hand, Experiment Finding, Tribhuvan University, p. 53
5. Simatupang, J.W., Wijaya, W., Tyler, D., Mavridis, C.: Simulation analysis of equivalent circuit model of skin-electrode impedance for transcutaneous electric simulation. Bull. Electric. Eng. Inf. **10**(4), 1936–1943 (2021)
6. Touillet, A., et al.: Characteristics of phantom upper limb mobility encourage phantom-mobility-based prosthesis control. Sci. Rep. **8**, Article number: 15459 (2018)
7. Tool, J., et al.: Classification of EMG signal based on time domain and frequency domain features. Int. J. Human Technol. **1**, 25–30 (2017)
8. Wang, J.Z., et al.: EMG signal classification for myoelectric teleoperating a dexterous robot hand. In: Annual International Conference of the IEEE Engineering in Medicine and Biology Society, Shanghai, China, pp. 5931–5933 (2005)
9. Paul, Y., et al.: Comparative analysis between SVM and KNN classifier for EMG signal classification on elementary time domain features. In: Proceeding 4th International Conference on Signal Processing, Computing and Control (ISPCC), Solan, India, pp. 169–175 (2018)
10. Mahmood, N.T., et al.: Upper prosthetic design based on EMG: a systematic review. IOP Conf. Ser.: Mater. Sci. Eng. 978 012025 (2020)
11. Li, X. et al.: Increasing the robustness against force variation in EMG motion classification by common spatial patterns. In: Proceedings 39th Annual International Conference of the IEEE Engineering in Medicine and Biology Society (EMBC), Jeju, South Korea, pp. 406–409 (2017)
12. Shi, C., et al.: i-MYO: A Hybrid Prosthetic Hand Control System based on Eye-tracking, Augmented Reality and Myoelectric signal. <https://doi.org/10.48550/arXiv.2205.08948>
13. Qi, S., et al.: Recognition of composite motions based on sEMG via deep learning. In: 14th IEEE Conference on Industrial Electronics and Applications, Xian, China, pp. 31–36 (2019)
14. Zhang, A., et al.: Combined influence of classifiers, window lengths and number of channels on EMG pattern recognition for upper limb movement classification. In: Proceeding 11th International Congress on Image and Signal Processing, BioMedical Engineering and Informatics, Beijing, China, pp. 1–5 (2019)
15. Adewuyi, A., et al.: An analysis of intrinsic and extrinsic hand muscle EMG for improved pattern recognition control. IEEE Trans. Neural Syst. Rehabil. Eng. **24**(4), 485–494 (2016)
16. Geng, Y., et al.: A strol. IEEE Access **6**, 38326–38335 (2018)
17. Nagaswathi, A., et al.: A machine learning system for classification of EMG signals to assist exoskeleton performance. In: Proceeding IEEE Applied Imagery Pattern Recognition Workshop (AIPR), Washington DC, USA, pp. 1–4 (2019)

18. Young, A.J., et al.: Classification of simultaneous movements using surface EMG pattern recognition. *IEEE Trans. Biomed. Eng.* **60**(5), 1250–1258 (2013)
19. Bao, T., et al.: Surface-EMG based wrist kinematics estimation. In: Proceeding IEEE 16th International Conference on Wearable and Implantable Body Sensor Networks (BSN), Chicago, USA, pp. 1–4 (2019)
20. Jaramillo-Yáñez, A., Benalcázar, M.E., Mena-Maldonado, E.: Real-time hand gesture recognition using surface electromyography and machine learning: a systematic literature review. *Sensors* **20**(9), 2467 (2020)
21. Oskoei, M.A., Hu, A.: Myoelectric control systems—a survey. *Elsevier Biomed. Sig. Proc. Control* **2**, 275–294 (2007)
22. Englehart, K. et al.: A robust, real-time control scheme for multifunction myoelectric control. *IEEE Trans. Biomed. Eng.* **50**(7), 848–854 (2003)
23. Smith, L.H.: Determining the optimal window length for pattern recognition-based myoelectric control: balancing the competing effects of classification error and controller delay. *IEEE* **192** (2010)
24. Nahid, N., et al.: Deep learning based surface EMG hand gesture classification for low-cost myoelectric prosthetic hand. In: Proceeding 2020 Joint 9th International Conference on Informatics, Electronics and Vision (ICIEV) and 2020 4th International Conference on Imaging, Vision and Pattern Recognition (icIVPR), Kitakyushu, Japan, pp. 1–8 (2021)
25. Amsüss, S., et al.: Self-correcting pattern recognition system of surface EMG signals for upper limb prosthesis control. *IEEE Trans. Biomed. Eng.* **61**(4), 1167–1176 (2014)
26. Shen, S., et al.: Movements classification of multi-channel sEMG based on CNN and stacking ensemble learning. *IEEE Access* **7**, 137489–137500 (2019)
27. Al-Timemy, A.H., et al.: Classification of finger movements for the dexterous hand prosthesis control with surface electromyography. *IEEE J. Biomed. Health Inf.* **17**(3), 608–618 (2013)
28. Zhang, X., et al.: Real-time implementation of a self-recovery EMG pattern recognition interface for artificial arms. In: Proceeding 35th Annual International Conference of the IEEE Engineering in Medicine and Biology Society (EMBC), Osaka Japan, pp. 5926–5929 (2013)
29. Matsubara, T., et al.: Bilinear modeling of EMG signals to extract user-independent features for multiuser myoelectric interface. *IEEE Trans. Biomed. Eng.* **60**(8), 2205–2213 (2013)
30. Liu, J., Zhou, P.: A novel myoelectric pattern recognition strategy for hand function restoration after incomplete cervical spinal cord injury. *IEEE Trans. Neural Syst. Rehabil. Eng.* **21**(1), 96–103 (2013)
31. Li, Z., et al.: Boosting-based EMG patterns classification scheme for robustness enhancement. *IEEE J. Biomed. Health Inf.* **17**(3), 545–552 (2013)
32. Pan, L., et al.: Continuous estimation of finger joint angles under different static wrist motions from surface EMG signals. *Biomed. Sig. Proc. Control* **14**, 265–271 (2014)
33. Emiliano-Noce, et al.: EMG and ENG-envelope pattern recognition for prosthetic hand control. *J. Neurosci. Meth.* **311**, 38–46 (2019)
34. Ogundokun, R.O., Maskeliunas, R., Misra, S., Damaševičius, R.: Improved CNN based on batch normalization and Adam optimizer. In: Proceedings of the International Conference on Computational Science and Its Applications, Malaga, Spain, Springer: Cham, Switzerland, pp. 593–604 (2022)

# Iterative Hard Thresholding Algorithm Using Norm Exponent



Bamrung Tausiesakul and Krissada Asavaskulkiet

**Abstract** Due to numerous data that is required to transfer in the information age, there is an increasing demand of computation and memory usage. Compressed sensing (CS) appears to be a promising technique in order to save both the computation and data storage. Iterative hard thresholding (IHT) is one of the signal recovery methods in the CS. Despite its fast computation, the IHT often delivers poor performance in the signal reconstruction accuracy. To solve this issue, we present an improved IHT in this work by using the fractional norm. Numerical simulation is demonstrated to illustrate better accuracy of the signal reconstruction than former approaches in various scenarios.

**Keywords** Compressive sensing · Iterative hard thresholding · Fractional norm

## 1 Introduction

As an emerging field, many applications draw on compressed sensing in science and engineering, e.g., imaging and vision [22], photonic mixer device [9], electronic defence [20], security and cryptosystem [26], radar [1, 18], earth observation [7], wireless networks [14, 16], biometric watermarking [27], healthcare [15], etc.

To cover the aforementioned applications, we consider the problem of determining an unknown signal in a vector form, denoted by  $\mathbf{x} \in \mathbb{R}^{N \times 1}$ , where  $N$  is the number of data points from discrete-time sampling. According to Fig. 1, the unknown signal  $\mathbf{x}$  is passed onto a system that has a linear transfer function in a matrix form as  $\mathbf{A} \in \mathbb{R}^{M \times N}$ , where  $M$  is the length of the data we can observe. However, during the transfer of data through the system, there might be an additive noise, denoted by  $\delta_b \in \mathbb{R}^{M \times 1}$ , that

---

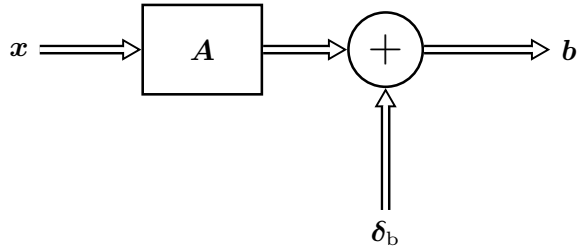
B. Tausiesakul

Department of Electrical Engineering, Faculty of Engineering, Srinakharinwirot University, 63 Mu 7, Rangsit-Nakhonnayok Road, Canal 16, Ongkharak, Nakhonnayok 26120, Thailand

K. Asavaskulkiet

Department of Electrical Engineering, Faculty of Engineering, Mahidol University, 999, Phutthamonthon Sai 4 Road, Salaya, Phutthamonthon, Nakhon Pathom 73170, Thailand  
e-mail: [krissada.asa@mahidol.edu](mailto:krissada.asa@mahidol.edu)

**Fig. 1** A noisy linear input-output system



can occur due to imperfect electronic elements or other environmental disturbance. Finally, the signal that can be observed by a sensor is sampled in time and collected in a vector, namely  $\mathbf{b} \in \mathbb{R}^{M \times 1}$ .

Typically, the relation between  $M$  and  $N$  plays a crucial role in Fig. 1. For  $M > N$ , the system is overdetermined and would encounter no serious issue in finding the unknown  $\mathbf{x}$ , whenever the transfer function matrix  $A$  is of full rank. Since the number of observed data points is greater than the length of the data we want to determine, this scenario is known as an overdetermined system. This category is well studied in the past. However, in the past few decades, numerous amounts of data have been increasingly flowing throughout everyday life due to the information age. There is a demand of compressing the data by setting  $M < N$ , which would cause an underdetermined system. This scenario would never have been solvable, except that one may know a priori knowledge of the desired signal  $\mathbf{x}$ . In many situations, it is discovered that the signal imposes only a limited number of nonzero elements, denoted by  $K$ , which can be even less than  $M$ . Even if the signal may not have zero in its elements, after a transformation technique one can find that the signal possesses only a few frequencies [5, 10] and this condition is sufficient to perform a sparse signal recovery. The remaining task in this framework appears to be how to recover the unknown data  $\mathbf{x}$ .

There are many techniques that have been proposed to recover the sparse data [4, 6, 8, 11–13, 23]. One of these is iterative hard thresholding (IHT). This iterative computation approach was proposed in [2, 3]. Let  $\cdot^\top$  be the transpose operator for a vector or a matrix. Let  $\cdot^{-1}$  be the inverse operator for a square matrix. In [24], the Moore-Penrose inverse (MPI) for an underdetermined case, denoted by  $A^\top(AA^\top)^{-1}$ , is proposed to cope with the traditional IHT. The inverse  $(AA^\top)^{-1}$  would have no serious issue, since the rank of  $AA^\top$  is equal to  $M$ , i.e., the matrix  $AA^\top$  is of full rank. In [19], the IHT is improved by incorporating another form of the MPI in the overdetermined case, i.e.,  $(A^\top A)^{-1} A^\top$ , into the conventional IHT. Unfortunately, the matrix inverse  $(A^\top A)^{-1}$  cannot be done easily, since the rank of  $A^\top A$  is only  $M$ . As its size is  $N \times N$ , the matrix  $A^\top A$  is rank-deficient for  $N > M$ . To make it of full rank, the matrix  $(A^\top A)^{-1} A^\top$  is regularized by a positive constant  $\varepsilon$  in the form of  $(A^\top A + \varepsilon I)^{-1} A^\top$ . In [28], the matrix  $A^\top$  is replaced by the pseudo inverse of its best rank- $M$  approximation, which requires an intensive computation of the singular value decomposition.

In this work, we pay attention to signal recovery methods, especially for higher precision or lower error from the reconstruction of a compressed signal. A new improved version of the IHT is presented. It adopts a fractional norm with a norm exponent  $p$ . According to earlier works, we adopt the case of  $p < 1$ , which would provide the benefit to signal sparsity recovery.

Contribution of this work is a new method of the sparse signal reconstruction. We provide a new updating formula that can be incorporated in the IHT. An iterative computation algorithm in a similar way to the IHT is introduced with the aim to increase the signal reconstruction accuracy. Numerical examples are conducted to demonstrate the benefit of this proposed method.

## 2 Iterative Hard Thresholding

With regard to the linear system, the relation among all variables in Fig. 1 can be written as

$$\mathbf{b} = \mathbf{A}\mathbf{x} + \boldsymbol{\delta}_b, \quad (1)$$

where  $\mathbf{x} \in \mathbb{R}^{N \times 1}$  is the vector of the desired signal, written as

$$\mathbf{x} = [x_1 \ x_2 \ \dots \ x_N]^T. \quad (2)$$

The vector  $\mathbf{x}$  might be sparse. In other words, some elements of  $\mathbf{x}$  can be zeros. We assume that the number of nonzero elements in  $\mathbf{x}$  is  $K$ , i.e.,

$$\lim_{p \rightarrow 0} \|\mathbf{x}\|_p^p = K, \quad (3)$$

where  $\|\cdot\|_p^p$  is the  $\ell_p$  norm and  $\lim_{p \rightarrow 0} \|\cdot\|_p^p$  is the pseudo zero norm that counts the number of nonzero elements in the vector. The compressive sensing problem is the minimization with respect to the unknown variable  $\mathbf{x}$  of the form

$$\begin{aligned} \hat{\mathbf{x}}_{\ell_0} &= \arg \min_{\mathbf{x}} \lim_{p \rightarrow 0} \|\mathbf{x}\|_p^p \\ \text{s.t. } \mathbf{x} &\in \begin{cases} \{\mathbf{u} | \mathbf{A}\mathbf{u} = \mathbf{b}\}, & \text{noiseless,} \\ \{\mathbf{u} | \|\mathbf{A}\mathbf{u} - \mathbf{b}\|_2 < \epsilon_b\}, & \text{noisy,} \end{cases} \end{aligned} \quad (4)$$

where  $\epsilon_b$  is a threshold that accounts for a noise energy. The pseudo zero norm  $\lim_{p \rightarrow 0} \|\mathbf{x}\|_p^p$  is a non-differentiable function. An approximation of the problem in (4) is given by the regularization in the form of

$$\hat{\mathbf{x}}_{\ell_0} \approx \arg \min_{\mathbf{x}} \|\mathbf{A}\mathbf{x} - \mathbf{b}\|_2^2 + \rho \lim_{p \rightarrow 0} \|\mathbf{x}\|_p^p, \quad (5)$$

where  $\rho$  is the regularization parameter. Proximal gradient method is a generalized form of the projection that can be used to solve various non-differentiable convex optimization problems [21]. By using the proximal technique, one can end up with a hard decision. The IHT algorithm is a gradient-descent method that converges linearly [2, 3]. Let  $\mathbf{h}_K(\mathbf{x}) : \mathbb{R}^{N \times 1} \mapsto \mathbb{R}^{N \times 1}$  be the vector that keeps only  $K$  elements of  $\mathbf{x}$ . All  $K$  elements in  $\mathbf{x}$  that are to be kept in  $\mathbf{h}_K(\mathbf{x})$  are largest in the absolute-value sense, compared to the remaining  $N - K$  elements of  $\mathbf{x}$ . The remaining  $N - K$  elements of  $\mathbf{h}_K(\mathbf{x})$  are finally set to be zeros. Let  $\|\cdot\|_2$  be the  $\ell_2$  norm of the vector. Let  $\mathbf{0}$  be the vector that contains only zeros of a corresponding size. The IHT algorithm can be summarized as follows.

---

**Algorithm 1** Iterative Hard Thresholding [2, 3]

---

**Input:**  $A \in \mathbb{R}^{M \times N}$ ,  $\mathbf{b} \in \mathbb{R}^{M \times 1}$ ,  $K \in \mathbb{Z}_+^{1 \times 1}$ ,  $I_{\max} \in \mathbb{Z}_+^{1 \times 1}$ ,  $\epsilon_{\min} \in \mathbb{R}_+^{1 \times 1}$ ,  $\mu \in \mathbb{R}_+^{1 \times 1}$   
**Output:**  $\hat{\mathbf{x}}_h \in \mathbb{R}^{N \times 1}$

```

 $\hat{\mathbf{x}}[0] \leftarrow \mathbf{0}$ 
 $i \leftarrow 0$ 
 $\epsilon_{\hat{\mathbf{x}}} \leftarrow \epsilon_{\min} + 1$ 
while  $\epsilon_{\hat{\mathbf{x}}} > \epsilon_{\min} \wedge i \leq I_{\max}$  do
     $i \leftarrow i + 1$ 
     $\hat{\mathbf{x}}[i] \leftarrow \mathbf{h}_K \left( \mathbf{x} + \mu A^T (\mathbf{b} - A\mathbf{x}) \Big|_{\mathbf{x}=\hat{\mathbf{x}}[i-1]} \right)$ 
     $\epsilon_{\hat{\mathbf{x}}} \leftarrow \frac{\|\hat{\mathbf{x}}[i] - \hat{\mathbf{x}}[i-1]\|_2}{\|\hat{\mathbf{x}}[i-1]\|_2}$ 
end while
return  $\hat{\mathbf{x}}[i]$ 

```

---

It is fruitful to realize that an iterative method, known as Landweber's iteration [17], for a linear system  $A\mathbf{x} \approx \mathbf{b}$  is given by

$$\mathbf{x}[i] = \mathbf{x}[i-1] + A^T(\mathbf{b} - A\mathbf{x}[i-1]), \quad (6)$$

where  $i$  is the iteration index. Comparing (6) to Algorithm 1, one can see that the IHT is an approach that applies the hard decision  $\mathbf{h}_K(\cdot)$  to the Landweber's iteration.

### 3 Iterative Hard Thresholding with Norm Exponent

In this work, we propose an iterative computation in the form of

$$\mathbf{x}[i+1] = \mathbf{x}[i] + A^T \mathbf{b} - \left( A^T A + \frac{1}{2} \rho p \mathbf{D}(|\mathbf{x}[i]|^{p-2}) \right) \mathbf{x}[i]. \quad (7)$$

The Algorithm 1 can thus be modified to adopt (7) as follows.

**Algorithm 2** Iterative Hard Thresholding with Norm Exponent

---

**Input:**  $A \in \mathbb{R}^{M \times N}$ ,  $\mathbf{b} \in \mathbb{R}^{M \times 1}$ ,  $K \in \mathbb{Z}_+^{1 \times 1}$ ,  $I_{\max} \in \mathbb{Z}_+^{1 \times 1}$ ,  $\epsilon_{\min} \in \mathbb{R}_+^{1 \times 1}$ ,  $\mu \in \mathbb{R}_+^{1 \times 1}$ ,  $\rho \in \mathbb{R}_+^{1 \times 1}$ ,  $p \in [0, 2]$

**Output:**  $\hat{\mathbf{x}}_h \in \mathbb{R}^{N \times 1}$

```

 $\hat{\mathbf{x}}[0] \leftarrow \mathbf{0}$ 
 $i \leftarrow 0$ 
 $\epsilon_{\hat{\mathbf{x}}} \leftarrow \epsilon_{\min} + 1$ 
while  $\epsilon_{\hat{\mathbf{x}}} > \epsilon_{\min} \wedge i \leq I_{\max}$  do
     $i \leftarrow i + 1$ 
     $\hat{\mathbf{x}}[i] \leftarrow \mathbf{h}_K \left( \mathbf{x} + \mu (A^\top \mathbf{b} - (A^\top A + \frac{1}{2} \rho p D(|\mathbf{x}|^{p-2})) \mathbf{x})|_{\mathbf{x}=\hat{\mathbf{x}}[i-1]} \right)$ 
     $\epsilon_{\hat{\mathbf{x}}} \leftarrow \frac{\|\hat{\mathbf{x}}[i] - \hat{\mathbf{x}}[i-1]\|_2}{\|\hat{\mathbf{x}}[i-1]\|_2}$ 
end while
return  $\hat{\mathbf{x}}[i]$ 

```

---

There are two additional parameters that we need to supply to Algorithm 2, such as  $\rho$  and  $p$ . Numerical simulation in the next section will demonstrate possible regions one can pick up a value for the regularization parameter  $\rho$  or the norm exponent  $p$ .

## 4 Numerical Examples

The performance metrics we use to compare different IHT algorithms include

- root-mean-squared-relative error (RMSRE), which is given by

$$\text{RMSRE} = \sqrt{\mathcal{E}_{\mathbf{A}, \mathbf{x}_0, \text{supp}(\mathbf{x}_0)} \left\{ \frac{\|\hat{\mathbf{x}} - \mathbf{x}_0\|_2^2}{\|\mathbf{x}_0\|_2^2} \right\}}, \quad (8)$$

where  $\mathcal{E}_{\mathbf{y}}\{\cdot\}$  is the expectation of the quantity  $\cdot$  with respect to the random variable  $\mathbf{y}$ ,  $\mathbf{x}_0 \in \mathbb{R}^{N \times 1}$  is the true value of  $\mathbf{x}$ ,  $\text{supp}(\mathbf{x}_0)$  is the set that contains nonzero indices of the elements in  $\mathbf{x}_0$ , and  $\|\cdot\|_2$  is the  $\ell_2$  norm,

- standard-deviation mean (SDM), which is given by

$$\text{SDM} = \frac{1}{N} \sum_{n=1}^N \sqrt{\mathcal{E}_{\mathbf{A}, \mathbf{x}_0, \text{supp}(\mathbf{x}_0), \delta_b} \left\{ (\hat{x}_n - \mathcal{E}_{\mathbf{A}, \mathbf{x}_0, \delta_b} \{ \hat{x}_n \})^2 \right\}}, \quad (9)$$

and

- computational time.

First, we consider the noiseless case, i.e.,  $\delta_b = \mathbf{0}$ . The expression in (1) becomes

$$\mathbf{A}\mathbf{x} = \mathbf{b}. \quad (10)$$

The linear least squares (LLS) criterion is the method that provides a closed-form solution, expressed by

$$\begin{aligned}
\hat{\mathbf{x}}_{\text{LLS}} &= \arg \min_{\mathbf{x}} \|\mathbf{x}\|_2^2 \quad \text{s.t. } \mathbf{A}\mathbf{x} = \mathbf{b} \\
&= \arg \min_{\mathbf{x}, \lambda} \left( \|\mathbf{x}\|_2^2 + \lambda^T(\mathbf{A}\mathbf{x} - \mathbf{b}) \right) \\
&= \arg \left( \frac{\partial}{\partial \mathbf{x}} \left( \|\mathbf{x}\|_2^2 + \lambda^T(\mathbf{A}\mathbf{x} - \mathbf{b}) \right) = \mathbf{0} \wedge \frac{\partial}{\partial \lambda} \left( \|\mathbf{x}\|_2^2 + \lambda^T(\mathbf{A}\mathbf{x} - \mathbf{b}) \right) = \mathbf{0} \right) \\
&= \arg \left( 2\mathbf{x} + \mathbf{A}^T\lambda = \mathbf{0} \wedge \mathbf{A}\mathbf{x} - \mathbf{b} = \mathbf{0} \right) \\
&= \arg \left( \mathbf{x} = -\frac{1}{2}\mathbf{A}^T\lambda \wedge \mathbf{A} \left( \underbrace{-\frac{1}{2}\mathbf{A}^T\lambda}_{\mathbf{x} = -\mathbf{A}^T\lambda} \right) = \mathbf{b} \right) \\
&= \arg \left( \lambda = -2(\mathbf{A}\mathbf{A}^T)^{-1}\mathbf{b} \wedge \mathbf{x} = -\frac{1}{2}\mathbf{A}^T \left( \underbrace{-2(\mathbf{A}\mathbf{A}^T)^{-1}\mathbf{b}}_{\lambda = -\mathbf{A}^T(\mathbf{A}\mathbf{A}^T)^{-1}\mathbf{b}} \right) \right) \\
&= \mathbf{A}^T(\mathbf{A}\mathbf{A}^T)^{-1}\mathbf{b}.
\end{aligned} \tag{11}$$

In Fig. 2, the RMSRE is shown as a function of the norm exponent  $p$ . One can see that there is no significant difference for various values of the norm exponent  $p$ . Therefore, in practice, one can choose any value of  $p$  along the x-axis shown in Fig. 2.

In Fig. 3, the acceptable value for the regularization parameter  $\rho$  is less than  $10^{-4}$ . It is obvious that for  $\rho < 10^{-4}$ , there is no significant difference to the RMSRE.

In Fig. 4, for a low compression ratio, the proposed IHT-FNR behaves similarly to the IHT initialized by the LLS and provides lower RMSRE than other methods.

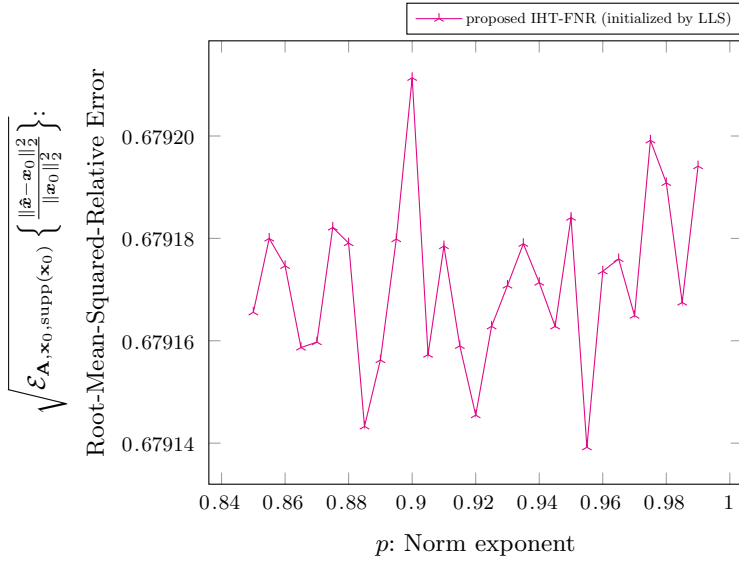
In Fig. 5, the IHT-FNR and the IHT initialized by the LLS have higher SDM than the IHT-MPI, the NSIHT, and the PHT, especially for a low compression ratio.

In Fig. 6, the IHT-FNR occupies the computer memory almost identical to that required by the PHT but less than the NSIHT memory consumption.

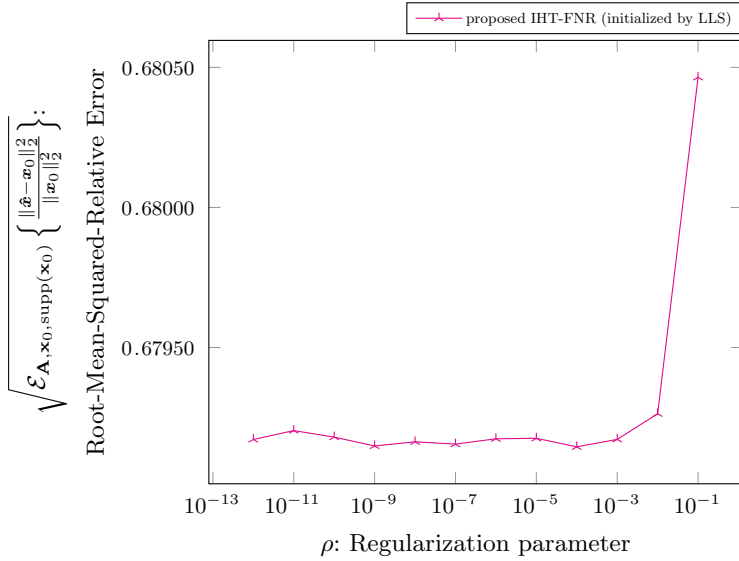
In Fig. 7, the proposed IHT-FNR takes less computational time than the PHT and the NSIHT.

The simulation setup that accounts for the additive noise is as follows.

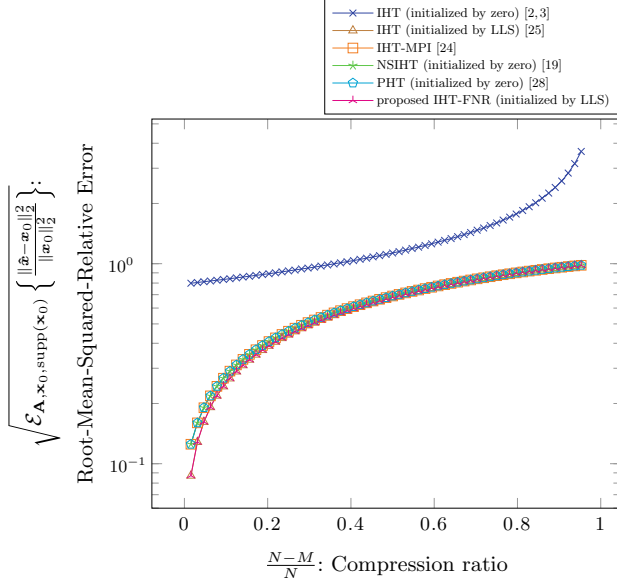
- Input:  $K, M, N, N_{\max}, \epsilon_{\min}, \epsilon, p, \rho, N_{\text{supp}(\mathbf{x}_0)}, N_A$ , and  $N_{\delta_b}$ .
- Random number generation:  $\mathbf{x}_0$  and  $\mathbf{A}$ .
- Random nonzero pattern generation:  $\text{supp}(\mathbf{x}_0)$ .
- Random noise generation:  $\delta_b$ .
- Signal reconstruction:  $\hat{\mathbf{x}}$ .
- Performance metric computation.



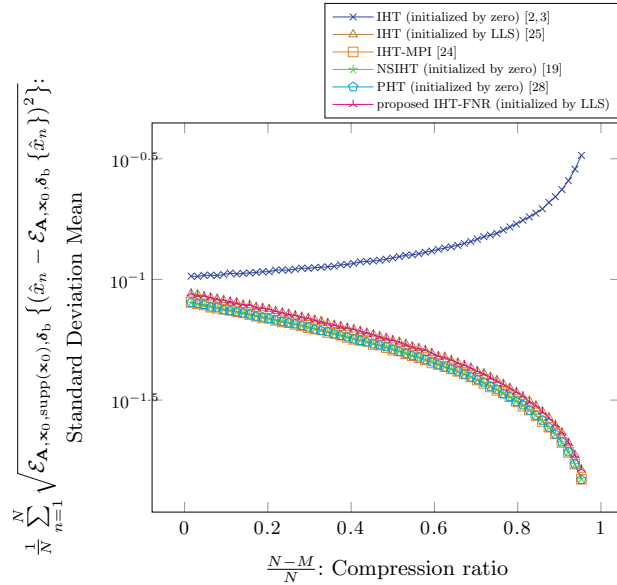
**Fig. 2** RMSRE as a function of  $p$  for  $K = 16$ ,  $M = 64$ ,  $N = 128$ , and  $\rho = 10^{-6}$ , from  $N_{\text{supp}(x_0)} = 1000$ ,  $N_A = N_{x_0} = 1000$ , and  $N_R = N_A N_{\text{supp}(x_0)} = 1,000,000$  independent runs



**Fig. 3** RMSRE as a function of  $\rho$  for  $K = 16$ ,  $M = 64$ ,  $N = 128$ , and  $\rho = 10^{-6}$ , from  $N_{\text{supp}(x_0)} = 1000$ ,  $N_A = N_{x_0} = 1000$ , and  $N_R = N_A N_{\text{supp}(x_0)} = 10,00,000$  independent runs

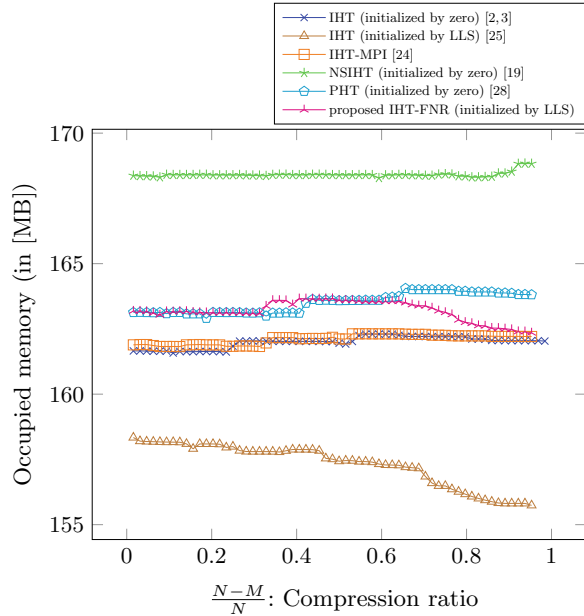


**Fig. 4** RMSRE as a function of compression ratio for  $K = 16$  and  $N = 128$  from  $N_{\text{supp}(x_0)} = 1000$ ,  $N_A = N_{x_0} = 1000$ , and  $N_R = N_A N_{\text{supp}(x_0)} = 1,000,000$  independent runs

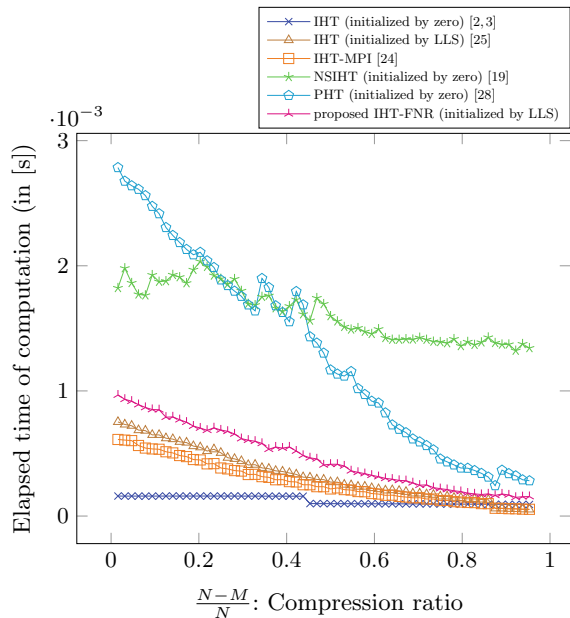


**Fig. 5** SDM as a function of compression ratio for  $K = 16$  and  $N = 128$ , from  $N_{\text{supp}(x_0)} = 1000$ ,  $N_A = N_{x_0} = 1000$ , and  $N_R = N_A N_{\text{supp}(x_0)} = 1,000,000$  independent runs

**Fig. 6** Occupied memory during computation as a function of compression ratio for  $K = 16$  and  $N = 128$  from  $N_{\text{supp}(x_0)} = 1000$ ,  $N_A = N_{x_0} = 1000$ , and  $N_R = N_A N_{\text{supp}(x_0)} = 1,000,000$  independent runs



**Fig. 7** Elapsed time of computation as a function of compression ratio for  $K = 16$  and  $N = 128$  from  $N_{\text{supp}(x_0)} = 1,000$ ,  $N_A = N_{x_0} = 1,000$ , and  $N_R = N_A N_{\text{supp}(x_0)} = 1,000,000$  independent runs



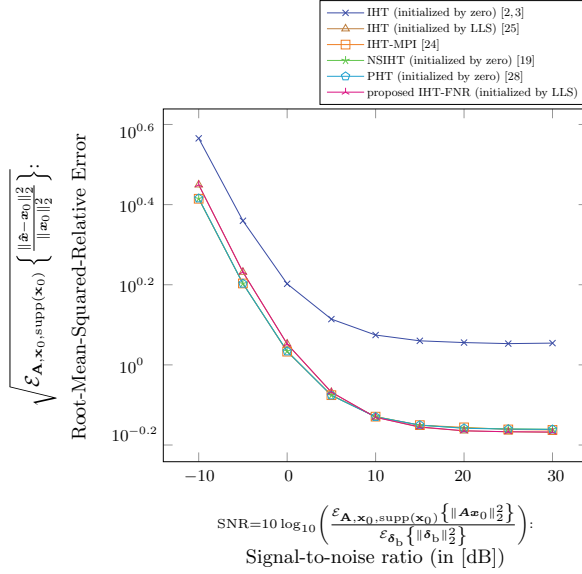


**Fig. 8** RMSRE as a function of SNR for  $K = 16$ ,  $M = 64$ , and  $N = 128$  from  $N_{\text{supp}(\mathbf{x}_0)} = 32$ ,  $N_A = N_{\mathbf{x}_0} = 313$ ,  $N_{\delta_b} = 100$ , and  $N_R = N_A N_{\text{supp}(\mathbf{x}_0)} N_{\delta_b} = 1,001,600$  independent runs

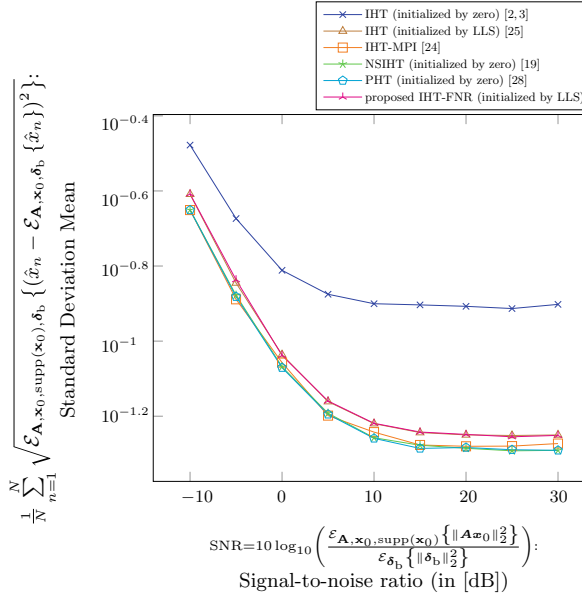


**Fig. 9** SDM as a function of SNR for  $K = 16$ ,  $M = 64$ ,  $N = 128$ ,  $\text{SNR} = 20$  dB, from  $N_{\text{supp}(\mathbf{x}_0)} = 32$ ,  $N_A = N_{\mathbf{x}_0} = 313$ ,  $N_{\delta_b} = 100$ , and  $N_R = N_A N_{\text{supp}(\mathbf{x}_0)} N_{\delta_b} = 1,001,600$  independent runs

**Fig. 10** Occupied memory during computation as a function of SNR for  $K = 16$ ,  $M = 64$ , and  $N = 128$  from  $N_{\text{supp}(x_0)} = 32$ ,  $N_A = N_{x_0} = 313$ ,  $N_{\delta_b} = 100$ , and  $N_R = N_A N_{\text{supp}(x_0)} N_{\delta_b} = 1,001,600$  independent runs

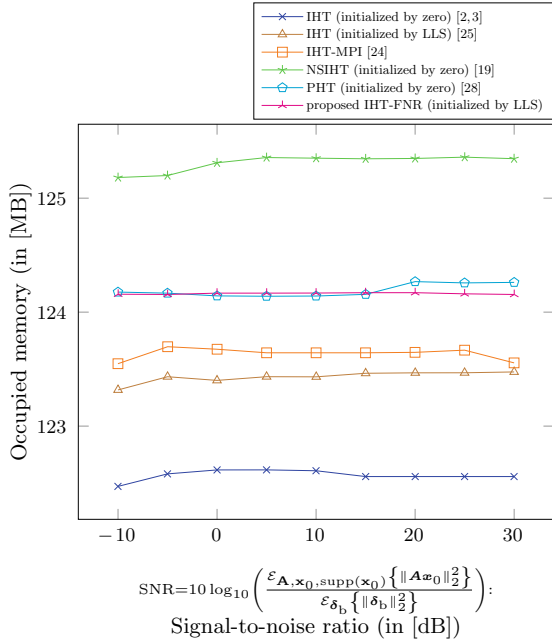
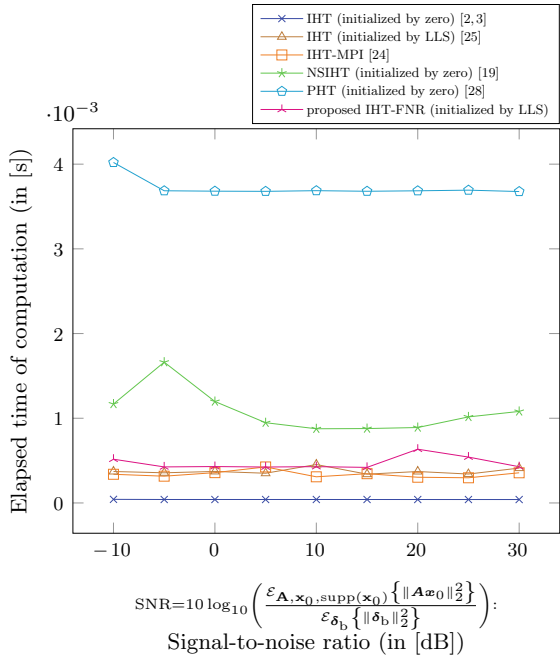


**Fig. 11** Elapsed time of computation as a function of SNR for  $K = 16$ ,  $M = 64$ , and  $N = 128$  from  $N_{\text{supp}(x_0)} = 32$ ,  $N_A = N_{x_0} = 313$ ,  $N_{\delta_b} = 100$ , and  $N_R = N_A N_{\text{supp}(x_0)} N_{\delta_b} = 1,001,600$  independent runs



In Fig. 8, one can see that the IHT with FNR and the IHT initialized by the LLS perform identically and have higher RMSRE than the IHT-MPI, the PHT, and the NSIHT for a low SNR. However, for a high SNR, both methods provide lower RMSRE than the others.

In Fig. 9, one can see that the IHT with FNR and the IHT initialized by the LLS perform identically and have higher SDM than the IHT-MPI, the PHT, and the NSIHT.

In Fig. 10, the IHT-FNR occupies the memory as same as the PHT but lower than that required by the NSIHT.

In Fig. 11, the IHT-FNR takes less computational time than the PHT and the NSIHT.

## 5 Conclusion

We propose an improved IHT for better signal reconstruction accuracy. It is shown that this method has a possible range of the norm exponent  $p$  and the regularization parameter  $\rho$ . Its computational time is less than the PHT and the NSIHT, while its RMSRE is lower than other methods on the second digit after the decimal in the noiseless case and on the fourth digit after the decimal in the noisy case. In the noiseless case, the memory occupied by the proposed method is lower than the IHT-MPI and the PHT.

## References

1. Amin, M. (ed.): Compressive Sensing for Urban Radar. CRC Press, Boca Raton, FL (2015)
2. Blumensath, T., Davies, M.E.: Iterative thresholding for sparse approximations. *J. Fourier Anal. Appl.* **14**(5–6), 629–654 (2008)
3. Blumensath, T., Davies, M.E.: Iterative hard thresholding for compressed sensing. *Appl. Comput. Harmon. Anal.* **27**(3), 265–274 (2009)
4. Boche, H., Calderbank, R., Kutyniok, G., Vybíral, J.: Compressed Sensing and its Applications: MATHEON Workshop 2013. Applied and Numerical Harmonic Analysis, Birkhäuser, Cham, Switzerland (2015)
5. Candès, E.J., Romberg, J., Tao, T.: Robust uncertainty principles: exact signal reconstruction from highly incomplete frequency information. *IEEE Trans. Inf. Theory* **52**(2), 489–509 (2006)
6. Carmi, A.Y., Godsill, S.J., Mihaylova, L.S. (eds.): Compressed Sensing & Sparse Filtering. Signals and Communication Technology. Springer, Berlin/Heidelberg, Germany (2014)
7. Chen, C.: Compressive Sensing of Earth Observations. Signal and Image Processing of Earth Observations. CRC Press, Boca Raton, FL (2017)
8. Coluccia, G., Ravazzi, C., Magli, E.: Compressed Sensing for Distributed Systems. Signal Processing. Springer, Berlin, Heidelberg, Germany (2015)
9. Conde, M.H. (ed.): Compressive Sensing for the Photonic Mixer Device: Fundamentals. Methods and Results. Springer, Wiesbaden, Germany (2017)
10. Donoho, D.L.: Compressed sensing. *IEEE Trans. Inf. Theory* **52**(2), 1289–1306 (2006)
11. Elad, M.: Sparse and Redundant Representations: From Theory to Applications in Signal and Image Processing. Springer, New York, NY (2010)

12. Eldar, Y.C., Kutyniok, G. (eds.): Compressed Sensing: Theory and Applications. Cambridge University Press, Cambridge, UK (2012)
13. Foucart, S., Rauhut, H.: A Mathematical Introduction to Compressive Sensing. Applied and Numerical Harmonic Analysis. Birkhäuser, New York, NY (2013)
14. Han, Z., Li, H., Yin, W. (eds.): Compressive Sensing for Wireless Networks. Cambridge University Press, Cambridge, UK (2013)
15. Khosravy, M., Dey, N., Duque, C.A.: Compressive Sensing in Healthcare, Advances in Ubiquitous Sensing Applications for Healthcare, vol. 11. Academic Press, London, UK (2020)
16. Kong, L., Wang, B., Chen, G.: When Compressive Sensing Meets Mobile Crowdsensing. Springer, Singapore (2019)
17. Landweber, L.: An iteration formula for Fredholm integral equations of the first kind. Amer. J. Math. **73**(3), 615–624 (1951)
18. Maio, A.D., Eldar, Y.C., Haimovich, A.M. (eds.): Compressed Sensing in Radar Signal Processing. Cambridge University Press, Cambridge, UK (2020)
19. Meng, N., Zhao, Y.B.: Newton-step-based hard thresholding algorithms for sparse signal recovery. IEEE Trans. Signal Process. **68**, 6594–6606 (2020)
20. Mishra, A.K., Verster, R.S.: Compressive Sensing Based Algorithms for Electronic Defence. Signals and Communication Technology, Springer, Cham, Switzerland (2017)
21. Parikh, N., Boyd, S.: Proximal algorithms. Found. Trends Optim. **1**(3), 123–231 (2014)
22. Patel, V.M., Chellappa, R.: Sparse Representations and Compressive Sensing for Imaging and Vision. Springer, New York, NY (2013)
23. Pfander, G.E.: Sampling Theory, A Renaissance: Compressive Sensing and Other Developments. Applied and Numerical Harmonic Analysis. Birkhäuser, Cham, Switzerland (2015)
24. Qiu, K., Dogandžić, A.: Sparse signal reconstruction via ECME hard thresholding. IEEE Trans. Signal Process. **60**(9), 4551–4569 (2012)
25. Tausiesakul, B.: Iterative hard thresholding using least squares initialization. In: Proceedings of IEEE International Conference on Communication Systems and Network Technologies 2022 (CSNT 2022). pp. 612–615. Indore, India, Apr 2022
26. Testa, M., Valsesia, D., Bianchi, T., Magli, E.: Compressed Sensing for Privacy-Preserving Data Processing. Signal Processing. Springer, Singapore (2019)
27. Thanki, R.M., Dwivedi, V.J., Borisagar, K.R. (eds.): Multibiometric Watermarking with Compressive Sensing Theory: Techniques and Applications. Signals and Communication Technology, Springer, Cham, Switzerland (2018)
28. Wen, J., He, H., He, Z., Zhu, F.: A pseudo-inverse-based hard thresholding algorithm for sparse signal recovery. IEEE Trans. Intell. Transp. Syst (2022)

# Unveiling the Root Cause of EV Charging Irregularities: A Statistical Approach



Ankit Bajaj, Dinesh Gopalani, Rachit Mathur, Hemanjaneya Reddy,  
Swapna Satyanarayan, and Ansuman Chand

**Abstract** The drive for mobility has caused an increase in greenhouse gas emissions, leading to a shift toward the adoption of electric vehicles (EVs). These vehicles are powered by efficient electric motors, which offer reduced upkeep and enhanced operation. However, the unstable nature of electricity demand and the proliferation of EV charging equipment providers have posed significant challenges in EV charging. Furthermore, charging interruptions are commonplace, with electrical vehicle supply equipment (EVSE) serving as a mysterious black box for EV owners. By analyzing EVSE and EV data during charging, sensitive signals of charging termination can be discovered. The present research paper aims to investigate endurance data to uncover the root cause of EV charging interruption and to address uncertainties in EV charging.

**Keywords** Cause effect analysis · Causal learning · Causal inference · Time series · Charging interoperability · Electrical vehicle · Electrical vehicle supply equipment

---

Supported by Mercedes-Benz Research and Development India

A. Bajaj (✉) · D. Gopalani

Department of Computer Science Engineering, Malaviya National Institute of Technology, Jaipur, India

e-mail: [ankitbajaj7250@gmail.com](mailto:ankitbajaj7250@gmail.com)

D. Gopalani

e-mail: [dgopalani.cse@mnit.ac.in](mailto:dgopalani.cse@mnit.ac.in)

R. Mathur · H. Reddy · S. Satyanarayan · A. Chand

Mercedes-Benz Research and Development, Bengaluru, India

e-mail: [rachit.mathur@mercedes-benz.com](mailto:rachit.mathur@mercedes-benz.com)

H. Reddy

e-mail: [hemanjaneya.reddy@mercedes-benz.com](mailto:hemanjaneya.reddy@mercedes-benz.com)

S. Satyanarayan

e-mail: [swapna.satyanarayan@mercedes-benz.com](mailto:swapna.satyanarayan@mercedes-benz.com)

A. Chand

e-mail: [ansuman.chand@mercedes-benz.com](mailto:ansuman.chand@mercedes-benz.com)

## 1 Introduction

The demand for electric vehicle (EV) market is burgeoning swiftly due to the government's incentives all over the world to cut down on pollution and the requirement for millions of barrels of oil. Electric vehicles boast a range of benefits, such as emitting nothing from the tailpipe, exceptional energy efficiency, low upkeep requirements, cost-efficient operating costs, and so on. Nevertheless, a user is always searching for an affordable, convenient, and eco-friendly system. According to Global EV Outlook 2021, the EV vendors' market has grown exponentially. Customers are encountering incongruity with EVs and charging stations. The user is discontented when they plug in the cable to charge, and if the charging does not kick off or terminates abruptly. For example, suppose that charging is commenced for 60 min. During the first 15 min, the charging will proceed uninterrupted. However, it may halt charging between the 16th and 28th minutes due to either delicate signals or error signals. Consequently, it becomes necessary to restart the charging manually. The charging process will then resume from the 29th to 35th minute and continue in this manner. Owing to unsatisfactory charging experiences, approximately 20% of EV owners desire to switch to IC vehicles in 2022 [1]. The naive solution for this problem is to drive the vehicle and check the behavior of the EV at every supply station to ensure compatibility. EVSE is a complex system that has long been shrouded in mystery, with limited knowledge of the data and information exchanged between the EVSE and EV during the charging process. To address this gap, we conducted rigorous testing during vehicle development, collected endurance data, and subsequently analyzed data to identify the root cause of charging termination. Our objective is to gather all pertinent signals and carefully study them, to ensure that we avoid any future issues with EV charging and EVSE interactions. By doing so, we can enhance the reliability and effectiveness of EV charging systems, contributing to a more sustainable and efficient transportation sector.

## 2 Basic Background

Electric vehicles (EVs) can be charged using either AC or DC charging systems. AC charging involves converting AC to DC using AC–DC converters, which are classified into three levels by SAE EV AC Charging Power Levels [2]. Level 1 uses on-board chargers and 110 V domestic plugs, taking 0.5–12.5 h to charge a modest EV. Level 2 requires an Electric Vehicle Service Equipment to establish a direct connection to the grid. Level 3, known as rapid chargers, can fully recharge an EV in under 30 min. Meanwhile, DC charging systems are more powerful and faster than AC systems, but require special wiring and installations. They can automatically adjust the voltage output to accommodate different EVs. However, EV charging connectors and plug types vary by region and model [3]. Worldwide, the most common charging connectors are Type 1 used in North America, Type 2 used in Europe, Chademo used

in Japan, Tesla Supercharger for Tesla models, CCS used in Europe and other parts of the world, and GB/T used in China.

The International Energy Agency stated that EVs have expanded approximately 50% every year since 2010, reaching over 5 million in 2016. Furthermore, the availability of charging infrastructure has a significant influence in driving demand, since it impacts the ease and expense of owning an electric vehicle. As of 2019, the global number of publicly available slow chargers was 5,98,000, with half of them located in China and 38% spread across seven other countries. Meanwhile, there were 2,64,000 publicly accessible fast chargers, with the majority (81%) found in China and the remaining 14% in six other countries [4]. The absence of adequate charging infrastructure in India is the primary obstacle to the economic viability of electric vehicles [5]. India only has 650 charging stations in comparison with China's over 456K in the same year [6].

The interaction between the EV and EVSE is regulated by two global standards: IEC 61851 and ISO/IEC 15118. IEC 61851 outlines the coordination of states between the EV and EVSE during a charge and is accountable for fundamental signaling, such as connection status or readiness for charging. However, more intricate information is left to the high-level communication defined in ISO/IEC 15118, which encompasses communication specifics in all seven layers of the OSI model. It is noteworthy that EV charging stations are contingent on devices that adhere to the international electrotechnical commission (IEC) 61850 standards. A conformance testing system has been implemented to guarantee that electric vehicle chargers adhere to the ISO/IEC 15118, IEC 61851, and IEC 61850-90-8 standards, ensuring compliance and conformity [7]. However, just because a device adheres to these standards, it does not ensure seamless integration with devices from different manufacturers.

In contemporary times, all charging substations have adopted the utilization of Intelligent Electronic Devices (IEDs) to automate their substation automation systems (SAS). This provides advanced measurement capabilities, predictive analysis, and complete control functionalities within the power system, rendering it more complex than conventional systems. The integration of IEDs from multiple manufacturers into a unified substation automation system is a feat that can be achieved through engineering. However, with the increasing requirement for seamless data sharing between production companies, the need for interoperability has become increasingly prevalent to ensure accurate real-time data transmission and eliminate vulnerabilities [8]. If compatibility among devices from multiple vendors can be achieved, power utilities will have the ability to incorporate devices from various manufacturers in charging stations [9].

### 3 Literature Review

In modern times, information holds immense significance as it serves as the cornerstone for various enterprises relying on data-driven verdicts. Companies are keen on exploring the causal relationship between different aspects of their business and its

outcomes. Consequently, researchers have invested substantial time and resources into developing causal learning algorithms. The causal learning approach surpasses conventional machine learning techniques due to its ability to reveal the underlying data-generating procedures. Conventional ML techniques are limited to learning correlation-based patterns and relationships from data. However, correlation is a poor surrogate for causality, as data may contain spurious correlations. Causal inference is a pivotal research area across several domains, including statistics, computer science, education, public policy, epidemiology, and economics, spanning decades [10].

Traditional methods for establishing causality, such as interventions and randomized controlled trials, may not always be practical or ethical. As a result, researchers have turned to observational data as a quicker alternative. Although researchers cannot control the subjects or treatments, they can still observe and record data to determine actions and outcomes. However, this method does not provide insight into the mechanisms behind actions. To address this, researchers have developed frameworks like the potential outcome framework and structural causal model, as well as powerful machine learning techniques. Various causal inference methods, including re-weighting, stratification, matching, tree-based, representation-based, multi-task learning, and meta-learning methods have been developed to help identify causes from effects [11].

Numerous methods have been employed in the pursuit of causal discovery. One such avenue is causal structure learning, which seeks to uncover causal relationships through the creation of structural equation models, including causal graphs [12]. However, if one lacks familiarity or understanding of the data labels' values, determining causality becomes challenging. To date, no algorithms exist that can solve such problems without proper comprehension of the dataset's values.

In this paper, we shall introduce a resolution to the quandary of EV charging incompatibility, using a comprehensive collection of EV charging and EVSE data. Presently, there are no available resources that can detect the underlying causes of charging discontinuation. Therefore, our investigation aims to bridge this gap in charging interoperability by devising a novel approach that can identify and rectify the issues of charging incompatibility. Additionally, our research paper will contribute to the field of causality analysis by addressing this research gap.

## 4 Methodology

### 4.1 Dataset

The dataset comprises time series information gathered through regular tapping. We employed the endurance dataset to determine the root cause of charging termination. This data was gathered during the testing phase of vehicle development. However, due to the limited availability of such datasets, the researchers resorted to creating simulated data using Hardware-In-the-Loop (HIL) technology. This approach can

Time[s]	S1	S2	S3	S4	S5	S6	S7	S8	S_effected_EV	S_effected_EVSE
Time	NAN	STATIC		BOOLEAN		RANGE		EFFECTED		
1.00001				0			1	4851	1	1
1.02555			4		5		2	5		2
1.25001		1								
1.28997			4	1		7	51		1	1
1.37894								78462		
1.39999		1				7			2	1
1.45557										
1.58888			4	1		78	1	0	1	2
1.58974						51	3			
1.59874					5			452452	2	1
1.59999						51	4		2	
1.66666				0				578		
1.70001		1			5		7		1	2
1.78749						78			2	
1.80584			4	1	7			7849161	1	1

**Fig. 1** Dataset visualization

significantly improve the real-time embedded controller's performance by accelerating testing and minimizing development time. The dataset comprises up to 1281 columns, each containing a unique signal, labeled using a specific naming convention which includes "CAN model name :: Node name :: Signal name." As an illustration, "CHAdemo\_xxi\_Di\_App\_B::H\_1xx9\_Charger\_2::Hxx10x\_Bx\_B4\_Charg\_syst\_err."

**Data Visualization:** We have categorized the signals based on their values for enhanced data representation and comprehension. Figure 1 has been provided as an exemplar for visualizing the dataset.

- **Time**—The dataset showcases time-based information. The primary column is designated as "time."
- **NAN Signal**—These signals hold no significant value and are thus unproductive.
- **Static Signal**—These signals possess a consistent value throughout. It is acknowledged that a static signal will have no influence on the termination of charging.
- **Boolean Signal**—These signals possess two distinct values.
- **Range Signal**—These signals can fluctuate between  $-x$  and  $+y$  in terms of value.
- **Effected Signal**—The critical signal relevant to the cessation of charging is this one. There are two crucial signals, one for the electric vehicle (EV) and one for the Electric Vehicle Supply Equipment (EVSE). The signal value 1 symbolizes a successful charging process, while signal value 2 represents a charging interruption.

## 4.2 Dataset Preprocessing

Due to the periodic collection of data, and the varied clock cycles associated with each signal, the dataset is inundated with an excessive number of empty or missing values. To address this issue, we are utilizing a technique called forward filling and backward filling.

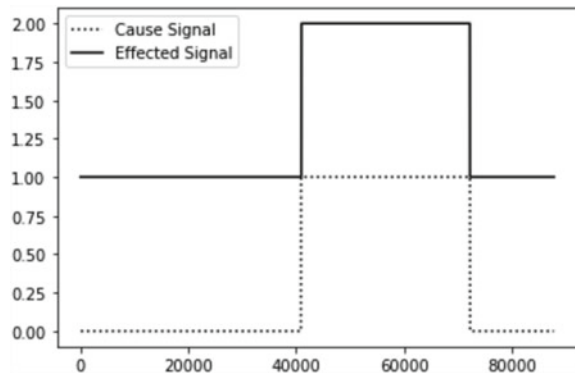
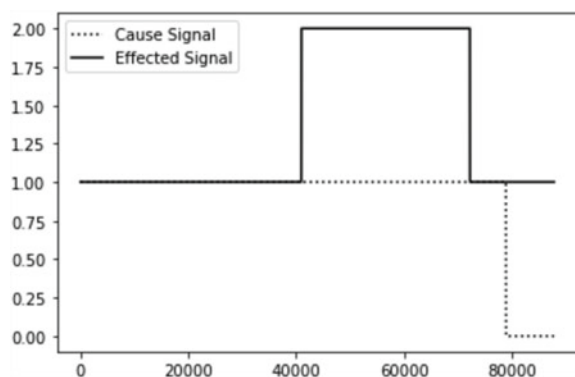
- Forward Filling—The Pandas dataframe.ffill() function is employed to rectify missing values in the dataframe. This ffill() technique substitutes NULL values with the value from the prior row or column (depending on the axis parameter setting). The term “ffill” stands for “forward replacement” and carries over the last valid observation.
- Backward Filling—This term refers to filling missing values with the subsequent data point. The NAN values present in the pandas dataframe will be backfilled using the dataframe.bfill() function.
- Eliminate NAN Signals—This implies that a signal without value is useless and remains blank during the charging process. It is recommended to remove this signal from the dataset.
- Eliminate Static Signals—This indicates that the value of the signal does not vary during charging. As a signal remains constant throughout the charging period, it will not impact the charging or canceling process. It is recommended to eliminate this type of signal for signal filtering purposes.
- Eliminate Irrelevant Signals—Certain signals are necessary to be displayed during the charging process, however, they may not hold significance in terms of analysis or may duplicate other signals. It is advisable to eliminate these signals to concentrate solely on the crucial signals.

### ***4.3 Proposed Scheme and Implementation***

This is a dilemma of cause and effect. The cause and effect analysis methodology enables one to pinpoint all probable causes behind an issue, thereby enabling the root cause to be identified and rectified. The objective is to precisely determine the cause behind the charging cessation. A signal indicating a fault serves as the cause signal, while the effected signal activates upon the occurrence of any faults. To date, we have tried various strategies and in this research paper, we outline several crucial techniques.

**Comparative Analysis:** In this research methodology, we employed the Pearson correlation method. This is a widely utilized method for determining linear correlation and is depicted by a numerical value ranging from  $-1$  to  $1$ . This value reflects the strength and direction of the relationship between two variables. As seen in our results, when the affected signal experiences spikes, there is a corresponding spike in the cause signal, resulting in a strong correlation. Our study took into account the cause signals that were most similar to the affected signal, thus providing a comprehensive analysis of the correlation between the two. Figure 2 illustrates a strong correlation between the causal signal and the affected signal

**Signal Advancing:** As depicted in the accompanying illustrations, it has been observed that the signals were impacted prior to the root cause, as demonstrated in Fig. 3. To conquer this issue, we employed a strategy of shifting the signal by

**Fig. 2** Absolute correlation**Fig. 3** Signal advancing

dividing its length, which was affected, through a process of hit and trial. By continuously averaging the correlation values, we were able to determine that the highest correlation was obtained by dividing the length of the affected signal three times. This hit and trial approach ultimately resulted in maximum correlation.

**Granger Causality:** The Granger causality test is a statistical procedure employed to establish whether one time series holds sway over another, thereby offering valuable prognostic information. However, it is important to note that the Granger causality test does not purport to elucidate the relationship between the variables in question, as it falls short of being a true causality analysis, such as a “cause and effect” examination. Furthermore, when interdependencies exist between multiple variables, the Granger causality test proves to be ineffective in forecasting. Additionally, this type of causality test cannot be executed on non-stationary data, and our data was determined to be non-stationary through the utilization of the Augmented Dickey-Fuller Test. Given these limitations of the Granger causality test, it can be concluded that this methodology is not appropriate for our data and problem statement [13].

**Weight of Evidence:** The “weight of evidence” methodology is a research approach that involves evaluating the credibility and strength of evidence from various sources

to reach a conclusion or make an informed decision. The WOE approach involves a systematic analysis of all available evidence, with each piece of evidence assigned a numerical weight based on its relevance, reliability, and credibility. The WOE scores for each piece of evidence are then combined to produce an overall score that reflects the level of confidence in the hypothesis or claim. This approach provides a robust and objective method for evaluating the evidence and determining the strength of a conclusion. By integrating multiple sources of evidence and taking into account the quality and quantity of the data, researchers can draw robust conclusions and make informed decisions. This technique is useful in various fields, including law, medicine, and environmental studies, where decision-makers must weigh multiple factors and uncertainties. The weight of evidence approach is a powerful tool for identifying patterns and trends, and it can help to improve our understanding of complex systems and phenomena [14].

The following is the formula to determine WOE and IV:

$$WOE = \ln(Event\% / Non\ Event\%) \quad (1)$$

$$IV = \sum (Event\% - Non\ Event\%) * \ln(Event\% / Non\ Event\%) \quad (2)$$

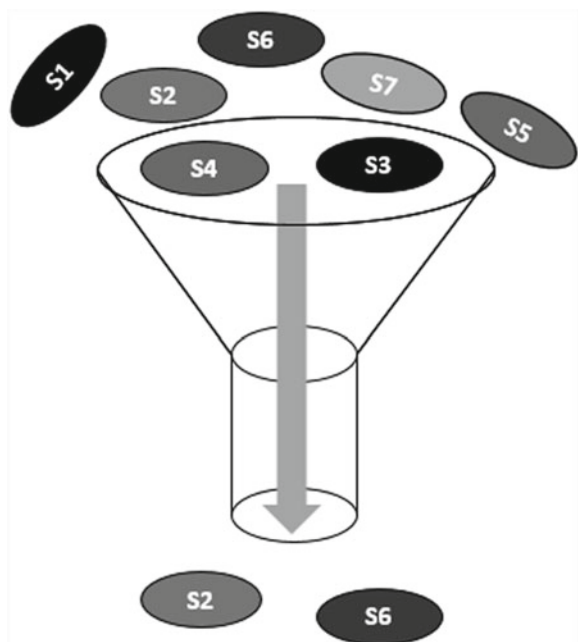
$$IV = \sum (Event\% - Non\ Event\%) * WOE \quad (3)$$

The computational efficiency of the Weight of Evidence (WoE) algorithm varies depending on the particular implementation and the magnitude of the dataset, yet it is generally acknowledged to exhibit a linear time complexity of  $O(n)$ , wherein n denotes the quantity of data points within the dataset.

This approach is commonly referred to as a metric for discerning the disparity between good and bad signals. As illustrated in Fig. 4, it depicts the extraction of favorable signals from a pool of all signals. This methodology utilizes a variety of indicators to determine the level of certainty regarding the presence of either favorable or unfavorable signals.

**Close Proximity Weight of Evidence:** This algorithm is employed to spot signal changes that transpire in close proximity to the corresponding consequences. As a result, it effectively distinguishes the underlying cause of a specific effect. This algorithm has the capacity to detect boolean value type signals, such as 0 or 1, 5 or 7, and 293 or 3433. Furthermore, the algorithm is competent in recognizing robust signals that take place in the vicinity of each effect spike. Another vital aspect of this methodology is the evaluation of the importance and informational worth of each signal in relation to the effect under scrutiny. This strategy presents vast potential for propelling the domain of signal analysis and facilitating more precise and dependable conclusions.

**Feed backward Weight of Evidence:** This approach is a newly developed algorithm that is capable of identifying the signal that has undergone the most changes during a changing event. This algorithm is designed to detect the backward signals that have

**Fig. 4** Signal filtration

changed in relation to the spikes of the affected signal. It is adept at detecting any class of range values signals, encompassing  $-y$  to  $+x$ . By utilizing this approach, the algorithm is able to accurately pinpoint the source of the changes and provide valuable insight into the underlying causes of these changes. This approach is a momentous progress in signal scrutiny and holds the possibility of significantly enhancing our grasp of multifaceted systems.

**Sequence Detection Algorithm:** A novel algorithm has been created to identify the series of signals that lead to the cessation of charging in a hierarchical manner. The algorithm accurately records the timing of signal transitions, as well as pinpoints the most influential signal that led to the charging termination. This innovative algorithm enables the identification of the order of signal ranks based on their impact on the charging process. Additionally, the algorithm generates hexadecimal ROE signal values that allow for the creation of a diagnostic trouble code (DTC). The DTC code can be utilized to efficiently identify and locate any on-board issues, providing a rapid and effective solution. By utilizing this algorithm, we can swiftly and effectively identify the location and nature of the problem and take remedial actions promptly.

A comparison Table 1 has been generated to present the Key Features, Benefits, and Drawbacks of each methodology

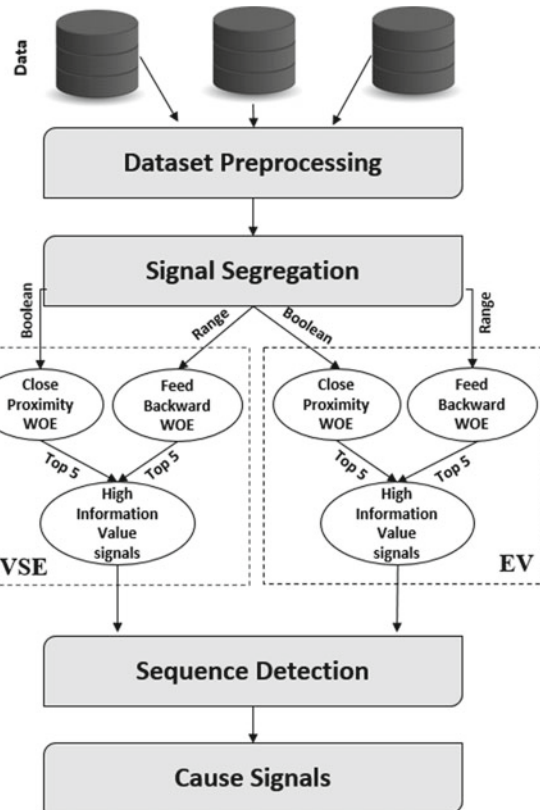
**Table 1** Comparison table

Approach	Key characteristics	Advantages	Limitations
Comparative analysis	All highly correlated signals found, but no clear cause signals identified	Good for identifying relationships between signals	Does not provide causal insights
Signal advancing	Cause signals identified, but not effective for real-time datasets	Effective for identifying cause and effect relationships	Limited applicability in real-time datasets
Granger causality	Does not provide causal insights, only measures statistical association	Useful for analyzing relationships between signals	Limited insights into causality
Weight of evidence	Achieved 90% accuracy for identifying delicate signals	Effective for identifying subtle signal patterns	Limited in scope, For finding rank-wise delicate signals
Sequence detection algo	Identifies the order of signal ranks based on their impact on charging	Useful for analyzing sequential relationships	Improves in the future according to the need

#### 4.4 Solution Workflow

The proposed method architecture aims to identify the root cause of charging termination or incompatibilities, and the workflow for the solution is presented in Fig. 5. The data required for the study was collected during the testing process of vehicle development, as well as from a simulation environment. The data was initially pre-processed, with a focus on filling blank entities and removing unnecessary signals, while emphasizing important signals. The dataset was then segregated into two categories of signals, and different Weight of Evidence (WOE) techniques were applied based on signal type. The top 5 high information value signals were then selected from each signal group. After that, the top 20 sensitive signals from both electric vehicle (EV) and Electric Vehicle Supply Equipment (EVSE) faults were collected. These cause signals were then ranked according to their sensitivity for termination of charging using a sequence detection algorithm. Finally, all these cause signals were gathered together as a comprehensive list.

**Fig. 5** Flow diagram of proposed analysis



## 5 Results

The present investigation has established that the utilization of the cause and effect analysis methodology is a potent strategy for pinpointing and remedying the underlying cause of issues. We have examined several approaches in this research and documented a select few in this paper. Through the employment of these methods, we successfully narrowed down a pool of more than 1281 signals to the top 20 signals pertaining to charging termination. To ensure the algorithm's veracity, we scrutinized over 100 datasets to identify the delicate signals. We successfully identified approximately 90% of the fragile and sensitive signals that impact charging. To validate the outcomes, we replicated the same behavior in Hardware-In-Loop (HIL) environment, which boosted our confidence in the accuracy of our findings. Furthermore, the creation of a new algorithm now allows for the automated detection of error signals, negating the necessity for manual validation by professionals.

**Table 2** Result table

Dataset number	Actual error signals	Comparative analysis	Signal advancing	WOE
1	2	1	1	2
2	3	0	1	3
3	2	0	1	2
4	2	0	0	2
5	3	1	2	3
6	1	0	0	1

Table 2 illustrates the findings of distinct methodologies when applied to a specific dataset. The table incorporates six distinct datasets to elucidate the results. Each dataset's actual error signal count is specified in the table alongside the outcomes of each approach employed.

## 6 Conclusion

After an exhaustive investigation, our team has determined that we have effectively identified and resolved the major cause of hindrances to charging efficiency. Through scrupulous log analysis, we precisely pinpointed the reason for the failure. In the course of this research, we accumulated a plethora of datasets from the testing phase of vehicle development, which can provide valuable insights for future analysis. Our team has developed an algorithm that effectively detects any cause of charging termination, resulting in optimal efficiency. A comprehensive examination of the log files enabled us to ascertain the root cause of previous malfunctions and resolve them effectively. The implementation of a charger sequence detection algorithm has allowed us to measure signal sensitivity, enabling us to terminate charging when necessary. As a result, we can now perform digital testing of electric vehicles, eliminating the need for physical testing, which will significantly reduce costs, save time, and reduce risks associated with testing. This will broaden the portfolio of EVSE players and increase the number of EVs in the market significantly.

**Acknowledgements** This work has been supported by Mercedes-Benz Research and Development India and Mercedes-Benz AG. We express our appreciation to Mercedes-Benz for furnishing the resources and infrastructure necessary to finalize this research. We accept that any opinions expressed in this paper are solely those of the authors.

## References

1. Hardman, S., Tal, G.: Understanding discontinuance among California's electric vehicle owners. *Nat. Energy* **6**(5), 538–545 (2021)
2. Un-Noor, F., Padmanaban, S., Mihet-Popa, L., Mollah, M.N., Hossain, E.: A comprehensive study of key electric vehicle (EV) components, technologies, challenges, impacts, and future direction of development. *Energies* **10**(8), 1217 (2017)
3. Falvo, M.C., Sbordone, D., Bayram, I.S., Devetsikiotis, M.: EV charging stations and modes: international standards. In: *2014 International Symposium on Power Electronics, Electrical Drives, Automation and Motion*, pp. 1134–1139. IEEE (2014)
4. Rivera, S., Kouro, S., Vazquez, S., Goetz, S.M., Lizana, R., Romero-Cadaval, E.: Electric vehicle charging infrastructure: from grid to battery. *IEEE Ind. Electron. Mag.* **15**(2), 37–51. <https://doi.org/10.1109/MIE.2020.3039039>
5. Mishra, S., Verma, S., Chowdhury, S., Gaur, A., Mohapatra, S., Dwivedi, G., Verma, P.: A comprehensive review on developments in electric vehicle charging station infrastructure and present scenario of India. *Sustainability* **13**(4), 2396 (2021)
6. Panchal, C., Stegen, S., Lu, J.: Review of static and dynamic wireless electric vehicle charging system. *Int. J. Eng. Sci. Technol.* **21**(5), 922–937 (2018)
7. Shin, M., Kim, H., Kim, H., Jang, H.: Building an interoperability test system for electric vehicle chargers based on ISO/IEC 15118 and IEC 61850 standards. *Appl. Sci.* **6**(6), 165 (2016)
8. Park, Y.-Y., Kim, S.-K., Jang, B.-T., Kim, N.-D., Kim, W.-J., Lee, N.-H.: Development of the testing automation system for verifying interoperability of digital substation. In: *2022 6th International Conference on Electric Power Equipment-Switching Technology (ICEPE-ST)*, pp. 363–366. IEEE (2022)
9. Bhattacharjee, T., Jamil, M., Alotaibi, M.A., Malik, H., Nassar, M.E.: Hardware development and interoperability testing of a multivendor-IEC-61850-based digital substation. *Energies* **15**(5), 1785 (2022)
10. Cheng, L., Guo, R., Moraffah, R., Sheth, P., Candan, K.S., Liu, H.: Evaluation methods and measures for causal learning algorithms. *IEEE Trans. Artif. Intell.* **3**(6), 924–943 (2022)
11. Yao, L., Chu, Z., Li, S., Li, Y., Gao, J., Zhang, A.: A survey on causal inference. *ACM Trans. Knowl. Discovery Data (TKDD)* **15**(5), 1–46 (2021)
12. Spirtes, P., Zhang, K.: Causal discovery and inference: concepts and recent methodological advances. *Appl. Inf.* **3**(1), 1–28 (2016)
13. Qiu, H., Liu, Y., Subrahmanyam, N.A., Li, W.: Granger causality for time-series anomaly detection. In: *2012 IEEE 12th International Conference on Data Mining*, pp. 1074–1079. IEEE (2012)
14. Gough, D.: Weight of evidence: a framework for the appraisal of the quality and relevance of evidence. *Res. Pap. Educ.* **22**(2), 213–228 (2007)

# Performance Analysis of Wireless Power Charging and Future Enhancement Techniques for Drones



Ahmed. O. MohamedZain, Jiehan Teoh, Kianmeng Yap,  
and Huangshen Chua

**Abstract** Drones' technology has become forefront in the industry development sector. It has been used in many applications such as forest fire monitoring, border security surveillance and delivery application. However, drone flights are limited to only a few minutes also high current consumption by drone's motors resulting in requiring batteries with high capacity. This represents a challenge for the drones to efficiently serve their purpose, researchers show more interest in developing a drone wireless charging method for longer flight duration. Many factors are to be considered such as power transfer efficiency, number of transmitter coils, frequency range and transfer distance; all these factors have been reviewed in this research. This paper aims to investigate and review the methods of wireless power transfer (WPT) and its capability to charge a drone's battery at all sizes. WPT is divided into three main types which are capacitive wireless power transfer (CWPT), radiative and non-radiative methods. Non-radiative technique is divided into three methods which are inductive wireless power transfer (IWPT), hybrid capacitive wireless and magnetic resonant wireless power transfer. The types of wireless charging technologies based on the distance between transmitter and receiver have been summarized. The advantages and disadvantages of each method have been introduced. Hybrid inductive and capacitive method using multiple transmitter antennas is a potential technology for the charging of drone's battery. Design of the WPT station has been proposed, which consists of four transmitters' antennas aims to increase the output power efficiency. Performance analysis of wireless power transfer module was conducted, and efficiency was calculated based on the distance between power transmitter (Tx) and power receiver (Rx). A maximum efficiency of 98% was achieved at 0 mm between

---

Ahmed. O. MohamedZain · J. Teoh · K. Yap (✉)

Department of Computing and Information Systems, School of Engineering and Technology,  
Research Centre for Human-Machine Collaboration, Sunway University, Bandar Sunway, 47500  
Petaling Jaya, Malaysia  
e-mail: [kmyap@sunway.edu.my](mailto:kmyap@sunway.edu.my)

H. Chua

School of Engineering, University of Wollongong Malaysia, Utropolis, Glenmarie, 40150 Shah  
Alam, Selangor, Malaysia

School of Engineering, UOW Malaysia KDU Penang University College, Jalan Anson, 10400  
George Town, Pulau Pinang, Malaysia

Tx and Rx, when using  $20\Omega$  as a load resistance. A minimum efficiency of 86% was achieved at 0 mm between Tx and Rx, when 35 and  $50\Omega$  were used as a load resistance respectively. The future development and future workforce strategies were proposed.

**Keywords** Wireless power transfer · Capacitive wireless power transfer · Drone · Inductive wireless power transfer · Hybrid inductive and capacitive

## 1 Introduction

The technology of drones has been used for many applications such as inspections and research [1], agriculture applications [2], environmental protection and rescue missions, and border monitoring for security purposes [3]. The area coverage by the single drone is around 15 km radius per 1 flight [3]. Therefore, in this application renewable energy such as solar panels can be applied [4] as power supply for the wireless power technology (WPT) charging process of the drone. At least three drones are required to efficiently cover an area of 30–45 km radius, since the drone flight time is around 30 min in normal weather when there is no wind, and the charging time is between 1 and 3.5 h depending on the drone battery capacity. Therefore, wireless power charging stations are needed. References [5, 6] have proposed drones for forest fire monitoring, in this application large area up to 30 km radius is covered by the drones. When the fire services department detects smoke or fire, the drones take off immediately to monitor for 20–30 min; while the first patch of drones is in mission, the second patch of drones is recharging. After 40 min, the second patch of drones take off to start monitoring. However, drones have become more required recently as the demand for their applications has increased sharply in many fields. Mostly LiPo batteries are used as an electrical power source [7] in most of the medium size drone as shown in Fig. 1 [8] but because of the high electrical power consumption of the drone's motors, the normal operation time of a drone is between 20 and 30 min [9]. This limits the drone flight range and operation time, and because of this, the drone might be unable to fulfil the purpose of its use in a specific application use [10]. In most cases, to continuously operate drone, the batteries are replaced or recharged [11] after its use. These batteries can be recharged by using wired power transfer which requires some substantial connections. Alternatively, by wireless power transfer, which does not require any physical connection. Even though the wired power transmission is more efficient than wireless power transmission in terms of power transmission, recently wireless power transmission techniques are utilized for its more minimal maintenance and increased safety (due to no physical connection of wires) [12].

To charge the drone using wireless power transmission, the drone is equipped with electromagnetic coils function as a wireless power receiver. These coils can be single or multiple depending upon the size and design of the charging system. In most cases, a wireless power transmission system is composed of a transmitting and a receiving side. Both transmitting and receiving sides are equipped with coils to



**Fig. 1** Medium size drone [13]

transfer the power from the source to load. Reference [14] have designed a 450 W wireless charger using inductive wireless power transfer method for a drone, with an 85 kHz frequency band. In this work the receiver coil was designed according to the shape of the charging port, the results show that wireless charging station is an enormous potential for drone's technology. Reference [15] have conducted a study on a drone charging system using wireless charging method; in this project, Reference [15] have constructed a 100 W inductive wireless charging station using single transmitter antenna and single receiver antenna, with a 13.56 MHz frequency band. The maximum transmitted power efficiency was 60%. Reference [16] have designed an automatic drone wireless charging station with single transmitter antenna and receiver antenna, in this work maximum current transmitted efficiency achieved by the charging station was 65%. Reference [17] have developed a self-charging wireless station for drones, three transmitter antennas and single receiver antenna, and average transmitted power efficiency was 75%. Reference [18] designed power wireless receiving side using single antenna for drone application, and results have shown that the maximum efficiency of the power transfer was 77%.

The aim of this research paper is to determine a new research area to be focused on and ways to improve wireless charging efficiency. The objectives are shown below.

Review the methods of wireless power transfer based on the distance between transmitter and receiver.

- Review the advantages and disadvantages of inductive wireless power transfer, capacitive wireless power transfer, magnetic resonance, hybrid inductive and capacitive power transfer and laser microwave, considering drone's battery charging.

- Review the advantages and disadvantages of capacitive wireless power transfer, considering drone's battery charging.
- Comparison of wireless power transfer (WPT) methods on drone's battery charging.
- Development trend of WPT methods on drone's battery charging.
- Performance analysis of the efficiency of wireless power transfer module (KT-B3-RX) at different distances between Tx and Rx and apply different values of load resistance.

## 2 Principles of Wireless Power Transfer Technology

Wireless power transfer (WPT) means transmitting electrical power through free space without any contact between the loads and the power source. The complete wireless charging process can be divided into two electrical circuits as shown in Fig. 3, the transmitter circuit, which transfers the input voltage to high frequency AC current. Therefore, the receiver circuit plays a role of converting the high frequency AC current into the receiver circuit to be converted into DC current. According to Ref. [19], two techniques are the most used in charging a drone battery. The techniques are wireless induction charging and contact-based charging. Wireless charging uses induction coils but requires the drone to land very precisely on a charging pad. Any differential orientation between the induction loops on the charging pad and the drone reduces power transfer efficiency. Currently the wireless power transfer is advancing towards two major directions: radiative wireless charging and non-radiative wireless charging. Radiative wireless charging consists of directive radio frequency charging such as laser microwave and non-directive radio frequency charging such as radio waves. Where non-radiative wireless charging consists of inductive coupling, magnetic resonant coupling, and hybrid inductive and capacitive. This paper discusses the advantages and disadvantages of radiative wireless charging and non-radiative charging and provides comparison on these technologies. The flow chart in Fig. 2 illustrates the methods of wireless power transfer technology. Where WPT divided into three main methods capacitive, radiative and non-radiative methods. Radiative methods categorized into two types which are laser microwaves and radio wave, where the distance between transmitter antenna and receiver antenna is large. The distance between transmitter and receiver antennas in non-radiative methods is relatively short as well as the capacitive method.

The resonance condition of the system can be controlled by the capacitance of  $C_1$  and  $C_2$  [20] as shown in Fig. 3. Thus, the capacitance values of  $C_1$  and  $C_2$  must be appropriately chosen to achieve the resonance condition at a considered frequency  $f_0$ , where the angular frequency can be calculated based on Eq. (1) [21, 22].

$$\omega_0 = 2\pi f_0 \quad (1)$$

$C_1$  and  $C_2$  can be calculated by using the equation in (2a) and (2b).

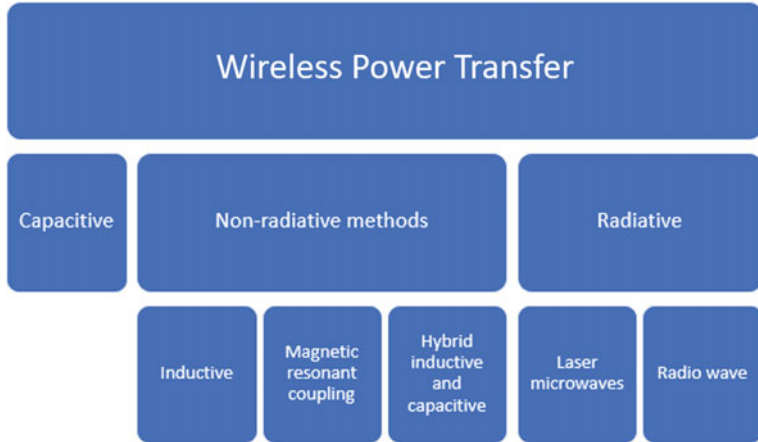
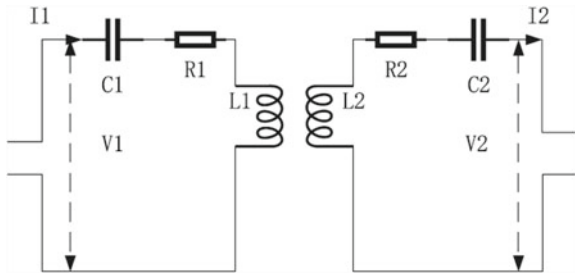


**Fig. 2** Current methods of WPT

**Fig. 3** Circuit structure of WPT system [20]



$$C_1 = \frac{1}{\pi \omega_0^2 L_1} \quad (2a)$$

$$C_2 = \frac{1}{\pi \omega_0^2 L_2} \quad (2b)$$

The self-inductance  $L_1$  can be calculated by feeding the primary coil with a current  $I_1$  not equal to 0 and imposing  $I_2$  equal to zero as shown in Eq. (3a). The self-inductance  $L_2$  can be calculated by feeding the secondary coil with a current  $I_2$  not equal to 0 and imposing  $I_1$  equal to zero as shown in Eq. (3b):

$$L_1 = l_m \left\{ \frac{v_{10}}{\omega_0 I_1} \right\} \quad (3a)$$

$$L_2 = l_m \left\{ \frac{v_{20}}{\omega_0 I_2} \right\} \quad (3b)$$

Equations (3a) and (3b) calculates the inductance, where  $l_m$  is the imaginary part.  $v_{10}$  and  $v_{20}$  are the voltage drops along the circuit.

$$M = \text{Im} \left\{ \frac{V_{20}}{\omega I_1} \right\} \quad (4)$$

$$k = \frac{M}{\sqrt{L_1 L_2}} \quad (5)$$

The mutual inductance,  $M$ , and the coupling factor  $k$  between the coils are calculated by Eqs. (4) and (5), respectively. The coils use a type of wire called a Litz wire conductor to reduce resistive loss inside the coil and to increase efficiency. The coil resistance  $R_1$  and  $R_2$  can be found in the wire datasheet. In the SS compensation circuit, the efficiency of the system  $\eta$  can be obtained in resonance condition for a load resistance,  $R_L$  by using Eq. (6) [22].

$$\eta = \frac{R_L (\omega_0^2 M^2)}{(R_2 + R_L)^2 \left( R_1 \frac{\omega_0^2 M^2}{R_2 + R_L} \right)} \quad (6)$$

## 2.1 Wireless Coil Design

The number of turns in the primary and secondary coils can be varied to maximize the wireless power transmission [23]. The best performance and maximum efficiency of the series-series topology (SS) compensation are when the number of turns in primary and secondary coils is the same [23]. The number of coils shall not be too much. This will lead to saturated mutual inductance, and the volume of the coil will be too large. The ratio of several turns of transmitting and receiving coils is assumed to be 1:1 [20].

Compact and light windings can be constructed by fixing the external diameter of the coil and spacing between coils. Transmitting coil diameter equals 8 cm, receiving coil diameter equals 8 cm and the spacing between coils is around 1 cm. These coils are designed to minimize weight and size to maintain high efficiency. These coils are perfectly aligned [24]. The coils design depends on the Litz cable which is placed on a soft ferrite structure [25]. This with a magneto plated wire (MPW) was proposed which this type of wire is a copper wire plated with a thin iron film and Litz wire with a copper wire [26]. An improvement of the transmission efficiency is required in the WPT. Thus, it is necessary to improve the coupling coefficient and quality factor of the coils. The quality factor is proportional to the inductance of the coils and angular frequency and inversely proportional to the resistance of the coils in the system. The resistance of the coils can be reduced to improve the quality factor. This resistance is the sum of the AC resistance due to the skin effect  $R_s$ , AC resistance

due to proximity effect  $R_p$  and DC resistance  $R_{dc}$ . A twisted plural copper wire with a small diameter (LCW) which is the Litz wire is generally used to reduce the AC resistance due to skin effect [26].

### 3 Method of Wireless Power Transfer Based on the Distance Between Transmitter and Receiver

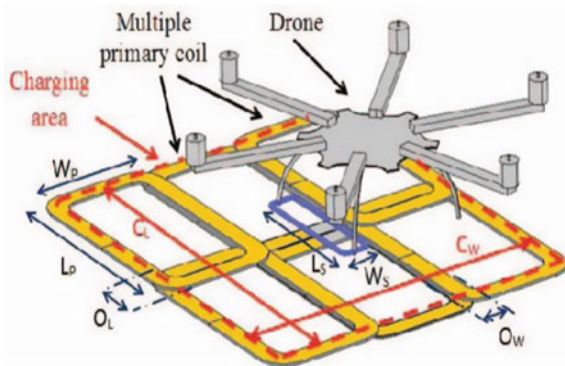
To minimize the impact of power losses, some wireless charging systems use sensors to determine the drone's position on the charging pad and adjust the position of the charging coil. Reference [15] have categorized wireless charging technology into four types based on the distance between the power transmitter and receiver. Table 1 shows the specifications of each type. Non-radiative methods mean transferring the electric power through one wavelength of the transmitter antenna [27].

In addition, the non-radiative method is using capacitive or inductive wireless power transfer. In the other hand, radiative method means transferring the electric power beyond one wavelength. Reference [9] have presented an example of wireless power transmission; in this project, the system was composed of a drone charging station with multiple power transmitters and one receiver to charge the battery of a drone; in this work, resonance inductive coupling-based wireless power transmission technique has been used. The block diagram in Fig. 4 illustrates the proposed system, in which the wireless charging consists of three main parts: first is the wireless power receiver attached to the drone battery, which acts as battery charger. Second is the

**Table 1** Types of wireless charging technologies based on the distance between transmitter and receiver

Method of charging	Transmission distance (metre)	Frequency range (hertz)	Applications
Contact-based charging technique (using inductive coupling)	1–10 cm	125 kHz–13.56 MHz	Electric toothbrushes, wireless shaver and drone's battery
Wireless power transmission-based charging technique (radiative method)	1–10 m	10–800 MHz	Cellular phones, drone's battery and electric stove
Wireless power transmission-based charging technique (non-radiative method)	2–10 m	10–800 MHz	Electric toothbrush, wireless shaver and drone's battery
Distance transmission	1–900 km	1–10 GHz	Radio frequency, radio power transmission and medical equipment

**Fig. 4** Method of WPT for drone's battery [27]



wireless power transmitter, which can be adjusted, based on the landing spot of the drone [28]. The third part is the control unit, which can measure the terminal voltage of each transmitting coil, align the centroid of the transmitting and receiving coil.

### 3.1 Inductive Wireless Power Transfer

Inductive wireless power transfer (IWPT) is the application of the electromagnetic induction where the primary coil is provided with an electric current to generate a magnetic field [29], where the secondary coil is placed within the magnetic field to induce current. Both primary and secondary coils are tightly coupled together and operate at similar frequency [30]. Inductive coupling has a very high transfer energy efficiency but in a very close distance [31], the higher distance between transmitter antenna and receiver antenna the less power transfer efficiency. Both transmitter and receiver must be tightly aligned to achieve high-energy transfer efficiency. IWPT consists of two parts transmitter and receiver coils. Both coils act as an electric transformer [32] based on Ampere's law and Faraday's law when the transmitter coil generates a magnetic field, the power can be transferred to the receiver coil. Relatively this method has a short range of power transfer. It can be applied in many applications such as charging a battery, toothbrush and industrial heater. Reference [33] have presented an inductive wireless power charger for drone battery. In this work, a solar panel was installed as a power supply for the system. The charger consists of six transmitters coils, with a capacity of maximum 700 mA. Also, in this work developing of a tethered robotic rover equipped with a 2D Lidar sensor to detect and localize a drone, and a robotic arm equipped with an inductive charging pad. Reference [33] have concluded that inductive power transfer charging method has the disadvantage of sensitivity to displacement. This could cause a power reduction on the receiver side; in some cases, the transferred power is zero. Furthermore, the inductive charging method has a low rate of transferred electric charge.

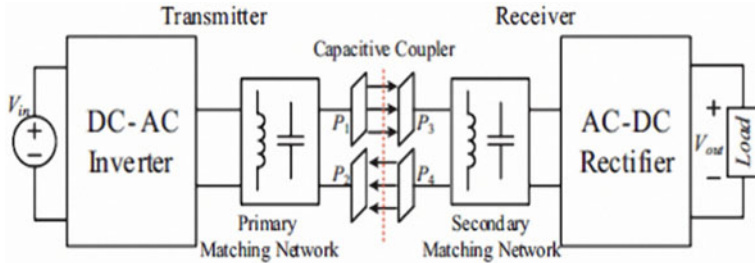


**Fig. 5** Capacitive wireless power transfer block diagram [37]

### 3.2 Capacitive Wireless Power Transfer

Reference [34] have conducted research and development on capacitive (or electric) coupling, which uses the electric field to transfer power wirelessly. Moreover, Reference [34] concluded that in capacitive wireless power transfer (CWPT) method drawbacks are the higher voltages, frequencies and field strengths compared to inductive wireless power transfer. However, it has many other advantages such as lower power losses [35], less heat production and less weight of the system. Reference [36] have investigated the power transfer density enhancement in large air-gap capacitive wireless power transfer systems. Figure 5 represents the simplified block diagram of CWPT. The air gap between the receiver coil and transmitter coil in this experiment was up to 70 mm and delivered output power of 45 W.

### 3.3 Coupled Magnetic Resonance

Coupled magnetic resonance (CMR) method has some similarity to IWPT method with only small differences in the resonant coils, which are tuned to resonate at the same frequency. Resonant magnetic coupling allows multiple charging and wider charging distance as compared to IWPT method. The transmitter and receiver are not required to be tightly aligned. However, when the charging distance increases, the efficiency of resonant charging decreases relatively [38]. Reference [39] have designed WPT using magnetic resonance coupling as shown in Fig. 6, and experimental results have shown that the efficiency of the WPT was 70%. In this method when the system contains more transmitters and receivers coils, the efficiency of the power transfer increases.

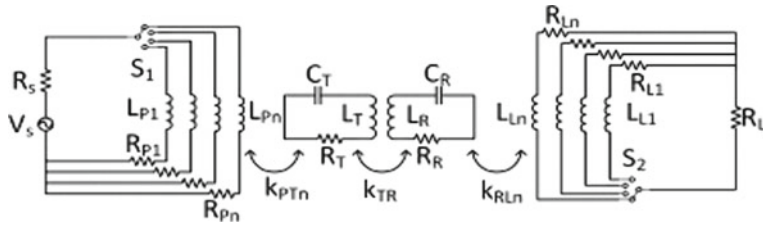


**Fig. 6** Coupled magnetic resonance circuit diagram [39]

### 3.4 Hybrid Inductive and Capacitive Power Transfer

This system combines both IWPT and CWPT, and each system has its own advantages and disadvantages. In IWPT, the current flows through the transmitter and receiver coils; therefore, an alternative current will be generated providing a channel of power transfer [32]. In some of the IWPT, an external capacitor is connected to smooth the flow of the output power [40]. CWPT has the advantage of flexibility in coupling structure [41], and it can transfer the power wirelessly using metal barriers. The maximum transferred distance of CWPT reaches several tens cm. resulting in requiring high voltage and frequency to achieve high power transfer efficiency. The hybrid system of IWPT and CWPT has been proposed by Ref. [42] to enhance the transferred efficiency of the wireless power transfer. CWPT needs inductors to tune the system, and IWPT requires values of capacitor to compensate the wireless power transfer. Therefore, hybrid system is one of the alternative solutions to enhance the output power transferred wirelessly. Figure 7 represents a hybrid system of inductive and capacitive power transfer proposed by Ref. [42], in this work the system was constructed to deliver DC output power which has achieved a maximum efficiency of about 8582%.

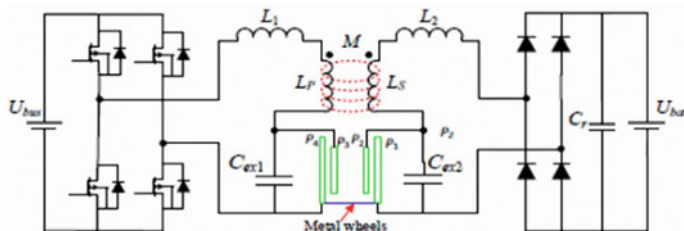


**Fig. 7** Hybrid system of IWPT and CWPT [42]

### 3.5 *Laser Microwave*

The laser microwave is one of the radiative wireless power transfer technologies, and it can transfer energy and data for long distances [43]. In power transfer application, laser microwave requires a strong directivity transmitter antenna [44], which enables efficient power transfer. Moreover, it has also been claimed that laser microwaves have a complication in maintaining efficient alignment. Therefore, it is unsuitable for charging a drone's battery.

## 4 Discussion and Development Trend

WPT has become a leading trend technology in most of the new applications devices, such as mobile phones and drones. However, it has many technical challenges, especially when it comes to charging drone's batteries. As shown in Table 2, recent researchers [14–18] have proposed and designed a WPTs for drones charging system by using several types of methods of charging. However, the power transfer efficiency was revealed to be one of the most intensive challenges in designing a WPT for drones. One of the main obstacles in terms of technical aspect is using a single coil for the transmitter side and single coil for the receiver side as shown in Table 3 which summarizes WPT power efficacy for drone's battery. Using single coils in the receiver antenna and transmitters antenna results in decreasing power transfer efficiency. Therefore, their results in terms of power transfer efficiency have not exceeded 75%. Super-capacitor is one of the useful elements which can be added to the design of the WPT system to increase the power transfer efficiency. Where super-capacitor reduces the possibility of voltage drop when the drone's battery is on charging process, especially when using green technology such as solar panels as power supply to the charging system. Super-capacitor can maintain a stable battery charging when the input voltage is dropped. Moreover, it differs from a regular capacitor in that it has very high capacitance. When voltage differential is applied to its positive and negative pins it charges it. Moreover, super-capacitor has a longer lifetime compared with normal battery. Among the various types of WPT method, hybrid capacitive and inductive are the most efficient.

Figures 8 and 9 represent a proposed study platform to find the best position of efficient WPT during drone's battery charging. To increase the power in the transmitter side (Tx) multiple transmitter antenna is proposed. Locating of the receiver antenna is the most important part to get the maximum power possible by placing the 4 Tx at different locations spot at (x-axis and y-axis) in the wireless charging station it allows to study the power transfer efficiency at different locations. Sensors to detect the output voltage and current are required for further analysis and therefore store all the data of the output power for Tx into SD card. LoRa module is proposed to be used to transfer and monitor the output power of the Tx. At the first stage adjusting

**Table 2** Efficiency of WPT for drone's batteries

References	Method	Power transfer efficiency	Number of Transmitter coils
[14]	IPT	NA	Single coil
[15]	IPT	60%	Single coil
[16]	IPT	65%	Single coil
[17]	CMR	75%	Three coils
[18]	CPT	77%	Modified single coil
[34]	CPT	50%	Single coil
[45]	CMR	71%	Two coils

**Table 3** Comparison of WPT methods on drone's battery charging

WPT technology	Type of WPT	Frequency range	Transfer distance	Power transfer efficiency	Application and capability for drones charging
Capacitive		Medium	Low	Low	Transfer distance and power level are low for drone's battery
Non-radiative	Inductive	Medium	Low	High	Transfer distance is low for drone's battery
	Hybrid inductive and capacitive	Medium	Medium	High	Capable for all size of drone's battery
	Magnetic coupled Resonant	Medium	Medium	Medium	Capable for medium size drone's battery
Radiative	Laser microwave	High	High	High	Requires large antennas, and direct path of transferring the power. Also, costly compared with other techniques
	Radio microwave	High	High	Low	Requires high-frequency band, which harmful to the human body

the locations of the Tx must be conducted manually, to study the performance of the output power.

#### 4.1 Drones Charging Network Scheduling Approach

Drones can be highly effective in many applications even with the current challenges such as lack of flight time duration. However, wireless charging stations for

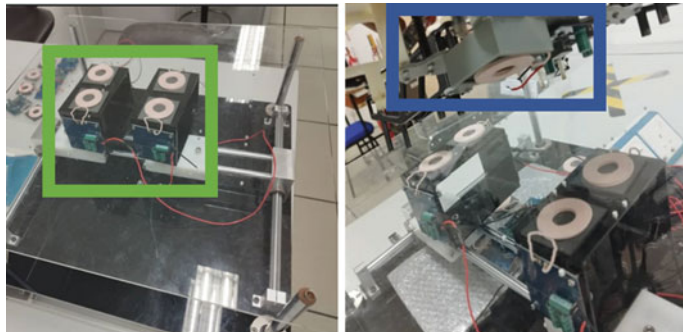


**Fig. 8** WPT charging station for drone

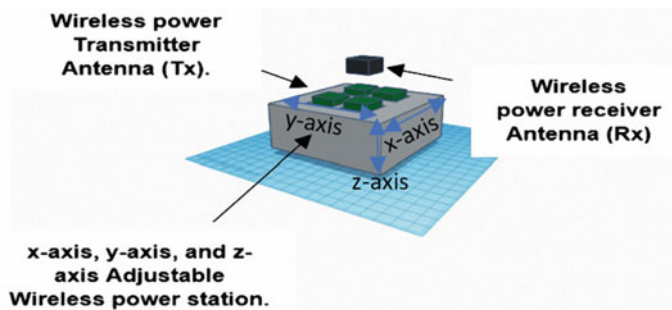


**Fig. 9** Concept design of WPT charging station for drone

drones requires scheduling for proper power distribution. Many studies have been conducted to enhance drones to be used in multiple applications, such as scheduling-drone charging for multi-drone network [46]. In this approach, scheduling of drones to be charged was simulated based on game theory and timestamp to charge the lowest drone battery. Reference [47] introduced a green charging station system for drone controller using reinforcement learning approach; in this work, current control has been applied to the wireless charging station to organize the charging time. Moreover, computing designs also were proposed by other researchers to enhance drone's performance in terms of organizing the charging time [48, 49]. Applying LoRa network communication to the charging system can solve the problem of long-distance communication between drone and charging station. The following diagram in Fig. 10 represents the overall design of the drone flight for monitoring application, where the charging system is part of the overall design. First the drone flight is initialized, then when the drone has reached the specified altitude, navigating to the destination will start automatically. During the time of the drone flight, there will be voltage sensor to detect the battery voltage of the drone every 3 s and send feedback through LoRa module. When the drone battery voltage is below the specified limit, automatically the drone will be navigated to the nearest charging

station. Therefore, autoland to the specified location of the charging station will take place, and wireless charging will start once the drone lands on the station.

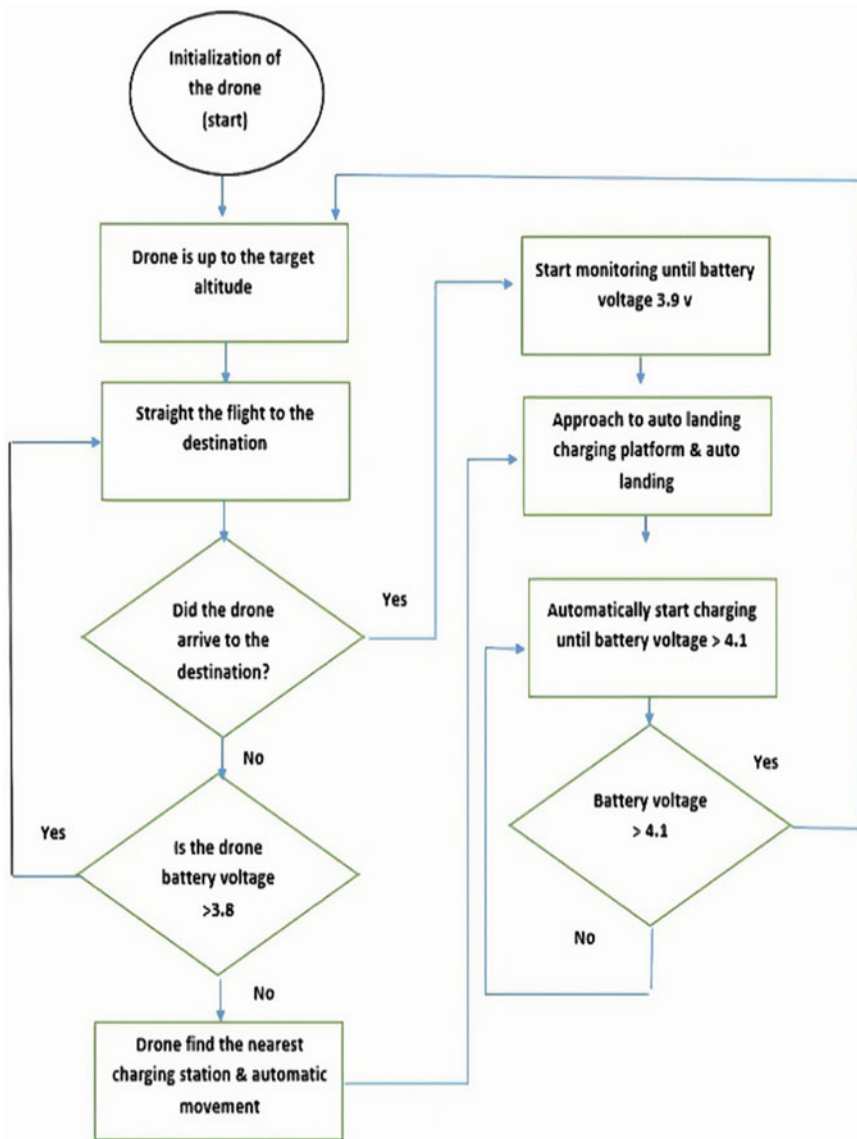


**Fig. 10** Overall design of the charging system

## 4.2 Proposed Wireless Sensor Network for Long-Distance Data Charging Acquisition

Wireless sensor network (WSN) has many structures such as mesh network system [50], star network system [51]. Network connection of LoRa system for wireless charging station is shown in Fig. 9. A mesh topology is proposed to be used in the LoRa end-nodes to communicate with the LoRa gateway. Once the drone takes off from its station, power must be monitored to estimate the flight duration and when the drone can return to the charging station. Reference [52] have studied the drone's power factor when the drone on-flight mode, and how much power is consumed when the drone take-off. To secure the data transmission process, each end-node has its own sync word, and at the same time, it helps to separate each device's data. When the LoRa gateway receives the transmitted data, it recognizes the device based on its sync word. Therefore, send the received data from end-node to the Arduino Mega controller. A Wi-Fi module can be used to provide an internet interface to the LoRa gateway. As shown in Fig. 11, the mesh network consists of three nodes; at first, node 1 communicates with the gateway as its parent. Once the communication is started between node 1 and the gateway, the gateway adds it as a one of the child-list. Therefore, the gateway request nodes in the child-list to send data. The gateway sends command D1 to node 1, then node 1 sends its data back as a D2 to the gateway. At the same time, the nearest node to node 1 is node 3. The same structure of communication is initialized between node 1 and node 3, node 3 considers node 1 as its parent and joins the network. By this sequence, the mesh network is constructed. Therefore, in the next round the gateway requires node 3 to collect its data using D3, D4, D5 and D6.

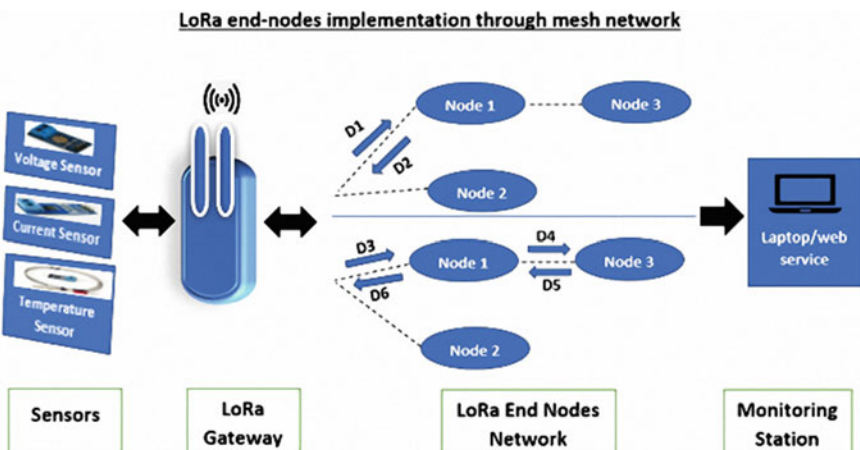


**Fig. 11** Overall design of LoRa transfer topology for the charging system

## 5 Results

This section presents a performance analysis of the wireless transfer module (KT-B3-RX) to assess its efficiency at various distances (0, 5, 10 and 15 mm) between the receiver (Rx) and transmitter (Tx). The obtained results, as shown in Table 4, indicate a maximum efficiency of 98% when the load resistance was set to  $20\ \Omega$  at 0 mm between Tx and Rx. Subsequent Tables 5, 6, 7, and 8 illustrate the efficiency achieved when different load resistance values of 30, 35, 45 and  $50\ \Omega$  were applied, respectively. Throughout the study cases, an input voltage of 21.4 was provided to the transmitter module.

**Table 4** Efficiency at different distance between Tx and Rx using  $20\ \Omega$  as a load

Distance between Tx and Rx (mm)	Input voltage (V)	Input current (A)	Output voltage (V)	Output current (A)	Output power (W)	Efficiency (%)
0	21.4	1.98	23.1	1.81	41.8	98
5	21.4	0	0	0	0	0
10	21.4	0	0	0	0	0
15	21.4	0	0	0	0	0

**Table 5** Efficiency at different distance between Tx and Rx using  $30\ \Omega$  as a load

Distance between Tx and Rx (mm)	Input voltage (V)	Input current (A)	Output voltage (V)	Output current (A)	Output power (W)	Efficiency (%)
0	21.4	1.3	23.3	1.17	27.26	97.9
5	21.4	1.32	23.3	1.18	27.5	97
10	21.4	1.36	23.3	1.18	27.5	94.5
15	21.4	1.37	23.4	1.18	27.6	94

**Table 6** Efficiency at different distance between Tx and Rx using  $35\ \Omega$  as a load

Distance between Tx and Rx (mm)	Input voltage (V)	Input current (A)	Output voltage (V)	Output current (A)	Output power (W)	Efficiency (%)
0	21.4	1.15	23.5	0.9	21.2	86
5	21.4	1.17	23.5	1.0	23.5	93.8
10	21.4	1.25	23.5	1.1	25.85	96.6
15	21.4	1.25	23.5	1.1	25.85	96.6

**Table 7** Efficiency at different distance between Tx and Rx using  $45\ \Omega$  as a load

Distance between Tx and Rx (mm)	Input voltage (V)	Input current (A)	Output voltage (V)	Output current (A)	Output power (W)	Efficiency (%)
0	21.4	0.86	23.6	0.76	17.9	97
5	21.4	0.86	23.6	0.76	17.9	97
10	21.4	0.91	23.6	0.76	17.9	92
15	21.4	0.95	23.6	0.76	17.9	88

**Table 8** Efficiency at different distance between Tx and Rx using  $50\ \Omega$  as a load

Distance between Tx and Rx (mm)	Input voltage (V)	Input current (A)	Output voltage (V)	Output current (A)	Output power (W)	Efficiency (%)
0	21.4	0.82	23.6	0.64	15.1	86
5	21.4	0.78	23.5	0.65	15.3	91.6
10	21.4	0.82	23.5	0.66	15.5	88
15	21.4	0.82	23.7	0.65	15.4	87.7

## 6 Conclusion

Three main types of WPT have been introduced in this review which are capacitive, radiative and non-radiative methods. Types of wireless charging technologies based on the distance between transmitter and receiver have been summarized. The advantages and disadvantages of each method have been introduced. Hybrid inductive and capacitive method using multiple transmitter antenna is a potential technology for the charging of drone's battery. For high efficiency performance of wireless power station of drone's battery, it is necessary to consider:

- Using hybrid system of IWPT and CWPT due to its high efficiency power transfer.
- Add a super-capacitor to the charging circuit to smooth out the flow of the current.
- Apply multiple transmitter antennas to the design, to increase the power efficiency of the WPT system.
- For longer distance transmission the LoRa network system has been proposed.

**Acknowledgements** This research is fully funded by Sunway University PhD Studentship Scheme. The research work is also supported by Research Centre for Human-Machine Collaboration (HUMAC) at Sunway University and University of Wollongong (UOW) University College Malaysia.

## References

1. Smith, T.F., Waterman, M.S.: Identification of common molecular subsequences. *J. Mol. Biol.* **147**, 195–197 (1981). [https://doi.org/10.1016/0022-2836\(81\)90087-5](https://doi.org/10.1016/0022-2836(81)90087-5); Yap, K.M., Eu, K.S., Low, J.M.: Investigating wireless network interferences of autonomous drones with camera based positioning control system. In: *6 International Computer Symposium* (2016). <https://doi.org/10.1109/ICS.2016.80>
2. Aydoğán Y.: Drone technology in agricultural mechanization *Int. Sci. J. Mech. Agric.* **38**(2), 36–38 (2018)
3. Rughu, S.I.R.U., Prmle, H., Hgx, Q., Udkpdq, P., Hgx, Q.: A novel approach for border security surveillance drone with live instruction monitoring. *IEEE*, 7–10 (2019)
4. Mohamedzain, A.O., Chua, H.S., Al-talib, A.A.M.: Outdoor experimental comparison between PV cell and combined system PV-TEG **32**(3), 279–283 (2020)
5. Allauddin, M.S., Kiran, G.S., Kiran, G.S.S.R., Srinivas, G., Mouli, G.U.R., Prasad, P.V.: Development of a surveillance system for forest fire detection and monitoring using drones. In: *IGARSS 2019–2019 IEEE International Geoscience and Remote Sensing Symposium*, pp. 9361–9363 (2019). <https://doi.org/10.1109/igarss.2019.8900436>
6. Simoes, D., Rodrigues, A., Reis, A.B., Sargent, S.: Forest fire monitoring through a network of aerial drones and sensors. In: *2020 IEEE International Conference on Pervasive Computing and Communications Workshops, PerCom Workshops 2020* (2020). <https://doi.org/10.1109/PerComWorkshops48775.2020.9156137>
7. Mohammed, O., Tahar, L.M.: Power management and control of a grid-connected DFIG based wind turbine/PV/battery hybrid renewable energy system. *Sci. Int. (Lahore)* 231–251 (2022)
8. Park, S., Zhang, L., Chakraborty, S.: Battery assignment and scheduling for drone delivery businesses. In: *Proceedings of the International Symposium on Low Power Electronics and Design* (2017). <https://doi.org/10.1109/ISLPED.2017.8009165>
9. Rohan, A., Rabah, M., Asghar, F., Talha, M., Kim, S.-H.: Advanced drone battery charging system. *J. Electric. Eng. Technol.* (2019). <https://doi.org/10.1007/s42835-019-00119-8>
10. Lu, M., Bagheri, M., James, A.P., Phung, T.: Wireless charging techniques for UAVs: a review, reconceptualization, and extension. *IEEE Access* **6**(c) 29865–29884 (2018). <https://doi.org/10.1109/ACCESS.2018.2841376>
11. Williams, A., Yakimenko, O.: Persistent mobile aerial surveillance platform using intelligent battery health management and drone swapping. In: *Proceedings—2018 4th International Conference on Control, Automation and Robotics, ICCAR 2018*, pp. 237–246 (2018). <https://doi.org/10.1109/ICCAR.2018.8384677>
12. Campi, T., Cruciani, S., Maradei, F., Feliziani, M.: Wireless charging system integrated in a small unmanned aerial vehicle (UAV) with high tolerance to planar coil misalignment. In: *2019 Joint International Symposium on Electromagnetic Compatibility, Sapporo and Asia-Pacific International Symposium on Electromagnetic Compatibility, EMC Sapporo/APEMC 2019*, pp. 601–604 (2019). <https://doi.org/10.23919/EMCTokyo.2019.8893934>
13. Mohamedzain, A.O., Chua, H., Yap, K., Uthayasurian, P., Jiehan, T.: Novel drone design using an optimization software with 3D model, simulation, and fabrication in drone systems research. *MDPI* **6**(4). <https://doi.org/10.3390/drones6040097>
14. Obayashi, S., Kanekiyo, Y., Nishizawa, K., Kusada, H.: 85-kHz band 450-W inductive power transfer for unmanned aerial vehicle wireless charging port. In: *2019 IEEE Wireless Power Transfer Conference, WPTC 2019*, pp. 80–84 (2019). <https://doi.org/10.1109/WPTC45513.2019.9055626>
15. Park, C.W., Chung, H.T.: A study on drone charging system using wireless power transmission. *Int. J. Trend Res. Dev.* **3**(6), 736–745 (2016)
16. Choi, C.H., Jang, H.J., Lim, S.G., Lim, H.C., Cho, S.H., Gaponov, I.: Automatic wireless drone charging station creating essential environment for continuous drone operation. In: *2016 International Conference on Control, Automation and Information Sciences, ICCAIS 2016*, pp. 132–136 (2017). <https://doi.org/10.1109/ICCAIS.2016.7822448>

17. Bin Junaid, A., Konoiko, A., Zweiri, Y., Sahinkaya, M.N., Seneviratne, L.: Autonomous wireless self-charging for multi-rotor unmanned aerial vehicles. *Energies (Basel)* **10**(6), 1–14 (2017). <https://doi.org/10.3390/en10060803>
18. Muhamar, A., Mostafa, T.M., Hattori, R.: Design of power receiving side in wireless charging system for UAV application. In: Proceeding—ICSEEA 2017 International Conference on Sustainable Energy Engineering and Application: ‘Continuous Improvement of Sustainable Energy for Eco-Mobility’, vol. 2018-Janua, pp. 133–139 (2017). [https://doi.org/10.1109/ICS\\_EEA.2017.8267698](https://doi.org/10.1109/ICS_EEA.2017.8267698)
19. Dominique, D., Dominique, F.: A position and orientation independent drone charging system. *J. Eng.* **2017**(9), 536–538 (2017). <https://doi.org/10.1049/joe.2017.0325>
20. Yan, Y., Shi, W., Zhang, X.: Design of UAV wireless power transmission system based on coupling coil structure optimization. *EURASIP J. Wirel. Commun. Netw.* **2020**(1) (2020). <https://doi.org/10.1186/s13638-020-01679-4>
21. Kim, H., et al.: Mitigation of frequency splitting phenomena using a matching capacitor in wireless power transfer system for automated guided vehicle. In: 2020 IEEE Wireless Power Transfer Conference, WPTC 2020, pp. 170–173 (2020). <https://doi.org/10.1109/WPTC48563.2020.9295565>
22. Campi, T., Cruciani, S., Feliziani, M., Maradei, F.: High efficiency and lightweight wireless charging system for drone batteries. In: 2017 AEIT International Annual Conference: Infrastructures for Energy and ICT: Opportunities for Fostering Innovation, AEIT 2017, vol. 2017-Janua, pp. 1–6 (2017). <https://doi.org/10.23919/AEIT.2017.8240539>
23. Campi, T., Dionisi, F., Cruciani, S., de Santis, V., Feliziani, M., Maradei, F.: Magnetic field levels in drones equipped with wireless power transfer technology. In: 2016 Asia-Pacific International Symposium on Electromagnetic Compatibility, APEMC 2016, pp. 544–547 (2016). <https://doi.org/10.1109/APEMC.2016.7522793>
24. Dai, J., Ludois, D.C.: Capacitive power transfer through a conformal bumper for electric vehicle charging. *IEEE J. Emerg. Sel. Top Power Electron.* **4**(3), 1015–1025 (2016). <https://doi.org/10.1109/JESTPE.2015.2505622>
25. Houran, M.A., Yang, X., Chen, W.: Magnetically coupled resonance WPT: review of compensation topologies, resonator structures with misalignment, and EMI diagnostics. *Electronics (Switzerland)* **7**(11). MDPI AG (2018). <https://doi.org/10.3390/electronics7110296>
26. Mizuno, T., Ueda, T., Yachi, S., Ohtomo, R., Goto, Y.: Dependence of efficiency on wire type and number of strands of litz wire for wireless power transfer of magnetic resonant coupling. *IEEE J. Ind. Appl.* **3**(1), 35–40 (2014). <https://doi.org/10.1541/ieejija.3.35>
27. Lu, X., Wang, P., Niyato, D., Kim, D.I., Han, Z.: Wireless charging technologies: fundamentals, standards, and network applications. *IEEE Commun. Surv. Tutor.* **18**(2), 1413–1452 (2016). <https://doi.org/10.1109/COMST.2015.2499783>
28. MohamedZain, A. O., Wei Hou, L., Chua, H., Yap, K., & Kim Boon, L. (2023). The Design and Fabrication of Multiple-Transmitter Coils and Single-Receiver Coils for a Wireless Power Transfer System to Charge a 3s LiPo Drone’s Battery. <https://doi.org/10.3390/en16093629>
29. Houran, M.A., Yang, X., Chen, W., Samizadeh, M.: Wireless power transfer: critical review of related standards
30. Kuehl, A., Kneidl, M., Seefried, J., Masuch, M., Weigelt, M., Franke, J.: Production concepts for inductive power transfer systems for vehicles. *Energies (Basel)* **15**(21), 7911 (2022). <https://doi.org/10.3390/en15217911>
31. Li, G., Jo, C.-H., Shin, C.-S., Jo, S., Kim, D.-H.: A load-independent current/voltage IPT charger with secondary side-controlled hybrid-compensated topology for electric vehicles. *Appl. Sci.* **12**(21), 10899 (2022). <https://doi.org/10.3390/app122110899>
32. Maulana, E., Abidin, Z., Djuriatno, W.: Wireless power transfer characterization based on inductive coupling method. In: 2018 Electrical Power, Electronics, Communications, Controls and Informatics Seminar, EECCIS 2018, pp. 164–168 (2018). [https://doi.org/10.1109/EEC\\_CIS.2018.8692901](https://doi.org/10.1109/EEC_CIS.2018.8692901)
33. Khonji, M., Alshehhi, M., Tseng, C.M., Chau, C.K.: Autonomous inductive charging system for battery-operated electric drones. In: e-Energy 2017—Proceedings of the 8th International

- Conference on Future Energy Systems, pp. 322–327 (2017). <https://doi.org/10.1145/3077839.3078462>
34. Mostafa, T.M., Muhamam, A., Hattori, R.: Wireless battery charging system for drones via capacitive power transfer. In: 2017 IEEE PELS Workshop on Emerging Technologies: Wireless Power Transfer, WoW 2017 (2017). <https://doi.org/10.1109/WoW.2017.7959357>
35. Institute of Electrical and Electronics Engineers, IEEE Microwave Theory and Techniques Society, Wireless Power Consortium, Q. IEEE PELS Workshop on Emerging Technologies: Wireless Power (2018) : Montréal, and Q. Wireless Power Congress (2018) : Montréal, 2018 IEEE Wireless Power Transfer Conference (WPTC) : WPTC, IEEE MTT-S Wireless Power Transfer Conference ; WoW, IEEE PELS Workshop on Emerging Technologies: Wireless Power ; WPC, Wireless Power Consortium : June 3–7, 2018, Montreal, Quebec, Canada
36. Kumar, A., Pervaiz, S., Chang, C.K., Korhummel, S., Popovic, Z., Afridi, K.K.: Investigation of power transfer density enhancement in large air-gap capacitive wireless power transfer systems. In: 2015 IEEE Wireless Power Transfer Conference, WPTC 2015 (2015). <https://doi.org/10.1109/WPT.2015.7140182>
37. Abramov, E., Zeltser, I., Peretz, M.M.: A network-based approach for modeling resonant capacitive wireless power transfer systems. CPSS Trans. Power Electron. Appl. **4**(1), 19–29 (2019). <https://doi.org/10.24295/cpsstpea.2019.00003>
38. Ching, T.W., Wong, Y.S.: Review of wireless charging technologies for electric vehicles. In: 2013 5th International Conference on Power Electronics Systems and Applications, PESA 2013, vol. 2 (2013). <https://doi.org/10.1109/PESA.2013.6828235>
39. Shi, L., Rasool, N., Zhu, H., Huang, K., Yang, Y.: Design and experiment of a reconfigurable magnetic resonance coupling wireless power transmission system. IEEE Microw. Wirel. Compon. Lett. **30**(7), 705–708 (2020). <https://doi.org/10.1109/LMWC.2020.2997068>
40. Anczewski, P., Miskiewicz, R.M., Moradewicz, A.J.: Inductive power transfer for unmanned aircraft vehicles. In: 2017 Progress in Applied Electrical Engineering, PAEE 2017 (2017). <https://doi.org/10.1109/PAEE.2017.8009025>
41. Wu, X., Su, Y., Hou, X., Qing, X., Zhu, W.: Load adaptation of capacitive power transfer system with a four-plate compact capacitive coupler. In: 2019 IEEE PELS Workshop on Emerging Technologies: Wireless Power Transfer, WoW 2019, pp. 324–329 (2019). <https://doi.org/10.1109/WoW45936.2019.9030647>
42. Luo, B., Long, T., Guo, L., Dai, R., Mai, R., He, Z.: Analysis and design of inductive and capacitive hybrid wireless power transfer system for railway application. IEEE Trans. Ind. Appl. **56**(3), 3034–3042 (2020). <https://doi.org/10.1109/TIA.2020.2979110>
43. Du, Y., Wang, K., Yang, K., Zhang, G.: Trajectory design of laser-powered multi-drone enabled data collection system for smart cities. In: 2019 IEEE Global Communications Conference, GLOBECOM 2019—Proceedings, pp. 1–6 (2019). <https://doi.org/10.1109/GLOBECOM38437.2019.9013552>
44. Agha, S. et al.: Micromachines A Comprehensive Review of Micro UAV Charging Techniques (2022). 10.3390/mi
45. Jawad, A.M., Jawad, H.M., Nordin, R., Gharghan, S.K., Abdullah, N.F., Abu-Alshaeer, M.J.: Wireless power transfer with magnetic resonator coupling and sleep/active strategy for a drone charging station in smart agriculture. IEEE Access **7**, 139839–139851 (2019). <https://doi.org/10.1109/ACCESS.2019.2943120>
46. Hassija, V., Saxena, V., Chamola, V.: Scheduling drone charging for multi-drone network based on consensus time-stamp and game theory. Comput. Commun. **149**(August 2019), 51–61 (2020). <https://doi.org/10.1016/j.comcom.2019.09.021>
47. Faraci, G., Raciti, A., Rizzo, S.A., Schembra, G.: Green wireless power transfer system for a drone fleet managed by reinforcement learning in smart industry. Appl. Energy **259**(August), 114204 (2020). <https://doi.org/10.1016/j.apenergy.2019.114204>
48. Uddin, Z., Altaf, M., Bilal, M., Nkenyereye, L., Bashir, A.K.: Amateur drones detection: a machine learning approach utilizing the acoustic signals in the presence of strong interference. Comput. Commun. **154**(November 2019), 236–245 (2020). <https://doi.org/10.1016/j.comcom.2020.02.065>

49. Kouroshnezhad, S., Peiravi, A., Haghghi, M.S., Jolfaei, A.: An energy-aware drone trajectory planning scheme for terrestrial sensors localization. *Comput. Commun.* **154**(November 2019), 542–550 (2020). <https://doi.org/10.1016/j.comcom.2020.02.055>
50. Lee, H.C., Ke, K.H.: Monitoring of large-area IoT sensors using a LoRa wireless mesh network system: design and evaluation. *IEEE Trans. Instrum. Meas.* **67**(9), 2177–2187 (2018). <https://doi.org/10.1109/TIM.2018.2814082>
51. Ochoa, M.N., Guizar, A., Maman, M., Duda, A.: Evaluating LoRa energy efficiency for adaptive networks: from star to mesh topologies. In: International Conference on Wireless and Mobile Computing, Networking and Communications, vol. 2017-October (2017). <https://doi.org/10.1109/WiMOB.2017.8115793>
52. Shen, C.H., Albert, F.Y.C., Ang, C.K., Teck, D.J., Chan, K.P.: Theoretical development and study of takeoff constraint thrust equation for a drone. In: IEEE Student Conference on Research and Development: Inspiring Technology for Humanity, SCOReD 2017—Proceedings, vol. 2018-January, pp. 18–22 (2018). <https://doi.org/10.1109/SCORED.2017.8305428>

# IIUM Gombak Driving Cycle for Motorcycle



Hafizi Malik  and Ahmad Syahrin Idris 

**Abstract** One such method can be used to assess the fuel rate for an internal combustion engine (ICE) vehicle within a specific area is to develop the driving cycle. For a full-battery electric vehicle (BEV), driving cycle is an important instrument for the evaluation of vehicle characteristics like energy consumption and range estimation. This research aims to experience the actual on-road driving of the selected routes and apply proper methods to construct a significant driving cycle that closely represents local driving patterns to evaluate the fuel rate of certain vehicles within the area. The study area was IIUM Gombak, and speed-time data was collected among selected local routes using a motorcycle. Two machine learning methods were used to construct the driving cycle which are k-means clustering and Markov chain. Results showed that the former method was better suited for the study area as it considered road geography as a significant aspect of traffic flow, where a fuel consumption of 4.50 L per 100 km was required. The study highlighted the importance of determining major aspects of traffic flow such as, but not limited to, road geography, work zones, and traffic volume, when choosing the method outcomes for a representative driving cycle.

**Keywords** Driving cycle · Machine learning · Fuel consumption

---

H. Malik

Department of Mechatronics Engineering, International Islamic University Malaysia, 53100 Gombak, Selangor, Malaysia

A. S. Idris ()

Department of Electrical and Electronic Engineering, University of Southampton Malaysia,  
Iskandar Puteri, Johor, Malaysia  
e-mail: [A.S.Idris@soton.ac.uk](mailto:A.S.Idris@soton.ac.uk)

## 1 Introduction

### 1.1 *Background*

Driving cycle is a speed rate graph developed from real-world driving experience usually used to assess traffic and vehicle engineering design as well as fuel rate and emission estimation by specific vehicle. Driving cycles have been applied in two ways, which are legislative and non-legislative. Some existing driving cycles have been used for legislative purposes only to control carbon emission by on-road vehicles so that they do not exceed the standard specification and essentially provided to the authorities. On the other hand, the latter type of driving cycle was constructed for the use of industry or environmentalists to estimate fuel consumption and exhaust emission helping the local community to design latest eco-driving car and measuring air pollution level. Moreover, it has been reported that the number of vehicles has surpassed the human population (33.3 million versus 32.6 million), causing even more traffic congestion [1]. Thus, driving cycle research to determine better regional vehicle specifications is critical. Commonly, two types of driving cycle methods were practiced as they are in a form of modal or transient [2]. Modal approach is a compilation of straight acceleration and constant speed and is not featured by real-world road behavior. Transient approach is an experimental-based mode cycle involving various speeds and acceleration typically representing an on-road driving condition.

It is common knowledge that a driving cycle only represents a specific region at where the testing is carried out [3]. Thus, it is not supposed to be applied to others unless they may have the same traffic pattern or characteristics but then, it is rare. So, every region or area needs its own driving cycle to provide information of local on-road driving conditions. Fuel rate, as well as energy distribution, depends on several aspects such as road and vehicle condition, driver behavior, and weather [4]. In this paper, road condition will be the major consideration as the independent variable.

The aim is to analyze and validate the actual on-road driving patterns and construct local driving cycle using appropriate machine learning methods tested them in terms of the authenticity and accuracy. The constructed driving cycle will be validated in terms of performance validation for fuel consumption and exhaust emission using advanced vehicle simulator (ADVISOR) simulation tool. During the operation, to match time and budget constraints, some resources may be limited, such as the variety of vehicles used, as only one will be used.

### 1.2 *Literature Review*

Various opinions are obtained on the definition of driving cycle. However, among all, they have some similarities as driving cycle is a speed-time graph representing traffic pattern within a specific area by specific vehicle. Driving pattern is how the driving

cycle looks like. Its characteristics differ from one area to another. Regardless of the difference, the process to develop the driving cycle is basically similar anywhere. There are four basic stages in constructing a representative driving cycle which are route selection, data collection, cycle construction, and cycle assessment [5].

Route selection could be done qualitatively or quantitatively [6]. A qualitative approach is based on the researcher's personal judgment corresponding on their daily routine such as the route could be based on home-to-work trips, population density, and road classification. This method is common to practice if the study primarily considers better flexibility as it does not involve any quantitative indicator. The quantitative method involves statistics approach such as traffic volume or emission statistics. The advantage of this method is that the selection provides ways to compare the competence of multiple routes and minimizes potential bias occurred due to researchers' individual judgment. However, this method may require extensive effort to survey the specific data unless it is provided by the local authorities.

Once the representative routes are selected, there are three well-known methods to collect data which are chase car method, on-board measurement, and the combination of both previous methods [7]. Chase car method is preferable due to its low resource requirement [6]. Two conditions must be considered for the method to be applied which are a trained driver and target vehicle. The trained driver must follow the selected vehicle along the predetermined routes and keep a constant distance as the speed allowing a time lag for both acceleration and deceleration phases to be reduced [8]. On the contrary, on-board measurement method is used for large-scale studies as it may require a lot of resources [6]. This method is able to collect accurate driving data directly during the operation as it gives a major advantage over the previous method.

The method to construct a driving cycle is variety. However, four methods that have been always practiced worldwide are micro-trip-based construction, segment-based construction, pattern classification construction, and modal construction. Micro-trip-based construction is defined as a trip between two adjacent stops [9]. A micro-trip is commonly composed of four driving components which are acceleration, deceleration, idle and cruise [10]. The cycle will be a combination of several micro-trips side by side done usually either based on random selection, best incremental, or hybrid.

Segment-based method considers the driving conditions or level of services (LOS) instead of the micro-trips. Thus, this method is most suitable for traffic engineering purposes rather than for emission testing. Since it combines the segments according to the roadway conditions, each segment can start or end at any speed. In the meantime, the connecting point of two consecutive segments has to be matched in terms of their speed and acceleration. This method is more applicable where there are less number of stop–go conditions since there is no need for two adjacent stops as the previous method.

Pattern classification method requires kinematic sequences to be classified into heterogeneous classes using statistical method [11]. To begin with, the classes will be categorized into several parameters which can vary in terms of LOS or the

traffic volume. Then, the succession probabilities are used to determine the likelihood between classes. The driving cycles are constructed by chaining the kinematic sequences randomly selected from each of the activity classes.

The last method would be the modal construction where a real-world driving is viewed as a sequence of four basic driving components. The snippets can start and end at any value which is quite similar to the segment-based method. The first step is to partition the speed data collected into snippets based on acceleration and then classify the snippets into modal bins using maximum likelihood estimation. Using the modal bins, a transition matrix that contains succession probabilities between different modes is created, and a driving cycle can be constructed using a Markov Chain considering the transition matrix [12].

## 2 Methodology

### 2.1 Overview

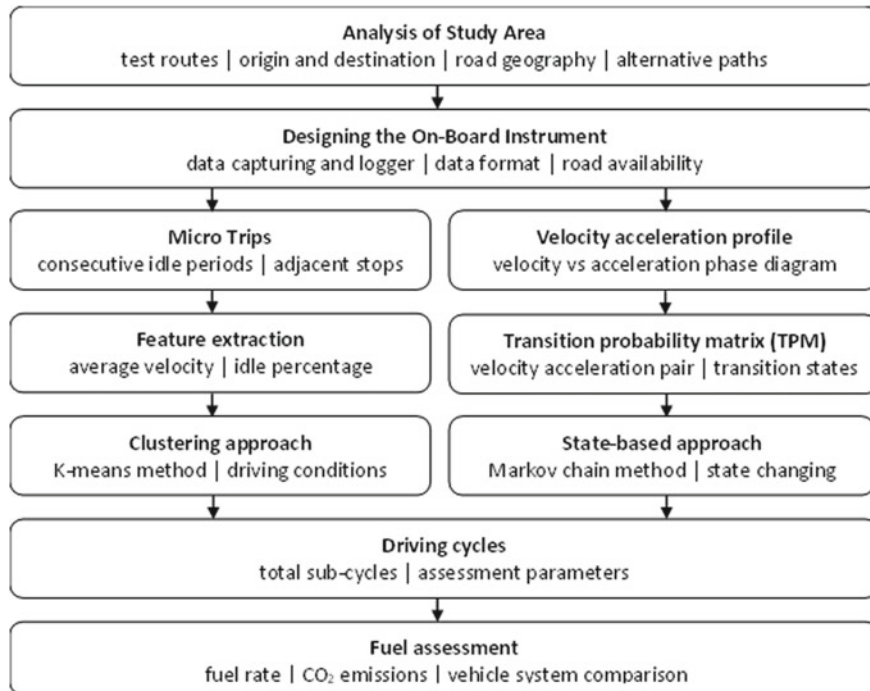
Based on Fig. 1, generation of driving cycles includes the process of selecting representative routes and collecting GPS data with the need of instruments for data logging. The data will be processed to the appropriate format and will be analyzed using several methods, with some of them being commonly used worldwide. Driving cycles are validated using proper process and the justified one is used to assess fuel rate on specific vehicle.

### 2.2 Study Area

The study revolves around driving cycles within IIUM Gombak. Due to less traffic volume within the study area, road geography has become the major consideration affecting the driving cycle pattern. Thus, the route selection is based on qualitative method as it does not involve any statistical record. Every route has the same origin and destination with different geographical paths. The selected routes are shown in Fig. 2.

### 2.3 On-Board System Development

For the data collection, an on-board measurement method is utilized as it is more applicable within IIUM Gombak compared to chase car method which needs multiple vehicles to correlate along the routes. An instrument, as the components are illustrated

**Fig. 1** Methodology flow chart**Fig. 2** Selected routes for on-road testing

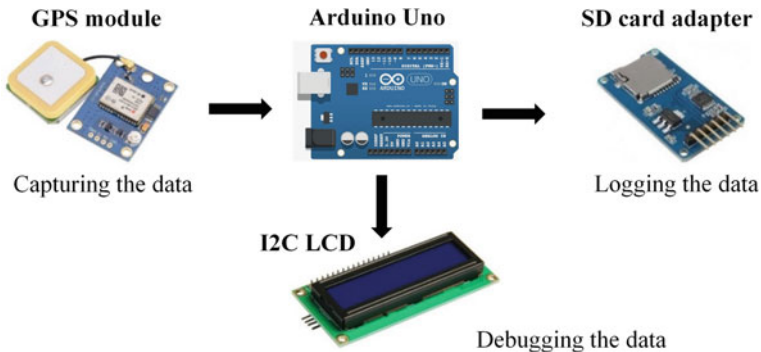


**Fig. 3** Components for the on-board system

in Fig. 3, is developed for data capturing in three data format which are time, coordinates, and speed. Therefore, to satisfy the requirements, GPS tracking is preferred regardless of its disadvantages which need unblocked sky and may provide intermittent data. Both disadvantages are negotiable as the operation will be carried out on the routes with an open sky and any loss data can be overcome and manipulated using interpolation method. All data collected during the real-world testing will be recorded onto SD card, and LCD will be attached to debug the data stored into the SD card.

## 2.4 Cycle Construction Methods

**K-Means Clustering.** The method begins with dividing the recorded data into micro-trips. Micro-trip is a trip between two consecutive idling periods (zero velocity and zero acceleration) or between adjacent stops. Then, driving features such as average speed and idle time percentage are extracted from each micro-trip. The two features are formulated as follows:

1. Average speed of a micro-trip ( $V_{\text{avg}}$ ),

$$V_{\text{avg}} = \frac{v_T}{n}, \quad (1)$$

where  $v_T$  is the total velocity of a micro-trip in meter per second and  $n$  is the duration of the micro-trip in seconds.

2. Idle time percentage of a micro-trip ( $t$ ),

$$t = \frac{t_o}{t_T}, \quad (2)$$

where  $t_o$  and  $t_T$  are the duration when the vehicle speed is zero and the total time of the micro-trip, respectively.

Upon the extraction, each micro-trip can be plotted in a form of average speed versus idle time percentage. The relationship can be seen as the greater the idle time percentage, the lower the average speed. Then, the micro-trips or data points of the feature graph will be clustered using k-means clustering. At the end of the process, the result should have the characteristics as follows:

1. Every cluster must consist of data points.
2. Every cluster must not share the same data points.
3. Every data point must be included into any clusters.

Thus, the steps of k-means clustering algorithm are described as follows [13]:

1. Initialize initial cluster centers,  $z_1, z_2, \dots, z_K$ , depending on the desired number of driving conditions,  $K$ , randomly from speed data points,  $\{x_1, x_2, \dots, x_n\}$ . In this study,  $K = 3$  was used because three speed conditions were considered: low, medium, and high.
2. Assign point  $x_i, i = 1, 2, \dots, n$  to cluster  $C_j, j$  is subset of  $\{1, 2, \dots, K\}$ , if  $\|x_i - z_j\| < \|x_i - z_p\|, p = 1, 2, \dots, K$ , and  $j \neq p$ . The data points will be clustered together with their nearest cluster centers,  $z_j$ .
3. Recompute new cluster centers,  $z_1^*, z_2^*, \dots, z_K^*$ , as follows:

$$z_i^* = \frac{1}{n_i} \sum_{x_j \in C_i} x_j, i = 1, 2, \dots, K, \quad (3)$$

where  $n_i$  is the number of elements belonging to cluster  $C_i$ . Basically, in the specific cluster, it takes the vectors of every element and averages them out by the total number of the elements.

4. If all data points remain in the same cluster for the next iteration where  $z_i^* = z_i, i = 1, 2, \dots, K$ , then exit. Otherwise, repeat Step 2. It is considered as the maximum number of iterations as it terminates.

After the micro-trips are clustered to the three driving conditions, the final driving cycle is constructed by selecting the nearest micro-trips to the cluster centers as the representative micro-trips for the specific driving condition. First, it is necessary to identify how much micro-trips will be selected for each cluster. Considering the final driving cycle should be proportionate to the length of the micro-trips of whole recorded driving data, the duration of each cluster will be formulated as follows:

$$t_i = \frac{t_{\text{driving cycle}}}{t_{\text{all}}} \sum_{j=1} t_{i,j}, \quad (4)$$

where  $t_i$  is duration of cluster number  $i = 1, 2, \dots, n$  in the final driving cycle,  $t_{\text{driving cycle}}$  is duration of the proposed final driving cycle,  $t_{\text{all}}$  is the duration of all

collected data,  $t_{i,j}$  is total duration of micro-trips number  $j$  in cluster number  $i$ , and  $n_i$  is the total number of micro-trips in cluster number  $i$ .

Once the final driving cycle is constructed, it must be validated by comparing it to the assessment parameter of speed data of each route. In this article, the parameters are limited to nine only as they are found to have considerable effect on the vehicle emission. The selected assessment parameters are average speed of the whole driving cycle, average running speed, average acceleration, average deceleration, idle percentage, cruise percentage, acceleration percentage, deceleration percentage and root mean square acceleration. The overall flowchart of clustering method is shown in Fig. 4.

**Markov Chain.** Markov chain is a stochastic method to generate the driving cycle. It is also known as state-based method that will construct the driving cycle (possible events) using the transition states (previous events) of the velocity-acceleration profile by predicting them to one another according to the probabilistic rule. Therefore, the first step is to generate transition probability matrix (TPM) from the velocity-acceleration profile of the collected speed data as illustrated in Fig. 5. The 2D profile shows that there are 204 data points or states existed based on the real-world driving.

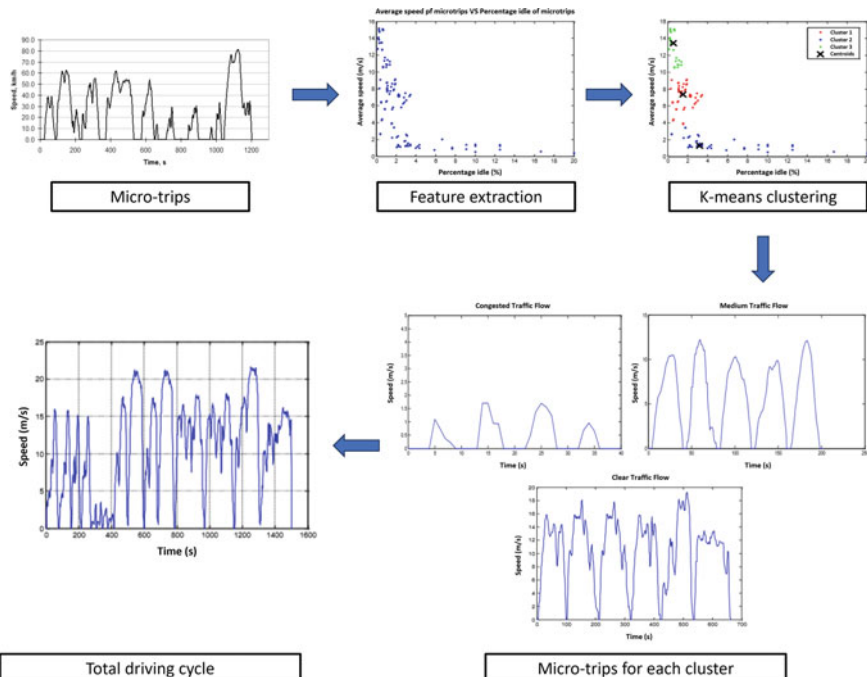


**Fig. 4** Clustering method flow chart

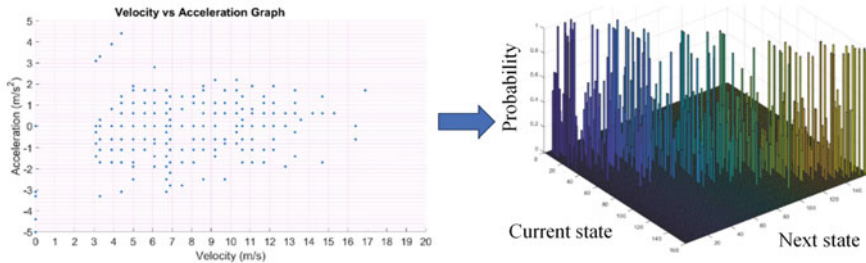


**Fig. 5** Conversion of velocity-acceleration profile to TPM

TPM is used to capture probabilities for transition from one state to another, in which each state is defined as a velocity-acceleration pair. First, a frequency matrix is created counting all the transitions from one state to another and then, it is converted to a transition matrix by dividing by the total of row frequencies. Thus, the total probability of each row should be one.

$$p_{i,j} = \frac{n_{i,j}}{\sum n_i}, \quad (5)$$

where  $p_{i,j}$  is the transition probability from state number  $i$  ( $i = 1$  to number of rows) to state number  $j$  ( $j = 1$  to number of columns),  $n_{i,j}$  is the number of frequencies at state  $(i, j)$ , and  $\sum n_i$  is total number of state frequencies in row  $i$ .

The final representation of the TPM is presented in Fig. 6. On the side are the previous events of velocity-acceleration pair while on the top are the possible events. Thus, a value of 0 indicates that it is not possible to transition from the previous events to the potential events based on real-world driving conditions. If the value is not zero, the particular transition is likely to occur. The size of TPM depends on the number of velocity-acceleration pairs equal to the number of available states.

$$n_r = n_c = n_{\text{velocity, acceleration pair}} = n_{\text{states}} = 204,$$

where  $n_r$  and  $n_c$  are the number of rows and column of TPM, respectively.

Upon the completion of TPM, cumulative sum of each row must be carried to ensure that elements from left to right within a row are non-decreasing for binning process later. Otherwise, it could lead to overlapping bins or intervals, which would introduce inconsistency in the binning process.

$$p_{\text{new}} = p_{i,j} + p_{i,j-1}, \quad (6)$$

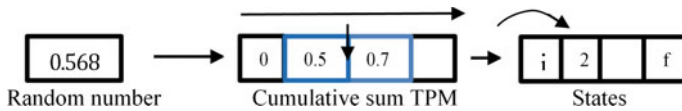
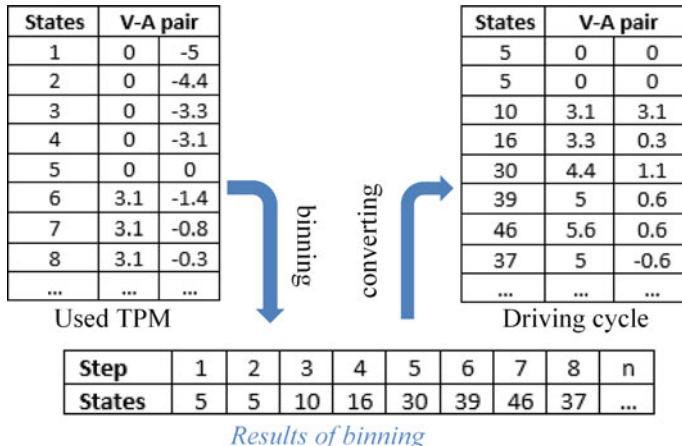
where  $p_{\text{new}}$  is new probability of row  $i$  and column  $j$  of TPM. Then, a set of random probability numbers is generated for the length of desired steps or duration. By using binning algorithm, it will determine where the generated random probabilities will fall in which bins of the TPM row by row, as illustrated in Fig. 7, and  $s_i = j$  if

		Velocity2, Acceleration2									
		0, -5	0, -4.4	0, -3.3	0, -3.1	0, 0	3.1, -1.4	3.1, -0.8	3.1, -0.3	3.1, 0	...
Velocity1, Acceleration1	0, -5	0	0	0	0	0	0	0	0	0	...
	0, -4.4	0	0	0	0	0	0	0	0	0	...
	0, -3.3	0	0	0	0	0	0	0	0	0	...
	0, -3.1	0	0	0	0	0.5	0	0	0	0	...
	0, 0	0	0	0	0	0.25	0	0	0	0	...
	3.1, -1.4	0	0	0	0	0	0	0	0	0	...
	3.1, -0.8	0	0	0	0.666667	0	0	0	0	0.333333	...
	3.1, -0.3	0	0	0	0.25	0	0	0	0	0.25	...
	3.1, 0	0	0	0	0.666667	0	0	0	0	0	...
...	...	...	...	...	...	...	...	...	...	...	

**Fig. 6** Snippet of generated TPM

$p_{i,j} < x_i < p_{i,j+1}$ , where  $s_i$  is the predicted state of TPM row  $i$  and second  $i$ ,  $x_i$  is the random probability number for second  $i$ , and  $p_{i,j}$  is the probability of TPM row  $i$  and column  $j$ .

The result should be in a set of states or velocity-acceleration pairs of the original TPM where the beginning and the end of the set must be zero velocity and zero acceleration pair. Then, the whole set will be converted to speed-time data to develop driving cycle as shown in Fig. 8.

**Fig. 7** State prediction of a row via binning algorithm**Fig. 8** Conversion of states to velocity-acceleration pairs

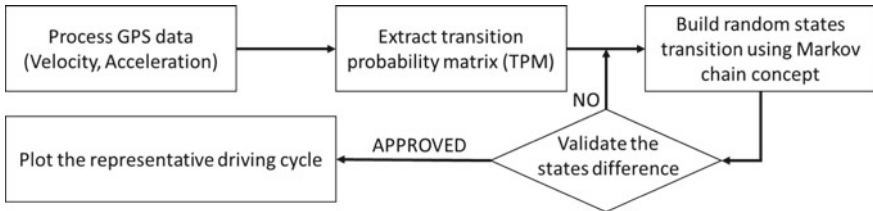


**Fig. 9** Stochastic method flow chart

Since stochastic method uses probabilistic approach, all trials of driving cycle generations will not be a good representation. Therefore, to choose the best result, the validation must be performed by comparing the number states of the input data and the generated driving cycle where both should be close. Figure 9 depicts the overall flowchart of stochastic method.

### 3 Results and Discussion

#### 3.1 Cycle Construction

**K-Means Clustering Method.** Driving features of speed data of every route are extracted and clustered accordingly to their driving conditions. Figure 10 shows the selected driving features of velocity profile of every route are extracted from micro-trips and clustered to their respective driving conditions. Figure 11 presents the driving cycles of every route which each is clustered to three driving conditions. Following that, all feature graphs are compiled and clustered to the three driving conditions as reflected in Fig. 12.

To develop the overall driving cycle, the share of each traffic condition needs to be formulated using (4) where  $t_{\text{driving cycle}} = 400$  s (desired final driving cycle),  $t_{\text{overall}} = 2000$  s (duration of all processed recorded data),  $t_{i,j}$  is 51, 316, and 1587 s for low-, medium-, and high-speed zones of all recorded data, respectively.

$$t_i = \frac{400}{2000} (51, 316, 1587)$$

$$t_i = 10.2, 63.2, 317.4 \text{ s.}$$

Therefore, the duration of low, medium, and high clusters or speed zones in the final driving cycle must be around 10.2, 63.2, and 317.4 s, respectively, and the total duration of final driving cycle will be approximately 390 s. To satisfy the requirements, only the nearest micro-trips to the cluster centers will be selected, and only 2 micro-trips, 6 micro-trips, and 7 micro-trips for low-, medium-, and high-speed

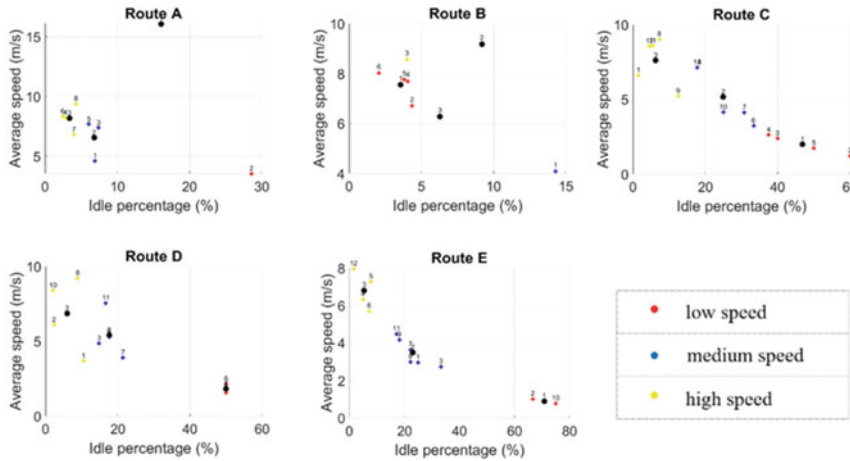


**Fig. 10** Feature extraction of every route

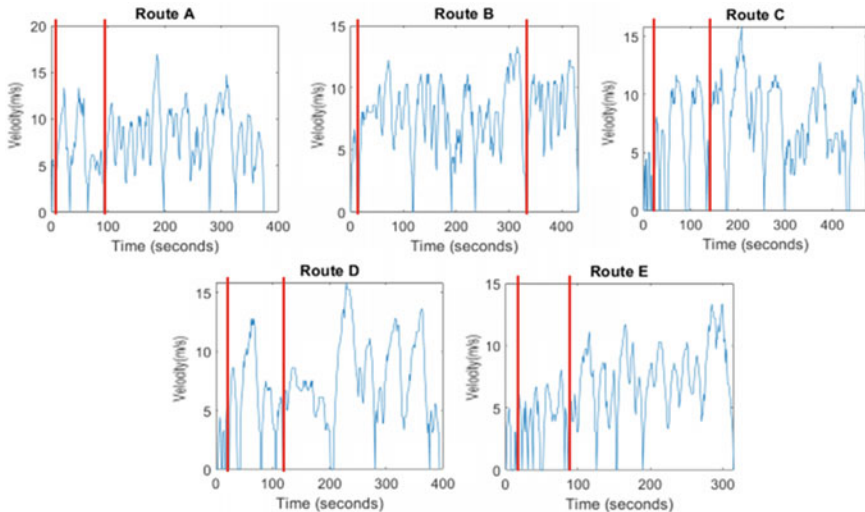


**Fig. 11** Driving cycles of every route. **a** low speed (1st portion), **b** medium speed (2nd portion), **c** high speed (3rd portion)

zones are combined together to develop the final driving cycle with total duration of 388 s presented in Fig. 13a.

**Markov Chain Method.** Compared to clustering method, stochastic method does not need evaluation of individual routes. This method focuses on state transition of velocity-acceleration pair. Therefore, only a relationship between the transition state of input and output data determines a valid driving cycle. After the TPM is developed,

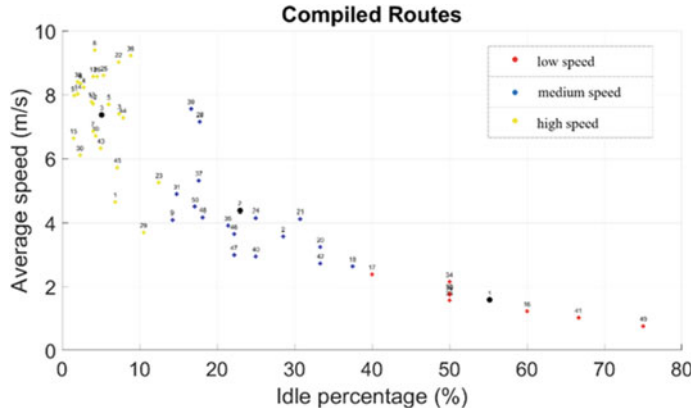


**Fig. 12** Clustering features of compiled routes

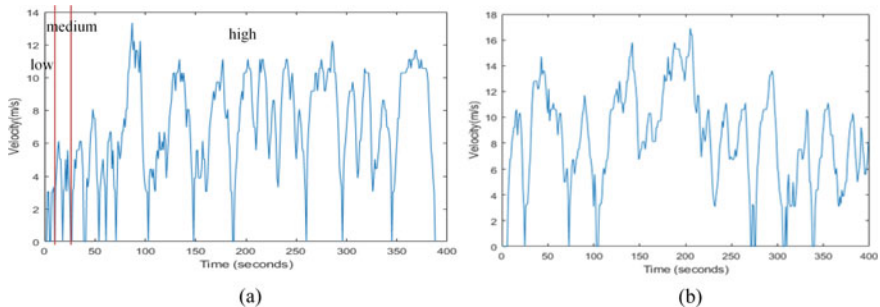


**Fig. 13** Final proposed IIUM driving cycle. **a** K-means clustering and **b** Markov chain

the Markov process is simulated for 400 steps so that we could have a driving cycle duration equivalent to the average duration of total recorded data of each route. One million driving cycles are generated and evaluated to the input data (the used TPM) using MATLAB. The validation process is formulated as follows:

$$\text{Deviation} = \frac{N_{\text{TPM}} - N_{\text{generated}}}{N_{\text{TPM}}} \times 100, \quad (7)$$

where  $N_{\text{TPM}}$  and  $N_{\text{generated}}$  are number of the used TPM states and number of the generated driving cycle state.

It calculates the deviation from the used TPM, and the generated driving cycle is acceptable as the deviation is close to the zero. It determines either the generated driving could undergo most of the recorded data states or not and to be the representative driving cycle. Throughout the process, the optimal generated driving cycle achieved a minimum deviation of 18.14% from the initial number of TPM states, comprising a total of 167 different states as shown in Fig. 13b. The deviation is

**Table 1** Experimental comparison between clustering and stochastic method

Aspects	Clustering method	Stochastic method
Processed data	Velocity-time profile	Velocity-acceleration profile
Input data	Driving features (average speed, idle percentage)	Transition probabilities matrix
Algorithm	Centroid-based algorithm	Binning algorithm
Validation	Assessment parameters difference	Number of states difference
Output data	Micro-trips based	Transition state based

computed using (7) as follows:

$$\text{Deviation} = \frac{204 - 167}{204} \times 100 = 18.1373\% .$$

**Comparisons.** For the clustering method, the structure of each micro-trip in the final driving cycle can be found in the original recorded data as it only clusters specific micro-trips into their respective driving conditions. Thus, the clustering method is more suitable for the area where its traffic flow is majorly controlled by a constant variable such as road geography as it predicts pattern within specific environment.

For stochastic method, the final driving cycle is developed in a form of transition states or velocity pairs as the original data is manipulated from one data point to another as it predicts pattern at any points, not specific speed zones like the clustering method, and is suitable for inconsistent or unpredictable traffic flow which may majorly be due to driver behavior. Moreover, stochastic method is also able to handle data with less or without stop–go conditions or micro-trips; thus, it seems more comprehensive than clustering method to analyze speed data of expressway which has a smaller number of stop–go conditions.

In contrast to [14], this study tested multiple methods rather than different procedures on a method (clustering) to find the optimal result of the most representative driving cycle. To summarize, based on the study area's high number of geographical obstacles such as road bumps and low number of drivers, the clustering method becomes more relevant for the development of the driving cycle with the area. Table 1 shows basic comparisons identified from both methods.

### 3.2 Fuel Consumption and Emission Analysis

Both final driving cycles are fed to the ADVISOR 2.0 to assess the fuel consumption and emission of specific vehicle model. ADVISOR is a tool for simulation and analysis of the vehicle model and the constructed driving cycle. Some vehicle models have been provided in the software including conventional, hybrid (parallel and series), and electric vehicle. Three major layouts are provided on the ADVISOR tool

to assess the fuel rate which are vehicle and parameters input window, driving cycle and simulation parameters window, and results window.

Figure 14 shows the simulation results of the generated driving cycles in terms of fuel performance from a period to another. Table 2 shows the fuel rate and emission of the generated driving cycles including the worldwide driving cycles. To compare between the generated driving cycles and the worldwide driving cycles, the generated driving cycles have higher fuel consumption twice from the worldwide driving cycles.

Based on the observation, it is due to the road geography within IIUM Gombak which has a lot of road bumps, as previously stated, as it is a university premise and is meant for safety purpose. However, this measure would not be practical on the long urban or rural road outside. Known that one aspect which has a significant effect on the fuel consumption as well as the carbon dioxide emission is the rate at when vehicle is accelerated. The more rapid or more frequent accelerations result in an increased fuel consumption, especially in this case, the road bumps trigger the occurrence more often. Regardless of the number of road bumps, fuel consumption can be reduced by lowering the average speed of the motorcycle while driving along the study area compared to driving outside, thereby reducing the gap value of rapid acceleration and deceleration across the road bumps.

From Table 2, it can also be concluded that generated driving cycle by the clustering method (IIUM1) has higher fuel rate than the stochastic method (IIUM2). In Fig. 14a, when the fuel rate graph (second row) is compared to the driving cycle graph (first row), it can be identified that more occurrence of rapid fuel rate due to rapid acceleration in a shorter timespan causing it to have more total fuel consumption compared to both graphs in Fig. 14b. Several simulations on motorcycle hybrid (HEV) are also done based on the setup suggested by some reliable sources despite not having resources to apply with a real HEV. Based on Table 3, the fuel consumption was reduced twice than the conventional one and CO<sub>2</sub> emission decreased a lot as the powertrain was powered with the help of electric batteries.

## 4 Conclusion

The real-world characteristics of motorcycle in IIUM Gombak were successfully collected from five routes which have been used to analyze and validate the on-road driving patterns for determining the representative driving cycles. The driving cycles are favorably established using two types of machine learning which are clustering method and stochastic method. K-means clustering method involves the evaluation of micro-trips of each route to categorize them into three driving conditions and the selection of appropriate micro-trips by using centroid-based method. Markov chain method involves the transition probability matrix (TPM) of velocity-acceleration pair and the binning of random probabilities on the cumulative sum of TPM rows for a number of desired steps. The generated driving cycles must be validated using assessment parameters and state transition differences, respectively, to be the representative driving cycle. Each driving cycle is successfully evaluated in terms of performance

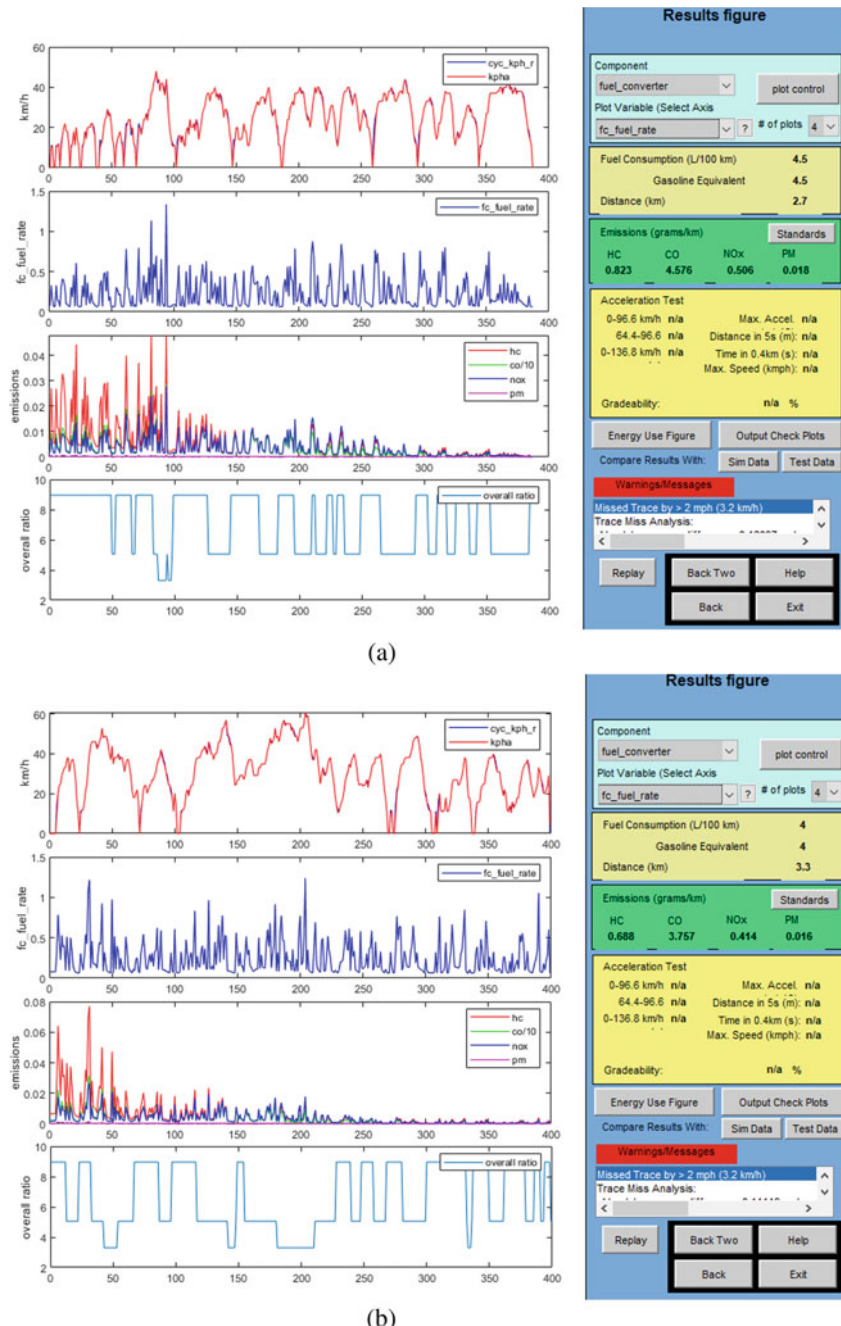


**Fig. 14** Results of the simulation. **a** clustering method and **b** stochastic method

**Table 2** Fuel rate and emission of the driving cycles

Driving cycle	Fuel economy (mpg)	Fuel consumption (l/100 km)	CO <sub>2</sub> emission (grams/km)
IIUM1	52.26	4.50	4.576
IIUM2	58.80	4.00	3.757
JP1015	82.40	2.85	0.874
FTP75	95.30	2.47	0.268
WLTC 3	92.70	2.54	0.226
WMTC	98.70	2.38	0.190

**Table 3** Fuel rate and emission on motorcycle hybrid

Driving cycle	Fuel economy (mpg)	Fuel consumption (l/100 km)	CO <sub>2</sub> emission (grams/km)
IIUM1	101.90	2.40	0.749
IIUM2	118.10	2.20	0.649

validation for their fuel rate emission with respect to the vehicle model, and the results are compared between both generated driving cycles and worldwide driving cycles in terms of the construction process and fuel assessment. The study identified that regular driving within IIUM consumes approximately 4.50 L of fuel for every 100 km using a conventional motorcycle. This fuel consumption is relatively high due to frequent speed bumps causing rapid acceleration and deceleration. The use of HEV can reduce the consumption about twice of the conventional. The study concluded that a clustering method would be more appropriate for this particular case representing the interval geographical area, specifically the road bumps, rather than predicting the varying possible traffic flow using methods such as Markov chain.

## References

1. Chan, D.: Vehicles outnumber people in Malaysia. New Straits Times (2022). <https://www.nst.com.my/>, accessed 9 Jun 2022
2. Huzayyin, O.A., Salem, H., Hassan, M.A.: A representative urban driving cycle for passenger vehicles to estimate fuel consumption and emission rates under real-world driving conditions. *Urban Clim.* **36** (2021)
3. Mafi, S., Kakaei, A., Mashadi, B., Moosavian, A., Abdolmaleki, S., Rezaei, M.: Developing local driving cycle for accurate vehicular CO<sub>2</sub> monitoring: a case study of Tehran. *J. Clean. Prod.* **336** (2022)
4. Tormos, B., Pla, B., Bares, P., Pinto, D.: Energy management of hybrid electric urban bus by off-line dynamic programming optimization and one-step look-ahead rollout. *Appl. Sci.* **12**(9) (2022)

5. Mahayadin, A.R.: Development of driving cycle construction methodology in Malaysia's urban road system. In: International Conference on Computational Approach in Smart Systems Design and Applications ICASSDA, pp. 1–5 (2018)
6. Tong, H.Y., Hung, W.T.: A framework for developing driving cycles with on-road driving data. *Transp. Rev.* **30**(5), 589–615 (2010)
7. Zhang, X., Zhao, D.J., Shen, J.M.: A synthesis of methodologies and practices for developing driving cycles. *Energy Proced.* **16**(PART C), 1868–1873 (2011)
8. Ho, S.H., Wong, Y.D., Chang, V.W.C.: Developing Singapore driving cycle for passenger cars to estimate fuel consumption and vehicular emissions. *Atmos. Environ.* **97**, 353–362 (2014)
9. Grüner, J., Marker, S.: A tool for generating individual driving cycles—IDCB. *SAE Int. J. Comm. Vehi.* **9**(2), 417–428 (2016)
10. Yuhui, P., Yuan, Z., Huibao, Y.: Development of a representative driving cycle for urban buses based on the K-means cluster method. *Clust. Comput.* **22**, 6871–6880 (2019)
11. Dai, Z., Niemeier, D., Eisinger, D.: Driving cycles: a new cycle-building method that better represents real-world emissions. U.C. Davis-Caltrans Air Quality Project (2008)
12. Galgamuwa, U., Perera, L., Bandara, S.: Developing a general methodology for driving cycle construction: comparison of various established driving cycles in the world to propose a general approach. *J. Transp. Tech.* **5**(4), 191–203 (2015)
13. Fotouhi, A., Montazeri-Gh, M.: Tehran driving cycle development using the k-means clustering method. *Scient. Iranica* **20**(2), 286–293 (2013)
14. Vámosi, A., Czégé, L., Kocsis, I.: Development of bus driving cycle for debrecen on the basis of real-traffic data. *Period. Polytech. Transp. Eng.* **50**(2), 184–219 (2022)

# Securing Wireless Communications in IoT: A Study of One-Step Majority Logic Decodable Codes for Physical Layer Security



Otmane El Mouaatamid, Mohamed Lahmer, Mostafa Belkasmi, and Karim Rkizat

**Abstract** Wireless communication networks for the Internet of Things (IoT) system face significant challenges in terms of reliability and security. Traditional networks rely on cryptographic protocols to address security, which primarily focus on upper layers in the OSI model without considering the physical layer. However, recent research has increasingly focused on physical layer security, as it offers a different approach to achieving secrecy in communication. The goal of physical layer security is to ensure that data transmission between legitimate nodes in a network remains confidential, even in the presence of malicious actors attempting to intercept the communication. One way to achieve secrecy is by utilizing the unique characteristics of the physical layer, such as thermal noise, interference, and fading channels. There are various approaches to physical layer security, and this paper focuses on information-theoretic methods for enhancing wireless system security against eavesdropping attacks. Error-correcting codes (ECC) also play a role in providing security, and various code classes can be employed for this purpose, such as polar codes and low-density parity-check (LDPC) codes. In this paper, we investigate the use of One-Step Majority Logic Decodable (OSMLD) codes in physical layer security for IoT applications. OSMLD codes are characterized by their low complexity in the majority decoding process. The main contributions of this work are the application of different types of OSMLD codes in the wiretap channel and the demonstration of the benefits of OSMLD codes in physical layer security for IoT applications.

**Keywords** Physical layer security · Eavesdropper attack · Wiretap channel · Internet of Things · OSMLD codes

---

O. El Mouaatamid (✉) · M. Belkasmi · K. Rkizat  
ICES Team, ENSIAS, Mohammed V University, Rabat, Morocco  
e-mail: [otmane\\_elmouaatamid@um5.ac.ma](mailto:otmane_elmouaatamid@um5.ac.ma)

M. Lahmer  
My Ismail University, Meknes, Morocco

## 1 Introduction

In the future 5G wireless communication, the Internet of Things (IoT) networks will provide a lot of interest as they can meet several requirements such as massive IoT and critical IoT [1]. The most challenging issue for the deployment of IoT application is security. Based on cryptographic solutions, the security requirements are authentication, availability, confidentiality, authorization, integrity, non-repudiation, and privacy. Furthermore, the IoT devices are characterized by their low complexity but the most cryptographic solutions need high computing power. In 1949, Shannon has established the communication theory and defined a fundamental Information-theoretic approach to secure communication view [2]. Across a public channel, we assume that a secure transmission of a  $k$ -bit message, referred to as  $M$ , takes place from Alice to Bob. We achieve perfect security if the message  $M$  is encoded in a way that ensures that no information about  $M$  is present in the transmitted word  $X$ , such that their mutual information is zero ( $I(M; X) = 0$ ). Based on this definition and in order to achieve perfect security, Shannon concluded that Bob and Alice should certainly share  $k$  bits of the key. This method marked the beginning of the key distribution challenge and formed the foundation of symmetric key cryptography security systems commonly used today. Physical layer security is an alternative technology. The primary objective of these techniques is to leverage the communication channel characteristics, such as thermal noise, interference, and the dynamic nature of fading channels. In addition, it enables a legitimate receiver to decode correctly and improve the communication security against eavesdropping attack [3]. In 1975, Wyner [4] was the first who represents the security system based on the physical layer; this model is named the wiretap channel. In the wiretap channel model, the main channel was presented between the sender, Alice, and the legitimate receiver, Bob, while the wiretap channel was defined between Alice and the passive eavesdropper Eve, this channel represents a degraded version of the main channel. We hypothesize that the main and the wiretap channels are modeled as discrete and memoryless systems. The principal goal of error-correcting codes is not only to provide reliable communication but also ensure the aspects of the security. Among the most known error-correcting codes are the low-density parity-check (LDPC) and Bose, Chaudhuri, and Hocquenghem (BCH) codes and polar codes, etc. To measure the quality of Bob's and Eve's channels, we use an important metric called the security gap. Furthermore, we must keep this parameter as small as possible to achieve a sufficient level of physical layer security. The security gap has been reduced using some techniques in coding theory.

In [5, 6], they proposed the puncturing technique for LDPC codes and demonstrated that this technique could reduce the security gap. However, among the disadvantages of the punctured code is the offering of less reliable performance than the non-punctured code and the need for a higher power to achieve better performance over the main channel. On the other hand, scrambled codes were proposed by [7, 8] for physical layer security. It consists of using a scrambling matrix which is inspired by the McEliece Cryptosystem [9]. They show that with scrambling information bits

within the transmitted codeword, it could decrease the signal power compared to the puncturing codes. Despite this, the scrambling techniques were unable to achieve significant improvement in the frame error rate as a measure of reliability [10].

In [11], Reed introduced the One-Step Majority Logic Decodable (OSMLD) codes. OSMLD codes are types of error-correcting codes that are characterized by their low complexity for simple decoding. In this paper, we investigate OSMLD codes for reliable and secure communication through the wiretap channel. Moreover, we analyze the performances of constructed OSMLD codes based on three constructions. The first is cyclic codes [12], the second is the quasi-cyclic OSMLD codes [13–15] from combinatorial design with higher rate decoded with majority logic decoding (MLGD), threshold decoding (TD), and iterative threshold decoding (ITD) algorithms [16, 17]. Our proposal could achieve a reduced security gap specifically for Cyclic Codes. The paper is organized as follows. Section 2 provides background information. Section 3 describes the system model. In Sect. 4, we present OSMLD codes on the wiretap channel. The results of our simulations are demonstrated in the final section, followed by the conclusion and some suggestions for future directions.

## 2 Preliminaries

### 2.1 OSMLD Codes

In [11], Reed discovered the One-Step Majority Logic Decodable (OSMLD) codes that are a class of multiple error-correcting codes found by Muller. In 1961, Mitchell et al. proved that the following codes may be decoded with a simple majority rule: the triple error-correcting code (15, 5), the error-correcting (21, 11) cyclic code that is studied by Green and San Soucie in [18, 19]. A majority of codes that can be decoded using majority logic are cyclic codes, but an algebraic method can also be applied to decode convolutional codes. In reference [20], the initial algorithms for majority logic decoding of convolutional codes which are referred to as self-orthogonal were presented.

#### 2.1.1 Cyclic-OSMLD Codes

Reflect on a linear code  $C$  that has an  $(n, k)$  configuration and is accompanied by a parity-check matrix  $H$ . The linear combination of rows in  $H$  forms a linear code with parameters  $(n, n-k)$ , referred as  $C^\perp$ . This code is also known as the null space of  $C$  or the dual code of  $C$ . The scalar product of any vector  $v$  in  $C^\perp$  and any vector  $w$  in  $C^\perp$  is equal to zero, as stated in reference [21]. Imagine a scenario where a codeword vector from  $C$  is sent through a binary symmetric communication channel. We consider that  $e(e_1, e_2, \dots, e_n)$  and  $r(r_1, r_2, \dots, r_n)$  represent the error vector and the received vector, respectively. With this, the received vector can be expressed as the sum of the original

codeword vector and the error vector:  $r = v + e$ . For any vector  $w$  in the dual code  $C^\perp$ , the construction of the linear sum of the received vector is:

$$A = \sum_{p=1}^n r_p w_p. \quad (1)$$

$A$  is known as the parity-check sum. By utilizing the fact that  $(w, v) = 0$ , the correlation between the parity-check sum  $A$  and the error digits in  $e$  can be determined:

$$A = \sum_{p=1}^n e w_p. \quad (2)$$

Let's consider that the dual code  $C_\perp$  contains  $J$  vectors with the following characteristics:

- (1) The  $j$ th component of each vector  $w_i$  is a 1.
- (2) For  $i \neq j$ , there is at most one vector whose  $i$ th component is a 1.

It is stated that the  $J$  vectors are arranged in a perpendicular manner at the  $j$ th digit location. These vectors are known as orthogonal vectors. In order to create  $J$  parity-check sums, we will use these  $J$  orthogonal vectors. For each  $i$  in set  $I, \dots, J$ ,

$A_i = \sum_{p \neq i}^n e_p + e_j$ , the error digit  $e_j$  will be examined by all the checksums above. The second property of orthogonal vectors states that any error digit other than  $e_j$  will be examined by at most one checksum. These  $J$  checksums are considered to be perpendicular on the error digit  $e_j$ . When the sum of all error digits  $A_i$  is zero for  $i \neq j$ , the value of  $A_i$  becomes equal to  $e_j$ . This information allows us to use the parity-check sums that are orthogonal on  $e_i$  for determining  $e_i$  or for decoding the received digit  $r_i$ .

### 2.1.2 Quasi-Cyclic-OSMLD Codes

It was stated that a code is considered quasi-cyclic if any cyclic shift of a codeword with  $p$  positions results in another valid codeword. Therefore, QC codes can be seen as a broader category of codes that includes cyclic codes as a special case when  $p$  equals 1. A type of QC code, referred to as  $(m_{k_0}, m_{k_0})$ , that has a minimum distance of  $d$  and is based on difference sets, can be defined by  $k_0$  distinct difference sets  $\{D_1, D_2, \dots, D_{k_0}\}$ . Each difference set,  $D_i$ , has the form  $(d_{i0}, d_{i1}, d_{i2}, \dots, d_{i(S-1)})$  and is selected from the set  $\{0, 1, 2, \dots, m_{k_0}\}$  as described in [21]. The parity-check matrix,  $H$ , in the systematic form of this code can be completely determined using these difference sets:

$$H = [P_1 P_2 \dots P_{k_0} I_{n-k}]. \quad (3)$$

The matrix  $P_i$  is derived from the set  $D_i$  by identifying the position of header of the matrix with a 1 in  $D_i$  and creating other rows through cyclic shift of the header. The identity matrix  $I$  is also involved in the process. The algorithm of majority logic decoding for QC codes resembles that of cyclic codes, but with some differences.

In cyclic codes, the decoding of error digits  $e_i$  is done through cyclical permutation of the  $r$  (received word), whereas in QC codes in systematic form, the process involves shifting each of the  $(n-k)$  bits by one position in a cyclical manner.

**Example 1** The QC code C(6,3,3) has a rate of 1/2 and is rooted in the Singer difference set DS {0,1} of order 2. The parity-check matrix  $H$ , in systematic form, can be noted  $[P \ I_3]$ .

$$\begin{matrix} 1 & 1 & 0 & 1 & 0 & 0 \\ 0 & 1 & 1 & 0 & 1 & 0 \\ 1 & 0 & 1 & 0 & 0 & 1 \end{matrix}$$

The parity-check sum perpendicular to  $e_3$  can be calculated from the parity-check matrix  $H$ .

$$A_1 = e_2 + e_3 + e_5$$

$$A_2 = e_1 + e_3 + e_6$$

### 3 System Model

As depicted in Fig. 1, a model known as the Gaussian wiretap channel serves as an apt representation of a physical layer security scheme. Developed by Wyner, Csiszar, and Korner in the 1970s, it has primarily been explored within the field of information and coding, separate from the advancements made in modern cryptography [4, 22]. The model includes three parties: the transmitter (Alice), and the two receivers (Bob and Eve). The connection between Alice and Bob is referred to as the main channel, while the link between Alice and Eve is known as the wiretap channel. The channels between Alice and Bob and between Alice and Eve are not identical in this model. Both channels are assumed to be discrete memoryless channels.

There are various methods used to evaluate the security of transmissions on a wiretap channel, one of which is the security gap metric. This metric is based on bit error rate (BER) and quantifies the difference in quality between the channels of the intended receiver (Bob) and the eavesdropper (Eve) in order to ensure both a secure transmission and a reliable reception for Bob [6]. The objective is to minimize the security gap in order to attain physical layer security. Let  $P_e^B$  and  $P_e^E$  be the average BER at Bob and Eve, respectively. As shown in Fig. 2, it is desirable that  $P_e^B$  should

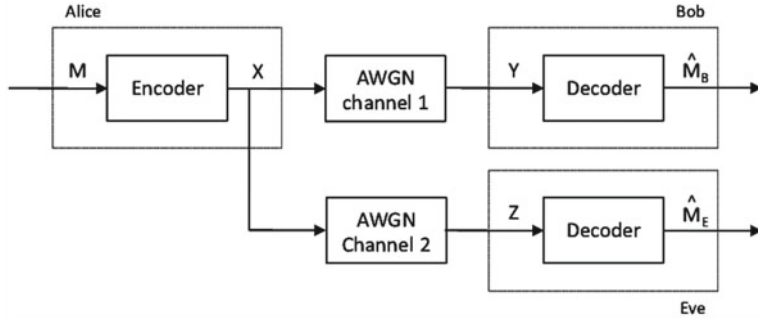


**Fig. 1** Wiretap channel

be lower than a given threshold  $P_{\text{err},\max}^B (\approx 0)$  in order to ensure reliability. On the other side,  $P_e^E$  should be larger than a given threshold  $P_{\text{err},\min}^E (\approx 0.5)$  to guarantee confidentiality. If  $P_e^E$  is close to 0.5 and the errors are i.i.d., Eve cannot extract much information from the received message. Hence, reliability and security are assured if the following conditions (4) and (5) can be satisfied:

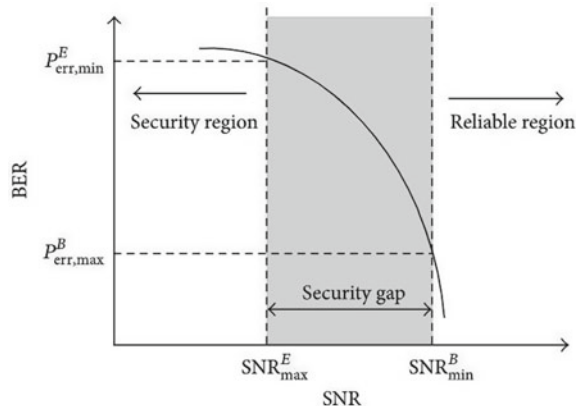
$$P_e^E \leq P_{\text{err},\max}^B = P_E(\text{SNR}_{B_{\min}}) \quad (4)$$

$$P_e^E \geq P_{\text{err},\min}^E = P_E(\text{SNR}_{B_{\max}}), \quad (5)$$

where  $\text{SNR}_{B_{\min}}$  is the reliability threshold that is the lowest signal-to-noise ratio for Bob, while  $\text{SNR}_{B_{\max}}$  is the security threshold which is the highest signal-to-noise ratio for Eve. Therefore, the security gap (in decibels) is defined below:

$$S_G = \text{SNR}_{B_{\min}} - \text{SNR}_{B_{\max}}.$$

**Fig. 2** Security gap



## 4 Simulations and Results

This section evaluates the simulation outcomes and analyzes the process of decoding QC-OSMLD and Cyclic-OSMLD codes with the standard and modified versions of the MLGD, TD, and ITD decoders. The parameters of communication system used in our simulations are presented in Table 1.

We show in Table 2 the security gap of QC-OSMLD codes and Cyclic-OSMLD codes decoded with the both versions of standard and modified MLGD, TD, and ITD decoders.

The results from this table show that in general, the modified version gives the best security gap, except for QC-OSMLD code decoded with ITD, in which the standard version is better than the modified version. The Cyclic-OSMLD code decoded with ITD modified shows the best security gap with  $S_G = 2$  dB (Fig. 3).

**Table 1** Parameters used in simulating a communication system

Parameter	Setting
Modulation	BPSK
Channel	Gaussian wiretap
Residual errors	200 errors
Transmitted blocks	1000 blocks
Iterations (ITD decoder)	10 iterations

**Table 2** Security gap's values of a cyclic (CC) and, quasi-cyclic codes under MLGD, TD, and ITD decoders

### Standard decoding

Decoder	Code	Parameters	SNR <sub>E<max></max></sub>	SNR <sub>B<min></min></sub>	SG1 (dB)
MLGD	QC	(681, 227, 21)	3	8	5
	CC	(819, 515, 30)	4	8	4
TD	QC	(681, 227, 21)	2	6.5	4.5
	CC	(819, 515, 30)	2	6.2	4.2
ITD	QC	(681, 227, 21)	2	4.6	2.6
	CC	(819, 515, 30)	2	4.5	4.5

### Modified decoding

Decoder	Code	Parameters	SNR <sub>E<max></max></sub>	SNR <sub>B<min></min></sub>	SG2 (dB)
MLGD	QC	(681, 227, 21)	6	9.2	3.24
	CC	(819, 515, 30)	6	9	3
TD	QC	(681, 227, 21)	6	10.2	4.2
	CC	(819, 515, 30)	6	10.1	4.1
ITD	QC	(681, 227, 21)	4	6.8	2.8
	CC	(819, 515, 30)	4	6	2

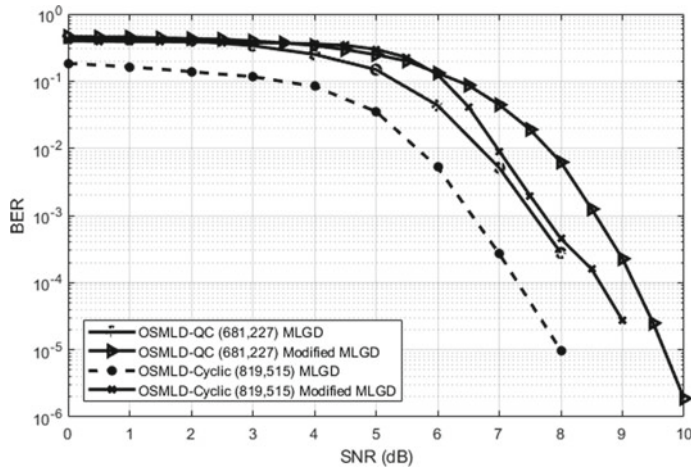


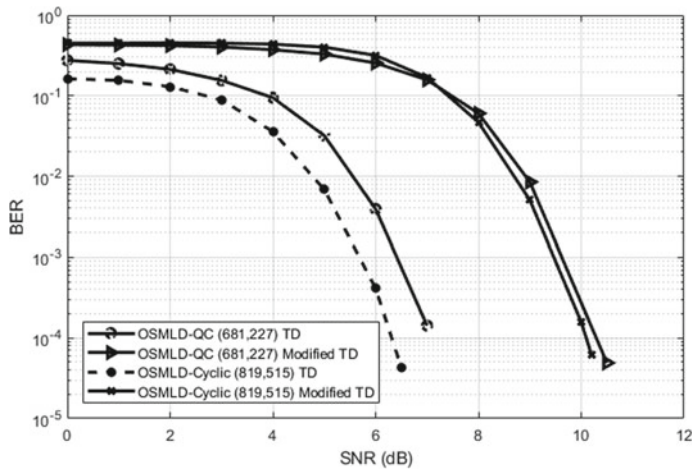
**Fig. 3** Simulated BER for OSMLD-QC(681,227) and OSMLD-cyclic(819,515) codes decoded with standard MLGD versus modified

The simulated bit error rate (BER) is a crucial metric in evaluating the performance of error-correcting codes. Figure 4 presents a comparison of the BER performance for two different codes: OSMLD-QC(681,227) and OSMLD-Cyclic(819,515) when decoded using both standard threshold decoding (TD) and a modified TD. The OSMLD-QC(681,227) and OSMLD-Cyclic(819,515) codes are commonly used in communication systems and have been shown to provide good error correction capabilities. The figure shows that the modified TD algorithm provides a significant improvement in BER performance compared to the standard TD algorithm for both codes.

The OSMLD-Cyclic(819,515) code outperforms the OSMLD-QC(681,227) code in terms of BER for both standard and modified TD decoding algorithms. This suggests that the OSMLD-Cyclic(819,515) code is better suited for applications that require high levels of error correction.

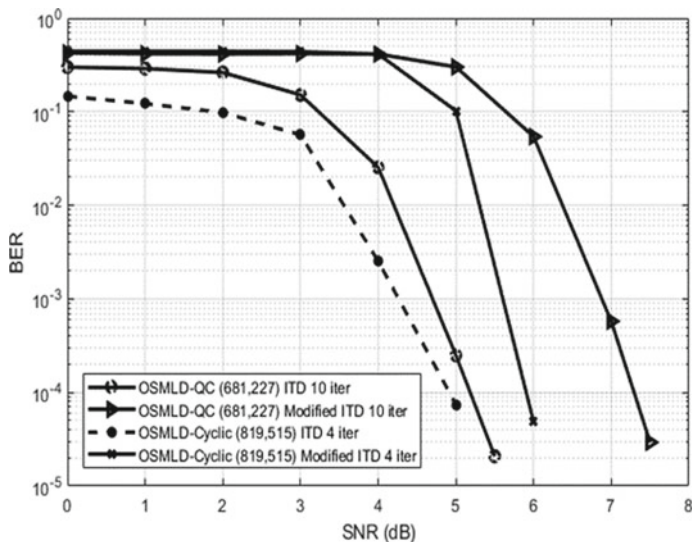
The results presented in Fig. 4 demonstrate the effectiveness of the modified TD algorithm in improving the BER performance of these error-correcting codes and highlight the importance of carefully selecting the appropriate code for a specific communication system based on its performance requirements.

Figure 3 presents the simulated bit error rate performance for decoding two codes, namely QC-OSMLD and Cyclic-OSMLD, using two versions of the MLGD standard and modified. The Cyclic-OSMLD codes exhibit the best error correction capability when decoded with the standard MLGD, as indicated by the results. However, in the context of physical layer security, the bit error rate remains significantly lower than 0.5 even at a low signal-to-noise ratio. On the other hand, the Cyclic-OSMLD code decoded with the modified MLGD or the QC-OSMLD code decoded with both standard and modified MLGD demonstrates good physical layer security performance, as the BER is close to 0.5 at lower SNR. Figures 3 and 5 illustrate that in the case



**Fig. 4** Simulated BER for OSMLD-QC(681,227) and OSMLD-cyclic(819,515) codes decoded with standard TD versus modified

of the modified TD and ITD, the QC-OSMLD and Cyclic-OSMLD codes do not perform well in terms of BER. However, unlike the standard version, the modified version maintains the BER close to 0.5 at low SNR and improves the slope of the curve, reducing the security gap.



**Fig. 5** Simulated BER for OSMLD-QC(681,227) and OSMLD-cyclic(819,515) codes decoded with standard ITD and modified

## 5 Conclusion and Future Directions

In this paper, we have presented an analysis of the performance of QC-OSMLD and Cyclic-OSMLD codes in the Gaussian wiretap channel. We have introduced a novel decoding method using MLGD, TD, and ITD decoders, which achieved a BER close to 0.5 at low SNR. Our focus in this work was primarily on the fundamental issue of a security gap in physical layer security, and we have analyzed different types of OSMLD codes (cyclic, quasi-cyclic, and non-cyclic) under different decoders (MLGD, TD, and ITD). The simulation results showed that Eve must operate at a bit error rate very close to 10-1 as soon as her SNR is only a few dB lower than Bob's, even if she can use a bitwise TD and ITD decoder. This finding highlights the importance of ensuring a secure communication channel between Bob and Alice, particularly in scenarios where the channel is susceptible to eavesdropping attacks. Our results also suggest that further investigation is needed into scrambling and punctured cyclic and quasi-cyclic-OSMLD codes with different lengths. We believe that such investigations can lead to the development of more secure and reliable communication channels for IoT networks. In our future work, we plan to implement OSMLD codes using scrambled and punctured techniques in the Gaussian wire-type channel. We will test this implementation in an IoT network scenario to evaluate the reliability and security against eavesdroppers attacks. We believe that this work will provide insights into the performance of OSMLD codes in practical scenarios and enable the development of more secure and reliable communication channels for IoT networks. Overall, our analysis highlights the importance of ensuring a secure communication channel between Bob and Alice, particularly in scenarios where the channel is susceptible to eavesdropping attacks. We hope that our findings will inspire further research in the development of more secure and reliable communication channels for IoT networks.

## References

1. Al-Fuqaha, A., Guizani, M., Mohammadi, M., Aledhari, M., Ayyash, M.: Internet of things: a survey on enabling technologies, protocols, and applications. *IEEE Comm. Surveys Tut.* **17**(4), 2347–2376 (2015) (Fourth quarter)
2. Shannon, C.E.: Communication theory of secrecy systems. *Bell Syst. Tech. J.* **28**, 656–715 (1949)
3. El Mouaatamid, O., Lahmer, M., Belkasmi, M.: Internet of Things Security: Layered classification of attacks and possible countermeasures. *Elect. J. Info. Techn.* **9** (2016)
4. Wyner, A.D.: The wire-tap channel. *Bell Syst. Tech. J.* **54**(8), 1355–1387 (1975)
5. Klinc, D., Ha, J., McLaughlin, S., Barros, J., Kwak, B.J.: LDPC codes for physical layer security. In: IEEE Global Telecommunications Conference GLOBECOM (2009)
6. Klinc, D., Ha, J., McLaughlin, S., Barros, J., Kwak, B.J.: LDPC codes for the Gaussian wiretap channel. *IEEE Trans. Inf. Forensics Secur.* **6**(3), 532–540 (2011)
7. Baldi, M., Bianchi, M., Chiarioluce, F.: Non-systematic codes for physical layer security. In: IEEE Information Theory Workshop, Ireland, Dublin (2010)

8. Baldi, M., Bianchi, M., Chiaraluce, F.: Coding with scrambling, concatenation, and HARQ for the AWGN wire-tap channel: security gap analysis. *IEEE Trans. Inf. Forensics Secur.* **7**(3), 883–894 (2012)
9. McEliece, R.J.: A public-key cryptosystem based on algebraic coding theory. *DSN Prog. Rep.* **44**, 114–116 (1978)
10. Baldi, M., Maturo, N., Ricciutelli, G., Chiaraluce, F.: Security gap analysis of some physical layer security for the internet of things based on one-step majority logic decodable codes 11 LDPC coded transmission schemes over the at and fast fading Gaussian wiretap channels. *EURASIP J. Wirel. Commun.* **1**, 1–12 (2015)
11. Reed, I.S.: A class of multiple-error-correcting codes and their decoding scheme. *IRE Trans. Inf. Th.* **pGIT-4**, 38–49 (1954)
12. Weldon, E., Jr.: Difference-set cyclic codes. *Bell Syst. Tech. J.* **45**(7), 1045–1055 (1966)
13. El Mouatamid, O., Lahmer, M., Belkasmi, M.: Construction and decoding of OSMLD codes derived from unital and oval designs. In: 2018 International Conference on Advanced Communication Technologies and Networking (CommNet), pp. 1–7. IEEE (2018)
14. Rkizat, K., Lahmer, M., Belkasmi, M., Nouh, S.: Construction and iterative thresh-old decoding for low rates quasi-cyclic one step majority logic decodable codes. In: Advanced Communication Systems and Information Security (ACOSIS), International Conference on, pp. 1–7, IEEE (2016)
15. Belkasmi, M., Lahmer, M., Ayoub, F.: Iterative threshold decoding of product codes constructed from majority logic decodable codes. In: 2006 2nd International Conference on Information and Communication Technologies, Vol. 2, pp. 2376–2381. IEEE (2006)
16. Green, J.H., San Soucie, R.L.: An error-correcting encoder and decoder of high efficiency. *Proc. IRE* **46**(10), 1741–1744 (1958)
17. Prange, E.: The Use of Coset Equivalence in the Analysis and Decoding of Group Codes, No. AFCRC-tr-59-164. Air Force Cambridge Research Labs Hanscom AFB (1959).
18. Massey, J.L.: Threshold decoding. No. tr-410. Massachusetts Inst of Tech Cambridge Research Lab of Electronics (1963)
19. Costello, D.J.: Error Control Coding: Fundamentals and Applications. Prentice Hall (1983)
20. Csiszar, I., Korner, J.: Broadcast channels with confidential messages. *IEEE Trans. Inf. Theory* **24**(3), 339 (1978)
21. Rkizat, K., Yatribi, A., Lahmer, M., Belkasmi, M.: Iterative threshold decoding of hig rates quasi-cyclic OSMLD codes. *Int. J. Adv. Comp. Sci. Appl.* **7** (2016)
22. Belkasmi, M., Lahmer, M., Benchrifa, M.: Iterative threshold decoding of parallel concatenated block codes. In: 4th International Symposium on Turbo Codes and Related Topics; 6th International ITG- Conference on Source and Channel Coding, pp.1–4. VDE (2006)

# IRS-Aided Cyclostationary Spectrum Sensing in Dynamic Spectrum Access Networks



Sanjeev Raghoonath and Sean Rocke

**Abstract** Green wireless communications aim to reduce the environmental impact of wireless communication systems while maintaining or improving their performance. One technique used in wireless communication systems is spectrum sensing which is an enabling technique that provides information on spectrum availability for cognitive radio. Cyclostationary spectrum sensing is a particular sensing approach that takes use of the built-in periodicities characteristic to most man-made signals. However, when channel fading conditions are severe, the interference can affect primary users and the wireless communication systems consume a significant amount of energy and generate greenhouse gas emissions, leading to various environmental and health impacts to maintain quality. To combat this issue, intelligent reflecting surface aided cyclostationary spectrum sensing is proposed. Cases where the line of sight between the primary user and its destination is known, were investigated. Receiver Output Characteristic curves were produced with and without the use of intelligent reflecting surfaces in cyclostationary spectrum sensing to determine if it retains the information from the primary user in severe channel fading conditions. Simulation results verify that the use of intelligent reflecting surfaces can improve the performance of cyclostationary detection for spectrum sensing.

**Keywords** IRS · Dynamic spectrum access · Cyclostationary spectrum sensing

## 1 Introduction

Servicing growing spectrum demand has been increasingly difficult with the growth of wireless communication devices and the increased desire for wideband applications. It has become an integral part of modern life, and the demand for wireless connectivity is growing rapidly. However, wireless communication systems consume a significant amount of energy and generate a substantial amount of greenhouse gas

---

S. Raghoonath (✉) · S. Rocke

Department of Electrical and Computer Engineering, The University of the West Indies,  
St. Augustine Campus., St. Augustine, Trinidad and Tobago  
e-mail: [sanjeev.raghoonath@my.uwi.edu](mailto:sanjeev.raghoonath@my.uwi.edu)

emissions. This not only contributes to climate change but also leads to other environmental and health impacts. Cognitive radio (CR) is a platform that enables intelligent reconfiguration of operational parameters to improve communications performance [1]. CR-based systems enable Dynamic Spectrum Access (DSA), through which unlicensed secondary users (SUs) can opportunistically access any vacant or under-utilized frequency bands allocated to licensed primary users (PUs) by using different operation modes while minimizing interference to the PU, among other things [2]. A critical aspect of DSA is awareness of the electrospace, which geolocation database mechanisms [3] or spectrum sensing [4] facilitate.

Unlike geo-database approaches, spectrum sensing offers an opportunity for in-situ radio environment awareness, either via separate sensing infrastructure or via the SUs which aim to exploit spectrum holes. Numerous sensing techniques have been explored in the literature including *inter-alia*: energy detection, matched filter detection, cyclostationary (CS) spectrum sensing, waveform-based sensing, collaborative sensing, and eigenvalue-based detection [4]. There have also been various studies involving variations such as collaborative spectrum sensing [5], random spectral sampling [6], and wideband sensing [7], for improving performance. In much of the techniques studied, the systems are assumed to operate in channels with various stochastic impairments including slow and fast fading, as well as node mobility issues. Under these circumstances, there is little control over the channel, and at best compensatory methods are employed for achieving currently reported levels of performance.

Recently, intelligent reflecting surfaces (IRSs) have been proposed and investigated as a key enabler for dynamically shaping the wireless propagation channel to improve communication performance, including increasing channel capacity to address the growing demand for wireless technologies [8]. IRS consists of passive reflective elements that can be independently controlled by adjusting amplitude and phase shifts to produce directed nulls or enhanced signals [9–11]. The ability of IRS to dynamically control the channel presents new opportunities for wireless communications systems.

Several functional benefits of IRS explored in the literature when used for wireless reconfiguration include coverage extension, adding extra paths to improve channel rank, refining channel statistics, and interference suppression [5]. IRS has also been identified to enhance spectral efficiency and energy efficiency in CR networks [12]. This can reduce their energy consumption of wireless communication systems by improving the signal quality and coverage, thereby reducing the need for high transmit power at the transmitter and high receive sensitivity at the receiver. This can lead to significant energy savings, especially in the context of green wireless communications. IRS comprising a planar array of reflecting cells does not perform any active processing of the incident signals before reflection occurs. This allows for mass deployment at a reduced cost with low energy consumption as the primary purpose of IRS is to be completely passive. However, as stated in [13], there exist limited information regarding the practical implementations of IRS which can detail more about the maintenance and durability of these IRS panels.

It is also a cutting-edge technology that could play a critical role in energy-efficient communication for future wireless networks. As seen in [14], the use of IRS can effectively improve the performance of wireless networking to meet the requirements of a sustainable energy system. As a result, IRS can reduce the amount of transmission power required to maintain a given signal quality, which can lead to a substantial reduction in the carbon footprint of wireless networks. Furthermore, IRS can enable wireless communication in areas that are difficult to reach or have poor signal quality, which can reduce the need for expensive infrastructure deployments. For example, IRS can be used in indoor environments to improve signal quality and reduce the need for additional access points. They can also be used in outdoor environments to extend coverage and capacity in areas with high interference or limited line-of-sight. By enabling wireless communication in these areas.

IRS can reduce the need for energy-intensive infrastructure, such as cell towers or fiber optic cables, which can further reduce the energy consumption of wireless networks. It can also be used with unmanned aerial vehicles to replace repeater towers as well as reduce the need for extensive coverage in dense urban areas. The authors in [15] were able to show that the use of the IRS in these types of environments were able to outperform the traditional systems whilst maintaining a lower power requirement than the traditional system. Although they indicated that the problem was complex to which traditional optimization methods could not be used, their proposed solution was able to show the improvement that IRS provided whilst ensuring that the system requirements were sustainable.

In addition, IRS can be easily integrated into existing wireless networks, making them a cost-effective and scalable solution for upgrading legacy systems. IRS can be deployed in various configurations, such as standalone or integrated with existing infrastructure, which can further reduce the need for additional hardware and reduce the overall energy consumption of wireless networks. As such, IRS can significantly reduce the operating costs of wireless networks, making them an attractive option for operators seeking to improve energy efficiency and reduce their carbon footprint. In summary, IRS has the potential to revolutionize the way we design and operate wireless networks, making them more energy-efficient, sustainable, and cost-effective.

Regarding spectrum sensing, there is increasing interest in the potential of IRS-based enhancements. In [16] IRS-enhanced energy detection was explored for single user and cooperative user spectrum sensing. The authors concluded that IRS-based spectrum sensing can offer improved detection performance. In [17] the authors proposed a codebook-driven, sequential approach to vary the IRS reflection over time. Coupled with a weighted energy detection method, the authors demonstrated the performance gains of their proposed system. Overall, these publications demonstrate the potential of IRS as a green wireless communications initiative. By improving the energy efficiency, capacity, and spectrum efficiency of wireless communication systems, IRS can help to reduce the environmental impact of wireless communications and promote sustainable development.

In this paper, IRS-aided cyclostationary spectrum sensing is comprehensively studied for single users. Performance analysis is presented through Receiver Operating Characteristic (ROC) curves using the probability of detection ( $P_d$ ) and proba-

bility of false alarm ( $P_{fa}$ ). These curves would be compared to the study conducted in [16] which investigated the use of IRS-enhanced energy detection (ED) in spectrum sensing. It is concluded that IRS can greatly enhance spectrum sensing in DSA networks. The remainder of this paper is as follows. Section 2 introduces the system model for spectrum sensing. Section 3 indicates the approach being used in IRS-enhanced cyclostationary spectrum sensing. Section 4 presents the simulation results to display the results of the sensing performed on various bands in the spectrum. Finally, the conclusion is presented in Sect. 5.

## 2 System Model

Figure 1a illustrates a spectrum sensing scheme in which IRS is used. In this scenario, a single SU is considered. The SU observes the received signal as the basis for PU detection. The IRS consists of L passive reflective elements for which the phase shifts of each element can be dynamically adjusted via a control system to achieve the intended outcome. When compared to the traditional system, the energy requirements for a repeater site, or even a higher transmit and higher receiver sensitivity requirement, can be seen from Fig. 1b.

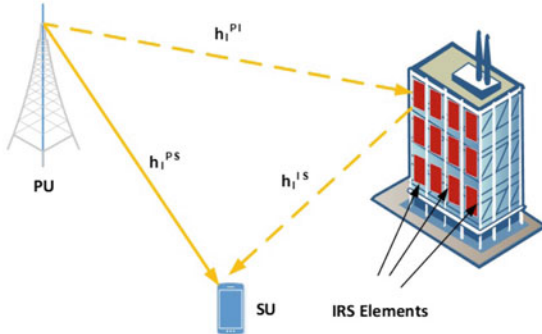
For each SU, sensing is formulated as a binary hypothesis test for detecting whether a PU is transmitting or not:

$$\begin{aligned} H_0 : y[n] &= w[n] \\ H_1 : y[n] &= \left[ \sum_{l=1}^L h_l^{PI} e^{j\varphi_l} h_l^{IS} + h^{PS} \right] s[n] + w[n] \end{aligned} \quad (1)$$

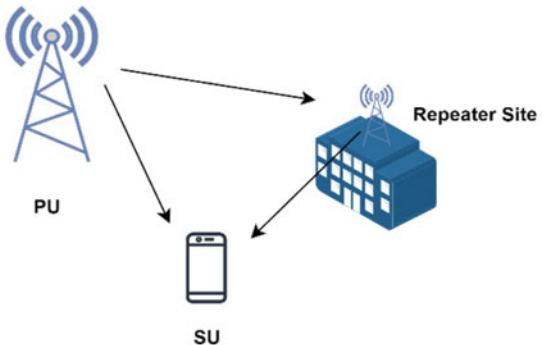
where  $H_0$  and  $H_1$ , respectively represent a spectrum hole or an instant when the PU is transmitting. The discrete-time observations of the received, transmitted, and noise signals are denoted by  $y[n]$ ,  $s[n]$ , and  $w[n]$ , respectively, where  $n = 1, \dots, N$ .  $E[||s[n]||_2^2]$  is the PU transmitting power,  $e^{j\varphi_l}$  denotes the phase shift of the  $l$ th element of the IRS,  $h_l^{PI}$  is the channel between the PU and the  $l$ th element of the IRS,  $h_l^{IS}$  is the channel between the  $l$ th element of the IRS and the SU, and  $h^{PS}$  is the channel between the PU and the SU. Noise and the channels are distributed as follows:  $w \sim N(0, \sigma^2)$ ,  $h_l^{PI} \sim CN(0, \sigma_{PI}^2)$ ,  $h_l^{IS} \sim CN(0, \sigma_{IS}^2)$  and  $h^{PS} \sim CN(0, \sigma_{PS}^2)$ , where  $\sigma_{PI}^2$ ,  $\sigma_{IS}^2$ , and  $\sigma_{PS}^2$  are the respective path loss coefficients, for  $h_l^{PI}$ ,  $h_l^{IS}$ , and  $h^{PS}$ .

In this work, it is assumed that each SU has a single antenna for sensing. Under practical considerations, it is reasonable to assume that the channel information for the coefficients  $h_l^{PI}$ ,  $h_l^{IS}$ , and  $h^{PS}$  are unknown. Furthermore, these may be difficult to determine without some form of information dissemination between the PU, SU, and IRS control elements. Thus, there is this additional challenge in spectrum sensing. To address this issue, the phases,  $\varphi_l$ , are taken as time-varying, according to some pre-defined sequence, effected by the IRS controller:

**Fig. 1** Spectrum sensing systems for PU detection



(a) PU detection with IRS.



(b) PU detection without IRS.

$$\varphi_l = \{\varphi_{(l,1)}, \varphi_{(l,2)}, \dots, \varphi_{(l,N)}\} \quad (2)$$

### 3 IRS-Enhanced Cyclostationary Detection Approach

For signal transmission as defined in (1) and (2), it is expected that there would be periodicities due to the characteristics of the transmitted signal [18]. Such signals can be characterized using the cyclic auto-correlation function (CAF), which is defined by [19]:

$$R_y^\alpha(\tau) = \lim_{N \rightarrow \infty} \frac{1}{(N+1)T_s} \sum_{n=-N/2}^{N/2} y[n]y[n-\tau]e^{-j2\pi\alpha n T_s} \quad (3)$$

For cyclostationary sensing, it can be shown that provided that the cyclic auto-correlation function (CAF) exists and has some non-zero values as a function of the auto-correlation delay,  $\tau$ ,  $y[n]$  contains second-order periodicities at cyclic frequency,  $\alpha$  [18]. On this basis, over a finite observation interval,  $NT_s$ , the power at cyclic frequency,  $\alpha$ , can be computed using:

$$R_y^\alpha(0) = \frac{1}{(N+1)T_s} \sum_{-N/2}^{N/2} y^2[n] e^{-j2\pi\alpha n T_s} \quad (4)$$

Based upon the above, a weighted cyclostationary sensing approach is proposed, and the resulting test statistic is defined as follows:

$$Y = \frac{1}{(N+1)T_s} \sum_{-N/2}^{N/2} \psi_n y^2[n] e^{-j2\pi\alpha n T_s} \quad (5)$$

where,  $\psi_n \geq 0$ . The resulting SU decision rule is given by:

$$Y \gtrless_{H_0}^{H_1} \lambda \quad (6)$$

where  $\lambda \geq 0$  is the decision threshold. Based upon (1), (4) and (5), it can be shown that  $Y$  follows a central chi-squared distribution under  $H_0$ , with  $N+1$  degrees of freedom. However, under  $H_1$ , without further restrictions on  $\psi_n$  an exact distribution involving the weighted summation of chi-squared variables would be difficult to put forth. However, for large  $N$ , the Central Limit Theorem applies, and a normal approximation can be used under  $H_1$ , without any further restrictions on the weights,  $\psi_n$ .

## 4 Performance Analysis

In this section, the performance of IRS-aided cyclostationary spectrum sensing for single users is examined. The passive reflective elements that exist on an IRS is harnessed between one PU and SU to enhance the PU's signal quality. The channel fading is assumed to be FSPL as seen in [16]. The number of passive reflective elements,  $M$ , as seen in [16], was modified to determine the effect it has on the cyclostationary detector as this form of sensing is the most reliable at lower SNR values and, unlike energy detection, cyclostationary sensing is not affected by noise uncertainty as seen in [20].

The simulation parameters were set as follows. The number of elements in the IRS,  $M$  is initially set to 16. This data was modulated using Quadrature Amplitude Modulation (QAM). This signal was then filtered using a raised cosine filter with a roll-off factor of 0.25, a symbol span of 10 symbols to capture the symbols, and four (4) samples per symbol. The modulation used in this study was 16—QAM.

The transmit power is set as  $\gamma_0 = -3$  dB similar to [21]. The channel losses in this study were due to the path loss fading model,  $\beta_\mu = \beta_0 (\frac{d_\mu}{D_0})^{-k_\mu}$ , where  $\beta_0 = 42$  dB is the reference path loss,  $D_0 = 1m$  is the reference distance,  $k_\mu$  = path loss exponent which is 3.5 and  $d_\mu$  is the distance. Additive White Gaussian Noise (AWGN) with a variance  $\sigma^2 = 1$  was also another form of noise that these signals experienced similar to [16, 22]. These conditions will simulate an ideal environment where the aim of this paper can be investigated. These distances,  $d_h$ ,  $d_g$ , and  $d_v$  representing PU-IRS, SU-IRS, and PU-SU, respectively, was set at 51 m, 51 m, and 100 m, respectively. These distances for the IRS from the transmitter are similar to that of [16].

The probability of detection was determined with the use of the following equation:

$$P_D = \frac{1}{\text{NoF}} \sum_{(n=1)}^N |Y| \geq \lambda[n] \quad (7)$$

where NoF is the number of frames,  $Y$  is the result of the signal that has been processed by the cyclostationary detector and  $\lambda$  is the threshold values that the result will be compared against to determine if the signal was successfully detected.

As stated in Sect. 3, the decision threshold of  $\lambda > 0$  was applied with the noise in the received signal as explained in [23]. The highest value of the received signal was set as the highest value determined by the path loss and the highest value of the transmitted signal.

The false alarm probability,  $P_{FA}$  was determined with the use of the following equation:

$$P_{FA} = \frac{1}{\text{NoF}} \sum_{(n=1)}^N |Y| \geq \lambda[n] \quad (8)$$

which is under the assumption that  $H_0$  holds while (7) holds for  $H_1$  as seen previously in Sect. 3.

This result would be compared with the threshold values to determine the false alarm probability. The false alarm and detection probabilities in Fig. 3 were determined by transmitting a signal through a Rician Channel Model. For the model, the following parameters were used: sample rate,  $f_s = 200$  GHz, and transmit frequency,  $f_c = 2.5$  GHz. The SNR range which was used as seen in Fig. 2 was  $-10$  to  $10$  dB similar to [16].

From Fig. 3, the ROC curves show that with increase in the SNR values, the performance of the cyclostationary detector improves. When compared to the values seen in Fig. 2, for the same SNR values, the ROC curves are similar. However, the performance of the CS detector shows small improvements with IRS than without IRS.

Although [16] produced missed detection probability ( $P_{MD}$ ) graphs, it can be comparable to the  $P_D$  graphs produced in this paper. A similar performance was seen with CS detector and the ED detector when IRS was utilized in relation to the SNR range used.

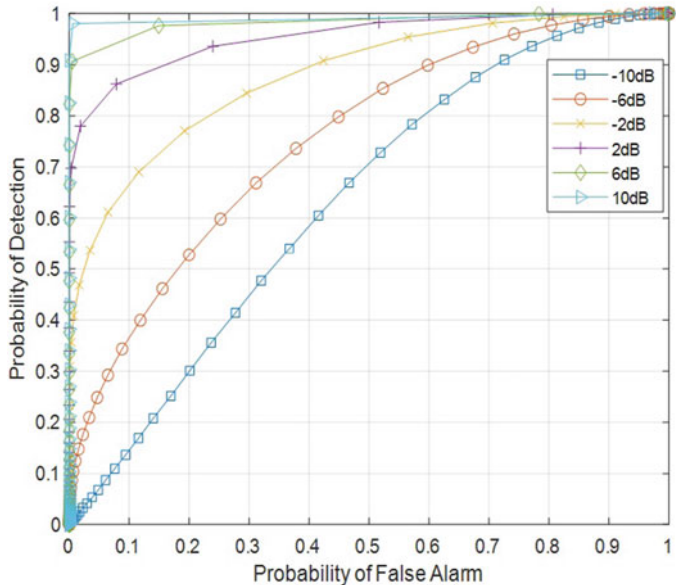


**Fig. 2** CS Detection with IRS for SNR values  $-10$  to  $10$  dB

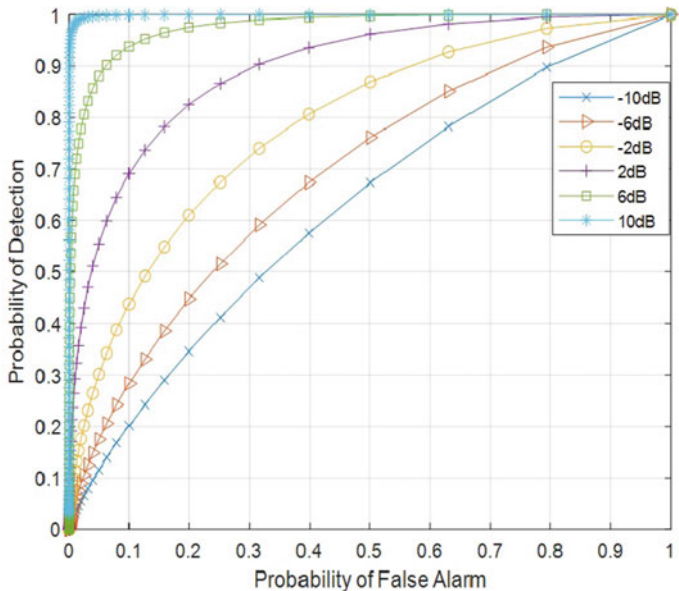


**Fig. 3** CS Detection without IRS for SNR values  $-10$  to  $10$  dB

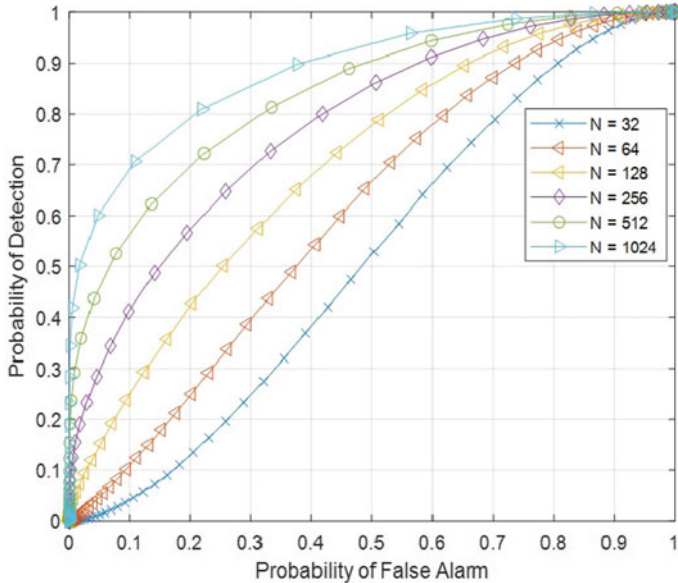
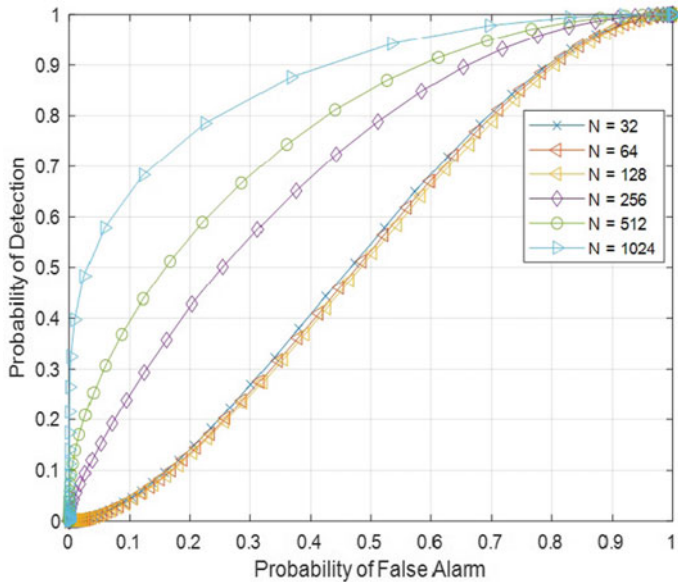


**Fig. 4** CS Detection with IRS for frame sizes with a SNR:  $-10$  dB

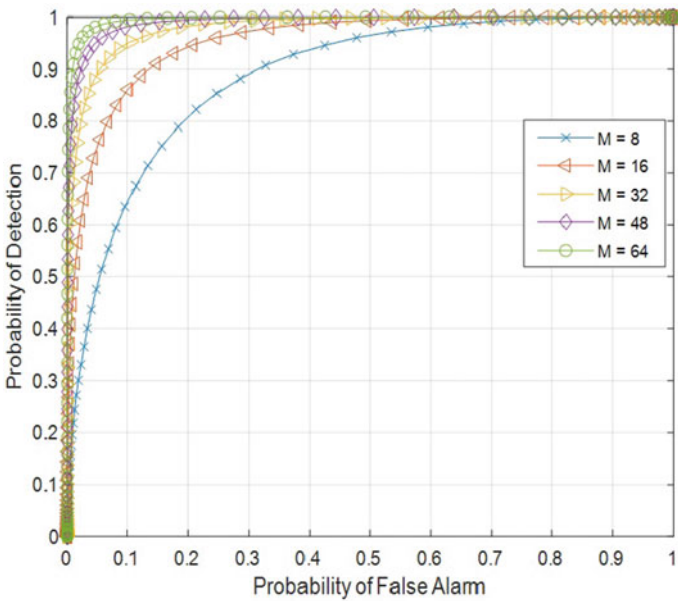
Figure 4 shows the effect of increasing the frame size,  $N$  has on the ROC curve of detection versus false alarm. The SNR was kept constant at  $-10$  dB where  $N = 32, 64, 128, 256, 512$  and  $1024$ . The ROC curves indicate that as the frame size increases, the reliability of the detector increases as the distance between the symbols will decrease.

Figure 5 shows the ROC curves for the variation of  $N$  without IRS. Similar to the trends seen in Figs. 2 and 3, the performance of the detector with IRS increases as opposed to without IRS. From Figs. 2, 3, 4 and 5, it is noted that the introduction of IRS has improved the performance of the cyclostationary detector.

Figure 6 shows the performance of the CS detector as the number of reflective elements are increased. At the same SNR value of  $-10$  dB, increasing the number of reflective elements improves the performance of the detector. When compared to [16], for the same quantity of reflective elements, the CS detector has an improved performance when compared to ED. Noting that the transmit SNRs,  $\gamma_0$  are the same, the ED ROC curves show small increases in performance whereas the CS detector achieves a greater performance for small increases in the number of reflective elements.



**Fig. 5** CS detection without IRS for frame sizes with a SNR:  $-10$  dB



**Fig. 6** CS detection with IRS with reflective elements,  $M$  with SNR:  $-10$  dB

## 5 Conclusion

In this paper, an innovative IRS-aided cyclostationary detection scheme was proposed for spectrum sensing. The performance of IRS-aided cyclostationary detection for single user spectrum sensing was investigated. An expression of the test statistic for IRS-aided cyclostationary detection with the line-of-sight between the PU and SU were both derived by using the cyclic auto-correlation function and the central limit theorem (CLT). The detection probability function was shown using this test statistic. Simulation results verified the accuracy of the theory and corroborated the benefit of using IRS for cyclostationary spectrum sensing.

A known limitation of this study is that more detailed analysis will be required for further investigations into multiple SUs, dense urban environments and environments where vehicular traffic is high. Additionally, the use of IRS as shown in this paper can potentially satisfy the system requirements without additional infrastructure being employed, thereby improving the energy efficiency. By promoting IRS as part of a green wireless communications system, the negative environmental, and health impacts of wireless communication systems can be minimized.

## References

1. Mitola, J., Maguire, G.Q.: Cognitive radio: making software radios more personal. *IEEE Pers. Commun.* **6**(4), 13–18 (1999)
2. Haykin, S., Thomson, D.J., Reed, J.H.: Spectrum sensing for cognitive radio. *Proc. IEEE Inst. Electr. Electron. Eng.* **97**(5), 849–877 (2009)
3. Yilmaz, H., Tugcu, T., Alagöz, F., Bayhan, S.: Radio environment map as enabler for practical cognitive radio networks. *IEEE Commun. Mag.* **51**(12), 162–169 (2013)
4. Yucek, T., Arslan, H.: A survey of spectrum sensing algorithms for cognitive radio applications. *IEEE Commun. Surv. Tutor.* **11**(1), 116–130 (2009)
5. Ghasemi, A., Sousa, E.S.: Collaborative spectrum sensing for opportunistic access in fading environments. In: First IEEE International Symposium on New Frontiers in Dynamic Spectrum Access Networks, 2005. DySPAN 2005. IEEE (2005)
6. Rocke, S., Wyglinski, A.: Random spectral sampling for compliance enforcement in dynamic spectrum access networks. *Wirel. Pers. Commun.* **96**(2), 2401–2425 (2017)
7. Sun, H., Nallanathan, A., Wang, C.X., Chen, Y.: Wideband spectrum sensing for cognitive radio networks: a survey. *IEEE Wirel. Commun.* **20**(2), 74–81 (2013)
8. Wu, Q., Zhang, R.: Towards smart and reconfigurable environment: Intelligent reflecting surface aided wireless network. *IEEE Commun. Mag.* **58**(1), 106–112 (2020)
9. Wu, Q., Zhang, S., Zheng, B., You, C., Zhang, R.: Intelligent reflecting surface-aided wireless communications: A tutorial. *IEEE Trans. Commun.* **69**(5), 3313–3351 (2021)
10. Ma, D., Ding, M., Hassan, M.: Enhancing cellular communications for UAVs via intelligent reflective surface. In: 2020 IEEE Wireless Communications and Networking Conference (WCNC). IEEE, May 2020
11. Ozdogan, O., Bjornson, E., Larsson, E.G.: Intelligent reflecting surfaces: physics, propagation, and pathloss modeling. *IEEE Wirel. Commun. Lett.* **9**(5), 581–585 (2020)
12. Yuan, J., Liang, Y.C., Joung, J., Feng, G., Larsson, E.G.: Intelligent reflecting surface-assisted cognitive radio system. *IEEE Trans. Commun.* **69**(1), 675–687 (2021)

13. Martinez-de Rioja, E., Vaquero, Álvaro F., Arrebola, M., Carrasco, E., Encinar, J.A., Achour, M.: Passive intelligent reflecting surfaces based on reflect array panels to enhance 5g millimeter-wave coverage. *Int. J. Microwave Wirel. Technol.* **15**(1), 3–14 (2023)
14. Liu, Q., Sun, S., Rong, B., Kadoch, M.: Intelligent reflective surface based 6G communications for sustainable energy infrastructure. *IEEE Wirel. Commun.* **28**(6), 49–55 (2021)
15. Asim, M., Abd El-Latif, A.A., ELAffendi, M., Mashwani, W.K.: Energy consumption and sustainable services in intelligent reflecting surface and unmanned aerial vehicles-assisted MEC system for large-scale internet of things devices. *IEEE Trans. Green Commun. Netw.* **6**(3), 1396–1407 (2022)
16. Wu, W., Wang, Z., Yuan, L., Zhou, F., Lang, F., Wang, B., Wu, Q.: IRS-enhanced energy detection for spectrum sensing in cognitive radio networks. *IEEE Wirel. Commun. Lett.* **10**(10), 2254–2258 (2021)
17. Lin, S., Zheng, B., Chen, F., Zhang, R.: Intelligent reflecting surface-aided spectrum sensing for cognitive radio. *IEEE Wirel. Commun. Lett.* **11**(5), 928–932 (2022)
18. Gardner, W.A.: The spectral correlation theory of cyclostationary time-series. *Signal Process.* **11**(1), 13–36 (1986)
19. Jang, W.M.: Simultaneous power harvesting and cyclostationary spectrum sensing in cognitive radios. *IEEE Access* **8**, 56333–56345 (2020)
20. Helif, S., Abdulla, R., Kumar, S.: A review of energy detection and cyclostationary sensing techniques of cognitive radio spectrum. In: 2015 IEEE Student Conference on Research and Development (SCOReD). IEEE, Dec 2015
21. Kudathanthirige, D., Gunasinghe, D., Amarasuriya, G.: Performance analysis of intelligent reflective surfaces for wireless communication. In: ICC 2020—2020 IEEE International Conference on Communications (ICC). pp. 1–6 (2020)
22. Digham, F.F., Alouini, M.S., Simon, M.K.: On the energy detection of unknown signals over fading channels. *IEEE Trans. Commun.* **55**(1), 21–24 (2007)
23. Venkatramana, P., Sree Vidyanikethan Engineering College, Reddy, S.N.: Efficient cyclostationary detection based spectrum sensing in cognitive radio networks. *Int. J. Eng. Trends Technol.* **19**(4), 195–200

# Prediction of Electricity Consumption Demand Based on Long-Short Term Memory Network



Amanullah Khan Siti Marwangi Mohamad Maharum ,  
Faezah Harun and Jawad Ali Shah

**Abstract** Long Short-Term Memory (LSTM) networks are widely recognized for their ability to capture and retain long-term dependencies within time series data, making them a valuable tool for dealing with complex relationships between elements over extended periods of time. This research proposes a KerasTuner-based LSTM network to predict future electricity consumption and maximum demand. Dataset used in this study is historical electricity consumption data of a plastic manufacturing plant in Malaysia, collected at 30-min intervals from 1st January 2017 to 31st December 2019. Both random selection and KerasTuner-based hyperparameter tuning were used to determine the best hyperparameters. The results demonstrated that the KerasTuner-based LSTM approach is effective in predicting future electricity consumption and captures the complex dependencies within the electricity consumption data. The evaluation metrics, training time, and limits of the future maximum demand indicated the effectiveness of the proposed model. This is proven when the proposed model outperformed other models and could improve the prediction accuracy while saving time. This research shows that the proposed model could serve as a valuable tool for predicting maximum electricity demand and could be applied in other industries to provide crucial insights for energy planning and management.

**Keywords** Electricity consumption prediction · Machine learning · Long short-term memory

---

A. Khan · S. M. M. Maharum · F. Harun  
Universiti Kuala Lumpur British Malaysian Institute, 53100 Gombak, Selangor, Malaysia  
e-mail: [sitimarwangi@unikl.edu.my](mailto:sitimarwangi@unikl.edu.my)

J. A. Shah  
International Islamic University, Islamabad 44000, Pakistan

## 1 Introduction

Energy prediction has become progressively essential to deal with problems such as the utilization of spare generating units, high fuel usage, and greater expenditures [1]. In addition, electrical energy cannot be stored in large quantities and it is crucial to generate the exact amount needed to meet the usage demand [2]. Energy or load prediction not only provides important information for policymakers to ensure efficient resource utilization but also helps in achieving better scheduling through generation units and demand response. Electrical load forecasting involves predicting electricity consumption based on historical load data, weather information, and other relevant factors.

The development of intelligent power networks and the improvements in metering devices have led to a growing interest in predicting short-term electricity consumption. This is because effective energy management strategies and the reduction of energy loss depend on an accurate prediction of future energy demand. Moreover, the analysis of past energy consumption data can provide valuable insights and predict future consumption trends [3]. To achieve this goal, it is necessary to establish high-precision forecasting models of electrical load that can accurately predict energy demand trends [4].

In this paper, a method of predicting future electricity consumption demand based on the LSTM network is proposed for an industrial facility. The outcomes of the proposed method could help consumers to determine the possible demand value that the consumption can reach. To achieve accurate predictions and make full use of the data on electricity consumption, the model employs different parameters including the use of dropouts, regularization, and early stoppings in conjunction with the LSTM. The goal of leveraging these parameters is to improve the performance of the LSTM model in predicting electricity consumption and future demand.

The rest of the paper is organized as follows. Section 2 presents the general overview of the models used for electricity forecasting, an introduction to LSTM and its significance for electricity prediction. Section 3 explains the methodology adopted in this research. It provides the general framework of the proposed predictive model, details of the dataset used, dataset processing description, the parameters, and the evaluation of electricity prediction based on LSTM. Section 4 presents the results analysis and performance evaluation of LSTM for prediction of electricity consumption and maximum demand. Finally, Sect. 5 concludes the paper and gives directions for future work.

## 2 Overview of Electricity Consumption Forecasting Models

Load forecasting has evolved from traditional methods to Machine Learning methods, including regression analysis, Artificial Neural Networks (ANN), and Deep Neural Networks (DNN). Back Propagation Neural Network (BPNN) is widely used

due to its strong adaptability and computing ability, but it can easily fall into a local extremum during training [5]. With the development of a smart grid, more extensive and complex load data of industrial enterprises are now available.

The LSTM has unique advantages in processing long sequences of load data compared to other neural networks [6]. It was introduced in 1997 for the first time [7]. It can be employed to effectively acquire knowledge about electricity consumption patterns using time series data [8]. In electricity consumption prediction, it is extensively used in household consumption [9], as well as in buildings [10] and industries [4]. LSTM is considered the most efficient approach in identifying periodic trends [11] and other fluctuations [9] in the behavior of consumption data [12].

The LSTM network has attracted considerable attention in the field of short-term load forecasting. Researchers have investigated its effectiveness both as an independent model and as part of a hybrid model that combines different techniques. A key advantage of the LSTM network is its ability to handle long sequence data by using memory cells that retain information over an extended period of time. This feature is particularly useful for load forecasting, where the amount of data can be large and complex. Moreover, LSTM outperforms traditional models such as regression analysis and ANN due to its recurrent nature.

Researchers have combined LSTM with other techniques to develop hybrid models, which have shown promising results and have become a popular research topic in load forecasting. These hybrid models include techniques like Convolution Neural Network (CNN) [13], a combination of Multilayer Perceptron (MLP) neural network, Adaptive Neuro-Fuzzy Inference System (ANFIS), and Seasonal Autoregressive Integrated Moving Average (SARIMA) [14], and eXtreme Gradient Boosting (XGboost) [15]. Although LSTM requires more computational resources than traditional methods, this is not necessarily an issue if the task requires high accuracy and performance.

### 3 Prediction of Electricity Consumption and Maximum Demand Using Proposed LSTM

Figure 1 shows the workflow of the proposed model in which the first step was to read the already collected data of the industrial plant. Secondly the pre-processing of the data and data normalization. Next, the network hyperparameters shall be determined by including the number of layers for the LSTM network, the number of units in each layer, the batch size, the regularization, and the dropout values. Finally, the model is trained with the best hyperparameters searched for the given data by the “KerasTuner” API using “RandomSearch”. Then, a trained model is obtained to predict future consumption and the estimated maximum demand.

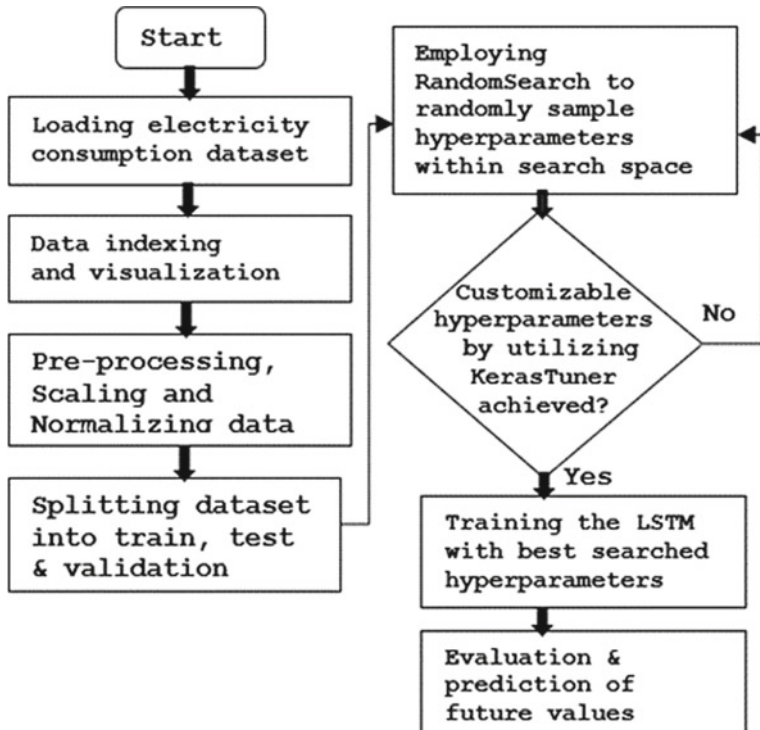


**Fig. 1** Flowchart of the proposed LSTM model for prediction of electricity consumption

### 3.1 The Dataset

In this work, an energy consumption dataset was obtained from a plastic manufacturing industry in Malaysia. The dataset consists of time-stamped data recorded every half hour for three years, starting from 1st January 2017 to 31st December 2019. The dataset comprises 52,560 rows and 2 columns, with the first column indicating the date and time of each reading and the second column indicating the amount of energy consumed in kilowatt-hour (kWh). Table 1 presents a summary of the dataset.

The dataset available for the energy consumption predictions is limited in terms of information, as it only contains power consumptions and timestamps. Moreover, the descriptive statistics of the dataset have high fluctuations and non-linearities, with a high standard deviation value of 500.045931 as shown in Table 2, which could be attributed to the non-linearities present in the dataset. Non-linear data usually have a higher standard deviation as it significantly deviates from the mean, resulting in a wider spread of the data. Therefore, accurate prediction of future energy consumption is challenging.

Figures 2, 3, and 4 respectively visualize the trends and patterns of irregular energy consumption data generated from the dataset over time using charts such as

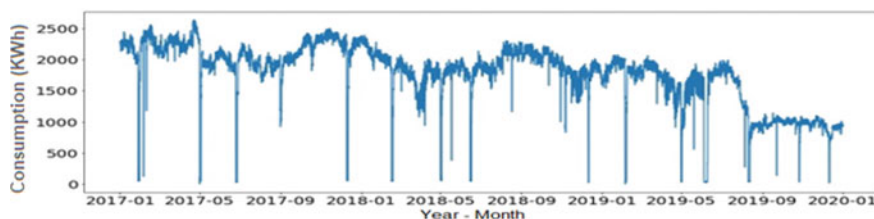
**Table 1** Summary of the dataset used for evaluation of the proposed LSTM model

Data entry	Date and time	Electricity consumption (kWh)
0	1 Jan 2017 12:00:00 AM	2283.95
1	1 Jan 2017 12:30:00 AM	2271.46
2	1 Jan 2017 01:00:00 AM	2275.90
3	1 Jan 2017 01:30:00 AM	2269.97
4	1 Jan 2017 02:00:00 AM	2290.45
...	...	...
52,556	31 Dec 2019 10:00:00 PM	925.50
52,557	31 Dec 2019 10:30:00 PM	941.57
52,558	31 Dec 2019 11:00:00 PM	957.20
52,559	31 Dec 2019 11:30:00 PM	948.27

**Table 2** Descriptive statistics of the dataset presented in Table 1

Statistical parameters	Electricity consumption (kWh)
Count	52,560.000000
Mean	1776.174421
Std.	500.045931
Min.	0.000000
25%	1673.722500
50%	1888.960000
75%	2101.980000
Max.	2636.770000
Count	52,560.000000
Mean	1776.174421

line graphs and boxplots. By examining these graphs, it is possible to gain a deeper understanding of the patterns and trends in energy consumption data over three years of the dataset.

**Fig. 2** Visualization of dataset in three years from January 2017 until December 2019

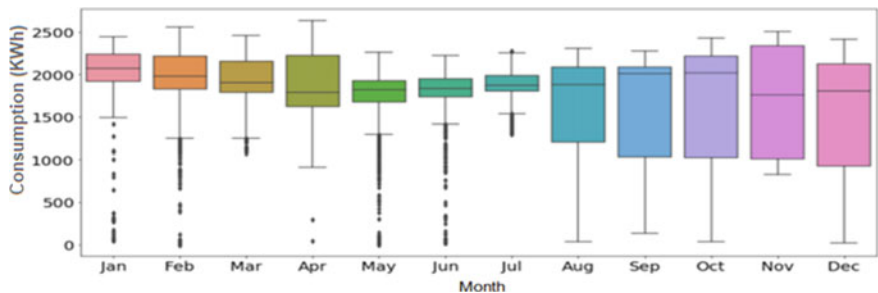
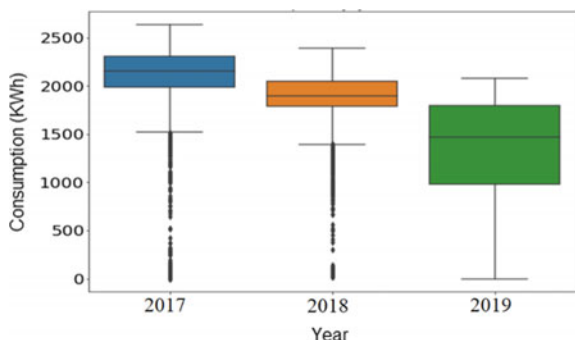


**Fig. 3** Boxplot of dataset according to months

**Fig. 4** Boxplot of dataset according to years



### 3.2 Pre-processing of Dataset

In this work, all simulations are performed in Python programming language by utilizing various libraries and functions for data processing, visualization, model building, and evaluation. First, the dataset is subjected to the necessary pre-processing steps to ensure its suitability for the model. Subsequently, the dataset is normalized and divided into training, testing, and validation sets. Specifically, this work assigned the first two years of the dataset as the training data, while the last year is assigned as the testing data.

The dataset is normalized and divided into training, testing, and validation sets. Specifically, an initial split assigned the first two years of the dataset as the training data, while the last year is assigned as the testing data. Then, the training data was further split into a new training data and validation data, where the validation data is derived from the training data and represents a portion (20%) of the data points from it. In this way, three sets of sequences were grouped in which the training data consists of 27,226 samples, the testing data consists of 16,511 samples, and the validation data consists of 6807 samples. Each sample consists of a sequence of 1008 time-steps and one feature. The value of the time-steps is adjustable and can affect the training time and the complexity of the model.

By applying these pre-processing techniques, the LSTM model could learn from the historical patterns and trends in the data and make accurate predictions. The original form of the input data was maintained, with a time interval of 30 min and no resampling was performed because estimating the maximum demand in Malaysia depended solely on the energy consumed in 30-min intervals. Therefore, the originality of the data is critical for accurate predictions.

### 3.3 Network Architecture

Python3 contains a wide range of pre-built layers, loss functions, and optimization algorithms that can be easily used to construct a neural network model, including the LSTM. Several libraries have been used in this work because they provide a wide range of tools for manipulating and analyzing data, building and training models, tuning hyperparameters, and evaluating model performance.

The “Sequential” module is used for initializing the neural network model, while the “LSTM” module is responsible for adding LSTM layer to the model. The “Dense” module is used to add a dense layer to the model that is fully linked, to construct a functional model more customization and definition of the model’s hyperparameters are needed. To achieve this, LSTM with customizable hyperparameters by utilizing KerasTuner is designed. The hyperparameter object is employed to define the hyperparameters that the tuner will look for. The ranges for hyperparameters are listed in Table 3.

To minimize the validation loss of the model, the tuner uses “RandomSearch” to randomly select the hyperparameters within the defined search space. Once the best hyperparameters are found, the LSTM is trained with them to achieve the desired output. The schematic block diagram in Fig. 5 shows how the LSTM model looks along with the best hyperparameters found. In the proposed model, this basic framework is used to generate the LSTM. The use of KerasTuner with LSTM offers an automated approach to tuning hyperparameters that can save time and potentially improve the performance of the proposed model.

**Table 3** The hyperparameters set in KerasTuner

Hyperparameter	Value
Batch size	(32, 64, 128)
Number of LSTM layers	Minimum 2, maximum 5
Units in each LSTM layer	Minimum 32, maximum 512, with a step of 32
Learning rate	(0.01, 0.001, 0.0001)
Dropout rate	Minimum 0, maximum 0.5, with a step of 0.1
L2 regularization rate	Minimum 0.000006, maximum 0.001

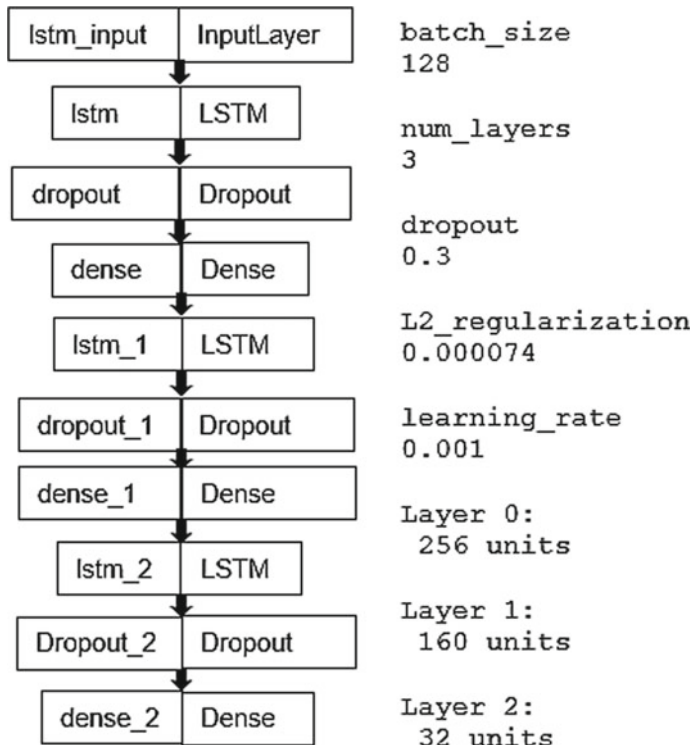


**Fig. 5** Architecture of the hyper-tuned LSTM

### 3.4 Evaluation Metrics

The accuracy of the prediction is evaluated using common evaluation metrics, such as Mean Absolute Error (MAE), Mean Square Error (MSE), Root Mean Square Error (RMSE) and R<sup>2</sup> (coefficient of determination).

### 3.5 Prediction of the Future Demand

To predict future electricity consumption, the LSTM model trained with the best hyperparameters gets the energy consumption data for the input sequence and reshapes it. The model is then used to generate a prediction for energy consumption. The prediction is then reshaped, concatenated, and appended to the input sequence. Another prediction is generated for each 30-min timestamp in the next week using the updated input sequence. The predictions are converted back to their original scale using the scaler and stored in a list. With that, the future consumption demand could be predicted.

## 4 Results and Discussions

In this work, the actual data from a manufacturing plant in Malaysia was used to develop and evaluate the proposed LSTM model. The proposed model showed good results in predicting future electricity consumption, particularly the maximum demand for one week in advance. As shown in Figs. 6 and 7, the proposed LSTM model demonstrated accurate predictions not only on the training data but also on the test data.

Table 4 presents the comprehensive results of LSTM models that were developed, in which hyperparameters for 11 LSTM models were randomly selected and one LSTM model was developed using KerasTuner. In the randomly selected hyperparameter models, Model-1 and Model-11, as well as the KerasTuner based model, successfully predicted future consumption demand limits that were quite close to the actual values.

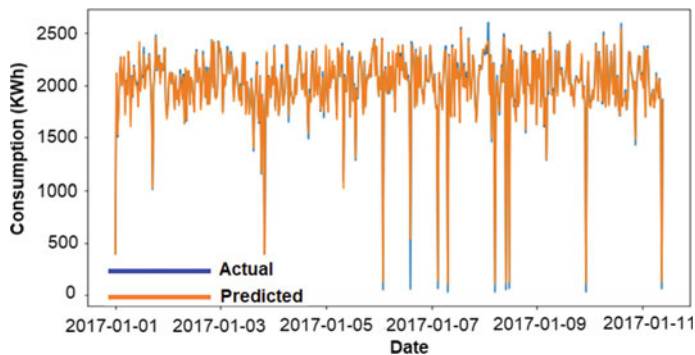


**Fig. 6** Predictions made on the training data

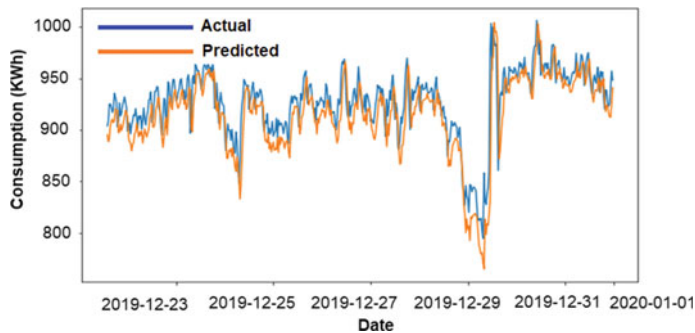


**Fig. 7** Predictions made on the testing data

**Table 4** Summary of performance evaluation

Models	Performance evaluation						
	MAE	MSE	RMSE	R-Squared	Time steps	Demand limits (KWh)	Training time
Model-1	0.11	0.23	0.15	0.98	240	2041 to 2769	About 4.5 min
Model-2	0.08	0.01	0.12	0.98	240	2436 to 4818	About 5.0 min
Model-3	0.04	0.01	0.09	0.99	240	2584 to 3152	About 8.0 min
Model-4	0.06	0.01	0.11	0.99	240	2542 to 3891	About 8.0 min
Model-5	0.05	0.01	0.11	0.99	240	1851 to 3650	About 9.5 min
Model-6	0.05	0.01	0.11	0.99	240	2096 to 3755	About 9.5 min
Model-7	0.06	0.01	0.11	0.99	240	2516 to 3886	About 10.0 min
Model-8	0.12	0.02	0.05	0.98	480	2732 to 3944	About 19.0 min
Model-9	0.06	0.01	0.11	0.99	720	2627 to 3021	About 21.0 min
Model-10	0.14	0.02	0.17	0.98	720	2451 to 3522	About 23.0 min
Model-11	0.07	0.01	0.11	0.99	720	1854 to 2767	About 21.0 min
Hyper-Tuned	0.06	0.01	0.12	0.99	1008	1794 to 2622	About 3.0 h

Overall, the Hyper-tuned LSTM model showed the best performance. The lower values of MAE, MSE, RMSE, and the higher value of  $R^2$  show the better performance of the proposed model. The most significant benefit of the Hyper-tuned LSTM model over randomly selected LSTM models is the time required for development and training. The training time column in Table 4 shows the time taken for all 12 LSTM models. Refining different hyperparameter combinations to find a satisfactory solution would take a lot of time and there is a probability that satisfactory results will not be obtained.

A randomly selected hyperparameter LSTM may have a shorter training time, but as the number of time steps increases, so does the training time, and a larger number of hyperparameters increase the complexity of model and training becoming more difficult. The Hyper-tuned LSTM model on the other hand automatically selects the best hyperparameters based on the input data. Therefore, the proposed model is the best in terms of training time and performance. The proposed model made an accurate prediction in both the training and testing datasets. The predicted values were used

**Fig. 8** Predictions of future electricity consumption

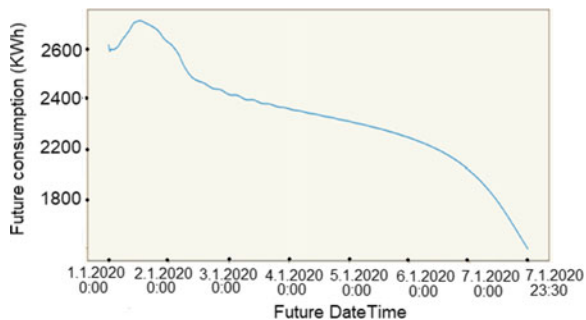


**Table 5** Details of prediction on future electricity consumption

Data	Date and time	Future electricity consumption (kWh)
0	2020-01-01 00:00:00	2622.366699
1	2020-01-01 00:30:00	2595.249756
2	2020-01-01 01:00:00	2605.430420
3	2020-01-01 01:30:00	2601.960205
4	2020-01-01 02:00:00	2602.956299
...	...	...
331	2020-01-07 21:30:00	1827.475830
332	2020-01-07 22:00:00	1819.210083
333	2020-01-07 22:30:00	1811.012329
334	2020-01-07 23:00:00	1802.897949
335	2020-01-07 23:30:00	1794.882080

to train the model for future predictions. Figure 8 shows the model's predictions for maximum electricity consumption in the future while Table 5 provides details of the predicted future time and consumption demand. These findings reflect the historical trends in the entire dataset.

## 5 Conclusion

As supported by the presented values in Tables 5 and 6 provides the comparison of real data versus the predicted data when the proposed LSTM model has made predictions for a week ahead of the available dataset. It can be observed that there are noticeable differences between the real values for the first week of the years 2017, 2018, and 2019, along with the predicted values for the first week of 2020. The real values for 2017 ranged from 2269.97 kWh to 2337.70 kWh. For 2018, the values

**Table 6** Comparison between dataset values and predicted electricity consumption in the coming year

Real values in 2017 (kWh)	Real values in 2018 (kWh)	Real values in 2019 (kWh)	Predicted values in 2020 (kWh)
2283.95	2341.09	1711.15	2622.3667
2271.46	2351.17	1711.15	2595.2498
2275.9	2346.34	1711.15	2605.4304
2269.97	2342.27	1711.15	2601.9602
...	...	...	...
2304.34	2319.3	1711.15	1819.2101
2337.7	2320.46	1711.15	1811.0123
2318.03	2329.1	1711.15	1802.898
2310.96	2346.03	1711.15	1794.8821

ranged from 2319.30 kWh to 2346.34 kWh while 2019 consists of constant values at 1711.15 kWh.

Notably, the predicted values for 2020 fall comfortably within these observed ranges, spanning from 1794.8821 to 2622.3667 kWh, the model exhibits an impressive ability to capture both high and low-demand periods accurately. The maximum predicted value of 2622.3667 kWh signifies the model's ability in identifying peak demand periods, while the minimum predicted value of 1794.8821 kWh demonstrates its effectiveness in recognizing periods of reduced energy consumption. This shows the model's capacity to adapt and learn from historical patterns and fluctuations in electricity consumption, leading to satisfactory performance.

The proposed model was trained and evaluated using real-time data of a Malaysian plastic manufacturing plant. Although the dataset contained only one feature, the proposed LSTM model performed very well in predicting future electricity consumption demand. This research highlights the importance of predicting electricity consumption and maximum demand in the future using HyperTuned-LSTM. By effectively forecasting values within the observed ranges and accurately capturing both high and low-demand periods, the model proves its adaptability to changing patterns and offers valuable insights for decision-making in the field of electricity consumption and demand forecasting.

For future work, it is possible to implement and improve the LSTM model by including additional input data associated with electricity usage, temperature data, and other relevant factors. To improve the performance of the LSTM model, various feature augmentation and development techniques are needed to extract, transform, and create new features from existing data. This would lead to a more comprehensive understanding of patterns and trends in the energy consumption of consumers. It is important that researchers focus on improving the efficiency of the LSTM algorithm specifically in the area of electricity consumption.

**Acknowledgements** This research project was conducted by student and staffs of Universiti Kuala Lumpur British Malaysian Institute (UniKL BMI) and its publication is financially supported by the university. Therefore, the authors would like to thank UniKL BMI for the provision of laboratory facilities and financial support.

## References

1. Jacob, M., Neves, C., Vukadinović Greetham, D.: Forecasting and assessing risk of individual electricity peaks. Springer Nature (2020).
2. Torres, J.F., Martínez-Álvarez, F., Troncoso, A.: A deep LSTM network for the Spanish electricity consumption forecasting. *Neural Comput. Appl.* **34**(13), 10533–10545 (2022)
3. Mahjoub, S., Chrifí-Alaoui, L., Marhic, B., Delahoche, L.: Energy consumption using LSTM multi-layer GRU and drop-GRU neural networks. *Sensors* **22**(11), 4062 (2022)
4. Wang, T., Chen, X., Wang, Y., Chen, Y., Chen, J., Sun, S.: Short-term load forecasting for industrial enterprises based on long short-term memory network. In: 2019 IEEE 3rd Conference on Energy Internet and Energy System Integration (EI2), pp. 1759–1764. IEEE (2019)
5. Wang, L., Wang, Z., Qu, H., Liu, S.: Optimal forecast combination based on neural networks for time series forecasting. *Appl. Soft Comput.* **66**, 1–17 (2018)
6. Waheed, W., Ghazali, R.: A novel error-output recurrent neural network model for time series forecasting. *Neural Comput. Appl.* **32**, 9621–9647 (2020)
7. Hochreiter, S., Schmidhuber, J.: Long short-term memory. *Neural Comput.* **9**(8), 1735–1780 (1997)
8. Lim, C. G., Choi, H. J.: Deep learning-based analysis on monthly household consumption for different electricity contracts. In: 2020 IEEE International Conference on Big Data and Smart Computing (BigComp), pp. 545–547. IEEE (2020)
9. Kong, W., Dong, Z.Y., Hill, D.J., Luo, F., Xu, Y.: Short-term residential load forecasting based on resident behaviour learning. *IEEE Trans. Power Syst.* **33**(1), 1087–1088 (2017)
10. Wang, X., Fang, F., Zhang, X., Liu, Y., Wei, L., Shi, Y.: LSTM-based short-term load forecasting for building electricity consumption. In: 2019 IEEE 28th International Symposium on Industrial Electronics (ISIE), pp. 1418–1423. IEEE (2019)
11. Wang, J.Q., Du, Y., Wang, J.: LSTM based long-term energy consumption prediction with periodicity. *Energy* **197**, 117197 (2020)
12. Shao, X., Kim, C.S.: Multi-step short-term power consumption forecasting using multi-channel LSTM with time location considering customer behavior. *IEEE Access* **8**, 125263–125273 (2020)
13. Rafi, S.H., Deeba, S.R., Hossain, E.: A short-term load forecasting method using integrated CNN and LSTM network. *IEEE Access* **9**, 32436–32448 (2021)
14. Chahkoutahi, F., Khashei, M.: A seasonal direct optimal hybrid model of computational intelligence and soft computing techniques for electricity load forecasting. *Energy* **140**, 988–1004 (2017)
15. Li, C., Chen, Z., Liu, J., Li, D., Gao, X., Di, F., Li, L., Ji, X.: Power load forecasting based on the combined model of LSTM and XGBoost. In: Proceedings of the 2019 the international conference on pattern recognition and artificial intelligence, pp. 46–51 (2019)

# A New Quantum-Resistant Electronic Voting Based on Fully Homomorphic Encryption



Meryem Cherkaoui Semmouni, Mostafa Belkasmi, Abderrahmane Nitaj,  
and Ali Azougaghe

**Abstract** The emergence of large quantum computers running Shor’s algorithm threatens the security of several cryptographic schemes in current use, including electronic voting. As a consequence, many post-quantum candidates that are quantum-resistant are actively investigated. Post-quantum schemes-based hard lattice problems are particularly promising. In this paper, we present and implement a new quantum-resistant electronic voting scheme and prove its efficiency and security by studying its algebraic complexity. Our scheme is based on a combination of two techniques: hard lattice problems and homomorphic encryption with Fan and Vercauteren system.

**Keywords** Lattice-based cryptography · Homomorphic encryption · Electronic voting · Fan and Vercauteren scheme

## 1 Introduction

The process of democratization is rapidly developing and promoting due to electronic voting. However, the increase of frauds and the increasing amount of attacks launched by hackers gave birth to privacy and authentication problems. Cryptography offers multiple solutions to overcome the sensitive data protection issues in e-voting. The traditional homomorphic encryption schemes based on factorization, discrete logarithm problem, and elliptic curve discrete logarithm problem are not secure in

---

M. C. Semmouni (✉) · M. Belkasmi · A. Azougaghe  
ICES Team, ENSIAS, Mohammed V University in Rabat, Rabat, Morocco  
e-mail: [meryem.semouni@um5s.net.ma](mailto:meryem.semouni@um5s.net.ma)

M. Belkasmi  
e-mail: [mostafa.belkasmi@um5.ac.ma](mailto:mostafa.belkasmi@um5.ac.ma)

A. Azougaghe  
e-mail: [aliazougaghe@gmail.com](mailto:aliazougaghe@gmail.com)

A. Nitaj  
LMNO, University of Caen Normandie, Caen, France  
e-mail: [abderrahmane.nitaj@unicaen.fr](mailto:abderrahmane.nitaj@unicaen.fr)

the future with quantum computers with Shor's algorithm [18]. As a consequence, the search for new post-quantum schemes that are resistant to quantum computers and quantum computation is extensively and rapidly developing.

Many works have been done on e-voting. Zhao et al. [21] presented an electronic voting system based on homomorphic encryption to ensure anonymity, privacy, and reliability, but there are still some unattended issues in their work, such as how to supervise the voting process to prevent conspiracy. Cervero et al. [10] presented an efficient homomorphic E-voting system over elliptic curves. Tohari et al. [1] proposed a mobile voting scheme where the users' votes are secured by using the elliptic curve cryptography (ECC). Azougaghe et al. [2] presented an electronic voting system based on Paillier homomorphic encryption to ensure privacy, confidentiality, and integrity. For electronic voting based on hard problems in lattices, Del Pino et al. [14] proposed a lattice-based homomorphic commitment electronic voting scheme that relies on the hardness of the M-LWE and M-SIS problems. In [11], a new post-quantum e-voting protocol was proposed. The construction of this scheme exploits the LWE-based homomorphic encryption.

In this paper, we propose to use cloud computing for data processing without any trusted third party to develop electronic voting. More specifically, homomorphic encryption is used as a fundamental tool to process data in a secured way. We present and implement the new quantum-resistant electronic voting scheme and prove its efficiency and security. Our new scheme is based on the hardness of problems in lattices and uses the scheme presented by Fan and Vercauteren [16].

The rest of this paper is organized as follows. In Sect. 2, we recall some facts on lattices, hard lattice problems, and post-quantum cryptography. In Sect. 3, we describe the homomorphic encryption concept and the Fan and Vercauteren scheme. In Sect. 4, we present the new electronic voting scheme, give an example of voting, and study the security of the new scheme. In Sect. 5, we present an implementation of our new scheme using SEAL library [9]. We conclude the paper in Sect. 6.

## 2 Lattice-Based Cryptography

In this section, we briefly describe some facts related to lattices.

### 2.1 Lattice

We start with the definition of a lattice.

**Definition 1** Let  $B = \{b_1, \dots, b_n\}$ ,  $b_i \in \mathbb{R}^m$  be a set of  $n$  linearly independent vectors of  $m$  coordinates with  $n \leq m$ . The lattice  $\mathcal{L}$  associated to  $B$  is the discrete additive subgroup of  $\mathbb{R}^m$  containing all integer linear combinations of the vectors of  $B$ , that is

$$\mathcal{L}(B) = \left\{ \sum_{i=1}^n x_i b_i \mid x_i \in \mathbb{Z} \right\}.$$

The integer  $n$  is the dimension of the lattice, and  $m$  is the rank. When  $m = n$ , the lattice is called full-rank. The basis  $B$  can be represented as a matrix  $B = [b_1, \dots, b_n]$ . The determinant of the lattice is defined by  $\det(\mathcal{L}) = \sqrt{B^T \cdot B}$  where  $B$  is considered here as the matrix of the vectors  $b_1, \dots, b_n$ .

## 2.2 Hard Lattice Problems

The security of various schemes is based on the hardness of specific problems in lattices such as SVP, CVP, and LWE (see [12] for more details). We list below the main hard problems.

1. **The Shortest Vector Problem (SVP):** Given a lattice basis  $B$ , find the shortest nonzero vector in  $\mathcal{L}(B)$ .
2. **The Closest Vector Problem (CVP):** Given a lattice basis  $B$  and a target vector  $v_0$  not in the lattice  $\mathcal{L}(B)$ , find  $v \in \mathcal{L}(B)$ , the closest vector to  $v_0$ .
3. **Learning With Errors Problem (LWE):** Let  $A$  be a  $n \times n$  matrix which is uniformly distributed in  $\mathbb{Z}/q\mathbb{Z}$  where  $q$  is a prime number. Let  $s$  and  $e$  be two unknown vectors. The LWE problem is to find  $s$  and  $e$  using  $A$  and  $As + e$ .
4. **Ring-Learning With Errors Problem (Ring-LWE):** Ring-LWE problem is similar to the LWE problem where the unknown parameters  $s$  and  $e$  are polynomials from the ring of polynomials  $\mathcal{R}_q = \mathbb{Z}_q[x]/(x^n + 1)$  where  $q$  is a prime number.

## 2.3 Post-Quantum Cryptography

In modular arithmetic and quantum computing, Shor's algorithm, invented in 1994 by Shor [18], is a quantum algorithm that can solve hard problems in classical cryptography such as the factorization problem and the discrete logarithm problem. Shor's algorithm reduces the problem of factorization to the problem of finding the period of a certain function using the quantum Fourier transform, which is infeasible with classical computers. Shor's algorithm is probabilistic, it gives the correct answer with a high probability, and the probability of failure can be decreased by repeating the algorithm. Most of the widely used public key cryptosystems, such as RSA [19], ElGamal [15], and EC-ElGamal [20], are vulnerable if Shor's algorithm is implemented in a practical quantum calculator. To overcome this problem, cryptosystems that are resistant to quantum computer are needed. The cryptography resistant to quantum computers is called post-quantum cryptography. A promising post-quantum

cryptography is based on lattices. Lattice-based cryptography is a novel and promising area of cryptography based on the hardness of some lattice problems, especially the shortest vector problem (SVP), the closest vector problem (CVP), and learning with errors problem (LWE). SVP, CVP, and LWE are known to be NP-hard problems, and there are no efficient quantum algorithms for solving them.

## 2.4 Post-Quantum Electronic Signature

With the progress in cryptanalysis, alternatives for currently used signature schemes such as RSA, DSA, and ECDSA have been invented. More especially, lattice-based signature schemes such as BLISS [13] and GLP [17] have been created. In [3], it is shown that both BLISS and GLP do not allow for good performance and provably secure instantiation at the same time as Ring-Tesla [8], so choosing parameters according to the security reductions for these schemes reduces their performance significantly.

A promising signature scheme is Tesla# [8], which is a strong candidate for post-quantum digital signature. It is provably secure with a security reduction to the ring-learning with errors (Ring-LWE) problem.

## 3 Homomorphic Encryption and Fan and Vercauteren Cryptosystem Scheme

### 3.1 Homomorphic Encryption

Homomorphic encryption is used to process the encrypted data and to ensure its privacy and confidentiality. A system is said to be homomorphic when computations, mainly addition and multiplication, can be made on the encrypted data without decrypting it. If decrypted, the final result is similar to if the computation was done on decrypted data.

**Definition 2** Let  $E$  be a homomorphic encryption algorithm. A cryptosystem is said to partially homomorphic if it verifies one of the following properties:

1. partially homomorphic additive:  $E(m_1 + m_2) = E(m_1) + E(m_2)$ ;
2. partially homomorphic multiplicative:  $E(m_1 m_2) = E(m_1)E(m_2)$ .

### 3.2 Fan and Vercauteren Cryptosystem Scheme

With the progress in cryptanalysis, alternatives to currently homomorphic additive schemes such as Brakerski scheme [5], Brakerski and Vaikuntanathan (BV)

scheme [6], Brakerski, Gentry, and Vaikuntanathan (BGV) scheme [7], and Fan and Vercauteren (FV) scheme [16] have been invented. They are all based on the LWE or the Ring-LWE problems and are considered as secure post-quantum schemes. The arithmetic of Fan and Vercauteren uses various parameters.

- $\mathcal{R} = \mathbb{Z}[x]/(x^{d'} + 1)$  is the ring of polynomials modulo  $x^{d'} + 1$ .
- $\mathcal{R}_q = \mathbb{Z}_q[x]/(x^{d'} + 1)$  is the ring of polynomials modulo  $q$  and modulo  $x^{d'} + 1$ .
- $\mathcal{R}_t = \mathbb{Z}_t[x]/(x^{d'} + 1)$  is the ring of polynomials modulo  $t$  and modulo  $x^{d'} + 1$ .
- $[\mathbf{a}]_t$  is the value modulo  $t$  of each component (or coefficient) of the vector  $\mathbf{a}$ .
- $[\lfloor \mathbf{a} \rfloor]$  is the vector where the components are the nearest integers to the components of the vector  $\mathbf{a}$ .

The Fan and Vercauteren scheme is based on the following three algorithms:

1. **Key Generation:** Let  $\chi$  be a distribution on  $\mathcal{R}$ ,  $t$  is chosen following the choice of the clear space to be encrypted ( $m$  is the clear in this case),  $\Delta = \left\lfloor \frac{q}{t} \right\rfloor$ ,  $a \leftarrow \mathcal{R}_q$  is sampled uniformly, and  $e \leftarrow \chi$ .
  - (a) The private key is an integer  $s_k \in \mathcal{R}_q$
  - (b) The public key is  $p_k = (b, a) \in \mathcal{R}_q^2$  where  $b = -(a \cdot s_k + e) \pmod{q}$ .
2. **Encryption:** To encrypt a message  $m \in \mathcal{R}_t$ , we sample  $u, e_1, e_2 \leftarrow \chi$  and compute

$$FV(m) = C = (c_0, c_1) = ([bu + e_1 + \Delta \cdot m]_q, [au + e_2]_q)$$

3. **Decryption:** To decrypt  $C = (c_0, c_1)$ , we compute  $m = \left\lfloor \left[ \frac{t \cdot [c_0 + c_1 s_k]_q}{q} \right] \right\rfloor_t$ .

The correctness of the decryption is guaranteed as follows:

$$\begin{aligned} \left\lfloor \left[ \frac{t \cdot [c_0 + c_1 s_k]_q}{q} \right] \right\rfloor_t &= \left\lfloor \left[ \frac{t \cdot [(bu + e_1 + \Delta \cdot m)_q + (au + e_2)_q s_k]_q}{q} \right] \right\rfloor_t \\ &= \left\lfloor \left[ \frac{t \cdot [(-(a \cdot s_k + e)u + e_1 + \Delta \cdot m)_q + (au + e_2)_q s_k]_q}{q} \right] \right\rfloor_t \\ &= \left\lfloor \left[ \frac{t \cdot [-(a \cdot s_k + e)u + e_1 + \Delta \cdot m + (au + e_2)s_k]_q}{q} \right] \right\rfloor_t \\ &= \left\lfloor \left[ \frac{t \cdot [-eu + e_1 + \Delta \cdot m + e_2 s_k]_q}{q} \right] \right\rfloor_t \\ &= \left\lfloor \left[ \frac{t \cdot [\Delta \cdot m + e_1 + e_2 s_k - eu]_q}{q} \right] \right\rfloor_t \\ &= \left\lfloor \left[ \frac{t \cdot [\lfloor \frac{q}{t} \rfloor \cdot m + e_1 + e_2 s_k - eu]_q}{q} \right] \right\rfloor_t \\ &= \lfloor [m + \widehat{e}] \rfloor_t \\ &= m. \end{aligned}$$

While  $\widehat{e}$  is small, we can find  $m$ . We note that the FV scheme is homomorphic with respect to the addition law. Indeed, if

$$\begin{aligned} C_1 &= \text{FV}(m_1) = ([bu^{(1)} + e_1^{(1)} + \Delta \cdot m_1]_q, [au^{(1)} + e_2^{(1)}]_q), \\ C_2 &= \text{FV}(m_2) = ([bu^{(2)} + e_1^{(2)} + \Delta \cdot m_2]_q, [au^{(2)} + e_2^{(2)}]_q), \end{aligned}$$

then

$$\begin{aligned} C_1 + C_2 &= \text{FV}(m_1) + \text{FV}(m_2) \\ &= (A, B) \end{aligned}$$

where

$$\begin{aligned} A &= [bu^{(1)} + e_1^{(1)} + \Delta \cdot m_1]_q + [bu^{(2)} + e_1^{(2)} + \Delta \cdot m_2]_q \\ &= [b(u^{(1)} + u^{(2)}) + e_1^{(1)} + e_1^{(2)} + \Delta \cdot (m_1 + m_2)]_q, \\ B &= [au^{(1)} + e_2^{(1)}]_q + [au^{(2)} + e_2^{(2)}]_q \\ &= [a(u^{(1)} + u^{(2)}) + e_2^{(1)} + e_2^{(2)}]_q \end{aligned}$$

from which we deduce

$$C_1 + C_2 = \text{FV}(m_1) + \text{FV}(m_2) = (A, B) = \text{FV}(m_1 + m_2)$$

## 4 The New Electronic Voting Scheme

### 4.1 Architecture and Scenario of the New Electronic Voting Scheme

In this section, we present our new scheme for electronic voting which is based on lattices.

The participating parties are the voters, the local trusted party, and the trusted party in the cloud. The voters encrypt and send their votes to the cloud that calculates the encrypted results using homomorphic properties, and then the local trusted party that generates and stores the election private key, decrypts encrypted results coming from the cloud and calculates the result of the vote.

Let  $v$  be the number of voters,  $m$  the number of candidates,  $P_i(x)$  is a polynomial in  $\mathcal{R}_t[x]$  with coefficient in  $\mathbb{Z}/2\mathbb{Z}$ , and  $v < t$ . We describe a scenario of the new electronic voting scheme as follows (the scenario is presented in Fig. 1).

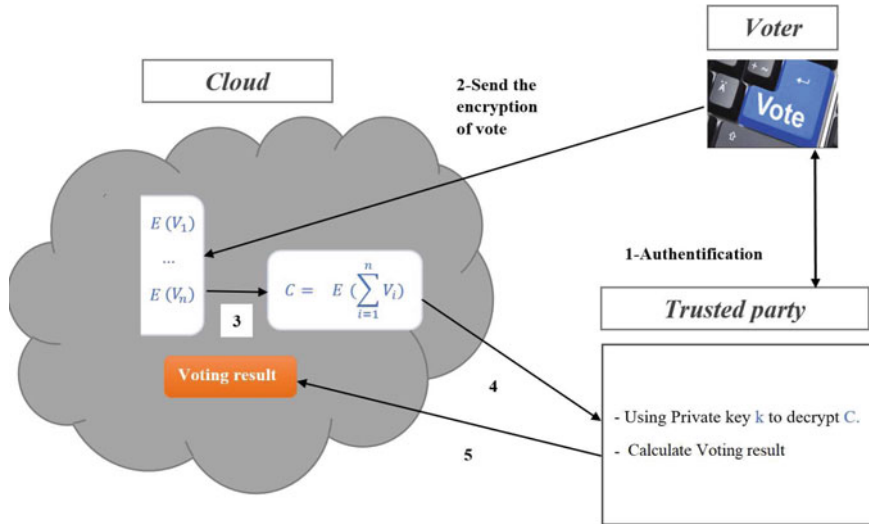


**Fig. 1** Scenario of a new voting system based on lattices

- First, each voter  $j$  with  $1 \leq j \leq v$  must be authenticated, using the electronic signature scheme Tesla# [8]. Each voter owns a private key for signing, and a correspondent public key, generated as follows:
  - The private key:*  $(s, e_1, e_2) \in \mathcal{R}_q^3$  sampled from  $D$  a distribution on  $\mathcal{R}_q$  .
  - The public key:*  $(t_1, t_2) \in \mathcal{R}_q^2$ , where  $t_1 = a_1 s + e_1$  and  $t_2 = a_2 s + e_2$ , and  $a_1, a_2 \in \mathcal{R}_q$  are two invertible ring elements.
- If the authentication with the trusted party is accomplished, the voter obtains the permission to vote.
- If the voter  $j$  wants to vote for candidate number  $i$  with  $1 \leq i \leq m$ , then the vote will be  $P_i$  where the polynomial  $P_i(x) \in \mathcal{R}_t[x]$  with coefficients in  $\mathbb{Z}/2\mathbb{Z}$ .
- The voter computes  $FV(P_i)$  using the FV scheme and sends it to the cloud.
- The system will do this process until the end of the voting process.
- The cloud applies the properties of homomorphic addition encryption to compute the encryption of the voting result as follows:

$$\begin{aligned}
 C &= FV(P_1) + \dots + FV(P_1) + \dots + FV(P_k) + \dots + FV(P_m) \dots + FV(P_m) \\
 &= FV(b_1 P_1) + \dots + FV(b_k P_k) \dots + FV(b_m P_m) \\
 &= FV \left( \sum_{i=1}^m b_i P_i \right).
 \end{aligned}$$

- The cloud sends the encrypted value  $C$  to the trusted party.

8. The trusted party decrypts  $C$  using the private FV key to obtain  $R = \sum_{i=1}^m b_i P_i$ , where  $b_i$  is the total number of votes for candidate  $i$ .
9. The trusted party applies Algorithm 1 to find each integer  $b_i$  from  $R$ , which corresponds to the number of votes for the candidate  $i$ .

## 4.2 Votes Calculation: General Case

We present now the method for solving the equation  $R = \sum_{i=1}^m b_i P_i$  for the integers  $b_i$ . We start with the definition of  $\text{Coef}(P_i)$ .

**Definition 3** For a polynomial  $P_i = \sum_{h=1}^d a_{ih}x^h$  we define the function  $\text{Coef}$  as  $\text{Coef}(P_i) = (a_{i1}, a_{i2}, \dots, a_{id})$ .

One can easily check that the function  $\text{Coef}$  is linear.

**Lemma 1** For  $1 \leq i \leq m$ , let  $P_i(x) = \sum_{h=1}^d a_{ih}x^h \in \mathcal{R}_t$  with  $d = \max_{1 \leq i \leq m}(\deg(P_i)) < d'$  representing the vote in favor of the candidate  $i$ , with coefficients in  $\mathbb{Z}/2\mathbb{Z}$ , satisfying,  $a_{ih}a_{i'h} = 0$  for  $i \neq i'$ , and  $v < t$ . Let  $R(x) = \sum_{i=1}^m b_i P_i(x)$  be the polynomial representing all votes. Then, the number of votes  $b_k$  in favor of the candidate  $k$  is

$$b_k = \frac{\langle \text{Coef}(P_k), \text{Coef}(R) \rangle}{\sum_{h=1}^d a_{kh}^2},$$

where  $\langle X, Y \rangle$  is the dot product of the vectors  $X$  and  $Y$ .

**Proof.** For  $1 \leq i \leq m$ , let  $P_i(x) = \sum_{h=1}^d a_{ih}x^h \in \mathcal{R}_t$  representing the vote in favor of the candidate  $i$ , with coefficients in  $\mathbb{Z}/2\mathbb{Z}$  and  $v < t$ .

Let  $P_k = \sum_{h=1}^d a_{kh}x^h$ . Then  $\text{Coef}(P_k) = (a_{k1}, \dots, a_{kd})$ . Similarly, let  $R(x) = \sum_{i=1}^m b_i P_i(x)$ . Then

$$R(x) = \sum_{i=1}^m b_i P_i(x) = \sum_{i=1}^m b_i \sum_{h=1}^d a_{ih}x^h = \sum_{h=1}^d \sum_{i=1}^m b_i a_{ih}x^h,$$

which leads to

$$\text{Coef}(R) = \left( \sum_{i=1}^m b_i a_{i1}, \dots, \sum_{i=1}^m b_i a_{id} \right).$$

Hence, the dot product of the vectors  $\text{Coef}(P_k)$  and  $\text{Coef}(R)$  is

$$\langle \text{Coef}(P_k), \text{Coef}(R) \rangle = \sum_{h=1}^d a_{kh} \sum_{i=1}^m b_i a_{ih} = \sum_{h=1}^d \sum_{i=1}^m b_i a_{kh} a_{ih}.$$

Since  $a_{kh}a_{ih} = 0$  for  $i \neq k$ , then

$$\langle \text{Coef}(P_k), \text{Coef}(R) \rangle = \sum_{h=1}^d b_k a_{kh}^2 = b_k \sum_{h=1}^d a_{kh}^2,$$

from which we deduce

$$b_k = \frac{\langle \text{Coef}(P_k), \text{Coef}(R) \rangle}{\sum_{h=1}^d a_{kh}^2}.$$

This terminates the proof.

The method for finding the integer values  $b_i$  in the polynomial equation  $R(x) = \sum_{i=1}^m b_i P_i(x)$  is presented in Algorithm 1

---

#### Algorithm 1 Algorithm to find result of vote

---

**Require:** The sum  $R(x) = \sum_{i=1}^m b_i P_i(x) = \sum_{h=1}^d \sum_{i=1}^m b_i a_{ih} X^h = \sum_{h=1}^d r_{ih} X^h$  ( $r_{ih} = \sum_{i=1}^m b_i a_{ih}$ ), the number  $m$  of candidates, the number  $v$  of voters, and  $P_i = \sum_{h=1}^d a_{ih} X^h \in \mathcal{R}_t$  (with coefficients in  $\mathbb{Z}/2\mathbb{Z}$  and  $d = \max_{1 \leq i \leq m} (\deg(P_i)) < d'$ ) is the vote for candidate  $i$  satisfying,  $a_{ih}a_{i'h} = 0$  for  $i \neq i'$ , and  $v < t$ .

**Ensure:** The numbers  $b_1, b_2, \dots, b_m$  of votes of the candidates.

- 1: **for**  $k = 1$  to  $m$  **do**
  - 2:   Compute  $\text{Coef}(P_k) = (a_{k1}, a_{k2}, \dots, a_{kd})$ .
  - 3:   Compute  $\text{Coef}(R) = (r_{11}, r_{12}, \dots, r_{1d})$ .
  - 4:   Compute  $b_k = \frac{\langle \text{Coef}(P_k), \text{Coef}(R) \rangle}{\sum_{h=1}^d a_{kh}^2}$  where  $\langle x, y \rangle$  is the dot product of the vectors  $x$  and  $y$ .
  - 5: **end for**
  - 6: **Return**  $b_1, b_2, \dots, b_m$ .
- 

### 4.3 A Numerical Example

1. In the following example, we describe the new scheme for five candidates and 20 voters:
  - $\mathcal{R}_{97} = \mathbb{Z}_{97}[x]/(x^{256} + 1)$  is the ring of polynomials modulo 97 and modulo  $x^{256} + 1$ .
  - $P_1 = X + X^6$  is the voting polynomial for candidate number 1.
  - $P_2 = X^2$  is the voting polynomial for candidate number 2.
  - $P_3 = X^4 + X^7$  is the voting polynomial for candidate number 3.
  - $P_4 = X^3 + X^8$  is the voting polynomial for candidate number 4.
  - $P_5 = X^9$  is the voting polynomial for candidate number 5.
2. Suppose that 5 voters have voted for the candidate 1, 6 voters for the candidate 2, 3 voters for candidate 3, 2 voters for the candidate 4, and 4 voters for the candidate 5.

3. The votes are encrypted using the FV scheme.

4. We have

$$\begin{aligned}
 FV(R) &= \underbrace{FV(X + X^6) + \dots + FV(X + X^6)}_{5 \text{ times}} + \underbrace{FV(X^2) + \dots + FV(X^2)}_{6 \text{ times}} \\
 &\quad + \underbrace{FV(X^4 + X^7) + \dots + FV(X^4 + X^7)}_{3 \text{ times}} \\
 &\quad + \underbrace{FV(X^3 + X^8) + \dots + FV(X^3 + X^8)}_{2 \text{ times}} \\
 &\quad + \underbrace{FV(X^9) + \dots + FV(X^9)}_{4 \text{ times}} \\
 &= FV(5(X + X^6) + 6X^2 + 3(X^4 + X^7) + 2(X^3 + X^8) + 4X^9) \\
 &= FV(4X^9 + 2X^8 + 3X^7 + 5X^6 + 3X^4 + 2X^3 + 6X^2 + 5X).
 \end{aligned}$$

5. After decryption we obtain:  $R = 4X^9 + 2X^8 + 3X^7 + 5X^6 + 3X^4 + 2X^3 + 6X^2 + 5X$ .

6. For the polynomials  $P_1, P_2, P_3, P_4$ , and  $P_5$ , we have  $\sum_{h=1}^9 a_{1h}^2 = 2$ ,  $\sum_{h=1}^9 a_{2h}^2 = 1$ ,  $\sum_{h=1}^9 a_{3h}^2 = 2$ ,  $\sum_{h=1}^9 a_{4h}^2 = 2$ , and  $\sum_{h=1}^9 a_{5h}^2 = 1$ , respectively. Then, since  $b_i = \frac{\langle \text{Coef}(P_i), \text{Coef}(R) \rangle}{\sum_{h=1}^9 a_{ih}^2}$ , we get:

$$\begin{aligned}
 b_1 &= \frac{\langle \text{Coef}(P_1), \text{Coef}(R) \rangle}{\sum_{h=1}^9 a_{1h}^2} \\
 &= \frac{\langle (1, 0, 0, 0, 0, 1, 0, 0, 0), (5, 6, 2, 3, 0, 5, 3, 2, 4) \rangle}{2} = 5,
 \end{aligned}$$

$$\begin{aligned}
 b_2 &= \frac{\langle \text{Coef}(P_2), \text{Coef}(R) \rangle}{\sum_{h=1}^9 a_{2h}^2} \\
 &= \frac{\langle (0, 1, 0, 0, 0, 0, 0, 0, 0), (5, 6, 2, 3, 0, 5, 3, 2, 4) \rangle}{1} = 6
 \end{aligned}$$

$$\begin{aligned}
 b_3 &= \frac{\langle \text{Coef}(P_3), \text{Coef}(R) \rangle}{\sum_{h=1}^9 a_{3h}^2} \\
 &= \frac{\langle (0, 0, 1, 0, 0, 1, 0, 0, 0), (5, 6, 2, 3, 0, 5, 3, 2, 4) \rangle}{2} = 3.
 \end{aligned}$$

$$\begin{aligned} b_4 &= \frac{\langle \text{Coef}(P_4), \text{Coef}(R) \rangle}{\sum_{h=1}^9 a_{4h}^2} \\ &= \frac{\langle (0, 0, 1, 0, 0, 0, 0, 1, 0), (5, 6, 2, 3, 0, 5, 3, 2, 4) \rangle}{2} = 2. \end{aligned}$$

$$\begin{aligned} b_5 &= \frac{\langle \text{Coef}(P_5), \text{Coef}(R) \rangle}{\sum_{h=1}^9 a_{5h}^2} \\ &= \frac{\langle (0, 0, 0, 0, 0, 0, 0, 0, 1), (5, 6, 2, 3, 0, 5, 3, 2, 4) \rangle}{1} = 4. \end{aligned}$$

#### 4.4 Votes Calculation: Monomials Case (optimal Case)

In this section, we propose an amelioration of the algorithm 1 that gives less operations to compute the number of votes. Each candidate  $i$  votes by the monomial  $P_i(x) = X^j$ , to obtain  $R = \sum_{k=1}^m b_k P_k(x)$ , with  $b_k$  is number of votes of candidate  $k$  calculated as in the following corollary.

**Corollary 1** For  $1 \leq i \leq m$  and  $1 \leq j \leq d$ , let  $P_i(x) = X^j$  representing the vote in favor of the candidate  $i$ , and  $v < t$ . Let  $R(x) = \sum_{i=1}^m b_i P_i(x)$  be the polynomial representing all votes. Then

(1) the number of votes  $b_k$  in favor of the candidate  $k$  is

$$b_k = \langle \text{Coef}(P_k), \text{Coef}(R) \rangle \text{ where } \langle x, y \rangle,$$

where  $\langle X, Y \rangle$  is the dot product of the vectors  $X$  and  $Y$ .

(2) The complexity of calculation is optimal.

**Proof.** 1. Let  $P_i(x) = X^j$  representing the vote in favor of the candidate  $i$ , and  $v < t$ . Let  $R(x) = \sum_{i=1}^m b_i P_i(x)$ . Then according to Lemma 1, we have

$$b_k = \frac{\langle \text{Coef}(P_k), \text{Coef}(R) \rangle}{\sum_{h=1}^d a_{kh}^2},$$

where  $\sum_{h=1}^d a_{kh}$  is the sum of the coefficient of  $P_k$ . In this case  $\sum_{h=1}^d a_{kh}^2 = 1$  because  $P_k$  is a monomial and

$$b_k = \langle \text{Coef}(P_k), \text{Coef}(R) \rangle.$$

2. The complexity of Step 4 of Algorithm 1 is equal to the complexity of

$$\frac{\langle \text{Coef}(P_k), \text{Coef}(R) \rangle}{\sum_{h=1}^d a_{kh}^2}.$$

Observe that in this new case, Step 4 becomes  $\langle \text{Coef}(P_k), \text{Coef}(R) \rangle$ , so we conclude that the case of monomials is best in terms of complexity.

This terminates the proof.

## 4.5 The Security of the New Scheme

In this section, we show that the proposed system achieves the security requirements.

**Authentication and uniqueness** Only people in the electoral roll can vote, and every participant can vote once at most.

1. Each voter authenticates with Tesla# [8].
2. If voter authenticates another time to vote, he is blocked for uniqueness.

**Privacy** Votes cannot be related to voter identities

1. All the votes are encrypted using the FV cryptosystem, so that no information can be obtained from an encrypted result.
2. Only trusted party which acts honestly can decrypt and has got the result of vote.
3. The algorithm used for authentication is Tesla#. Hence, no information leaks from it.

**Fairness** No partial results can be revealed before the end of the voting period, no vote is decrypted before the ending of the voting period, and only trusted party can decrypt.

**Verifiability** Correctness of the process can be checked

1. The algorithm of the calculation of result is public, and anyone can verify its correctness.
2. The correctness of decryption is proved.

### Post-quantum security

All cryptographic schemes applying FV for encryption and Tesla# for authentication are resistant to quantum attacks. As a consequence, our scheme is secure and resistant to quantum attacks.

**Table 1** Complexity

Vote encryption	Ciphertext addition	Result decryption	Results computing
$\mathcal{O}(d'^2 \log(d'))$	$\mathcal{O}(vd' \log(d'))$	$\mathcal{O}(d'^3)$	$\mathcal{O}(md)$

## 5 Complexity and Performance of the Scheme

### 5.1 Complexity Study of the New Scheme

The key technical barrier to realizing homomorphic encryption-based representation matching is the computational complexity of the FV scheme, especially the votes encryption addition. Fundamentally, the addition of two votes in the plaintext transforms to addition of two polynomials of degree  $d'$ , the degree of the modulus polynomial  $x^{d'} + 1$  and  $v$  is the voters number. Table 1 presents the complexity of different vote treatment phases.

In our electronic voting scheme, we can use the RNS Variant of FV [4]; in this case, the decryption complexity becomes  $\mathcal{O}(d'^2 \log(d'))$  instead of  $\mathcal{O}(d'^3)$  in FV based scheme.

### 5.2 Implementation and Performance of the New Scheme

SEAL library [9] is an open-source library, developed in 2015 in C++ by a Microsoft Teams. It implements FV cryptosystem with no external library dependencies. In SEAL, the user chooses the security level, the plaintext modulus (no limit for the choice), and the degree.

In this section, we give the results of our experiments: First we compare the calculation vote function presented in Algorithm 1, and we show how this function is efficient, especially for the monomials case. Second, we implement our e-voting scheme using SEAL library, starting with the encrypting of votes, the additive homomorphic encryption, and the decryption of final result.

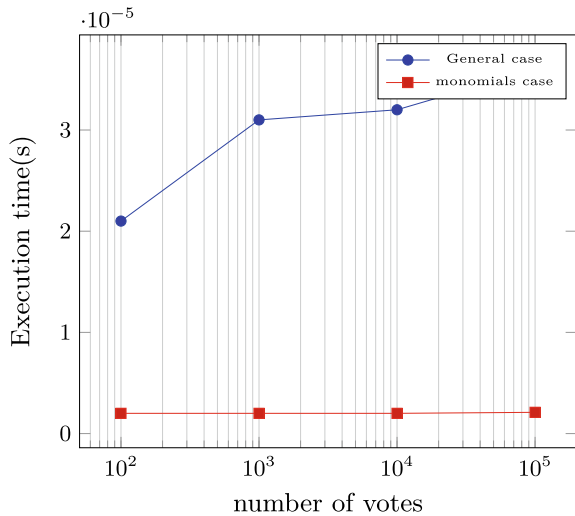
We have implemented the algorithm using SEAL library with C++ and have experimented with it in a computer with an Intel Core i5 5200 2.20 GHz CPU with 8GB of RAM running ubuntu 20.04 as OS. The parameters of FV cryptosystem for 128 bits of security are chosen as follows:  $d' = 4096$ ,  $t = 100090$ ,  $q = 110$ .

In our scheme, the homomorphic addition is efficient, as shown in Table 2. The execution time is only equal to 9 seconds for 100000 encrypted votes.

In Fig. 2, we present a comparison of the execution times between the monomials case and the general case 1 of our calculation vote function. The monomials case remains better even if the number of voters becomes higher.

**Table 2** Homomorphic addition execution time (s)

	m	v			
		$10^2$	$10^3$	$10^4$	$10^5$
Execution time	3	0.008880	0.090728	0.896139	8.973199
	5	0.008725	0.087658	0.907500	8.813361
	9	0.008707	0.088323	0.906385	8.902762

**Fig. 2** Algorithm 1 execution time

The average execution time of FV encryption cryptosystem is fast and does not exceed one second as shown in Fig. 3. Also, the execution time of decryption of the final result is very fast, around 5 ms as shown in Fig. 4.

## 6 Conclusion

We presented a new secure electronic voting scheme based on Fan and Vercauteren cryptosystem which is an additive homomorphic cryptosystem to guarantee privacy. We implemented our scheme and proved its efficiency. We have also shown that our scheme is correct and secure against quantum attacks.

**Fig. 3** Encryption execution time

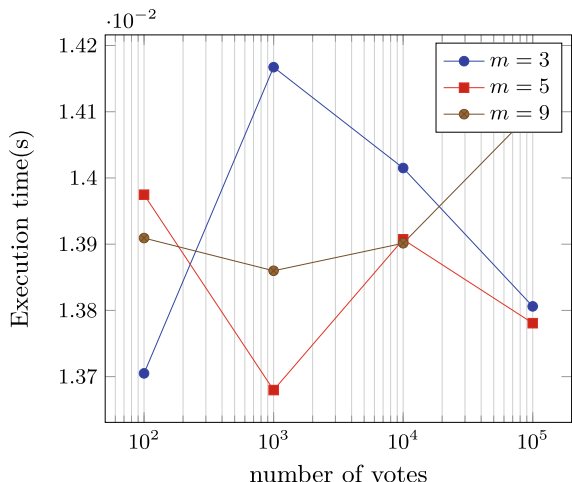
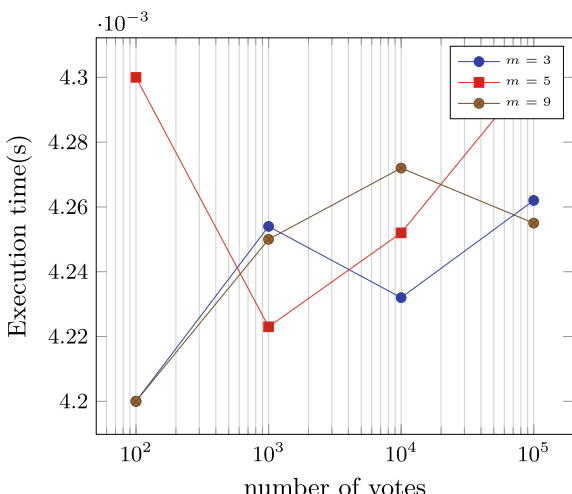


**Fig. 4** Decryption execution time



## References

1. Ahmad, T., Hu, J., Han, S.: An efficient mobile voting system security scheme based on elliptic curve cryptography. In: 2009 Third International Conference on Network and System Security, pp. 474–479. IEEE (2009)
2. Azougaghe, A., Kartit, Z., Hedabou, M., Belkasmi, M., Benmiloud, M., Marraki, M.: An Efficient Electronic Voting System in a Cloud Computing Environment (2015)
3. Akleylek, S., Bindel, N., Buchmann, J., Kramer, J., and Marson, G. A.: An efficient lattice-based signature scheme with provably secure instantiation. In: International Conference on Cryptology in Africa, pp. 44–60. Springer, Cham (2016)
4. Bajard, J.-C., et al.: A full RNS variant of FV like somewhat homomorphic encryption schemes. In: International Conference on Selected Areas in Cryptography. Springer, Cham (2016)

5. Brakerski, Z.: Fully homomorphic encryption without modulus switching from classical gapsvp. In: Cryptology ePrint Archive, Report 2012/078 (2012). <http://eprint.iacr.org/>
6. Brakerski, Z., Vaikuntanathan, V.: Efficient fully homomorphic encryption from (standard) lwe. In: Cryptology ePrint Archive, Report 2011/344 (2011). <http://eprint.iacr.org/>
7. Brakerski, Z., Gentry, C., Vaikuntanathan, V.: (Leveled) fully homomorphic encryption without bootstrapping. ACM Trans. Comput. Theory (TOCT) **6**(3), 13 (2014)
8. Barreto, P.S., Longa, P., Naehrig, M., Ricardini, J.E., Zanon, G.: Sharper ring-LWE signatures. In: Cryptology ePrint Archive, Report 2016/1026 (2016)
9. Chen, H., Laine, K. and Player, R.: Simple encrypted arithmetic library-SEAL v2. 1. In: International Conference on Financial Cryptography and Data Security. Springer, Cham (2017)
10. Cervero, M. A., Mateu, V., Miret, J. M., Sebe, F., Valera, J.: An efficient homomorphic E-Voting system over elliptic curves. In: International Conference on Electronic Government and the Information Systems Perspective, pp. 41–53. Springer, Cham (2014, August)
11. Chillotti, I., Gama, N., Georgieva, M., Izabachène, M.: A homomorphic LWE based e-voting scheme. In: Post-Quantum Cryptography, pp. 245–265. Springer, Cham (2016)
12. Chris P., et al.: A decade of lattice cryptography. Found. Trends Theoret. Comput. Sci. **10**(4), 283–424 (2016). <https://web.eecs.umich.edu/~cpeikert/pubs/lattice-survey.pdf>
13. Ducas, L., Durmus, A., Lepoint, T., Lyubashevsky, V.: Lattice signatures and bimodal Gaussians. In: Canetti, R., Garay, J.A. (eds.) Advances in Cryptology—CRYPTO 2013, volume 8042 of Lecture Notes in Computer Science, pp. 40–56. Springer, Santa Barbara (CA), USA (2013)
14. Del Pino, R., Lyubashevsky, V., Neven, G., Seiler, G.: Practical quantum-safe voting from lattices. In: Proceedings of the 2017 ACM SIGSAC Conference on Computer and Communications Security, pp. 1565–1581. ACM (2017)
15. ElGamal, T.: A public key cryptosystem and a signature scheme based on discrete logarithms. IEEE Trans. Inf. Theory **31**(4), 469–472 (1985)
16. Fan, J., Vercauteren, F.: Somewhat practical fully homomorphic encryption. In: Cryptology ePrint Archive, Report 2012/144 (2012). <http://eprint.iacr.org/>
17. Guneyşu, T., Lyubashevsky, V., and Poppellmann, T.: Practical lattice-based cryptography: A signature scheme for embedded systems. In: Prouff, E., Schaumont, P. (eds.) Cryptographic Hardware and Embedded Systems—CHES 2012, volume 7428 of Lecture Notes in Computer Science, pp. 530–547. Springer (2012)
18. Shor, P.W.: Polynomial-time algorithms for prime factorization and discrete logarithms on a quantum computer. SIAM J. Comput. **26**, 1484–1509 (1997)
19. Rivest, R.L., Shamir, A., Adleman, L.: A method for obtaining digital signatures and public-key cryptosystems. Commun. ACM **21**(2), 120–126 (1978)
20. Sunuwar, R., Samal, S.K.: ElGamal Encryption using Elliptic Curve Cryptography. University of Nebraska, Lincoln, Cryptography and Computer Security (2015)
21. Zhao, Y., Pan, Y., Wang, S., et al.: An anonymous voting system based on homomorphic encryption. In: 2014 10th International Conference on Communications (COMM), pp. 1–4. IEEE (2014)

# Mitigation of Electromagnetic Interference from DC-DC Converters for Electric Vehicle Application



Satabda Chaudhuri, Ishan Mukherjee, and S. Hemamalini

**Abstract** Electromagnetic interference (EMI) produced by power electronic components like DC-DC converters and associated switching components is a major problem in electric vehicles. Most techniques for mitigation of EMI are to use a single filter. This study focuses on combining filter circuits to mitigate EMI. Two filter combinations are considered in this paper. Module 1 is a combination of snubber circuit and line impedance stabilization network (LISN), and Module 2 is a PI filter with snubber circuit and LISN. Simulation studies are done for a buck converter with the filter modules and the filter performances are compared.

**Keywords** EMI · Converters · LISN · Snubber circuit · PI filter · FFT

## 1 Introduction

Electromagnetic interference has rapidly increased as a result of the usage of advanced electronic devices (EMI). The two types of EMI are conducted emissions and radiated emissions. Conducted emissions are electromagnetic emissions that are connected to the equipment's power source. Moreover, the conducted disturbance may be split into two groups namely differential mode and common mode [1].

However, electromagnetic interference (EMI) and electromagnetic compatibility (EMC) issues in EVs continue to limit the growth potential of the EV sector. The regulation of EMI is the primary objective of this paper. The primary sources of EMI include emissions from motor drive, and other power electronic emissions, particularly from switching elements. Most of the times vehicles maintain the proper

---

S. Chaudhuri · I. Mukherjee · S. Hemamalini (✉)

School of Electrical Engineering, Vellore Institute of Technology Chennai, Chennai, India

e-mail: [hemamalini.s@vit.ac.in](mailto:hemamalini.s@vit.ac.in)

S. Chaudhuri

e-mail: [satabda.chaudhuri2019@vitstudent.ac.in](mailto:satabda.chaudhuri2019@vitstudent.ac.in)

I. Mukherjee

e-mail: [ishan.mukherjee2019@vitstudent.ac.in](mailto:ishan.mukherjee2019@vitstudent.ac.in)

EMI/EMC standards, but it is necessary to understand them first. IGBTs and power MOSFETs, which are primarily gate-controlled devices used in switched-mode power converters, are the principal sources of electromagnetic interference (EMI). Due to the high-frequency spectrum of the pulses produced by these converter systems, which are used to reduce power losses, they emit electromagnetic emissions [2].

The amplitudes of the high bandwidth of the components are constrained by the regulations defined criteria. The two modes that the EMI filter normally consists of are the differential mode (DM) and the common mode (CM), in which the created noise and interference are conveyed. Each of these two components has its own design. The CM filter approach is used in this study. Similar engineering may be used to create the DM filter [3].

The primary negative impact of using switch-mode power supply (SMPS) is EMI. Due to the switching activities of the semiconductor devices and resultant discontinuous currents, EMI noise is inherent in switching power supply. EMI control is one of the most challenging SMPS design concerns, in addition to functional difficulties, resilience, cost, temperature, and space limits. For this type of distortion, communication and navigation-related issues arise due to the disturbance that has occurred in the controllers. Even it may cause fatal effects in the vehicle control systems. So, noise is generated using oscillators for an ideal condition of SMPS in EVs and this noise is reduced using filter components [4].

According to Kotny, the idea of PI filter-based filtering methods is the possible approach to filter out the noises. For that the conception about power electronics and designing techniques is required. But those techniques are tedious to operate for high-frequency range of operations and issues are mentioned in [5].

A different approach is deduced for the filtration technique. Here the proposed solution is a developed module with different filtering approaches. Three types of filtering techniques are implemented all together in a module which are RC snubber circuit, PI filter, and LISN networks [6].

In this paper, a combination of filter circuits is used to mitigate the EMI noise. Two modules are developed, one with snubber circuit and LISN network and another with a PI filter with snubber circuit and LISN network. Simulation studies are done for the proposed filter circuits, and their performances are compared.

## 2 Design specifications for EMI Mitigation

The government of the nation where the electronic gadget is being marketed regulates EMI to stop its adverse effects on other devices. There are European standards (for example, EN55022) in Europe, while FCC part 15 is in the USA. The two types of EMI in SMPS are conducted EMI and radiated EMI. Noise is dispersed across conductors, parasitic impedances, power connections, and ground connections when EMI is transmitted. Unwanted noise is associated via radio transmission for radiated

EMI. In particular, the concepts of the conducted component of EMI as produced by a step-down switching component are discussed in [7].

Conducted EMI is caused by the DC-DC converters running normally. Apart from the input or output capacitor, it does not include circuit parasitics. PCB layout alone would not lessen conducted EMI. Moreover, the current level at input and output ports is the only factor in conducted EMI and the voltage level is unrelated. To put it in another way, a lower input voltage results in a larger input current and a worse input conducted EMI for a buck converter with the same power level. A low-pass filter must typically be added between a power converter and the input supply in order to comply with the current EMI requirements [8, 9].

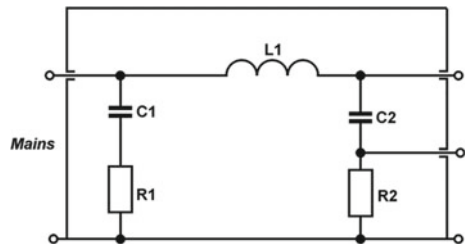
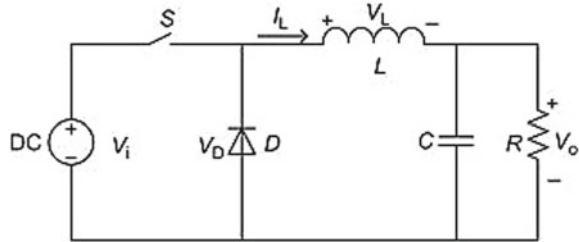
A passive LC filter with an inductor is attached to the SMPS's input side. The voltage ripple caused by the intermittent current flowing through the input capacitors is the source of the input port EMI noise. The switching frequency of the converter is the fundamental frequency of the voltage ripple. The noise spectrum contains higher-order harmonics of the fundamental frequency as well. It should be noted that some harmonics and the basic switching frequency are above the permitted range. An extra attenuation in terms of filtration needed with the desired limit is determined by the peak of the fundamental component over the target value [10, 11].

From the perspective of regulatory test requirements, the measuring frequency ranges from 10 kHz up to 30 MHz. Sometimes, there can be system needs that fall under the purview of the SMPS input filter that is above the frequency range of the regulation specification. These system requirements need to be reviewed and taken into account. Maintaining controlled conducted differential EMI performance over 30 MHz is discussed in fulfilling the standards for separately tested radiated EMI [12].

In this work, a simulation-based application of different RC filter topologies has been included with a buck converter, and the results have been compared to justify the possible application of them as a noise filtration technique which defines the conclusion of the study.

## 2.1 Line Impedance Stabilization Network

The significance of a LISN is to provide an impedance at the input side in order to obtain consistent measurements of the noise present at the measurement port. This is important because the testing device and the power supply's impedance function as a voltage divider. The impedance of the power source varies with the supply cable behind it. According to Fig. 1, the design consists of two capacitors 8 uF and 250 nF, coupled with a 50 uH inductor, along with a 1000 Ω resistor.

**Fig. 1** Simplified LISN**Fig. 2** Simplified buck converter

## 2.2 Buck Converter

A buck converter of 0.8 kW and 400 V of input power rating with an output of 50 V (duty cycle of 0.458) is selected for the application. The converter has a diode and a MOSFET as switching elements in the circuit. The converter is shown in Fig. 2.

## 2.3 Snubber Circuit

In buck converters, many high-frequency noises are generated at switch nodes. A snubber circuit provides one way of eliminating such harmonic noise. The snubber circuit is capable to filter out till 2.7 GHz of frequency noises. It consists of a RC network which has a  $5\ \Omega$  resistor with a  $1\text{nF}$  capacitor in parallel of the switch as shown in Fig. 3.

## 2.4 PI Filter

A shunt capacitor is placed at the input side of a Pi filter, which is then followed by a  $L$ -section filter. The rectifier's output is provided straight across a capacitor. The input side capacitor, followed by a choke coil and a second shunt capacitor, filters the pulsing DC output voltage. The way the components are assembled recalls the

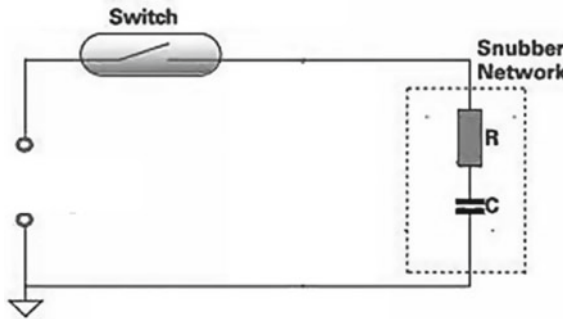


**Fig. 3** Simplified RC snubber network

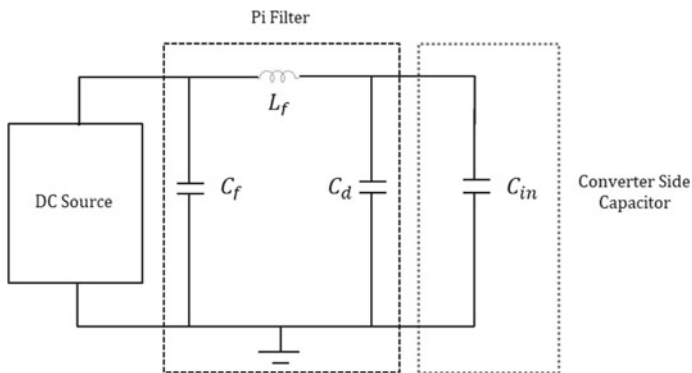


**Fig. 4** Simplified input side PI filter

form of the Greek letter PI as shown in Fig. 4. Moreover, the capacitor on the input side is also known as a capacitor input filter.

In this application, PI filter is designed in such a way to nullify the low to medium range of noises till 20 MHz generated by the LISNs from the switching node and the source side.

Identification of the noise level is the first step in the standard process for building an input filter for a buck converter followed by required degree of attenuation. After this, the choice of the filter inductance  $L_f$  can be 1  $\mu\text{H}$  to 10  $\mu\text{H}$  as per the guidelines. Then the filter capacitance  $C_f$  and damping capacitance  $C_d$  are calculated.

Calculation of  $L_f$  and  $C_{in}$  has a significant influence on the supply's regular operation as it may result in input instability of the SMPS. In order to prevent the impact of the input filter on the converter's stability, a damping capacitance  $C_d$  is added. The necessary EMI filter attenuation is given in (1).

$$|\text{Att}|_{\text{dB}} = 20 \log \left( \frac{\frac{1}{\pi^2 f_s C_{in}} \sin(\pi D)}{1 \mu V} \right) - V_{\max} \quad (1)$$

where  $f_s$  is the switching frequency,  $C_{\text{in}}$  is the converter's input side capacitor and  $D$  is the duty cycle. Similarly,  $I$  is the DC inductor current component, which corresponds to the output current in the case of a buck converter. For low and medium power applications, the inductor's value ( $L_f$ ) is typically in the range of 1–10  $\mu\text{H}$  since it determines the resonance frequency of the EMI filter. Choose the greatest value that satisfies the requirements for amperage and physical size. For  $C_f$  the highest among in between  $C_{fa}$  and  $C_{fb}$  which is derived using (2) and (3) has been considered.

$$C_{fa} = \frac{C_{\text{in}}}{\left( C_{\text{in}} L_f \left( \frac{2\pi f_s}{10} \right)^2 - 1 \right)} \quad (2)$$

$$C_{fb} = \left( \frac{1}{L_f} \right) \left( \frac{10^{\frac{|\text{Att}|_{\text{dB}}}{40}}}{2\pi f_s} \right)^2 \quad (3)$$

$C_{fa}$  guarantees that the input filter's resonance frequency is at least a decade below the switching frequency.  $C_{fb}$  assures correct attenuation of the EMI filter and is derived from an approximation. The largest value in that range of  $C_{fa}$  and  $C_{fb}$  is chosen as per our design-specified requirement.

The transfer function of a switching regulator is changed by the addition of an input filter. In order to prevent the input filter from significantly affecting the SMPS loop gain, the filter's output impedance must be suitably low. The filter LC parasitic heavily influences the peak of the impedance at the resonance corner frequency. Damping is needed when the output impedance is very high at the resonating frequency (that is,  $Q$  of filter formed by  $C_{\text{in}}$  and  $L_f$  is too high.) An electrolytic capacitor  $C_d$  can be used as a damping device in the circuitry, and it should be selected using (4).

$$C_d \geq 4 \times C_{\text{in}} \quad (4)$$

The converter is designed with a switching frequency ( $f_s$ ) of 20 MHz.

In addition, there are few external parasitic components that have been used after the snubber unit to normalize the output waveform after reduction of noise and to minimize the transients.

### 3 Synthesis of the Filter Modules

The need for high-speed electronics operating at high frequencies is causing EMI, which manifests as both conducted interference and radiated interference. The use of EMI filters is currently the best method for reducing conducted interference. For this reason, it is essential to synthesize an adequate filter module [1].

There are two types of module combinations considered in this work as shown in Figs. 5 and 6.

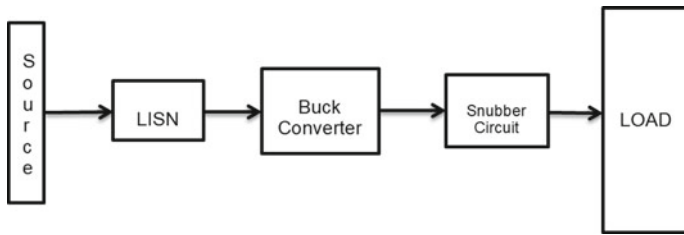


**Fig. 5** Simplified diagram of module 1-buck converter with RC snubber

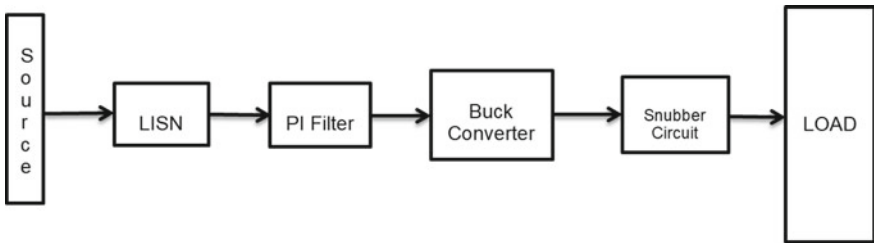


**Fig. 6** Simplified diagram of module 2-buck converter with RC snubber and PI filter

- Module 1-Buck Converter with RC snubber.
- Module 2-Buck Converter with RC snubber and PI filter.

The design specifications of the system components are mentioned in Table 1 and the same is used for simulation.

## 4 Operation of the Modules

Consider two factors, namely emission and immunity, in order to comprehend the consequences of EMI (also known as susceptibility). The electromagnetic energy that a radiofrequency source emits is measured by its emissions. Immunity refers to how much an external electromagnetic energy source will interfere with an electrical device's ability to function. The gadget will be resistant to EMI up to a certain point and vulnerable after that point [13–15]. Radio frequency interference, electrostatic discharge, and power disruptions are the three types of EMI issues that occur most frequently. The focus of the operation of the modules is how much noise they can reduce for different testing conditions and the best efficient way of filtration.

**Table 1** Design specifications

Type	Specifications	Module 1	Module 2
Buck converter	C11 = 100 uF M2 (MOSFET) L8 = 10 nH D3 (Diode) C12 = 1 pF	Included	Included
LISN	L10 = 50 uH = L11 C15 = 8 uF = C17 C14 = 250 nF = C16 R9 = 1000 Ω = R10	Included	Included
Snubber circuit	R7 = 5 Ω C13 = 1 nF	Included	Included
Input PI filter	L6 = 10 uH C9 = 100 uF C2 = 100 uF	Not Included	Included
External parasitic	L1 = 100 uH C10 = 100 uF D2 (Diode)	Included	Included
Load resistor Type1	R1 = 0.08 Ω	Not included	Included
Load resistor Type5	R5 = 0.9 Ω	Included	Not included

#### 4.1 Module 1-Buck Converter with RC Snubber

In this module, as shown in Fig. 7, LISN 1 is connected to the source to generate a noise in the network which delivers the power to the buck converter and to inject a noise from the converter side LISN 2 is incorporated. To nullify the noises in the output waveform, a RC snubber network is added across the output side of the converter in addition with few parasitic connections across the output side to limit the switching waveforms and their peaks and a reverse bias diode to limit the dual power flow [16].

#### 4.2 Module 2-Buck Converter with RC Snubber and PI Filter

In this module, as shown in Fig. 8, it is different in terms of its filtration topologies as it has a PI filter before the buck converter to nullify the medium frequency noises to a good extent. The noises are generated in the source by LISN 1 and then it has been received by the input side of the PI filter. Accordingly, the noises having higher strength have been reduced by the PI filter [17–19]. But due to the LISN 2 in the switching terminal, it injects a noise there which affects the output of the converter. To nullify the effect, a RC snubber circuit is implemented. Due to the injection near the MOSFET, it generates the noise partially.

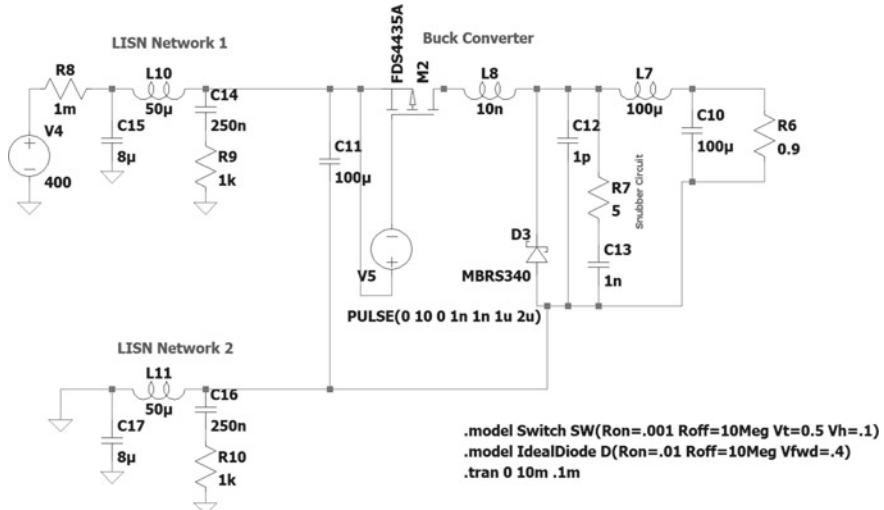


**Fig. 7** Module 1-buck converter with RC snubber circuit

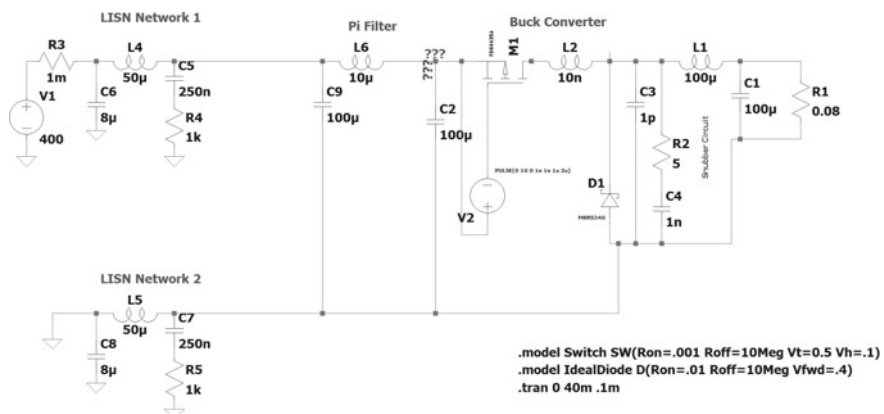


**Fig. 8** Module 2-buck converter with RC snubber circuit and PI filter circuit

## 5 Results and Analysis

The simulation results for Module 1 with snubber circuit as their filtering element are shown in Fig. 9. The input voltage is 400 V and the output voltage is 64.0429 V with a settling time of 7.425 ms. The FFT analysis of the input and output voltage spectrum is shown in Figs. 10 and 11, respectively. It is observed that the noises are reduced at the lower frequency except for the higher frequencies (lesser than 100 kHz). But at the same time, the higher frequency noises are not altered much by the snubber as it looks like a single low-pass filter operation.

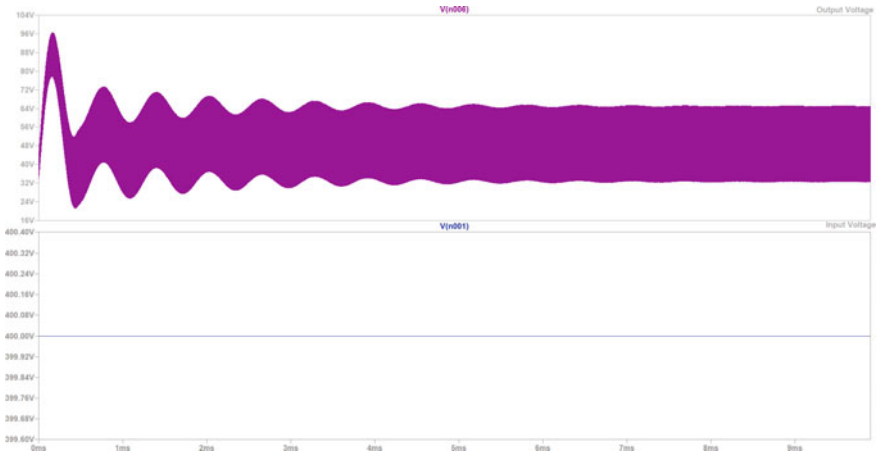


**Fig. 9** Output and input voltages of module 1-buck converter with RC snubber where X-axis depicts about voltage and Y-axis depicts about time in seconds

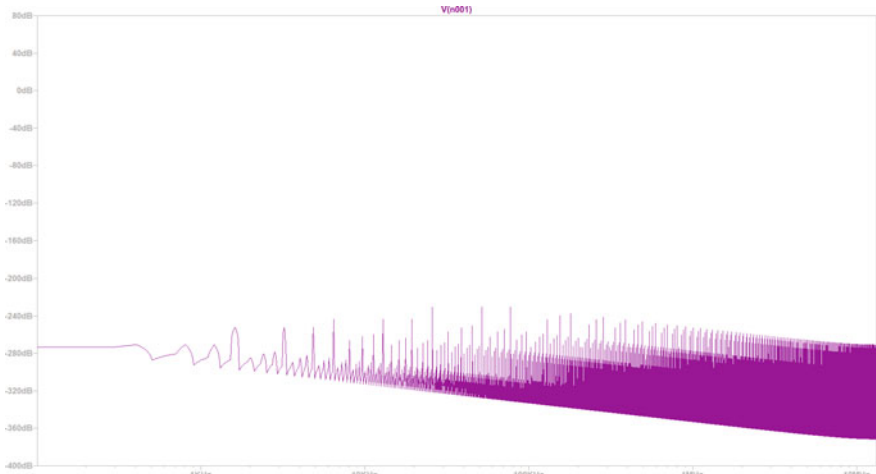


**Fig. 10** FFT analysis of input voltage of module 1 with noises more than 100 kHz

The simulation results for Module 2 with snubber circuit and PI filter as their filtering element are shown in Fig. 12. The input voltage is 400 V, the output is of 48.47 V, and the settling time is 29.1667 ms. The FFT analysis of the input and output voltage is shown in Figs. 13 and 14. The waveform analyser shows that the waveform of the output and input is totally different as per the working of the modules. The noises injected by the different LISN networks irrespective of the frequencies have been cancelled out due to the incorporation of PI filter with the snubber circuit. In comparison to Fig. 10, the higher frequencies are almost cancelled by the PI Filter as

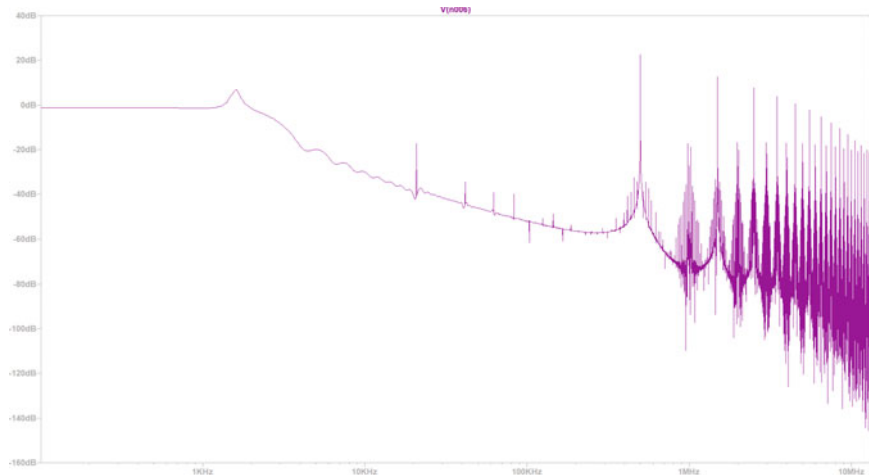


**Fig. 11** FFT analysis of output voltage of module 1

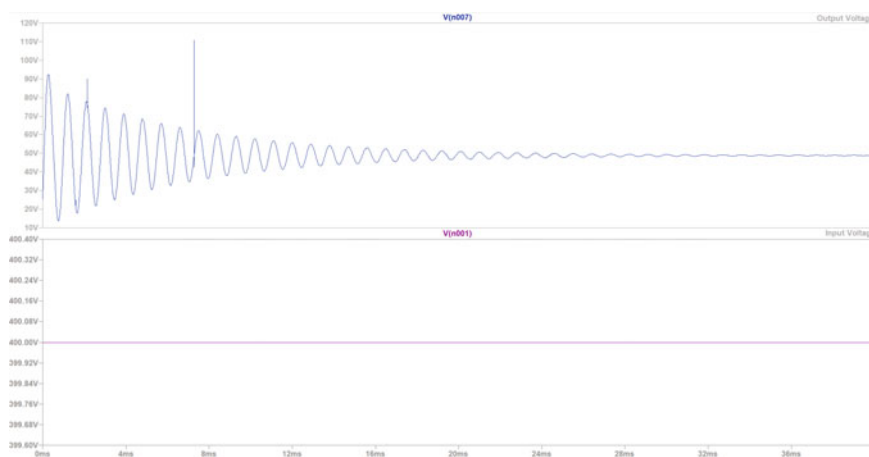


**Fig. 12** Input and output voltages of module 2

seen in Fig. 14. The snubber circuit cancels the other type of frequencies ranging from low to high noises till 20 MHz. The output is very smooth and even the FFT analysis gives us much detailed view of the filtration validating that the second module is better than the first module.

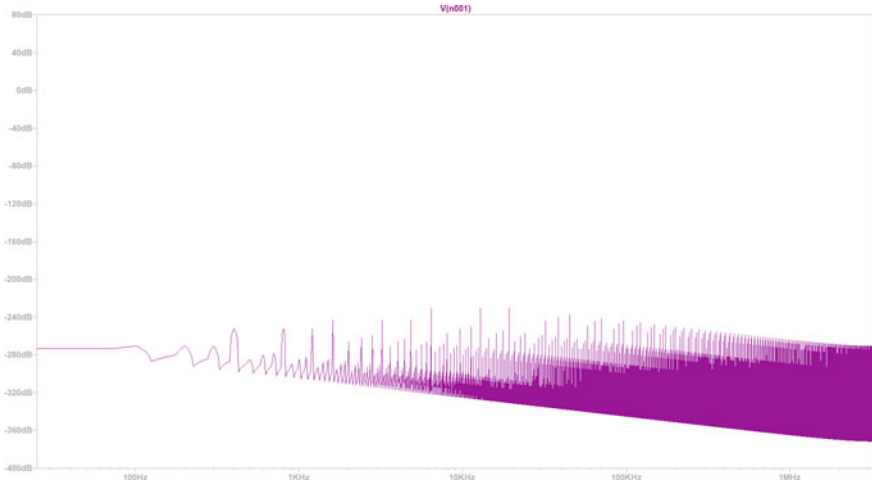


**Fig. 13** FFT analysis of input voltage waveform of module 2

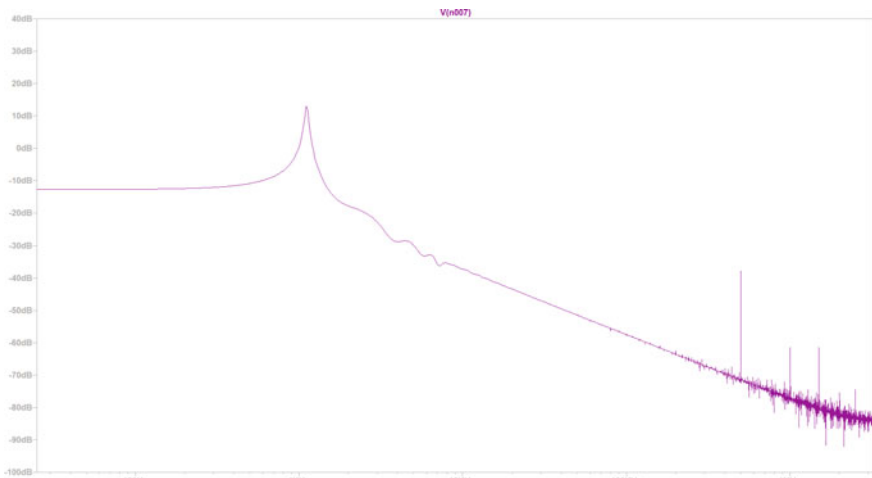


**Fig. 14** FFT Analysis of output voltage of module 2

## 6 Conclusion

The results show that the combination of a model buck converter with an input PI filter may be utilized to minimize noises that were high enough to have an impact on the drive system. The output waveforms and FFT analysis revealed that the PI filter implementation greatly lowered the quantity of noise present in the output voltage. In this paper, a new filter is proposed by combining PI filters along with a

high-frequency filter such as RC snubber network which is based on not only high-frequency noise filtration but also smoothening the waveform by almost mitigating all the types of noises. The influence of the passive components' parasitic elements on the performance of the EMI filter is simulated and analysed. The results showed that the PI filter combined with snubber circuit is an approach that nullifies the noises and introduces a new approach in terms of filtration in power electronic applications.

## References

1. Jayasree, P.V.Y., Priya, J.C., Poojita, G.R., Kameshwari, G.: EMI filter design for reducing common-mode and differential-mode noise in conducted interference. *Int. J. Electron. Communicat. Eng.* **5**(3), 319–329 (2012)
2. Consoli, A., Musumeci, S., Oriti, G., Testa, A.: An innovative EMI reduction design technique in power converters. *IEEE Trans. Electromagn. Compat.* **38**(4), 567–575 (1996). <https://doi.org/10.1109/15.544311>
3. Zhang, D., Fan, T., Ning, P., Wen, X.: An automatic EMI filter design methodology for electric vehicle application. *IEEE Energy Conv. Cong. Exposit. (ECCE)*, 4497–4503 (2003). <https://doi.org/10.1109/ECCE.2017.8096772>
4. AN-2162 simple success with conducted EMI from DC-DC converters. Application Report SNVA489C, November (2011). Revised April 2013, [https://www.ti.com/lit/an/snva489c/snv\\_a489c.pdf?ts=1647707545790](https://www.ti.com/lit/an/snva489c/snv_a489c.pdf?ts=1647707545790)
5. Kotny, J.-L., Duquesne, T., Idir, N.: Design of EMI Filters for DC-DC Converter (2003). <https://doi.org/10.1109/VPPC.2010.5729047>
6. Switching regulator series, snubber circuit for buck converter IC, application note. ROHM Semiconductors (2016). [https://fscdn.rohm.com/en/products/databook/applinote/ic/power/switching\\_regulator/buck\\_snubber\\_app-e.pdf](https://fscdn.rohm.com/en/products/databook/applinote/ic/power/switching_regulator/buck_snubber_app-e.pdf)
7. Lopa, S., Hossain, S., Hasan, M., Chakraborty, T.: Design and simulation of DC-DC converters. *Int. Res. J. Eng. Tech.* **3**, 62–70 (2016)
8. Watson, J.D., Watson, N.R.: Impact of electric vehicle chargers on harmonic levels in New Zealand. *IEEE Innov. Smart Grid Tech—Asia (ISGT-Asia)*, 1–6 (2017). <https://doi.org/10.1109/ISGT-Asia.2017.8378374>
9. Li, L., Wang, B., Deng, Y.: Model establishment and harmonic analysis of electric vehicle charger. In: 2018 13th IEEE Conference on Industrial Electronics and Applications (ICIEA), pp. 2204–2209 (2018). <https://doi.org/10.1109/ICIEA.2018.8398076>
10. Kumar, M.S., Rani, A.J.: Reduction of conducted electromagnetic interference by using filters. *Comp. Elect. Eng.* **72**, 169–178 (2018). ISSN 0045-7906. <https://doi.org/10.1016/j.compeleceng.2018.09.002>
11. Chen, W., Yang, X., Wang, Z.: A novel hybrid common-mode EMI filter with active impedance multiplication. *IEEE Trans. Industr. Electron.* **58**(5), 1826–1834 (2011). <https://doi.org/10.1109/TIE.2010.2053341>
12. Yuan, J., Dorn-Gomba, L., Callegaro, A.D., Reimers, J., Emadi, A.: A review of bidirectional on-board chargers for electric vehicles. *IEEE Access* **9**, 51501–51518 (2021). <https://doi.org/10.1109/ACCESS.2021.3069448>
13. Mutoh, N., Nakanishi, M., Kaneko, M., Nakashima, J.: EMI noise control methods suitable for electric vehicle drive systems. *IEEE Trans. Electromagn. Compat.* **47**(4), 930–937 (2005). <https://doi.org/10.1109/TEMC.2005.857893>
14. Pliakostathis, K.: Research on EMI from Modern Electric Vehicles and their Recharging Systems, pp. 1–6 (2020). <https://doi.org/10.1109/EMCEUROPE48519.2020.9245742>

15. Cuellar, C., Idir, N.: Reduction of the parasitic couplings in the EMI filters to improve the high frequency insertion loss. In: IECON 2018—44th Annual Conference of the IEEE Industrial Electronics Society, Washington, DC, USA, pp. 5766–5771 (2018). <https://doi.org/10.1109/IECON.2018.8591234>
16. Kostov, K., Kyrya, J., Suntio, T.: Analysis and design of EMI filters for DC-DC converters using chain parameters. In: 10th European Conference on Power Electronics and Applications (EPE 2003), Toulouse, France, 2–4 September (2003)
17. Zhang, H., Young, S.: Speed up the design of EMI filters for switch-mode power supplies, **54**(2), April (2020)
18. Bocock, G.: Modular EMI filter selection for AC-DC converters. Published 12th August, 2020. <https://eepower.com/technical-articles/modular-emi-filter-selection-for-ac-dc-converters/#>, Downloaded on 10<sup>th</sup> August, 2022
19. IEC 60939-1: Passive filter units for electromagnetic interference suppression—part 1: generic specification (2010). <https://webstore.iec.ch/publication/3947#additionalinfo>

# Deep Learning-Based Bioimpedance Spectroscopy Using Start of Frame Delimiter in Human Body Communications



Aaron Roopnarine and Sean Rocke

**Abstract** Bioimpedance spectroscopy (BIS) is a frequency-based technique which has been extensively used in medical and agricultural applications. BIS involves estimation of the power spectral density (PSD), to determine the frequency response of biological material modelled as an impedance. This PSD is then used to determine other biological parameters of interest. A deep-learning-based BIS technique is proposed for body area networks (BAN) using the IEEE 802.15.6 Human Body Communications (HBC) specification. The proposed technique uses the start of frame delimiter (SFD) from the HBC physical layer (PHY) frame to perform BIS. A deep-learning-based strain gauge was developed based on this SFD-BIS framework as a proof of concept. Results show an average RMSE of around 3.87 N and an average absolute error of 1.20 N for all noise variations explored. The relatively low error showed the feasibility of this approach validating this proof of concept. This has great potential when applied to cyber-physical systems.

**Keywords** Bioimpedance spectroscopy · Channel estimation · Channel sensing · Deep learning · Sensor design · Strain gauge

## 1 Introduction

Bioimpedance spectroscopy (BIS) is the analysis of the electrical properties of biological materials across frequency [1–3]. BIS methods show great potential when applied to body composition estimation since they are safe, non-invasive and more accurate than anthropometric methods [3, 4]. Furthermore, BIS offer several practical advantages for rapid development applications: the instrumentation is portable, instrumentation maintenance and measurements are safe and easy to perform, results are obtained immediately and measurements can be repeated with great inter-

---

A. Roopnarine (✉) · S. Rocke

The University of the West Indies, St. Augustine, Trinidad and Tobago  
e-mail: [aaron.roopnarine@sta.uwi.edu](mailto:aaron.roopnarine@sta.uwi.edu)

S. Rocke  
e-mail: [sean.rocke@sta.uwi.edu](mailto:sean.rocke@sta.uwi.edu)

observer reproducibility [3]. BIS has proven to be an incredible tool in clinical applications such as: diagnosing diseases (e.g. breast cancer related lymphedema (BCRL) [5] and cutaneous melanoma [6]), estimating body analyte (e.g. glucose [7, 8], cholesterol [9], and creatinine [10]) concentrations, predicting all-cause mortality for patients with diseases [11, 12], among others. BIS has also proven useful in determining presence and concentration of the staphylococcus aureus bacteria, the main cause of bovine mastitis, in milk [13] and aiding in dielectric material classification [14].

Body area networks (BANs) utilize sensor nodes to provide real-time patient health tracking. At each sensor node, separate devices employ BIS to acquire the medical data (the sensor) from communicating the sensed data to the intended node (the transceiver) [15]. More devices affect energy efficiency and sensor size which are important factors in sensor design especially in the area of medical telemetry [16]. What if channel estimation techniques can eliminate the need for some BIS sensor integrated chips in the sensor node? Channel estimation utilizes pilot signals sent to determine the channel response which is typically used to optimize error performance [17]. This channel response is an electrical parameter from the body. If there is sufficient correlation and sensitivity to biological parameters (i.e. the channel state), it can be used for BIS eliminating the need for the sensor.

Human body communication (HBC) is a communication mode used in BANs. HBC uses the human body as the transmission medium to communicate data [18]. HBC systems achieve higher data rates, greater spectral efficiency and greater power efficiency when compared to RF-based BANs [19]. From the extents of the literature surveyed, little to no emphasis has been placed on using channel estimation data for analysis of channel state especially in the HBC band (18.375–23.625 MHz). With regard to channel estimation in the HBC band, Zhang et al. [20] investigated dynamic channel estimation showing that dynamic pilot interval adjustment according to channel variances reduces the number of pilots required in a frame with minimal effect on estimation accuracy. However, for this scheme to be implemented, the PHY frame structure of the IEEE 802.15.6 must be changed which can cause discord with transceivers that use HBC channels. Additionally, the method for channel estimation was not specified.

Now that the link between BIS, channel estimation, and HBC has been proffered, this concept must be proved by measuring a relevant biological parameter. Unintentional accidental deaths is among the top 5 leading causes of deaths in the United States of America [21]. Monitoring the forces applied to the skin may help prevent some accidents as these may alert professionals or guardians about such incidents through considering where the force is applied and the magnitude of such. Advances in medical telemetry, through the use of wearable sensors, has proven effective athlete performance optimization through monitoring bio-mechanical and physiological parameters affecting athlete performance for coaching, e.g. impact force measurement to the brain to help prevent brain injury and bio-mechanical force detection as a teaching tool [22]. Thus, monitoring forces applied to the body is helpful in optimization of athlete training as trainers will get a better idea of the pressures on the trainee's body.

Recently, deep learning as proven to be an alternative to conventional parameter estimation in sensors and channel modelling. These models emulate the true distribution of the channel resulting in more accurate results [23–25].

In this work, the force applied channel is estimated. To the best of the authors' knowledge there is no work whereby channel sensing techniques have been applied to HBC. The authors propose the use of the start frame delimiter (SFD) specified in the IEEE802.15.6 standard at the receiver node, as the basis for channel estimation which can be leveraged for BIS. This concept is implemented by using a deep-learning framework which uses the received SFD frame to estimate the force applied to the skin; effectively producing a system that can simultaneously transfer information and measure. Thus the research contributions are:

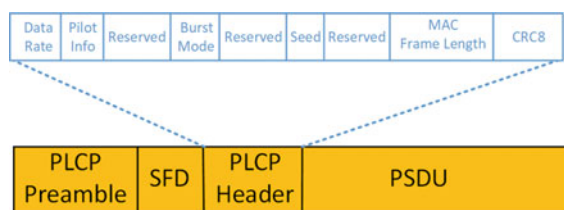
- Proposing a framework for SFD-BIS
- Establishing the link between the applied force and the channel response through the use of finite element model analysis
- Developing a deep-learning-based strain gauge as a use case of the SFD-BIS framework for BIS.

In Sect. 2, develops the system model for achieving channel estimation using the IEEE802.15.6 standard framework. Section 3, proposes the neural network (NN) architecture to be used for BIS. Section 4, presents and evaluates the results from implementing is estimation technique. Section 5 concludes the paper.

## 2 System Model

The IEEE 802.15.6 HBC transmitter constructs a packet consisting of a physical layer convergence protocol (PLCP) preamble, Starter Frame Delimiter (SFD)/Rate Indicator (RI), PLCP header, physical layer service data unit (PSDU) or physical layer (PHY) payload, and pilot sequences as shown in Fig. 1 [18]. This packet is sent using the frequency selective digital transmission (FSDT) scheme where data is spread in the frequency domain, centred at 21 MHz, using frequency selective spread codes. This binary chip sequence,  $s(n)$  of length  $N$ , is sent in the HBC band (18.375–23.625 MHz) band by applying a transmit mask through bandpass filtering, with filter response  $h_{Tx}(n)$ , as shown in Eq. (1):

**Fig. 1** IEEE 802.15.6 HBC PHY packet structure



$$x(n) = h_{Tx}(n) * s(n). \quad (1)$$

The transmitted signal,  $x(n)$  is sent through the electrodes into the body channel of impulse response,  $h(n)$ , and additive noise,  $w(n)$ , as given by (2) to produce the received signal,  $y(n)$  [26]:

$$y(n) = h(n) * x(n) + w(n). \quad (2)$$

The receiver detects the received chips and demodulates the received signal through correlation with the spread codes and selecting the sequence with the minimum hamming distance [27]. Since the receiver structure is not restricted in the IEEE 802.15.6 standard, several compliant receivers have been successfully designed and implemented [27–30]. However, these designs do not employ channel estimation.

The PLCP preamble, SFD and pilot sequences are known, pre-generated fixed gold code sequences, which can be utilized in channel estimation. Consequently, if the transmitted sequence in the frequency domain,  $X(k)$ , is known, the channel response,  $H(k)$ , is determined using the received sequence,  $Y(k)$ , from (3):

$$H(k) = \frac{Y(k)}{X(k)}. \quad (3)$$

These gold code sequences consist of frequency components in the HBC band and can be used to reconstruct the channel response which can be utilized in BIS-based sensing applications.

Displacements, stresses, and strains are related through the differential equation shown in (4).

$$0 = \nabla \cdot (FS)^T + \mathbf{F}_V, F = I + \nabla \mathbf{u} \quad (4)$$

where  $S$  is second Piola-Kirchhoff stress [ $\text{N}/\text{m}^2$ ],  $F$  is the deformation gradient,  $I$  is the unit tensor,  $\mathbf{F}_V$  is the force per unit volume vector [ $\text{N}/\text{m}^3$ ] and  $\mathbf{u}$  is the displacement field [m] [31].

Forces applied to tissue affects the geometry and density of its tissue components which will, in turn, affect electric field distributions governed by the current conservation equation based on Ohm's law—and by extension Kirchhoff's conservation laws for the voltages, currents, and charges—as shown in (5), (6) and (7).

$$\nabla \cdot \mathbf{J} = Q_{j,v} \quad (5)$$

$$\mathbf{J} = \sigma \mathbf{E} + j\omega \mathbf{D} + \mathbf{J}_e \quad (6)$$

$$\mathbf{E} = -\nabla \cdot \mathbf{V} \quad (7)$$

where  $Q_{j,v}$  is an external current source [ $\text{A}/\text{m}^3$ ],  $\mathbf{J}$  is current density [ $\text{A}/\text{m}^2$ ],  $\mathbf{J}_e$  is an externally generated current density [ $\text{A}/\text{m}^2$ ],  $\sigma$  is the electrical conductivity [ $\text{S}/\text{m}$ ],

$E$  is the electric field intensity [V/m],  $D$  is electric displacement [ $C/m^2$ ],  $V$  is scalar electric potential [V] and  $\omega$  is angular frequency [rad/s].

Consequently, force should have an effect on the channel response.

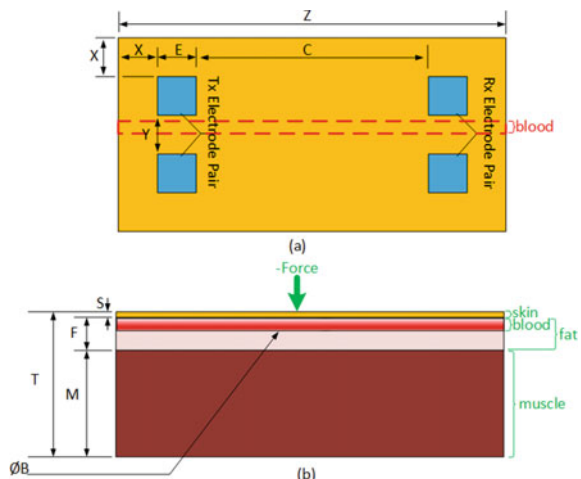
### 3 Proposed Approach: SFD–BIS

The channel response is integral in bioimpedance spectroscopy as bioimpedance and scatter parameters can be derived from it and be used to relate to a measurement parameter, e.g. glucose concentration [14, 32]. This section covers the design and training of the deep-learning-based SFD-BIS force estimation system.

In this study, a Finite Element Model (FEM) was constructed using COMSOL multiphysics to derive the channel response of the human body when subject to different forces. The geometry and dimensions are shown in Fig. 2 and Table 1. The dielectric tissue properties (permittivity  $\epsilon$  and conductivity  $\sigma$ ) were configured using the Cole-Cole model shown in [33, 34]. The mechanical tissue properties (Young's modulus  $E$ , Poisson's ratio  $\nu$ , and density  $\rho$ ) were configured based on typical ranges in the literature [35–49]. This channel was then deformed with typical forces applied to the skin ( $-30$  N to  $+30$  N in  $1$  N increments), shown in Fig. 2b, and the channel response recorded for each variation [50]. Positive forces emulate a pinch or muscle contraction/relaxation from body movement, while negative forces emulate a pressing force on the skin from sitting on leaning on a surface. The magnitudes of these forces were chosen to based on typical forces applied to the human skin [50].

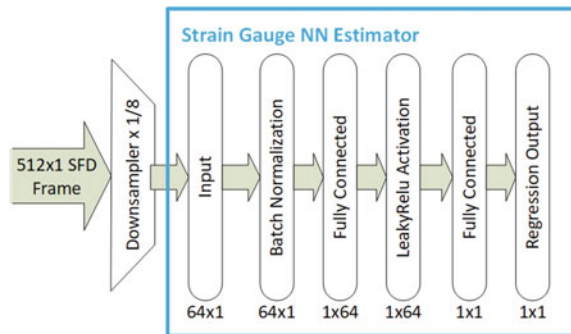
For each unique channel response derived under varying forces, IEEE 802.15.6 compliant frames were passed under varying SNRs (1dB to 500dB) to emulate channel conditions and augment the data collected. The SFD sequence was extracted for

**Fig. 2** The geometry design for the proposed FEM model through **a** Plan view, **b** Coronal section view



**Table 1** The geometry dimensions for the FEM model proposed

Dimension	Value (mm)	Dimension	Value (mm)
A	50	F	8.5
Diameter B	3.2	M	27.5
Z	340	T	37.5
C	300	S	1.5
D	25	X	10
E	10	Y	10

**Fig. 3** The NN architecture proposed for SFD-BIS force estimation

each channel for the purpose of NN training, validation, and testing. 60% of the data was reserved for training, 30% for validation, and 10% for testing. Each of these extracted SFD sequences correspond to a specific force applied to the skin.

The NN architecture designed, shown in Fig. 3, is based on regression-based deep-learning networks with low complexity used to estimate parameters [51, 52]. Figure 3 shows the type and size of each layer utilized in the final deep network. The SFD frame extracted was down-sampled to reduce the number of neurons and learnables, as shown in Fig. 3, required for training given the limited training data as well as reduce the complexity of the network's complexity for low power applications.

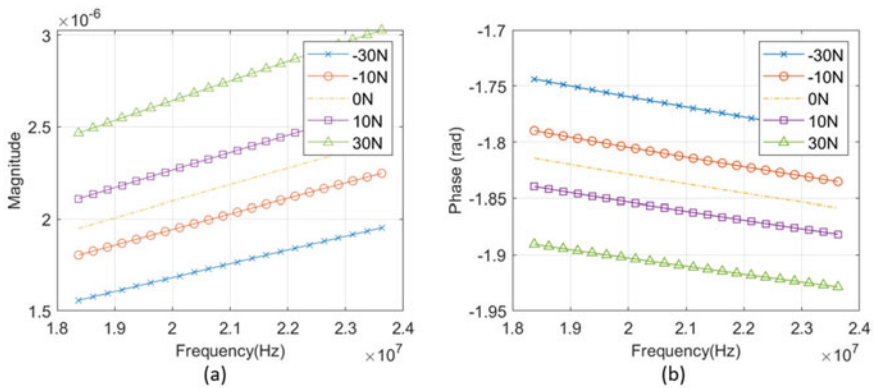
The designed network was constructed using MATLAB and trained using the training configurations: stochastic gradient decent (SGDM) optimization, a total of 30 epochs before training weight updates, an initial learning rate of  $1 \times 10^{-5}$  and a learning rate drop factor of 0.1. The performance of the network was then evaluated.

The end result is a regression-based deep-learning network that takes in the SFD frame, extracted from the channel at the receiver, and outputs the predicted force that the skin is experiencing.

## 4 Results and Analysis

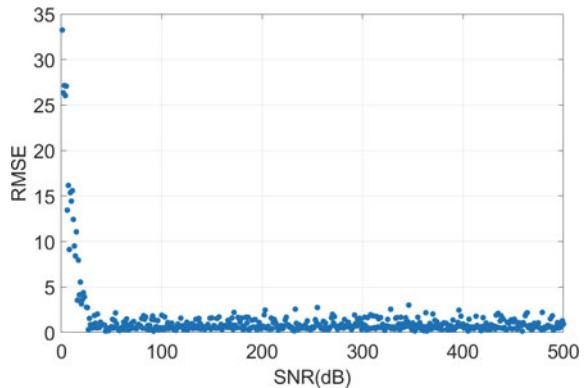
Figure 4 shows the channel response recorded when different forces were applied on the skin of the FEM model derived. These results corroborate with the underlying theory in Sect. 2 showing force applied affects the channel response. Furthermore, from the magnitude response, increasing the downward force on skin decreases the channel gain. This is intuitive since by pressing the skin, molecules are forced closer together further impeding the path of conductive currents and hence decreasing the channel gain.

Figure 5 shows the accuracy of the deep-learning-based strain gauge when compared to the ground truth testing data. Intuitively, as the signal quality improves, the accuracy of the strain gauge improves. Further, from inspection, the strain gauge's



**Fig. 4** The channel response for different forces of the human body FEM model where **a** is the magnitude response and **b** is the phase response

**Fig. 5** The RMSE performance of the deep-learning-based strain gauge when predicting forces at different SNRs



estimation were not very far off from the ground truth yielding an average root mean squared error (RMSE) of around 3.87N and an average absolute error of 1.20N for all SNR variations. Consequently, this serves as a proof of concept for SFD-BIS.

## 5 Conclusion

A SFD-BIS system was proposed and this proof of concept was investigated for BIS-based applications. The results show a clear relationship between the force applied to the skin and the channel response. Furthermore, the relatively low error rate of the deep-learning-based strain gauge estimator serves as a proof of concept for the SFD-BIS framework proposed. The results show that there is potential for use in cyber-physical systems. Despite focus on the HBC band, the concept can be applied to other bands also. For further work we recommend applying some form of hyper-parameter optimization for the current NN architecture to improve accuracy. Exploration of other force types, e.g. torsion, since this study is only limited to push and pull forces to the skin, should also be explored. Further, only the magnitude of the SFD frame is incorporated for reduced complexity of the NN architecture to facilitate low powered applications. In further work we recommend exploring the incorporation of phase response for improved accuracy. Additionally, an FEM model is used to train the deep-learning-based strain gauge, further empirical validation of that FEM model is required using live human subjects or body phantoms to reinforce training data. Finally, this NN-based SFD-BIS framework can be applied to measure body analyte concentration (e.g., glucose level and creatinine level).

## References

1. Margo, C., Prado, J., Kouider, M., Rouane, A., Nadi, M.: Bioimpedance spectroscopy for cell characterization in the 50hz-5mhz frequency range. In: 2006 Ph.D. Research in Microelectronics and Electronics, pp. 441–444 (2006)
2. Grimnes, S., Martinsen, Ø.G.: Selected applications. In: Grimnes, S., Martinsen, Ø.G. (eds.) Bioimpedance and Bioelectricity Basics, 3rd edn, Academic Press, Oxford, pp. 405–494 (2015). [Online]. Available: <http://www.sciencedirect.com/science/article/pii/B9780124114708000106>
3. Naranjo-Hernández, D., Reina-Tosina, J., Min, M.: Fundamentals, recent advances, and future challenges in bioimpedance devices for healthcare applications. *J. Sens.* **2019**, 9210258 (2019). [Online]. Available: <https://doi.org/10.1155/2019/9210258>
4. Moissl, U.M., Wabel, P., Chamney, P.W., Bosaeus, I., Levin, N.W., Bosy-Westphal, A., Korth, O., Müller, M.J., Ellegård, L., Malmros, V., Kaitwatcharachai, C., Kuhlmann, M.K., Zhu, F., Fuller, N.J.: Body fluid volume determination via body composition spectroscopy in health and disease. *Physiol. Meas.* **27**(9), 921–933 (2006). [Online]. Available: <https://doi.org/10.1088/0967-3334/27/9/012>
5. Shah, C., Vicini, F.A., Arthur, D.: Bioimpedance spectroscopy for breast cancer related lymphedema assessment: clinical practice guidelines. *Breast J.* **22**(6), 645–650 (2016)

6. Mohr, P., Birgersson, U., Berking, C., Henderson, C., Trefzer, U., Kemeny, L., Sunderkötter, C., Dirschka, T., Motley, R., Frohm-Nilsson, M., Reinhold, U., Loquai, C., Braun, R., Nyberg, F., Paoli, J.: Electrical impedance spectroscopy as a potential adjunct diagnostic tool for cutaneous melanoma. *Skin Res. Technol.* **19**(2), 75–83 (2013). [Online]. Available: <https://onlinelibrary.wiley.com/doi/abs/10.1111/srt.12008>
7. Li, J., Igbe, T., Liu, Y., Nie, Z., Qin, W., Wang, L., Hao, Y.: An approach for noninvasive blood glucose monitoring based on bioimpedance difference considering blood volume pulsation. *IEEE Access* **6**, 51119–51129 (2018)
8. Sulla, T.R., Talavera, S.J., Supo, C.E., Montoya, A.A.: Non-invasive glucose monitor based on electric bioimpedance using afe4300. In: 2019 IEEE XXVI International Conference on Electronics, Electrical Engineering and Computing (INTERCON), pp. 1–3 (2019)
9. Ain, K., Wibowo, R.A., Soelistiono, S., Muniroh, L.: Measurement of cholesterol concentration based on bioimpedance with ad5933-eval. In: 2017 5th International Conference on Instrumentation, Communications, Information Technology, and Biomedical Engineering (ICICI-BME), pp. 1–4 (2017)
10. Ramsaroop, Z., Rocke, S., Gayapersad, N., Persad, J.: Csrr-based microwave sensor for non-invasive, continuous monitoring of renal function. In: Loughborough Antennas Propagation Conference (LAPC), pp. 1–5 (2016)
11. Kim, E.J., Choi, M.J., Lee, J.H., Oh, J.E., Seo, J.W., Lee, Y.K., Yoon, J.W., Kim, H.J., Noh, J.W., Koo, J.R.: Extracellular fluid/intracellular fluid volume ratio as a novel risk indicator for all-cause mortality and cardiovascular disease in hemodialysis patients. *PLoS One* **12**(1), e0170272 (2017)
12. Demirci, C., Açıci, G., Demirci, M.S., Özkahya, M., Töz, H., Duman, S., Sipahi, S., Erten, S., Tanrisev, M., Ok, E.: Impedance ratio: a novel marker and a powerful predictor of mortality in hemodialysis patients. *Int. Urol. Nephrol.* **48**(7), 1155–1162 (2016). [Online]. Available: <https://doi.org/10.1007/s11255-016-1292-1>
13. Porto, R.W., Ayres, L.C., Neuenfeld, R.H., Carvalho, C.W., Geller, A.M., Oliveira, W.C.: Electrical bioimpedance scanning in bacterial diagnosis and mastitis detection. In: 2020 IEEE International Instrumentation and Measurement Technology Conference (I2MTC), pp. 1–6 (2020)
14. Ansari, M.A.H., Jha, A.K., Akhter, Z., Akhtar, M.J.: Multi-band rf planar sensor using complementary split ring resonator for testing of dielectric materials. *IEEE Sens. J.* **18**(16), 6596–6606 (2018)
15. Yaghoubi, M., Ahmed, K., Miao, Y.: Wireless body area network (wban): A survey on architecture, technologies, energy consumption, and security challenges. *J. Sens. Act. Netw.* **11**(4) (2022). [Online]. Available: <https://www.mdpi.com/2224-2708/11/4/67>
16. Amjad, O., Bedeer, E., Ikki, S.: Energy-efficiency maximization of self-sustained wireless body area sensor networks. *IEEE Sens. Lett.* **3**(12), 1–4 (2019)
17. Gizzini, A.K., Chafii, M.: A survey on deep learning based channel estimation in doubly dispersive environments. *IEEE Access* **10**, 70595–70619 (2022)
18. IEEE Standards Association and others: Ieee standard for local and metropolitan area networks-part 15.6: wireless body area networks. *IEEE Stand. Inf. Technol. IEEE* **802**(6), 1–271 (2012)
19. Pereira, M.D., Alvarez-Botero, G.A., de Sousa, F.R.: Characterization and modeling of the capacitive hbc channel. *IEEE Trans. Instrum. Meas.* **64**(10), 2626–2635 (2015)
20. Zhang, Y., Kou, B., Fan, D., Liu, Y., He, Z., Chen, X.: A dynamic pilot interval adjustment scheme for hbc channel estimation. In: 2016 IEEE/CIC International Conference on Communications in China (ICCC Workshops), pp. 1–5 (2016)
21. Centers for Disease Control and Prevention (CDC): Underlying cause of death, 1999–2020 results. deaths occurring through 2020. National Vital Statistics System - Mortality data (2020) via CDC WONDER, Tech. Rep. (2020). [Online]. Available: <https://www.cdc.gov/nchs/fastats/accidental-injury.htm>
22. Seshadri, D.R., Li, R.T., Voos, J.E., Rowbottom, J.R., Alfes, C.M., Zorman, C.A., Drummond, C.K.: Wearable sensors for monitoring the internal and external workload of the athlete. *NPJ Digit. Med.* **2**, 71 (2019)

23. Seyedsalehi, S., Pourahmadi, V., Sheikhzadeh, H., Foumani, A.H.G.: Propagation Channel Modeling by Deep Learning Techniques (2019)
24. Manikandan, S., Poongavanam, N., Vivekanandhan, V., Mohanaprkash, T.: Performance comparison of various wireless sensor network dataset using deep learning classifications. In: 2022 IEEE 2nd International Conference on Mobile Networks and Wireless Communications (ICM-NWC), pp. 1–4 (2022)
25. Kalita, D., Mirza, K.B.: Glucose prediction using wide-deep lstm network for accurate insulin dosing in artificial pancreas. In: 2022 44th Annual International Conference of the IEEE Engineering in Medicine & Biology Society (EMBC), pp. 4426–4429 (2022)
26. IEEE Standards Association and others: Ieee p802.15 working group for wireless personal area networks (wpans): channel model for body area network (ban). In: IEEE, Report IEEE P802.15-08-0033-04-0006 (2008)
27. Kang, T., Oh, K.-I., Park, H., Kang, S.: Review of capacitive coupling human body communications based on digital transmission. *ICT Express* **2**(4), 180–187 (2016), special Issue on Emerging Technologies for Medical Diagnostics. [Online]. Available: <http://www.sciencedirect.com/science/article/pii/S2405959516301710>
28. Zhao, B., Lian, Y., Niknejad, A.M., Heng, C.H.: A low-power compact ieee 802.15.6 compatible human body communication transceiver with digital sigma-delta iir mask shaping. *IEEE J. Solid-State Circ.* **54**(2), 346–357 (2019)
29. Cho, H., Lee, H., Bae, J., Yoo, H.: A 5.2mw ieee 802.15.6 hbc standard compatible transceiver with power efficient delay-locked-loop based bpsk demodulator. In: 2014 IEEE Asian Solid-State Circuits Conference (A-SSCC) , pp. 297–300 (2014)
30. Shikada, K., Wang, J.: Development of human body communication transceiver based on impulse radio scheme. In: 2012 2nd IEEE CPMT Symposium Japan, pp. 1–4 (2012)
31. Multiphysics cyclopedia (2018). [Online]. Available: <https://www.comsol.com/multiphysics/stress-and-equations-of-motion?parent=structural-mechanics-0182-202>
32. Saha, S., Cano-Garcia, H., Sotiriou, I., Lipscombe, O., Gouzouasis, I., Koutsoupidou, M., Palikaras, G., Mackenzie, R., Reeve, T., Kosmas, P., et al.: A glucose sensing system based on transmission measurements at millimetre waves using micro strip patch antennas. *Sci. Rep.* **7**(1), 1–11 (2017)
33. Gabriel, S., Lau, R., Gabriel, C.: The dielectric properties of biological tissues: Iii. parametric models for the dielectric spectrum of tissues. *Phys. Med. Biol.* **41**(11), 2271 (1996)
34. Gabriel, C.: Compilation of the dielectric properties of body tissues at rf and microwave frequencies. U.S. Air Force, Tech. Rep. U.S. Air Force Report AFOSR-TR-96 (1996)
35. Kearney, S.P., Khan, A., Dai, Z., Royston, T.J.: Dynamic viscoelastic models of human skin using optical elastography. *Phys. Med. Biol.* **60**(17), 6975–6990 (2015)
36. Liang, X., Boppart, S.A.: Biomechanical properties of *in vivo* human skin from dynamic optical coherence elastography. *IEEE Trans. Biomed. Eng.* **57**(4), 953–959 (2010)
37. ClinMed International Library: Young's modulus and poisson's ratio for the tissues. Online repository of medical research. [Online]. Available: <https://clinmedjournals.org/articles/jor/jor-4-048-table1.html>
38. Wang, K., Chen, Y., Huang, S., Wang, L., Niu, W.: Subcutaneous fat thickness remarkably influences contact pressure and load distribution of buttock in seated posture. *J. Healthc. Eng.* **2021**, 4496416 (2021)
39. Takaza, M., Moerman, K.M., Gindre, J., Lyons, G., Simms, C.K.: The anisotropic mechanical behaviour of passive skeletal muscle tissue subjected to large tensile strain. *J. Mech. Behav. Biomed. Mater.* **17**, 209–220 (2013). [Online]. Available: <https://www.sciencedirect.com/science/article/pii/S1751616112002457>
40. Karimi, A., Sera, T., Kudo, S., Navidbakhsh, M.: Experimental verification of the healthy and atherosclerotic coronary arteries incompressibility via digital image correlation. *Artery Res.* **16**, 1–7 (2016). [Online]. Available: <https://www.sciencedirect.com/science/article/pii/S1872931216300369>
41. Pawlaczyk, M., Lelonkiewicz, M., Wieczorowski, M.: Age-dependent biomechanical properties of the skin. *Postepy Dermatol. Alergol.* **30**(5), 302–306 (2013)

42. Pailler-Mattei, C., Bec, S., Zahouani, H.: In vivo measurements of the elastic mechanical properties of human skin by indentation tests. *Med. Eng. Phys.* **30**(5), 599–606 (2008)
43. Agache, P.G., Monneur, C., Leveque, J.L., De Rigal, J.: Mechanical properties and Young's modulus of human skin in vivo. *Arch. Dermatol. Res.* **269**(3), 221–232 (1980)
44. Comley, K., N Fleck, A.: A micromechanical model for the young's modulus of adipose tissue. *Int. J. Solids Struct* **47**(21), 2982–2990 (2010). [Online]. Available: <https://www.sciencedirect.com/science/article/pii/S0020768310002465>
45. Nightingale, K., McAleavy, S., Trahey, G.: Shear-wave generation using acoustic radiation force: in vivo and ex vivo results. *Ultrasound Med. Biol.* **29**(12), 1715–1723 (2003). [Online]. Available: <https://www.sciencedirect.com/science/article/pii/S0301562903010809>
46. Lima, K.M.M.E., Costa Júnior, J.F.S., Pereira, W.C.A., Oliveira, L.F.: Assessment of the mechanical properties of the muscle-tendon unit by supersonic shear wave imaging elastography: a review. *Ultrasonography* **37**(1), 3–15 (2018)
47. Ebrahimi, A.P.: Mechanical properties of normal and diseased cerebrovascular system. *J. Vasc. Interv. Neurol.* **2**(2), 155–162 (2009)
48. ITIS Foundation: Tissue Properties. Online Database. [Online]. Available: <https://itis.swiss/virtual-population/tissue-properties/database/density/>
49. Chawla, A., Mukherjee, S., Karthikeyan, B.: Mechanical properties of soft tissues in the human chest, abdomen and upper extremities. *J. Mech. Eng. Inst. Eng.* (2006)
50. Lee, K.-S., Jung, M.-C.: Total force of pinch and grasp by hand postures. In: Advances in Physical Ergonomics and Human Factors, ser. Advances in Intelligent Systems and Computing. Springer International Publishing, pp. 208–212 (2017)
51. Hu, S., Hirose, A.: Proposal of millimeter-wave adaptive glucose-concentration estimation system using complex-valued neural networks. In: IGARSS 2018—2018 IEEE International Geoscience and Remote Sensing Symposium, pp. 4074–4077 (2018)
52. Xiao, X., Yu, Q., Li, Q., Song, H., Kikkawa, T.: Precise noninvasive estimation of glucose using uwb microwave with improved neural networks and hybrid optimization. *IEEE Trans. Instrum. Meas.* **70**, 1–10 (2021)

# Reliability-Based Single Bit-Flipping Decoding Algorithm for LDPC Codes



Soufian Addi , Mostafa Belkasmi , Ahlam Berkani ,  
and Ahmed Azouaoui 

**Abstract** In this work, we present a new bit-flipping iterative Low-Density Parity-Check (LDPC) decoder based on reliability. The proposed decoder, called Reliability-based Single Bit-Flipping Decoding Algorithm, introduces the idea of separating the hard decision from the soft decision while processing flipping metrics, where the initial belief about received signals during decoding operations will efficiently contribute to the refinement of the final decision. We demonstrate through simulations over the binary-input Additive White Gaussian Noise (AWGN) channel that our decoder offers efficient trade-offs between BER performance and decoding complexity. It exhibits better decoding performance than known BF algorithms like Gradient Descent Bit Flipping (GDBF) and Single Bit Flipping (SBF) and presents a polynomial complexity, which proves its efficiency.

**Keywords** Low-density parity-check codes (LDPCs) · Bit-flipping decoding · Hard-decision decoding · Soft-decision decoding · Reliability · Performance

## 1 Introduction

5G network systems [1, 2] are the new communication systems adopted or in the way of adoption in all over the world. It promises more consistent user experience: multi-gigabit per second peak data rates, vast network bandwidth, ultra-low latency, and increased reliability. One of the most innovative aspects in 5G is the use of LDPC codes to insure the best transmission's errors correction [3]. The LDPC codes [4] are currently considered one of the best next generation Error-Correcting Codes

---

S. Addi  · M. Belkasmi

ICES Team, ENSIAS College, Mohammed V University in Rabat, Rabat, Morocco  
e-mail: [soufian.addi@gmail.com](mailto:soufian.addi@gmail.com)

A. Berkani

Faculty of Sciences, Mohammed V University in Rabat, Rabat, Morocco

A. Azouaoui

Chouaib Doukkali University, El Jadida, Morocco

(ECCs) that allow data transmission to reach Shannon's limit [5, 6]. Their discovery returns firstly to Gallager in his pioneer PhD thesis in 1962 [4] and secondly to MacKay [7, 8] who brought them back into prominence in 1996. The most promising aspect when using LDPC codes is that they have been shown near-Shannon's limit-capacity performance when the Sum-Product Algorithm (SPA) [7, 9] is used for decoding. In addition to 5G network systems, many other state-of-the-art communication systems adopt the LDPC codes in their standards, such as second-generation satellite broadcasting systems (DVB-S2) [10] and IEEE 802.11n systems.

Even if the SPA [11] decoding offers Shannon's limit when using LDPC codes, its complexity stays very high which pushes many researches in order to find a comparative performance with lower costs. One of the well-known "light" decoders is Bit-Flipping (BF) algorithm. The BF algorithm, proposed by Gallager [4], is a hard-decision algorithm [12] that flips a set of bits based on the values computed by the flipping function (FF) for each iteration. However, even if the BF algorithm is much simpler than the probabilistic SPA algorithm (soft decision), its Bit Error Rate (BER) performance is far from optimal.

Therefore, in order to reduce the performance gap, many variants of Gallager's BF algorithms have been proposed. We can cite the Candidate Bit-Based Bit Flipping (CBBF) [13], where we calculate a reliability of unsatisfied parity-check equations in addition to the reliability of each bit used in classical BF. There is also the Weighted Candidate Bit-Based Bit Flipping (WCBBF) [14] where authors used a weighted reliability of the parity check equations, and the weights are prefixed integers. And another work is Single Bit Flipping (SBF) [15] which flips a single bit chosen carefully in each iteration. All of these decoders belong to hard-decision variants of the original Gallager's BF algorithm.

When using the hard-decision decoding algorithms [16, 17], quantizing the received data as the set of binary elements belonging to the transmitted data leads to the loss of some reliable informations on the channel belief, which causes considerable performance degradation compared to the soft decision. Also, any improvement in performance can induce a large increase in complexity compared to the soft-decision algorithms. That is why attention has been moved toward soft-decision decoding, and researchers become then more interested in simplifying soft-decision version of BF decoding algorithms. In this category, we use both hard and soft informations during the decoding process. The first work was the Weighted Bit-Flipping (WBF) decoder [18], and we cite in this class the Modified Weighted Bit Flipping (MWBF) [19], Reliability Ratio-Based Weighted Bit-Flipping algorithm (RRWBF) [20, 21], Gradient Descent Bit Flipping (GDBF) [22], Noisy Gradient Descent Bit-Flip Decoding (NGDBF) [23], Dynamic Weighted Bit-Flipping decoding algorithms (DWBF) [24], Hybrid Weighted Bit-Flipping algorithm [25], Mixed Modified Weighted Bit-Flipping decoding algorithm [26], Two-bit weighted bit-flipping decoding algorithm [27], Classification-based algorithm for bit-flipping decoding algorithm [28], High-throughput bit-flipping decoding Algorithm [29], Reliability variance-based weighted bit-flipping algorithms [30], A NEW Reliability Ratio

Weighted Bit-Flipping Algorithm [31], and improved noisy Gradient Descent Bit-Flipping algorithm [32]. All these works achieve different degrees of enhancements from WBF in performance and convergence rate.

In this paper, we introduce a new reliability-bit-based bit-flipping algorithm for decoding LDPC codes called Reliability-based Single Bit Flipping algorithm (RSBF). It offers efficient trade-offs between BER performance and decoding complexity. Its main idea comes from our belief that weightiness of information in the magnitude of the received signal can be lost or mitigated if combined with hard metrics, and this magnitude or the weight of the received bits reflects the faith of the channel behavior. Therefore, concatenating the hard metric and soft metric will keep soft information active and efficient and can be used for the final decision for each iteration. The metric has been used largely in the decoding decision or stopping criterion [33]. Our decoder will choose the bit with smallest absolute weight to flip in each iteration.

The rest of this paper is organized as follows. In Sect. 2, we will provide our motivations and details about the proposed algorithm. The simulation results, parameter optimization, and complexity study are presented in Sect. 3, before concluding in Sect. 4.

## 2 The Proposed Algorithm

### 2.1 Preliminaries

First, let  $C$  denoted by  $(n;k)$  be an LDPC code over binary field GF(2).  $C$  is defined by the null space of an  $m \times n$  parity-check matrix  $H = [H_{ji}]$ . We assume that the  $C$  is a regular code which means that  $H$  has column weight  $d_c$  and row weight  $d_r$  with  $M = n-k$ . We also assume that codeword  $c_i = (c_0, c_1, \dots, c_{n-1})$  is modulated by a Binary phase-shift keying (BPSK) modulator and transmitted over an Additive White Gaussian Noise (AWGN) channel. The vector  $r_n = (r_0, r_1, \dots, r_{n-1})$  is the sequence of soft channel values obtained at the receiver. The demodulator makes hard-decisions  $w_n(r_i)$ ,  $k = 1, \dots, n$ , where  $w_n(r_i) = 1$  if  $r_i \geq 0$ , else  $w_n(r_i) = 0$ , and  $w_n'$  is the vector obtained after each iteration of flipping.

We introduce  $\widehat{w}_n \in \{-1,1\}$  the bipolar value sequence of the hard decision  $w_n$  and  $\hat{w}_n^l \in \{-1,1\}$  the bipolar value sequence of the hard decision  $w_n$  with  $l^{\text{th}}$  position flipped, and the two definitions are expressed as follows:

$$\widehat{w}_n \triangleq \{(1 - 2w_1, \dots, 1 - 2w_n) : w_i \in \{0, 1\}\}. \quad (1)$$

$$\hat{w}_n^l \triangleq \{(1 - 2w_1, \dots, 2w_{l-1}, \dots, 1 - 2w_n) : w_i \in \{0, 1\}\}. \quad (2)$$

The syndrome  $s$  defined by  $s = w_n \cdot H^T$  is calculated at the receiver stage. If the syndrome  $s = w_n \cdot H^T = 0$ , we can say that  $w$  is the most likely transmitted codeword. Else, the decoding process begins.

The set of code bits that participates in the  $j$ th check is denoted by  $N(j) = \{i : h_{j,i} = 1\}$  and the set of checks which contains the  $i^{\text{th}}$  code bit is denoted by  $M(i) = \{j : h_{j,i} = 1\}$ .

## 2.2 Bit-Flipping Algorithm

The Bit-Flipping algorithm proposed by Gallagar [4] is a simple hard-decision algorithm for the LDPC codes [34] that chooses the bit to flip based on the number of unsatisfied check equations: Bits with a number that exceeds the defined threshold ( $T$ ) will be chosen because we suppose that they are most likely the incorrect bits. Once all the parity-check equations are satisfied, the algorithm is terminated which means that a valid codeword has been found or the maximum number of iterations  $I_{\max}$  is reached.

The main part in the BF algorithm is the cost function represented by the reliability metric of the corresponding bit decision called the “Flipping Function” (FF) (3). It depends on the binary-valued checksums of the Variable Nodes (VNs) connected with Check Nodes (CNs).

For the BF algorithm, the FF can be expressed by the following formula:

$$e_i^{\text{BF}} = \sum_{j \in M(i)} (2s_j - 1). \quad (3)$$

The steps of the BF algorithm are as follows:

---

**Algorithm 1:** BF algorithm**Step 0:** initial all parameters**Step 1:** Calculate  $s = s_1, s_2, \dots, s_m \leftarrow w_n \cdot H^T$ , If  $s = 0$ , then the algorithm terminates**Step 2:** calculate  $e_i^{\text{BF}}$ **Step 3:** If  $\max e_i^{\text{BF}} < T$ , then the algorithm terminates**Step 4:** Flip all bits  $w_n$  with  $e_i^{\text{BF}} >= T$ ,  $I \leftarrow I + 1$  and  $w_n \leftarrow w_n'$ , with  $w_n'$  is the vector obtained after the flipping**Step 5:** If  $I > \text{Imax}$  the algorithm terminates. Else Go to Step 1

---

## 2.3 Motivations

The AWGN channel used in this research has a “Gaussian distribution”, also commonly called the “normal distribution” (see Fig. 1).

In time domain, the probability distribution of the noise samples is Gaussian with a zero mean, because the samples can acquire both positive and negative values, and in addition, the values close to zero have a higher chance of occurrence, while the values far away from zero are less likely to appear.

The modulation and demodulation BPSKs used consist on a bipolar signal that may assume either of two polarities  $\{1, -1\}$ , neither of which is zero.

As a result, if the received signal magnitude is near to 0, that means the probability of the noise away from zero is more likely happened and the noise has been added to the original signal.

The distribution of an output of a binary bipolar channel, in Fig. 2, leads to the idea of using the magnitude of the received bits as metric where the magnitude of the bits near the polarities  $\{1, -1\}$  is considered as more reliable and the magnitude of the bits near  $\{0\}$  has less reliability and more probably erroneous or affected by the large noise amplitude.

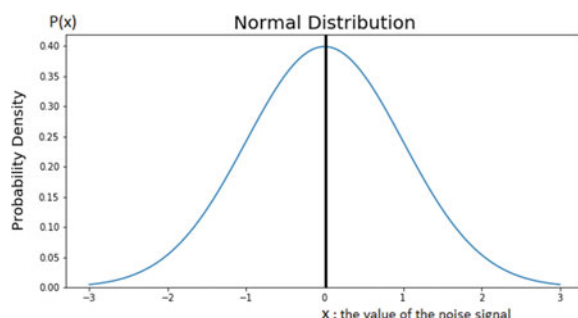
We can deduct from previous paragraphs that the symbol amplitude of the received word provides additional information on its reliability and can be used for decision-making in BF decoding. The majority of soft-decision bit-flipping decoders combine hard metrics with weighted metrics to decide which bits to flip. But this combination is always done in the same treatment. The contribution of the reliability of the received words can be used separately to decide, and this is the main object of this paper.

In the next sub-section, we will propose a new algorithm based on reliability of the received signal as soft metrics: the Reliability-Bit based Bit Flipping (RSBF).

The proposed algorithm will separate the FF processing of the hard calculation with the soft one (see Fig. 3) in contrary with the known soft BF decoding algorithms where they combine them to have unique metric for the FF.

The raison to separate the calculation of the two kinds of metrics is our belief that the weightiness of information in the magnitude of the received signal can be lost or

**Fig. 1** Gaussian or normal distribution



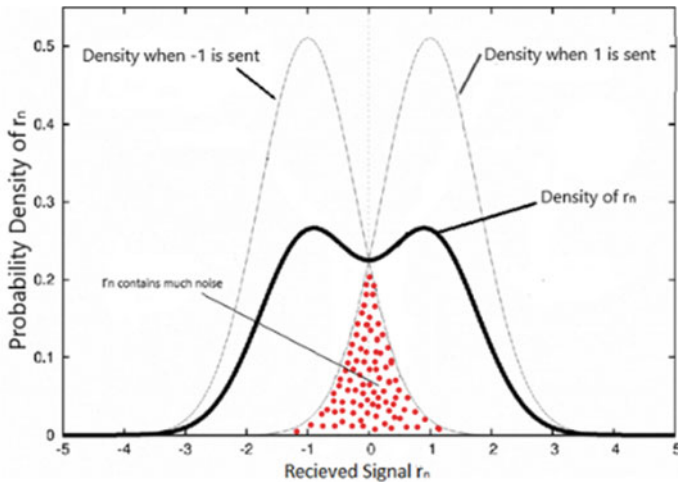
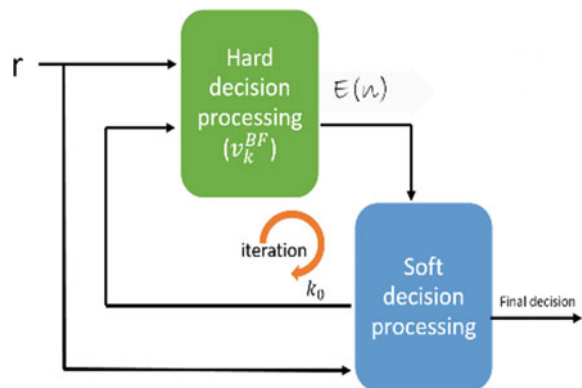


**Fig. 2** Distribution of  $r_n$

**Fig. 3** Separation of hard processing and soft processing in our proposed decoder



mitigated if combined with hard metric, therefore concatenating the hard metric and soft metric will keep soft information active and efficient.

## 2.4 The Proposed RSBF Algorithm

The RSBF algorithm will calculate the check-based message about  $r_n$  by FF in (3) in first stage. Then, we consider the set of bits positions that satisfy the threshold calculated by:

$$E(n) = \{i : e_i^{\text{BF}} \geq T, 0 \leq i \leq n\}. \quad (4)$$

In second stage, the RSBF algorithm will select one bit from the set of bits gotten from the (4), and this selection will be based on choosing the bit with minimum magnitude that we consider as reliability measurement. Since we believe that the bit with minimum magnitude  $|r_i|$  has less reliability to be correct and susceptible to be erroneous.

The FF of the RSBF algorithm will chose the bit with smallest magnitude  $|r_i|$ , so we can express the FF by the following general formula:

$$e_n^{\text{RSBF}} = K_0 = \operatorname{argmin}(|r_i|), \quad i \in E(n) \quad (5)$$

The RSBF algorithm selects the bit to be flipped based on Formula (4) then Formula (5) successively unlike the known Soft BF where they combine the hard and soft metrics.

The steps of the RSBF algorithm are as follows:

---

**Algorithm 2:** RSBF algorithm

- 
- Step 0:** initial all parameters
- Step 1:** Calculate  $s = s_1, s_2, \dots, s_m \leftarrow w_n \cdot H^T$ , If  $s = 0$ , then the algorithm terminates
- Step 2:** calculate the  $E(n)$ . If  $E(n)$  is empty, then the algorithm terminates
- Step 3:** Calculate  $e_n^{RSBF}$
- Step 4:** Flip the bit reported by the emRSBF function.  $I \leftarrow I + 1$  and,  $w_n \leftarrow w_n'$ , with  $w_n'$  is the vector obtained after the flipping
- Step 5:** If  $I > I_{max}$ , the algorithm terminates. Else Go to Step 1
-

### 3 Results and Discussion

The decoding performance of the proposed new decoding algorithm is illustrated in this work through simulations. Three regular LDPC codes [35] (see Table 1) are considered and used to this end. The first and second codes (Code1 and Code2) are difference-set codes family [18], where the third one (Code3) is a pseudorandom LDPC code [36] or Gallager code.

Intensive simulations on decoder were carried out. The entire transmission chain is used in simulations, and the proposed decoder has been implemented using C language [37]. The transmission chain used contains an AWGN channel with a BPSK modulation and demodulation. For simulations, Monte Carlo method [38] was chosen.

The decoding performance of the proposed algorithm is given in terms of Bit Error Rate (BER) as a function of Signal-to-Noise Ratio (SNR). Table 2 shows the default simulation's parameters used in this work.

#### 3.1 Optimization of the Threshold Parameter

The threshold T is a very important parameter in BF decoding since it affects directly the number of bits flipped in each iteration and then affects the performance of decoding. Its value has to be specified before starting to decode, that is why we tried to search through simulations the best value for each code used in this study.

**Table 1** Parameters of LDPC codes

Code	$N$	$K$	$M$	Rate	$d_c$
Code1	73	45	73	0.616	9
Code2	1057	813	1057	0.77	33
Code3	1057	813	244	0.77	3

**Table 2** Simulations' parameters

Simulation parameters	Value
Simulation method	Monte Carlo
Channel	AWGN
Modulation	BPSK
Minimum number of transmitted blocks	1000
Minimum number of residual bit errors	200
Max iterations (Imax)	45

In order to optimize  $T$ , we observe BER performance at some fixed value of SNR. These values of SNR depend on the decoding algorithm and the chosen codes, where the threshold  $T$  range depends on dc parameter of the codes such as:  $T \in [1, d_c]$ .

In order to find the best value  $T$  for each one of the three LDPC codes, we fixed the SNR values according to the used code and required the decoding performance of  $\text{BER} \leq 10^{-5}$ . Figures 4, 5, and 6 illustrate the influence of the parameter  $T$  in BER performance of the proposed RSBF decoder when used with Code1, Code2, and Code3, respectively, and Table 3 shows our choice of the best value of  $T$  which will be used in the next simulations in this study.

We can deduce from the Table 3 that the best value of the threshold parameter is always determined by:  $T \geq \frac{d_c}{2}$ .

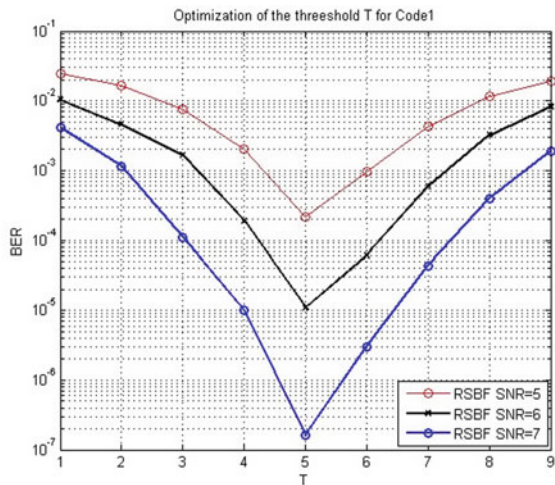
The number  $\frac{d_c}{2}$  comes from the fact that:

- $d_c$  represents the maximum participation number of single bit in the parity check equations or a bit node participate to a  $d_c$  check nodes;
- And the  $E(\mathbf{n})$  value represents the participation of a given bit in the parity check equations that are not satisfied.

Consequently, the best scenario is to correct bit with  $E(\mathbf{n}) \geq \frac{d_c}{2}$ , that means we will satisfy the majority of parity check equations that are not satisfied ( $E(\mathbf{n})$ ) and we will unsatisfied the residue equations ( $d_c - E(\mathbf{n})$ ) and leave them to the next iterations.

However, if we flip bit with  $E(\mathbf{n}) \leq \frac{d_c}{2}$ , we will satisfy a number of equations fewer ( $E(\mathbf{n}) \leq (d_c - E(\mathbf{n}))$ ) than unsatisfying new parity-check equations and this will lead to spread errors in later iterations, therefore, making correction more difficult.

**Fig. 4** Optimization of the threshold  $T$  for Code1



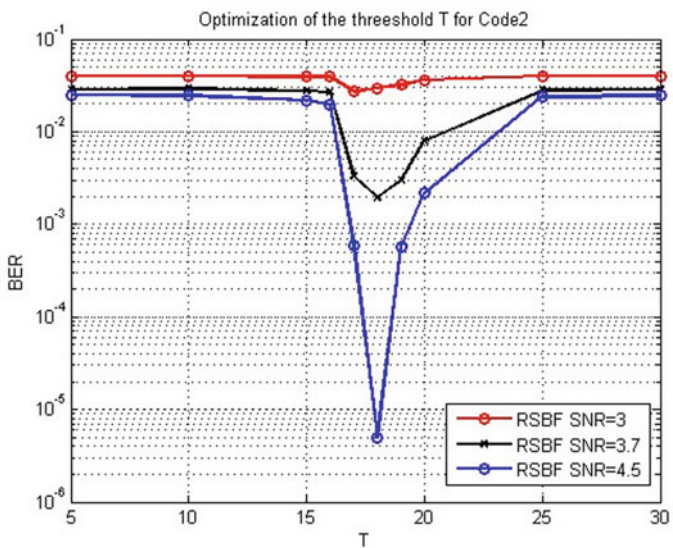


**Fig. 5** Optimization of the threshold  $T$  for Code2

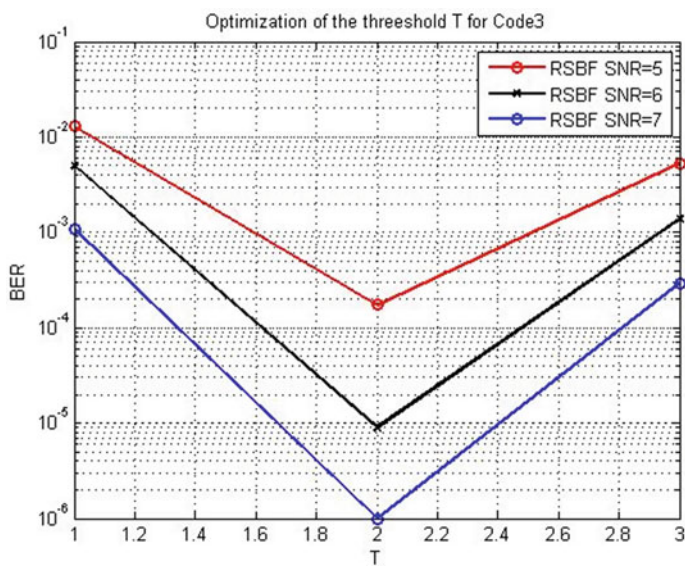


**Fig. 6** Optimization of the threshold  $T$  for Code3

**Table 3** Values of optimized threshold  $T$  for Code1, Code2, and Code3

Code	$T$	$d_c$
Code1	$5 = \lceil d_c/2 \rceil$	9
Code2	$18 \approx \lceil d_c/2 \rceil$	33
Code3	$2 = \lceil d_c/2 \rceil$	3

### 3.2 Performance Study for AWGN Channel

Figure 7 benchmarks our decoder performance against some known bit-flipping decoders for the Code1. As shown, our decoder has a better BER performance than SBF and light advantage in comparison with GDBF. It presents a gain of 0.75 and 0.2 db, respectively, at BER  $2.10^{-5}$ .

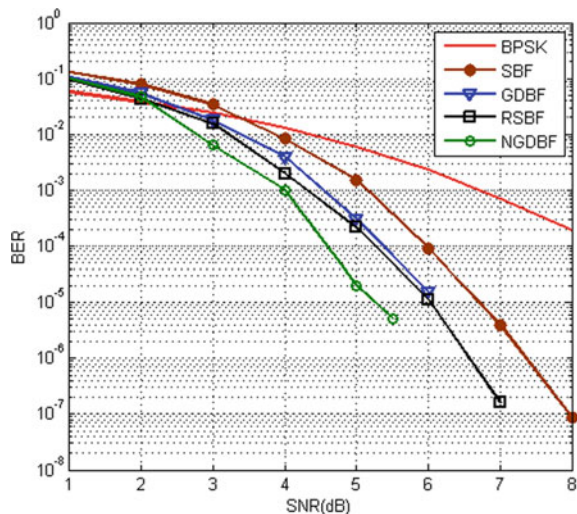
Figure 8 shows results for the Code2 where our decoder achieves coding gain of 0.75 and 1.2 db over the GDBF and the SBF algorithms, respectively, at BER  $2.10^{-5}$ .

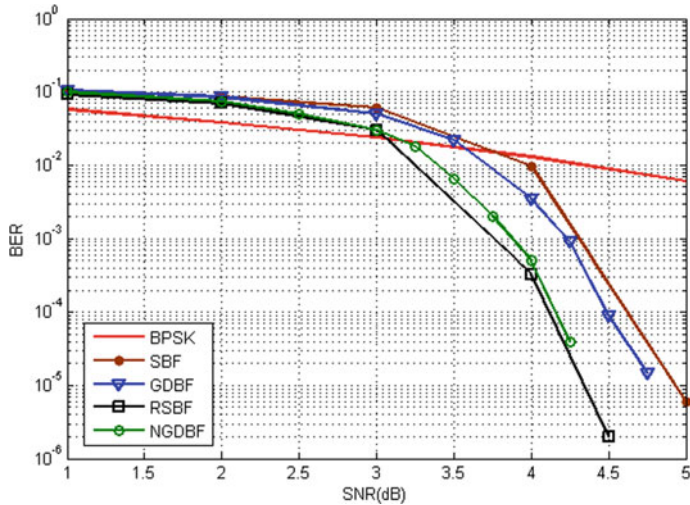
Furthermore, our decoder presents a gain of 0.1db at BER  $2.10^{-5}$  with the known NGDBF for these codes, unlike for the Code1 code where we loss 0.8db of performance at  $2.10^{-5}$ . This observation may imply that longer codes will gain larger improvement over NGDBF.

Figure 9 scales our decoder against some known bit-flipping decoders for the Code3. The figure shows that our decoder outperforms the other algorithms in BER performance. As RSBF achieves coding gain of 2.2, 1.7, 0.8, and 0.8 db for BF, SBF, CBBF, and WBF, respectively, at BER  $10^{-5}$ .

These results may show that it is important to keep the reliability values of received signals during decoding operations since it is the initial belief on the information

**Fig. 7** Performance comparison of our decoder (RSBF) with the state-of-the-art decoders for Code1





**Fig. 8** Performance comparison of our decoder (RSBF) with the state-of-the-art decoders for Code2

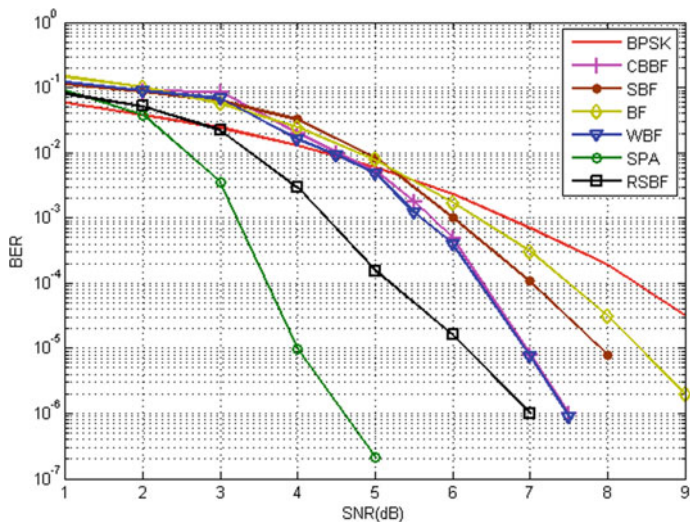


**Fig. 9** Performance comparison of our decoder (RSBF) with the state-of-the-art decoders for Code3

reliability. On the other hand, the obtained results may imply the relationship of the codes length in improving the performance for our new decoder.

**Table 4** Complexity of the BF decoding algorithms

BF algorithms	Complexity
Complexity	$O(I_{\text{tr}}(m.n))$
SBF	$O(I_{\text{tr}}(m.n))$
WBF	$O(I_{\text{tr}}(m.n))$
RSBF	$O(I_{\text{tr}}(m.n))$
GDBF	$O(I_{\text{tr}}(m.n^2))$
NGDBF	$O(I_{\text{tr}}(m.n^2))$

### 3.3 Complexity Study

Let  $C$  denoted by  $(n,k)(d_r, d_c)$  be a regular binary LDPC code over binary field GF (2).  $C$  is the null space of an  $m \times n$  parity-check matrix  $H = [H_{m,n}]$  which has  $d_c$  1 in each column, and  $d_r$  1 in each row with  $m = (n-k)$ , and  $I_{\text{tr}}$  the average number of iterations.

Table 4 illustrates the analytic complexity of our decoder RSBF, as well as the known BF algorithms. It shows that the complexity is polynomial in  $n$ ,  $m$ , and  $I_{\text{tr}}$  for all algorithms.

The complexity of the RSBF and other BF variants algorithms (excluding the GDBF & NGDBF) is same. As a result, we can say that the RSBF is better than the other BF variants, because he provides better BER performance for theoretically same complexity if we consider that the number of iterations is identical for all BF variants. Moreover, the RSBF is low complex besides the GDBF and NGDBF and provides better BER performance compared to GDBF for the Code1 and Code2 and NGDBF for the Code2 as shown in the previous section.

## 4 Conclusion

In this work, we present a new BF decoding algorithm based on the reliability of the received signal which we call the Reliability-based Single Bit-Flipping Decoder (RSBF). It can be regarded as new way to make decision on the bit to be flipped by separating hard decision from the soft decision, because we think that the initial belief about received signals during decoding operations will efficiently contribute in the refine of the final decision.

The proposed algorithm shows better decoding performance than known BF algorithms, such as the Single BF algorithm, Gradient Descent Bit Flipping, and the Noisy Gradient Descent Bit Flipping, for several LDPC codes.

Our algorithm gives also an effective trade-off between performance and decoding complexity. It requires only binary logical operations and integer additions and hence can be implemented with simple combinational logic circuits.

The obtained results open new horizons for future works to strengthen our proposed algorithm by providing iterations complexity study or testing large code length.

## References

- Shafi, M., et al.: 5G: a tutorial overview of standards, trials, challenges, deployment, and practice. *IEEE J. Sel. Areas Commun.* **35**(6), 1201–1221 (2017). <https://doi.org/10.1109/JSAC.2017.2692307>
- Hajiyat, Z.R.M., Sali, A., Mokhtar, M., Hashim, F.: Channel coding scheme for 5G mobile communication system for short length message transmission. *Wirel. Pers. Commun.* **106**(2), 377–400 (2019). <https://doi.org/10.1007/s11277-019-06167-7>
- Richardson, T., Kudekar, S.: Design of low-density parity check codes for 5G new radio. *IEEE Commun. Mag.* **56**(3), 28–34 (2018). <https://doi.org/10.1109/MCOM.2018.1700839>
- Gallager, R.: Low-density parity-check codes. *IRE Trans. Inf. Theory* **8**(1), 21–28 (1962). <https://doi.org/10.1109/TIT.1962.1057683>
- Shannon, C.E.: A mathematical theory of communication. *Bell Syst. Tech. J.* **27**(3), 379–423 (1948). <https://doi.org/10.1002/j.1538-7305.1948.tb01338.x>
- Tanner, R.: A recursive approach to low complexity codes. *IEEE Trans. Inf. Theory* **27**(5), 533–547 (1981). <https://doi.org/10.1109/TIT.1981.1056404>
- MacKay, D.J.C., Neal, R.M.: Near Shannon Limit Performance of Low Density Parity Check Codes
- MacKay, D.J.C.: Good error-correcting codes based on very sparse matrices. *IEEE Trans. Inf. Theory* **45**(2) (1999)
- Li, H., Guo, J., Guo, C., Wang, D.: A low-complexity min-sum decoding algorithm for LDPC codes. In: 2017 IEEE 17th International Conference on Communication Technology (ICCT), pp. 102–105 (2017). <https://doi.org/10.1109/ICCT.2017.8359612>
- Morello, A., Mignone, V.: DVB-S2: the second generation standard for satellite broad-band services. *Proc. IEEE* **94**(1), 210–227 (2006). <https://doi.org/10.1109/JPROC.2005.861013>
- Hemati, S., Leduc-Primeau, F., Gross, W.J.: A relaxed min-sum LDPC decoder with simplified check nodes. *IEEE Commun. Lett.* **20**(3), 422–425 (2016). <https://doi.org/10.1109/LCOMM.2016.2517142>
- Jose, R., Pe, A.: Analysis of hard decision and soft decision decoding algorithms of LDPC codes in AWGN. In: 2015 IEEE International Advance Computing Conference (IACC), Jun., pp. 430–435 (2015). <https://doi.org/10.1109/IADCC.2015.7154744>
- Dong, G., Li, Y., Xie, N., Zhang, T., Liu, H.: Candidate bit based bit-flipping decoding algorithm for LDPC codes. In: 2009 IEEE International Symposium on Information Theory. pp. 2166–2168 (2009). <https://doi.org/10.1109/ISIT.2009.5205798>
- Zhu, Q., Wu, L.: Weighted candidate bit based bit-flipping decoding algorithms for LDPC codes. In: 2013 3rd International Conference on Consumer Electronics, Communications and Networks, Xianning, pp. 731–734 (2013)
- Addi, S., Berkani, A., Azouaoui, A., Belkasmi, M.: New hard decision decoder of LDPC codes using single bit flipping algorithm. In: 2017 International Conference on Wireless Networks and Mobile Communications (WINCOM), pp. 1–5 (2017). <https://doi.org/10.1109/WINCOM.2017.8238191>
- Liu, Y., Zhang, M.: Hard-decision bit-flipping decoder based on adaptive bit-local threshold for LDPC codes. *IEEE Commun. Lett.* **23**(5), 789–792 (2019). <https://doi.org/10.1109/LCOMM.2019.2909207>
- Ouakili, H.E., Touati, H., Kadi, A., Mehdaoui, Y., Alami, R.E.: New low-density-parity-check decoding approach based on the hard and soft decisions algorithms. *Int. J. Electr. Comput. Eng. IEECE* **13**(2), Art. no. 2 (2023). <https://doi.org/10.11591/ijece.v13i2.pp1639-1646>

18. Kou, Y., Lin, S., Fossorier, M.P.C.: Low-density parity-check codes based on finite geometries: a rediscovery and new results. *IEEE Trans. Inf. Theory* **47**(7), 2711–2736 (2001). <https://doi.org/10.1109/18.959255>
19. Zhang, J., Fossorier, M.P.C.: A modified weighted bit-flipping decoding of low-density parity-check codes. *IEEE Commun. Lett.* **8**(3), 165 (2004)
20. Guo, F., Hanzo, L.: Reliability-ratio based weighted bit-flipping decoding for low-density parity check codes. *Electron. Lett.* **40**(21), Art. no. 21 (2004)
21. Guo, F., Hanzo, L.: Reliability ratio based weighted bit-flipping decoding for LDPC codes. In: 2005 IEEE 61st Vehicular Technology Conference, vol. 1, pp. 709–713 (2005). <https://doi.org/10.1109/VETECS.2005.1543385>
22. Wadayama, T., Nakamura, K., Yagita, M., Funahashi, Y., Usami, S., Takumi, I.: Gradient descent bit flipping algorithms for decoding LDPC codes, pp. 1–6 (2009). <https://doi.org/10.1109/ISITA.2008.4895387>
23. Sundararajan, G., Winstead, C., Boutillon, E.: Noisy gradient descent bit-flip decoding for LDPC codes. *IEEE Trans. Commun.* **62**(10), 3385–3400 (2014). <https://doi.org/10.1109/TCOMM.2014.2356458>
24. Chang, T.C.-Y., Su, Y.T.: Dynamic weighted bit-flipping decoding algorithms for LDPC codes. *IEEE Trans. Commun.* **63**(11), 3950–3963 (2015). <https://doi.org/10.1109/TCOMM.2015.2469780>
25. Roberts, M.K., Jayabalan, R.: An improved low complex hybrid weighted bit-flipping algorithm for LDPC codes. *Wirel. Pers. Commun.* **82**(1), 327–339 (2015). <https://doi.org/10.1007/s11277-014-2210-4>
26. Huang, H., Wang, Y., Wei, G.: Mixed modified weighted bit-flipping decoding of low-density parity-check codes. *IET Commun.* **9**(2), 283–290 (2015). <https://doi.org/10.1049/iet-com.2014.0192>
27. Oh, J., Ha, J.: A two-bit weighted bit-flipping decoding algorithm for LDPC codes. *IEEE Commun. Lett.* **22**(5), 874–877 (2018). <https://doi.org/10.1109/LCOMM.2018.2809718>
28. Elsanadily, S., Mahran, A., Elghandour, O.: Classification-based algorithm for bit-flipping decoding of GLDPC codes over AWGN channels. *IEEE Commun. Lett.* **22**(8), 1520–1523 (2018). <https://doi.org/10.1109/LCOMM.2018.2840146>
29. Kalipatnapu, S., Chakrabarti, I.: High-throughput bit flipping decoder for structured LDPC codes. *IET Commun.* **13**(14), 2168–2172 (2019). <https://doi.org/10.1049/iet-com.2019.0229>
30. Harita, D., Rajan, K.P.: Reliability variance based weighted bit flipping algorithms for LDPC. In: 2019 9th International Conference on Cloud Computing, Data Science & Engineering (Confluence), pp. 593–595 (2019). <https://doi.org/10.1109/CONFLUENCE.2019.8776988>
31. Aqil, C., Akharraz, I., Ahaitouf, A.: A new reliability ratio weighted bit flipping algorithm for decoding LDPC codes. *Wirel. Commun. Mob. Comput.* **2021**, e6698602 (2021). <https://doi.org/10.1155/2021/6698602>
32. Biazaran, R., Helgert, H.J.: Improved noisy gradient descent bit-flipping algorithm over Rayleigh fading channel. *Int. J. Electr. Comput. Eng. IJECE* **12**(3), Art. no. 3 (2022). <https://doi.org/10.11591/ijece.v12i3.pp2699-2710>
33. Berkani, A., Belkasmî, M.: A reduced complexity decoder using compact genetic algorithm for linear block codes. In: 2016 International Conference on Advanced Communication Systems and Information Security (ACOSIS), pp. 1–6 (2016). <https://doi.org/10.1109/ACOSIS.2016.7843925>
34. Razi, M., Benhayoun, M., Mansouri, A., Ahaitouf, A.: An improvement and a fast DSP implementation of the bit flipping algorithms for low density parity check decoder. *Int. J. Electr. Comput. Eng. IJECE* **11**(6), Art. no. 6 (2021). <https://doi.org/10.11591/ijece.v11i6.pp4774-4784>
35. Xu, J., Chen, L., Djurdjevic, I., Lin, S., Abdel-Ghaffar, K.: Construction of regular and irregular LDPC codes: geometry decomposition and masking. *IEEE Trans. Inf. Theory* **53**(1), 121–134 (2007). <https://doi.org/10.1109/TIT.2006.887082>
36. Prabhakar, A., Narayanan, K.: Pseudorandom construction of low-density parity-check codes using linear congruential sequences. *IEEE Trans. Commun.* **50**(9), 1389–1396 (2002). <https://doi.org/10.1109/TCOMM.2002.802537>

37. Ritchie, D.M., Johnson, S.C., Lesk, M.E., Kernighan, B.W.: UNIX time-sharing system: the C programming language. *Bell Syst. Tech. J.* **57**(6), 1991–2019 (1978). <https://doi.org/10.1002/j.1538-7305.1978.tb02140.x>
38. Geweke, J.: Chapter 15 Monte Carlo simulation and numerical integration. In: *Handbook of Computational Economics*, vol. 1, pp. 731–800. Elsevier (1996). [https://doi.org/10.1016/S1574-0021\(96\)01017-9](https://doi.org/10.1016/S1574-0021(96)01017-9)

# Design of an Automated System for Door Set Measurement Using IoT Technologies: A Manufacturer's Perspective



Takahiro Usuzuki, Sivajothi Paramasivam, Tamil Moli Loganathan, and Hari Krishnan Munisamy

**Abstract** Small and medium-sized based manufacturing industry, despite being the most important industry in an economy is still grappling with unsteady processes, futile effort on controlling disturbances and erroneous deviation of its end-product resulting in waste of raw materials. Thus, necessitates to push Industry 4.0 (I4.0) higher at their agenda to increase manufacturing efficiency. Considering this, the manufacturer in this study is a mid-tier supplier of high-quality wood door for residential spaces and who frequently deals with modular and customizable door sets. This study makes the following contributions: (1) develop a microcontroller-driven automated system to accurately measure dimensions of door sets; (2) establish a communication to store-retrieve raw data using IoT technologies and (3) develop graphical user interface as diagnostic tool that generates statistical reports as data analytics. A low-cost ESP8266 (ESP) microcontroller Wi-Fi module interfaces with a rotary encoder used to monitor the displacement of door set for error deviation. Data is sent using IoT-based ThingSpeak application. Results satisfactorily record accuracy on error deviation which set between 0 and 0.6 mm based on the percentages of doors. Statistical reports, such as error deviation, percentage of doors within the allowed error, and production rate were remotely accessed to gauge productivity status. Emerging technologies of automation and Internet of Things that underpin concepts introduced by I4.0 are viewed as an antidote to manufacturing issues as

---

T. Usuzuki · S. Paramasivam (✉)

University Of Wollongong Malaysia, Jalan Kontraktor U1/14, 40150 Shah Alam, Selangor, Malaysia

e-mail: [siva@uow.edu.my](mailto:siva@uow.edu.my)

UOW Malaysia Penang University College, Jalan Anson, 10400 Georgetown, Pulau Pinang, Malaysia

T. M. Loganathan

Politeknik Banting Selangor, Jalan Sultan Abdul Samad, Persiaran Ilmu, 42700 Banting, Selangor, Malaysia

H. K. Munisamy

Midahdor, Lot 41060, Jalan Haji Abdul Samat 2, Mukim Kapar, Klang Utara, 42200 Kapar, Selangor, Malaysia

it facilitates the creation of smart monitoring and controlling system for improved productivity yield.

**Keywords** Industry 4.0 · IoT technologies · Data analytics · Graphical user interface · Statistical reports

## 1 Introduction

Advancement of technological development is the catalyst for small and medium enterprises (SMEs) to invest in novel technologies to strategically restructure their manufacturing process. In fact, global manufacturing SMEs are urged to increase reliance on innovative systems to sustain business dominance and a competitive edge. This is imperative in tandem with the industrial climate which is currently being transformed by digital technologies that have significantly improved the way products and services are conceived [1]. Consequently, necessitates exploitation of digital innovation in the manufacturing and production section.

Small and medium-sized businesses (SMEs) are the lifeblood of manufacture-driven economy of many nations. In this relation, local policymakers are recognizing the crucial significance of digitalization towards growth in economy segment and efforts are being made through Industry 4WRD: National Policy 2018 to foster digital transformation among manufacturers [2]. Thus, charting a strategic roadmap to propel Malaysia towards an industrial landscape pivots on automated and digitalization environment. Statistically, the majority of SMEs fall under the category of manufacturing; making up 98.5% of Malaysia's industrial sector, and contributed 38.3% to the national gross domestic product in 2018 [3]. However, the interest in implementing I4.0 concepts is moderately low, of which 15% to 20% of companies, especially young firms, are aggressive towards embracing technologies underpinning I4.0. The reason being majority is less prepared for the transformation towards new wave of technologies and its associated implementation framework [2, 4].

Typically, manufacturers are often challenged to produce products and service of high quality in view of gaining greater consumer loyalty and market confidence. Thus, in meeting such desirable aspirations, the operation of production lines must be executed at its optimized potential using digital technologies and reliable analytics [5]. In this context, products produced and dispatched to the customers are expected to fulfil the primary objective, which revolves around measuring the favourable impact of production. As such, flaws or defects in production line must be constantly monitored with accurate interpretation from any evidence gathered during testing activities to allow the prediction of future failure. Thus, necessitates modernization of the manufacturing process using digital technologies and data analytics to address issues related to production errors, drop in production performance and low response time to customers demand and preference [6, 7].

Against such a background, this project revolves on providing digital technologies base solutions to improve productivity of a mid-tier SME manufacturer who adopts

conventional method to produce high-quality modular and customizable wood door sets in harsh environment settings, subsequently provides the following contributions: (1) develop a microcontroller and rotary encoder integrated system to perform measurement of dimensions of door sets; (2) establish communication using TCP protocol to store-retrieve raw data via integration of cloud and IoT technologies and (3) develop a graphical user interface as diagnostic tool that generates statistical reports providing real-time data analytics.

SMEs of manufacturing based are constantly pressured to push I4.0 higher at their agenda as many were still grappling with unsteady processes, futile effort on controlling disturbances and adopting solutions for deviation control to produce quality finish of end-product [3]. Consequently, as faced by other non-technological driven SMEs, they experience waste of raw materials, customer dissatisfaction and drop in revenues. Therefore, an industry of such nature was selected for this study [8, 9].

Emerging technologies of automation and Internet of Things that underpin concepts introduced by I4.0 are viewed as a boon for exploitation by many manufacturing based [10].

## 2 Industry 4.0 as Solution for Improvement

The emergence and development of digital technologies driven by I4.0 provides an opportunity for small and medium-sized businesses (SMEs) to leverage the application of technologies to improve the sustainability of manufacturing operations. The reason being that many manufacturing industries have evolved over the years and have resulted in the emergence of new practices. Hence, it is imperative that the manufacturing industry gains complete visibility into the entire process, from supply to the end customer, to optimize their output.

Every industrial revolution pivots strongly to bolster productivity and efficiency of industry. The first industrial revolution signifies the phase-in of the use of machines in the manufacturing processes driven by water and steam. The second industrial revolution revolves around the utilization of machines powered by electrical energy to drive industrial processes, which has a direct bearing on low cost and resource aspects. The third industrial revolution reveals the breakthrough of partial programmable logic controller (PLC) automation and digital technology of good computing power with heavy reliance on human intervention and input. The industry I4.0 (the fourth industrial revolution) is a concept that revolves around autonomous decision-making processes, monitoring assets and processes in real-time and establishing connectivity between machines, devices and factories in an industrial setting [11–13].

I4.0 is the rise of digital industrial technology and is closely associated in making manufacturing operations smarter and more automated. The goal of I4.0 is to drive SMEs to modernize their operations and improve productivity to sustain business competitiveness [13, 14]. This entails shifting the manufacturing processes to leverage on effective use of digitization and quality control tools.

The building block of I4.0 focuses on technology that encompasses advanced and innovative technologies such as advanced sensors, big data analytics, intelligent robotics, 3D printing, machine learning and cloud computing, cybersecurity and the Internet of Things (IoT) [1, 3, 15, 16].

Considerable works indicated that reliance on I4.0-based solutions yields positive impacts such as increased operational efficiency, products becoming customized, processes being networked, reduced human-based errors and doing so at a depth that reveals accurate machine conditions and trends in production [2, 17, 18].

## 2.1 Automation and Data Analytics in SME Manufacturing

Manufacturer of this study typically uses heavy machinery, equipment and other items at the production site in a harsh environment to create their door set product.

As shown in Fig. 1, the challenging situation involves addressing production errors such as the inaccuracy of dimensioning of door sets during the process of manufacturing customizable door sets, which contributes to the waste of raw material. The reason being this woodwork manufacturer does not have access to some data on the production floor. In this case, its end-to-end production processes were operating but driven in a non-smart and interactive manner. The manufacturer would realize an occurrence of issue when the finished door sets re-enter the production floor due to misfitting. Hence, these warrant manufacturers face such situations to embrace and adopt elements of I4.0 to help increase visibility in both effective usage of their raw materials and to streamline operational processes.

Automated machine data collection is driving the next generation of manufacturing analytics. It improves automation of industrial processes, increases data gathering and self-monitoring and is subsequently capable of being used to analyze and diagnose issues without human intervention [19]. In gaining these desirable intents, manufacturers are investing in technology that pivots on data gathering and processing, and the dissemination of that data within an interconnected production system.

Automation is increasingly accessible to manufacturing SMEs as technology becomes relatively cost-effective. Coupled with sensors and IoT technology, such integration provides valuable insight into equipment health, operational efficiencies



**Fig. 1** Operational flow of door set by manufacturer

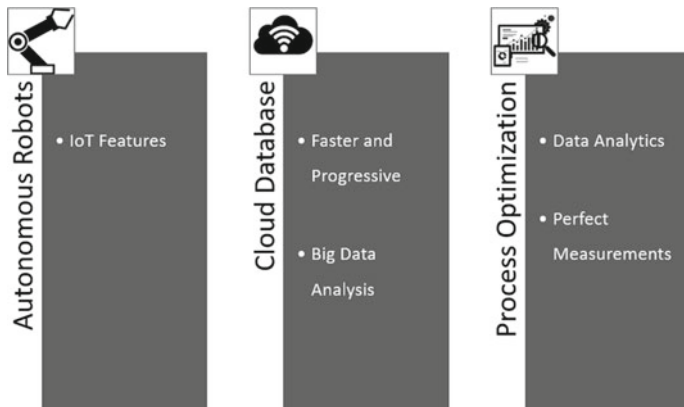


**Fig. 2** Industry 4.0 manufacturing solutions [11]

and quality of output. Subsequently, the dynamics of modern manufacturing demands greater integration of data analytics to deliver automated production processes that increase productivity and quality control [20–22].

In fact, automated machine data collection is driving the next generation of manufacturing analytics as shown in Fig. 2.

SME manufacturers positively affect their operations using IoT and automation technologies, primarily driven by the need to access real-time insights and information throughout the manufacturing process. This includes the use of sensors and IoT devices to track inventory and monitor production processes or implement automation systems to handle routine tasks. With the rising adoption of interconnected environments, solutions such as cloud database technology are used to store, sort and retrieve massive amounts of data machines and equipment produced every day during normal operations. Such communication promotes the integration and synchronization of all resources along the value chain [4, 23]. Subsequently, entails the use of data analytics to access and analyze data to gain insights on machines' performance and efficiency for various decision-making purposes [11].

Quality compliance is a crucial part of a manufacturing environment and can be a bridge between waste reduction and the desired finished product. Thus, the case of the mid-tier supplier in this study focuses on improvement measures at the production line which revolves on real-time data monitoring, tracking the status and positions of wood door as well as to hold the instructions to control production processes. In this connection, the main developments that affect manufacturing are the Internet of Things (IoT), which describes the way objects use the Internet to communicate, and cloud databases secure and compile massive amounts of data for intelligent analytical compiling.

The focus on most of these I4.0 enablers is geared to fostering innovation through further development of the ecosystem and supporting SMEs for restructuring and modernization of their respective production capabilities.

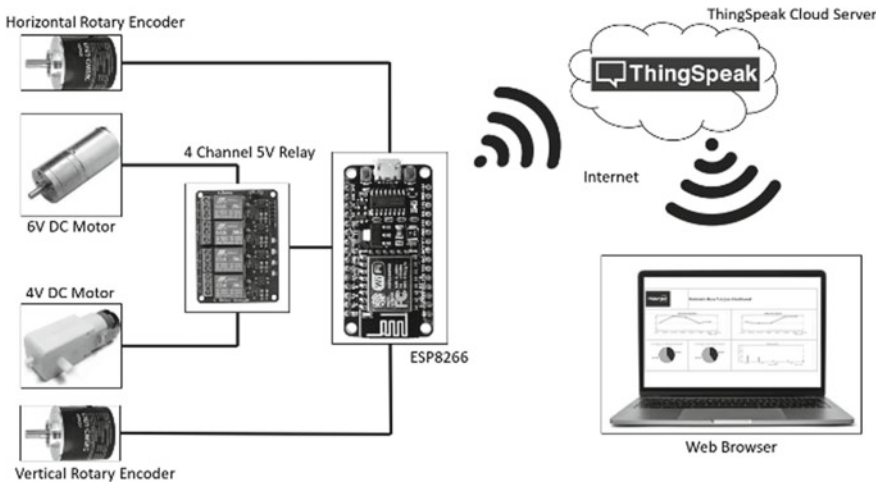


**Fig. 3** System layout—components and connections

### 3 Methodology

#### 3.1 Overview of System

The overview of the system which shows the components and interface is shown in Fig. 3. At the heart of the system is the microcontroller, where the Node Micro-Controller Unit (NodeMCU) which was built around the ESP8266 allows connection to the Internet. The system utilized sensors such as OMRON rotary encoders and infrared sensors as well as relays to carry out the data acquisition process. ThingSpeak cloud server was used for cloud database and computing, and HTML was used for data analytics web browser.

#### 3.2 Hardware Development

The system was implemented in a “harsh” environment in an actual production setting located in Klang. In this context, “harsh” indicates the production area was a dusty, loud and sometimes dark manufacturing environment. As such, surrounding factors were considered and compared with the capabilities of infrared sensors and ultrasonic sensors, which were the most widely used distance measurement sensors. However, the two sensors were not able to meet the requirements of a door manufacturing setting.

Using the measurement of the velocity of the shaft, rotary encoders were used and able to measure linear distances based on the circumference of a gear. The electric signals were calculated in pulses per revolution (PPR).

$$\text{PPM} = \frac{\text{PPR}}{2\pi r}, \quad (1)$$

where

PPM pulse per meter, which is the pulses per 1 m of the circumference travelled,  
 PPR pulse per revolution which is indicated in the data sheet,  
 $r$  radius of the rotating tip.

Using the PPI value obtained from Eqs. (1) and (2), subsequently this value is used to obtain the linear distance ( $L$ ).

$$L = \frac{\text{Pulses}}{\text{PPM}} \quad (2)$$

where

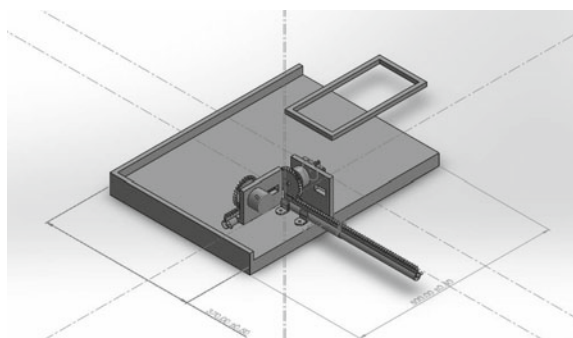
$L$  linear distance,  
 Pulse number of pulses output by the encoder.

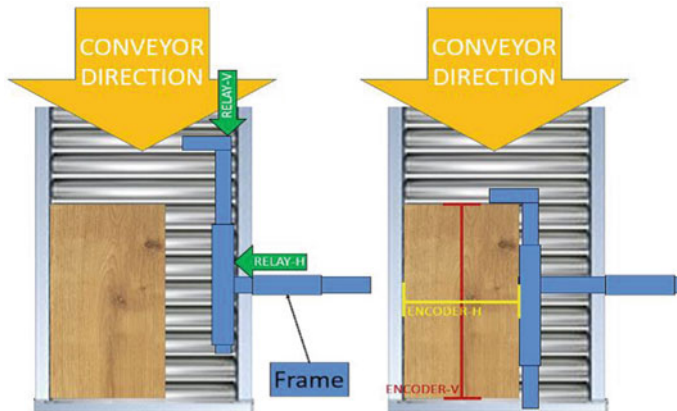
Aluminium material was used to create the mechanical frame for this prototype system due to its low-cost and light weight properties.

Figure 4 shows the illustration of the prototype that is to be developed where the width of the conveyor belt was assumed to be 370 mm and the length of the conveyor belt to be 500 mm.

Figure 5 shows the actual set-up of implementation. The frame was attached to the side of the conveyor system and moved towards the manufactured door to calculate the distance travelled. The maximum distance, which was the whole width of the conveyor system, was calibrated by the software where it would then deduct the distance travelled from the total distance. Therefore, giving the measurements of the manufactured doors. This was the concept which was reflected in the prototype.

**Fig. 4** Illustration of the prototype in solidworks drawing





**Fig. 5** Actual implementation of system

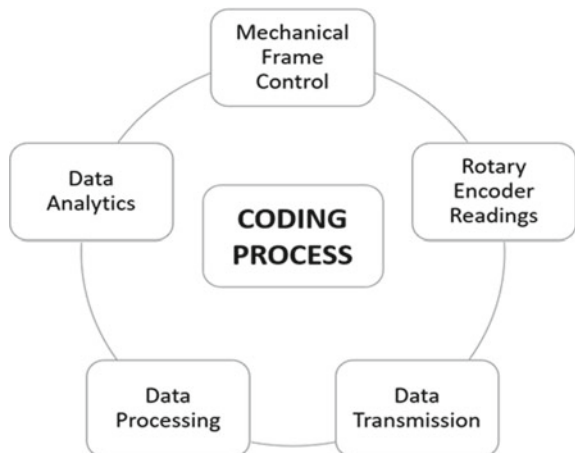
### 3.3 Software Development

Figure 6 shows the phases of the coding process for the system. Each of the coding processes is done separately and compiled at the end to work in unison.

The mechanical frame control and rotary encoder readings as well as data transmission were coded into the microcontroller using C++, while the data processing was coded into the cloud server using MATLAB. In addition, the data analytics were coded in the web browser using HTML.

**Mechanical Frame Control.** This part of the microcontroller coding was responsible for the movement of the aluminium mechanical frame. It would utilize relays to switch the DC motors on and off as well as switch on and off LEDs to indicate if

**Fig. 6** Coding process



the system was ready to accept another sample or was still processing the previous sample. The LEDs consisted of two colours, red and green where green meant all previous processes were finished and data was sent to the cloud. While, red meant it was still processing the previous sample.

**Rotary Encoder Readings.** This was also part of the microcontroller code and was used to process the number of pulses through the rotary encoder. An interrupt function was used where, when the trigger pin for the rotary encoder was HIGH, it would interrupt the code and check for the status of the direction pin. When the direction pin was HIGH, it would add + 1 to the variable and if it was LOW, it would add -1 to the variable. This was done for both the vertical and horizontal variables to obtain accurate values of the samples for their height and width, respectively.

**Data Transmission.** Data transmission was coded into the microcontroller to allow it to send data to the cloud. The use of ThingSpeak and ESP8266 Wifi libraries allows effective data transmission. By default, the NodeMCUs' integrated ESP8266 module uses MQTT protocols to transmit data. MQTT was used due to its capability to adapt to unstable connections. The code also contained the procedures to connect to a wireless network using a mobile hotspot, in which the SSID and password were keyed into and stored in a variable during set-up.

**Data Processing.** This first code in the cloud would take the data which was transmitted from the microcontroller and calculate information such as production rate. This process was done in the cloud because the production rate was calculated based on the number of samples obtained in the last 10 min. Since the microcontroller has a limit to how much data it can store at one time, it was better to accumulate data in the cloud and process it at the same time. The graphs and charts were also produced here and linked to the data analytics dashboard using links for remote access.

**Data Analytics.** Data analytics was one of the most crucial aspects of the system because the prime intention was to provide the manufacturer with data to address flaws in the production line. Since the cloud was able to output charts and graphs with remotely accessible capabilities, the data analytics dashboard was coded using HTML and critical and relevant data and information were displayed.

### **3.4 Network Development**

In step 1 of Fig. 7, the ESP8266 establishes a session with the cloud server. Thus, enabling the ESP8266, and cloud to communicate and identify the presence of another entity in the network. This is the 15 s set in the ESP8266 coding where it waits for the network to respond to its request.

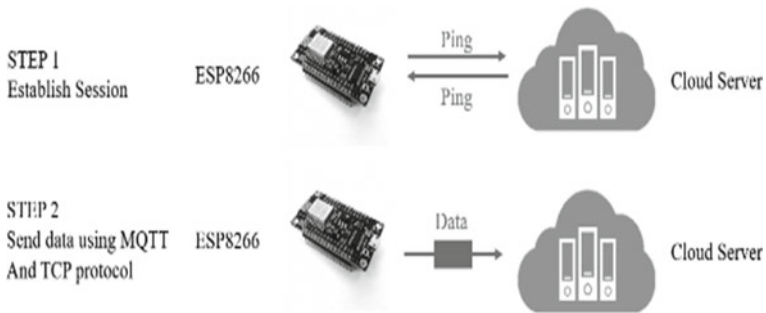


**Fig. 7** Establishing session

In step 2 of Fig. 7, the data is sent to the cloud via MQTT. MQTT is used as it has a built-in protocol in ESP8266 and adopts push-based message transfers which is well-supported by existing TCP/IP connections.

In order to make the system automated, the whole process is stepped up in a loop. Figure 8 shows the data loop for the system. It starts by measuring the data which is the data acquisition at the manufacturing line. The data is then sent to the cloud to be processed into graphs and charts but also to be stored as raw data for the measurements and errors in the products. The graphs and charts produced in cloud are then sent to a website via HTTP links for the manufacturer to observe. This loop will ensure data is always flowing into the server whenever there is a product manufactured.

**Fig. 8** Data loop to form an automated system



## 4 Results and Discussion

### 4.1 Design Performance

Based on the manufacturers' specifications, the desired precision of the system was 0.1 mm. A gear was needed to produce 0.1 mm linear distance for every pulse. Therefore, a 2000 PPR rotary encoder was chosen. Using these details to substitute into Eq. 1 and Eq. 2, the size of the gear was determined.

$$0.1 \text{ mm} = \frac{1}{\text{PPM}} \quad (3)$$

Since the rotary encoder needs to pulse once every 0.1 mm, the pulse will be equal to "1", and the linear distance will be equal to "0.1 mm".

$$\text{PPM} = \frac{1}{0.1 \text{ mm}} = 10 \text{ pulses per mm} \quad (4)$$

After rearranging the equation, PPM is equal to 10 pulses per mm. This value is then substituted into Eq. (1).

$$10 = \frac{2000}{2\pi r} \quad (5)$$

$$r = \frac{2000}{10 * 2\pi} = 31.83 \text{ mm} \quad (6)$$

At the base of a series of testing, sample measurement and their deviation were captured as given in Table 1.

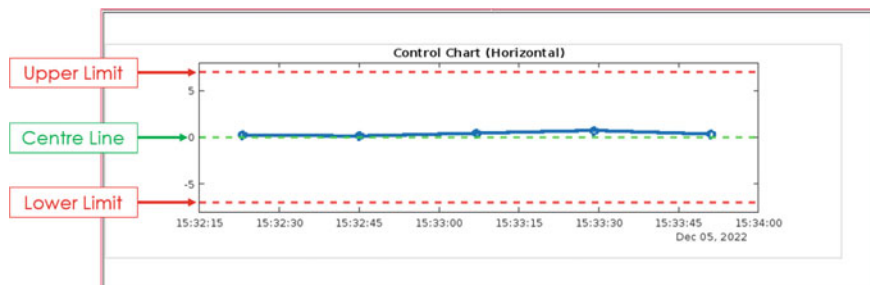
### 4.2 GUI Design and Output

Once the data was obtained from the samples, they were sent to the cloud and processed. After the process was done, the cloud was then tasked with producing the data analytics charts.

The control chart in Fig. 9 is produced by the browser-based GUI. It shows the horizontal error deviation of the samples. The x-axis shows the time of production, and the y-axis shows the error value in mm. The y-axis has a straight line through it which indicates the upper and lower limit of error in terms of positive and negative values, respectively. This was the part of the GUI that would allow the manufacturer to gauge the equipment's condition in their factory. If they see the points in the control charts increasing, it indicates the need to check the machines and to look for calibration errors or malfunction in the manufacturing lines' system.

**Table 1** Sample measurements and system deviations

Samples	Horizontal measurements	Vertical measurements	Horizontal deviation	Vertical deviation
1	202.10	328.40	0.10	-0.10
2	202.00	327.40	0.00	-1.10
3	202.00	328.80	0.00	0.30
4	202.00	329.50	0.00	1.00
5	202.50	327.70	0.50	-0.80
6	202.70	328.10	0.70	-0.40
7	201.40	327.50	-0.60	-1.00
8	202.10	328.00	0.10	-0.50
9	201.70	328.20	-0.30	-0.30
10	201.60	327.60	-0.40	-0.90
11	202.50	327.80	0.50	-0.70
12	201.60	328.90	-0.40	0.40
13	201.50	328.00	-0.50	-0.50
14	202.40	327.50	0.40	-1.00
15	201.60	326.70	-0.40	-1.80

**Fig. 9** Control chart: horizontal error deviation of samples

Since the scenario simulates the ideal performance of the manufacturing line, there were no machining errors shown in the control charts above and all samples were close to the centre line which indicated their error was close to zero.

In addition, pie charts generated by the GUI were used to visualize the data in terms of percentages as shown in Fig. 10.

The pie chart was set to take the errors in the last six samples and calculated if the errors were above 5 mm or below 5 mm, depending on the error range, it would show “Good” or “Bad”, respectively. Since the data is presented in terms of percentages, the manufacturer can easily identify the ratio between the good and bad doors.

However, a 6 mm board was used to offset the horizontal measurement to simulate a machining error in the horizontal side of the door.

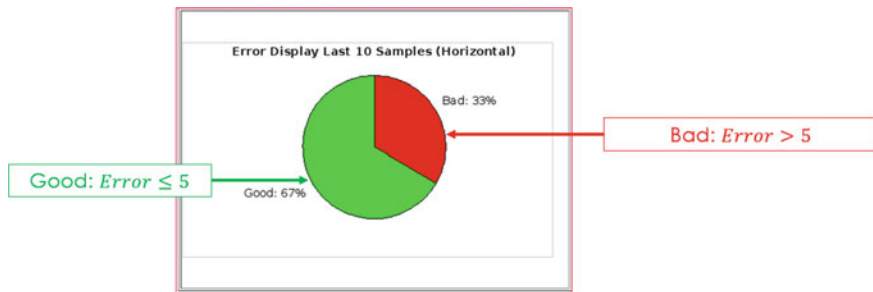


**Fig. 10** Pie chart representation from GUI

The results in Fig. 11 show that the points in the control charts increase, thus, it indicates the need to check the machines and to look for calibration errors or malfunction in the manufacturing lines' system. Hence, early identification using the control charts can provide them the necessary data to intervene these defects before they reach the customer.

The testing for the production rate was done separately in another test where the system was fed in varying quantities of samples during every 10-min intervals and since the system could not run the production rate analysis automatically, the process was started manually and the system took the number of samples from the past 10 min and plotted the production rate bar chart. This is shown in Fig. 12.

Furthermore, the data can also help in the maintenance of the machines, reducing critical breakdowns which contribute to an increase in machine lifespan and making better decisions for future developments based on the current performance of their production line.

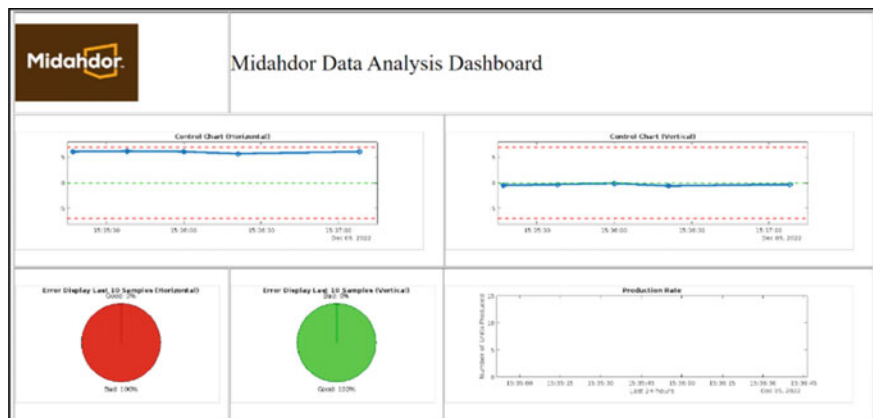


**Fig. 11** Machining error detection due to offset range

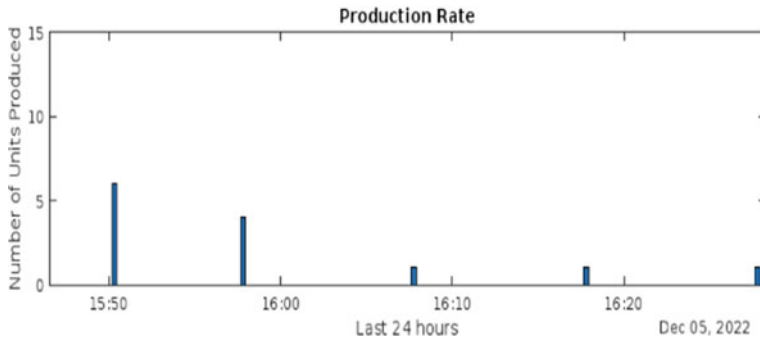


**Fig. 12** Production rate produced by GUI

## 5 Conclusion

In conclusion, this paper highlights the development of an IoT-based automated system with a GUI that adopts elements of I4.0 as a viable solution to issues faced by the mid-tier wood door set manufacturer. Without this intervention, the manufacturer does not have access to some data on the production floor. Hence, the only way they could know if there is a problem is when the products, they sent out come back due to misfitting.

In-depth research was done on the importance of digital technologies in the manufacturing industry which shed light on its potential to allow the manufacturer to grow through reduction in wastage, on time delivery and increasing customer satisfaction. Considering this, several pillars of IR 4.0 were chosen and utilized in the design, which included IoT, data analysis and the cloud to solve the manufacturer's problem. The proposed design managed to overcome the problem by measuring each manufactured door and providing real-time data analytics to the manufacturer using IoT and the cloud.

**Acknowledgements** I would like to thank Dr. Sivajothi A/L Paramasivam and Mr. Hari Krishnan A/L Munisamy, the Facility Manager of Midahdor to provide this industrial case study and technical insights of the door set production system. I would like to take this opportunity to thank Mr. David Teh Chu Yeau, the General Manager of Midah Industries to provide access to the physical facilities of the production lines to carry out the design and investigative work to develop the automated prototype system. I am extremely thankful to them for providing such support and guidance, although they had busy schedules.

This is to also thank the Postgraduate and Research Centre (PGRC), UOWM for funding the publication.

## References

1. Chavez, Z., Hauge, J.B., Bellgran, M.: Industry 4.0, transition or addition in SMEs? A systematic literature review on digitalization for deviation management. *Int. J. Adv. Manufact. Tech.* **119**, 57–76 (2022)
2. Wong, A.P.H., Kee, D.M.H.: Driving factors for Industry 4.0 readiness among manufacturing SMEs in Malaysia. *Info. Intell. Manufact. Informat.* **13**(3), 552 (2022)
3. Ling, Y.M., Abdul Hamid, N.A., Chuan, L.T.: Is Malaysia ready for Industry 4.0? Issues and challenges in manufacturing industry. *Int. J. Integrat. Eng.* **12**(7), 134–150 (2020)
4. Balakrishnan, B., Othman, Z., Ahmad Zaidi, M.Z.: Review of IR4.0 readiness and adoption in Malaysian manufacturing sector. *Int. J. Bus. Econ.* **3**(2), 24–35 (2021)
5. Alexopoulos, K., Nikolakis, N., Xanthakis, E.: Digital transformation of production planning and control in manufacturing SME's—the mold shop case. *Appl. Sci.* **12**, 10788 (2022)
6. Ragazou, K., Passas, I., Sklavos, G.: Investigating the strategic role of digital transformation path of SMEs in the era of COVID-19: a bibliometric analysis using R. *Sustainab.* **14**, 11295 (2022)
7. TabedzKa, J.: Industry 4.0—policy based approaches to efficient implementation in SME. *Eng. Manage. Product. Serv.* **13**(4), 72–78 (2021)
8. Tuselim, N.H.M., Ya'acob, S.: An exploratory study and impact of digitalisation on Malaysian SMEs. *Open Int. J Informat.* **10**(1), 122–134 (2022)
9. Sued, N.M.: Barriers of supply chain digitalization from the perspective of Malaysian SMEs. *J. Tech. Manag. Technopreneurship* **8**, 1–6 (2020)
10. Salah, B.: Real-time implementation of a fully automated industrial system based on IR 4.0 concept. *Actuat.* **10**(12), 319 (2021)
11. Javaid, M., Haleem, A., Singh, R.P., Rab, S., Suman, R.: Significance of sensors for industry 4.0: roles, capabilities, and applications. *Sensors Internat.* **2**, 1–12 (2021)
12. Rehman, S.U., Ejaz, S.: An implementation of 9 pillars of industry 4.0 in conventional footwear industry model. *Int. J. Eng. Appl. Sci. Tech.* **4**(2), 283–286 (2020)
13. Yang, F., Gu, S.: Industry 4.0, a revolution that requires technology and national strategies. *Comp. Intell. Syst.* **7**, 1311–1325 (2021)
14. Bidnur, C.V.: A study on industry 4.0 concept. *Int. J. Eng. Res. Tech. (IJERT)* **9**(4), 613–618 (2020)
15. Adam, A., Yusof, Y., Iliyas, M., Saif, Y., Hatem, N.: Review on manufacturing for advancement of industrial revolution 4.0. *Int. J. Integrat. Eng.* **10**(5), 93–98 (2018)
16. Yazdi, I. A., Couzon, P., Nguyen,N.Q., Ouazene, Y., Yalaoui, F.: Industry 4.0: revolution or evolution? *Am. J. Operat. Res.* **10**, 241–268 (2020)
17. Jovanovski, D.B., Seykova, D., Boshnyaku, A., Fischer, D.C.: 'The impact of industry 4.0 on the competitiveness of SMEs. *Int. Scient. J. Industry 4.0* **4**(5), 250–255 (2019)
18. Nwaiwu, F., Duduci, M., Chromjakova, F., Otekhile, C.A.F.: Industry 4.0 concepts within the Czech SME manufacturing sector: an empirical assessment of critical success factors. *Bus.: Theory Pract.* **21**(1), 58–70 (2020)
19. Othman, N., Nor, F.M., Zan, U.M.S.M.: Industrial revolution 4.0 and economic wellbeing: a systematic literature review. In: 8th International Conference on Management and Muamalah, pp 435–448 (2021)
20. Abdulaziz, Q. A., Mad Kaidi, H., Masrom, M., Hamzah, H.S., Sarip, S., Dzilyauddin, R.A., Muhammad-Sukki, F.: Developing an IoT framework for industry 4.0 in Malaysian SMEs: an analysis of current status, practices, and challenges. *Appl. Sci.* **13**, 1–19 (2023)
21. Falahat, M., Cheah, P.K., Jayabalan, J., Lee, C.M.J., Kai, S.B.: Big data analytics capability ecosystem model for SMEs. *Sustain.* **15**, 360 (2023)
22. Moyne, J., Iskandar, J.: Big data analytics for smart manufacturing: case studies in semiconductor manufacturing. *Processes* **5**, 1–20 (2017)
23. Zamani, S.Z.: Small and medium enterprises (SMEs) facing an evolving technological era: a systematic literature review on the adoption of technologies in SMEs. *Eur. J. Innov. Manag.* **25**(6), 735–757 (2022)

# Classification of Helpful and Unhelpful Online Customer Reviews Using XLNet and BERT Variants



Muhammad Bilal , Muhammad Haseeb Arshad, and Muhammad Ramzan

**Abstract** The majority of businesses have made public appearances on various social media platforms as a result of recent advances in e-commerce and the popularity of social media websites. Customers can share their experiences in the form of online customer reviews, which can assist potential customers in determining the quality of a company and making purchasing decisions. Due to the large volume of published reviews, it becomes difficult for customers to read all of the reviews and assess the quality of the business, resulting in the problem of information overload. Several solutions have been proposed in the literature by researchers using statistical and machine learning techniques to predict the helpfulness of online customer reviews. However, most of the existing solutions are based on the use of various business, review, and reviewer features, which lead to generalizability issues. Moreover, very limited studies have examined the effectiveness of state-of-the-art pre-trained language models for the classification of helpful and unhelpful reviews. Therefore, this study aims to examine the effectiveness of XLNet, Albert, DistilBert, and Roberta for review helpfulness prediction using textual features. The models were fine-tuned using a publicly available dataset of Yelp reviews. The results showed that XLNet achieved the highest *F1*-score of 0.730 compared to a benchmark of 0.717 achieved by the BERT base model.

**Keywords** Helpfulness · Classification · XLNet · Albert · Roberta · DistilBert

---

M. Bilal (✉)

Department of Computing and Information Systems, School of Engineering and Technology,  
Sunway University, Petaling Jaya, Malaysia  
e-mail: [muhhammadb@sunway.edu.my](mailto:muhhammadb@sunway.edu.my)

M. H. Arshad

Department of Computer Science, National University of Computer and Emerging Sciences,  
Chiniot-Faisalabad Campus, Chiniot, Pakistan

M. Ramzan

Department of Software Engineering, University of Sargodha, Sargodha, Pakistan

M. Bilal

School of Electronics and Computer Science, University of Southampton Malaysia, Iskandar Puteri, Malaysia

## 1 Introduction

The world has become a global village as a result of technological advancements and the popularity of social media platforms [1]. People in almost every field are using social media to share their thoughts and to communicate with one another. The use and reliance on social media for communication, content creation, information exchange, entertainment, social networking, news, and reviews are growing by the day [2, 3]. E-commerce platforms enabled customers and businesses to buy and sell products and services from anywhere globally [4]. The growing use and popularity of social media platforms have resulted in massive amounts of User-Generated Content (UGC). Online customer reviews on review websites such as Amazon, Yelp, and TripAdvisor are a major source of UGC [5, 6].

Social media users are encouraged to share their opinions on many review and e-commerce platforms about various services and products. Online reviews not only assist buyers in reducing purchase anxiety, but they also assist vendors in understanding the needs of their customers [7]. Customer feedback can help businesses address customer concerns about product quality, service, and the shopping experience. Profit margins can be increased by making decisions based on customer purchasing history [8]. Massive amounts of online customer reviews are published on various websites on a daily basis, but they do not always cover all areas and topics of interest. People from various backgrounds may use and react differently to online customer reviews [9, 10].

The number of online reviews is rapidly increasing, making it difficult for businesses and potential customers to analyze all of them. A single business or product may receive thousands of reviews, far exceeding cognitive abilities, making it extremely difficult to read them all to find the most helpful and appropriate reviews. Furthermore, a review may include a range of perspectives that depends on people's experiences. The review platforms attempted to address this issue by crowdsourcing helpful and unhelpful votes, but the majority of online reviews were unable to receive helpful or unhelpful votes [11]. The helpfulness of a review can be determined by a number of factors such as the reviewer's experience, writing style, length of review, timeframe. Online review platforms attempt to publish reviews in such a way that users receive the most relevant and valuable reviews to aid them in making decisions [9]. Online review platforms like Yelp have also implemented a mechanism to detect and highlight potentially fake reviews [12].

Customers who are exposed to a large number of conflicting and varying quality reviews may become confused and fail to make a decision. There is no standardized format for posting product reviews on social media or e-commerce sites. Each client has a unique writing style, terminology, and so on. As a result, finding and assessing helpful reviews are difficult. Researchers using various techniques have proposed a wide range of solutions to determine the helplessness of online customer reviews [11]. Existing solutions are proposed based on the features from the review, business, and reviewer categories. A few studies also attempted to investigate the impact of various textual and psychological features on review helpfulness. Different psychological

preferences, such as the Matthew Effect and the Ratchet Effect, can also have an impact on the helpfulness of a review [13].

Existing solutions on review helpfulness prediction lack generalizability due to the use of platform-specific review, business, product, and reviewer features. Furthermore, the majority of existing solutions rely on traditional machine learning techniques. Few recent studies [14, 15] classified helpful and unhelpful reviews using the Bidirectional Encoder Representations from Transformers (BERTs) base model, but there is still a need to investigate the effectiveness of other versions of BERT and pre-trained language models for the task of review helpfulness prediction. The aim of this study is to provide a generalized solution using only textual features in order to overcome the limitations of previous studies.

The remaining sections of the paper are organized as follows. Section 2 provides a comprehensive review of the existing review helpfulness prediction literature. Section 3 explains the research methodology. The findings of the study are discussed in Sect. 4. Lastly, the conclusion is provided in Sect. 5.

## 2 Literature Review

Customers and review platforms spent a significant amount of time deciding whether a review is helpful or not because there could be a large number of reviews on a website for any business, product, or service. Helpful reviews can get buried beneath low-quality reviews, making it difficult to distinguish between helpful and unhelpful reviews. A number of techniques for predicting review helpfulness have been proposed by researchers to overcome the problem of information overload. Liu et al. [16] created a nonlinear regression model for predicting usefulness and determining the most useful review for any given topic. The proposed technique was found to be effective when tested on the IMDB movie review dataset. Online customer reviews can assist consumers in making purchasing decisions by providing a better understanding of a product and reflecting on the experiences of others who have used that product. A previous study investigated the factors that contribute to the usefulness of online customer reviews, as well as how these factors influenced consumers [17].

A study [18] was conducted in collaboration with a marketing firm to assess information overload introduced by online customer reviews that significantly influences customer purchase decisions. It was discovered that the influence of perceived review quality grows as customers read more reviews. It does, however, increase until a certain number of reviews are read and then significantly decrease as the number of reviews read increases. Furthermore, the study reported important characteristics of a review that make it useful. Yi and Oh [19] measured review helpfulness as the number of attributes discussed in the review and investigated the impact of review rating on customer perceived helpfulness. To extract aspects from the text and their impact on helpfulness votes, as well as to make system improvement recommendations, word-level bigram analysis was used. The proposed approach was evaluated

using 21,125 reviews written for 14 wireless earbuds. The findings revealed that there is a positive relationship between the number of attributes and helpfulness for reviews with low ratings.

Bilal and Almazroi [14] proposed a generalized method based on the fine-tuned BERT base model to address the problem of limited generalization encountered by existing approaches due to the combination of handcrafted characteristics for online reviews. Furthermore, the performance of a fine-tuned BERT-based model was compared to bag-of-words-based approaches. In this study, a benchmark dataset of 10,000 Yelp reviews was created. The BERT-based classifier outperformed the bag-of-words-based classifiers in categorizing helpful and unhelpful Yelp reviews. Furthermore, findings on the significance of different review lengths for review usefulness were discussed. A study [20] proposed novel reviewer social network strength-based attributes, as well as several previously unexplored business measures, to investigate their impact on review usefulness prediction. The results revealed that Gradient-Booted Trees with all features produced the best results. In addition, the findings on the significance of existing and newly proposed features were presented.

Olmedilla et al. [21] proposed a 1D convolutional neural network (CNN) to predict whether a review is neutral, helpful, or unhelpful. CNN was used to perform cluster analysis and categorize the data into distinct groups. The experiment was conducted on 1164 internet reviews from the category Cars and Motorcycles. The experimental results showed that the proposed approach archived an accuracy of 66%. The clustering results show that helpful reviews provide details about cars and their features, whereas unhelpful reviews were mostly written on car-related companies. This demonstrates that the details and topics discussed in the review can have a significant impact on the usefulness of online customer reviews. Kashyap et al. [22] argued that existing solutions for predicting review usefulness did not capture the key characteristics of review usefulness. Using key review characteristics, a mixed-method approach was proposed.

The number of helpfulness votes received by a single online customer review varies over time. As a result, a study has collected Amazon product reviews and tracked the review helpfulness count over a six-week period to examine the helpful votes and choose a better target. The experimental results for classifying helpful and unhelpful reviews using BERT show promising results not only within the same domain but also across domains [15]. A study reported that existing studies on review helpfulness prediction did not take into account consistency between the text of reviews and the star rating associated with them. To avoid loss of consistency and information, a CCN-based model was proposed that used textual review features and a high-dimensional feature vector generated for the star rating. The results of experiments using an Amazon review dataset revealed that CNN outperformed other models [23].

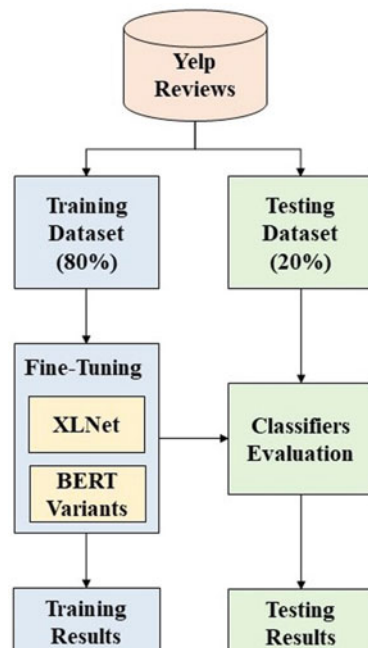
A big portion of online customer reviews not only contains textual reviews but also contains images. Most of the existing studies ignored the information exchange between review text and accompanied images. Predicting the helpfulness of online customer reviewing using a multimodal approach is a difficult task due to the link of information contained in review text and images. The perception of the helpfulness

of such reviews varies from individual to individual. Some may perceive a review helpful solely based on text, while for others, the review may appear helpful by considering along with the image. The information being delivered by the images can complement or substitute the information being contained in the review text. A study [24] proposed a novel technique for predicting review usefulness through the use of a multimodal approach that captures the interaction of information in review text and image. The complementary and substitute nature of the information was extracted from images and then used to predict usefulness in conjunction with the review text. The findings of the study demonstrated that the proposed method outperformed existing models.

### 3 Research Methodology

The overall sequence of stages in the research methodology is illustrated in Fig. 1. The three key stages include dataset preparation, fine-tuning, and evaluation. Each stage is described in detail in the sections below.

**Fig. 1** Stages in the research methodology



### 3.1 Dataset

This study makes use of the benchmark dataset [14] of 10,000 Yelp business reviews. This dataset is a subset of the 6,990,280 reviews in the publicly available Yelp open dataset [25]. The benchmark dataset is well balanced, with 5000 helpful and 5000 unhelpful reviews. The dataset is divided into 80% training and 20% testing datasets.

### 3.2 Fine-Tuning

In this stage, 10% of the training dataset is used to validate pre-trained models that have been fine-tuned using the training dataset. The models fine-tuned in this study included XLNet [26], Albert [27], DistilBert [28], and Roberta [29]. A quick overview of the models used in this study is provided in the following paragraphs. All models are fine-tuned using Google Colab and GPU (Tesla T4). The reviews are first tokenized with model-specific tokenizers. Each model is fine-tuned using six different sequence lengths: 64, 128, 256, 320, 348, and 512. The batch size of 32 is used for sequence lengths of 64–320, while the batch size of 16 is used for sequence lengths of 384 and 512 for all models due to limited memory. The epoch size is set to 4 and the learning rate of 2e-5 is used for all models with the AdamW optimizer.

XLNet: A study [26] proposed a generalized autoregressive language model, XLNet, used to learn representations of text sequences without supervision. When using the BERT, some limitations include ignoring the relationship between the masked positions and having a problem with pre-train fine-tune. This method overcomes the limitation of BERT and makes it possible to learn in both directions by increasing the expected likelihood across all possible factorization orders. The autoregressive language modeling and autoencoding methods are combined in the generalized autoregressive pre-training method XLNet. The XLNet considerably improved across prior pre-training targets on a number of different Natural Language Processing (NLP) tasks such as question answering, analyzing sentiment, natural language inference, and document ranking.

Albert: To address the two difficulties of reduced memory usage and slower BERT training, a study [27] proposed parameter-reduction techniques known as Albert. Extensive empirical data suggest that the proposed Albert model is significantly easier to scale than the typical BERT model. Furthermore, Albert consistently supports tasks that involve multi-sentence input, as well as the usage of self-supervised loss and inter-sentence coherence. Despite having fewer parameters than the BERT large model, Albert outperformed it on the benchmark datasets.

DistilBERT: A study [28] proposed DistilBERT a method for pre-training the general-purpose language representation model, that can be fine-tuned to achieve better performance than state-of-the-art while reducing the computational training time and BERT resource constraints. The suggested model size has been reduced for the BERT model by 40%, and speed increased by 60%. To take advantage of

the inductive biases that larger models develop during pre-training, this model introduced a triple loss that combines language modeling, distillation, and cosine-distance losses. The suggested model is also cheaper to pre-train and is smaller, faster, and lighter. The proposed model's suitability for on-device computation experiments and a comparative on-device study has been demonstrated.

**RoBERTa:** A study [29] suggested a replication study of BERT pre-training that thoroughly considers the effect of training data size and a number of significant hyper-parameters. They found that despite BERT's severe undertraining, it could perform on par with or better than every model that had been released before it. The upgraded pre-training strategy known as RoBERTa produces cutting-edge outcomes on NLP benchmark datasets. These findings highlight the significance of early, unconsidered design decisions and raise questions about more recent advances.

### 3.3 *Evaluation*

The evaluation of fine-tuned XLNet, Albert, DistilBert, and Roberta is performed using a testing dataset. The test dataset, like the training dataset, is tokenized using a model-specific tokenizer. The batch size of 32 is used for all models for testing. The evaluation metrics used in this study are accuracy (Accur.), precision (Precis.), recall, and *F1*-score. Each metric is calculated for all models for sequence lengths of 64, 128, 256, 320, 348, and 512. The *F1*-score is used as the primary evaluation metric in this study. Furthermore, the other metrics are provided as additional measures for future research to compare the results.

## 4 Results and Discussion

This section reports and discusses the experimental results in depth. First, the training and validation results for all four models are presented and discussed. Following that, the performance of each of the four models in comparison to the benchmark results is thoroughly discussed. Table 1 displays the training and validation results for Albert for each batch size, sequence length, and epoch. The training loss decreases from epoch 1 to epoch 4 for all sequence lengths, whereas the validation loss varies from one epoch to the next differently for all sequence lengths. The validation loss for epoch 1 with sequence length 64 is 0.637, which is reduced to 0.417 in epoch 4. While the validation loss in epoch 1 is 0.618, it is reduced to 0.598 in epoch 2. The validation accuracy increased from 0.646 in epoch 1 to 0.680 in epoch 2. After that, it is reduced to 0.669 in epoch 3 and then increased to 0.670 in epoch 4. It is interesting to see how the model leads to overfitting after epoch 2 as validation loss increases from epoch 3. The highest validation accuracy of 0.736 is obtained in epoch 1 with a sequence length of 128.

**Table 1** Training and validation results of Albert

Batch size	Seq. len	Epoch	Train. loss	Valid. loss	Valid. accur
32	64	1	0.637	0.616	0.646
		2	0.598	0.598	0.680
		3	0.520	0.618	0.669
		4	0.417	0.648	0.670
	128	1	0.596	0.555	0.736
		2	0.551	0.555	0.734
		3	0.466	0.575	0.708
		4	0.344	0.614	0.718
	256	1	0.597	0.563	0.714
		2	0.567	0.561	0.716
		3	0.486	0.564	0.728
		4	0.367	0.590	0.719
	320	1	0.585	0.562	0.723
		2	0.547	0.563	0.714
		3	0.468	0.577	0.715
		4	0.331	0.632	0.680
16	384	1	0.573	0.562	0.720
		2	0.554	0.576	0.709
		3	0.505	0.566	0.715
		4	0.445	0.577	0.718
	512	1	0.593	0.597	0.711
		2	0.569	0.622	0.686
		3	0.501	0.577	0.701
		4	0.370	0.655	0.705

Table 2 shows the DistilBert training and validation results for various batch sizes, sequence lengths, and epochs. The training loss continues to decrease for all sequence lengths at all epochs. The sequence length of 384 in epoch 1 achieves the highest validation accuracy of 0.734. In epoch 1, for a sequence length of 384, the training loss is 0.569 and the validation loss is 0.558. The training and validation results for Roberta are given in Table 3. The training loss is seen decreasing from epoch 1 to epoch 4 for all sequence lengths. The validation loss decreases and then increases for all sequence lengths except for the sequence lengths of 512. The best validation accuracy of 0.740 is achieved in epoch 4 for the sequence length of 320. The training loss of 0.442 and the validation loss of 0.570 are obtained in epoch 4 using the sequence length of 320. The validation accuracy fluctuates using all sequence lengths in different epochs.

Table 4 shows the XLNet training and validation results. The training loss, like the other three models, decreases from epoch 1 to epoch 4 for all sequence lengths.

**Table 2** Training and validation results of DistilBert

Batch size	Seq. len	Epoch	Train. loss	Valid. loss	Valid. accur
32	64	1	0.626	0.612	0.676
		2	0.575	0.604	0.678
		3	0.494	0.621	0.681
		4	0.435	0.658	0.681
	128	1	0.593	0.557	0.729
		2	0.551	0.554	0.726
		3	0.485	0.569	0.716
		4	0.433	0.598	0.710
	256	1	0.582	0.559	0.729
		2	0.548	0.552	0.723
		3	0.481	0.577	0.718
		4	0.434	0.601	0.708
	320	1	0.579	0.558	0.733
		2	0.549	0.556	0.726
		3	0.483	0.576	0.724
		4	0.433	0.600	0.701
16	384	1	0.569	0.558	0.734
		2	0.539	0.572	0.729
		3	0.445	0.628	0.710
		4	0.341	0.700	0.693
	512	1	0.569	0.556	0.730
		2	0.541	0.565	0.724
		3	0.459	0.608	0.710
		4	0.363	0.672	0.698

Except for the sequence length of 512, the validation loss for XLNet decreases and then increases for all sequence lengths. The validation loss for a sequence length of 512 increases from 0.556 in epoch 1 to 0.613 in epoch 2. The validation loss decreases to 0.590 in epoch 3 and then increases to 0.738 in epoch 4. XLNet achieves the best validation accuracy of 0.745 in epoch 2 with a sequence length of 128. It is interesting to note that for all four models, the validation loss for shorter sequence lengths decreases at first and then begins to increase, whereas, for longer sequence lengths, the validation loss increases from beginning to end. Similarly, for shorter sequence lengths, validation accuracy increases with epoch size, while for longer sequence lengths, the opposite trend is observed.

Table 5 shows the evaluation results for all models, as well as the benchmark results. Using a test dataset of 2000 Yelp reviews, the accuracy, precision, recall, and *F1*-score of all models are calculated over six different sequence lengths. It is interesting to note that different models achieved the best results at different sequence

**Table 3** Training and validation results of Roberta

Batch size	Seq. len	Epoch	Train. loss	Valid. loss	Valid. accur
32	64	1	0.618	0.598	0.683
		2	0.576	0.595	0.679
		3	0.505	0.617	0.688
		4	0.440	0.667	0.665
	128	1	0.603	0.580	0.705
		2	0.567	0.549	0.730
		3	0.498	0.554	0.736
		4	0.438	0.579	0.729
	256	1	0.589	0.567	0.716
		2	0.557	0.558	0.714
		3	0.506	0.571	0.724
		4	0.432	0.595	0.734
	320	1	0.586	0.568	0.708
		2	0.559	0.555	0.730
		3	0.506	0.555	0.716
		4	0.442	0.570	0.740
16	384	1	0.578	0.571	0.735
		2	0.561	0.568	0.724
		3	0.494	0.547	0.736
		4	0.396	0.601	0.728
	512	1	0.575	0.556	0.735
		2	0.558	0.568	0.726
		3	0.496	0.571	0.730
		4	0.398	0.620	0.736

lengths, in contrast to the previous study's [14] findings, which did not compare the results for different models based on sequence lengths. The BERT base model achieved the benchmark *F1*-score of 0.717 with a sequence length of 320. Albert had the highest *F1*-score of 0.707 with sequence lengths of 128 and 512, while DistilBert had the highest *F1*-score of 0.693 with a sequence length of 128. Albert and DistilBert both failed to outperform the existing results of the BERT base model. Roberta received the best *F1*-score of 0.718 with a sequence length of 384, which was slightly higher than the previous benchmark. By archiving an *F1*-score of 0.730 with a sequence length of 256, XLNet outperforms all other models. A comparison of the *F1*-score achieved by all four models along with the benchmark results of the BERT base model is given in Fig. 2.

**Table 4** Training and validation results of XLNet

Batch size	Seq. len	Epoch	Train. loss	Valid. loss	Valid. accur
32	64	1	0.627	0.668	0.620
		2	0.591	0.594	0.690
		3	0.514	0.616	0.680
		4	0.439	0.654	0.686
	128	1	0.599	0.551	0.738
		2	0.566	0.541	0.745
		3	0.507	0.545	0.740
		4	0.438	0.581	0.733
	256	1	0.608	0.570	0.721
		2	0.562	0.546	0.741
		3	0.508	0.559	0.730
		4	0.443	0.598	0.716
	320	1	0.585	0.576	0.713
		2	0.556	0.548	0.733
		3	0.490	0.561	0.726
		4	0.407	0.617	0.715
16	384	1	0.590	0.554	0.725
		2	0.558	0.578	0.718
		3	0.456	0.610	0.730
		4	0.338	0.735	0.714
	512	1	0.586	0.556	0.720
		2	0.561	0.613	0.701
		3	0.468	0.590	0.725
		4	0.368	0.738	0.699

**Table 5** Evaluation results

Classifier	Seq. len	Accur	Precis	Recall	<i>F</i> 1-score
BERT [14]	64	0.668	0.650	0.725	0.685
	128	0.694	0.690	0.703	0.696
	256	0.692	0.677	0.735	0.705
	320	0.707	0.693	0.743	0.717
	384	0.683	0.673	0.711	0.691
	512	0.697	0.709	0.666	0.687
Albert	64	0.667	0.670	0.656	0.663
	128	0.706	0.705	0.708	0.707
	256	0.702	0.699	0.710	0.704
	320	0.689	0.685	0.700	0.692
	384	0.701	0.694	0.717	0.705
	512	0.707	0.706	0.708	0.707
DistilBert	64	0.665	0.659	0.681	0.670
	128	0.689	0.684	0.702	0.693
	256	0.686	0.688	0.679	0.683
	320	0.685	0.688	0.676	0.682
	384	0.687	0.686	0.688	0.687
	512	0.684	0.683	0.686	0.685
Roberta	64	0.675	0.653	0.743	0.695
	128	0.705	0.696	0.728	0.712
	256	0.706	0.694	0.737	0.715
	320	0.701	0.692	0.724	0.708
	384	0.705	0.686	0.753	0.718
	512	0.697	0.680	0.745	0.711
XLNet	64	0.671	0.635	0.800	0.708
	128	0.697	0.686	0.724	0.705
	256	0.708	0.678	0.790	0.730
	320	0.698	0.672	0.775	0.720
	384	0.699	0.675	0.767	0.718
	512	0.687	0.655	0.787	0.715

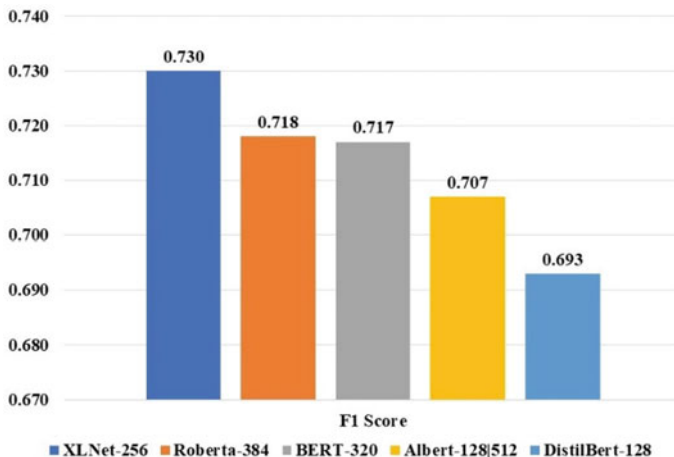


**Fig. 2** Comparison of best *F1*-scores for all models

## 5 Conclusion

In this study, XLNet and three BERT variants, Albert, DistilBert, and Roberta, are fine-tuned to examine their effectiveness in classifying helpful and unhelpful online customer reviews. All four models are fine-tuned for six different sequence lengths: 64, 128, 256, 320, 384, and 512. This study uses a benchmark dataset of 10,000 Yelp business reviews for fine-tuning and testing. The validation results revealed that the best results are obtained at various sequence lengths. XLNet achieves the highest validation accuracy of 0.745 with a sequence length of 128. Based on test dataset evaluations, XLNet achieved an *F1*-score of 0.730, outperforming all models, including the BERT base model's previous benchmark *F1*-score of 0.717. Furthermore, when compared to the BERT base model, Roberta obtained a slightly higher *F1*-score of 0.718. Albert and DistilBert, on the other hand, failed to outperform the existing. The previous benchmark *F1*-score was obtained with a sequence length of 320, whereas the best *F1*-score obtained in this study was obtained with a sequence length of 256. With a sequence length of 320, XLNet also achieves the second-highest *F1*-score of 0.720. XLNet outperforms BERT and its variants in the classification of helpful and unhelpful reviews, as well as in other popular tasks using benchmark datasets reported in the literature. Future research will focus on predicting the usefulness of online customer reviews using cross-platform transfer learning.

## References

1. Naeem, M.: Do social media platforms develop consumer panic buying during the fear of Covid-19 pandemic. *J. Retail. Consum. Serv.* **58**, 102226 (2021)

2. Stawicki, S.P., Firstenberg, M.S., Papadimos, T.J.: The growing role of social media in international health security: the good, the bad, and the ugly. In: Global Health Security: Recognizing Vulnerabilities, Creating Opportunities, pp. 341–357 (2020)
3. Bilal, M., et al.: Social profiling: a review, taxonomy, and challenges. *Cyberpsychol. Behav. Soc. Netw.* **22**(7), 433–450 (2019)
4. Taneja, B.: The Digital Edge for M-Commerce to Replace E-Commerce, in Emerging Challenges, Solutions, and Best Practices for Digital Enterprise Transformation, pp. 299–318. IGI Global (2021)
5. Lee, P.S., Chakraborty, I., Banerjee, S.: Artificial intelligence applications to customer feedback research: a review. *Artific. Intell. Mark.* 169–190 (2023)
6. Guan, C., Hung, Y.-C., Liu, W.: Cultural differences in hospitality service evaluations: mining insights of user generated content. *Electron. Market.* 1–21 (2022)
7. Billiore, S., Anisimova, T.: Panic buying research: a systematic literature review and future research agenda. *Int. J. Consum. Stud.* **45**(4), 777–804 (2021)
8. Zhang, J., Zhang, J., Zhang, M.: From free to paid: customer expertise and customer satisfaction on knowledge payment platforms. *Decis. Support Syst.* **127**, 113140 (2019)
9. Bilal, M., et al.: Profiling users' behavior, and identifying important features of review "helpfulness." *IEEE Access* **8**, 77227–77244 (2020)
10. Yang, B., et al.: Exploiting user experience from online customer reviews for product design. *Int. J. Inf. Manage.* **46**, 173–186 (2019)
11. Bilal, M., et al.: Predicting helpfulness of crowd-sourced reviews: a survey. In: 2019 13th International Conference on Mathematics, Actuarial Science, Computer Science and Statistics (MACS). IEEE (2019)
12. Wu, Y., et al.: Fake online reviews: literature review, synthesis, and directions for future research. *Decis. Support Syst.* **132**, 113280 (2020)
13. Qin, J., Zheng, P., Wang, X.: Comprehensive helpfulness of online reviews: a dynamic strategy for ranking reviews by intrinsic and extrinsic helpfulness. *Decis. Support Syst.* **163**, 113859 (2022)
14. Bilal, M., Almazroi, A.A.: Effectiveness of fine-tuned BERT model in classification of helpful and unhelpful online customer reviews. *Electron. Commer. Res.* 1–21 (2022)
15. Wu, S.-H., Chen, Y.-K.: Cross-domain helpfulness prediction of online consumer reviews by deep learning model. In: 2020 IEEE 21st International Conference on Information Reuse and Integration for Data Science (IRI). IEEE (2020)
16. Liu, Y., et al.: Modeling and predicting the helpfulness of online reviews. In: 2008 Eighth IEEE International Conference on Data Mining. IEEE (2008)
17. Mousavizadeh, M., et al.: An investigation of peripheral and central cues of online customer review voting and helpfulness through the lens of elaboration likelihood model. *Inf. Syst. Front.* 1–21 (2022)
18. Hu, H.-F., Krishen, A.S.: When is enough, enough? Investigating product reviews and information overload from a consumer empowerment perspective. *J. Bus. Res.* **100**, 27–37 (2019)
19. Yi, J., Oh, Y.K.: The informational value of multi-attribute online consumer reviews: a text mining approach. *J. Retail. Consum. Serv.* **65**, 102519 (2022)
20. Bilal, M., et al.: Profiling reviewers' social network strength and predicting the "helpfulness" of online customer reviews. *Electron. Commer. Res. Appl.* **45**, 101026 (2021)
21. Olmedilla, M., Martínez-Torres, M.R., Toral, S.: Prediction and modelling online reviews helpfulness using 1D convolutional neural networks. *Exp. Syst. Appl.* **198**, 116787 (2022)
22. Kashyap, R., Kesharwani, A., Ponnam, A.: Measurement of online review helpfulness: a formative measure development and validation. *Electron. Commerc. Res.* 1–34 (2022)
23. Li, X., Li, Q., Kim, J.: A review helpfulness modeling mechanism for online E-commerce: multi-channel CNN end-to-end approach. *Appl. Artif. Intell.* **37**(1), 2166226 (2023)
24. Xiao, S., et al.: Complementary or substitutive? A novel deep learning method to leverage text-image interactions for multimodal review helpfulness prediction. *Exp. Syst. Appl.* **208**, 118138 (2022)

25. Yelp Open Dataset: Available from: <https://www.yelp.com/dataset>. Accessed 02 May 2023
26. Yang, Z., et al.: Xlnet: generalized autoregressive pretraining for language understanding. *Adv. Neural Inf. Proc. Syst.* **32** (2019)
27. Lan, Z., et al.: Albert: a lite bert for self-supervised learning of language representations. arXiv preprint [arXiv:1909.11942](https://arxiv.org/abs/1909.11942) (2019)
28. Sanh, V., et al.: DistilBERT, a distilled version of BERT: smaller, faster, cheaper and lighter. arXiv preprint [arXiv:1910.01108](https://arxiv.org/abs/1910.01108) (2019)
29. Liu, Y., et al.: Roberta: a robustly optimized bert pretraining approach. arXiv preprint [arXiv:1907.11692](https://arxiv.org/abs/1907.11692) (2019)

# Characterization and Absorption Test of Cellulose from Oil Palm Empty Fruit Bunch for Potential Use in Oil Spill Clean-Up



N. F. Afandi, Adrian Wei-Yee Tan, Pravin Mariappan, Savisha Mahalingam, and Abreeza Manap

**Abstract** Empty fruit bunch (EFB) is among the major agricultural waste from the oil palm industry, but its cellulose extract has the potential to clean up hazardous and large-scale oil spills. This research aims to extract cellulose from the oil palm empty fruit bunch fiber and study the water absorption rate of the cellulose. First, extraction processes were conducted using 15% sodium hydroxide (NaOH) and 10% hydrogen peroxide ( $H_2O_2$ ). Then, the morphology of empty fruit bunch fiber, crystalline index, and phase identification was characterized using scanning electron microscopy (SEM), and X-Ray diffraction (XRD), respectively. The extracted cellulose was found to have a smaller diameter (8–50  $\mu m$ ). Alkaline treatment assisted in the removal of hemicellulose, while bleaching aided in the removal of lignin and discoloration. As a result, the extracted cellulose showed a high crystalline index of 30.67%. Moreover, the water absorption rate of the extracted cellulose is calculated, and the maximum water absorption rate of the extracted cellulose was recorded at 269.50%. Hence, this research provides an efficient method for extracting cellulose from oil palm empty fruit bunch fiber and the highest yield of water absorption from the extracted cellulose, primarily used as aerogel in oil spill cleaning.

**Keywords** Oil palm · Empty fruit bunch · Absorption rate

---

N. F. Afandi (✉) · P. Mariappan · A. Manap

Department of Mechanical Engineering, College of Engineering, Universiti Tenaga Nasional, Jalan IKRAM-UNITEN, 43000 Kajang, Selangor, Malaysia  
e-mail: [nurfanizan@uniten.edu.my](mailto:nurfanizan@uniten.edu.my)

N. F. Afandi · S. Mahalingam · A. Manap

Institute of Sustainable Energy, Universiti Tenaga Nasional, Jalan IKRAM-UNITEN, 43000 Kajang, Selangor, Malaysia

A. W.-Y. Tan

School of Engineering, University of Southampton Malaysia, Iskandar Puteri, 79100 Johor, Malaysia

## 1 Introduction

Oil spills on the ocean have been a key concern globally due to their severe hazardous and long-term impact on the ecosystem, which ends up in the food chain and adversely affects all living health. Spilled oil would damage living organisms since it is toxic in its chemical constituents. Numerous approaches are available to absorb, adsorb, and clean up the oil spill. According to Thai et al. [1], existing oil spill cleaning techniques include chemical, bioremediation, and physical methods. Chemical methods, such as solidifiers and in-situ burning (IBS) are common methods for cleaning oil spills. However, solidifiers are limited to small spills near shorelines and cannot be used where the oil cannot be immersed immediately [2]. Meanwhile, IBS is deliberated as the last preference form since safety is the primary concern since the marine habitat takes longer to recover from the formation of the viscous-tar-like residue. The bioremediation method uses microorganisms that occur naturally or deliberately to consume and decompose contaminants in the ecosystem to break the polluted area. This approach is well-known for its efficiency and cost-effectiveness in eliminating oil with less environmental harm [3].

Nevertheless, physical methods such as absorption were considered the most effective oil spill cleaning approach. The oil absorbents can be classified as inorganic material, synthetic polymer, and natural fiber. Inorganic material comprises vermiculite, exfoliated graphite, fly, and ash, while synthetic organic material includes polypropylene and polyurethane. Natural fibers, such as cotton, wood fiber, and sugarcane bagasse were used in oil spill cleaning [4]. Even though these materials can absorb the oil spill very well, researchers would focus on natural cellulose-based aerogel for oil spill cleaning. Nguyen et al. [4] revealed that cellulose-based aerogel has encouraging potential as it is a renewable oil absorbent, abundantly available, low cost, and has high capacity for oil absorption.

Biomass lignocellulose was recognized for possible use in the chemical and biomaterial industry. It has high potential to be used in aerogel production. Cellulose is a linear homopolymer with high solution viscosity, high crystallization tendency, and the ability to form fibrillary strands [5]. The cellulose is extracted from the biomass by eliminating the amorphous polymer (lignin and hemicellulose) and the impurities from the biomass before being used as a natural material for oil spill cleaning. One of the biomasses that can be used in cellulose extraction is the oil palm fruit bunch (OPEFB). The waste of the OPEFB becomes a major concern and utilizing the waste can reduce the landfilled at low economic value. Hasanuzzaman et al. [6] reported that empty fruit bunches (EFB) are sturdy lingo-cellulosic waste for producing bioethanol and creating electricity through thermo-chemical or chemical alteration methods. Moreover, many researchers focus on using cellulose derived from OPEFB as a sound absorber, but more studies are needed in water absorption applications, especially for oil spill cleaning.

Thus, this research aims to extract cellulose from the oil palm empty fruit bunch fiber and study the water absorption rate of the cellulose to be used in aerogel production. First, alkaline and bleaching treatments were used to extract cellulose from

empty fruit bunch (EFB) fiber. Then, the morphological, phase identification, and crystalline index changes in the raw material were characterized after alkaline treatment and extracted cellulose. Next, the moisture content and water absorption rate of cellulose derived from EFB were determined before being used in aerogel oil spill cleaning.

## 2 Methodology

The oil palm empty fruit bunch (OPEFB) fiber mats were obtained from the Malaysian Palm Oil Board (MPOB). The pre-treatment was done by cutting the OPEFB into smaller lengths and dried for three days at room temperature. Then, the OPEFB was immersed in distilled water to eliminate the dirt and sand particles until the water turned colorless. The fiber was dried again at room temperature for two days. The dried OPEFB were weighed to 5 g for each sample. The dried sample was treated at 90–100 °C with continuous stirring using a 5:100 (g/ml) fiber-to-solution ratio with 15% sodium hydroxide (NaOH), with a magnetic stirrer. The sample was cooled in the fuse chamber for 30 min after the alkali treatment. Subsequently, the cooled sample was rinsed with distilled water for multiple times. The sample was filtered and dried at room temperature. Then, a bleaching treatment was applied using 10% hydrogen peroxide (H<sub>2</sub>O<sub>2</sub>) at 90–100 °C for one hour with continuous stirring of a constant fiber-to-solution ratio of 5:100 (g/ml). After the treatment, the sample was cooled in the fuse chamber for 30 min before being rinsed several times with distilled water. The extracted cellulose was then dried in a furnace at 60 °C for one hour [7].

Then, the morphology of samples was analyzed using scanning electron microscopy (SEM, JEOL JSM-6010) PLUS/LV at 15 kV. The phase identification and crystalline index were characterized using X-Ray diffraction (XRD, D8 Advance, and Bruker AXS). The samples were scanned from 5° to 60° by utilizing Cu K $\alpha$  radiation ( $\lambda = 1.54060 \text{ \AA}$ ) at 2 $\theta$ . Then, the moisture content of the OPEFB is calculated based on:

$$\text{Moisture content}(\%) = \frac{w_h - w_o}{w_o} \times 100 \quad (1)$$

where the  $w_h$  (g) is the final weight of the cellulose, whereas  $w_o$  (g) is the initial weight of the cellulose. Meanwhile, the absorption test, based on UNE-EN ISO 62:2008, is determined by:

$$M_t(\%) = \frac{m_t - m_l}{m_l} \times 100 \quad (2)$$

where  $M_t$  (g/g) is the water absorption rate of the cellulose at individual time  $t$  (min),  $m_t$  (g) is the weight of the sample after absorption, and  $m_l$  (g) is the weight of the dried cellulose.

### 3 Results and Discussions

#### 3.1 Analysis of Extracted Cellulose from OPEFB

Figure 1 shows the discoloration of the OPEFB before and after the treatments. The discoloration on the sample was because of the elimination of lignin and hemicellulose following the extraction treatment. According to Chen et al. [8], hemicellulose removal from the sample will cause mild discoloration, while lignin removal causes severe discoloration. The color of plant fiber is influenced by the content of phenolic substances such as lignin and hemicellulose [8]. Alkali treatments were conducted to eliminate hemicellulose, lignin, and foreign substances from the empty fruit bunch sample. Thus, the alteration of color is less significant than after the bleaching treatment was carried out. Bleaching treatments were carried out to remove lignin from the sample and will cause major changes in the discoloration. The white residues that can be observed in Fig. 2 indicate the removal of lignin from the sample. The sample must be filtered several times to obtain pure cellulose.

The surface morphology of the raw empty fruit bunch, after alkali treatment and the extracted cellulose sample, is shown in Fig. 3. The raw empty fruit bunch sample has a diameter of 50–600 with an irregular surface before the treatment. Figure 3a indicates that several foreign contaminants are bound to the surface of the raw empty fruit bunch surface before the treatment.

There was no significant transformation in the sample diameter after the alkali treatment was done. Major fluctuations in the fiber morphology can be observed in Fig. 3b after the alkaline treatment, whereby the sample became clean, and the roughness on the sample surface was reduced because of the elimination of impurities

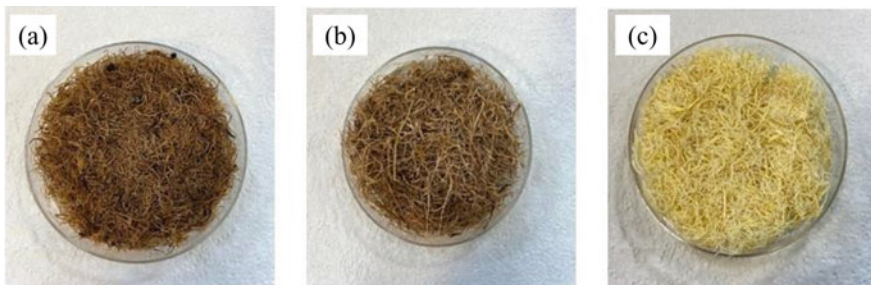


**Fig. 1** Oil palm empty fruit bunch **a** Raw material, **b** After alkaline treatments, and **c** Extracted cellulose

**Fig. 2** Bleaching treatment of the extracted cellulose

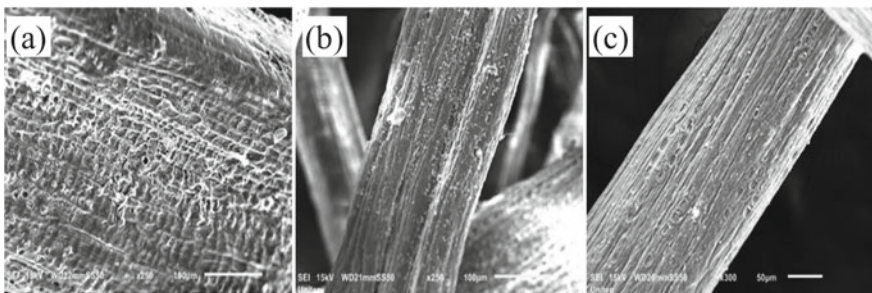


**Fig. 3** Surface morphology of **a** Raw empty fruit bunch, **b** After alkali treatment, and **c** Extracted cellulose

from the surface. Figure 3b also indicates that the foreign substances are no longer stuck to the sample surface. However, there are signs of damage on the samples, which might result from the foreign material adhesion. The extracted cellulose sample has a smaller diameter of 8–50  $\mu\text{m}$ , and the sample surface is smoother, as shown in Fig. 3c.

Alkaline treatment with 4% of NaOH could help extract foreign substances from the rice husk sample, as reported by Johar et al. [9]. However, this research showed that the sample diameter of 170  $\mu\text{m}$  does not change after alkaline treatment. However, after contact with bleaching treatment, the diameter of the samples was decreased to 7  $\mu\text{m}$  [9].

Alkaline treatment using 15% NaOH (w/w) at high temperatures plays a key part in extracting the foreign particles from the surface of the sample without causing any changes in the diameter length. Oushabi et al. stated that this is attributable to the fact that the alkaline treatment has removed only a small amount of lignin. In addition, the alkaline treatment enhances the thermal conductivity of the date palm fiber since the waxy layer and other impurity components were removed from the surface of the sample [10]. Kumneadklang et al. stated that the fiber treatment

typically breaks the lignocellulosic complex by alkaline and bleaching treatment, solubilizing the lignin and hemicellulose to reveal the exposed cellulose to more porosity and surface area. Thus, this will lead to an increment in the cellulosic fiber being arranged and distributed separately, making them more available for cellulose extraction [7].

According to Watkins et al., lignin is a compulsory material in plant fiber. After removing lignin, the fiber sample prevails bound to each other, resulting in an unchanged sample diameter [11]. In contrast, Alemdar et al. stated that bleaching treatment significantly removes lignin. In addition, the discharge of the impurities by splitting the bonds between hemicellulose and lignin triggers the fibers to break down into individual fibers, making the diameter smaller [12].

### 3.2 Cellulose Crystallinity

Cellulose crystallinity was used to estimate the fiber thermal stability, absorptive capacity, elasticity, and extra physical belongings that are significant for industrial applications. Referring to Fig. 4, the main peak at  $22.5^\circ$  raises the crystalline structure of the extracted cellulose, whereas the low intensity at  $16.5^\circ$  denotes the amorphous background on the sample. Table 1 gives the crystalline index value for all the three samples. The XRD analysis results displayed a crystallization level of 22.53% for the oil palm empty fruit bunch before treatment and slightly rose after the alkaline treatment (26.75%) and extracted cellulose (30.36%).

Figure 4 shows that the core peak at  $22.5^\circ$  for the extracted cellulose sample is sharper than the empty fruit bunch fiber sample before and after the alkaline treatment. According to Sheltami et al., this is due to the increased removal of amorphous polymers, which makes the crystal structure in cellulose samples clearer than other

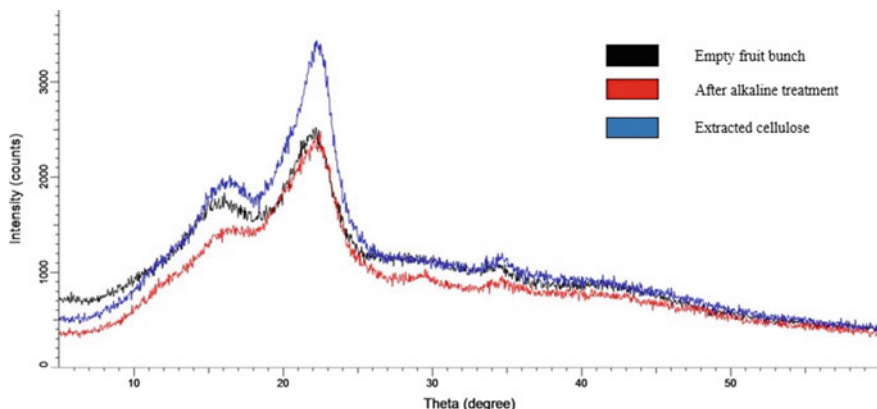


**Fig. 4** X-ray diffraction pattern of the raw empty fruit bunch, after alkaline treatment, and extracted cellulose

**Table 1** Crystal index for empty fruit bunch before treatment, after alkaline treatment, and extracted cellulose

Sample	$2\theta (I_{\text{am}})$ ( $^{\circ}$ )	$2\theta (I_{002})$ ( $^{\circ}$ )	$X_c$ (%)
Empty fruit bunch	16.5	22.2	22.53
After alkali treatment	16.5	22.2	26.75
Extracted cellulose	16.5	22.5	30.36

$I_{\text{am}}$ : Peak intensity of the amorphous material;  $I_{002}$ : Peak intensity of the crystalline material;  $X_c$ : Crystalline index

samples [13]. The crystallinity increase can be measured by eliminating the hemicelluloses and lignin in the amorphous areas. The higher crystalline index indicates a higher absorption rate of the cellulose.

Table 1 also gives that the intensity of cellulose crystals extracted was lower than the intensity of cellulose extracted from empty fruit bunch (38%), reported by Ngadi et al. [14], which added acetic acid to acidify the sodium hydroxide for the alkaline treatment. Ngadi et al. obtained a higher crystalline index than this research due to the addition of acetic acid to sodium hydroxide for the alkaline treatment. This causes the alkaline agent to be more reactive to eliminate the noncellulosic fiber, for example, hemicellulose and lignin from the empty fruit bunch fiber.

### 3.3 Moisture Content

Water content and interaction with the components of any cellulosic material have a significant impact on the physical properties. The approach of water molecules engaging with and dispersing cellulose within cellulosic material is often complex, and their dynamic structure is crucial to its application [15]. Table 2 indicates the moisture content of the extracted cellulose after the bleaching treatment was done. Moisture content was conducted to study the structural changes in the extracted cellulose. Significant crystal structure changes can be observed due to the moisture content on the sample. Fotie et al. reported that moisture content on the cellulose affects the mobility of the water and swelling behavior in the sample [16]. As mentioned by Rongpipi et al. [17], moisture absorption for cellulose occurs mainly by hydrogen bonding of water to active hydroxyls in less-ordered areas on the membranes of elementary fibers and its spontaneous fibrillary transformations at a relative humidity below 50–60%. The recovery of moisture from cellulose is thus a more straightforward indicator of cellulose adequacy to reactants. The variation in final weight was due to inconsistency in the filtration period. Each sample took about 5–8 min to undergo the filtration treatment. The sample was cellulose; thus, it started to absorb water during the filtration treatment, which resulted in differences in the final weight. The higher the moisture content percentage, the lower the moisture content in the sample. Samples with higher moisture content are suitable for the absorption test since it has a low amount of moisture in the sample, as samples need to be fully dried before the absorption test.

**Table 2** Moisture content of extracted cellulose after bleaching treatment (%)

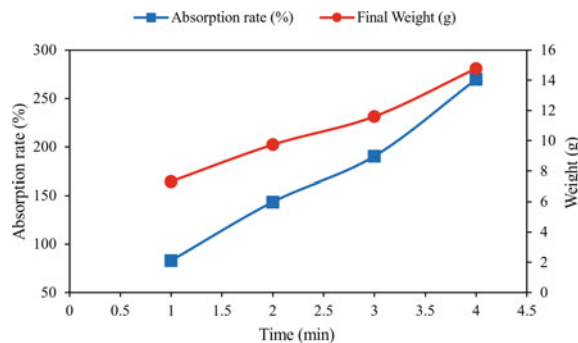
Sample	Initial weight (g)	Final weight (g)	Moisture content (%)
1	5	13.70	174.0
2	5	15.18	203.6
3	5	14.71	194.0
4	5	14.23	184.6
Average	5	14.45	189.05

### 3.4 Water Absorption Rate

Most natural cellulose structures are crystalline and amorphous domains, variable proportion and liable on both the source and history. According to Maslinda et al. [18], amorphous cellulose samples were often used in a model experiment to study the cellulose behavior under various conditions. Amorphous cellulose is characterized by a nanoporous structure with an exposed hydroxyl site that tends to make it strongly water-absorbent. Water absorption in hydrophilic polymers like cellulose is a complicated procedure driven mainly by hydrogen bond formation and breaking. Because of the porous character and flexibility of the biopolymers, water molecules can easily be absorbed and attracted by strong hydrogen bond energy [18]. Factors that affect the water absorption rates include the weight of the sample, period of immersion, and sample structure. Thus, this research studied the period of immersion of the sample.

Figure 5 shows the absorption capabilities of the extracted cellulose as a function of time. The absorption capabilities gradually increased with a longer immersion period, where the absorption rate increased from 83 to 269.5% with an immersion period of 1–4 min, respectively. This has proved that a material immersion time affects the absorption rate. High water absorption can be observed in 4 min immersion due to the post-treatment degradation of cellulose, resulting in rupture cells, porous, and improved hydrophilic structure of the cellulose.

**Fig. 5** Water absorption rate and weight of extracted cellulose as a function of time



An increase in the hydrophilic of cellulose will increase the absorption. However, the extracted cellulose must undergo a cross-linking agent to be hydrophilic before aerogel fabrication for oil spill cleaning. Weight gain changes can be recognized for all four samples, which indicates the Fickian diffusion principle. As mentioned by Moon et al., water absorption is one of the critical problems restricting implementations for cellulose-based materials, as this affects the stability of mechanical properties, chemical stability, and dimensional stability. Available hydroxyl groups on the layer of cellulose sample are usually considered the primary site of water absorption and are thus susceptible to loss of mechanical properties [19].

## 4 Conclusions

This study emphasizes the synthesization of green and cost-effective techniques to extract cellulose from oil palm empty fruit bunch (OPEFB). The extraction of cellulose was done by alkaline and bleaching treatment. The use of alkali and bleaching treatment for extracting cellulose from empty fruit bunch has generated a significant amount of 40.5% of cellulose (w/w). Furthermore, the analysis of the extracted cellulose indicates that the alkaline treatment helps to eliminate hemicellulose while the bleaching treatment helps to eliminate lignin from the empty fruit bunch fiber mat. Based on this research, several conclusions can be summarized below:

- Cellulose was successfully extracted from an empty fruit bunch (EFB) using a cost-effective method.
- NaOH treatment proved to be a successful approach in eliminating lignin and hemicellulose from the sample.
- Cellulose is proven to have a hydrophilic characteristic that can absorb water, and the period of immersion impacts the sample water absorption capabilities.
- SEM results showed detailed cellulose results from the chemical treatment. XRD analysis indicated the increase in crystallinity index because of the elimination of lignin and hemicellulose from the sample.
- Compared with previous research, a chemical treatment used in the study could improve the properties of the extracted cellulose.
- The extracted cellulose has the potential as a low-cost feedstock for bioconversion for oil spill application.

**Acknowledgements** This work was supported by Tenaga Nasional Berhad (TNB) and UNITEN through the BOLD Research Grant under the project code of J510050002/2022031.

## References

1. Thai, Q.B., Nguyen, S.T., Ho, D.K., Du Tran, T., Huynh, D.M., Do, N.H., Luu, T.P., Le, P.K., Le, D.K., Phan-Thien, N., Duong, H.M.: Cellulose-based aerogels from sugarcane bagasse for oil spill-cleaning and heat insulation applications. *Carbohydr. Polym.* **228**, 115365 (2019)
2. Merv, F.: *The Basics of Oil Spill Clean up*. CRC Press (2013)
3. Yang, S.-Z., Jin, H., Wei, Z., He, R., Ji, Y.J., Li, X.M., Yu, S.P.: Bioremediation of oil spills in cold environments: a review. *Pedosphere* **19**, 371–381 (2019)
4. Nguyen, S.T., Feng, J., Le, N., Le, A., Hoang, N., Tan, V.B.C., Duong, H.: Cellulose aerogel from paper waste for crude oil spill cleaning. *Ind. Eng. Chem. Res.* **52**, 18386–18391 (2013)
5. Granström, M.: *Cellulose Derivatives: Synthesis, Properties and Applications*. Ph.D. thesis, University of Helsinki (2009)
6. Hasanuzzaman, M., Hossain, M.F., Rahim, N.A.: Palm oil EFB: green energy source in Malaysia. *Appl. Mech. Mater.* **619**, 376–380 (2014)
7. Kumneadklang, S., O-thong, S., Larpkiattaworn, S.: ScienceDirect characterization of cellulose fiber isolated from oil palm frond biomass. *Mater. Today Proc.* **17**, 1995–2001 (2019)
8. Chen, Y., Tshabalala, M.A., Gao, J., Stark, N.M., Fan, Y.: Color and Surface chemistry changes of pine wood flour after extraction and delignification. *BioResources* **9**(1), 2937–2948 (2014)
9. Johar, N., Ahmad, I., Dufresne, A.: Extraction, preparation and characterization of cellulose fibres and nanocrystals from rice husk. *Ind. Crops Prod.* **37**(1), 93–99 (2012)
10. Oushabi, A., Sair, S., Oudrhiri Hassani, F., Abboud, Y., Tanane, O., El Bouari, A.: The effect of alkali treatment on mechanical, morphological and thermal properties of date palm fibers (DPFs): study of the interface of DPF–Polyurethane composite. *South African J. Chem. Eng.* **23**, 116–123 (2017)
11. Watkins, D., Nuruddin, M., Hosur, M., Tcherbi-Narteh, A., Jeelani, S.: Extraction and characterization of lignin from different biomass resources. *J. Mater. Res. Technol.* **4**(1), 26–32 (2015)
12. Alemdar, A., Sain, M.: Isolation and characterization of nanofibers from agricultural residues—wheat straw and soy hulls. *Bioresour. Technol.* **99**(6), 1664–1671 (2008)
13. Sheltami, R.M., Abdullah, I., Ahmad, I., Dufresne, A., Kargarzadeh, H.: Extraction of cellulose nanocrystals from mengkuang leaves (*Pandanus tectorius*). *Carbohydr. Polym.* **88**(2), 772–779 (2012)
14. Ngadi, N., Lani, N.S.: Extraction and characterization of cellulose from empty fruit Bunch (EFB) fiber. *Jurnal Teknologi* **68**(5), 35–39 (2014)
15. Sahputra, I.H., Alexiadis, A., Adams, M.J.: Effects of moisture on the mechanical properties of microcrystalline cellulose and the mobility of the water molecules as studied by the hybrid molecular mechanics-molecular dynamics simulation method. *J. Polym. Sci. Part B Polym. Phys.* **57**(8), 454–464 (2019)
16. Fotie, G., Rampazzo, R., Ortenzi, M.A., Checchia, S., Fessas, D., Piergiovanni, L.: The effect of moisture on cellulose nanocrystals intended as a high gas barrier coating on flexible packaging materials. *Polymers (Basel)* **9**(9), 1–16 (2017)
17. Rongpipi, S., Ye, D., Gomez, E.D., Gomez, E.W.: Progress and opportunities in the characterization of cellulose—an important regulator of cell wall growth and mechanics. *Front. Plant Sci.* **9**, 1–28 (2019)
18. Maslinda, A.B., Abdul Majid, M.S., Ridzuan, M.J.M., Afendi, M., Gibson, A.G.: Effect of water absorption on the mechanical properties of hybrid interwoven cellulosic-cellulosic fibre reinforced epoxy composites. *Compos. Struct.* **167**, 227–237 (2017)
19. Moon, R.J., Martini, A., Nairn, J., Simonsen, J., Youngblood, J.: Cellulose nanomaterials review: Structure, properties and nanocomposites. *Chem. Soc. Rev.* **40**(7), 3941–3994 (2011)

# Comparative Study of Various Deep Learning Models for Structural Anomaly Detection



Nitin Mohariya, Rushikesh Gade, and Jimson Mathew

**Abstract** Efficient detection and segmentation of wall cracks play a crucial role in building maintenance and construction. However, the implementation of vision transformers (ViT) for crack classification often presents challenges due to its high computational complexity, making it unsuitable for deployment on low-efficiency devices. To address this issue, we propose a novel approach that leverages knowledge distillation (KD) to create a computationally efficient ensemble model comprising a convolutional neural network (CNN) and ViT. In our framework, the teacher model is the ViT, which possesses exceptional classification capabilities, while the student model is a CNN designed to reduce complexity and enhance inference efficiency. By employing KD, we transfer knowledge from the ViT to the CNN, enabling the student model to approximate the performance of the more complex teacher model. This approach reduces the training time and computational requirements without significantly sacrificing classification accuracy. Following the classification stage, we employ a UNet segmentation model on the crack-detected images to accurately identify and delineate the damaged areas within a cracked surface. By analyzing the segmented images, we can calculate essential metrics such as the percentage of crack area and the length of the cracks. These metrics provide valuable insights into the severity of the cracks, facilitating the development of effective strategies for repair and prevention. Experimental results on a diverse dataset demonstrate that our ensemble model achieves competitive crack detection and segmentation performance while maintaining efficiency. The proposed approach not only reduces the complexity associated with ViT deployment but also provides an accurate and comprehensive analysis of wall crack severity. These findings have significant implications for building maintenance and construction industries, enabling proactive measures to mitigate structural damage and ensure safer and more sustainable infrastructure.

---

N. Mohariya (✉) · R. Gade · J. Mathew  
Indian Institute of Technology Patna, Bihta 801103, India  
e-mail: [nitin\\_2111mt03@iitp.ac.in](mailto:nitin_2111mt03@iitp.ac.in)

R. Gade  
e-mail: [rushikesh\\_2111mt07@iitp.ac.in](mailto:rushikesh_2111mt07@iitp.ac.in)

J. Mathew  
e-mail: [jimson@iitp.ac.in](mailto:jimson@iitp.ac.in)

**Keywords** Wall crack detection · Wall crack segmentation · Vision transformers · Knowledge distillation · Ensemble model · Convolutional neural network · UNet · Severity analysis · Building maintenance · Infrastructure

## 1 Introduction

Anomaly detection is the process of identifying data examples that drastically deviate from the bulk of data instances. It is also known as outlier identification or novelty discovery. Anomaly detection plays increasingly essential roles, emphasized in numerous fields like data mining, machine learning, and computer vision. This is due to the growing need and applications in broad areas such as risk management, security, health, and AI safety. Recent years have seen deep learning extending the capabilities of many learning tasks with its impressive powers in learning expressive representations of complicated data, including high-dimensional data, spatial, and graph data. For the purpose of anomaly detection, deep learning aims to develop feature representations or anomaly scores through neural networks. Numerous deep anomaly detection techniques have been developed, and they have been shown to perform noticeably better than traditional anomaly detection techniques when it comes to tackling challenging identification issues in a range of real-world situations. This work aims to explore various deep learning models and implement them in anomaly detection. CNN have been the standard approach for image classification in the field of image processing, consistently achieving state-of-the-art results on a variety of image classification problems. The transformer is now garnering a lot of interest in Natural Language Processing (NLP). Transformer employs an attention mechanism on input sequence data as a deep learning model. Dosovitskiy applies a typical transformer directly to photos by slicing images into patches and successively inserting them into the transformer. In this paper, we'll explore both CNN and vision transformer. With the aid of a knowledge distillation-based model, we will deploy these models on low-computing hardware devices like smartphones for anomaly detection after we obtain the best classification results utilizing these models through real-time analysis on a drone.

## 2 Problem Definition

The advent of new technology has revolutionized nearly every aspect of our lives, yet the construction industry has struggled to keep pace with these advancements. Presently, manual inspections remain the predominant method for assessing a building's structural integrity. In essence, engineers still rely on visual examinations and extensive photography to identify cracks, a laborious, costly, and subjective process. Compounding the issue are safety concerns arising from limited access to certain building components. Fortunately, unmanned aerial vehicles (UAVs), commonly

known as drones, have been deployed to capture images in areas where accessibility is challenging. However, the task of scrutinizing each photograph for evidence of damage still requires considerable human effort and time.

This is where our innovative approach to inspection processes comes into play. Leveraging the power of artificial intelligence, specifically deep learning, we have trained our robots to assume the arduous task of identifying cracks in building photographs, thereby relieving humans of this painstaking responsibility. Our research has focused on developing deep learning models like convolutional neural networks (CNN) and vision transformers for detecting anomalies. Additionally, we aim to deploy these models on resource-constrained devices such as smartphones, and to achieve this, we have created a KD-based model that significantly reduces the parameters of the original model while maintaining its accuracy. Furthermore, a segmentation model will be utilized to detect cracks, enabling precise measurements of their length and area. This comprehensive approach seeks to enhance the efficiency and effectiveness of crack classification, as detailed in our research paper.

### 3 Related Work

The process of identifying anomalies, which refers to unusual events or observations that are statistically different from the remaining observations, is commonly referred to as anomaly detection. The first study to confirm programmable computing came to the conclusion that a machine could master the game of checkers and overcome a human opponent in 1959 [1]. The advancement in the field of computer science with massive amounts of data and powerful computational hardware like GPU has allowed artificial intelligence to flourish in this area [2]. The majority of the recent deep learning techniques have shown promise in a variety of tasks, including classification (objects, news) [3, 4] and surveillance [5, 6]. In order to monitor a structure for the correct maintenance, structural pictures are utilized for a variety of tasks, including the automatic detection of cracks, classification of the fractures, and measurement of the crack attributes. The edges information [7], morphological procedures [8], statistical techniques, digital image correlation [9], and pattern matching [10] may all be used to identify fractures in pictures. The CNN is the most extensively used, well-established, and advanced DL technique. CNNs worked spectacularly in computer vision applications and were effectively used to classification challenges [3]. The development of vision-based methods for detecting concrete cracks has been thoroughly studied, and several popular methods have been suggested. Early methods for detecting cracks in images include edge detection [7], thresholding and segmentation [11], and peculation-based techniques [12]. Concrete crack detection has been significantly impacted and improved by machine learning advancements. Machine learning, as opposed to earlier methods, can learn deep features and carry out statistical inference without manually adjusting parameters. The two main steps in traditional machine learning methods for crack detection are feature extraction and classification. Image processing methods are used to extract pertinent

crack information (features) from the images, which are then assessed by different classifiers. Traditional machine learning techniques [13, 14] have been the foundation of many crack detection studies [15–18]. However, the classifier may not produce accurate results if the extracted features do not accurately represent the cracks. Deep learning techniques have greatly increased the adaptability and robustness of traditional methods and have demonstrated excellent performance in crack detection problems [19–21]. Through a multi-layer neural network, deep convolutional neural network (CNN) models are able to extract pertinent features from the input data [22]. With the emergence of transformers in the field of NLP has revolutionized the domain due to its attention model. Transformer [23] has demonstrated SoTA performance in several NLP tasks and is proposed for machine translation tasks. Transformer-based models use attention mechanisms to process long-range dependencies and aggregate the data from all the tokens. There have been numerous attempts to adapt the transformer architecture to computer vision tasks, motivated by the success of transformer-based models in the NLP field. ViT, put forth by Dosovitskiy et al. [24], has outperformed CNN-based methods and achieved the SoTA performance on image classification tasks. As a deep learning model, transformer uses an attention mechanism on the input sequence data. By cutting images into patches and placing them into the transformer one at a time, Dosovitskiy applies a conventional transformer directly to images. This method was inspired by the transformer's better performance in NLP tasks. When a large amount of data is used to pre-train the proposed ViT model and transferred to a smaller basis, it exhibits superior performance compared to state-of-the-art CNNs in the task of image classification. In the presence of diverse noisy signals, the performance of CNN-based models significantly declined, as evidenced by a decrease in the mean dice score. However, the use of ViT proved to be beneficial as it improved the robustness of the encoder-decoder network in such situations [25]. In addition, image segmentation is a fundamental task in computer vision, enabling the extraction of meaningful information from visual data. Over the years, various segmentation algorithms have been developed, among which the UNet architecture [26] has gained significant attention and popularity. This research paper aims to optimize the parameters and size of a model to make it suitable for deployment on low computational hardware. This will be achieved by implementing a knowledge distillation (KD)-based approach, while ensuring that the model's predictive accuracy remains nearly unchanged. Additionally, a segmentation model will be utilized for crack detection, enabling the identification of crack length and area. Through this process, the paper aims to enhance the efficiency and effectiveness of crack classification.

## 4 Dataset Description

Surface fractures in concrete are a severe flaw in civil construction. Building inspections are carried out to assess the stiffness and tensile strength of the structure. Finding the cracks and assessing the health of the building are important aspects of

crack detection in the inspection of structures. In this paper, we have used a surface crack detection dataset [27]. The next section provides a full explanation of this dataset.

#### 4.1 Surface Crack Detection Dataset

Images of diverse concrete surfaces, both with and without cracks, are present in the dataset. For image classification, the picture data are split into two categories: negative (without crack) and positive (with crack). Each class includes 20,000 photos, for a total of 40,000 ( $227 \times 227$ ) RGB-channelled images. Using the approach suggested by Zhang et al. (2016), the dataset is created from 458 high-resolution photos ( $4032 \times 3024$  pixels). In terms of surface quality and lighting, high-resolution photos were found to show significant variation. No random rotation, flipping, tilting, or another kind of data augmentation is used. Sample images from both classes are depicted in Figs. 1 and 2.

#### 4.2 Crack Segmentation Dataset

We trained the UNet architecture using a dataset of images of building walls with cracks. The dataset consists of 150 images ( $256 \times 256$ ) of building walls with various types and sizes of cracks. Figure 3 represents the same. In order to train the UNet model, a dataset of images with corresponding masks is required. The masks represent the ground truth labels for each image, an indication of the location object or the

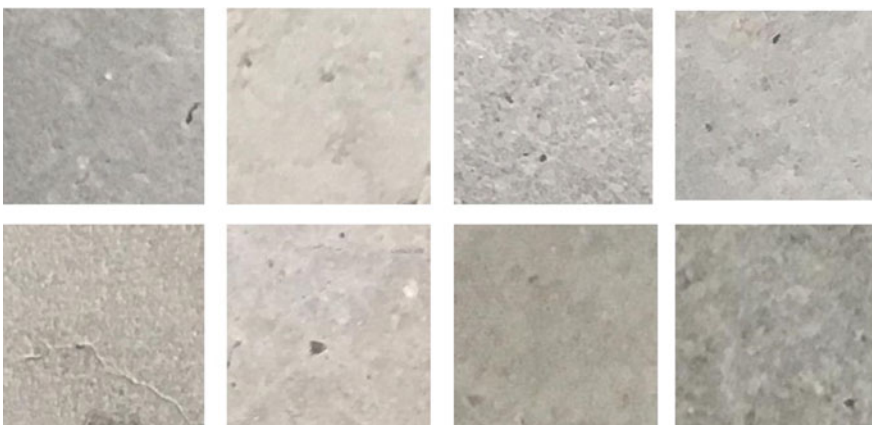


**Fig. 1** Sample images from the dataset representing the class ‘Negative’

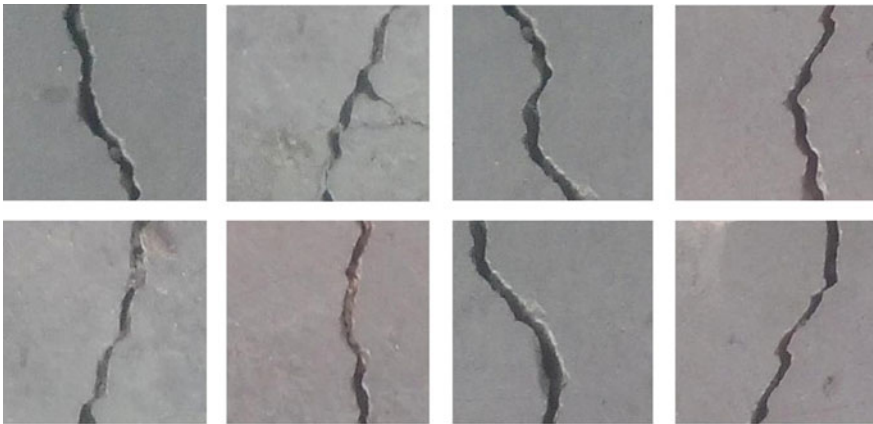


**Fig. 2** Sample images from the dataset representing the class ‘Positive’

region of interest (ROI) within the image. The UNet mask is a binary image where the object or ROI is represented in white color and the background is represented in black color.

We manually created the binary masks using morphological operations such as erosion, dilation, opening, closing, and adjusting intensity levels to ensure accuracy and facilitate the model’s training for semantic segmentation of wall cracks. We split the 130 images for training and 20 images for testing. Using augmentation techniques such as random horizontal and vertical flips, Shift scale rotation, Random brightness contrast for the input images, and its binary mask using the Albumentation augmentation tool. Then we again split the training images with augmentation into train and validation split with 80:20 percent.

## 5 Proposed Model

Basically, we started with pre-processing the surface crack detection dataset having 40k images labeled as positive and negative. The CNN model as well as the vision transformer were customized and trained for the purpose of classification and their accuracy was observed. Vision transformer had large parameters and a huge model size. Thus knowledge distillation-based model was developed to reduce the parameters as well as model size to deploy on devices with low computational power such as smartphones. The model was deployed on a smartphone connected via drone and real-time analysis of anomaly was monitored on the smartphone. Figure 4 explains the approach followed.

In this section, our proposed method and its architecture are explained. We will explore and optimize CNN and vision transformers for their optimum performance.

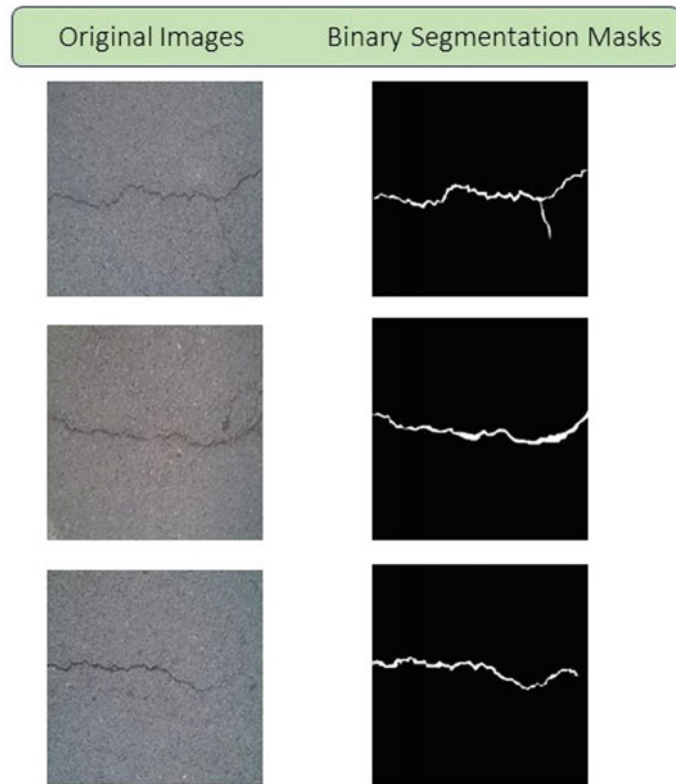


**Fig. 3** Original Images from dataset (left) and corresponding binary segmentation masks (right)

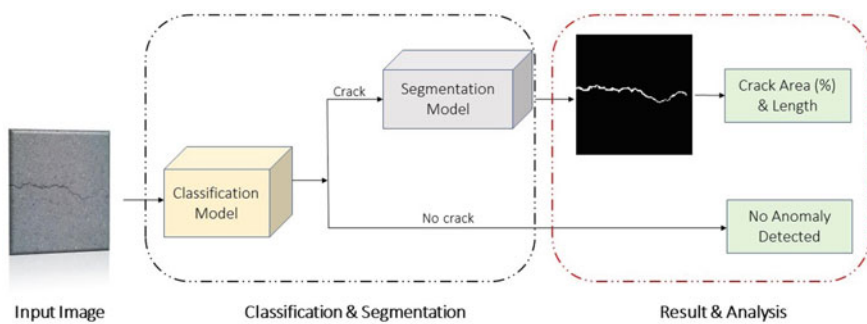


**Fig. 4** An integrated approach: combining classification and segmentation for accurate anomaly detection and precise crack length and area calculation

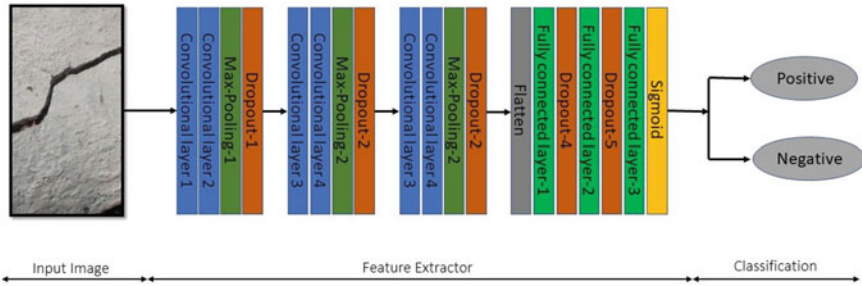


**Fig. 5** Convolutional neural network architecture

**Table 1** Training parameters of the proposed CNN model

Training parameters	Values
Train:Validation:Test split	8:1:1
Image size	120×120
optimizer	Adam
Loss function	Binary cross-entropy
Epochs	150

At last, we will discuss the architecture of the knowledge distillation-based model that will be good enough to deploy on low computational hardware devices.

### 5.1 Convolutional Neural Network Model

The CNN model used for the classification of an anomaly in structures is as shown in Fig. 5. The input image is fed into the CNN with the ratio of training, validation, and testing set as 80:10:10. The input image was resized to 120x120. The architecture consists of six convolution layers, three max-pooling layers, adam as an optimizer, and loss function as binary cross-entropy. In this, we have used stride as 1 and no padding is used. Moreover, the output is depicted in terms of classification as a “Positive” or “Negative” image with an accuracy percentage. Table 1 represents various training parameters of the proposed CNN model.

### 5.2 Vision Transformer Model

In the vision transformer model, all the steps were followed while implementation as per Dosovitskiy [24]. The architecture for the vision transformer is depicted in Fig. 6. The image was resized to 85x85 and was divided into 9 patches. After that

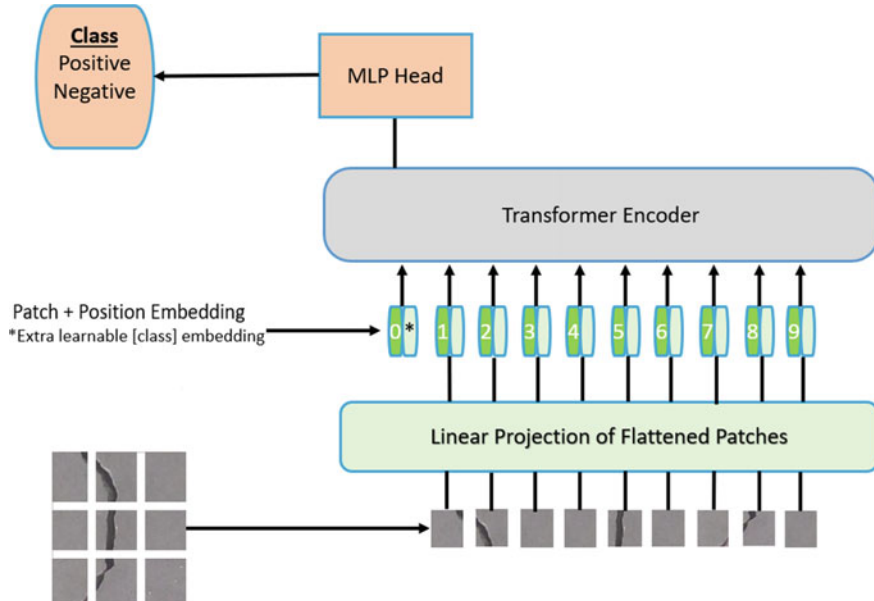


**Fig. 6** Vision transformer architecture

flattened patches were linearly projected followed by patch and position embedding to maintain the sequence of patches. These were fed to the transformer encoder and the encoder was connected to a multi-layer perceptron that would predict the class of the input image.

### 5.3 Knowledge Distillation-Based Model

Model compression technique known as "knowledge distillation" trains a tiny model to imitate a bigger, previously-trained model. The large model serves as the teacher in this training environment, while the smaller model serves as the student. Bucila et al. [28] originally put forth the idea of knowledge distillation, then after that Hinton et al. [29] generalized it. By minimizing a loss function with the distribution of class probabilities predicted by the teacher model as the aim, distillation transfers information from the teacher model to the student. That is the result of applying a softmax function on the logits from the teacher model. In our architecture, the teacher model is a vision transformer and the student model is CNN. The complete working of the model is depicted in the Fig. 7.

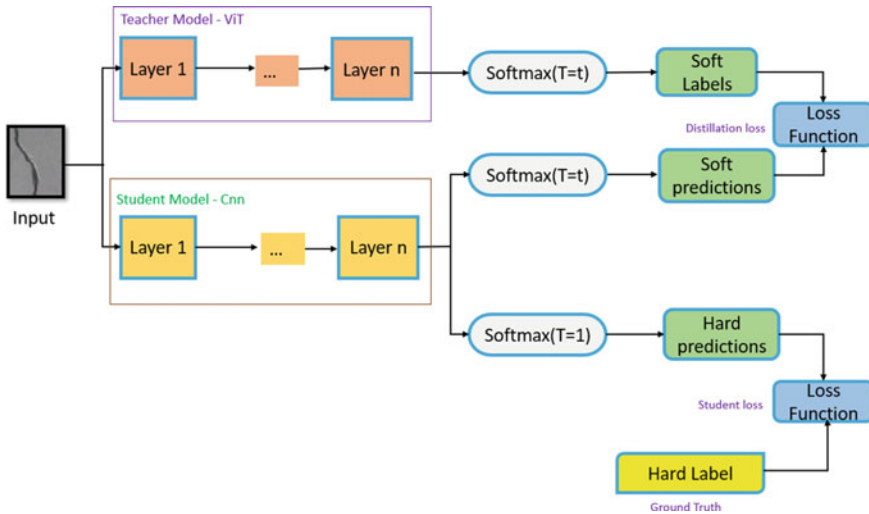


**Fig. 7** Knowledge distillation-based architecture

#### 5.4 UNet Segmentation Model

In recent years, semantic segmentation has become a well-known technique for automatically detection and segmenting wall cracks in images. To calculate the percentage of damaged area in an image in terms of pixels, we are utilizing the UNet Binary Segmentation model. The model generates a binary mask that distinguishes between the cracks and the background in the image. By analyzing the pixels in binary masks, we can determine the percentage of the total image area that contains our crack. This approach allows us for accurate and automated calculation of the damaged area in the image, which can be useful for various application such as assessing the severity of damage in building structures.

Our UNet model takes an input image of size  $256 \times 256$  as shown in Fig. 8 and applies convolutional layers to extract features. These features are then flattened (512) and passed through skip connections to preserve high-level information from earlier layers. The model then transposes the convolution of the feature maps to the original image size to generate a segmentation map. The skip connections enable the model to combine information from different levels of the feature hierarchy, allowing it to perform accurate segmentation for regions of interest (ROI). We used binary cross-entropy (BCE) loss as the loss function for training the UNet model. BCE has commonly used for binary segmentation tasks and measures the difference between the predicted mask and the ground truth mask. Adam optimizer with a learning rate of 0.01 for training the model. The Adam optimizer is popular for its efficient convergence and handling of noisy gradients.

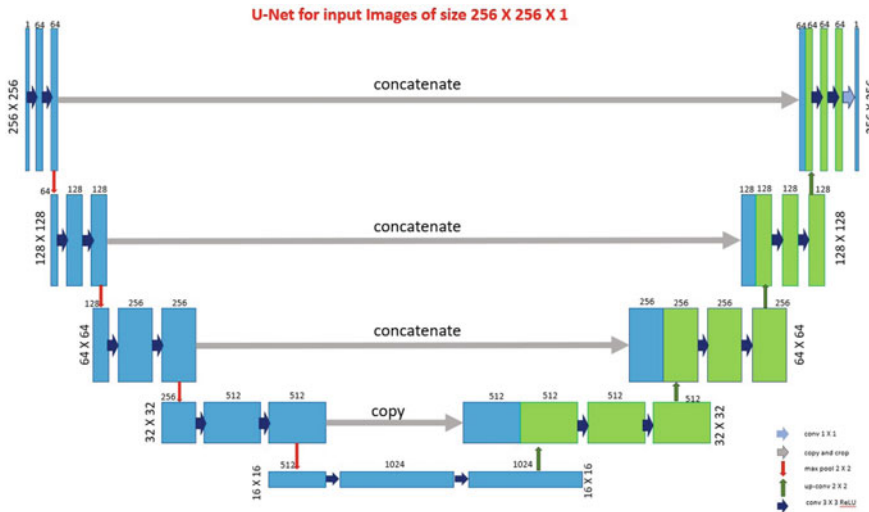


**Fig. 8** UNet architecture

## 6 Results

Results were acquired through the GPU and tensorflow framework of the 2.8.2 version. On testing our customized models which are CNN, vision transformer, and knowledge distillation based on the crack surface detection dataset, the following results were obtained as depicted in Table 2. The CNN model outperformed the vision transformer when the model was trained on 20k images. But when both the models were trained on the same dataset with 40k images then the vision transformer yielded better results as compared to CNN. The knowledge distillation-based model was able to predict its accuracy almost the same as the vision transformer though its parameter was reduced from 86 to 8 M.

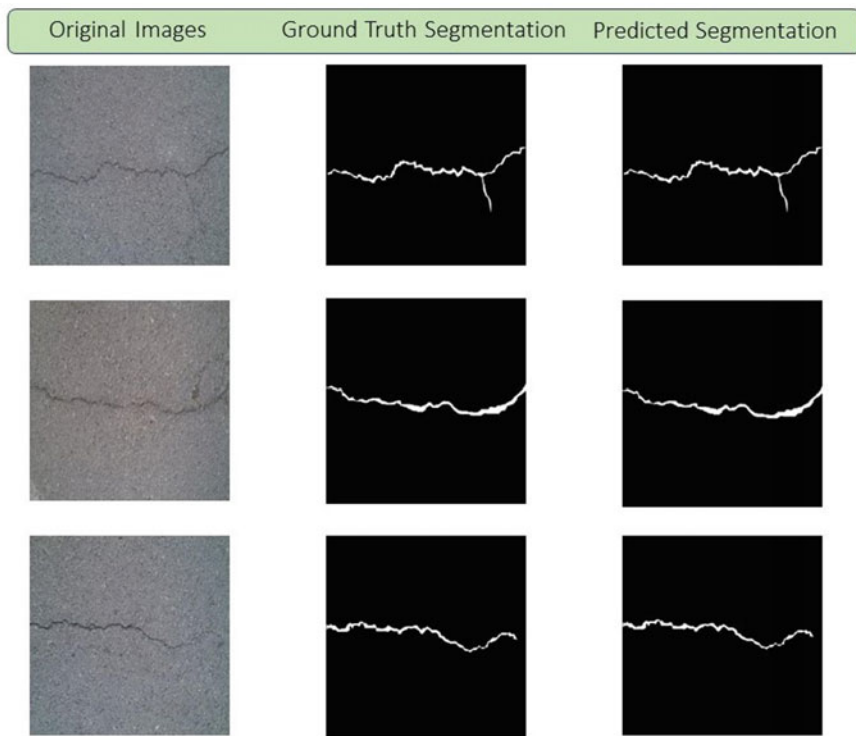
The provided Table 3 presents the performance metrics for the UNet model, specifically highlighting its results in terms of IOU, Dice coefficient, and accuracy (Fig. 9).

**Table 2** Comparison study for various models performance

	CNN	ViT	KD-based
Size of the dataset (k)	40	40	40
Number of parameters (M)	1	90	6
Training time (min)	15	170	25
Validation accuracy	0.97	0.995	0.991

**Table 3** Outcomes for different segmentation metrics

Metrics	Results
Accuracy score	97.649
Precision	88.48
Recall	86.27
F1 score	88.48
IoU (Jaccard index)	79.34
Dice similarity score	88.379

**Fig. 9** Resulting images showing original images, corresponding ground truth segmentation, and their predicted segmentation

## Crack Analysis On Segmented Output

1. Crack Area: When analyzing an image for damage or cracks area, the first step is to segment the image and create a binary image where damaged areas are represented by white pixels and undamaged areas are represented by black pixels. Once the binary image is obtained, the next step is to calculate the area of damage. The Eq. (1) given below represents the formula to calculate the area of damage in an image.

$$\text{Area of damage} = \frac{\text{Number of white pixels}}{\text{Total number of pixels}} \times 100\% \quad (1)$$

This percentage represents the area of damage relative to the total area of the image. This method of area calculation is commonly used in image analysis and provides a simple and effective way to quantify the extent of damage or cracks in an image. Figure 10 displays the results for crack images by calculating their area.

2. Crack Length: The next step in crack analysis involves calculating the length of the crack. To do this, a loop is run over the binary image to identify the co-ordinates of the white pixels, which represent the crack. Once the co-ordinates are obtained, the Linear Regression (LR) algorithm from “Scikit-Learn” is applied to these pixel co-ordinates to obtain the equation of the line. By passing the  $X$  co-ordinates of the pixels again through the fitted equation, we can obtain the corresponding  $Y$  co-ordinates, which allow us to plot the line representing the crack length as shown in Fig. 11.

The co-ordinates of the line may be in a random order, so they are sorted in increasing order and any co-ordinates that lie outside of the image size are trimmed. After trimming, the first and last co-ordinates in the list are selected, and the distance formula Eq. (2)

$$d = \sqrt{(x_2 - x_1)^2 + (y_2 - y_1)^2} \quad (2)$$

is used to calculate the approximate length of the crack in pixels. It is possible that there may be some small patches of pixels that are not actually part of the crack, but rather surrounding noise. However, these outliers are automatically handled by LR algorithm. This is because the equation of the line fitted with the actual crack pixels will dominate the outliers. As a result, when the co-ordinates of both the crack and the outliers are passed through the fitted line equation, their predictions will still follow the line.

By combining this crack length calculation with the area calculation method, it is possible to obtain a more comprehensive analysis of the damage in the image.

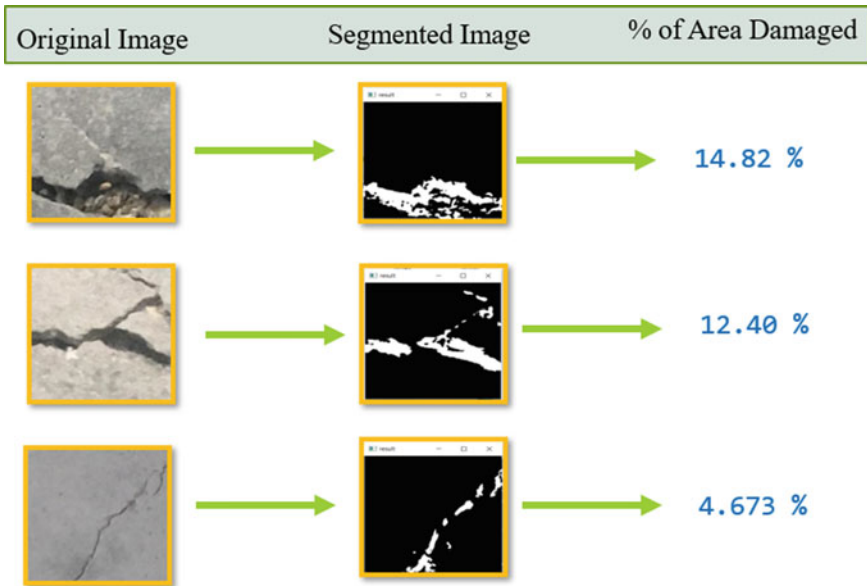


**Fig. 10** Given image displays the segmented image results, along with the corresponding calculated area of damage

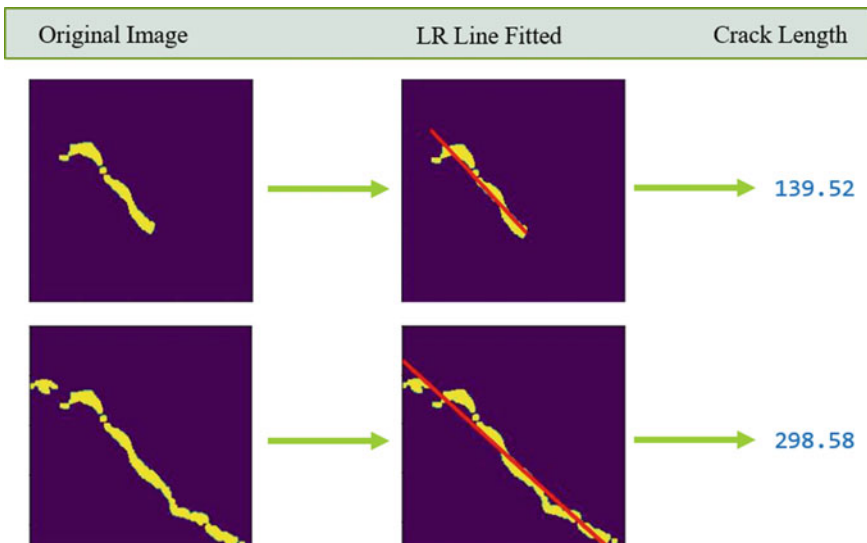


**Fig. 11** Crack length calculation

## 7 Conclusion

In this study, we compared the performance of two popular models used in computer vision, the vision transformer and the CNN. We found that while the vision transformer had higher accuracy, it had a larger model size and required more computational power, making it difficult to deploy on hardware with limited resources. To address this issue, we proposed a knowledge distillation-based model where we used the vision transformer as the teacher model and the CNN as the student model. By distilling knowledge from the larger teacher model, we were able to significantly reduce the size and parameters of the student model while maintaining comparable accuracy. We then deployed this knowledge distillation-based model to perform real-time classification of structural cracks. When a crack was detected, the image was subjected to a segmentation model for further analysis. Our model was able to detect cracks and perform segmentation to accurately calculate the area of the damaged structure and the length of the crack.

However, we recognize that there is still room for improvement. For instance, we aim to train the model on more diverse datasets to increase its robustness and accuracy, making it more effective in detecting structural anomalies. Moreover, we plan to incorporate sensors and other equipment to further enhance the accuracy of crack area detection. Additionally, we will explore techniques for the depth estimation of cracks, which will help us better understand the severity of the damage and provide more accurate results. By improving the model's effectiveness, we hope to contribute to the development of more accurate and reliable tools for structural anomaly detection.

## References

1. Samuel, A.L.: Some studies in machine learning using the game of checkers. II-recent progress. *IBM J. Res. Dev.* **11**(6), 601–617 (1967)
2. Goodfellow, I., Bengio, Y., Courville, A., Bengio, Y.: Deep learning (Go to reference in article) (2016). <http://www.deeplearningbook.org>
3. LeCun, Y., Boser, B., Denker, J., Henderson, D., Howard, R., Hubbard, W., Jackel, L.: Handwritten digit recognition with a back-propagation network. In: *Advances in Neural Information Processing Systems*, vol. 2 (1989)
4. Dyrmann, M., Karstoft, H., Midtiby, H.S.: Plant species classification using deep convolutional neural network. *Biosyst. Eng.* **151**, 72–80 (2016)
5. Sreenu, G., Durai, S.: Intelligent video surveillance: a review through deep learning techniques for crowd analysis. *J. Big Data* **6**(1), 1–27 (2019)
6. Pan, J., Yin, Y., Xiong, J., Luo, W., Gui, G., Sarı Hikmet: Deep learning-based unmanned surveillance systems for observing water levels. *IEEE Access* **6**, 73561–73571 (2018)
7. Abdel-Qader, I., Abudayyeh, O., Kelly, M.E.: Analysis of edge-detection techniques for crack identification in bridges. *J. Comput. Civil Eng.* **17**(4), 255–263 (2003)
8. Yamaguchi, T., Nakamura, S., Saegusa, R., Hashimoto, S.: Image-based crack detection for real concrete surfaces. *IEEJ Trans. Electr. Electron. Eng.* **3**(1), 128–135 (2008)
9. Gehri, N., Mata-Falcón, J., Kaufmann, W.: Automated crack detection and measurement based on digital image correlation. *Construct. Build. Mater.* **256**, 119383 (2020)

10. Adhikari, R.S., Moselhi, O., Bagchi, A.: Image-based retrieval of concrete crack properties for bridge inspection. *Autom. Constr.* **39**, 180–194 (2014)
11. Kamaliardakani, M., Sun, L., Ardakani, M.K.: Sealed-crack detection algorithm using heuristic thresholding approach. *J. Comput. Civil Eng.* **30**(1), 04014110 (2016)
12. Yamaguchi, T., Nakamura, S., Hashimoto, S.: An efficient crack detection method using percolation-based image processing. In: 2008 3rd IEEE Conference on Industrial Electronics and Applications, pp. 1875–1880. IEEE (2008)
13. O’Byrne, M., Ghosh, B., Schoefs, F., Pakrashi, V.: Regionally enhanced multiphase segmentation technique for damaged surfaces. *Comput.-Aided Civil Infrastruct. Eng.* **29**(9), 644–658 (2014)
14. O’Byrne, M., Schoefs, F., Ghosh, B., Pakrashi, V.: Texture analysis based damage detection of ageing infrastructural elements. *Comput.-Aided Civil Infrastruct. Eng.* **28**(3), 162–177 (2013)
15. Moon, H-G., Kim, J-H., et al.: Intelligent crack detecting algorithm on the concrete crack image using neural network. In: Proceedings of the 28th ISARC, pp. 1461–1467 (2011)
16. Liu, S.-W., Huang, J.H., Sung, J.C., Lee, C.C.: Detection of cracks using neural networks and computational mechanics. *Comput. Methods Appl. Mech. Eng.* **191**(25–26), 2831–2845 (2002)
17. Sinha, S.K., Fieguth, P.W.: Neuro-fuzzy network for the classification of buried pipe defects. *Autom. Constr.* **15**(1), 73–83 (2006)
18. Wei, W., Liu, Z., He, Y.: Classification of defects with ensemble methods in the automated visual inspection of sewer pipes. *Pattern Anal. Appl.* **18**, 263–276 (2015)
19. Kalfarisi, R., Wu, Z.Y., Soh, K.: Crack detection and segmentation using deep learning with 3d reality mesh model for quantitative assessment and integrated visualization. *J. Comput. Civil Eng.* **34**(3), 04020010 (2020)
20. Maeda, H., Sekimoto, Y., Seto, T.: Lightweight road manager: smartphone-based automatic determination of road damage status by deep neural network. In: Proceedings of the 5th ACM SIGSPATIAL International Workshop on Mobile Geographic Information Systems, pp. 37–45 (2016)
21. Ali, L., Alnajjar, F., Al Jassmi, H., Gocho, M., Khan, W., Adel Serhani, M.: Performance evaluation of deep CNN-based crack detection and localization techniques for concrete structures. *Sensors* **21**(5), 1688 (2021)
22. Fei, Y., Wang, K.C.P., Zhang, A., Chen, C., Li, J.Q., Liu, Y., Yang, G., Li, B.: Pixel-level cracking detection on 3d asphalt pavement images through deep-learning-based cracknet-v. *IEEE Trans. Intell. Transport. Syst.* **21**(1), 273–284 (2019)
23. Ashish, V.: Attention is all you need. *Adv. Neural Inf. Process. Syst.* **30**, I (2017)
24. Dosovitskiy, A., Beyer, L., Kolesnikov, A., Weissenborn, D., Zhai, X., Unterthiner, T., Dehghani, M., Minderer, M., Heigold, G., Gelly, S., et al.: An image is worth 16x16 words: transformers for image recognition at scale (2020). [arXiv:2010.11929](https://arxiv.org/abs/2010.11929)
25. Shamsabadi, E.A., Xu, C., Rao, A.S., Nguyen, T., Ngo, T., Dias-da Costa, D.: Vision transformer-based autonomous crack detection on asphalt and concrete surfaces. *Autom. Constr.* **140**, 104316 (2022)
26. Ronneberger, O., Fischer, P., Brox, T.: U-net: convolutional networks for biomedical image segmentation. In: Medical Image Computing and Computer-Assisted Intervention—MICCAI 2015: 18th International Conference, Munich, Germany, 5–9 Oct 2015, Proceedings, Part III 18, pp. 234–241. Springer (2015)
27. F Özgenel, Ç., Gönenç Sorguç, A.: Performance comparison of pretrained convolutional neural networks on crack detection in buildings. In: ISARC. Proceedings of the International Symposium on Automation and Robotics in Construction, vol. 35, pp. 1–8. IAARC Publications (2018)
28. Bucila, C., Caruana, R., Niculescu-Mizil, A.: Model compression christian. KDD (2006)
29. Hinton, G., Vinyals, O., Dean, J., et al.: Distilling the knowledge in a neural network. *2(7)* (2015) [arXiv:1503.02531](https://arxiv.org/abs/1503.02531)

# Cutting Temperature in Machining of Ti-6Al-4V Alloy and Its Predictive Model



Elango Natarajan , Manickam Ramasamy, S. Ramesh, Chun Kit Ang, and V. Kaviarasan

**Abstract** Titanium alloy (Ti-6Al-4V) is a biomaterial which has an incomparable weight-strength ratio, corrosion resistance, and thermal resistance than any other commonly used metals. It is one of the reasons for using it in implants, aerospace, defense applications. The induced cutting temperature during machining is higher as it is one of the hard materials. It is chemically active, and it tends to react with tool material. But it must be confronted as it has wide industrial applications. This research was intended to investigate the cutting temperature during turning of Ti alloy and analyze the significance of cutting parameters such as cutting speed, feed rate, and depth of cut. The Taguchi  $L_{27}$  orthogonal array was utilized in conducting experiments. The range of parameters and their effect on cutting temperature were statistically analyzed. At this end, a predictive model using ANFIS was developed and validated. Performance metric RMSE was found to be very minimal (9.31994e-05).

**Keywords** ANFIS · Machining · Ti alloy · Predictive model · Temperature

## 1 Introduction

Titanium and its alloys are extensively used in various sectors such as aerospace, defense, and biomedical industries due to their excellent characteristics like high strength-to-weight ratio, fracture toughness, corrosion, and good fatigue resistance. Ti alloys are preferred and used in medical implants because of their low bioactivity that prolongs the healing process [1]. Low modulus  $\beta$ -Ti alloys are found

---

E. Natarajan · M. Ramasamy · C. K. Ang  
Faculty of Engineering, Technology and Built Environment, UCSI University, 56000 Kuala Lumpur, Malaysia  
e-mail: [elango@ucsiuniversity.edu.my](mailto:elango@ucsiuniversity.edu.my)

S. Ramesh  
Department of Mechanical Engineering, Jerusalam College of Engineering, Chennai, India

V. Kaviarasan  
Sona College of Technology, Salem, India

suitable for dental implants because of its toughness and hardness [2]. Though Ti alloys have many superior properties, they have a limitation of low wear resistance. But it can be overcome by plasma-assisted surface treatment [3]. Ramesh et al. [4] investigated the machining of titanium alloy and reported how it plays a crucial role in the aerospace industry. Though we appreciate their incomparable mechanical properties, we find difficulty in manufacturing components to near net shape. Because of high cutting temperature and low heat conductivity of the material, tool-workpiece boundary reaches 1000 °C in high-speed cutting [5]. High cutting temperature stimulates different heat-related phenomena and causes rapid tool wear. Besides, it decreases hardness, early failure of the cutting tool. Jianxin et al. [6] revealed in his research paper that Tungsten and Cobalt elements in carbide cutting tool started diffusing at 600 °C and the penetrating depth reached 20 microns at 800 °C. The diffusion of these elements through chip interface affected tool substrate and subsequently increased tool wear. Generally, turning machine tools are most of the time used for different machining operations. Lou and Wu [7] reported that ultra-precision polishing was better than ultra-precision turning of optically graded Ti alloy. Ultra-precision polishing may be better and usable for polishing operation, but other operations like subtractive manufacturing processes, turning machine is unavoidable. A study of Agarwal et al. [8] revealed that cryogenic cutting is better than wet turning in terms of reduced carbon emission by 22% at higher cutting speeds.

Comparing dry, MQL, and liquid nitrogen condition in turning of Ti alloy, Gupta et al. [9] reported that dry condition produced more built-up edge (BUE) and hence hybrid condition could be applied for achieving optimal results. Shastri et al. [10] used Cohort Intelligence algorithm to optimize turning parameters and reported that this meta-heuristic algorithm works well for minimizing cutting force, tool wear, and surface roughness. Gupta et al. [11] in their another research reported that PSO algorithm could be used for optimization of turning parameters as it results closer result to desirability. Singh et al. [12] used analytic hierarchy process, which is known as a multi-attribute decision-making method and optimized the cutting parameters under MQL condition. Akkuş and Yaka [13] used S/N analysis for analyzing and optimizing surface roughness, energy consumption, and tool wear. Ramesh et al. [14] evaluated the cutting tools (PVD and CVD) and reported that PVD tool produces short chip and CVD produces long chip. They investigated the cutting temperature too during machining of Ti alloy with either tool.

From the above literature, it is derived that optimization of cutting parameters for minimizing surface roughness, cutting force, tool wear has been sufficiently researched. But research on cutting temperature is still open for the research. As cutting temperature has direct influence on other response parameters, this research is aimed to investigate the cutting temperature during turning of Ti alloy and analyze the results using desirability function approach. As such, the paper is organized as follows: Material and experimental method are presented in Sects. 2.1 and 2.2, while analysis of experimental data is presented in Sect. 2.3. Prediction model and microscopic results are presented and discussed in Sect. 3.

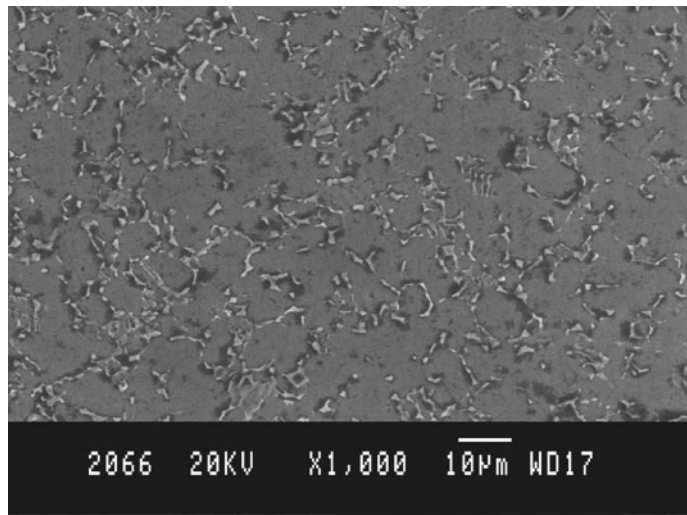


**Fig. 1** SEM microstructure of Ti-6Al-4V alloy

**Table 1** Chemical composition of Ti-6Al-4V alloy in weight %

Si	Mn	Cr	Mo	Al	Cu	Fe	V	Zr	Sn	Titanium (Ti)
0.051	0.02	0.0	0.01	6.18	0.02	0.2	3.88	0.0	0.0	89.585

## 2 Materials and Experimentations

### 2.1 Materials

Ti-6Al-4V alloy rod in the size of 90 mm in diameter and 160 mm in length was purchased from Titanium Industries, Inc., Wood Dale, Illinois. It is an annealed titanium alloy designated as ASTM B348, and it includes majorly about 6% aluminum, 4% vanadium, and 90% titanium. Figure 1 illustrates the SEM micrograph of the purchased Ti alloy. The exact chemical composition of Ti-6Al-4V is shown in Table 1.

### 2.2 Experimentation

Twenty-seven turning operations were carried out using CNC lathe operated at room temperature. These cutting conditions in all these experiments were based on  $L_{27}$  Taguchi orthogonal array derived prior to the experimentation, where three levels

of cutting speed ( $V$ ), feed ( $f$ ), and depth of cut ( $d$ ) were used as input parameters. We attempted three trials in each condition and recorded the cutting temperature using Raytek non-contact infrared (IR) thermometer (Model: MX2). Table 2 details the experimental results, where average of three trials is shown against cutting temperature.

**Table 2** Experimental results

Trial no.	Cutting speed ( $V$ ) (m/min)	Feed ( $f$ ) (mm/rev)	Depth of cut ( $d$ ) (mm)	Cutting temperature ( $T$ ) (°C)
1	10	0.065	0.5	436
2	10	0.065	0.75	454
3	10	0.065	1	462
4	10	0.13	0.5	463
5	10	0.13	0.75	477
6	10	0.13	1	486
7	10	0.22	0.5	469
8	10	0.22	0.75	476
9	10	0.22	1	498
10	40	0.065	0.5	484
11	40	0.065	0.75	503
12	40	0.065	1	547
13	40	0.13	0.5	529
14	40	0.13	0.75	587
15	40	0.13	1	607
16	40	0.22	0.5	592
17	40	0.22	0.75	630
18	40	0.22	1	634
19	70	0.065	0.5	603
20	70	0.065	0.75	657
21	70	0.065	1	692
22	70	0.13	0.5	663
23	70	0.13	0.75	712
24	70	0.13	1	809
25	70	0.22	0.5	789
26	70	0.22	0.75	897
27	70	0.22	1	1037

### 2.3 Analysis of Experimental Results

Analysis of Variance (ANOVA) analysis was carried out after measuring the responses from the experiments. It was done to identify the most influencing cutting parameter. Table 3 shows the ANOVA results, where we can notice that cutting speed is the most influencing parameter (69.35%) on cutting temperature, while noticing depth of cut as least influencing parameter. On analyzing cutting parameters, linear terms, and quadratic terms, it is understood that most of the terms are statistically significant ( $p < 5\%$ ), and moreover,  $R^2 = 97.63$ . Uncoded regression equation is shown below:

$$\begin{aligned} T = & 697.7 - 224.1V - 114.2f - 52.8d + 47.4V \times V \\ & + 10.8f * f + 0.8d \times d + 56.67V \times f \\ & + 33.75V \times d + 11.75f \times d \end{aligned} \quad (1)$$

Signal-to-noise (S/N ratio) is the concept that has high visibility in design of experiments (DoEs). It finds the variation of the response with the input parameters being represented by the process average and the noise being represented by the standard deviation of that output. It is a measure of the magnitudes relative to the standard deviation. Larger S/N value represents that the magnitude is large relative to the noise, and hence, it is significant. It is evident that speed is the most significantly influencing parameter in the current research (Fig. 2).

## 3 Prediction Model Development and Results

All three input parameters have some influence against the cutting temperature, and hence, the rise in cutting temperature was increased. Microscopic analysis image of PVD tool which was operated at  $v = 40$  m/min,  $s = 0.065$  mm/rev, and  $a = 0.5$  for about 10 min is shown in Fig. 3. It clearly shows a worn-out insert, which was supposedly caused by the high speed. Based on Taguchi optimization, cutting speed of 10 m/minute, feed of 0.065 mm/rev, depth of cut 0.5 mm were obtained as optimal levels to attain minimum cutting temperature.

Further to develop a prediction model, adaptive network-based fuzzy interference system (ANFIS) in MATLAB was used. Artificial neural network (ANN) is one of the most well-known predictive models which can estimate output response more efficiently [14, 15]. Elango et al. [16] used ANFIS and reported that performance of the model is increased using ANFIS. For the model development, 80% of the data was used for training and 20% was used for testing. Grid partitioning and hybrid optimization method were used where the hybrid method is a combination of the error propagation method and the least squares. Different member functions (MFs), different types of MF, and different epochs were attempted till least root mean square error (RMSE = 9.31994e-05) was obtained. A simple network model with three MFs

**Table 3** Analysis of variance

Source	DF	Adj SS	Adj MS	F-value	P-value	Contribution (%)
V	2	400,119	200,060	59.27	0.000	69.35
f	2	78,578	39,289	11.64	0.000	13.62
d	2	30,756	15,378	4.56	0.023	5.33
Error	20	67,504	3375			11.70
Total	26	576,957				100.00
Source	DF	Adj SS	Adj MS	F-Value	P-Value	
Model	9	563,312	62,590	77.98	0.000	
Linear	3	495,246	165,082	205.67	0.000	
V	1	386,614	386,614	481.66	0.000	
f	1	77,881	77,881	97.03	0.000	
d	1	30,752	30,752	38.31	0.000	
Square	3	14,206	4735	5.90	0.006	
V × V	1	13,506	13,506	16.83	0.001	
f × f	1	697	697	0.87	0.364	
d × d	1	4	4	0.00	0.947	
Two-way interaction	3	53,859	17,953	22.37	0.000	
V × f	1	38,533	38,533	48.01	0.000	
V × d	1	13,669	13,669	17.03	0.001	
f × d	1	1657	1657	2.06	0.169	
Error	17	13,645	803			
Total	26	576,957				
S		28.3315		R-sq		97.63%
R-sq(adj)		96.38%		R-sq(pred)		92.93%

as shown in Fig. 4 was found to be better in performance. Figure 5 shows the training error, rules, and testing error, where we can witness 436 °C for the input condition of cutting speed = 10 m/minute, feed = 0.065 mm/rev, depth of cut = 0.5 mm. The same result was obtained experimentally as well.

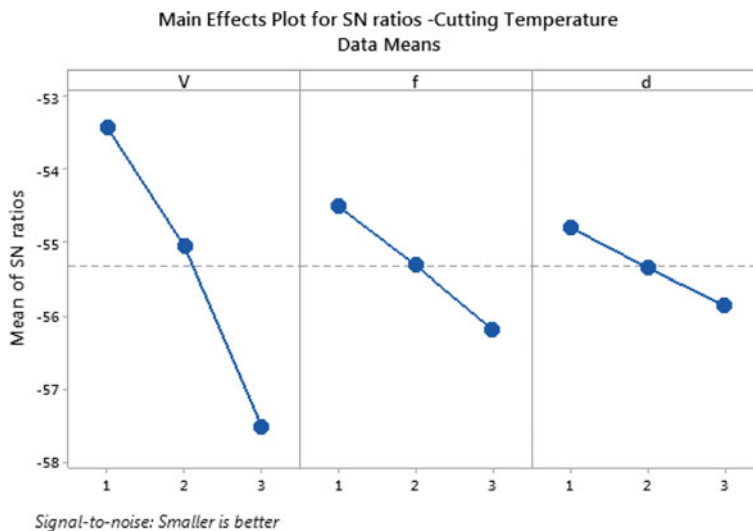


**Fig. 2** S/N ratio relative to standard deviation (noise)

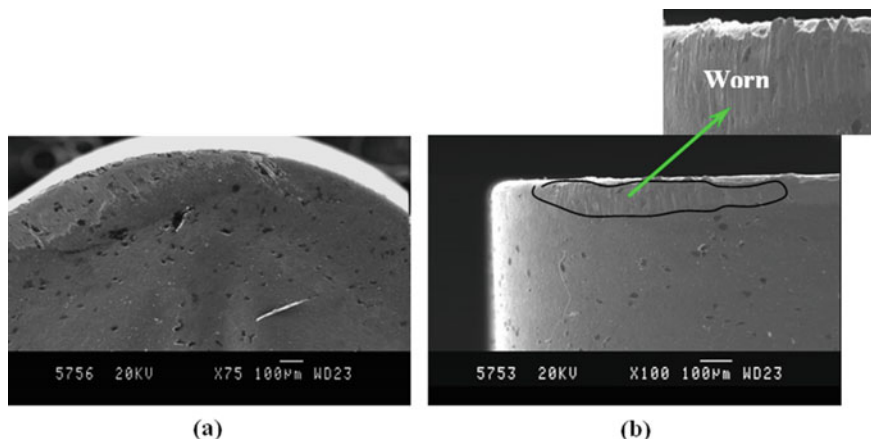


**Fig. 3** SEM micrograph **a** rake surface **b** worn-out PVD insert (operated at  $v = 40$  m/min,  $s = 0.065$  mm/rev, and  $a = 0.5$  mm for 10 min)

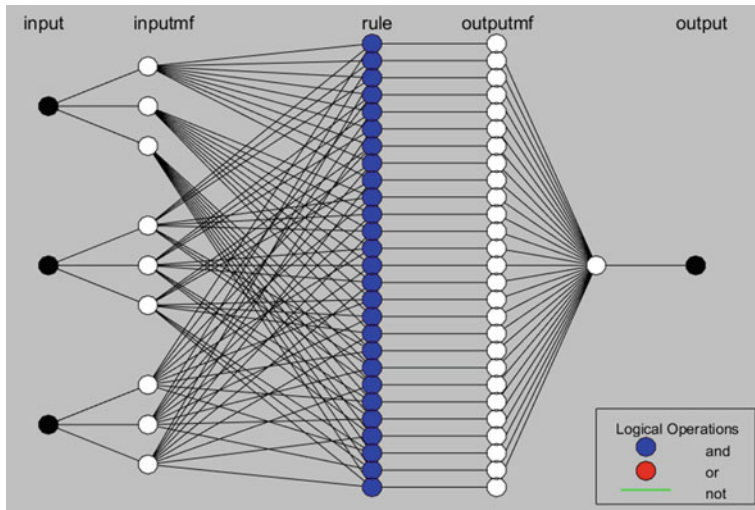


**Fig. 4** Network architecture

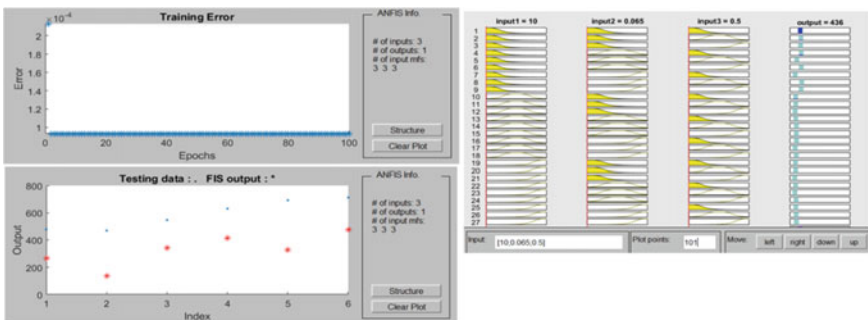


**Fig. 5** Training errors at 100 epochs, rules, and testing error

## 4 Conclusion

This research is attempted to investigate the machinability of Ti-6Al-4V alloy which is supposedly the hardest to machine. The Taguchi method was used to analyze and predict the optimal cutting parameters against the minimal cutting temperature. Based on Taguchi optimization, cutting speed of 10 m/minute, feed of 0.065 mm/rev, depth of cut 0.5 mm were obtained as optimal levels to attain minimum cutting temperature. Besides, it is observed that increase in cutting speed influences the higher cutting temperature. ANFIS predictive model was developed which can predict the cutting temperature against any input data. In overall, the developed model seems significant and effective with  $R^2 = 98\%$ .

**Funding** This work was supported by CERVIE, UCSI University, under REIG grant, REIG-FETBE-2022/018.

## References

1. Pesode, P., Barve, S.: A review—metastable  $\beta$  titanium alloy for biomedical applications. *J. Eng. Appl. Sci.* **70**(25), (2023). <https://doi.org/10.1186/s44147-023-00196-7>
2. Zhang, L., Chen, L.: A review on biomedical titanium alloys: recent progress and prospect. *Adv. Eng. Mater.* **21**(4) (2019)
3. Drouet, M., Pichon, L., Vallet, Y., Le Bourhis, E., Christiansen, T.L.: Surface engineering of titanium alloy TiAl6V4 by multi-interstitial diffusion using plasma processing. *Euro. J. Mater.* **2**(1), 1–11 (2022). <https://doi.org/10.1080/26889277.2021.2010504>
4. Ramesh, S., Karunamoorthy, L., Palanikumar, K.: Measurement and analysis of surface roughness in turning of aerospace titanium alloy (gr5). *Measur. J. Int. Measur. Conf.* **45**(5), 1266–1276 (2012)
5. You, S.H., Lee, J.H., Oh, S.H.: A study on cutting characteristics in turning operations of titanium alloy used in automobile. *Int. J. Precis. Eng. Manuf.* **20**, 209–216 (2019). <https://doi.org/10.1007/s12541-019-00027-x>
6. Jianxin, D., Yousheng, L., Wenlong, S.: Diffusion wear in dry cutting of Ti–6Al–4V with WC/Co carbide tools. *Wear* **265**, 1776–1783 (2008)
7. Lou, Y., Wu, H.: Effect of parameters on surface roughness during the ultra-precision polishing of titanium alloy. *PLoS ONE* **17**(8), e0272387 (2022). <https://doi.org/10.1371/journal.pone.0272387>
8. Agrawal, C., Wadhwa, J., Pitroda, A., Pruncu, C.I., Sarikaya, M., Khanna, N.: Comprehensive analysis of tool wear, tool life, surface roughness, costing and carbon emissions in turning Ti–6Al–4V titanium alloy: cryogenic versus wet machining. *Tribol. Int.* **153** (2021). <https://doi.org/10.1016/j.triboint.2020.106597>
9. Gupta, M.K., Nieslony, P., Korkmaz, M.E. et al.: Comparison of tool wear, surface morphology, specific cutting energy and cutting temperature in machining of titanium alloys under hybrid and green cooling strategies. *Int. J. of Precis. Eng. and Manuf.-Green Tech.* (2023). <https://doi.org/10.1007/s40684-023-00512-9>
10. Shastri, A., Nargundkar, A., Kulkarni, A.J. et al.: Optimization of process parameters for turning of titanium alloy (Grade II) in MQL environment using multi-CI algorithm. *SN Appl. Sci.* **3**(226) (2021). <https://doi.org/10.1007/s42452-021-04197-0>
11. Gupta, M.K., Sood, P.K., Sharma, V.S.: Machining parameters optimization of titanium alloy using response surface methodology and particle swarm optimization under minimum-quantity lubrication environment. *Mater. Manuf. Proc.* **31**(13), 1671–1682 (2016). <https://doi.org/10.1080/10426914.2015.1117632>
12. Singh, R., Dureja, J.S., Dogra, M., Randhwara, J.S.: Optimization of machining parameters under MQL turning of Ti-6Al-4V alloy with textured tool using multi-attribute decision-making methods. *World J. Eng.* **16**(5), 648–659 (2019). <https://doi.org/10.1108/WJE-06-2019-0170>
13. Akkuş, H., Yaka, H.: Optimization of cutting parameters in turning of titanium alloy (grade 5) by analysing surface roughness, tool wear and energy consumption. *Exp. Tech.* **46**, 945–956 (2022). <https://doi.org/10.1007/s40799-021-00525-6>
14. Palanikumar, S., Boppana, R., K., S. et al.: Analysis of chip formation and temperature measurement in machining of titanium alloy (Ti-6Al-4V). *Exp. Tech.* **47**, 517–529 (2023). <https://doi.org/10.1007/s40799-021-00537-2>
15. Sangwan, K.S., Saxena, S., Kant, G.: Optimization of machining parameters to minimize surface roughness using integrated ANN-GA approach. *Procedia CIRP* **29**, 305–310 (2015)
16. Elango, S., Varadaraju, K., Natarajan, E., Gnanamuthu, E.M.A., Durairaj, R., Mariappan, P.: PTFE in wet and dry drilling: two-tier modeling and optimization through ANFIS. *Math. Prob. Eng.* **10** (2022)

# Tools for Automated Structural Health Monitoring Using Deep Learning and Computer Vision Techniques



Rushikesh Gade, Surbhi Raj, and Jimson Mathew

**Abstract** Structural Health Monitoring (SHM) is a critical task in the management of buildings, bridges, and civil infrastructures. With the evolution of Artificial Intelligence (AI), SHM through AI is gaining popularity from past few years. Therefore, this work aims in providing SHM solution for wall defects through computer vision techniques. The work presents the development of mobile application to fully automate SHM procedure for inspection of building, finding defects, and its analysis. For crack detection purpose, MobileNetV2 as an algorithm is incorporated to determine two anomaly condition of whether the wall has crack or not. Mobilenet showed good result with an accuracy of 95%. The defect detected image is then segmented with the U-Net algorithm that resulted a Dice Similarity of 0.88, to determine the area of the damaged portion. The work also comprises real-time SHM of the walls using You Only Look Once version 5 (YOLOv5) for various defects such as crack, spalling, and seepage. To integrate these algorithms into mobile application, the models are converted into TensorFlow Lite (TFLite) format with the aim to reduce the size of the model and computational power. The proposed software has potential to significantly improve efficiency and effectiveness of SHM, providing a user-friendly and accessible solution for defect detection and analysis on mobile devices.

**Keywords** SHM · CV · MobileNetV2 · U-Net · YOLOv5

## 1 Introduction

The deterioration of infrastructure, such as cracks in concrete, spalling of concrete, corrosion of steel, and seepage, is a persistent problem that may harm the durability and safety of structures over time. If the life expectancy of infrastructure can be

---

R. Gade (✉) · S. Raj · J. Mathew  
Indian Institute of Technology Patna, Bihta 801103, India  
e-mail: [rushikesh\\_2111mt07@iitp.ac.in](mailto:rushikesh_2111mt07@iitp.ac.in)

S. Raj  
e-mail: [surbhi\\_2021cs36@iitp.ac.in](mailto:surbhi_2021cs36@iitp.ac.in)

J. Mathew  
e-mail: [jimson@iitp.ac.in](mailto:jimson@iitp.ac.in)

accurately assessed through inspection, it may be possible to prevent accidents by taking timely preventive measures. Traditional manual inspection methods are often time-consuming, labor-intensive, and prone to human error. So, in order to address this problem, automated inspection using computer vision (CV) and deep learning (DL) have emerged as a promising solution. This paper presents the development of mobile application for automated inspection of structural health of infrastructure. Using these tools, proactive maintenance planning and cost-effective prevention actions can be planned based on prior knowledge of the life expectancy and severity of deterioration. The mobile application allows user to upload the images of infrastructure captured from mobile camera or from gallery. Using CV, the application detects defects and summarizes the overall health of the infrastructure. Due to space limitation and computing capability of mobile devices, the models used in mobile application are optimized to be lightweight and efficient. This paper presents a detailed methodology for developing mobile, which will include DL algorithms for computer vision. The paper discusses the implementation details of each instrument, presents the study's findings, and explores the potential implications for the automation of structural health inspection.

## 2 Problem Definition

The problem at hand is to develop a platform that allows users to upload images or videos of their buildings to identify the defects and the extent of the affected area using deep learning and computer vision techniques, as there is a lack of such tools that are publicly available, which can assist people in identifying the defects and help them take necessary actions to mitigate the damage.

## 3 Related Work

Through the literature it has been seen that Structural Health Monitoring is been done through various means such as manual inspection, sensors and Unmanned Aerial Vehicle (UAVs). Bao et al. [1] have proposed a framework based on CV and DL technique for SHM in civil infrastructure. In the proposed approach, time series vibrational data are acquired which are then converted into image vectors. These image vectors are then be used by the deep neural network for the anomaly detection in bridges. In similar manner, Tang et al. [2] have proposed a method for SHM of the bridges by stacking the time domain and frequency domain of the time series data to create a 2D image space. These stacked data are then fed to the CNN network for data anomaly classification. Hung et al. [3] have proposed a technique for the anomaly detection of three-story frame by acquiring raw acceleration time series data from it. The time series data are then utilized by the combined CNN and LSTM network for the damage identification results. However, with health monitoring and anomaly

detection with the help of the sensors is tedious as it requires installation cost, time, and maintenance. Hence, researchers are now relying on health monitoring with the help of camera feed through UAVs, mobile robots, etc. Loupos et al. [4] have presented an autonomous system for tunnel inspection through a robotic platform. One of the tasks carried out is crack detection, which is accomplished using two steps DL technique and a heuristic approach using the image captured by the camera feed mounted on the robot. Wang et al. [5] have proposed a DL-based technique for damage detection of damaged glazed tiles in historic building. The approach used Masked Region-based CNN (R-CNN) for tiles detection and damage segmentation results. Nguyen et al. [6] have presented a solution for the concrete spall severity based on computer vision approach. Two Artificial Intelligence (AI)-based technique known as Extreme Gradient Boosting Machine (XGBoost) and Deep Convolutional Neural Network (DCNN) are incorporated for classifying images into shallow spall and deep spall. Kim et al. [7] have proposed a method for bridge inspection using UAVs based on DL technique. Camera images from the UAV camera feed are then trained on to the pre-trained R-CNN for identifying and quantifying the cracks in structure. Su et al. [8] have proposed a segmentation-based crack detection in bridges. This approach has used Convolutional Block Attention Module (CBAM) U-Net for the segmentation purpose which is further then post-processed using Gaussian fuzzy, Otsu, and medial skeletonization algorithms for accurately getting damaged detection results.

## 4 Dataset Description

The dataset comprises 5600 photos that were taken with a mobile device's camera as shown in Fig. 1. The pictures were sorted into two categories: pictures with wall cracks and pictures without wall cracks. Images are captured from different places to make a robust dataset. The dataset consists of 2800 photos depicting wall cracks and an equal number of photos (2800) showing walls without any cracks. To create a diverse and realistic dataset that can accurately represent real-world circumstances, the photographs were taken from various vantage points and lighting situations. In order to enable multi-class classification, a dataset of photographs depicting non-damaged objects was collected for comparison, as well as original images of various forms of defects, such as spalling, seepage, and wall cracks. 93 photographs of wall cracks, 26 images of seepage, 70 images of spalling, and 41 images of undamaged structures made up the initial dataset. Obtaining images for the spalling class proved to be challenging, requiring web searching and snapshots from video uploads on Internet as potential sources. We have applied data augmentation techniques to increase the size and diversity of the dataset by using the Python Albumentations library [9]. The transformations like shift-scale-rotate transformations, rotation, random blur, random gamma, random brightness or contrast adjustments, and horizontal flipping. By generating three augmented versions of each original image in the dataset, a larger and more diverse set of images was created for training and testing purposes. The incorporation of these enhanced photos is expected to enhance the model's ability to generalize and perform well on unseen data.



**Fig. 1** Captured images for dataset generation of crack and non-crack conditions

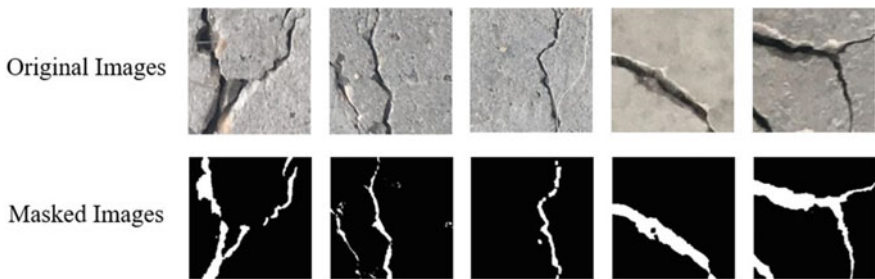


**Fig. 2** Generated masks for segmentation

A dataset of images of building walls with cracks was used to perform crack analysis using image segmentation technique U-Net architecture. It consists of images of building walls with various types and sizes of cracks. In order to train the U-Net model, a dataset of images with corresponding binary masks is required. The generated masks for 150 crack images are shown in Fig. 2 which represent the ground truth labels for each image, indicating the crack location or the region of interest (ROI) within image. The U-Net mask is a binary image where the object or ROI is represented in white color and background is represented in black color. The wall crack images were standardized to  $256 \times 256$  in order to maintain consistency with the input requirements of the architecture. Then created the binary masks manually using morphological operations such as erosion, dilation, opening, closing, adjusting intensity levels to ensure accuracy and facilitate the training of the model for semantic segmentation of wall cracks. The dataset of 150 images was split into a training set of 130 images and a testing set of 20 images. To improve the generalization ability of the model, augmentation techniques such as random horizontal and vertical flips, shift scale rotation, and random brightness contrast were applied to the input images and their corresponding binary masks using the Albumentation augmentation tool. The augmented training set was further split into a train set of 104 images and a validation set of 26 images, with an 80:20% split ratio (Fig. 3).

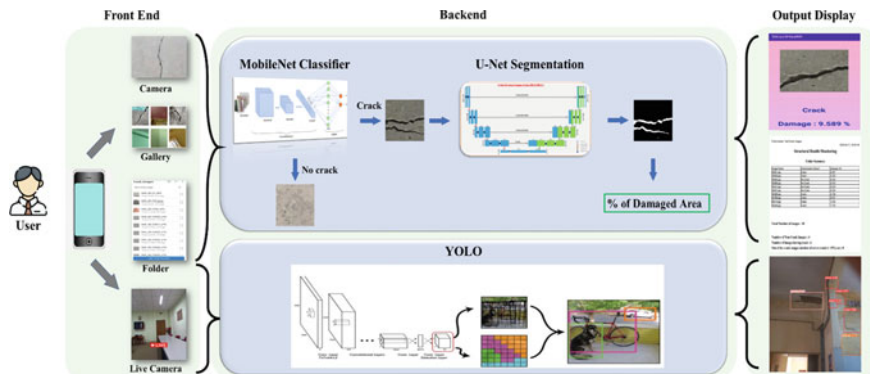


**Fig. 3** Pipeline for structural health monitoring

## 5 Software Architecture

StructHealth is an android application. This app is created with the help of Android Studio, which is powerful integrated development environment (IDE) for creating native Android applications.

One of the main components of android studio is the Graddle Build System, which allows for flexible and efficient project configuration and management. Android Studio supports a wide range of programming languages, including Java and Kotlin, making it a versatile tool for developers with different coding backgrounds. It includes support for external libraries. By leveraging these libraries and tools, developer can streamline their development process. The app includes wide range of features using machine learning (ML) and DL models to enhance the app's functionality. The implementation of MobileNetV2 for crack detection helps to identify cracks in images captured by the app, then using U-Net model for crack image segmentation, allows to calculate the area of damaged regions in the image. Also, the integration of YOLOv5 for the detection of spalling, crack, and seepage, enables us to identify these issues in real time using the app's camera feature. One notable feature for our app is the ability for user to upload folder of images containing building images, which app summarizes by providing the total images count, number of crack images, it's percentage of damage for each image and allows user to download it in PDF format. This feature enables users to quickly and easily access the state of their buildings and infrastructure, helping them take actions to address any issues detected.

## 6 Software Functionalities

### 6.1 Crack Classification Model

For the classification purpose of crack and non-crack images, we use MobileNetV2 CNN model. It is an opensource and freely available. It is lightweight and efficient, so for mobile devices with limited processing power and memory it's an ideal choice. MobileNetV2 is optimized for mobile devices, and its architecture is designed to run quickly and efficiently with high accuracy in image classification tasks, despite its small size, due to its separable architecture. In this study, pre-trained MobileNetV2 model from Keras is fine-tuned for a binary classification for crack and non-crack images. The model requires input images of size  $224 \times 224 \times 3$ , and only the final layers of the pre-trained model were modified to suit the specific task. The Adam optimizer and categorical cross-entropy loss function were used for training. The images were scaled within a range of  $-1$  to  $1$ . The model was trained for a specific number of epochs using a batch size of 32, and the model with the best validation accuracy was saved. The model achieved a high training accuracy of 98.78% and a validation accuracy of 94.92% during the training process (Table 1).

### 6.2 Segmentation Model

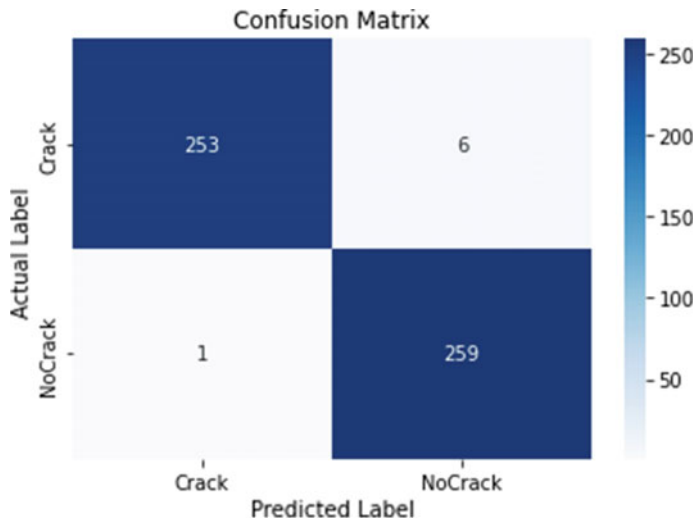
In recent years, semantic segmentation has become a well-known technique for automatically detection and segmenting wall cracks in images. U-Net binary segmentation model generates a binary mask that can be used to distinguish between the cracks and the background in the image. Our model takes an input image of size  $256 \times 256$  and applies convolutional layers to extract features. These features are then flattened (512) and passed through skip connections to preserve high-level information from earlier layers. The model applies the transpose convolution that upsamples the feature maps. It is essential for upscaling a low-resolution feature map to match the original dimension of the image. The skip connections enable the model to combine information from different levels of feature hierarchy, allowing it to perform accurate segmentation for region of interest (ROI). Binary cross-entropy (BCE) is used as the loss function for training the U-Net model. BCE commonly

**Table 1** Training parameters of proposed U-Net [13] architecture

Training parameters	Values
Image size	$224 \times 224 \times 3$
Epochs	10
Optimizer	Adam
Loss function	Categorical cross-entropy

**Table 2** Training parameters of proposed U-Net [13] architecture

Training parameters	Values
Train:validation:Test split	80:10:10
Image size	256 × 256
Epochs	55
Optimizer	Adam
Learning rate	0.0001
Loss function	BCE

**Fig. 4** Confusion matrix for the MobileNetV2 [12]

used for binary segmentation tasks and measures the difference between predicted mask and the ground truth mask. This model is trained using TensorFlow framework where Adam as optimizer with a learning rate of 0.0001 for training the model for 55 epochs. The Adam optimizer is popular for its efficient convergence and handling noisy gradients [10]. The various result metrics obtained for the segmentation task are as in Table 2 (Figs. 4, 5, and 6).

### 6.3 You Only Look Once (YOLO)

The application utilizes YOLOv5 for the real-time detection of building defects. Because of fast and accurate object detection capabilities of YOLOv5, it is widely used in object detection-based task. Also, it is lightweight algorithm so that it suits for embedded and mobile applications such as Android App. With the help of annotation

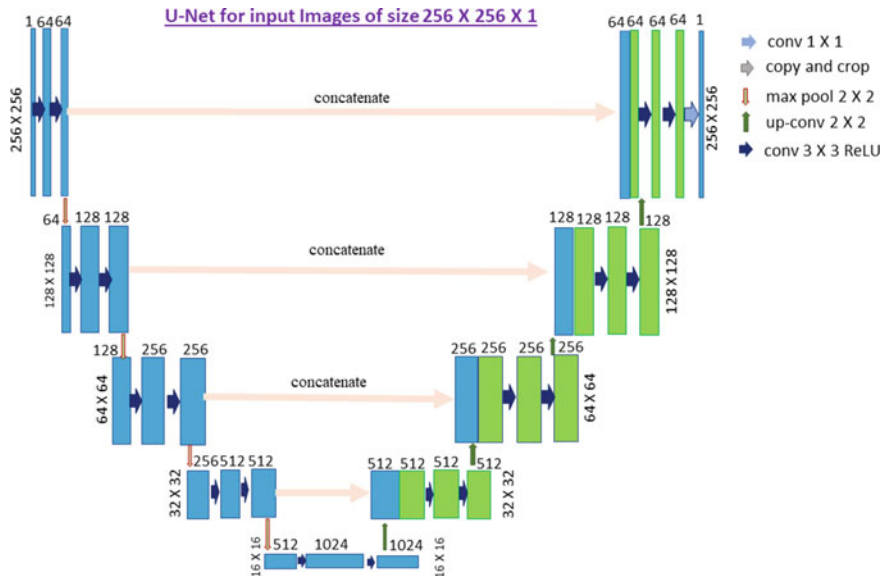


**Fig. 5** U-Net architecture [13]

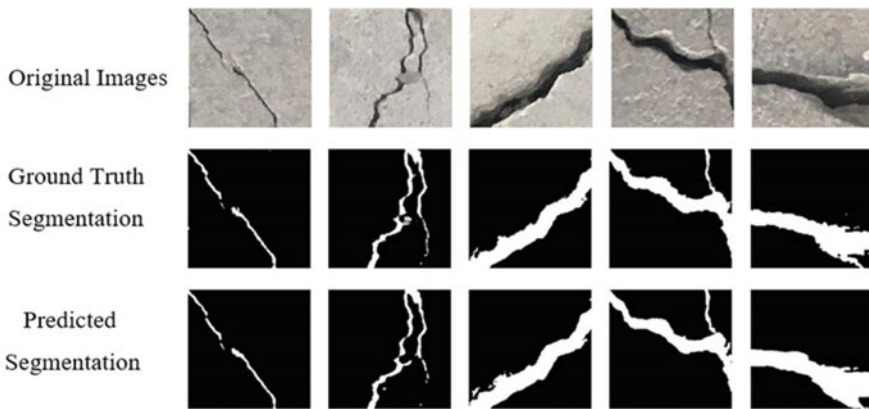


**Fig. 6** U-Net [13] predicted masks on sample images

tool “LabelImg” [11], 180 building images were annotated for three classes of defects crack, seepage, and spalling. Input image size for the model is  $256 \times 256$ . Then, it is trained for 80 epochs with the batch size of 16. The goal of this algorithm implementation is to enable on-the-spot building defect detection, which can lead to improve maintenance and implementation of the safety precautions. Evaluation of performance of algorithms is given in Tables 3 and 2.

**Table 3** Results of U-Net [13] Segmentation

Performance metrics	Scores
Accuracy	0.975
Precision	0.961
Recall	0.802
F1	0.87
Dice Similarity	0.8748
Jaccard score	0.875

**Table 4** Yolo performance

Class	Precision	Recall	mAP50	mAP50-95
Crack	0.860	0.827	0.909	0.602
Spalling	0.935	0.998	0.993	0.803
Seepage	0.923	0.949	0.984	0.679
All	0.906	0.925	0.962	0.695

## 7 Software Integration

The mobile application is developed with Android Studio software with Android Emulator Revision 32.1.12 and Android SDK platform tools-revision 34.0.1. To optimize the model for mobile deployment, we converted them from TensorFlow to TFLite model. It helps us in reduction in model size.

As can be seen from Figs. 7 and 8, the classification model showed a significant reduction in size of 76.99% after converting it into both TFLite model and TFLite optimized model. Furthermore, the inference time with TFLite also reduced by a remarkable 256 times. On the other hand, for the U-Net model, the TFLite model size was reduced by 66.68 %, but its inference time increased by 6 times. Similarly, for the TFLite optimized model, while the model size reduced significantly, the inference time increased significantly. Therefore, after consideration of both size and time factors, we decided to choose TFLite models for both algorithms, as they offered good balance between model size and faster inference. TFLite models are considerably smaller than original TensorFlow models, which has reduced the mobile applications overall storage footprint and permitted quicker model loading. The application required permissions for camera, folder, and Internet access. As part of applications functionality for crack analysis user can capture image or upload from gallery or can upload folder containing multiple images.

The application processes each image in the folder performing crack classification, then calculates the percentage of damaged area in the image with the help of segmentation. After scanning through all the images in folder, results are displayed in list format on the screen. User has option to download summary in PDF format also.

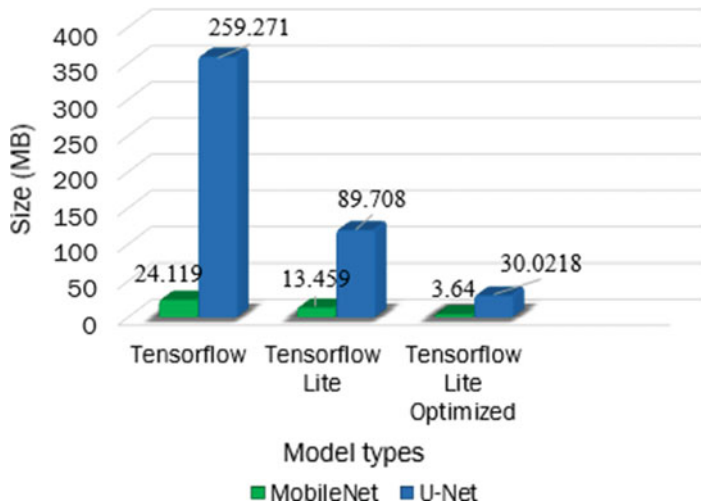


Fig. 7 Model size comparison

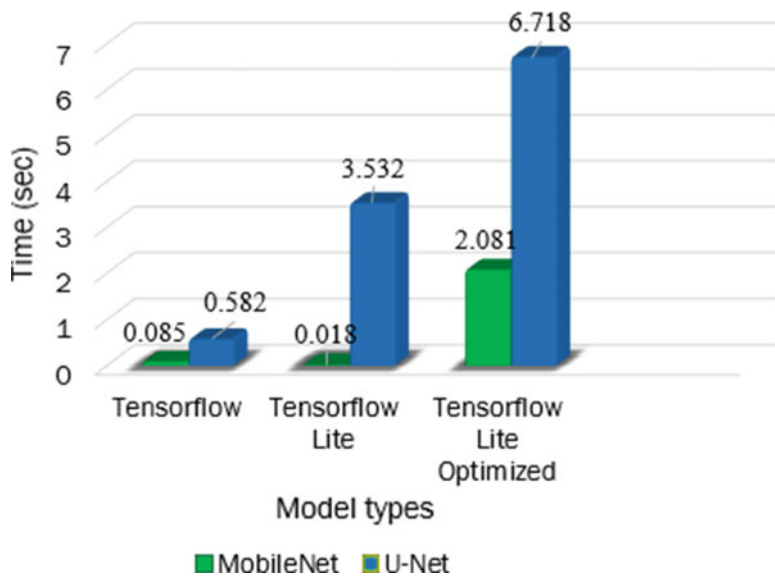
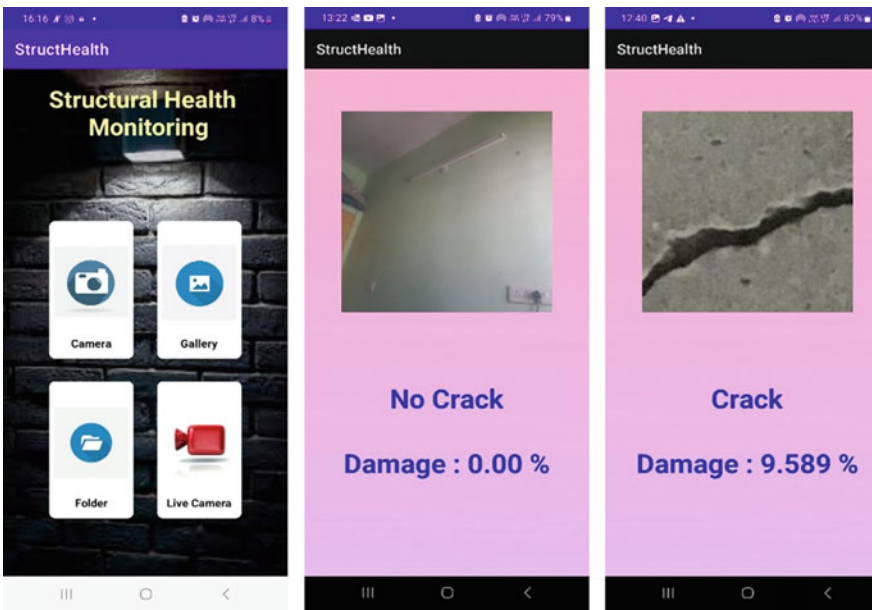


Fig. 8 Inference time comparison



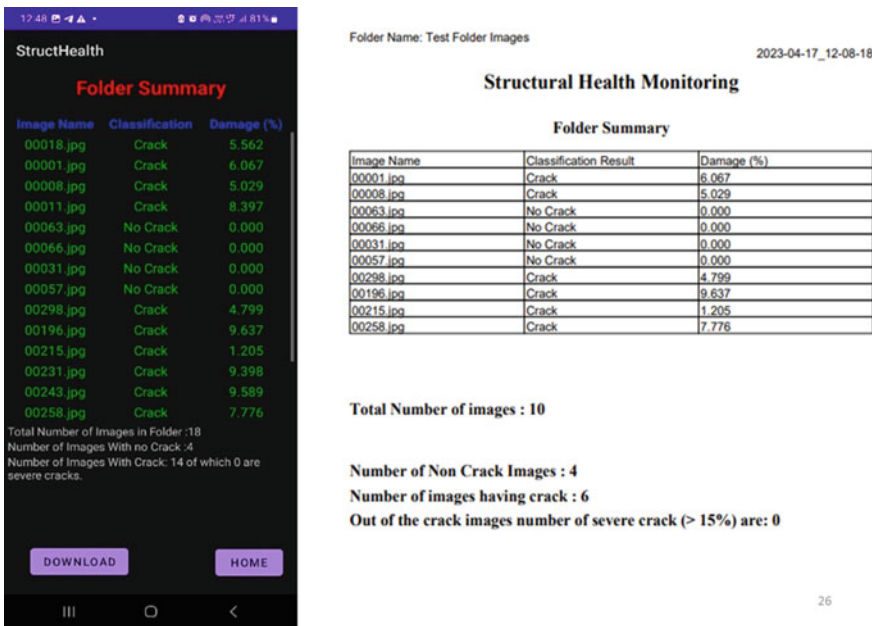
**Fig. 9** Mobile application interface

Utilizing iTextPDF library to facilitate the PDF operations, including generating and saving summary in PDF format.

It includes information like the folder name and the time this folder was downloaded. The name of the image, the categorization (crack or no crack), and the percentage of the damaged region are all listed in a table. A brief report also includes the number of photos processed and the number of images with and without cracks along with the crack analysis by providing the severity of the crack.

Our Java-based Android application uses YOLOv5 for real-time building defect detection. After training our YOLOv5 model, we converted our saved PyTorch model to TensorFlow Lite format as it provides a lightweight and efficient way to run machine learning models on mobile and embedded devices. This resulted the model size of 13.5 Mb. We were able to integrate YOLOv5 into our application using a dependency file that provides the necessary classes and methods for running the YOLOv5 model. The dependency file includes classes for loading and running the YOLOv5 model, as well as classes for preprocessing the input image and drawing bounding boxes around detected defects. We were able to use these classes to quickly and easily integrate YOLOv5 into our application (Figs. 9, 10 and 11).

By using a dependency file, we were able to avoid the need for manual integration of the YOLOv5 model, which can be a complex and time-consuming process. Instead, we were able to simply import the necessary classes and methods from the dependency file, and use them to perform building defect detection in real time.



26

Fig. 10 YOLO real-time detection



Fig. 11 YOLO real-time detection

## 8 Conclusion and Future Scope

An application developed for SHM using deep learning and computer vision techniques showed promising results. A few of its features make it an ideal tool for engineers and building maintenance personnel, such as defect detection and analysis, real-time defect identification, and analyze multiple building images simultaneously. The use TFLite models makes the application faster and lightweight, which is essential for mobile application as they provide optimized inference performance with reduced memory and computational requirements.

The future direction for this work includes expanding the model to identify additional types of building defects and incorporating a feature for suggesting remedial actions based on the severity of the identified defects. Also, in the future expanding the dataset to include a wider variety of building images with different types of defects could improve the model's ability to generalize and identify previously unseen images, which will help model to become more accurate and robust.

**Acknowledgements** We thank IIT Patna, India, for utilizing resources.

## References

1. Bao, Y., Tang, Z., Li, H., Zhang, Y.: Computer vision and deep learning-based data anomaly detection method for structural health monitoring. *Struct Health Monitor* **18**(2), 401–421 (2019)
2. Tang, Z., Chen, Z., Bao, Y., Li, H.: Convolutional neural network-based data anomaly detection method using multiple information for structural health monitoring. *Struct Control Health Monitor* **26**(1), e2296 (2019)
3. Hung, D.V., Hung, H.M., Anh, P.H., Thang, N.T.: Structural damage detection using hybrid deep learning algorithm. *J. Sci. Technol. Civil Eng. (STCE)-HUCE* **14**(2), 53–64 (2020)
4. Loupos, K., Doulamis, A.D., Stentoumis, C., Protopapadakis, E., Makantasis, K., Doulamis, N.D., Amditis, A., Chrobocinski, P., Victores, J., Montero, R., et al.: Autonomous robotic system for tunnel structural inspection and assessment. *Int. J. Intell. Robot. Appl.* **2**, 43–66 (2018)
5. Wang, N., Zhao, X., Zou, Z., Zhao, P., Qi, F.: Autonomous damage segmentation and measurement of glazed tiles in historic buildings via deep learning. *Comput.-Aided Civil Infrastruct. Eng.* **35**(3), 277–291 (2020)
6. Nguyen, H., Hoang, N.-D.: Computer vision-based classification of concrete spall severity using metaheuristic-optimized extreme gradient boosting machine and deep convolutional neural network. *Autom. Constr.* **140**, 104371 (2022)
7. Kim, I.-H., Jeon, H., Baek, S.-C., Hong, W.-H., Jung, H.-J.: Application of crack identification techniques for an aging concrete bridge inspection using an unmanned aerial vehicle. *Sensors* **18**(6), 1881 (2018)
8. Huifeng, S., Wang, X., Han, T., Wang, Z., Zhao, Z., Zhang, Pengfei: Research on a u-net bridge crack identification and feature-calculation methods based on a CBAM attention mechanism. *Buildings* **12**(10), 1561 (2022)
9. Buslaev, A., Iglovikov, V.I., Khvedchenya, E., Parinov, A., Druzhinin, M., Kalinin, A.A.: Albu-  
mentations: fast and flexible image augmentations. *Information* **11**(2), 125 (2020)

10. Haji, S.H., Abdulazeez, A.M.: Comparison of optimization techniques based on gradient descent algorithm: a review. *PalArch's J Archaeol Egypt/Egyptol* **18**(4), 2715–2743 (2021)
11. Tzutalin: LabelImg. Free Software. MIT License (2015)
12. Sandler, M., Howard, A., Zhu, M., Zhmoginov, A., Chen, L.-C.: MobileNetV2: Inverted 368 Residuals and Linear Bottlenecks. arXiv, 21 Mar 2019. <https://doi.org/10.48550/arXiv.1801.04381>
13. Ronneberger, O., Fischer, P., Brox, T. U-net: Convolutional networks for biomedical image segmentation. In *Medical Image Computing and Computer-Assisted Intervention—MICCAI 2015: 18th International Conference, Munich, Germany, October 5–9, 2015, Proceedings, Part III* 18 (pp. 234–241). Springer International Publishing (2015)

# Public Blockchain-Based Data Integrity Protection for Federated Learning in UAV Networks Using MAVLink Protocol



Jing Huey Khor, Michail Sidorov, Shaw Zuan Law, Sui Yuan Tan, and Peh Yee Woon

**Abstract** The utilization of federated learning in unmanned aerial vehicle (UAV) networks facilitates collaborative training of machine learning models by multiple UAVs while ensuring privacy preservation. However, the existing solutions for securing local model updates, such as heavy computation homomorphic encryption, secure multiparty computation, and differential privacy, are not feasible for UAV networks with limited computational resources and data capacity. To address this issue, a new lightweight protocol has been proposed, which protects the integrity of non-privacy sensitive local model updates in UAV networks using the MAVLink protocol over WiFi and LoRa communication technologies. The lightweight protocol has been designed using the SHA256 hash function and integrated with a public blockchain for integrity verification purposes. A proof of concept has been presented to demonstrate the proposed protocol's capability of protecting the integrity of local model updates in UAV networks. Furthermore, the security of the proposed protocol has been analyzed and shown to be secure against adversary-in-the-middle and replay attacks. The computation cost of the proposed protocol has also been evaluated and found to be supported by UAV networks.

**Keywords** Public blockchain · Data integrity · MAVLink · UAV · Federated learning

---

J. H. Khor (✉) · S. Z. Law · S. Y. Tan · P. Y. Woon  
Connected Intelligence Research Group University of Southampton Malaysia (UoSM), 79100  
Iskandar Puteri, Johor, Malaysia  
e-mail: [J.Khor@soton.ac.uk](mailto:J.Khor@soton.ac.uk)  
URL: <https://www.southampton.ac.uk/my/index.page>

M. Sidorov  
Department of Computer Science (IDI), Norwegian University of Science and Technology, 7034  
Trondheim, Norway

## 1 Introduction

Unmanned aerial vehicles (UAVs) are used for various tasks, including surveillance, inspection, and delivery. However, since the data collected by UAVs may contain sensitive information, such as personal information or trade secrets, it is not suitable to be shared with a central server. Therefore, federated learning has been utilized in UAVs networks to ensure data privacy. In a federated learning setup, the data is distributed across multiple UAVs, and the models are trained locally on each UAV without sharing the data with a central server. The local model updates are then aggregated to produce a global model that reflects the collective knowledge of all the UAVs.

Local models are susceptible to a variety of security attacks, including poisoning attacks (e.g. label-flipping [21], backdoor [22]), which subsequently affect the accuracy of a global model. Several approaches have been introduced to mitigate these attacks on federated learning models, including differential privacy, secure multiparty computation (SMPC), and homomorphic encryption. However, these approaches are typically not suitable for UAVs that have limited computational resources. Thus, a lightweight solution should be used for applications that use non-privacy sensitive data [3, 4].

Local models are often packaged into a set of model parameters and transmitted from UAVs to the server via unmetered network. For example, WiFi is considered as unmetered network as it does not have any explicit data usage limits and charges associated with their usage [2]. The MAVLink protocol has gained popularity among UAVs due to its simple message structure that can be supported by various communication technologies, such as WiFi, LoRa, Ethernet, serial communication, and more. MAVLink v2.0 can support a payload size of up to 255 bytes [9]. However, the size of the local model can vary, typically ranging from 1000 to 8000 kB for edge devices, depending on the complexity of the model [14]. Thus, the payload size limit of the MAVLink protocol makes it challenging to transmit large models over WiFi or other wireless networks.

Currently, none of the related works address the issue of integrity in local model updates with the MAVLink protocol. Therefore, this paper proposes a new lightweight protocol that incorporates public blockchain to guarantee non-privacy-sensitive federated learning local model updates using dual communication mode for UAV networks that utilize MAVLink protocol. The contributions of this paper are:

1. A new custom MAVLink message has been designed to include federated learning local model update signature as a packet payload.
2. A new lightweight protocol that guarantees the integrity of unencrypted non-privacy-sensitive federated learning model updates in UAV networks based on WiFi and LoRa dual communication mode.
3. A proof of concept to verify the feasibility of the proposed solution.
4. Performance analysis of the proposed protocol to evaluate the computation cost and security protection for local model updates.

The structure of the remaining paper is as follows: Sect. 2 examines the latest related work. Section 3 provides an overview of the standard MAVLink 2.0 and proposes a customized message ID to protect the integrity of federated learning. Section 4 describes a new lightweight protocol for protecting the integrity of local model updates in federated learning. Section 5 presents the proof of concept of the proposed lightweight protocol, and Sect. 6 analyzes its performance. Finally, Sect. 7 concludes the paper.

## 2 Related Works

Communication is crucial in federated learning since model parameters are shared with the server. If the parameters are not protected, a malicious UAV can use them to reconstruct the data of the UAVs via model-inversion adversarial attacks. Researchers proposed to use differential privacy [5, 10], homomorphic encryption [5, 13, 15, 16], and SMPC [1, 12, 18] to preserve privacy while sharing local model updates.

When using differential privacy, the UAVs add a small amount of random noise to the gradient information before sending it to the central aggregator. This noise is generated using a specific algorithm, such as Gaussian [10] or Laplace random noise [5] to ensure that the overall privacy of the data is preserved while still allowing the central aggregator to perform meaningful computations on the data.

Several research works have proposed the use of SMPC to enable multiple parties to jointly perform a computation on their private data while keeping their inputs confidential from each other. For example, SMPC has been utilized to ensemble model evaluation across hospitals to guarantee the privacy of models produced by each hospital [18]. In SMPC-based federated learning, the ElGamal encryption and Diffie–Hellman key exchange protocol have been used to preserve data privacy and parameter privacy [12]. Chen et al. improved privacy preservation in federated learning by isolating participants from model parameters, making it more resistant to generative adversarial networks [1]. However, SMPC is computationally expensive due to the complex functions involved, which may limit their applicability in scenarios where parties have limited computing power.

Homomorphic encryption is a type of public key encryption scheme that allows computation on ciphertexts without decrypting them. There are different types of homomorphic encryption, including fully (e.g. learning with error (LWE) [15]) and partially homomorphic encryption (e.g. Paillier [5, 13, 16]). While fully homomorphic encryption allows for multiple types of operations on ciphertexts, partially homomorphic encryption supports either addition or multiplication. The Paillier homomorphic encryption is more popular than LWE homomorphic encryption because multiplication is computationally more expensive than addition [16].

Although the methods mentioned above can help preserve data privacy, federated learning alone does not provide tamper-proof attributes to ensure data integrity. Verifiable computation is a cryptography tool meant to secure the integrity of computations on authenticated data. It enables a client to delegate to another entity the

computation of a function. The other entity evaluates the function and returns the result with a proof that the computation of the function was carried out correctly. Blockchain can be used to enhance the security and variability of verifiable computation. By storing the computation results and proofs on the blockchain, clients can verify that the computation was performed correctly and that the results have not been tampered with. Other than using the blockchain-based verifiable computation, local models can be stored on private blockchain to ensure their integrity due to its immutable features [18]. Permissioned blockchain has been proposed to be used to enhance the security and reliability of model parameters. Lu et al. developed a hybrid blockchain architecture which consists of the permissioned blockchain and the local directed acyclic graph for efficient data sharing in Internet of vehicle [11].

Linear homomorphic hash (LHH) has been utilized to verify final aggregation results to prevent attackers from tampering with the final aggregation results. In addition, digital signature has been used to ensure the integrity of LHH [15, 20]. Although blockchains and LHH have been deployed to guarantee the integrity of federated learning models and aggregation results, none of the existing research focuses on ensuring the integrity of federated learning models through a public blockchain in UAV systems using MAVLink protocol.

### 3 MAVLink Protocol

#### 3.1 MAVLink 2.0 Overview

MAVLink 2.0 is an update to the existing MAVLink 1.0 protocol, offering backward compatibility along with offers several key improvements. Figure 1 shows the MAVLink 2.0 packet format, which enhances MAVLink communication flexibility and security in UAVs systems through its updated features. MAVLink 2.0 includes packet signing, which helps to achieve message authentication. MAVLink 2.0 also has the ability to reduce the packet size through empty-byte payload truncation feature.

Another major enhancement is the increase in Message ID (MSG ID) size from 1 to 3 bytes, allowing support for over 16,777,216 unique message definitions. This is a significant improvement over the 256 message definitions supported by MAVLink 1.0. Although MAVLink 2.0 can support over 16 million MSG IDs, the common message set in MAVLink 2.0 contains 221 MSG IDs to cover a range of functionalities

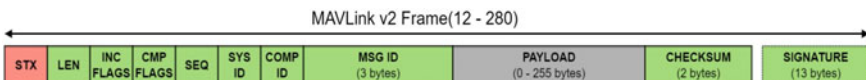


**Fig. 1** MAVLink 2.0 Packet format

STX (1 byte)	LEN (1 byte)	INC FLAGS (1 byte)	CMP FLAGS (1 byte)	SEQ (1 byte)	SYS ID (1 byte)	COMP ID (1 byte)	MSG ID (3 bytes)	PAYOUT FL Signature (6 bytes)	CHECKSUM (2 bytes)	SIGNATURE (13 bytes)
-----------------	-----------------	--------------------------	--------------------------	-----------------	--------------------	---------------------	---------------------	-------------------------------------	-----------------------	-------------------------

**Fig. 2** Custom MAVLink message ID 3 for federated learning signature payload

such as UAV control, telemetry, mission planning. Thus, the remaining unused MSG IDs can be used for custom message sets.

### 3.2 Proposed MAVLink 2.0 Custom Message

In this paper, Message ID 3 is used to define a custom message for guaranteeing the integrity of federated learning model updates. This custom message consists of a 6-byte payload as shown in Fig. 2, to represent a federated learning signature (FL\_sig) in the following section. This signature is obtained by taking the first 48 bits of a SHA256 hash of a complete federated learning model update (FL\_updates), as shown in Eq. 1.

$$\text{FL\_sig} = \text{SHA256\_48}(\text{FL\_updates}) \quad (1)$$

SHA256 hash function is an industry-standard one-way hash function used to produce a 256-bit hash value from any input message. It is widely used for digital signatures and message authentication code to guarantee data integrity. FL\_updates typically consist of two main components, namely model weights and training statistics. The model weights contain the updated weights and biases of the federated learning model after training on the local data. These parameters represent the changes made to the model during training and are the primary means by which the global model is updated. Training statistics contain local training information, such as loss value, accuracy, number of iterations, and learning rate during training. The current timestamp for the model updates is also included in the local training information to prevent replay attacks.

## 4 Proposed Lightweight Protocol for Preserving Local Model Update Integrity

Federated learning has been used to improve the accuracy and robustness of the federated learning models by training them on a diverse range of data from different UAVs. The proposed lightweight protocol is designed to be integrated with a public blockchain. The dual communication mode in this paper utilizes both WiFi and LoRa communication technology for enhancing the signal coverage of UAV networks. Since LoRa is a long-range communication protocol, it can easily extend

**Table 1** Notations used in the proposed protocol

Notations	Description
SHA256	SHA256 hash function
SHA256_48	The first 48 bits of a SHA256 hash
FL_sig	A 48 bits federated learning signature
FL_updates	Federated learning local model updates

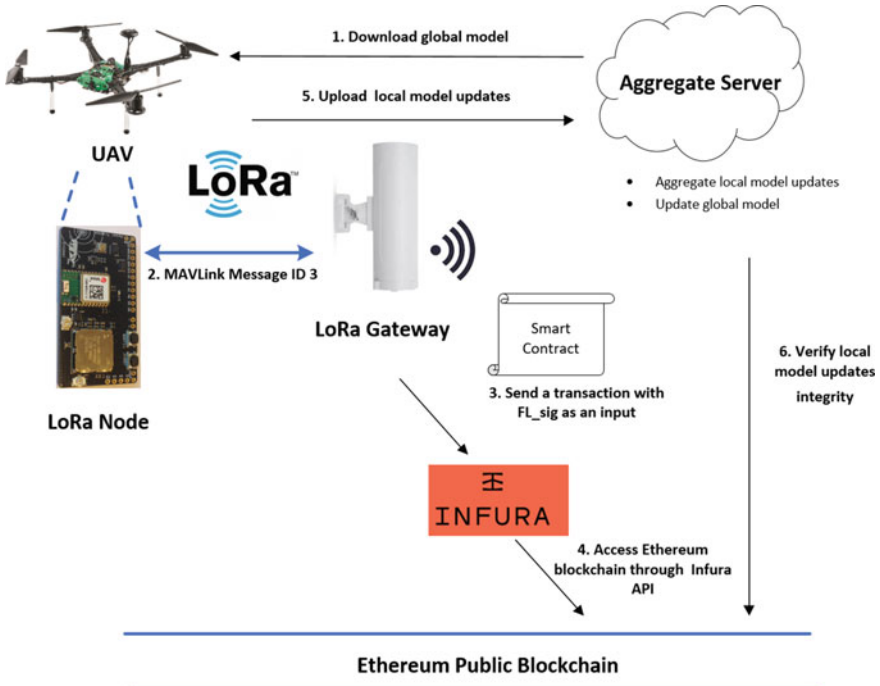
the coverage provided by short-range WiFi. WiFi is typically used for communication within a few hundred meters, LoRa; however, can transmit data over distances of 3.8 kilometers depending on the conditions and line of sight [17]. MAVLink 2.0 protocol is implemented on top of these two communication technologies since it is lightweight and suitable for UAV networks. However, as mentioned in Sect. 1, MAVLink is not suitable for large-size payloads; thus, the full local model updates are sent to the aggregate server using WiFi. Since UAVs might navigate outside of WiFi signal coverage, LoRa is used to send the hash of local model updates (FL\_sig), which is included as a payload in a customized MAVLink message.

Table 1 shows the notations used in the proposed protocol. The proposed protocol consists of two phases: signature generation and integrity verification. Each phase involves four parties, including UAV with embedded LoRa and WiFi modules, LoRa gateway, aggregate server, and public blockchain. The overall signature generation and verification process is illustrated in Fig. 3. The UAV performs local model training using TensorFlow Federated and computes FL\_sig using SHA256 hash function. The aggregate server aggregates local model updates from participated UAVs and updates the global model.

#### 4.1 Signature Generation Phase of Federating Learning Model Updates

The signature generation phase describes the steps needed for UAVs to generate a FL\_sig from local model updates. The steps are described as follows:

1. UAV downloads a global model from an aggregate server.
2. UAV trains the model locally using its own data.
3. UAV hashes the local model updates using the SHA256 hash function and extracts the first 48 bits as a federated learning signature.
4. The 48 bits federated learning signature, FL\_sig, is then included as a payload for MAVLink message ID 3.
5. UAV sends a MAVLink packet with MAVLink message ID 3 from an embedded LoRa node to a LoRa gateway.
6. The LoRa gateway then makes a transaction with the FL\_sig as an input on the Ethereum blockchain.



**Fig. 3** Proposed lightweight protocol for signature generation and integrity verification

7. UAV sends the locally trained model updates, FL\_updates, back to the aggregate server when it is within WiFi coverage.

#### 4.2 Integrity Verification Phase of Federated Learning Model Updates

The integrity verification phase is used to describe the steps needed to verify the integrity of local model updates to prevent any modification by attackers. The steps are as follows:

1. Aggregate server compares the computed federated learning signature with the one stored on the blockchain.
2. If they are equal, the local model update integrity is verified. The local model updates will be combined with other verified local model updates collected from other participating UAV to create a new global model.
3. The new global model is then distributed to all of the UAVs for further training and iteration.

4. This process is repeated until the global model reaches the desired level of accuracy and robustness, while still preserving data privacy on each individual UAV.

## 5 Proof of Concept

A decentralized web application was created using Hypertext Markup Language (HTML) as shown in Fig. 4. A smart contract named *FederatedLearning.sol* was designed as shown in Fig. 5. This contract has two local variables, namely *modelHash* (bytes6 data type) and *owner* (address data type). It contains two functions and one constructor, described below:

1. Constructor: sets the contract owner as the address that deploys the contract.
2. *setSignature (bytes6 updateHash)* function: stores the first 48 bits of the hash in the *modelHash* state variable.
3. *verifyModelIntegrity (bytes6 updateHash)* function: verifies the integrity of the model by comparing the first 48 bits of the SHA256 hash of the local model updates to the stored *modelHash* state variable.

Program to interact with the smart contract was written in JavaScript. It provides an interface to the Ethereum Goerli testnet blockchain. This allows data from the blockchain to be read through a smart contract and send transactions to update the state of the smart contract. The smart contract is written using the Solidity programming language and was deployed to the Ethereum Goerli testnet through an Infura

Timestamp	From	To	Signature	Integrity	Transaction Hash
Apr-19-2023 16:33:36	0xb8c9a8c350336e5833ed73f76a8fe62a3d00f153	0x959c6fea56af0e27fe2dd97957f3205397bca437	0x2899d508e4df	Verified	0xccd394b9155a50d5cf57d5fe3d784579424555c5c7230149879aca5e9babd28

**Fig. 4** Decentralized web application for integrity of local model updates verification

```
function setSignature(bytes6 updateHash) public onlyOwner {
    modelHash = updateHash;
}
```

**Fig. 5** A snippet of *setSignature* function from *FederatedLearning.sol* contract

endpoint. Infura is a web service that enables developers to access the Ethereum blockchain through remote Ethereum nodes. This avoids the need to set up and maintain own Ethereum node.

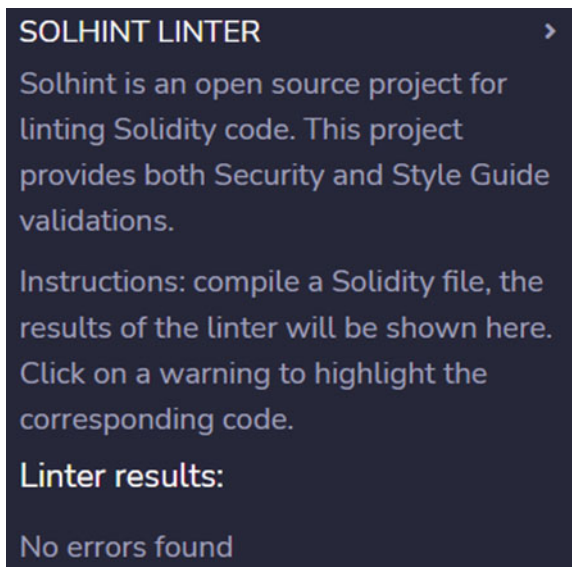
## 6 Performance Analysis

### 6.1 Smart Contract Analysis

The security of the *FederatedLearning.sol* smart contract, built for the Ethereum blockchain, has been thoroughly analyzed using two industry-standard security analysis tools: Solhint and Mythril. Solhint is a static analysis tool that provides an extensive range of validation rules to detect syntax-related security vulnerabilities in smart contracts. Its rich set of validation rules covers a wide variety of security issues, including uninitialized storage pointers, insecure hashes, and gas-related vulnerabilities. Analysis using Solhint is presented in Fig. 6. Linter result shows that no syntax errors were found in the *FederatedLearning.sol* contract.

Furthermore, a dynamic analysis was conducted using Mythril via Docker image. Mythril employs a range of techniques, including concolic analysis, taint analysis, and control flow checking, to detect various types of security vulnerabilities, such as integer underflows and overflows, reentrancy attacks, and owner-overwrite-to-Ether-withdrawal [8]. As depicted in Fig. 7, the comprehensive analysis in Mythril revealed no security issues in the *FederatedLearning.sol* smart contract.

**Fig. 6** Solhint linter results



```
C:\Users\JKhor>docker run -v C:/Users/JKhor:/tmp mythril/myth analyze /tmp/FederatedLearning.sol
The analysis was completed successfully. No issues were detected.
```

**Fig. 7** Mythril security analysis results

## 6.2 Protocol Security Analysis

The federated learning local model updates are hashed using the industry standard SHA256 hash functions. The security and performance of the SHA256 have been formally analyzed in numerous other works. It is unlikely that 2nd preimage collision attacks will be possible for at least the next decade using SHA256 to secure the secret key. The strength of the SHA256 hash function to resist 2nd preimage collision attacks is estimated to be between 201 and 256 bits [7].

The adversaries might attempt to perform adversary-in-the-middle (AITM) attacks on federated learning local model updates that are sent between UAV and aggregate server in a WiFi communication channel to compromise global model accuracy. However, such attacks are unsuccessful because the federated learning local model updates have been hashed with a SHA256 and the first 48 bits of hash value have been included in the payload of MAVLink message 3. The aggregate server can verify the integrity of the local model updates by comparing the hashed of the received model updates and the ones stored on the blockchain before including them for the global model updates.

The adversaries might attempt to capture the federated learning model updates that are transmitted in a communication channel and replay them which consequently results in the aggregate server receiving multiple copies of the same model update. This can be mitigated by including a timestamp in the model updates. The model updates will then be hashed using SHA256 and stored on the blockchain. If the adversaries replay the same model updates, a duplicate model update hash value will be found on the blockchain. Hence, the replay message will not be included in the global model update.

## 6.3 Computation Cost Analysis

In [20], data integrity protection was achieved using digital signature algorithms and hash functions. However, the specific digital signature algorithms used in [20] were not described in detail. Typically, digital signature algorithms use public key cryptographic algorithms to generate digital signatures. It is worth noting that while the SHA256 hash function only takes 0.0001 seconds to complete on low-power IoT devices [6], the computation time for ECC-160 public key cryptographic algorithm is much higher, taking approximately 1.61 s to complete [19].

**Table 2** Performance evaluation of the proposed protocol with other related works

Description	Proposed protocol	[18]	[20]
<i>Secure from</i>			
AITM attack	Yes	Yes	Yes
Replay attack	Yes	Yes	Yes
Blockchain integration	Yes	No	No
Secure smart contract	Yes	NA	NA
Privacy protection (algorithm)	NA	Homomorphic encryption, double masking	Symmetric encryption
Integrity protection (algorithm)	Hash function	Digital signature algorithm, hash function	Digital signature algorithm, hash function
Computation cost (s)	0.0001 <sup>a</sup>	1.61 <sup>a</sup>	1.61 <sup>a</sup>

<sup>a</sup>Estimated value based on the related works

#### 6.4 Comparative Analysis

The proposed protocol has been evaluated and compared with other related works, as shown in Table 2. The proposed protocol outperforms other related works in terms of computation cost. The use of SHA256 hash function ensures the integrity of the local model updates, as any modifications to the model would result in a different hash value. By incorporating the protocol with a public blockchain, the integrity of the local model updates can be verified by anyone on the network. This adds an additional layer of transparency and accountability, as any attempts to tamper with the model updates would be detectable by the aggregate server.

### 7 Conclusions

In this paper, a lightweight protocol has been proposed for protecting the integrity of local model updates in federated learning for UAV networks. The protocol has been designed using the SHA256 hash function and utilizes a public blockchain to provide integrity verification. A proof of concept has been conducted to validate the proposed protocol, and the security of the protocol has been analyzed theoretically, demonstrating its effectiveness in mitigating AITM and replay attacks. The computation cost of the protocol has been evaluated, and a comparative analysis with related work has shown its suitability for UAV networks.

Future work will concentrate on the development of a lightweight symmetric encryption algorithm to ensure the privacy of local model updates for resource-constrained IoT devices. Popular datasets such as EMNIST, NIST, and CIFAR-10 will be utilized to evaluate the performance of encryption algorithms in preserving privacy.

## References

1. Chen, Z., Fu, A., Zhang, Y., Liu, Z., Zeng, F., Deng, R.H.: Secure collaborative deep learning against GAN attacks in the internet of things. *IEEE IoT J.* **8**(7), 5839–5849 (2021). <https://doi.org/10.1109/JIOT.2020.3033171>
2. Cui, Y., Guo, J., Li, X., Liang, L., Jin, S.: Federated edge learning for the wireless physical layer: opportunities and challenges. *China Commun.* **19**(8), 15–30 (2022). <https://doi.org/10.23919/JCC.2022.08.002>
3. Hadian, M., Altuwaiyan, T., Liang, X., Zhu, H.: Privacy-preserving task scheduling for time-sharing services of autonomous vehicles. *IEEE Trans. Veh. Technol.* **68**(6), 5260–5270 (2019). <https://doi.org/10.1109/TVT.2019.2909468>
4. Hosseinalipour, S., Brinton, C.G., Aggarwal, V., Dai, H., Chiang, M.: From federated to fog learning: distributed machine learning over heterogeneous wireless networks. *IEEE Commun. Mag.* **58**, 41–47 (2020)
5. Jia, B., Zhang, X., Liu, J., Zhang, Y., Huang, K., Liang, Y.: Blockchain-enabled federated learning data protection aggregation scheme with differential privacy and homomorphic encryption in IIoT. *IEEE Trans. Ind. Inf.* **18**(6), 4049–4058 (2022). <https://doi.org/10.1109/TII.2021.3085960>
6. Khor, J.H., Sidorov, M., Ho, N.T.M., Chia, T.H.: Public blockchain-based lightweight anonymous authentication platform using zk-SNARKS for low-power IoT devices. In: 2022 IEEE International Conference on Blockchain (Blockchain), pp. 370–375 (2022). <https://doi.org/10.1109/Blockchain55522.2022.00058>
7. Khor, J.H., Sidorov, M., Ong, M.T., Chua, S.Y.: Public blockchain-based data integrity verification for low-power IoT devices. *IEEE IoT J.* 1–1 (2023). <https://doi.org/10.1109/JIOT.2023.3259975>
8. Khor, J., Masama, M.A., Sidorov, M., Leong, W., Lim, J.: An improved gas efficient library for securing IoT smart contracts against arithmetic vulnerabilities. In: Proceedings of the 2020 9th International Conference on Software and Computer Applications. ICSCA 2020, pp. 326–330. Association for Computing Machinery, New York, NY, USA (2020). <https://doi.org/10.1145/3384544.3384577>
9. Koubâa, A., Allouch, A., Alajlan, M., Javed, Y., Belghith, A., Khalgui, M.: Micro air vehicle link (MAVlink) in a nutshell: a survey. *IEEE Access* **7**, 87658–87680 (2019). <https://doi.org/10.1109/ACCESS.2019.2924410>
10. Liu, Y., Peng, J., Kang, J., Iliyasu, A.M., Niyato, D., El-Latif, A.A.A.: A secure federated learning framework for 5g networks. *IEEE Wirel. Commun.* **27**(4), 24–31 (2020). <https://doi.org/10.1109/MWC.01.1900525>
11. Lu, Y., Huang, X., Zhang, K., Maharjan, S., Zhang, Y.: Blockchain empowered asynchronous federated learning for secure data sharing in internet of vehicles. *IEEE Trans. Veh. Technol.* **69**(4), 4298–4311 (2020). <https://doi.org/10.1109/TVT.2020.2973651>
12. Ma, X., Zhang, F., Chen, X., Shen, J.: Privacy preserving multi-party computation delegation for deep learning in cloud computing. *Inf. Sci.* **459**, 103–116 (2018). <https://doi.org/10.1016/j.ins.2018.05.005>
13. Ma, Z., Ma, J., Miao, Y., Li, Y., Deng, R.H.: Shieldfl: Mitigating model poisoning attacks in privacy-preserving federated learning. *IEEE Trans. Inf. Forensics Secur.* **17**, 1639–1654 (2022). <https://doi.org/10.1109/TIFS.2022.3169918>

14. Pandey, S.R., Nguyen, M.N.H., Dang, T.N., Tran, N.H., Thar, K., Han, Z., Hong, C.S.: Edge-assisted democratized learning toward federated analytics. *IEEE IoT J.* **9**(1), 572–588 (2022). <https://doi.org/10.1109/JIOT.2021.3085429>
15. Ren, Y., Li, Y., Feng, G., Zhang, X.: Privacy-enhanced and verification-traceable aggregation for federated learning. *IEEE IoT J.* **9**(24), 24933–24948 (2022). <https://doi.org/10.1109/JIOT.2022.3194930>
16. Shin, Y.A., Noh, G., Jeong, I.R., Chun, J.Y.: Securing a local training dataset size in federated learning. *IEEE Access* **10**, 104135–104143 (2022). <https://doi.org/10.1109/ACCESS.2022.3210702>
17. Sidorov, M., Khor, J.H., Nhut, P.V., Matsumoto, Y., Ohmura, R.: A public blockchain-enabled wireless LoRa sensor node for easy continuous unattended health monitoring of bolted joints: implementation and evaluation. *IEEE Sens. J.* **20**(21), 13057–13065 (2020). <https://doi.org/10.1109/JSEN.2020.3001870>
18. Stephanie, V., Khalil, I., Atiquzzaman, M., Yi, X.: Trustworthy privacy-preserving hierarchical ensemble and federated learning in healthcare 4.0 with blockchain. *IEEE Trans. Ind. Inf.* pp. 1–10 (2022). <https://doi.org/10.1109/TII.2022.3214998>
19. Wander, A., Gura, N., Eberle, H., Gupta, V., Shantz, S.C., Sun: Energy analysis of public-key cryptography on small wireless devices (2004)
20. Wang, R., Lai, J., Zhang, Z., Li, X., Vijayakumar, P., Karuppiah, M.: Privacy-preserving federated learning for internet of medical things under edge computing. *IEEE J. Biomed. Health Inf.* **27**(2), 854–865 (2023). <https://doi.org/10.1109/JBHI.2022.3157725>
21. Zhang, J., Ge, C., Hu, F., Chen, B.: RobustFL: Robust federated learning against poisoning attacks in industrial IoT systems. *IEEE Trans. Ind. Inf.* **18**(9), 6388–6397 (2022). <https://doi.org/10.1109/TII.2021.3132954>
22. Zhao, L., Hu, S., Wang, Q., Jiang, J., Shen, C., Luo, X., Hu, P.: Shielding collaborative learning: mitigating poisoning attacks through client-side detection. *IEEE Trans. Depend. Secure Comput.* **18**(5), 2029–2041 (2021). <https://doi.org/10.1109/TDSC.2020.2986205>

# Improving Production Rate by Analyzing Wire-Electrical Discharge Machining Parameters and Developing a Prediction Model



S. Suresh , S. Ramesh, Elango Natarajan , Chun Kit Ang, Kanesan Muthusamy, and D. Velmurugan

**Abstract** This research aims to investigate the machinability of a SiC-reinforced Al6061-T6 composite by wire-cut electric discharge machining (Wire-EDM) and to develop a predictive model using artificial neural network (ANN). The machine parameters such as current (I), pulse-on time ( $T_{on}$ ), pulse-off time ( $T_{off}$ ), and wire feed (EF) are examined and optimized for a high material removal rate (MRR). The experiments are designed using Taguchi L<sub>16</sub> orthogonal array, and experiments are conducted at room temperature. The MRR obtained at different experiments is analyzed using statistical tools. An ANN model was then developed, and its performance was evaluated by comparing prediction results with experimental results. Visual graphs were used to show the combined impact of Wire-EDM factors on machinability performance. The suggested model reduces the time needed to set the process parameter values, improving production rate and process effectiveness.

**Keywords** Wire-EDM · Artificial neural network · Al6061-T6 · Silicon carbide · Nanoparticles

---

S. Suresh

Department of Mechanical Engineering, Erode Senguthar Engineering College, Erode, India

S. Ramesh

Department of Mechanical Engineering, Jerusalem College of Engineering, Chennai, India

E. Natarajan · C. K. Ang · K. Muthusamy

Faculty of Engineering, Technology and Built Environment, UCSI University, 56000 Kuala Lumpur, Malaysia

e-mail: [elango@ucsiuniversity.edu.my](mailto:elango@ucsiuniversity.edu.my)

D. Velmurugan

Department of Mechanical Engineering, Muthayammal Engineering College, Rasipuram, India

## 1 Introduction

Lightweight alloys are increasingly significant in many mechanical industries, including shipbuilding, aerospace, and automobiles. Aluminum alloys are in high demand due to industry requirements due to their high specific stiffness and strength, are lightweight, easily cast and machined, and have good heat conductivity [1–3]. The 6061-T6 alloy is becoming increasingly popular among these aluminum alloys due to its outstanding features, including high strength-to-weight ratio, excellent weldability/machinability, heat conductivity, and higher oxidation/corrosion resistance [4–6]. The alloys of metals are reinforced with particulate ceramics or fibers to achieve combined properties and formed as metal matrix composites. The properties of these materials have excellent applications in various areas like missiles, jets and cutting tools, nuclear reactors, and aerospace components production [7–9]. Ceramic particles such as  $\text{Al}_2\text{O}_3$  [10, 11], silicon carbide [12],  $\text{SiO}_2$  [13], fly ash, zircon, boron carbide, and other reinforcements enhance the metal matrix composite's mechanical and tribological properties.

Wire-electrical discharge machining (Wire-EDM) is the most popular unconventional machining technique in modern industries for producing complex shapes on modern materials with excellent quality and accuracy. In this process, the material from the workpiece is removed using the electro-discharge erosion effect of electrical sparks between the electrode wire and the work material [14]. The voltage has been supplied between the electrode wire and the chosen work material with dielectric fluid to melt the work material surface by the discharge of sparks on it. Because the electrode wire continually moves from one end to the other, the material is continuously removed [15, 16]. The operator's skill and manufacturer recommendations heavily influence the selection of Wire-EDM machining parameters. As a result, experimental techniques are required to optimize the machining parameters for newer materials.

Many direct and indirect factors, including pulse-on/off timing, peak current, wire tension, gap voltage, discharge frequency, mechanical and thermal characteristics of the wire electrode, workpiece, etc., influence this process. Most researchers have focused on how WEDM input parameters affect several responses, such as materials removal rate (MRR), kerf width, and surface roughness [8]. Deepak et al. [17] studied the process parameter effects on the wire-EDM of artificially aged Al6061/B4C composites using response surface methods methodology. They reported the impact of crucial parameters such as pulse-on/off time and current to obtain high MRR. Hammami et al. [18] investigated the effect of wire-EDM parameters of 2017-T451 and 7075-T651 aluminum alloys. They reported that the pulse-on and -off time significantly influenced the surface roughness of the machined sample. Rozenek et al. [19] reported an experimental investigation on the surface roughness for machining metal matrix composite AlSi7Mg reinforced with SiC and  $\text{Al}_2\text{O}_3$ . Pulse-on time, pulse-off time, discharge current, and voltage were considered process parameters. The result of the investigation showed that the feed rate and surface roughness increase trend with increasing discharge energy. Pramanik [20] conducted the wire-EDM

of SiC particles (700 nm) reinforced with 6061 aluminum alloy. It is revealed that significant variations in the wire diameter cause the uncontrolled spark due to small reinforced particles in the electrode gap. Moreover, the unreinforced matrix material experienced the most negligible reduction in electrode diameter.

Due to the electric discharge, the wire's diameter is more significant when it first enters the slit/kerf and gradually lowers as the machining process moves along. As a result, the wire's diameter changes as the slit/kerf increases, getting bigger at the top and smaller at the bottom. The MMC with macro-size SiC-reinforced particles shows the most wire electrode wear, resulting in the largest taper. The matrix material had a minor taper and the slightest loss in wire electrode diameter. The size of the reinforcing particles on wire-EDM of MMCs dramatically influences the process capability in terms of wear of the electrode, surface integrity, and material removal rate (MMR) [21, 22]. As reinforcement size increases, MRR drops, whereas more significant considerable reinforcements can prevent the melting of the matrix material.

Many optimizations have been conducted to predict the machining performance or improve the machinability of aluminum MMCs with different reinforcing particles, e.g., weight-based constrained algorithm [23], Taguchi's approach [24], Taguchi's-based gray relational analysis [25], RSM [26, 27], Gorilla Troops Optimizer[28], adaptive neuro-fuzzy inference system [29], particle swarm optimization [30], and ANN [31]. Based on a detailed survey of the literature, it was proved that the artificial neural network (ANN)-based model had been used to effectively predict the mechanical properties of metals and alloys [31–33].

In recent years, much research [22, 34–36] has been conducted on the Wire-EDM processing of different AMMCs with macro-size reinforcements. But limited research has been observed on the Al alloys, especially Al6061-T6 alloy with reinforcements of nanoparticles. This research investigates the effects of crucial parameters such as current ( $I$ ), pulse-on time ( $T_{on}$ ), pulse-off time ( $T_{off}$ ), and wire feed (WF). It develops optimal settings to enhance the productivity of 6061-T6/nano-SiC MMC in terms of MRR. The regression model is established to predict MRR by using artificial neural network (ANN).

## 2 Experimental Procedure

### 2.1 Base Material and Material Matrix Composite Preparation

The base material employed in this work was 6061-T6 aluminum alloy. Its chemical composition (%) is Si = 0.2, Fe = 0.22, Cu = 2.0 max, Mn = 0.1, Mg = 2.1–2.9, Zn = 5.1–6.1, Ti = 0.1 max, Cr = 0.2, and Al remaining. The aluminum matrix was reinforced with 6wt% of silicon carbide (SiC) nanoparticles with an average

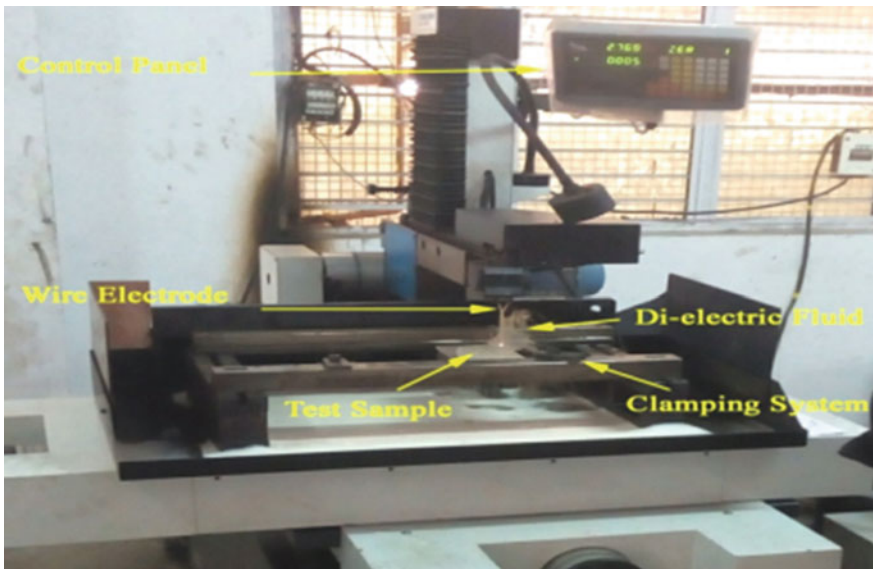


**Fig. 1** Wire-cut EDM process

particle size of 50 nm using stir casting method. Silicon carbide (SiC) is a high-performance monolithic ceramic of low density ( $2.52 \text{ g/cm}^3$ ) combined with high strength and hardness. Common applications of SiC are water pump seals, bearings, pump components, and extrusion dies. SiC offers a higher life for the component when compared with  $\text{Al}_2\text{O}_3$ . We adopted the metal matrix composite (MMC) samples preparation method used by Prakash et al. [37].

## 2.2 Wire-EDM Experimental Setup

The experiments were conducted using a computer numerically controlled wire-cut EDM machine (Make: Concord Wire-EDM, Model: DK7732). A cylindrical wire made of brass (diameter = 0.18 mm) was used as an electrode. A dielectric fluid (distilled water) was flooded between the wire gap and the workpiece to flush away the debris. The wire-EDM experimental setup is shown in Fig. 1.

## 2.3 Design of Experiment (DoE) and Experimentation

The machining parameters such as current ( $I$ ), pulse-on time ( $T_{\text{on}}$ ), pulse-off time ( $T_{\text{off}}$ ), and wire feed (WF) were considered input parameters. Table 1 shows the

wire-EDM process parameters and their levels of setting. The levels were chosen based on previous studies and existing literature [36, 38]. The pressure of dielectric fluid and the thickness of the samples were kept constant during the experiments. The experiments were designed by using Taguchi L<sub>16</sub> orthogonal array. Test samples were machined following the experimental plan depicted in Table 2.

The MRR acquired for each trial was calculated during machining using the weight loss method indicated by Eq. 1. The weight of the workpiece before ( $W_b$ ) and after ( $W_a$ ) machining was calculated using an electronic mass balance (Accuracy: 0.001 g). Computed MRR is also presented in Table 2.

$$\text{MRR} = \frac{W_b - W_a}{t} \left( \frac{\text{mg}}{\text{s}} \right) \quad (1)$$

**Table 1** Process parameter and its levels

Process parameters	Units	Symbol	Levels			
			L1	L2	L3	L4
Pulse-on time ( $T_{\text{on}}$ )	μs	A	20	30	40	50
Pulse-off time ( $T_{\text{off}}$ )	μs	B	10	15	20	25
Current ( $I$ )	A	C	3	4	5	6
Wire feed (WF)	mm/min	D	1	2	3	4

**Table 2** Experimental plan for machining and the respective MRR

Trail no.	Pulse-on time (μs)	Pulse-off time (μs)	Current (A)	Wire feed (mm/min)	MRR (mg/s)
1	20	10	3	1	0.344
2	30	15	3	2	0.452
3	40	20	3	3	0.532
4	50	25	3	4	0.585
5	20	15	4	3	0.415
6	30	10	4	4	0.514
7	40	25	4	1	0.339
8	50	20	4	2	0.513
9	20	20	5	4	0.829
10	30	25	5	3	0.595
11	40	10	5	2	0.713
12	50	15	5	1	0.577
13	20	25	6	2	0.354
14	30	20	6	1	0.339
15	40	15	6	4	1.163
16	50	10	6	3	1.028

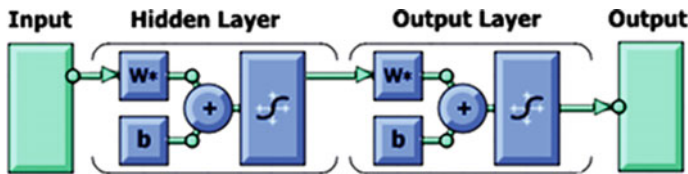


**Fig. 2** ANN-two layer model for MRR prediction

## 2.4 Artificial Neural Network (ANN)

The computational capability of an artificial neural network (ANN) was used to model the WEDM process for predicting the response variables (MRR) involved in the machining of AA6061-6/SiC composites. The neural network is a highly parallel distributed processing technique based on the biological neural network concept. It compresses with the ability to accumulate, learn, and adapt to information to archive it for future Refs. [39–41]. In the present work, all calculations and plots were carried out using MATLAB.

ANN-two layer network as shown in Fig. 2 was used for developing predictive model pertaining to wire-EDM process to predict MRR. In the present research, there are four inputs: current, pulse-on time, pulse-off time and wire feed, and one output (response); MRR. A hidden layer presented between the input and output layer has a varying number of neurons.

## 3 Result and Discussion

### 3.1 Analysis of Variance

ANOVA analysis determines each control parameter's effect on the process parameter's influence on MRR. Table 3 shows the significance of input parameters by the F-test with a confidence level of 95%. The  $F$  value helps to determine the role of Wire-EDM's input variables in the development of MRR. The p-value aids in assessing the relevance of a particular variable or set of variables in the MRR response. A variable or combination of factors is considered sensitive in causing a response of MRR if the p-value is less than 0.05 for that variable or combination of variables. If a p-value is greater than or equal to 0.1, it is considered insignificant, and there would be no sensitivity in producing an MRR response. The statistical model is effective if more than 50% of the factors are significant.

The most dominant input factors on MRR are wire feed ( $F$  value = 1673.57), current ( $F$  value = 363.88), pulse-off time ( $F$  value = 207.95), and pulse-on time ( $F$  value = 183.66), according to the ANOVA table. All four factors considered have p-values less than 0.05, indicating that they all significantly influence the MRR.

**Table 3** ANOVA result for the response of MRR

Source	DF	Adj SS	Adj MS	F value	P-value
Model	13	0.897669	0.069051	1255.82	0.001
Linear	4	0.189441	0.047360	861.33	0.001
$T_{on}$	1	0.010098	0.010098	183.66	0.005
$T_{off}$	1	0.011434	0.011434	207.95	0.005
A	1	0.020008	0.020008	363.88	0.003
WF	1	0.092022	0.092022	1673.57	0.001
Square	4	0.053417	0.013354	242.87	0.004
$T_{on} \times T_{on}$	1	0.000000	0.000000	0.00	0.960
$T_{off} \times T_{on}$	1	0.041773	0.041773	759.72	0.001
$A \times A$	1	0.033201	0.033201	603.82	0.002
WF $\times$ WF	1	0.040721	0.040721	740.58	0.001
2-way interaction	5	0.180302	0.036060	655.82	0.002
$T_{on} \times T_{off}$	1	0.040707	0.040707	740.32	0.001
$T_{on} \times A$	1	0.001488	0.001488	27.06	0.035
$T_{on} \times WF$	1	0.036426	0.036426	662.47	0.002
$T_{off} \times A$	1	0.014863	0.014863	270.32	0.004
$A \times WF$	1	0.077345	0.077345	1406.65	0.001
Error	2	0.000110	0.000055		
Total	15	0.897779			

### 3.2 Contour Plot Analysis and Validation

Figure 3a–f indicates the contour plot of each input parameter for MRR. Figure 3a depicts the effect of pulse-on time and pulse-off time on the response of MRR under the current of 4.5 A and wire feed of 2.5 mm/min. The MRR shows a continuous increase of an increasing pulse-on time. A reverse trend is observed for a pulse-off time; i.e., the value of MRR is shown to increase with a decrease in pulse-off time. Similarly, the response surface plot of MRR versus pulse-on time and current has been shown in Fig. 3b, which implies that MRR can be maximized by the current of 4.8A and pulse-on time of 48  $\mu$ s, respectively. Repeatedly, the response surface plot of MRR versus pulse-on time and wire feed has been shown in Fig. 3c. In this case, MRR can be increased by setting the pulse-on time and wire feed close to 24  $\mu$ s and 4 mm/min, respectively.

The response surface plot of MRR versus pulse-off time and current has been illustrated in Fig. 3d, which indicates that MRR can be maximized by setting pulse-off time and current near 16  $\mu$ s and 4.8 A, respectively. Again, the response surface plot of MRR versus pulse-off time and wire feed has been shown in Fig. 3e. In this case, MRR accedes to a higher value by setting pulse-off time and wire feed close to 20  $\mu$ s and 4 mm/min, respectively. Figure 3f depicts the effect of current and

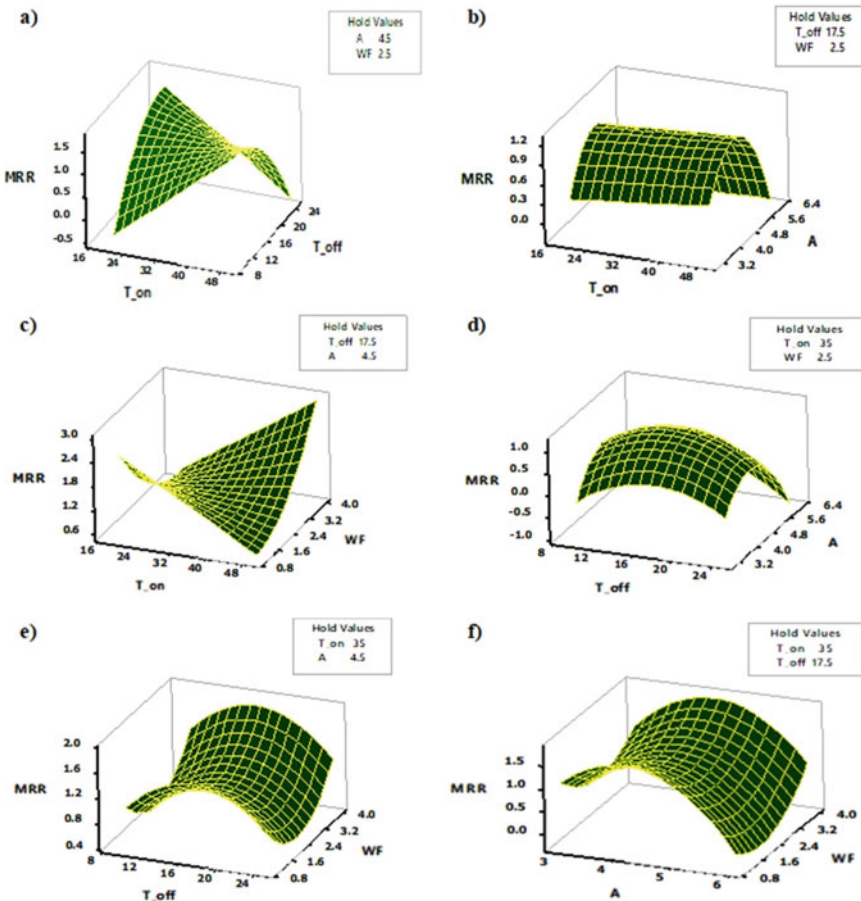


**Fig. 3.** 3D surface plot for MRR versus **a**  $T_{on}$  &  $T_{off}$ , **b**  $T_{on}$  & A, **c**  $T_{on}$  & WF, **d**  $T_{off}$  & A, **e**  $T_{off}$  & WF, **f** A & WF

wire feed under the pulse-on and -off time of  $3.5 \mu\text{s}$  and  $17.5 \mu\text{s}$ , respectively. MRR increases with a decrease of wire feed at the current near 4 A. Thus, from the contour plots of Fig. 3, it is understood that wire feed and current are the parameters mainly influencing MRR.

### 3.3 Experimental Results

Table 4 summarizes experimental findings and ANN predicted MRR where we can notice that the error percentage between experimental result and the ANN predicted result is less than 5%. Equation 2 is the regression equation representing the response

parameter MRR and process parameters. The coefficients of determination ( $R^2$ ), actual  $R^2$ , and predicted  $R^2$  are similar, implying that the analysis is accurate for the specified input parameters, and there is no additional factor impact in the study.

$$\begin{aligned} \text{Regression Equation for MRR} = & -10.581 + 0.05852 T_{\text{on}} + 0.7215 T_{\text{off}} \\ & + 3.859 A - 3.108 WF - 0.000001 T_{\text{on}} \\ & \times T_{\text{on}} - 0.010219 T_{\text{off}} \times T_{\text{off}} - 0.4486 A \times A \\ & + 0.23663 WF \times WF - 0.009246 T_{\text{on}} \times T_{\text{off}} \\ & - 0.001991 T_{\text{on}} \times A + 0.04675 T_{\text{on}} \times WF - 0.011051 T_{\text{off}} \\ & \times A + 0.08609 A \times WF \end{aligned} \quad (2)$$

In Fig. 4, a regression graph depicts the relationship between the ANN model network output and desired targets. The dotted line [ $Y$  (output) =  $T$  (goal)] in this graph signifies the optimum condition for a specific sample. In addition, the solid line displays the linear regression line between outcomes and targets that best fits the data. More outputs fit with marks, as evidenced by the more solid line next to the dotted line. Regression coefficients for the MRR model based on the data are

**Table 4** Comparison of experimental results and ANN predicted data

Trail no.	Pulse-on time (μs)	Pulse-off time (μs)	Current (A)	Wire feed (mm/min)	Experimental MRR (mg/s)	ANN predicted MRR	% of error
1	20	10	3	1	0.344	0.33	4.181
2	30	15	3	2	0.452	0.412	8.850
3	40	20	3	3	0.532	0.498	6.353
4	50	25	3	4	0.585	0.603	3.147
5	20	15	4	3	0.415	0.421	1.495
6	30	10	4	4	0.514	0.494	3.891
7	40	25	4	1	0.339	0.368	8.555
8	50	20	4	2	0.513	0.521	1.520
9	20	20	5	4	0.829	0.797	3.883
10	30	25	5	3	0.595	0.575	3.361
11	40	10	5	2	0.713	0.713	0.000
12	50	15	5	1	0.577	0.629	9.050
13	20	25	6	2	0.354	0.326	8.014
14	30	20	6	1	0.339	0.367	8.355
15	40	15	6	4	1.163	1.163	0.000
16	50	10	6	3	1.028	0.956	6.968
Model summary	S	R-sq (%)	R-sq(adj) (%)	R-sq(pred) (%)			
MRR	0.0074152	94.99%	92.91%	90.61%			

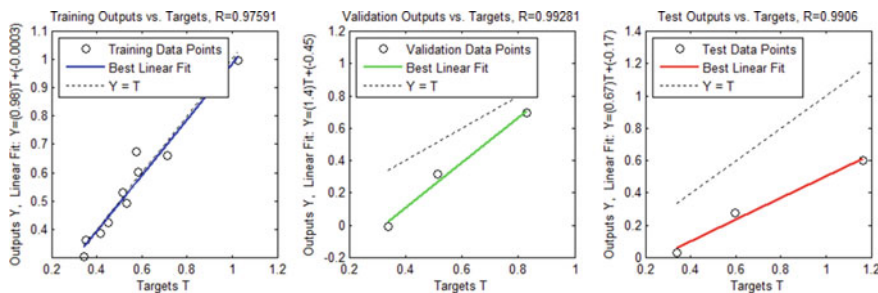


**Fig. 4** Network regression analysis for prediction

0.9906 for the test data, 0.97591 for the training set, and 0.99281 for the validation set. According to the plotted graphs, the network's learning is correct and the ANN model is accurate enough to forecast.

## 4 Conclusion

In the present investigations, MMC was fabricated by the bottom-poured stir casting process with a SiC reinforcement of 6%. Al6061-T6/nano-SiC MMC was machined by wire-cut EDM, and a prediction model was developed for obtaining the highest MRR using ANN. The degree of impact of machining variables on response parameters was figured out using the ANOVA. It is indicated that wire feed and current are the most crucial input parameters with the highest impact on MRR. The regression equation obtained shows the very least percentage of errors while comparing the experimental results and predicted outputs indicating the accuracy of the analysis.

**Acknowledgements** The authors would like to express their gratitude to the Ministry of Higher Education Malaysia for funding this research project through Fundamental Research Grant Scheme (FRGS) with the project code of FRGS/1/2020/SS0/UCSI/02/2.

## References

1. Tisza, M., Czinege, I.: Comparative study of the application of steels and aluminium in lightweight production of automotive parts. *Int. J. Light. Mater. Manuf.* **1**, 229–238 (2018). <https://doi.org/10.1016/j.ijlmm.2018.09.001>
2. Okokpujie, I.P., Tartibu, L.K.: A mini-review of the behaviour characteristic of machining processes of aluminium alloys. *Mater. Today Proc.* **62**, 4526–4532 (2022). <https://doi.org/10.1016/j.matpr.2022.05.006>
3. Suresh, S., Venkatesan, K., Natarajan, E., Rajesh, S., Lim, W.H.: Evaluating weld properties of conventional and swept friction stir spot welded 6061-T6 aluminium alloy. *Mater. Express* **9**, 851–860 (2019). <https://doi.org/10.1166/mex.2019.1584>

4. Suresh, S., Natarajan, E., Vinayagamurthi, P., Venkatesan, K., Viswanathan, R., Rajesh, S.: Optimum tool traverse speed resulting equiaxed recrystallized grains and high mechanical strength at swept friction stir spot welded AA7075-T6 lap joints. In: Natarajan, E., Vinodh, S., Rajkumar, V. (eds.) Materials, Design and Manufacturing for Sustainable Environment, pp. 547–555. Springer Nature Singapore, Singapore (2023)
5. Suresh, S., Natarajan, E., Franz, G., Rajesh, S.: Differentiation in the SiC filler size effect in the mechanical and tribological properties of friction-spot-welded AA5083-H116 alloy. *Fibers* **10**, 109 (2022). <https://doi.org/10.3390/fib10120109>
6. Suresh, S., Natarajan, E., Shanmugam, R., Venkatesan, K., Saravanan Kumar, N., Anto Dilip, A.: Strategized friction stir welded AA6061-T6/SiC composite lap joint suitable for sheet metal applications. *J. Mater. Res. Technol.* **21**, 30–39 (2022). <https://doi.org/10.1016/j.jmrt.2022.09.022>
7. Suresh, S., Venkatesan, K., Rajesh, S.: Optimization of process parameters for friction stir spot welding of AA6061/Al2O3 by Taguchi method. In: AIP Conference Proceedings, pp. 1–10 (2019). <https://doi.org/10.1063/1.5117961>
8. Mandal, K., Bose, D., Mitra, S., Sarkar, S.: Experimental investigation of process parameters in WEDM of Al 7075 alloy. *Manuf. Rev.* **7**, 30 (2020). <https://doi.org/10.1051/mfreview/2020021>
9. Nтуранабо, F., Масу, L., Баптист Кирабира, J.: Novel applications of aluminium metal matrix composites. In: Aluminium Alloys and Composites. IntechOpen (2020). <https://doi.org/10.5772/intechopen.86225>
10. Suresh, S., Venkatesan, K., Natarajan, E.: Influence of SiC nanoparticle reinforcement on FSS welded 6061-T6 aluminum alloy. *J. Nanomater.* **2018**, 1–11 (2018). <https://doi.org/10.1155/2018/7031867>
11. Suresh, S., Venkatesan, K., Natarajan, E., Rajesh, S.: Influence of tool rotational speed on the properties of friction stir spot welded AA7075-T6/Al2O3 composite joint. In: Materials Today: Proceedings, pp. 62–67 (2020). <https://doi.org/10.1016/j.matpr.2019.08.220>
12. Suresh, S., Venkatesan, K., Natarajan, E., Rajesh, S.: Performance analysis of nano silicon carbide reinforced swept friction stir spot weld joint in AA6061-T6 alloy. *SILICON* **13**, 3399–3412 (2021). <https://doi.org/10.1007/s12633-020-00751-4>
13. Lazar, P., Sengottuvelu, R., Natarajan, E.: Assessments of secondary reinforcement of epoxy matrix-glass fibre composite laminates through nanosilica ( $\text{SiO}_2$ ). *Materials (Basel)* **11**, 2186 (2018). <https://doi.org/10.3390/ma11121286>
14. Nagarajan, P., Murugesan, P.K., Natarajan, E.: Optimum control parameters during machining of LM13 aluminum alloy under dry electrical discharge machining (EDM) with a modified tool design. *Mater. Sci.* **25**, 407–412 (2019). <https://doi.org/10.5755/j01.ms.25.4.20899>
15. Patel, J.D., Maniya, K.D.: A Review on: Wire cut electrical discharge machining process for metal matrix composite. *Procedia Manuf.* **20**, 253–258 (2018). <https://doi.org/10.1016/j.promfg.2018.02.037>
16. Sagare, S., Pawar, S., Ghuge, N., Kolambe, C.: Analysis of wire electrical discharge machining parameter optimization for hardness and dimensional deviation. *Mater. Today Proc.* (2023). <https://doi.org/10.1016/j.matpr.2023.01.292>
17. Deepak, D., Gowrishankar, M.C., Shreyas, D.S.: Investigation on the wire electric discharge machining performance of artificially aged Al6061/B4C composites by response surface method. *Mater. Res.* **25**, (2022). <https://doi.org/10.1590/1980-5373-MR-2022-0010>
18. Hammami, D., Louati, S., Masmoudi, N., Bradai, C.: Influence of WEDM process parameters on aluminum alloy's surface finish. *Int. J. Adv. Manuf. Technol.* **126**, 453–469 (2023). <https://doi.org/10.1007/s00170-023-10929-w>
19. Rozenek, M., Kozak, J., Dąbrowski, L., Łubkowski, K.: Electrical discharge machining characteristics of metal matrix composites. *J. Mater. Process. Technol.* **109**, 367–370 (2001). [https://doi.org/10.1016/S0924-0136\(00\)00823-2](https://doi.org/10.1016/S0924-0136(00)00823-2)
20. Pramanik, A.: Electrical discharge machining of MMCs reinforced with very small particles. *Mater. Manuf. Process.* **31**, 150529083745005 (2015). <https://doi.org/10.1080/10426914.2015.1048360>

21. Garg, R.K., Singh, K., Anish, S., Sharma, V., Ojha, K., Singh, S.: Review of research work in sinking EDM and WEDM on metal matrix composite materials. *Int. J. Adv. Manuf. Technol.* **50**, 611–624 (2010). <https://doi.org/10.1007/s00170-010-2534-5>
22. Pramanik, A., Basak, A.K., Islam, N.: Effect of reinforced particle size on wire EDM of MMCs. *Int. J. Mach. Mach. Mater.* **17**, 139 (2015). <https://doi.org/10.1504/IJMMM.2015.070918>
23. Mandal, K., Sekh, M., Bose, D., Mitra, S., Sarkar, S.: Statistical analysis of process parameters and multi-objective optimization in wire electrical discharge machining of Al 7075 using weight-based constrained algorithm. *Int. J. Interact. Des. Manuf.* (2022). <https://doi.org/10.1007/s12008-022-01120-8>
24. Karthik, R., Rangasamy, V., Jayavel, B., Nadanasabapathi, S., Arivazhagan, R.: Optimization of WEDM parameters for machining of AZ31B Mg alloy using Taguchi Method. *IOP Conf. Ser. Mater. Sci. Eng.* **1013**, 12005 (2021). <https://doi.org/10.1088/1757-899X/1013/1/012005>
25. Mathew Paulson, D., Saif, M., Zishan, M.: Optimization of wire-EDM process of titanium alloy-Grade 5 using Taguchi's method and grey relational analysis. *Mater. Today Proc.* **72**, 144–153 (2023). <https://doi.org/10.1016/j.matpr.2022.06.376>
26. Suresh, P., Venkatesan, R., Sekar, T., Elango, N., Sathyamoorthy, V.: Optimization of intervening variables in MicroEDM of SS 316L using a genetic algorithm and response-surface methodology. *Strojnoški Vestn. J. Mech. Eng.* **60**, 656–664 (2014). <https://doi.org/10.5545/sv-jme.2014.1665>.
27. Preetham, N.S., Muniappan, A., Jayakumar, K.S., Maridurai, T.: WITHDRAWN: experimental investigation of machining conditions on surface roughness in WEDM of aluminum hybrid composite by RSM. *Mater. Today Proc.* (2021). <https://doi.org/10.1016/j.matpr.2021.07.328>
28. Natarajan, E., Kaviarasan, V., Lim, W.H., Ramesh, S., Palanikumar, K., Sekar, T., Mok, V.H.: Gorilla troops optimizer combined with ANFIS for wire cut EDM of aluminum alloy. *Adv. Mater. Sci. Eng.* **2022**, 1–14 (2022). <https://doi.org/10.1155/2022/3072663>
29. Phate, M., Toney, S., Phate, V.: Response surface modelling and effective application of adaptive neuro-fuzzy inference system to Analyze surface roughness of Al/Gr/Cp5 MMC machined using WEDM. *Aust. J. Mech. Eng.* **21**, 653–667 (2023). <https://doi.org/10.1080/14484846.2021.1913852>
30. Suresh, S., Elango, N., Venkatesan, K., Lim, W.H., Palanikumar, K., Rajesh, S.: Sustainable friction stir spot welding of 6061-T6 aluminium alloy using improved non-dominated sorting teaching learning algorithm. *J. Mater. Res. Technol.* **9**, 11650–11674 (2020). <https://doi.org/10.1016/j.jmrt.2020.08.043>
31. Thankachan, T., Soorya Prakash, K., Malini, R., Ramu, S., Sundararaj, P., Rajandran, S., Rammasamy, D., Jothi, S.: Prediction of surface roughness and material removal rate in wire electrical discharge machining on aluminum based alloys/composites using Taguchi coupled grey relational analysis and artificial neural networks. *Appl. Surf. Sci.* **472**, 22–35 (2019). <https://doi.org/10.1016/j.apsusc.2018.06.117>
32. Thankachan, T., Prakash, K., Pleass, C., Ramasamy, D., Prabakaran, B., Jothi, S.: Artificial neural network to predict the degraded mechanical properties of metallic materials due to the presence of hydrogen. *Int. J. Hydrogen Energy* **42** (2017). <https://doi.org/10.1016/j.ijhydene.2017.09.149>
33. Thankachan, T., Prakash, K., Jothi, S.: Artificial neural network modeling to evaluate and predict the mechanical strength of duplex stainless steel during casting. *Sādhānā* **46** (2021). <https://doi.org/10.1007/s12046-021-01742-w>
34. Prakash, C., Senthil, P., Manikandan, N., Palanisamy, D.: Machinability investigations of aluminum metal matrix composites (LM26 + Graphite + Flyash) by using wire electrical discharge machining process. In: *Recent Advances in Materials and Modern Manufacturing. Lecture Notes in Mechanical Engineering*. Springer, Singapore, pp. 983–991 (2022). [https://doi.org/10.1007/978-981-19-0244-4\\_91](https://doi.org/10.1007/978-981-19-0244-4_91)
35. Naidu, B.V.V., Natarajan, M., R, R., SOMSOLE, L.N., Pasupuleti, T.: Machinability studies on wire electrical discharge machining of aluminium based metal matrix composite for automotive applications. In: *SAE Technical Papers*, p. 5 (2022). <https://doi.org/10.4271/2022-28-0353>

36. Hillary, J.J.M., Sundaramoorthy, R., Ramamoorthi, R., Chelladurai, S.J.S.: Investigation on microstructural characterization and mechanical behaviour of aluminium 6061—CSFA/Sicp hybrid metal matrix composites. *SILICON* **14**, 11561–11576 (2022). <https://doi.org/10.1007/s12633-022-01881-7>
37. Prakash, S., Sasikumar, R., Natarajan, E., Suresha, B.: Influence of feeding techniques in bottom tapping stir casting process for fabrication of alumina nano-filler-reinforced aluminium composites. *Trans. Indian Inst. Met.* **73**, 1265–1272 (2020). <https://doi.org/10.1007/s12666-020-01975-z>
38. Raju, K., Balakrishnan, M., Priya, C.B., Sivachitra, M., Narasimha Rao, D.: Parametric optimization of wire electrical discharge machining in AA7075 metal matrix composite. *Adv. Mater. Sci. Eng.* **2022**, 1–8 (2022). <https://doi.org/10.1155/2022/4438419>
39. Chokshi, P., Dashwood, R., Hughes, D.J.: Artificial Neural Network (ANN) based microstructural prediction model for 22MnB5 boron steel during tailored hot stamping. *Comput. Struct.* **190**, 162–172 (2017). <https://doi.org/10.1016/j.compstruc.2017.05.015>
40. Bhattacharyya, T., Brat Singh, S., Sikdar (Dey), S., Bhattacharyya, S., Bleck, W., Bhattacharjee, D.: Microstructural prediction through artificial neural network (ANN) for development of transformation induced plasticity (TRIP) aided steel. *Mater. Sci. Eng. A* **565**, 148–157 (2013). <https://doi.org/10.1016/j.msea.2012.11.110>
41. Lee S-I, Shin S-H, Hwang B (2021) Application of artificial neural network to the prediction of tensile properties in high-strength low-carbon Bainitic steels. *Metals (Basel)* **11**, 1314 (2021). <https://doi.org/10.3390/met11081314>

# Computer-Aided Potato Disease Detection by Using Deep Learning Techniques



Fareeha Razaq, Muhammad Bilal , Muhammad Ramzan ,  
Muhammad Naveed, and Samreen Razzaq

**Abstract** Potato is the most widely grown and consumed food throughout the world. There are a number of potato crop diseases that affect production, and these diseases differ in symptoms, circumstances, and controls. Early detection and recognition of disease information can aid in disease prevention and production. This paper presents deep learning models using proposed CNN and pre-trained models for potato disease detection and classification. The proposed model is more efficient and accurate at detection and classification. To perform classification, we used two datasets: PLD and PlantVillage. The Xception CNN model serves as the foundation for our proposed model. It achieved 1.00 accuracy, 0.99 precision, 1.00 recall, and 0.99 F1-score on the PLD dataset. On the PlantVillage dataset, it achieved 1.00 accuracy, 1.00 precision, 1.00 recall, and 1.00 F1-score. We also compared the results of Inception-ResNet-V2, MobileNet-V2, VGG-19, Inception-V3, and Xception models with the performance of our proposed model. For three classes of potato leaves, the proposed CNN model produced more accurate results than other pre-trained models.

**Keywords** Deep learning · Plant diseases · Transfer learning · Potato

---

F. Razaq · S. Razzaq

Department of Computer Science, University of Sargodha, Sargodha, Pakistan

M. Bilal

Department of Computing and Information Systems, School of Engineering and Technology,  
Sunway University, Petaling Jaya, Malaysia

e-mail: [muhammadb@sunway.edu.my](mailto:muhammadb@sunway.edu.my)

M. Ramzan · M. Naveed

Department of Software Engineering, University of Sargodha, Sargodha, Pakistan  
e-mail: [mramzansf@gmail.com](mailto:mramzansf@gmail.com)

M. Bilal

School of Electronics and Computer Science, University of Southampton Malaysia, Iskandar Puteri, Malaysia

## 1 Introduction

The impact of diseases on agriculture has considerably reduced agricultural production and quality. Potato is an essential vegetable in many countries. Potato, as the major food crop, has the potential to feed millions of people, particularly in developing countries [1]. It's a very important food crop in the whole world. Potato production has recently been reduced due to multiple diseases such as early blight, late blight, black dot, dry rot, gangrene, etc., which cause a significant loss of cropped plants. Potato is known as an agronomically important crop in Pakistan, with a total 1.79 million acres covered area and a tuber production of 3.85 million tons [2].

Potato plants are normally affected by fungi which cause two types of diseases early blight and late blight in it [3]. *Phytophthora infestans* causes late blight in potato plants, while *Alternaria solani* causes early blight [4]. Proper plant disease diagnosis at the initial stages prevents crop damage and the threat to human food security. Farmers typically detect these diseases manually by focusing on how the color of the potato leaves changes, which is typically inadequate because it takes too much time and can lead to incorrect detection. Therefore, we need to develop a technological solution that can detect the disease automatically and accurately at the early stages. Our agriculture system has been dramatically improved by the introduction of computer-aided systems. However, some areas of agriculture still need improvement to diagnose diseases more efficiently and accurately. The early and precise detection of diseases in different plants can assist in the prevention of loss.

With advancements in agricultural technology and the use of machine learning in identifying plant diseases, it is becoming increasingly vital to conduct research relevant to sustainable agricultural development. The use of image processing techniques in agriculture is rapidly rising, from simple field management to the detection of crop diseases. ML methods identify diseases because they rely heavily on data and give us better results. However, the ML algorithms need extracted features from the images, and then classification is performed on these features. These extracted features represent raw data that extracted machine algorithms and use features to perform different tasks such as classification [5].

In this study, we employed a proposed deep learning-based model CNN to classify potato leaf diseases. The proposed model shows better accuracy and efficiency for plant leaf disease categorization and detection. We considered the detection and classification of three classes: early blight, healthy, and late blight. We used pre-trained models, Inception-ResNet-V2, Inception-V3, MobileNet50, VGG-19, and Xception models and suggested the Xception-based CNN model to conduct classification on two datasets separately. The results of six separately trained models are then compared, and the best-performing model is determined. Our proposed method detects potato leaf diseases more accurately, consistently, and efficiently, and it requires less effort, which contributes to success.

## 2 Literature Review

For potato disease detection, different deep learning and machine learning-based techniques using a variety of datasets have been discussed in this section.

Asif et al. [6] proposed a model based on the sequential model to identify classes of potato leaves. The authors used the YOLOv5 technique for image segmentation. The proposed deep learning model obtained 97.56% accuracy by using only one data augmentation technique. 98.28% accuracy was achieved by using two augmentation techniques, and 99% accuracy was achieved using five data augmentation techniques. The maximum accuracy was achieved with seven data augmentation techniques which were 99.75%. Sutrapakti et al. [7] described a model which performed classification on different color and texture features. The authors performed segmentation through the k-means clustering algorithm and then used the maximum and minimum color variance process to get color features. This study achieved 91.67% maximum accuracy. Barman et al. [8] performed experiments on augmented and non-augmented datasets for agriculture images. The proposed model achieved a maximum of 96.75% accuracy on the augmented dataset and 96.98% accuracy on the non-augmented dataset, respective to the overfitting. Rozqi et al. [9] proposed a model to identify the classes of potato leaf disease. The author experimented by splitting the training and testing dataset into 70:30 and 80:20 divisions on 1125 images of three classes. The proposed model achieved 92% validation accuracy and 97% training accuracy. Sholihati et al. performed classification on five classes of potato leaves [10]. The dataset PlantVillage dataset has been used and is available on Kaggle. The proposed methodology contains extracting ROI, data augmentation, and then classification through the VGGNet model. The accuracy achieved 91%. Chugh et al. [11] proposed Inception-V3-based enhanced CNN model for the classification of potato leaf diseases. The data has been split into 80% data for training purposes and 20% for validation. In this study ‘Adam Optimizer and ‘softmax’ functions achieved 90% accuracy. Mohamed et al. [12] introduced a system to detect potato plant diseases early to reduce potato crop production losses by employing a diagnosis and detection system. The authors carefully curated and extracted images of potato plants from the entire dataset of the PlantVillage. This study performed training on 70% of the images and used the remaining images with 20% for testing and 10% for validation. The proposed model achieved 98.2% accuracy.

Ferentinos et al. [13] used deep learning methods to train models on 25 different plant images. They used numerous model architectures, with the best performance achieving a success rate of 99.53%. Fuentes et al. [14] described the model by using three detectors such as Faster R-CNN, R-FCN, and SSD. The proposed method merged these architectures with a CNN model named VGG net and ResNet. They performed classification on nine different tomato diseases and pest datasets. This study concluded that data augmentation and data annotation gives better performance. Barbedo et al. [15] investigated the main factors influencing the design and efficiency of deep neural-based networks used in plant pathology. In the given method, it has been described that one of the primary benefits of the deep learning approach is that

the symptoms do not need to be recognized in the image. Supian et al. [16] reviewed leaf plant disease classification. The findings concluded that if image preprocessing, segmentation, and feature extraction were done before performing classification, then results could be improved.

Hassanien et al. [17] proposed the model and achieved better accuracy after applying the Gaussian process. The CNN model undergoes hyperparameters problems, and the Gaussian filter could improve the results. The performance of the pre-trained VGG-16 model is evaluated using nine different types of diseased datasets. Raigonda et al. [18] introduced a model which is based on the gray-level co-occurrence matrix (GLCM). They used the self-captured images dataset in the given study. The proposed methodology includes preprocessing techniques, feature extraction with GLCM, feature reduction, extracting ROI, detecting points, and then classification. The proposed work gives 93.51% accuracy.

Adi et al. [19] suggested proposed CNN and pre-defined models and their results on classification by using the vegetable leaf disease dataset. This research focuses on CNN, GAN, and ANN to detect plant diseases. The results showed that by applying proposed models, researchers could achieve 95% accuracy on average. Sharma et al. [20] used machine learning and image preprocessing techniques combined to get the results. The ML algorithms SVM, KNN, Naïve Bayes, and decision tree have been used for the classification. The SVM algorithm provides the best accuracy of 92.9%. Jhonson et al. [21] presented an automated system based on mask R-CNN architecture. 1423 images were collected and used the Mask R-CNN model to differentiate the background and extract ROI. Then converted RGB images to different color spaces and created a separate model for each color space. The proposed approach achieved 98% accuracy with the mask R-CNN model and by using LAB color space.

Lee et al. [22] proposed a CNN model to classify potato leaf's diseased images. The proposed methodology contains data augmentation by random movements and flipping, image preprocessing techniques like Gaussian filter, normalization, color conversion, extracting ROI, and then classification. The value of the optimizer and layers were fine-tuned, and the best accuracy achieved after different experiments was 99%. Rashid et al. [23] proposed a work in which first segments the potato leaf from a potato plant with YOLOv5. The potato leaves dataset performed classification into three classes. The results obtained by the suggested method were 99.75% accuracy. The proposed model gives 93.90% accuracy by using the PlantVillage dataset without augmentation. By training the proposed model with the PLD dataset and testing on the PlantVillage dataset, the model achieved 86% accuracy. Tarik et al. [24] research consists of 2034 images of potato and potato leaves which were collected from a garden and divided into seven classes. The author used a sequential model-based CNN model to perform classification. The proposed model achieved 99.39% accuracy.

**Table 1** Images distribution in PlantVillage and PLD dataset

Class name heading	No. of images (PlantVillage)	No. of images (PLD)
Early Blight	1000	1628
Late Blight	1000	1424
Healthy	152	1020
Total	2152	4070

### 3 Proposed Research Methodology

The proposed research describes a method for classification and detecting potato leaf diseases using deep learning techniques. The basic steps include data acquisition, preprocessing, data splitting, the proposed model for feature extraction, and classification.

#### 3.1 Dataset Acquisition

Two types of datasets have been used ‘Potato Leaf Disease (PLD) Dataset’ [9] and ‘PlantVillage Dataset’ [25]. Both datasets have the same number of classes. Images in the PLD dataset have been taken from the Central Region of Pakistan, while the PlantVillage dataset was developed by Penn State University (US) and EPFL (Switzerland). The distribution of our datasets is given in Table 1.

#### 3.2 Dataset Preprocessing

Various preprocessing techniques have been used to improve the results. The dataset preprocessing was done to improve the dataset’s reliability. An image dataset may include an unneeded region of interest, lighting issues, and irrelevant objects. As a result, before training the model, images must be preprocessed to obtain the desired data format. The CNN models take input images size of 224 by 224, so we resized all images size of 224 by 224. We also normalized the images because pixel values range from 0 to 255, and giving CNN raw pixel values results in slower model training. In the image normalization process, we used the re-scaling technique to normalize the low-pixel images and high-pixel images, fairness across all images, and scaling all images to an equal pixel range. By normalization, we change the range of pixel values, e.g., we enhance the images with poor contrast [26].

The PlantVillage dataset has an unbalanced image distribution because the ‘Healthy Leaves’ class has 152 images, while the other two classes have an equal number of images. The unbalanced dataset could lead to inaccurate results. To avoid overfitting, we used rotations, shearing, vertical flips, and horizontal flips to augment

the data. Consequently, we have increased the number of images in the ‘Healthy Leaves’ class to 1000. Moreover, only the PlantVillage dataset was used for the augmentation techniques.

### 3.3 Split Dataset

In this research, the dataset has been divided into training data, validation data, and testing data. We used 80% training data, 10% test, and 10% validation data.

### 3.4 Selected CNN Models and Proposed CNN Model

In this research, we proposed an Xception-based model for classifying potato leaf diseases. For classification, we also used the pre-trained Xception, Inception-V3, MobileNet-V2, Inception-Resnet-V2, and EfficientNetB0 models. Compare the proposed model’s performance with that of selected pre-trained CNN models to determine which model produces the best results. We trained these selected CNN models on three classes (early blight, healthy, and late blight) of the PLD and PlantVillage datasets using a free GPU Tesla K80 provided by Google Colab.

**Inception-ResNetV-2.** The pre-trained model Inception-ResNet-V2 employs a sophisticated architecture to extract critical features from images. It is a mixture of two networks, i.e., residual connections [27] and an updated version of Inception architecture’s version. Inception CNN models themselves are well-known for having multi-branch architectures. In each branch, they have a set of filters that are fused with concatenation. The internal architecture of the Inception module is seen to have a powerful illustrative capability in its dense layers. For training extremely deep architectures, the residual model is very famous, and the Inception-Resnet-V2 model makes good use of residual connections [28]. The network’s inner module consists of three blocks, i.e., the Inception-Resnet-A block, Inception-Resnet-B block, and Inception-Resnet-C block. The original network is stable because the residuals are scaled down before being added to the last layer.

**Inception-V3.** Inception-V3 CNN architecture is built around Inception modules. To reduce overfitting, the classifier is built with a dropout layer and a dense layer where a sigmoid is used as an activation function. Inception-V3 is primarily concerned with consuming as few computing resources as possible. These architectures were found to be faster and more accurate, with the number of parameters created.

**MobileNet-V2.** MobileNet-V2 is a CNN architecture that is made for mobile devices. It is designed on an inverted residual structure having residual connections among bottleneck layers [29]. As a cause of nonlinearity, the middle expansion layer filters features using lightweight depth-wise convolutions. The model’s architecture

comprises a fully convolution layer in start having 32 filters, and this layer is followed by 19 remaining bottleneck layers.

**VGG-19.** The VGGNet, a deep neural network, is multi-layered. There are 19 trainable layers in the VGG-19. It is a CNN-based model which has been trained on the ImageNet dataset. VGG-19 is beneficial because of its simple design, which has three convolutional layers on top to enhance the depth of the model. In the VGG-19 model, the max-pooling layers are used as a handler to reduce volume. 4096 neurons are used in two FC layers. In this model, convolutional layers are used for the extraction of features in the training phase, and to reduce feature dimensionality, max-pooling layers are connected with some convolutional layers. To extract features from the input images, the first convolutional layer used 64 kernels ( $3 \times 3$  filter size). The feature vector is created using FC layers [30].

**Xception.** Xception models take images in  $299 \times 299$  sizes. It is 126 and 36 convolutional layers deep, to extract features. To reduce the number of parameters, the FC layer is replaced with any other layer, and the ‘softmax’ function is used to output the result. 36 convolutional layers are organized into 14 modules, except the last and first modules. Each module has a linear skip connection around it. The 36 convolutional layers are split into three sections: entry flow, middle flow, and exit flow. The data is routed eight times between the entry flow and the middle flow, and finally, it comes to the exit flow. The entry flow is made up of eight convolutional layers. The entry flow is made up of eight convolutional layers, with the middle layer being the most important.

**Xception-based proposed CNN Model.** Xception is a CNN model, and it is 71 layers deep. We have added some layers to the Xception pre-trained model to achieve the best results. The structure of our enhanced pre-trained Xception model is as follows:

The total number of parameters that this model is taking is 20,867,627. In which trainable params are 20,813,099 and non-trainable params are 54,528. The structure-added layers have been modified. The input layer is the initial layer which is taking the image of size ‘ $224 \times 224 \times 3$ ’ as input and giving the output of the same size image. We have used ‘None’ as it denotes additional dimensions for batch processing. The global max-pooling layer enhanced model uses One GlobalMaxPooling2D layer. It is taking input shape as (None, 224, 224, 3) and producing output into (None, 7, 7, 2048). This layer works the same as flatten layer. In a model, global pooling can be used to aggressively summarize the presence of a feature in an image. The dropout layer has (None, 2048) neurons. It can be used as activity regularization to encourage sparse representations in auto-encoder models. It is giving output as (None, 2048).

## 4 Results and Discussion

We evaluated the results of the proposed and pre-trained model using several performance evaluation measures: accuracy, precision, recall, and F1-score. The proposed model shows the best performance when compared with other trained models in this research.

### 4.1 Experimental Setup

All implementation has been done with Python on Google Colab. All models are trained with optimizer ‘Adam’, loss function ‘categorical cross entropy’, epoch ‘100’, 80% training data. The system used for research work has Intel(R) Core(TM) i3-2370 M CPU@2.40 GHz processor with 1 TB hard disk and 8 GB RAM. For implementation, we used Tensorflow API with version 2.9.2 and Python libraries because it supports modularity and reusability. The Python libraries used in this research problem implementation are TensorFlow, Scikit-learn pandas, and NumPy. Matplotlib is used for graph plotting. Scikit-learn is the most popular ML library.

## 5 Performance Evaluation Measures

In this research, we evaluate the performance of trained CNN models by using different measures such as accuracy, precision, recall, and F1-score. True positive, false positive, true negative, and false negative calculate all the values of performance measures. The proposed Xception-based enhanced CNN model evaluated three classes of both datasets separately to classify three potato leaf classes. Results obtained achieved 1.00 validation accuracy and 1.00 training accuracy on the PLD dataset, while the same model achieved validation 1.00 accuracy and 1.00 training accuracy on the PLD dataset. The training accuracy of the PLD dataset and PlantVillage dataset is given in Table 2.

The proposed model achieved 1.00 validation accuracy and 1.00 training accuracy on the PLD dataset, while the same model achieved validation 1.00 accuracy and 1.00 training accuracy on the PLD dataset. The training accuracy of the PLD dataset and PlantVillage dataset is given in Table 2. The model of accuracy of the PLD dataset and PlantVillage dataset is shown in Fig. 1.

**Table 2** Training accuracy and validation accuracy proposed model

Dataset	Epoch	Training accuracy	Validation accuracy
PLD	100	1.00	1.00
PlantVillage	100	1.00	1.00

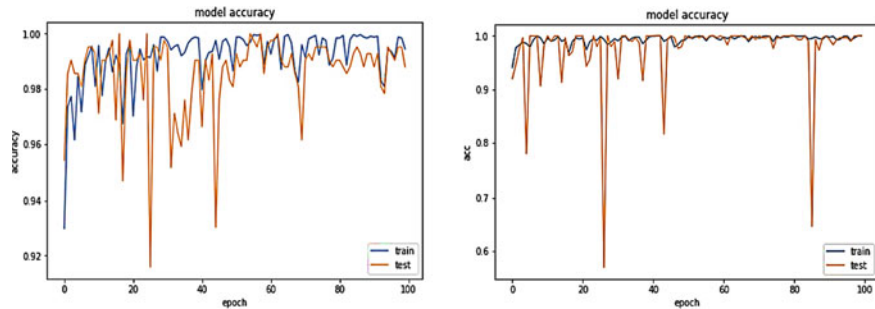


**Fig. 1** Model accuracy of proposed model on PLD dataset PlantVillage dataset

The confusion matrix to find out the FP, FN, TP, and TN values and the confusion matrix of the PLD dataset and PlantVillage dataset are shown below in Fig. 2.

The ROC curve shows the classification performance and plots on two parameters, i.e., FPR and TPR. The ROC curves are shown in Fig. 3 for the PLD dataset and PlantVillage dataset, respectively.

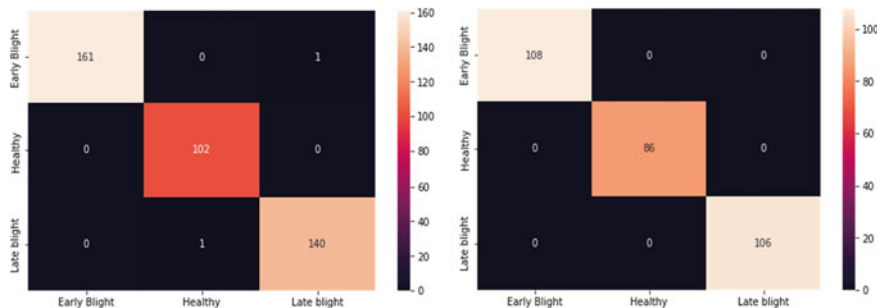


**Fig. 2** Confusion matrix of proposed model on PLD dataset and PlantVillage dataset

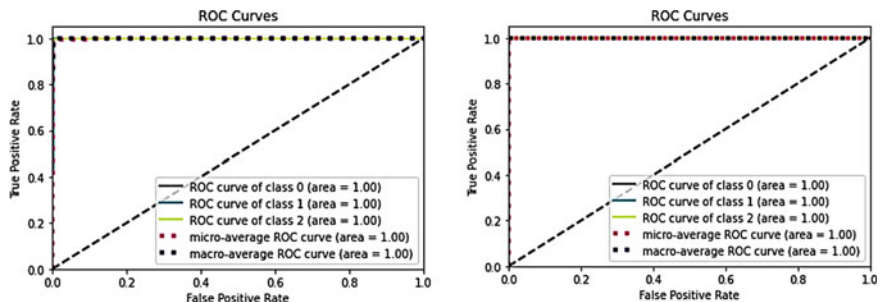


**Fig. 3** ROC curves of proposed model on PlantVillage dataset and PLD dataset

### Recall, Accuracy, F1-Score Results Using PLD Dataset.

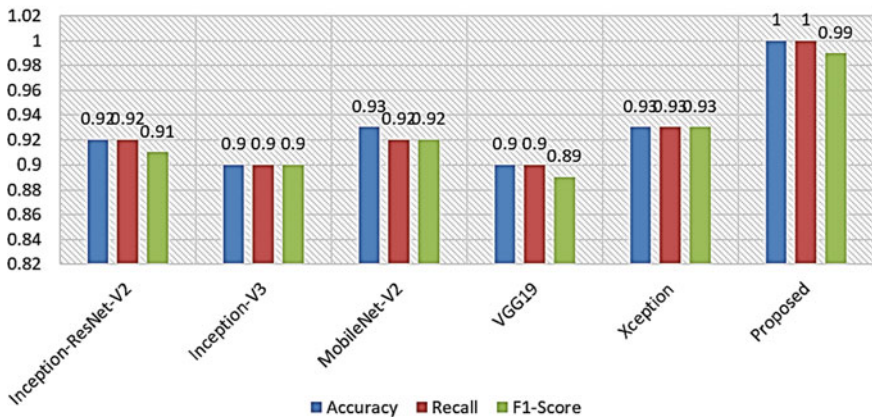


**Fig. 4** Recall, accuracy, and F1-score using PLD dataset

### Recall, Accuracy, F1-Score Results Using PlantVillage Dataset.

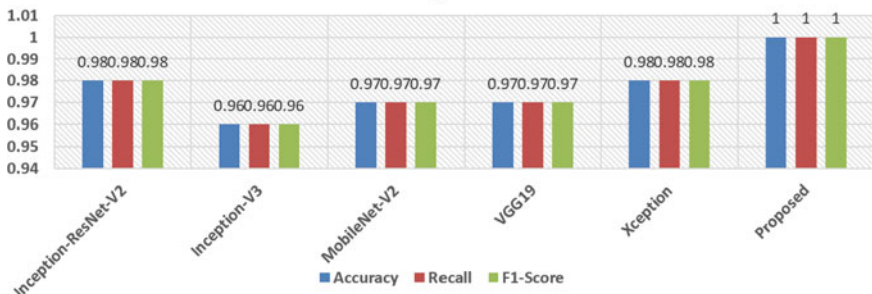


**Fig. 5** Recall, accuracy, and F1-score using PlantVillage dataset

Recall, accuracy, and F1-score for both datasets have been shown in Figs. 4 and 5.

### 5.1 Performance Comparison of Proposed Work

We compare our proposed research work with between used models, as given in Tables 3 and 4. Also, the existing work has been compared with the current existing work, as given in Table 5. The comparison showed that our proposed work has better performance than the existing work. It achieved an accuracy of 1.00, precision of 1.00, recall of 1.00, and F1-score of 1.00 on the PlantVillage dataset.

**Table 3** Performance comparison selected pre-trained CNN models and proposed CNN model on PLD dataset

CNN models	Accuracy	Macro average			Weighted average		
		Precision	Recall	F1-score	Precision	Recall	F1-score
Inception-ResNet-V2	0.92	0.91	0.92	0.91	0.92	0.92	0.92
Inception-V3	0.90	0.90	0.90	0.90	0.91	0.90	0.90
MobileNet-V2	0.93	0.92	0.92	0.92	0.93	0.93	0.93
VGG-19	0.90	0.89	0.90	0.89	0.90	0.90	0.90
Xception	0.93	0.93	0.93	0.93	0.93	0.93	0.93
Proposed	1.00	0.99	1.00	0.99	1.00	1.00	1.00

**Table 4** Performance comparison selected pre-trained CNN models and proposed on PlantVillage dataset

CNN models	Accuracy	Macro average			Weighted average		
		Precision	Recall	F1-score	Precision	Recall	F1-score
Inception-ResNet-V2	0.98	0.98	0.98	0.98	0.98	0.98	0.98
Inception-V3	0.96	0.96	0.96	0.96	0.97	0.96	0.96
MobileNet-V2	0.97	0.96	0.97	0.97	0.97	0.97	0.97
VGG-19	0.97	0.97	0.97	0.97	0.97	0.97	0.97
Xception	0.98	0.98	0.98	0.98	0.98	0.98	0.98
Proposed	1.00	1.00	1.00	1.00	1.00	1.00	1.00

## 6 Conclusion and Future Work

Potato is considered one of the four major cultivated crops. Potato plants get affected by fungi which may lead to certain production losses. Therefore, we have proposed a CNN-based model which can classify and detect the disease and give us better results. By identifying diseases in their early stages, which may result in severe crop yield losses, deep learning algorithms significantly boost crop production. In our research, we took two datasets one is PLD, which is collected from the area of Central Punjab in Pakistan, and the PlantVillage dataset, collected by authors from the US and Switzerland. We compared our research work with current existing work. The comparison showed that our proposed work has better performance than the existing work. In the future, our research can be extended to classify several diseases of potato plants, which will be able to detect the severity of the disease also. For easy use, we will develop a website and an Android app that farmers will be able to use and know the type of disease.

**Table 5** Performance comparison selected pre-trained CNN models and proposed with existing work

References	Year	Model	Dataset	No. of classes	No. of images	Accuracy
[7]	2022	CNN proposed	PlantVillage	3	2150	99.07%
[19]	2021	Machine learning	PlantVillage	3	2250	96.0%
[21]	2021	Machine learning	PlantVillage	2	1000	92.90%
[24]	2021	CNN proposed	PlantVillage	3	2152	99.39%
[34]	2021	CNN proposed	PlantVillage	3	2152	98.30%
[34]	2022	ResNet50	PlantVillage	3	2152	97%
[31]	2022	VGG16	PlantVillage	3	2152	97.89%
[33]	2022	DenseNet121	PLD	3	4082	98.34%
[32]	2022	Inception-V3	PLD	3	1500	98.34%
	–	CNN proposed	PLD	3	2152	1.00
	–	CNN proposed	PlantVillage	3	4082	1.00

## References

- Naz, S., Ahmad, S., Abbas, G., et al.: Modeling the impact of climate warming on potato phenology. *Eur. J. Agron.* **132**, 126404 (2022)
- Demissie, Y.T.: Integrated potato (*Solanum Tuberosum L.*) late blight (*Phytophthora Infestans*) disease management in Ethiopia. *Am. J BioSci.* **7**(6), Art. no. 6 (2019)
- Tiwari, D., Ashish, M., Gangwar, N., Sharma, A., Patel, S., Bhardwaj, S.: Potato leaf diseases detection using deep learning. In: 2020 4th International Conference on Intelligent Computing and Control Systems (ICICCS), pp. 461–466 (2020)
- Gold, K.M., Townsend, P.A., Chlus, A., et al.: Hyperspectral measurements enable pre-symptomatic detection and differentiation of contrasting physiological effects of late blight and early blight in potatoes. *Remote Sens.* **12**(2), 286 (2020)
- Shruthi, U., Nagaveni, V., Raghavendra, B.K.: A review on machine learning classification techniques for plant disease detection. In: 2019 5th International Conference on Advanced Computing & Communication Systems (ICACCS) (2019)
- Asif, M.K.R., Rahman, M.A., Hena, M.H.: CNN based disease detection approach on potato leaves. In: 2020 3rd International Conference on Intelligent Sustainable Systems (ICISS), pp. 428–432 (2020)
- Sutapakti, U., Bunpeng, A.: Potato leaf disease classification based on distinct color and texture feature extraction. In: 2019 19th International Symposium on Communications and Information Technologies (ISCIT), pp. 82–85 (2019)
- Barman, U., Sahu, D., Barman, G.G., Das, J.: Comparative assessment of deep learning to detect the leaf diseases of potato based on data augmentation. In: 2020 International Conference on Computational Performance Evaluation (ComPE), pp. 682–687 (2020)

9. Rozaqi, A.J., Sunyoto, A.: Identification of disease in potato leaves using convolutional neural network (CNN) algorithm. In: 2020 3rd International Conference on Information and Communications Technology (ICOIACT), pp. 72–76 (2020)
10. Sholihati, R.A., Sulistijono, I.A., Risnumawan, A., Kusumawati, E.: Potato leaf disease classification using deep learning approach. In: 2020 International Electronics Symposium (IES), pp. 392–397 (2020)
11. Chugh, G., Sharma, A., Choudhary, P., Khanna, R.: Potato leaf disease detection using Inception-v3. *Int. Res. J. Eng. Technol.* **07**(11), 4 (2020)
12. Mohamed, A.P.S.I., O.U. for M. S., Msa, A.: Potato leaf disease diagnosis and detection system based on convolution neural network. *Int. J. Rec. Technol. Eng. (IJRTE)* **9**(4), 254 (2020)
13. Ferentinos, K.P.: Deep learning models for plant disease detection and diagnosis. *Comput. Electron. Agric.* **145**, 311–318 (2018)
14. Fuentes, A., Yoon, S., Kim, S.C., Park, D.S.: A robust deep-learning-based detector for real-time tomato plant diseases and pests recognition. *Sensors* **17**(9), Art. no. 9 (2017)
15. Barbedo, J.G.A.: Factors influencing the use of deep learning for plant disease recognition. *Biosys. Eng.* **172**, 84–91 (2018)
16. Ahmad Supian, M.B., Madzin, H., Albahari, E.: Plant disease detection and classification using image processing techniques: a review. In: 2019 2nd International Conference on Applied Engineering (ICAE), pp. 1–4 (2019)
17. Shoib, M., Shah, B., Ei-Sappagh, S., et al.: An advanced deep learning models-based plant disease detection: a review of recent research. *Front. Plant Sci.* **14**, 875 (2023)
18. Faria, F.T.J., Moin, M.B., et al.: Classification of potato disease with digital image processing technique: a hybrid deep learning framework. In: 2023 IEEE 13th Annual Computing and Communication Workshop and Conference (CCWC), pp. 0820–0826. IEEE (2023)
19. Adi, M., Singh, A.K., Reddy, et al.: An overview on plant disease detection algorithm using deep learning. In: 2021 2nd International Conference on Intelligent Engineering and Management (ICIEM), pp. 305–309. IEEE (2021)
20. Sharma, S., Anand, V., Singh, S.: Classification of diseased potato leaves using machine learning. In: 2021 10th IEEE International Conference on Communication Systems and Network Technologies (CSNT), pp. 554–559 (2021)
21. Johnson, J., Sharma, G., Srinivasan, S., et al.: Enhanced field-based detection of potato blight in complex backgrounds using deep learning. *Plant Phenomics* (2021)
22. Lee, T.-Y., Lin, I.-A., Chang, J.-Y., et al.: High efficiency disease detection for potato leaf with convolutional neural network. *SN comput. Sci.* **2**(4), 297 (2021)
23. Rashid, J., Khan, I., Ali, G., Almotiri, S.H., et al.: Multi-level deep learning model for potato leaf disease recognition. *Electronics* **10**(17), Art. no. 17 (2021)
24. Tarik, M.I., Akter, S., Mamun, A. A., Sattar, A.: Potato disease detection using machine learning. In: 2021 Third International Conference on Intelligent Communication Technologies and Virtual Mobile Networks (ICICV) (2021)
25. <https://www.kaggle.com/datasets/emmarex/plantdisease>
26. Sharma, P., Hans, P., Gupta, S.C.: Classification of plant leaf diseases using machine learning and image preprocessing techniques. In: 2020 10th International Conference on Cloud Computing, Data Science & Engineering (Confluence), pp. 480–484 (2020)
27. He, K., Zhang, X., Ren, S., Sun, J.: Deep residual learning for image recognition. In: 2016 IEEE Conference on Computer Vision and Pattern Recognition (CVPR), pp. 770–778 (2016)
28. Szegedy, C., Ioffe, S., Vanhoucke, V., Alemi, A.: Inception-v4, Inception-ResNet and the Impact of Residual Connections on Learning (2016)
29. Sandler, M., Howard, A., Zhu, M., Zhmoginov, A., Chen, L.-C.: MobileNetV2: Inverted Residuals and Linear Bottlenecks. arXiv, 21 Mar 2019. <https://doi.org/10.48550/arXiv.1801.04381>
30. Mateen, M., Wen, J., Nasrullah, Song, S., Huang, Z.: Fundus image classification using VGG-19 architecture with PCA and SVD. *Symmetry* **11**(1), Art. no. 1 (2019)
31. Chakraborti, K., Mukherjee, R., Chakraborty, C., et al.: Automated recognition of optical image based potato leaf blight diseases using deep learning. *ScienceDirect* (2022)

32. Al-Akkam, R.M.J., Altaei, M.S.M.: Plants leaf diseases detection using deep learning. *Iraqi J. Sci.*, pp. 801–816 (2022)
33. Soumo, A.E., Ndeda, R., Aoki, S., et al.: (PDF) Comparison of deep learning architectures for late blight and early blight disease detection on potatoes. *Open J. Appl. Sci.* (2022)
34. Sarker, Md Rahmatul Kabir Rasel, et al.: A deep transfer learning-based approach to detect potato leaf disease at an earlier stage. *Second International Conference on Advances in Electrical, Computing, Communication and Sustainable Technologies (ICAECT)*, IEEE (2022)

# An Investigation into the Technical Feasibility of Incorporating Wind Energy for Electric Vehicle Charging Systems



Belal Aldabagh , Nur Hasalli Binti Ibrahim ,  
and Azizul Rahman Bin Abd Aziz

**Abstract** The primary objective of this research project was to investigate the potential application of wind energy as a solution for reducing charging time and extending the driving range of electric vehicles (EVs). To harness the benefits of the aerodynamic characteristics around the vehicle, a vertical-axis wind turbine was designed and positioned beneath the vehicle, with an inlet located at the front grille. The turbine blades were designed using the NACA4415 airfoil profile and fabricated using 3D printing technology. Experimental measurements were conducted in a subsonic wind tunnel to evaluate the velocity-to-voltage relationship. The experimental results revealed a significant increase in speeds, reaching up to 50% improvement when a nozzle was incorporated into the system. However, at a wind speed of 11.14 m/s, the speed increment dropped to 10% due to wind speed instability. At lower wind speeds of 12 m/s, the power output was measured at 11.28 W, which is considered relatively low. The utilization of a nozzle at the turbine inlet successfully enhanced the wind velocity, resulting in a power output increase of up to 19 kW. The highest recorded wind velocity was 33.33 m/s. Consequently, the integration of a nozzle at the inlet of the wind turbine demonstrated its potential to provide a greater supply of wind energy, thereby generating higher power output within the EV system.

**Keywords** Electric vehicle · VAWT · NACA 4415 · Wind velocity

## 1 Introduction

An internal combustion engine (IC) is a heat engine that transforms the chemical energy in fuel into thermal energy, which is then transformed into mechanical energy, which drives the motion of a car. The pistons inside the cylinders are connected to the crankshaft, which rotates to cause the pistons to move vertically. A timing belt connects the crankshaft to the camshafts, which are in charge of controlling the

---

B. Aldabagh · N. H. B. Ibrahim · A. R. B. A. Aziz

School of Engineering, UOW Malaysia, Jalan Kontraktor U1/14, Glenmarie, 40150 Shah Alam, Malaysia

e-mail: [hasalli.i@uow.edu.my](mailto:hasalli.i@uow.edu.my)

intake valves, which allow the air-fuel mixture to enter the cylinder, and the exhaust valves, which enable the release of combustion by-products from the cylinder. An exhaust piping system is used to direct the gases into the environment in order to discharge these by-products. The exhaust piping system from the exhaust valve transports the combustion process's gases to the outside environment [1]. The exhaust gases emitted during the combustion process contain a substantial volume of carbon dioxide, contributing significantly to global carbon dioxide emissions associated with fossil fuel usage in transportation and goods production, as identified by Leach et al. [2]. Carbon dioxide, classified as a potent greenhouse gas, exacerbates global warming by trapping heat within the atmosphere, as highlighted by the Green Vehicle Guide published by the Australian Government Institute.

Since the advent of the first industrial revolution and continuing to the present day, numerous inventions and developments have emerged, demanding substantial energy consumption to support progress [3]. In 2019, the transportation sector accounted for 30% of global energy consumption, encompassing various vehicles. Addressing this challenge through the adoption of cleaner energy sources to power vehicles can play a pivotal role in mitigating global warming [3]. Electric vehicles (EVs) represent a promising solution as they are environmentally friendly, eliminating the need for petrol combustion and subsequent emissions. Consequently, many countries, including those in Europe and America are actively promoting the widespread adoption of EVs. Measures such as limiting emission levels from manufacturers' vehicles and establishing an extensive network of charging stations are being implemented [4]. EVs can be classified into several categories: battery electric vehicles (BEVs), which primarily rely on battery packs as their main energy source; hybrid electric vehicles (HEVs), which combine an internal combustion engine with a battery pack, utilizing the battery at lower speeds and the engine at higher speeds; plug-in hybrid electric vehicles (PHEVs), which are similar to HEVs but primarily rely on the battery pack, only resorting to the engine when the battery is depleted; and fuel cell electric vehicles (FCEVs), which operate based on fuel cell technology [4]. This paradigm shift in the automotive industry towards EVs reflects a pivotal transition towards a more sustainable transportation future.

The limited driving range of battery electric vehicles (BEVs) posed a significant challenge, as owners had to contend with frequent charging. Recent years, however, have witnessed a surge in research efforts that aimed at enhancing the performance of lithium-ion batteries to extend the driving range of these vehicles. As of 2017, the driving range typically ranged from 100 to 500 km, depending on the specific car brand [4]. However, this range is subject to various influencing factors, including driving conditions, weather conditions, battery age, and more. Once the battery is depleted, the charging process commences, with the charging duration varying based on charger configuration, infrastructure, and operational power level [4]. Numerous research studies have been conducted to minimize charging time, but the time required to charge an EV still exceeds that of refuelling a conventional internal combustion engine (ICE) vehicle [5–7].

Batteries are one of the main energy sources in electric cars and there have been many research papers that seek out to improve and choose the most suitable type of

battery that has characteristics such as a long lifespan, does not affect the environment, supports fast charging, provides enough driving range, and provides enough energy to the vehicle. Many research papers are still going on to improve these aspects of the batteries. There are multiple types of batteries since the first usage of the electric vehicle until present and each one of these batteries varies based on each type's characteristics. Some of the most used batteries are lead-acid, nickel-metal hydride, and lithium-ion [7].

Charging an electric car faces lots of concerns in terms of the charging duration, the amount of current, and voltage and by following certain standards such as SAE J2929 and ISO 26262. Many researchers have been paying attention to developing a charging mechanism to ease the life of EV owners. Mainly, the charging process could happen by alternating-current (AC), direct-current (DC), and wireless chargers. AC chargers provide an alternating current flux to the vehicle which then requires an AC-DC converter to supply the batteries with direct current to start the charging process. This type of charger is considered the slow type of charger due to the time consumption during the process of AC-DC conversion. Direct current chargers are charging faster than AC chargers since it provides greater power. However, this type of charger requires a special type of wiring and installation which does not suit all the existing vehicles; even though it can be obtained easily if the car support DC chargers even as home chargers that could be installed in a garage perhaps [4].

The wind turbine in this project is an essential part and it must be designed in such a way that it generates enough power to recharge the EV's battery. In terms of the blades' design, there are mainly two types of wind turbines based on their blades' design being as horizontal axis wind turbines (HAWT) and vertical axis wind turbines (VAWT). VAWTs are a common option in the market for small applications such as urban areas where they can be installed on a rooftop of a house, for example, for electricity generation. They are also less complicated in terms of their components compared with HAWT since they do not need to be perpendicular to the wind direction. Hence, there is no need for yaw, pitch control, or gearbox. As a result, maintenance will be easier to conduct and will not cost as much as the HAWT system [8].

Due to the high emissions of carbon dioxide, researchers are willing to involve renewable energy possible in most of our life aspect that needs fossil fuel to be run, such as cars. Electric vehicles were introduced as a replacement for ICE cars but there has been a desire to use renewable energy, such as solar and wind energy sources, in the vehicle as a secondary or primary energy source. Thus, many experimental and numerical research papers have been made to test the viability of renewable energy to be used in an EV. For example, Quartey [9] made a theoretical study on installing a horizontal wind turbine on the top of an electric vehicle. The design simply contains a tunnel that the turbine will be placed in, a blade that has a chord length of 200 mm, a shaft that connects to the generator with a material of carbon steel, and the generator that is mounted to be in line with the shaft. The power of the shaft is calculated by focusing on the car's velocity and neglecting the surrounding wind velocity which gave a power of 4 kW. Figure 1 illustrates a conceptual design of the idea.

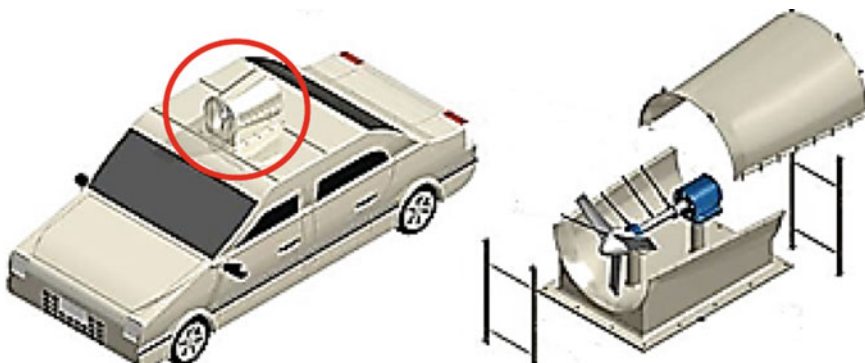


**Fig. 1** Wind turbine placed on the roof of an electric car

The author has conducted some calculations to figure out the expected output power of the turbine. Figure 2 shows the shaft power with respect to some velocities assuming the velocity of the vehicle is equivalent to the wind velocity.

Based on the study, the small-scale vertical-axis wind turbine with helical-shaped blades and with an expected output power of 100 W, the system is designated at a relatively low tip speed ratio at 1:1 that is targeted to be used in an urban environment at a rated wind speed of 9 m/s and a rotational speed of 170 RPM. The basic dimensions were determined through a momentum-based design method according to the IEC 61400-2 protocol [10]. This study shows that the higher the wind velocity, the more power is harvested, as shown in Fig. 3.

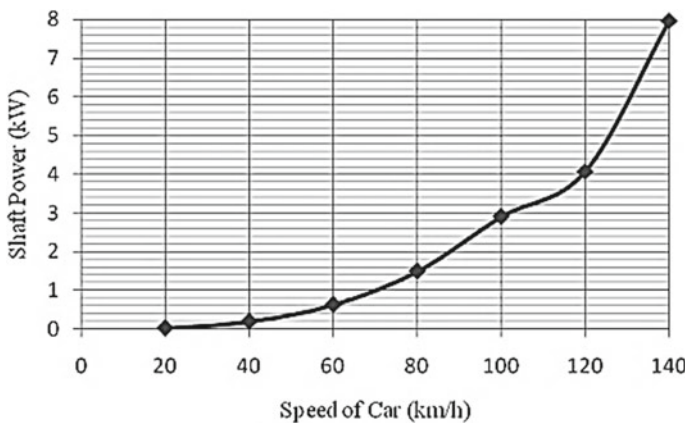


**Fig. 2** Speed of car against shaft power

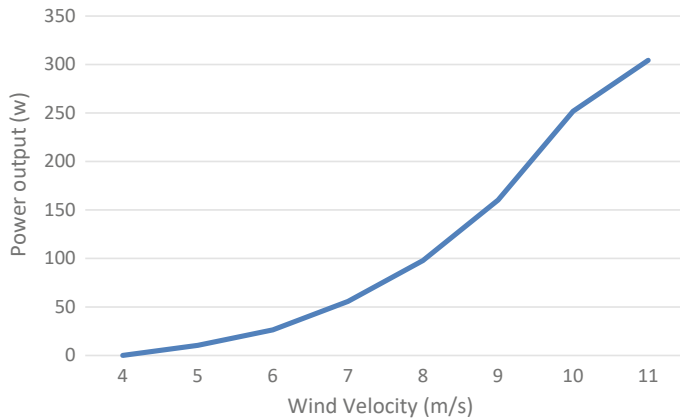


**Fig. 3** Power output at different wind speed

## 2 Methodology

This project has gone through some procedures to validate the idea of taking advantage of the kinetic energy stored in the wind that is striking the frontal bumper of a vehicle. Taking advantage of the energy will be by placing a wind turbine so that rotation occurred, and energy will be obtained to recharge the battery pack of the electric vehicle. The processes had to be started based on the conceptual design to illustrate the expected shape of the turbine's body system and set the turbine's parameters. Then, the turbine was printed using a 3D printer to build the whole turbine system. An experiment has been conducted using a wind tunnel to analyze the different speeds that affect and compare with the research study.

The selection of an appropriate airfoil is a crucial aspect of this project, considering the availability of various standardized airfoil profiles suitable for diverse applications. National Advisory Committee for Aeronautics (NACA) and National Renewable Energy Laboratory (NREL) are prominent sources of standardized airfoils. A comparative analysis highlighting different airfoil types and their respective characteristics has been presented [11]. Furthermore, according to research on NACA subsonic airfoils, pressure and velocity have a significant impact on how well the system performs aerodynamically, with pressure and velocity being highest at the leading edge and decreasing as they approach the trailing edge point [12]. In this project, it is imperative to identify an airfoil capable of withstanding the high-pressure conditions associated with high-speed wind, necessitating a high Reynolds number. Figure 4 presents a comparison between NACA and NREL airfoil standards specifically for VAWT applications under high Reynolds number conditions. The evaluation criteria include a significantly high lift-to-drag ratio ( $Y$ -axis) and minimal line fluctuation to minimize vibrations at high speeds. Upon examining the graphs, it is evident that most of the airfoils exhibit fluctuations, except for NACA 4415. Furthermore, some NACA airfoils demonstrate higher ratios compared with NREL

airfoils. Notably, NACA 4415 exhibits notably attractive characteristics, showcasing both reduced fluctuations and a high lift-to-drag ratio. Consequently, NACA 4415 has been selected as the preferred airfoil for implementation in this project.

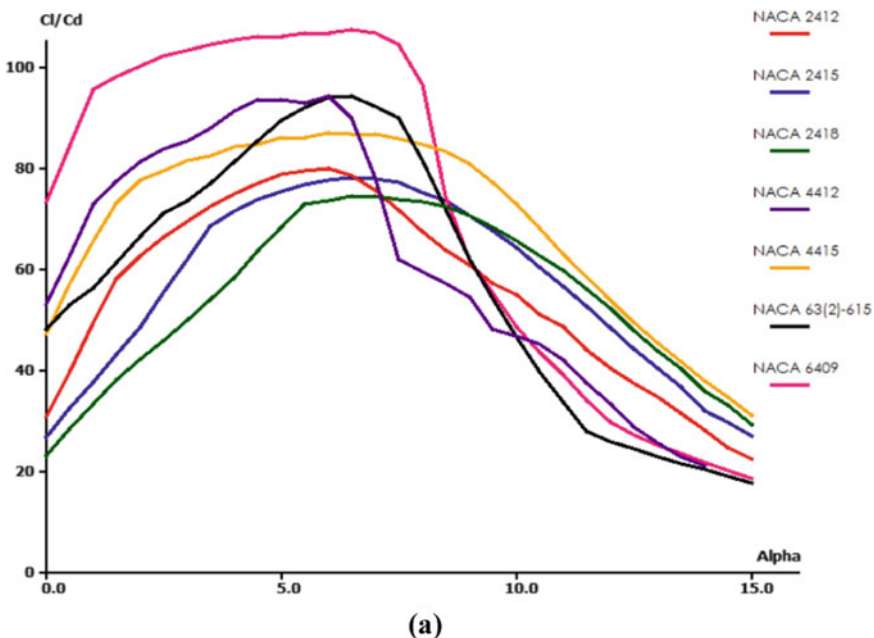
In terms of the generator, one of the commonly used generators in the projects of small to medium wind turbines is the permanent magnet synchronous generator (PMSG) [13]. As shown in Fig. 5, the system contains the blades, illustrated as horizontal but vertical in this project, in addition to a PMSG generator that both works as a convertor of wind into mechanical energy, a generator-side converter that rectifies the three-phase AC electrical voltage into DC, as well as a boost converter. In addition, an MPPT controller is in the system which extremely enhances the output power and a grid-side converter that turns DC electrical voltage into AC. The last stage of this system is supposed to be connected to the lithium-ion batteries for the recharging process.

The design of the vertical-axis wind turbine consists of four main parts; the base, the cylinder, the vanes that are attached to the cylinder, and the nozzle. Figure 6 is an illustration of the 3D model of the VAWT system for the electric vehicle that has been fabricated using the 3D printer.

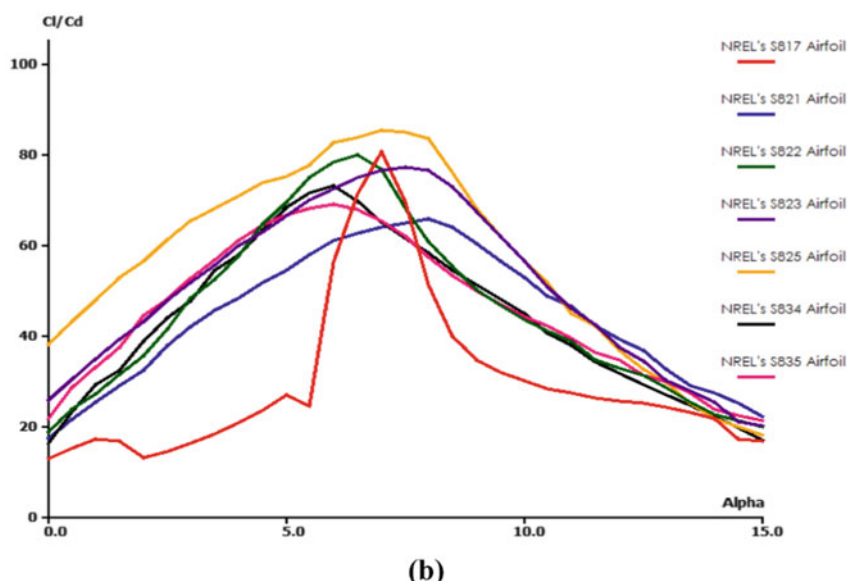
The body of the VAWT turbine consists of an inlet area that connects to the nozzle and leads to the turbine blades. The nozzle is placed in order to gain higher wind speed at the vehicle's low speed. Figure 7 is an illustration of the design.

The fabrication of the prototype involved utilizing the polylactic acid (PLA) material and employing a 3D printer. To ensure stability, the prototype was assembled with a motor and placed on a wooden base, preventing contact with the ground surface. Additionally, a multimeter was integrated with the prototype to accurately measure the voltage output. The experimental investigation took place within a subsonic wind tunnel, where the prototype was positioned in the designated testing area. The wind was applied at varying speeds to assess the corresponding voltage output. The experiment encompassed both nozzle-equipped and nozzle-free conditions to evaluate the impact of wind speed on the voltage output. Multiple velocity measurements were recorded while maintaining a constant dynamic pressure. Figure 8 illustrates the experimental set-up of the vertical axis wind turbine (VAWT) system within the subsonic wind tunnel. Safety measures were implemented during the wind tunnel experiment to protect researchers and equipment. Strict adherence to safe operating parameters and regular inspection prevented potential structural damage or equipment malfunction.

Data collection was conducted to facilitate the integration of the VAWT system beneath the electric vehicle while maintaining optimal aerodynamic performance. The placement of the turbine's inlet in the electric vehicle can be observed in Fig. 9.



(a)



(b)

**Fig. 4** Glide ratio versus angle of attack at Reynolds Number of 330,000 for **a** NACA and **b** NREL airfoils, respectively

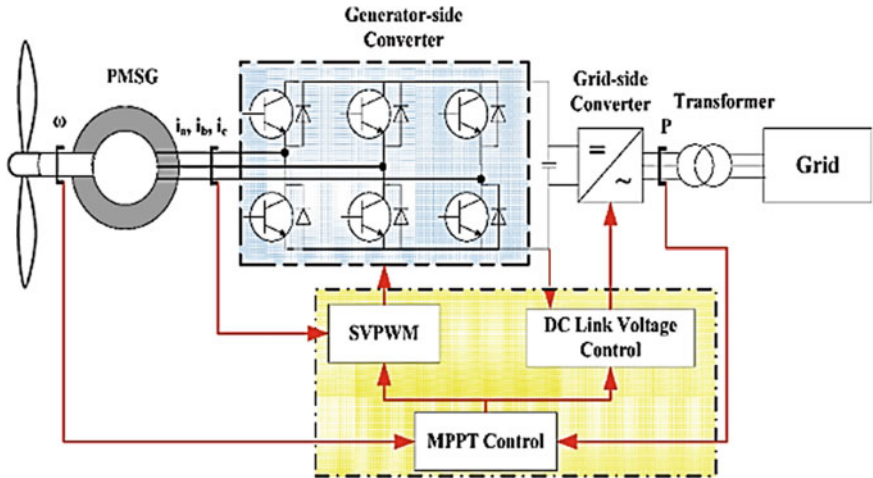


**Fig. 5** Diagram of full system small-scale wind turbine

### 3 Result and Discussion

The data that were collected from the experiment using subsonic wind tunnel consists of two different parts which is with nozzle and without nozzle. The constant range of velocity has been used to ensure the stability of the wind velocity under steady condition when flowing around the wind turbine system either with or without nozzle. Table 1 gives an experimental data for the VAWT turbine without nozzle which shows that the voltage increases when the wind velocity increases.

The same range of velocities that were used during the experiment were used to record the data for the VAWT with nozzle in Table 2 where the values of voltage are higher than the VAWT without nozzle.

In Fig. 10, the experiment data in between the VAWT with and without nozzle has been compared where the value of the voltage is increased when the wind velocity increases. The stability of the rotor is crucial because the data obtained from the experiment are ideal and after doing several experiments the fluctuation happens in the multimeter due to the instability. The velocity of the VAWT with a nozzle is higher than the VAWT without a nozzle which shows the implementation of the nozzle in the VAWT system is able to increase the amount of velocity and produce more energy to the system.

The experimental results indicate a linear relationship between velocity and voltage output. Table 3 displays the percentage increment in multimeter readings at a constant velocity. The nozzle demonstrates high efficiency at lower speeds, resulting in a 50% increase in millivoltage. However, as the velocity increases, the percentage increment decreases, reaching 10% at the highest recorded velocity during the experiment. Despite this decrease, the nozzle remains effective at lower speeds by compensating for the low-power output. Moreover, as the velocity increases, the

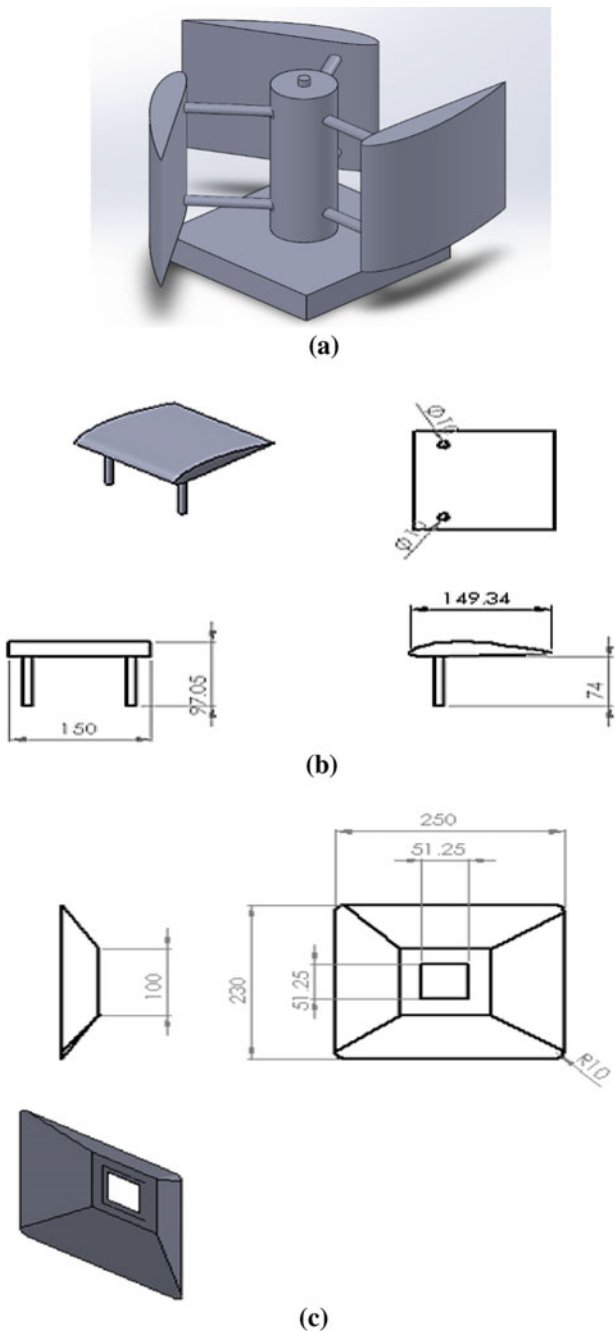


**Fig. 6** Conceptual design of the **a** assembled components of VAWT system, **b** blade component based on NACA4415, and **c** Nozzle system

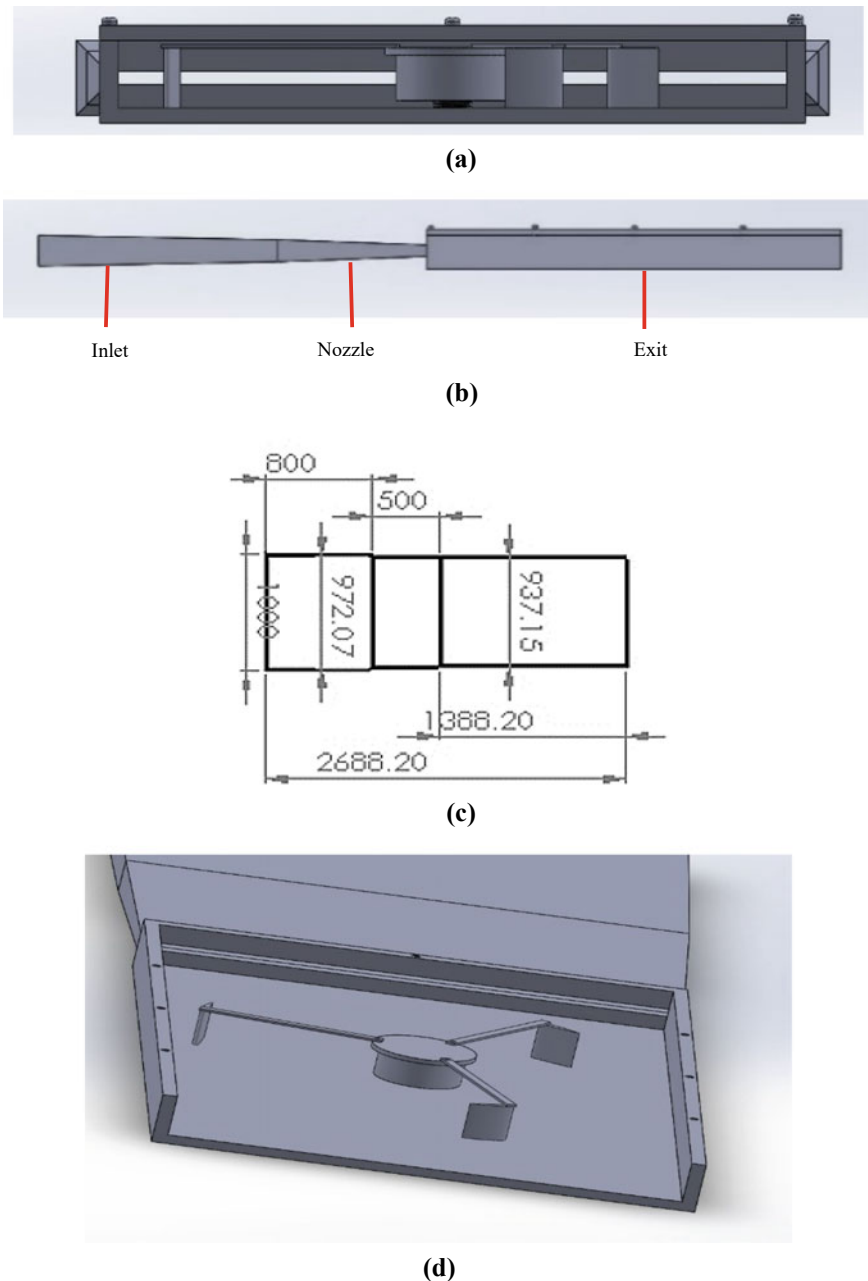


**Fig. 7** Illustration of the conceptual design for different view **a** front view (exit), **b** side view, **c** dimension of the nozzle, and **d** top view of the VAWT turbine system

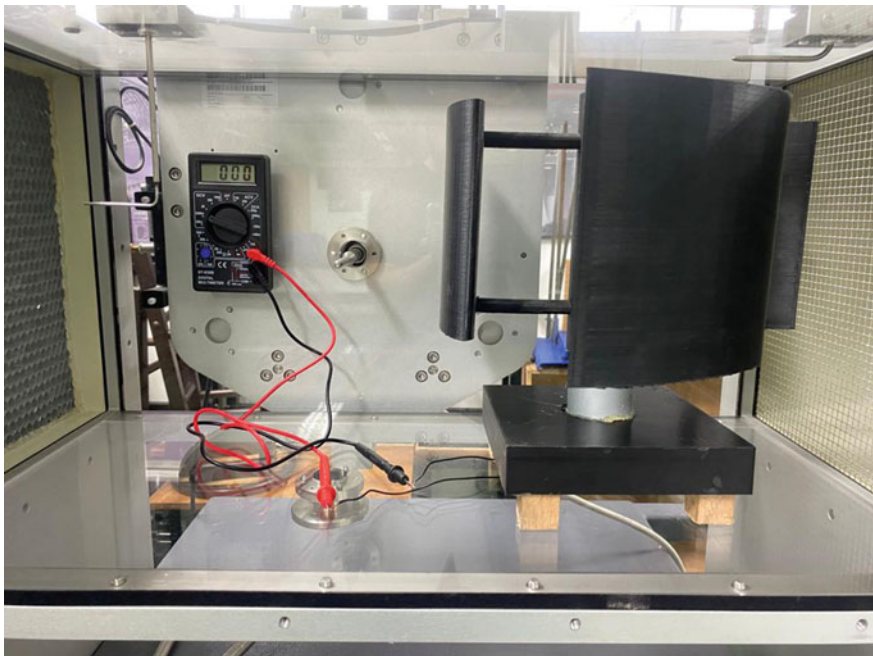


**Fig. 8** Prototype of the VAWT system inside the subsonic wind tunnel

**Fig. 9** Placement of the VAWT turbine's inlet



power output rises, enabling the turbine system to sufficiently recharge the battery without requiring the use of a nozzle.

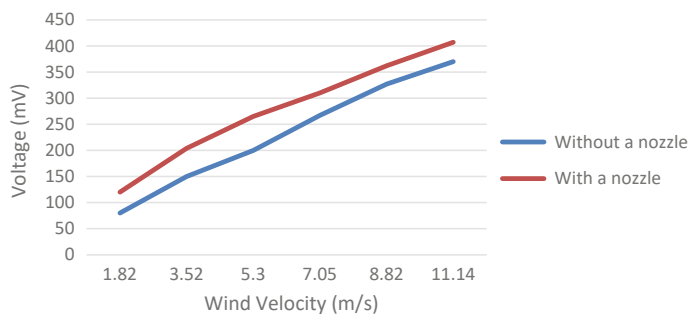
To validate the experimental work, the comparison with other researcher has been done for the small-scale turbine system [9]. Calculations were made based on

**Table 1** Experimental data without nozzle

Velocity (m/s)	$\Delta P_1$ (mmH <sub>2</sub> O)	Voltage (mV)
1.82	0.2	80
3.52	0.75	150
5.30	1.7	200
7.05	3	267
8.82	4.7	327
11.14	7.5	370

**Table 2** Experimental data with nozzle

Velocity (m/s)	$\Delta P_1$ (mmH <sub>2</sub> O)	Voltage (mV)
1.82	0.2	120
3.52	0.75	204
5.30	1.7	265
7.05	3	310
8.82	4.7	362
11.14	7.5	407

**Fig. 10** Comparison data of VAWT with and without nozzle**Table 3** Percentage of increment between the multimeter readings with and without the nozzle

Velocity (m/s)	Voltage without nozzle (mV)	Voltage with nozzle (mV)	Percentage of increase (%)
1.82	80	120	50
3.52	150	204	36
5.30	200	265	32.5
7.05	267	310	16.10
8.82	327	362	10.70
11.14	370	407	10

Quartey, the reference that measures for the HAWT on top of the EV. Firstly, the maximum tip speed ratio is found by:

$$\gamma = \frac{4\pi}{B} = \frac{4\pi}{3} = 4.189, \quad (1)$$

where  $B$  is the number of blades.

Using Betz limit of 59% and at 4.189, the pressure coefficient is 0.38; adding augmentation of 1.38;  $C_{ps} = 1.38 + 0.38 = 1.76$  ( $C_{ps}$  is the shaft power coefficient).

The area of the prototype: ( $D = 0.24366$  m).

$$A = \frac{\pi d^2}{4} = \frac{\pi 0.24366^2}{4} = 0.04663. \quad (2)$$

Shaft power, rotational speed, and the torque can be calculated by, respectively:

$$P_s = \frac{C_{ps}\rho AV^3}{2}, \quad (3)$$

$$\omega = \frac{\gamma V}{R}, \quad (4)$$

$$\tau = \frac{P_s}{\omega}. \quad (5)$$

Table 4 gives the shaft power, rotational speed, and torque at each speed of the experiment. On the other hand, Table 5 gives the same data but at velocities similar to the reference data that was used for the calculation.

To make the comparison clear, a line-graph has been generated with the calculated shaft power of each of the two designs to show the mechanism of increase and difference. Figure 11 shows the difference in the increase of shaft power in both the turbines systems. As usual, the shaft power is increasing by the rise of velocity. The increment of the shaft power of Quartey's turbines system is stiffer compared with the prototype which also means that the stiffer the line is, the more potential to harvest more energy the higher the speed is. The difference in the increase could be

**Table 4** Calculated data, related to experiment based on the constant velocities

Velocity (m/s)	$P_s$ (mV)	$\omega$ (mV)	$\tau$ (Nm)
1.82	0.30	62.58	0.0048
3.52	2.19	121.03	0.0181
5.30	7.48	182.23	0.0410
7.05	17.61	242.41	0.0603
8.82	34.49	303.26	0.114
11.14	69.49	383.04	0.181

**Table 5** Calculated data, related to experiment based on the other researcher velocity value [9]

Velocity (m/s)	$P_s$ (mV)	$\omega$ (mV)	$\tau$ (Nm)
5.55	8.59	191.24	0.045
11.11	68.93	382.83	0.180
16.66	232.44	574.07	0.405
22.22	551.46	765.65	0.720
27.77	1076.49	956.89	1.125
33.33	1861.19	1148.48	1.620

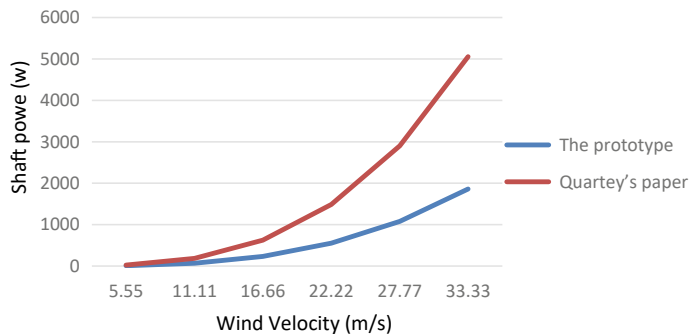


**Fig. 11** Comparison in shaft power between the prototype and Quartey's project

explained by the difference between the rotational radius where Quartey has designed the system to be bigger than the prototype of this project.

In terms of the conceptual design, it was validated by comparing the calculation by Castillo [14] that intended to design a small-scale vertical-axis wind turbine with the same calculation but with this project's turbine parameters. The process of calculation starts with finding the swept area, where  $R$  is the radius and  $L$  is the length of the turbine.

$$S = 2RL = 2 \times 0.392 \times 0.08 = 0.0627. \quad (6)$$

Wind power, rotational speed, tip speed ratio (TSR), and solidity are found by the following formulas, respectively:

$$P_w = \frac{\rho S V^3}{2}, \quad (7)$$

$$\omega = \frac{V}{2\pi R}, \quad (8)$$

$$\text{TSR} = \frac{R\omega}{V}, \quad (9)$$

$$\sigma = \frac{Nc}{R}. \quad (10)$$

Table 6 gives the original data of Javier Castillo, whereas Table 7 gives the same data but based on the dimensions of this project's conceptual design. The main difference in the design is that the turbine is considerable bigger than the designed wind turbine in this project; the chord, diameter, and the length are having higher values. The data of the conceptual design are lower than the illustrated data and again the main difference is in the design parameters which made an influence on the calculated data. The blade length, for example, of the conceptual design is 96% smaller than the design in the paper which was due to some limitation of NACA 4415 profile.

**Table 6** Data calculated and illustrated in a research paper [14]

Design parameters		Calculated parameters	
Rotor radius (m)	1	Tip speed ratio	2
Blade length (m)	2	Swept area	4
Blade chord (m)	0.2	Solidity	0.8
Power coefficient	0.17		
Number of blades	4	Rated blade speed (m/s)	12
		Actual rotational speed (rad/s)	12
Air constants		Actual rotational speed (rpm)	114.59
Air density (kg/m <sup>3</sup> )	1.225		
Wind speed (m/s)	6	Wind power (W)	529.2
Conversion factors		Power output (W)	89.964
rad/s → rpm	× 9.54		

**Table 7** Data calculated of the conceptual design

Design parameters		Calculated parameters	
Rotor radius (m)	0.392	Tip speed ratio	0.158
Blade length (m)	0.08	Swept AREA	0.0627
Blade chord (m)	0.08	Solidity	0.612
Power coefficient	0.17		
Number of blades	3	Rated blade speed (m/s)	12
		Actual rotational speed (rad/s)	4.87
Air constants		Actual rotational speed (rpm)	46.46
Air density (Kg/m <sup>3</sup> )	1.225		
Wind speed (m/s)	6	Wind power (W)	66.36
Conversion factors		Power output (W)	11.28
rad/s → rpm	× 9.54		

The rate of blade speed has been considered at 12 m/s which is equivalent to the vehicle speed at 43.2 km/s. This value is relevantly low and the higher the vehicle's speed the more output energy will be captured. Indeed, the rated blade speed should be even higher than the vehicle's speed due to the nozzle placed at the entrance of the turbine. As shown in Table 8, the calculations have been done but at rated blade velocity of 33.33 m/s (=120 km/h); it is clearly shown that the power output is higher than the one in the paper, 266% more.

The calculations that were conducted on the prototype to compare the results with Quartey's project were conducted on the conceptual design to find the actual difference between the two projects. As seen in Table 9, the overall data are extremely higher than the prototype and Quartey's project. If comparing the torque at 33.33 m/s, the torque at the HAWT was 5.832 Nm, whereas 54.13 Nm from the study.

Figure 12 shows a comparison data between the conceptual design and the HAWT by measuring the effect of the shaft power at different level of wind speed. There is an obvious difference in the power of the shaft in both projects where both power values are increasing by the rise of the wind velocity, but the curve of the conceptual design seems to be increasing in a sharper angle than the HAWT. That proves the VAWT is more efficient when used in small-scale applications. Also, the diameter

**Table 8** Data calculated the conceptual design at rated speed of 33.33 m/s

Design parameters		Calculated parameters	
Rotor radius (m)	0.392	Tip speed ratio	0.159
Blade length (m)	0.08	Swept area	0.0627
Blade chord (m)	0.08	Solidity	0.612
Power coefficient	0.17		
Number of blades	3	Rated blade speed (m/s)	33.33
		Actual rotational speed (rad/s)	13.532
Air constants		Actual rotational speed (rpm)	129.09
Air density (g/m <sup>3</sup> )	1.225		
Wind speed (m/s)	33.33	Wind power (W)	1421.93
Conversion factors		Power output (W)	241.7
rad/s → rpm	× 9.54		

**Table 9** Shaft power, rotational speed, and torque calculated based on the conceptual design

V (m/s)	P <sub>s</sub> (W)	ω (rad/s)	τ (Nm)
5.55	89.01	59.31	1.501
11.11	714.01	118.72	6.014
16.66	2407.63	178.32	13.50
22.22	5712.13	237.45	22.78
27.77	11,150.48	296.75	37.57
33.33	19,278.43	356.17	54.13

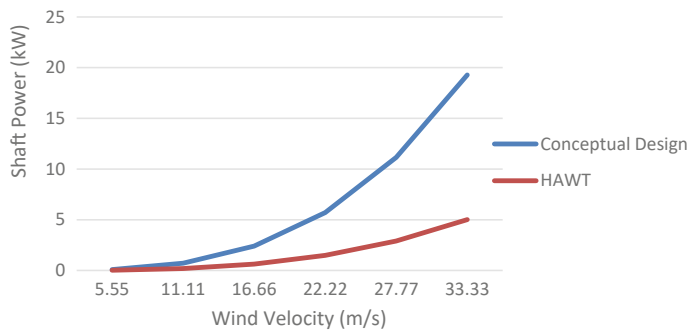


**Fig. 12** Comparison between the effects of shaft power on the conceptual design versus the HAWT

of the conceptual design is almost the double of the HAWT which also gives it an advantage.

## 4 Conclusion

In conclusion, this project aimed to address the challenges of recharging electric vehicles efficiently and extending their range. The first objective involved selecting a suitable small-scale wind turbine system that harnesses the kinetic energy in wind for EV battery charging. A thorough literature review guided the selection of optimal system components, including the blade profile and generator. The system was meticulously designed using SOLIDWORKS to seamlessly integrate beneath an electric vehicle, with the addition of a nozzle at the turbine entrance. Calculations based on the conceptual design were conducted, and comprehensive comparisons were undertaken to validate its effectiveness. Notably, at lower speeds such as 12 m/s, the power output was modest at 11.28 W. However, the inclusion of the nozzle proved advantageous, enhancing wind velocity, and thereby increasing power output. At higher speeds, such as 33.33 m/s, the power output demonstrated significant improvement, reaching approximately 19 kW. The second objective involved physical validation through the construction of a prototype and performance testing based on voltage output. The prototype building process encountered various challenges related to sizing and turbine stability, which were meticulously addressed. While high-speed testing was hindered by stability concerns, performance calculations were employed and compared with findings from existing research. The results highlighted the nozzle's effectiveness, particularly at lower speeds, where it exhibited a remarkable 50% voltage increment at a speed of 1.82 m/s. In summary, the implementation of the nozzle within the VAWT enhances power generation for sustainable electric vehicle charging. This project underscores the potential for utilizing wind energy as a viable solution for improving the efficiency and range of electric vehicles, contributing to a more sustainable transportation ecosystem.

**Acknowledgements** This research work is supported by UOW Malaysia.

## References

1. Gupta, H.N.: Fundamentals of internal combustion engines, 2nd edn. PHI Learning Private Limited (2013)
2. Leach, F., Kalghatgi, G., Stone, R., et al.: The scope for improving the efficiency and environmental impact of internal combustion engines. *Transp. Eng.* **1**(100005), 1–17 (2020)
3. Holmberg, K., Erdemir, A.: The impact of tribology on energy use and CO<sub>2</sub> emission globally and in combustion engine and electric cars. *Tribol. Int.* **135**, 389–396 (2019)
4. Un-Noor, F., Padmanaban, S., Mihet-Popa, L., et al.: A comprehensive study of key electric vehicle (EV) components, technologies, challenges, impacts, and future direction of development. *Energies* **10**(8), 1–82 (2017)
5. Aghajani-Eshkevari, S., Azad, S., Nazari-Heris, M., et al.: Charging and discharging of electric vehicles in power systems: an updated and detailed review of methods, control structures, objectives, and optimization methodologies. *Sustainability* **14**(4), 2137 (2022)
6. Ullah, I., Liu, K., Yamamoto, T., et al.: Prediction of electric vehicle charging duration time using ensemble machine learning algorithm and Shapley additive explanations. *Int. J. Energy Res.* **46**(11), 15211–15230 (2022)
7. Shahjalal, M., Shams, T., Tasnim, M.N., et al.: A critical review on charging technologies of electric vehicles. *Energies* **15**, 8239 (2022)
8. Hasan, M.M.: Design and performance analysis of small scale horizontal axis wind turbine for nano grid application. Master thesis, Georgia Southern University (2017)
9. Quartey, G., Adzimah, S.K.: Generation of electrical power by a wind turbine for charging moving electric cars. *J. Energy Technol. Policy* **4**(3), 1–11 (2014)
10. Han, D., Heo, Y.G., et al.: Design, fabrication, and performance test of a 100-W helical-blade vertical-axis wind turbine at low tip-speed ratio. *Energies* **11**(6), 1517 (2018)
11. Islam, M.R., Bashar, L., et al.: Comparison and selection of airfoils for small wind turbine between NACA and NREL's series airfoil families. *Int. J. Res. Electric. Electron. Commun. Eng.* **4**(2), 1–11 (2019)
12. Ibrahim, N.H., Amari, M.D., Shamsuddin, Z.S.: Study of subsonic airfoil based on the assessment of lift-to-drag (L/D) force ratio. *Int. J. Eng. Technol.* **8**(1.1), 53–58(2019)
13. Syahputra, R., Soesanti, I.: Performance improvement for small-scale wind turbine system based on maximum power point tracking control. *Energies* **12**(20), 3938 (2019)
14. Castillo, J.: Small-scale vertical axis wind turbine design. Degree thesis, Tampere University of Applied Sciences (2011)

# Surface-Modified PDMS-Aluminum Triboelectric Generator



Emaediong Sylvanus Udofo, Anas A. Ahmed, Yusri Md Yunos,  
and Mohamed Sultan Mohamed Ali

**Abstract** This study investigates the performance characteristics of a triboelectric generator utilizing a polydimethylsiloxane (PDMS)-aluminum (Al) bilayer system operating in contact-separation mode. The primary objective is to evaluate the influence of surface modification on the output voltage of the generator. The experimental procedure involves the preparation of an Al layer and PDMS samples with a  $4 \times 4 \text{ cm}^2$  area and a thickness of 2 mm, which were subjected to surface modifications using abrasive paper with grit sizes of 240 CW, 400 CW, 600 CW, and 800 CW. The findings of this study demonstrate that treating the PDMS sample with a 600 CW grade as the negative tribo-material, in combination with treating the Al layer with an 800 CW grade as the p-type material, resulted in a significant 50% increase in output voltage compared with the untreated configuration. This enhanced performance can be attributed to the formation of micro-structured surfaces on both the PDMS and Al layers through surface treatments which facilitates electron transfer within the triboelectric generator. The outcomes of this investigation provide valuable insights into the impact of surface treatment on the performance of PDMS-Al triboelectric generators. The findings contribute to the fundamental understanding of energy harvesting devices and offer opportunities for optimizing the design and fabrication of more efficient triboelectric generators.

**Keywords** Contact-separation · Surface-modified · Polydimethylsiloxane · Aluminum · Triboelectric generator

---

E. S. Udofo · A. A. Ahmed · Y. M. Yunos · M. S. Mohamed Ali  
Faculty of Electrical Engineering, Universiti Teknologi Malaysia, UTM Johor Bahru, 81310  
Johor, Malaysia

M. S. Mohamed Ali (✉)  
Department of Electrical Engineering, College of Engineering, Qatar University, Doha, Qatar  
e-mail: [m.sultan@qu.edu.qa](mailto:m.sultan@qu.edu.qa); [sultan\\_ali@fke.utm.my](mailto:sultan_ali@fke.utm.my)

## 1 Introduction

With the growing demand for self-powered systems, wearable devices, and low-power portable devices, the need for alternative energy sources has become increasingly urgent. While battery-powered devices have been developed, their environmental impact, short lifespan, and size restrictions continue to pose significant challenges [1]. Frequent recharging or replacement further limits their longevity. In response, researchers have investigated various energy harvesting methods such as piezoelectric, thermoelectric, and electromagnetic [2], but these methods have limitations in terms of low-voltage output, high cost, low efficiency, fragility, and limited flexibility [3]. Recently, triboelectricity has attracted significant attention for its potential in energy harvesting at low frequencies, due to its ability to harness available ambient mechanical energy. Triboelectric generators offer several advantages, including relatively high output power, cost-effectiveness, lightweight design, and the ability to utilize a wide range of materials sources with simple fabrication processes [4]. The phenomenon of gaining and losing electrons due to frictional contact is observed in a wide range of materials including wood, polymers, metals, and silk. This effect has led to the development of triboelectric generators (TEGs) using a diverse range of materials [5].

Triboelectric generators operate in four major modes: sliding mode, free-standing mode layer mode, single-electrode mode, and contact-separation mode. Researchers have explored the use of various techniques to improve the triboelectric performance of materials. For instance, electrospun polyvinylidene fluoride (PVDF) with micro-structured polyvinyl alcohol were explored to enhance output performance [6]. Materials used to improve TEG's contact surfaces have been widely explored to upgrade its output performance [7–9]. Improved stretchable graphene-based TEG through the regulation of surface nanostructure has also been explored [10]. The suitability of a material for TEG fabrication depends on its ability to generate a charge imbalance through the transfer of electrons, which is contingent on the polarity difference of material pairs. Consequently, the material selection for TEGs is vast, offering a broad range of options for device design and optimization [11, 12]. Surface modification is also reported to be considered as a critical strategy for enhancing the output performance of triboelectric devices, as it can impact the surface charge density and the material's capacity for gaining or losing electrons [12]. This can be achieved through physical or chemical methods such as surface patterning, coating, ion implantation, lithography, and laser patterning techniques. These methods enable the controlled introduction of surface features at the micro-nanoscale, allowing for precise manipulation of the electro-frictional properties of the material.

Among the widely used materials for triboelectric energy harvesting, polydimethylsiloxane (PDMS) has been shown to be a very desirable material due to its high flexibility, biocompatibility, easy surface modification capability, and high electronegativity. Utilization of polyethylene terephthalate (PET) and aluminum (Al) as a positive layer, coupled with sandpaper treated PDMS, has exhibited remarkable efficacy in enhancing the triboelectric output [13]. Surface modification techniques,

involving line, pillar, and hexagonal cone morphologies on the surfaces of PDMS and polymethyl methacrylate (PMMA) through contact-separation-based methods have also been successfully implemented [5]. Additionally, the high-performance output of TEG has been achieved by creating longitudinal paths of electrostatic charges within the contacting layers through the formation of internal-space-charge zones, achieved by embedding ravines and gullies in crisscrossed gold layers on the near-surface of the tribo-layer [7]. Moreover, surface texturing techniques in conjunction with constant dielectric control have been employed to further enhance the performance of PDMS-based TEGs [14]. Another study has demonstrated the use of abrasive paper to create micro-structured surface PDMS and human skin as a positive layer to harvest electrical energy for wearables [15]. Additionally, the doping of a carbon nanotube with abrasive paper patterned PDMS to improve the triboelectric output was investigated. Recently, plasma-treated polytetrafluoroethylene for improved TEG performance was also reported [16]. However, all these studies only focused on the polymer surface patterning chemistry (negative tribo-material) to improve the TEG output performance, without much emphasis on the positive tribo-material.

This study presents an approach for investigating the output performance of micro-structured PDMS films as negative tribo-material and Al layer as the positive tribo-material. The effect of varying micro-structured surfaces of both negative and positive tribo-materials was examined to enhance the performance of TEG. To achieve this, the micro-structured PDMS and Al surfaces were patterned to pose different surface roughness. The findings from this study provide a valuable contribution to the development and improvement of triboelectric output performance in energy harvesting. The paper outlines the principle of operation, fabrication process, experimental setup, results, discussion, and conclusion.

## 2 Experimental Work

The fabrication process of the surface-modified PDMS-Al TEG is depicted in Fig. 1. The PDMS film was produced by thoroughly mixing the resin and hardener in a weight ratio of 10:1. The mixture was stirred at a speed of 200 rpm for a duration of 30 min. To eliminate any entrapped air bubbles, the solution underwent a vacuum process for 5 min. Subsequently, the prepared PDMS solution was cast onto 3D-printed molds, where each mold was mounted on an abrasive paper of varying grit sizes (240 CW, 400 CW, 600 CW, and 800 CW) as shown in Fig. 1a. The PDMS film was then dried at a temperature of 120 °C on a hotplate for a period of 1 h. The resulting PDMS layer with the dimensions of 4 cm (width) × 4 cm (length) × 0.2 cm (thickness) was used as the negative tribo-material. On the other hand, 50- $\mu\text{m}$ -thick Al layer with a lateral size of 4 cm × 4 cm was used as the positive tribo-material. The Al layer was pressed on abrasive papers having grit size of 240 CW, 400 CW, 600 CW, and 800 CW through a laminating machine to modify the Al surface (Fig. 1c).

This approach provides a promising strategy for surface modification and treatment to enhance the performance of triboelectric generators.

To ensure proper functionality and stability, the PDMS layer affixed with Al tape, serving as an electrode and the Al layer pressed on the abrasive paper were securely mounted on acrylic plates as depicted in Fig. 1c. The TEG assembly was then positioned on a vibration exciter. This setup operated in a contact-separation mode, whereby a signal generator was connected to a power amplifier, which in turn was coupled with the vibration exciter. This setup facilitated the generation of periodic linear motion, involving the pressing and releasing of the TEG components. The

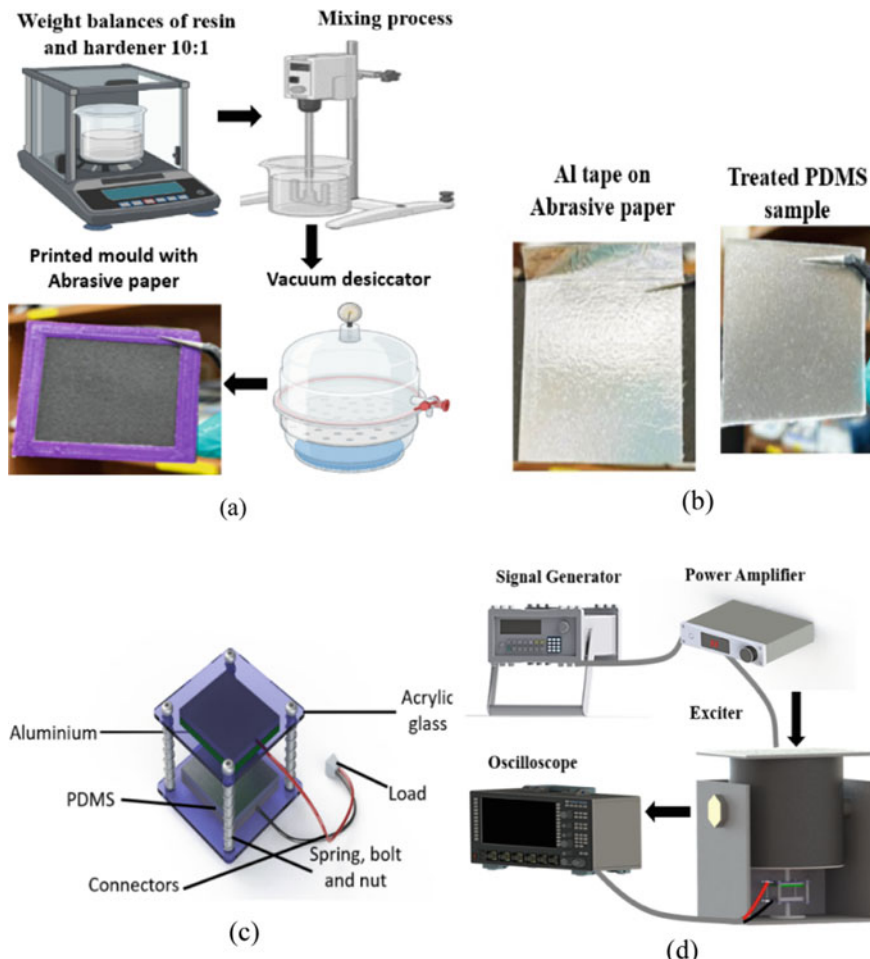


**Fig. 1** Fabrication process of surface-modified TEG (a–c) and Triboelectric measurement setup (d)

TEG positioned on the exciter was connected to a digital oscilloscope to investigate the triboelectric characteristics as illustrated in Fig. 1d.

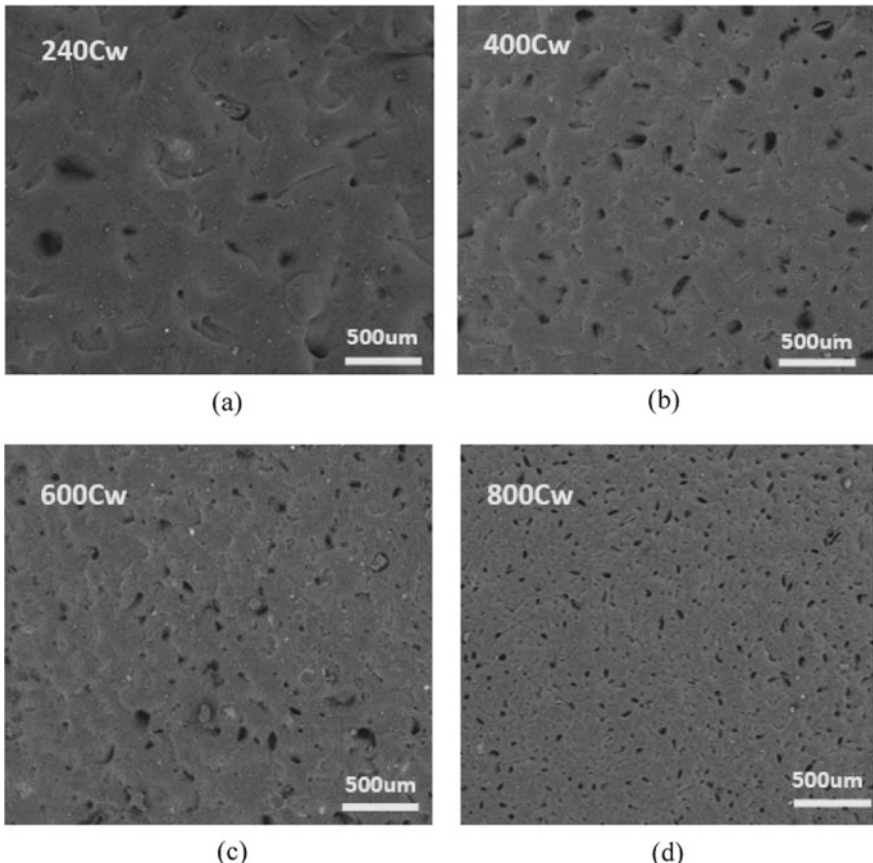
### 3 Results and Discussion

Figure 2 displays scanning electron microscopy (SEM) images depicting the surface modification of PDMS utilizing different grit sizes of abrasive paper. The images clearly demonstrate that the choice of abrasive paper significantly influences the characteristics of the PDMS surface. It is observed that higher grit size of the abrasive paper results in a smoother surface texture of the PDMS layer, while lower grit size produces rougher surfaces. It is anticipated that these observed variations in surface morphology have implications on the surface contact area and electric charge distribution of thermoelectric generators (TEG), thereby affecting their surface properties and tribo-material combinations.

As mentioned earlier, the surfaces of the positive (Al) and negative (PDMS) tribo-materials were modified using abrasive papers with different grit sizes, aiming to enhance the surface charge transfer and triboelectric characteristics of the TEG. Figure 3 compares the output voltage of the TEGs fabricated with different grit sizes at fixed frequency (8 Hz) and fixed applied force (2 N). Two sets of TEGs were fabricated; these are the fully modified TEG (Fig. 3a) and half-modified TEG (Fig. 3b). In the fully modified TEG, the surfaces of PDMS and Al were modified with the same grit size of 240 CW, 400 CW, 600 CW, and 800 CW, whereas in the half-modified TEG, only the surface of PDMS was modified with different grit sizes. From Fig. 3c, it is clear that the performance of the half-modified TEG is higher than the performance of fully modified TEG. The output voltage of the fully modified TEG increased from 22 to 32 V, whereas the output voltage of the half-modified TEG increased from 25 to 40 V with the increase of grit size from 240 to 800 CW. This could be related to the effective contact area of the two surfaces, where it is expected to be less for the fully modified TEG.

To gain a clear picture on the influence of the surface modification of the tribo-materials on the TEG triboelectric performance, a different combination of the surface-modified tribo-materials (PDMS and Al) was investigated as shown in Fig. 4. The surface of Al layer was modified in steps starting from grit size of 240 CW up to 800 CW. PDMS samples modified with different grit sizes were used for each modified Al layer. For the 240 CW modified Al combined with PDMS modified with 400 CW, 600 CW, 800 CW grit size, the output voltage was measured to be almost the same (30 V) (Fig. 4a). When 400 CW modified Al was combined with 240 CW modified PDMS, the output voltage increased to ~40 V (Fig. 4b). For higher grit size of Al modified layer, higher output voltages of 50 V and 68 V were measured for the 600 CW modified Al combined with 400 CW modified PDMS and 800 CW modified Al combined with 600 CW modified PDMS, respectively.

It is clear that the surface modification of tribo-materials strongly affects the triboelectric properties of TEGs, and a subtle surface modification can help in achieving



**Fig. 2** SEM images of surface-modified PDMS with different grit size of abrasive paper **a** 240 CW, **b** 400 CW, **c** 600 CW, and **d** 800 CW

highly efficient TEGs. The improvement in the triboelectric performance upon changing the surfaces of both tribo-materials can be assigned to the enhancement in the effective contact area between the positive (Al) and negative tribo-materials. Referring to Fig. 4, it can be concluded that higher output voltage can be recorded when the surfaces of both Al and PDMS were modified by an abrasive paper with higher grit size. This implies that higher grit size leads to patterning the tribo-material surface with smaller microstructures, thus increasing the contact points when the positive and negative tribo-surfaces are brought into contact as illustrated schematically in Fig. 5. As a result, more channels between Al and PDMS are developed which facilitate the electron transfer from the positive tribo-material (Al) to the negative tribo-material (PDMS), resulting in a higher triboelectric performance.

The high output voltage observed in Fig. 4d can be explained following the schematic illustration shown in Fig. 5. When the surfaces of Al and PDMS are

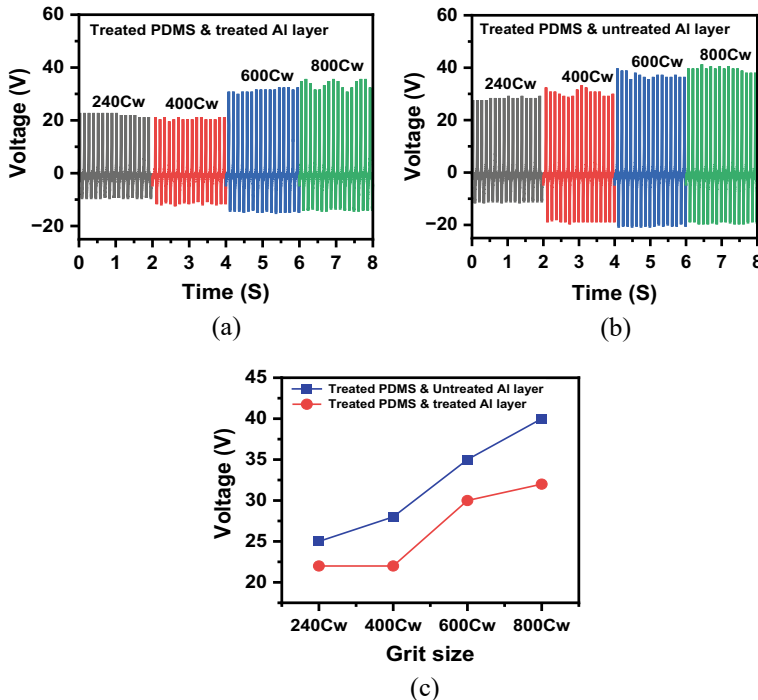


**Fig. 3** Output voltage of **a** Fully modified TEG, **b** Half-modified TEG, **c** Comparison between fully modified and half-modified TEGs

engineered to suitable microstructures, the microfeatures of the two surfaces match each other when brought into contact, resulting in nearly perfect contact area. This enhances the flow of electrons from Al to PDMS, where Al gains positive charges and PDMS gains negative charges. When the Al surface begins to move away from PDMS (releasing state) the potential difference between the two surfaces would be developed which results in the current flow through a resistor (red arrow). When the two surfaces reach an equilibrium (released state), current vanishes. By forcing the Al surface to move toward PDMS (pressing state), the current flows in the opposite direction and when the TEG reaches an equilibrium (pressed state), the current vanishes and in this case the TEG completes one cycle.

The power density is an important parameter to evaluate the performance of TEGs. It is expressed as:

$$P_d = \frac{V^2}{RA}$$

where  $P_d$  is the power density,  $V$  is the voltage drop across the resistor  $R$ , and  $A$  is the surface area of the TEG. The power density was measured by connecting various load resistors to the TEGs and the voltage drop across the resistor was recorded by

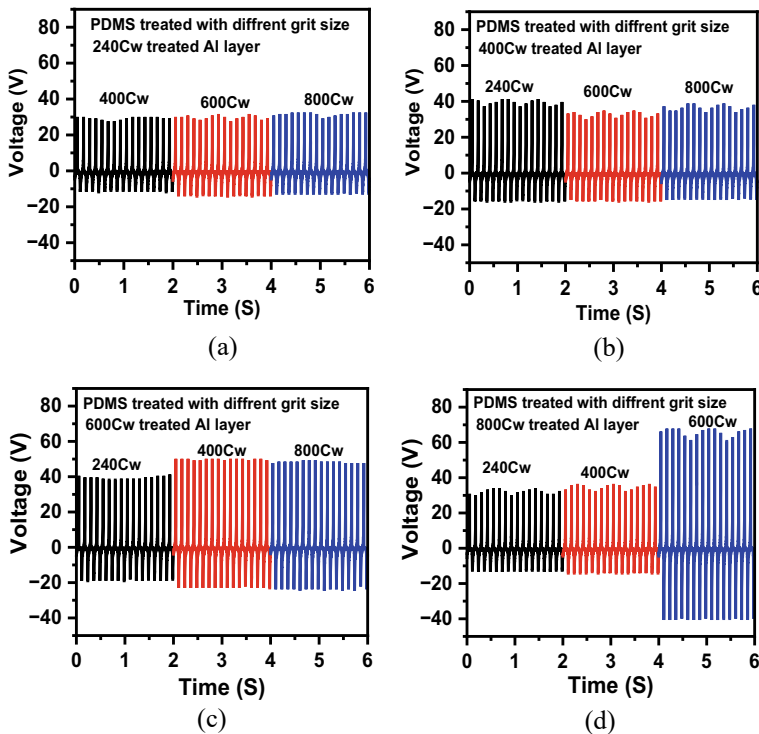


**Fig. 4** Influence of surface modification of tribo-materials on the output voltage of TEG

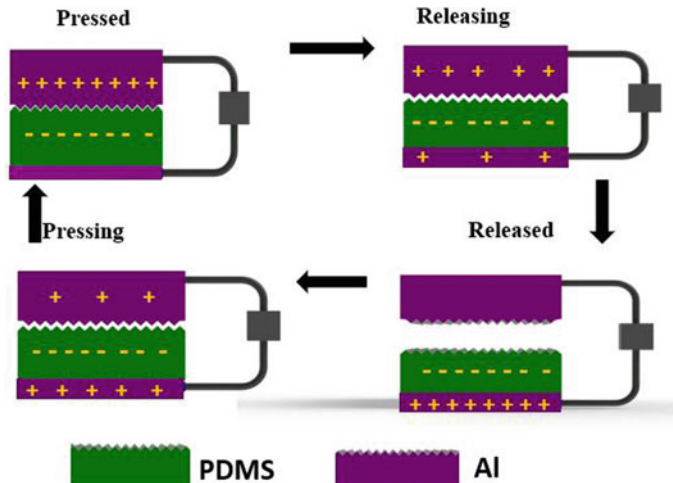


**Fig. 5** Working principle of surface-modified contact-separation mode TEG

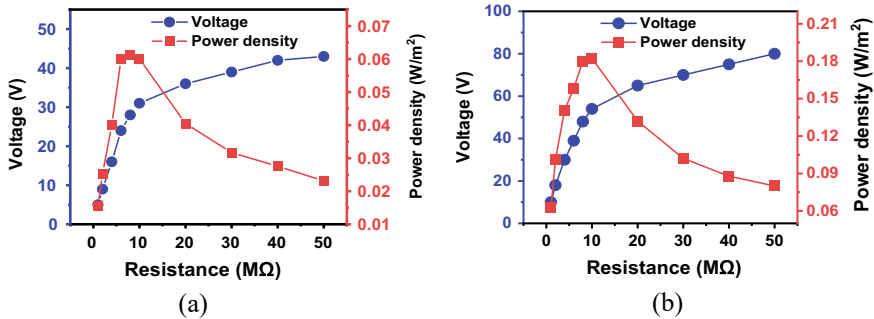


**Fig. 6** Voltage and power density at different values of load resistance, **a** Untreated Al combined with 600 CW treated PDMS, **b** 800 CW treated Al combined with 600 CW treated PDMS

a digital oscilloscope. Figure 6 shows the voltage and the power density at different values of load resistance for untreated Al layer combined with 600 CW treated PDMS (Fig. 6a) and 800 CW treated Al combined with 600 CW treated PDMS. It is observed that the fully treated TEG (Fig. 6b) showed higher performance than the half-treated TEG (Fig. 6a), where its power density was calculated to be 0.182 W/m<sup>2</sup>, whereas the power density of half-treated TEG was calculated to be 0.061 W/m<sup>2</sup>. This enhancement in the performance originates from the improved contact area between the Al and PDMS tribo-surfaces which was obtained through surface modification.

## 4 Conclusion

This work was carried out to improve the surfaces of the positive (Al) and negative (PDMS) tribo-materials using abrasive paper with different grit sizes (240 CW, 400 CW, 600 CW, and 800 CW). The triboelectric performance of a different combination of Al and PDMS tribo-materials was investigated. The results showed that the performance of the half-modified TEG, in which the Al was untreated and the PDMS was modified with grit size 200 CW, 400 CW, 600 CW, and 800 CW is higher than the fully modified TEG in which both Al and PDMS were modified with the same grit size. This was assigned to imperfect contact area between the modified surfaces. The best triboelectric performance was recorded for 800 CW modified Al combined with 600 CW modified PDMS. This can be related to the microstructured surfaces that enhance the effective contact area, where higher contact points can be obtained in this case, resulting in improved surface charge transfer from Al to PDMS.

**Acknowledgements** This work was supported by Ministry of Higher Education under Fundamental Research Grant Scheme FRGS/1/2022/TK07/UTM/02/42 and Universiti Teknologi, Malaysia under UTM Fundamental Research Grant Q.J130000.3823.22H55.

## References

1. Luo, J., Lin, Z.: Recent advances in triboelectric nanogenerator based self-charging power systems. *Energy Storage Mater.* **23**(March), 617–628 (2019). <https://doi.org/10.1016/j.ensm.2019.03.009>
2. Zhu, G., Yang, R., Wang, S., Wang, Z.L.: Flexible high-output nanogenerator based on lateral ZnO nanowire array. *Nano Lett.* **10**(8), 3151–3155 (2010). <https://doi.org/10.1021/nl101973h>
3. Wang, Z.L.: Triboelectric nanogenerators as new energy technology and self-powered sensors—Principles, problems and perspectives. *Faraday Discuss.* **176**, 447–458 (2014). <https://doi.org/10.1039/c4fd00159a>
4. Wang, Z.L., Wang, A.C.: On the origin of contact-electrification. *Mater. Today* **30**(xx), 34–51 (2019). <https://doi.org/10.1016/j.mattod.2019.05.016>
5. Mahmud, M.A.P., Lee, J.J., Kim, G.H., Lim, H.J., Choi, K.B.: Improving the surface charge density of a contact-separation-based triboelectric nanogenerator by modifying the surface morphology. *Microelectron. Eng.* **159**, 102–107 (2016). <https://doi.org/10.1016/j.mee.2016.02.066>
6. Patnam, H., Dudem, B., Graham, S.A., Yu, J.S.: High-performance and robust triboelectric nanogenerators based on optimal microstructured poly (vinyl alcohol) and poly(vinylidene fluoride) polymers for self-powered electronic applications. *Energy* **223**, 120031 (2021). <https://doi.org/10.1016/j.energy.2021.120031>
7. Lai, M., et al.: Enhancing the output charge density of TENG via building longitudinal paths of electrostatic charges in the contacting layers. *ACS Appl. Mater. Interfaces* **10**(2), 2158–2165 (2018). <https://doi.org/10.1021/acsmami.7b15238>
8. Lin, L., et al.: Triboelectric active sensor array for self-powered static and dynamic pressure detection and tactile imaging. *ACS Nano* **7**(9), 8266–8274 (2013). <https://doi.org/10.1021/nn4037514>
9. Yan, S., Lu, J., Song, W., Xiao, R.: Flexible triboelectric nanogenerator based on cost-effective thermoplastic polymeric nanofiber membranes for body-motion energy harvesting with high humidity-resistance. *Nano Energy* **48**(January), 248–255 (2018). <https://doi.org/10.1016/j.nanoen.2018.03.031>
10. Chen, H., Xu, Y., Zhang, J., Wu, W., Song, G.: Enhanced stretchable graphene-based triboelectric nanogenerator via control of surface nanostructure. *Nano Energy* **58**(2018), 304–311 (2019). <https://doi.org/10.1016/j.nanoen.2019.01.029>
11. Shi, Q., Sun, Z., Zhang, Z., Lee, C.: Triboelectric nanogenerators and hybridized systems for enabling next-generation IoT applications. *Research* **2021**, 1–30 (2021). <https://doi.org/10.34133/2021/6849171>
12. Fan, X., et al.: Flexible and wearable power sources for next-generation wearable electronics. *Batter. Supercaps* **3**(12), 1262–1274 (2020). <https://doi.org/10.1002/batt.202000115>
13. Lee, C.J., Choi, A.Y., Choi, C., Sim, H.J., Kim, S.J., Kim, Y.T.: Triboelectric generator for wearable devices fabricated using a casting method. *RSC Adv.* **6**(12), 10094–10098 (2016). <https://doi.org/10.1039/c5ra21749k>
14. Fang, Z., Chan, K.H., Lu, X., Tana, C.F., Ho, G.W.: Surface texturing and dielectric property tuning toward boosting of triboelectric nanogenerator performance. *R. Soc. Chem.* **00**(2013), 1–3 (2017). <https://doi.org/10.1039/C7TA07696G>
15. Rasel, M.S.U., Park, J.Y.: A sandpaper assisted micro-structured polydimethylsiloxane fabrication for human skin based triboelectric energy harvesting application. *Appl. Energy* **206**(April), 150–158 (2017). <https://doi.org/10.1016/j.apenergy.2017.07.109>
16. Ahmed, A.A., et al.: Low-pressure air plasma-treated polytetrafluoroethylene surface for efficient triboelectric nanogenerator. *Mater. Today Sustain.* **21**, 100330 (2023)

# Investigating the Performance of Control Strategies for Voltage and Frequency Regulation in Decentralized Power Generation System



P. G. Arul, Lenin Gopal, Filbert H. Juwono, and Vun Jack Chin

**Abstract** An imbalance between generation and load often occurs in decentralized power generation systems. This imbalance causes voltage and frequency deviations, which affect the stable operation of the system. This paper proposes control strategies for the system sources to regulate the voltage and frequency by balancing the active and reactive power. Various scenarios of power generation and load-demand conditions are considered to investigate the performance of the proposed control strategies. A simulation was conducted using PSCAD/EMTDC software to assess the feasibility of the proposed control strategies. Results indicate that the suggested control strategies are effective in maintaining system voltage and frequency under various operating conditions. The embedded decoupled current control approach in the proposed control strategies realizes fast compensation for transient disturbances.

**Keywords** Distributed power generation · Control strategies · Voltage and frequency stability

## 1 Introduction

In recent years, renewable power technologies have been gaining attention as a means to diversify energy supply and reduce dependence on conventional power generation. Among the various technologies, solar photovoltaic (PV) and wind are more appropriate for small off-grid applications due to their significant benefits in harvesting power from locally available energy resources. However, the intermittent nature of these energy sources and changes in load-demand can affect the voltage

---

P. G. Arul (✉) · L. Gopal · V. J. Chin  
Connected Intelligence Research Group, University of Southampton Malaysia (UoSM), 79100  
Iskandar Puteri, Johor, Malaysia  
e-mail: [a.p.gurusamy@soton.ac.uk](mailto:a.p.gurusamy@soton.ac.uk)

F. H. Juwono  
Department of Electrical and Electronic Engineering, Xi'an Jiaotong-Liverpool University,  
Suzhou, Jiangsu, China  
e-mail: [Filbert.Juwono@xjtlu.edu.cn](mailto:Filbert.Juwono@xjtlu.edu.cn)

and frequency stability of the system. In literature, a number of control techniques have been suggested for the parallel operation of inverters to regulate the voltage and frequency.

In order to enable parallel inverters to share power effectively, a control strategy based on the average current sharing technique has been suggested in [1, 2]. In this approach, current is measured from each inverter and then delivered to the current sharing bus, where it is used to generate a reference current. This reference current is then distributed among the inverters to ensure power sharing is carried out in an optimal and efficient manner. In addition, the output voltage of each inverter is regulated at a common voltage reference to balance the deviation in amplitude or phase angle of the output voltage due to output impedance. However, the average current sharing technique shows inaccurate load sharing and poor voltage regulation when implemented with parallel inverters of different power ratings. In [3], master-slave control approach is proposed for parallel operated inverters. A active power sharing and reactive power sharing buses are used to interconnect the parallel inverters. In this approach, the stable slave source with the highest output power automatically becomes the master source to drive the power buses and provide reference for other inverters. A good load sharing and high system reliability are achieved. However, this approach has a disadvantage of synchronization error [4].

The conventional active power–frequency (P–f) and reactive power–voltage (Q–V) droop control technique for the parallel operation of inverters is discussed in [5–7]. In this technique, the active and reactive powers are drooped to obtain the frequency and amplitude of the reference voltage. The droop control technique is an effective method for sharing the active and reactive powers between parallel inverters [8–10].

In this paper, conventional droop control is used to determine the amplitude and frequency of reference voltage for the energy storage inverter. For PV and wind inverters, the active power reference is derived from the maximum power point (MPP) controller [11]. Decoupled current control approach is used for the effective control of active and reactive powers.

## 2 Control Description

### 2.1 Frequency and Voltage Droop Control

The power supplied by the energy storage can be calculated as:

$$P_B = P_L - P_{(PV+W)} \quad (1)$$

$$Q_B = Q_L - Q_{(PV+W)}. \quad (2)$$

Based on the control relationship, the frequency droop is introduced by the active power derived, while the voltage droop is introduced by the reactive power derived as shown in Fig. 1.

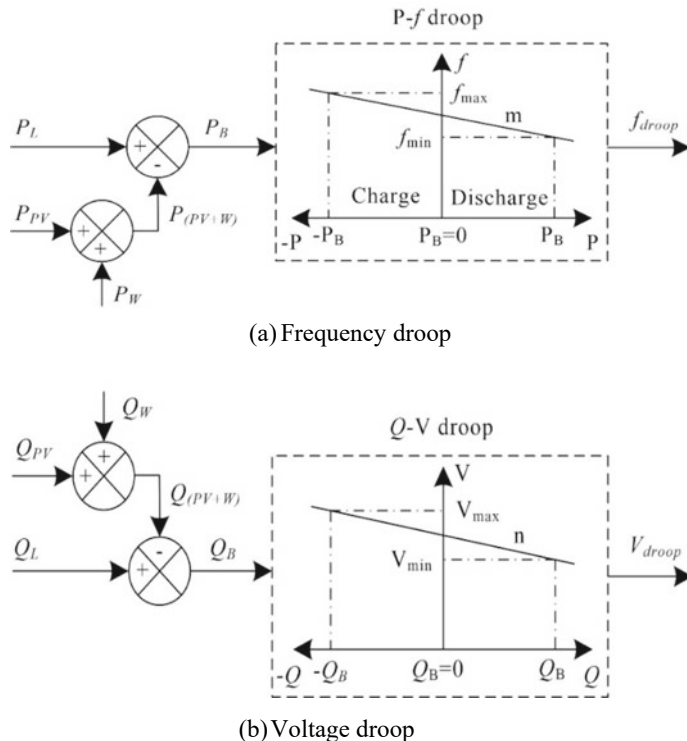


**Fig. 1** Frequency and voltage droop control

The system stability can be achieved by regulating the droop control coefficients  $m$  and  $n$  to ensure that they are within the acceptable limits. This will help in controlling the system within the desired range and maintaining its stability.

## 2.2 Power Control Loop

In the proposed active and reactive power control strategy, the active power is controlled at the MPP reference values, and the reactive power is controlled at the set reference value. The MPP reference values are obtained by using maximum power point tracking based on an incremental conductance algorithm. The error value obtained by comparing the MPP power,  $P_{MPP}$ , and the measured value of active power at the VSI output is controlled to produce the d-axis reference current as shown in Fig. 2 based on the following control equation.

**Fig. 2** Active power control loop

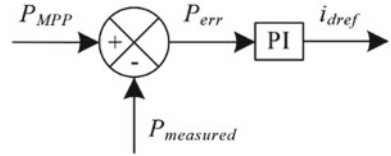
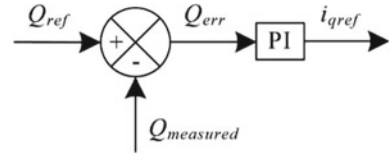


**Fig. 3** Reactive power control loop



$$i_{dref} = \left( k_{pP} + \frac{k_{iP}}{s} \right) (P_{MPP} - P_{\text{measured}}) \quad (3)$$

Similarly, the error value obtained by comparing the set reference value of the reactive power and the measured value of the reactive power at the load side is controlled to produce the q-axis reference current as shown in Fig. 3 based on the following control equation.

$$i_{qref} = \left( k_{pQ} + \frac{k_{iQ}}{s} \right) (Q_{\text{ref}} - Q_{\text{measured}}) \quad (4)$$

### 2.3 Current Control Loop

The current control loop for the proposed control strategies is shown in Fig. 4.

The current control loop is executed in the  $d$ - $q$  reference frame using control laws outlined in Eqs. 5 and 6. The  $d$ - $q$  controlled voltages attained from the current control loop are then transformed into abc controlled voltages that are essential for the PWM generator to generate the desired control signal.

$$V_{d\text{con}} = \left( k_{pd} + \frac{k_{id}}{s} \right) (i_{d\text{ref}} - i_d) - \omega L_f i_q + V_d \quad (5)$$

$$V_{q\text{con}} = \left( k_{pq} + \frac{k_{iq}}{s} \right) (i_{q\text{ref}} - i_q) + \omega L_f i_d + V_q \quad (6)$$

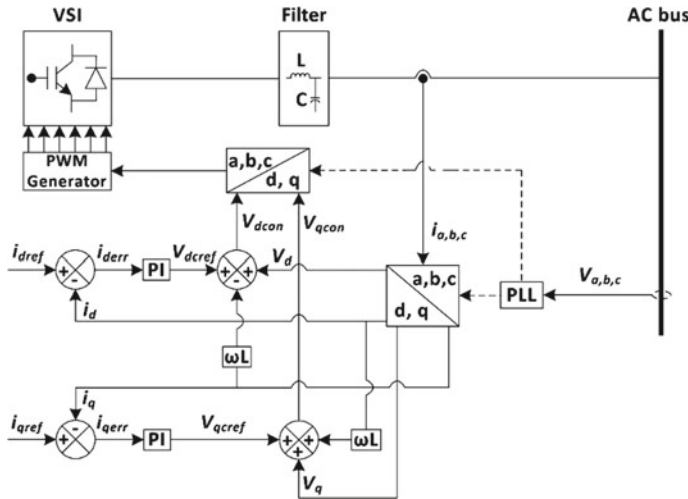


**Fig. 4** Current control loop

### 3 Results and Discussion

The performance of the proposed control strategies for the PV, wind turbine, and battery energy storage is investigated using PSCAD/EMTDC software. Various scenarios of power generation and load-demand conditions are considered to evaluate the response of the proposed control strategies. For all scenarios, the gain values of controllers are determined by trial and error and kept constant. The power electronic converters are operated at switching frequency of 3 kHz and a sampling time of 0.3 ms, which allow the controllers to detect and respond quickly to variations in power generation and load-demand.

#### 3.1 No Disturbance in Generation and Load

In this case, a constant irradiance of  $1000 \text{ W/m}^2$  for the PV panel and a constant wind speed of  $12 \text{ m/s}$  for the wind turbine are considered. The system is operated to supply a constant load of  $1 \text{ kW}$ . Figure 5 shows the active and reactive powers of the system sources and the load. The load active and reactive powers are shown in Fig. 5a. Initially, zero power injection from the PV and wind sources is considered. As shown in Fig. 5b, the battery energy storage is discharged to supply  $1 \text{ kW}$  to the load under the initial operating condition. At  $t = 2 \text{ s}$ , the battery power drops by  $0.5 \text{ kW}$  with an increase in the PV output power as shown in Fig. 5c. Because the power generated by the PV is less than the load-demand, the battery energy storage supplies the balance power to satisfy the total load-demand by adjusting the frequency droop.

During discharge, the frequency at the P-*f* droop is adjusted below 50 Hz. At  $t = 5$  s, the battery power further drops by 0.8 kW with an increase in the wind output power as shown in Fig. 5d. Because the total output power generated from the PV and wind turbine sources is greater than the load-demand, the battery energy storage starts to absorb the excess power. During charge, the frequency at the P-*f* droop is adjusted above 50 Hz according to the droop control settings. However, the reactive power of the system sources is maintained at zero as shown in Fig. 5.

Figure 6 shows the bus voltage under no disturbance in generation and load condition. It is clear from Fig. 6 that the bus voltage is maintained at the rated voltage of 0.4 kV by the voltage controller.

Figure 7 shows the frequency of the bus voltage. When the PV and wind sources are connected to the common AC bus, the frequency deviates slightly and returns back to the steady state.

### 3.2 Disturbance in Generation and Load

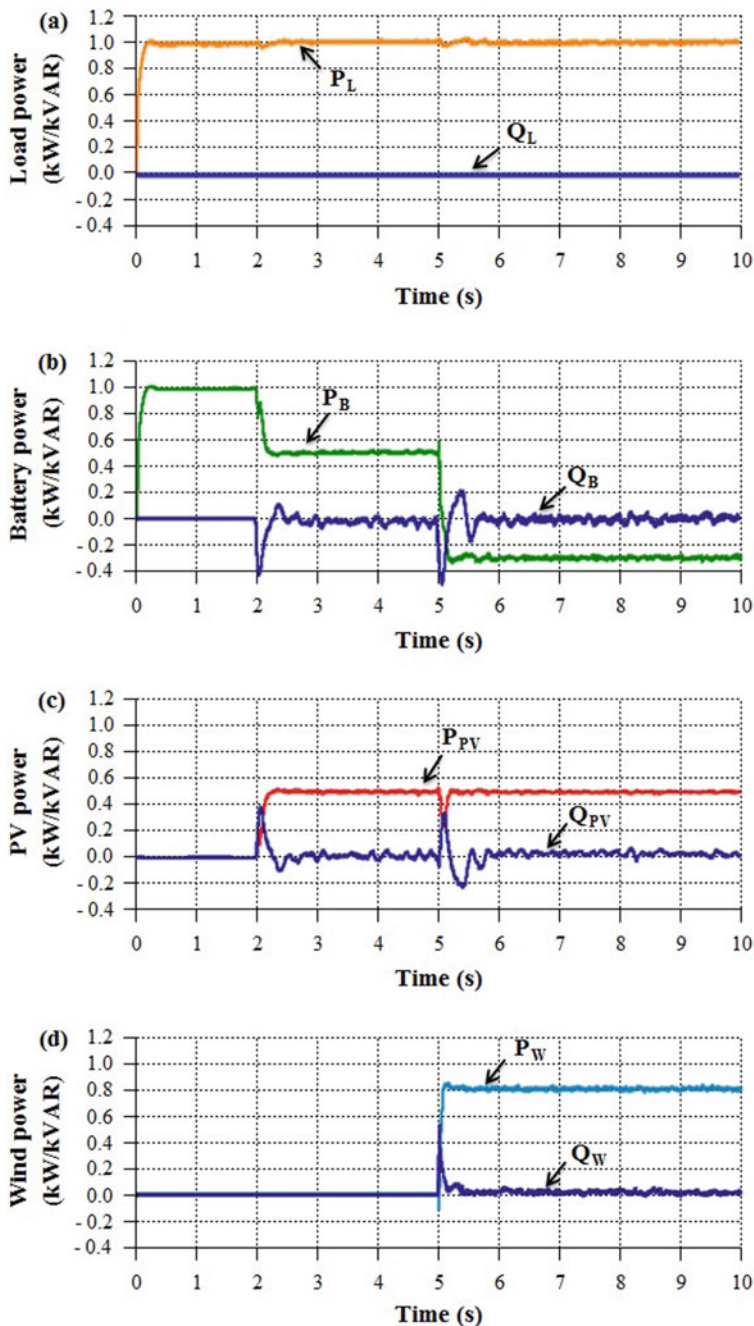
In this case, the performance of the proposed control strategies is investigated by considering the following scenarios.

#### Constant Power Generation and Variable Load

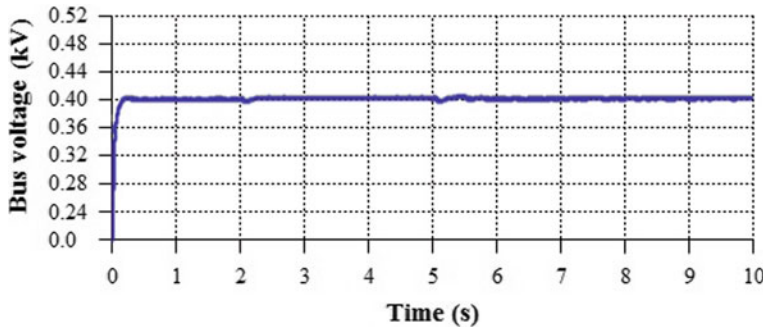
Figure 8 shows the active and reactive powers of the system sources under constant power generation and variable load condition. In this scenario, constant irradiance of 1000 W/m<sup>2</sup> for the PV panel and constant wind speed of 12 m/s for the wind turbine are considered. The load is considered to be 1 kW for  $0 < t < 7$  s and then varied from 1 kW to 0.5 kW at  $t = 7$  s as shown in Fig. 8a. Initially, the battery is discharged to supply the load load-demand. At  $t = 2$  s, the PV injects 0.5 kW as shown in Fig. 8c. The wind turbine injects 0.8 kW at  $t = 5$  s as shown in Fig. 8d. The battery power supplies the shortage of power as well as absorbs the excess power to balance the power variations as shown in Fig. 8b.

Figure 9 shows the bus voltage under constant power generation and variable load condition. It is clear from Fig. 9 that the bus voltage is maintained at the rated voltage of 0.4 kV.

Figure 10 shows the frequency of the bus voltage. During the presence of RESs and changes in load-demand, the frequency deviates slightly and returns back to the steady state quickly.



**Fig. 5** Active and reactive powers under no disturbance in generation and load condition: **a** load power, **b** battery power, **c** PV power, and **d** wind power



**Fig. 6** Bus voltage under no disturbance in generation and load condition

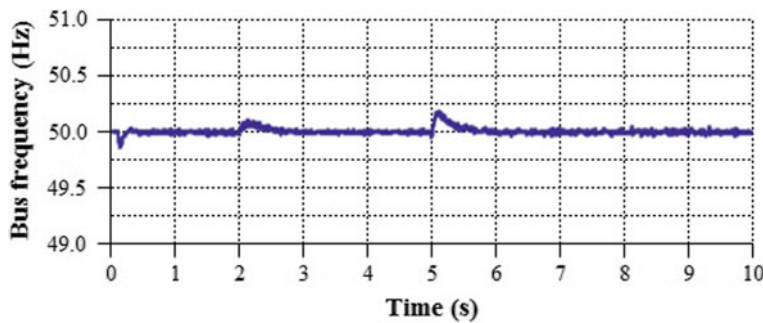


**Fig. 7** Bus frequency under no disturbance in generation and load condition

### Variable Power Generation and Constant Load

This scenario considers variable irradiance for the PV panel and wind speed for the wind turbine. The solar irradiance is varied from  $1000 \text{ W/m}^2$  to  $800 \text{ W/m}^2$  for  $7 < t < 9 \text{ s}$ , and the wind speed is varied from 12 m/s to 9 m/s for  $12 < t < 15 \text{ s}$ . The load is kept constant at 1 kW. Figure 11c, d show the power generated from the PV and wind turbine sources for the varying solar irradiance and wind speed. The battery energy storage reacts to the variations in output power generated from the PV and wind turbine sources to balance the load-demand as shown in Fig. 11b.

The voltage at the common AC bus is shown in Fig. 12. It is observed from Fig. 12 that the system sources adjust their reactive power and maintain the common AC bus voltage of 0.4 kV.

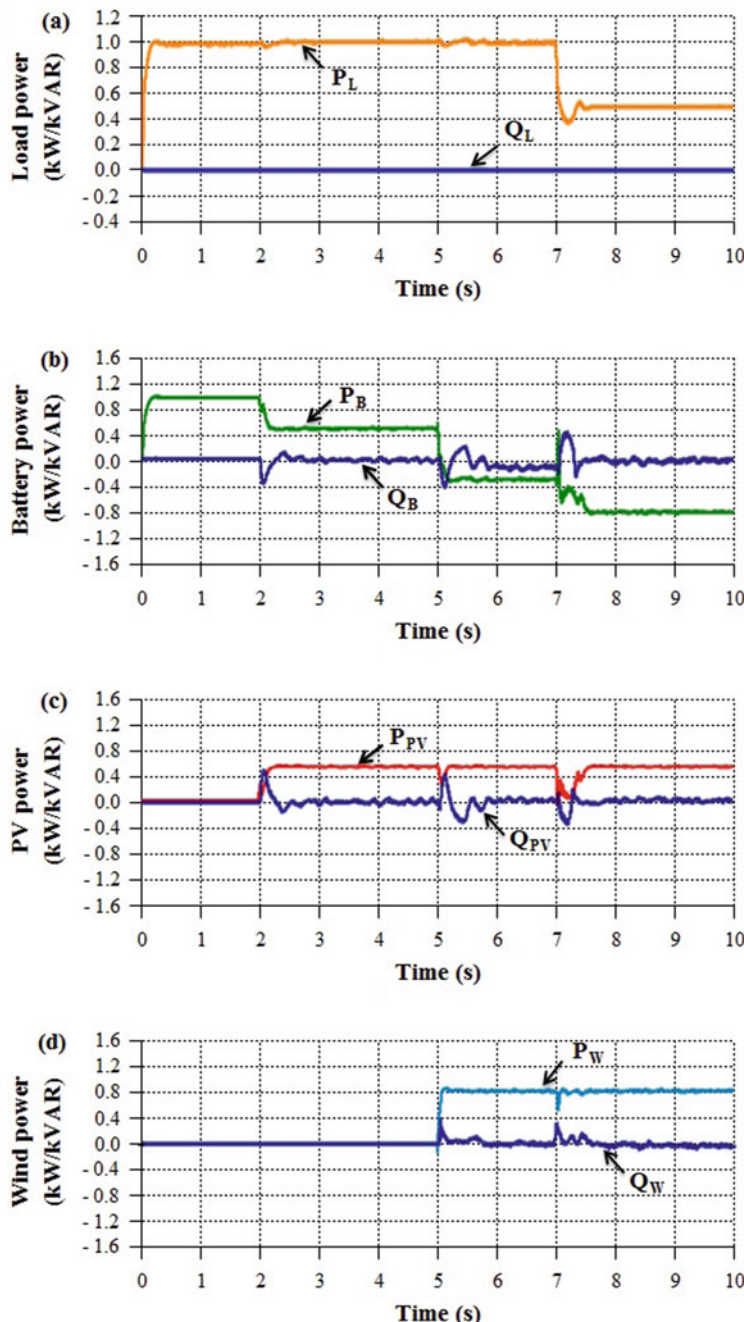


**Fig. 8** Active and reactive powers under constant generation and variable load condition: **a** load power, **b** battery power, **c** PV power, and **d** wind power

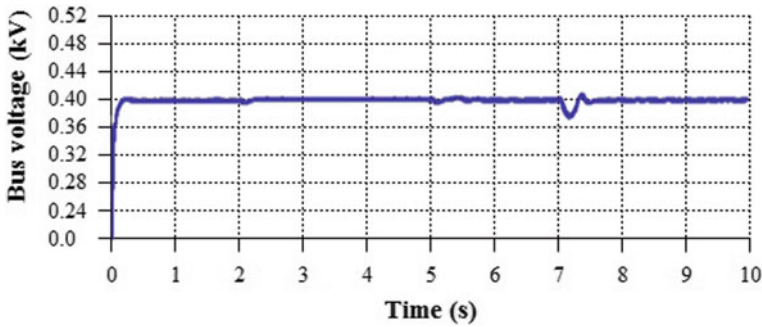


**Fig. 9** Bus voltage under constant generation and variable load condition

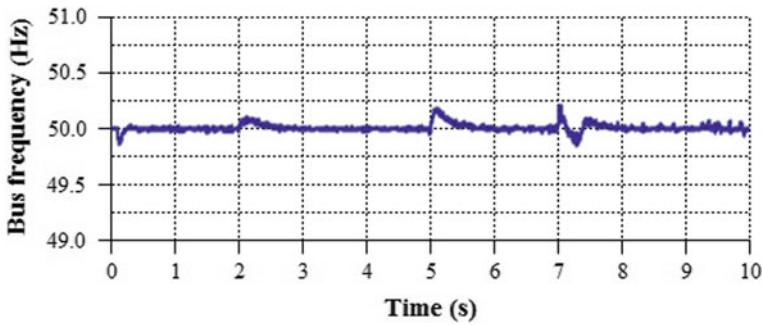
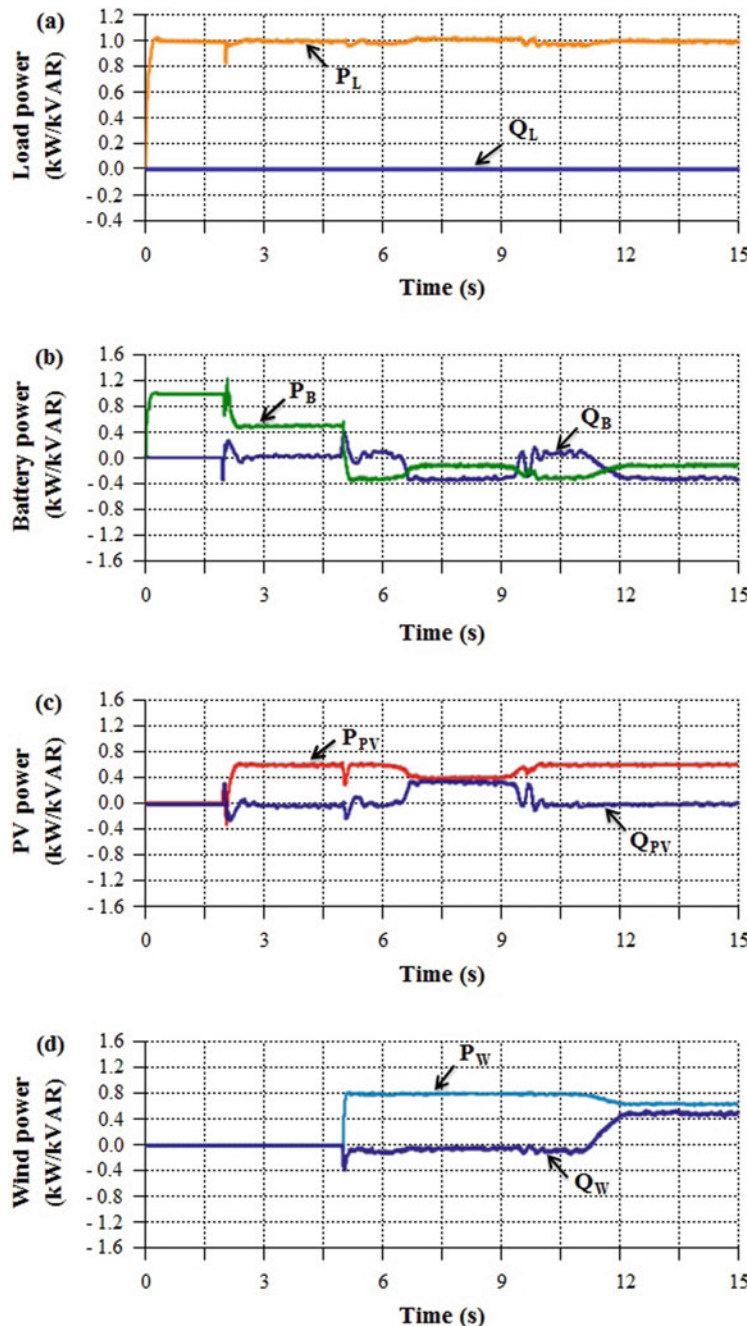


**Fig. 10** Bus frequency under constant generation and variable load condition

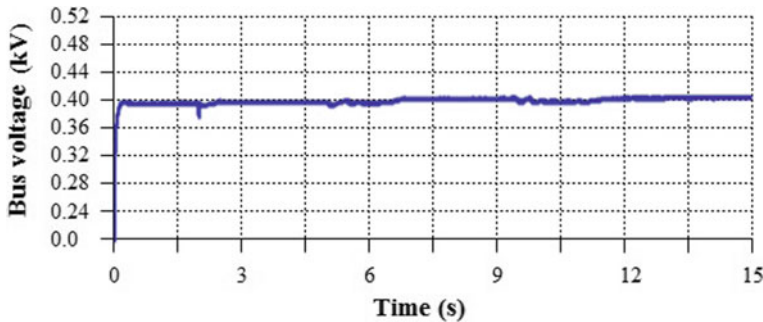
Figure 13 shows the frequency of the bus voltage. Result shows the frequency is regulated within the acceptable limits under the variable generation and constant load condition.

#### Variable Power Generation and Variable Load

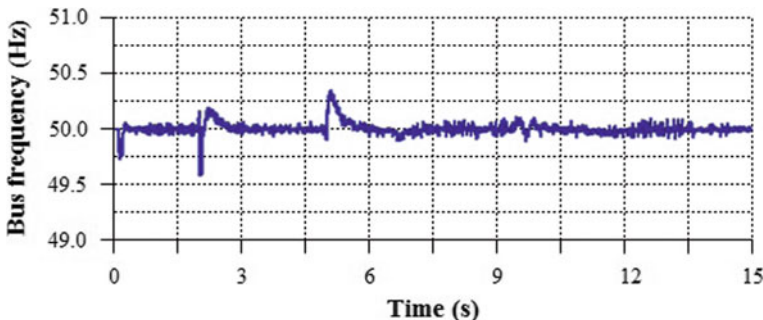
In this scenario, the output power generated from the PV and wind turbine sources is varied by varying the solar irradiance for PV panel and the wind speed for wind turbine. The solar irradiance is varied from  $1000 \text{ W/m}^2$  to  $800 \text{ W/m}^2$  for  $7 < t < 9 \text{ s}$  and the wind speed is varied from  $12 \text{ m/s}$  to  $9 \text{ m/s}$  for  $12 < t < 15 \text{ s}$ . Also, the load is varied from  $1 \text{ kW}$  to  $0.5 \text{ kW}$  at  $t = 8 \text{ s}$ . The output power response of the system sources to the variable power generation and variable load is shown in Fig. 14.



**Fig. 11** Active and reactive powers under variable generation and constant load condition: **a** load power, **b** battery power, **c** PV power, and **d** wind power



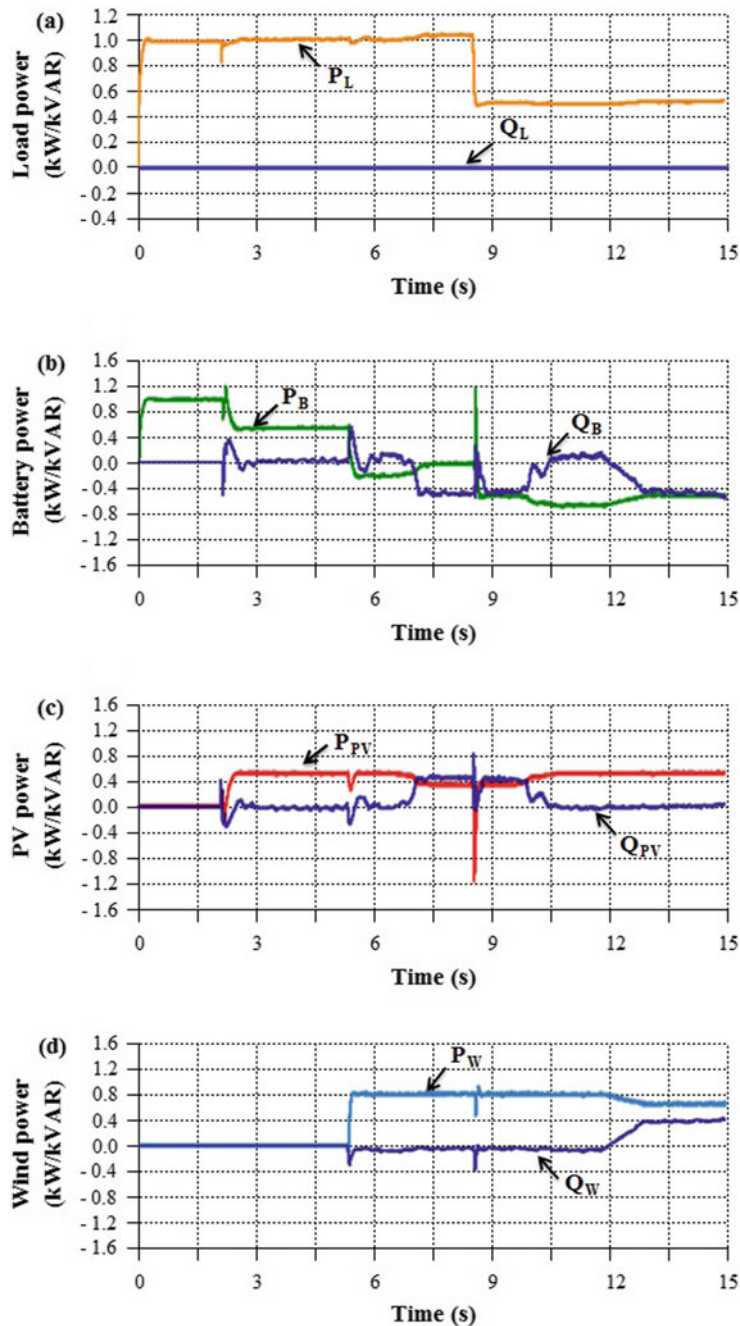
**Fig. 12** Bus voltage under variable generation and constant load condition



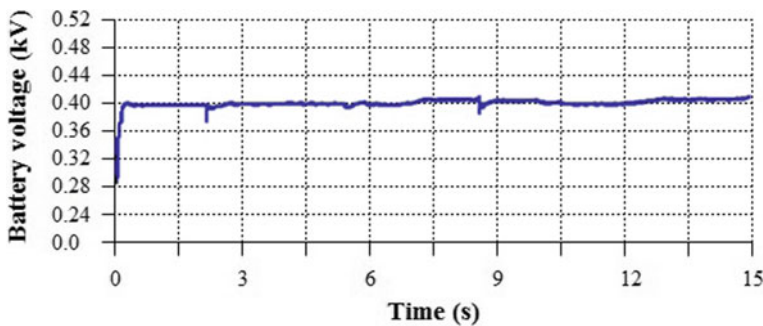
**Fig. 13** Bus frequency under variable generation and constant load condition

Figure 14c shows that the PV power drops at  $t = 7$  s due to the irradiance variation. Figure 14d shows that the wind power drops at  $t = 12$  s due to the wind speed variation. According to the drop in PV and wind turbine output powers, the battery energy storage supplies the deficit power to balance the load by adjusting the droop. It can be seen from Fig. 14 that the proposed control strategies are capable to balance the power under variable generation and variable load condition.

Due to the decrease in irradiance and wind speed, the voltage at the output terminal of the PV and wind turbine decreases. In order to maintain the output terminal voltage at the bus voltage of 0.4 kV, the PV and wind turbine inverters inject the required reactive power as shown in Fig. 14c, d. The regulation of active and reactive power maintains the bus voltage and frequency to be stable as shown in Figs. 15 and 16.



**Fig. 14** Active and reactive powers of the system sources under variable generation and variable load condition: **a** load power, **b** battery power, **c** PV power, and **d** wind power



**Fig. 15** Bus voltage under variable generation and variable load condition

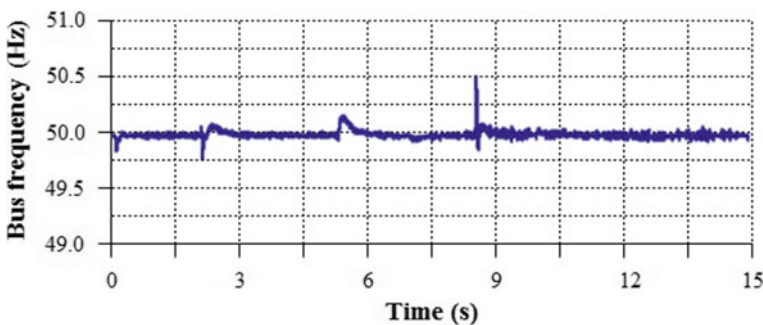


**Fig. 16** Bus frequency under variable generation and variable load condition

#### 4 Conclusion

In this paper, the performance of the proposed control strategies to regulate the bus voltage, bus frequency, and load sharing is investigated under various scenarios of power generation and load-demand conditions. The voltage and frequency control strategy with droop concept provides a stable bus voltage and frequency response along with the load sharing. The active and reactive power control strategy with maximum power point tracking operates the PV and wind turbine sources at the MPP and injects maximum available power from the sources. The proposed control strategies with decoupled current control provide independent control of active and reactive powers as well as fast compensation for transient disturbances.

Although the system can handle variations, they cause an increased overshoot in system responses. Additionally, variations in generation and load-demand can cause oscillation in the steady response of system parameters. Decreasing the overshoot and amplitude of oscillations results in an increased stability margin. This can be achieved by enhancement in the controller design.

## References

1. Qinglin, Z., Zhongying, C., Weiyang, W.: Improved control for parallel inverter with current-sharing control scheme. In: 2006 CES/IEEE 5th International Power Electronics and Motion Control Conference, Shanghai, China, pp. 1–5 (2006)
2. Roslan, A.M., Ahmed, K.H., Finney, S.J., Williams, B.W.: Improved instantaneous average current-sharing control scheme for parallel-connected inverter considering line impedance impact in microgrid networks. *IEEE Trans. Power Electron.* **26**(3), 702–716 (2011)
3. Li, D., Man Ho, C.N.: A delay-tolerable master–slave current-sharing control scheme for parallel-operated interfacing inverters with low-bandwidth communication. *IEEE Trans. Ind. Appl.* **56**(2), 1575–1586 (2020)
4. Chunjiang, Z., Guitao, C., Zhongnan, G., Weiyang, W.: An alternating-master-slave parallel control research for single phase paralleled inverters based on CAN bus. In: 2006 CES/IEEE 5th International Power Electronics and Motion Control Conference, Shanghai, China, pp. 1–5 (2006)
5. Meng, X., Liu, J., Liu, Z.: A generalized droop control for grid-supporting inverter based on comparison between traditional droop control and virtual synchronous generator control. *IEEE Trans. Power Electron.* **34**(6), 5416–5438 (2019)
6. Ling, Y., Li, Y., Xiang, J.: Load support by droop-controlled distributed generations. *IEEE Trans. Industr. Electron.* **68**(9), 8345–8355 (2021)
7. De Brabandere, K., Bolsens, B., Van den Keybus, J., Woyte, A., Driesen, J., Belmans, R.: A voltage and frequency droop control method for parallel inverters. *IEEE Trans. Power Electron.* **22**(4), 1107–1115 (2007)
8. Vasquez, J.C., Guerrero, J.M., Savaghebi, M., Eloy-Garcia, J., Teodorescu, R.: Modeling, analysis, and design of stationary-reference-frame droop-controlled parallel three-phase voltage source inverters. *IEEE Trans. Industr. Electron.* **60**(4), 1271–1280 (2013)
9. Zhang, W., Zheng, Z., Liu, H.: Droop control method to achieve maximum power output of photovoltaic for parallel inverter system. *CSEE J. Power Energy Syst.* **8**(6), 1636–1645 (2022)
10. Liu, B., Wu, T., Liu, Z., Liu, J.: A small-AC-signal injection-based decentralized secondary frequency control for droop-controlled islanded microgrids. *IEEE Trans. Power Electron.* **35**(11), 11634–11651 (2020)
11. Arul, P.G., Ramachandaramurthy, V.K.: Mitigating techniques for the operational challenges of a standalone hybrid system integrating renewable energy sources. *Sustain. Energy Technol. Assess.* **22**, 18–24 (2017)

# Exploring the Feasibility of Recycled Carbon Fiber for Damage Sensing in Composite Materials



Ting Yang Ling, Fan Zhang, and Khong Wui Gan

**Abstract** Small subcritical damage in composite materials can serve as warning signs for potential catastrophic failures, making their detection crucial. However, identifying these signs poses significant challenges due to the complex nature of composite structures. Meanwhile, recycled carbon fiber, which possesses inherent electrical conductivity, can be exploited as both a structural and sensing material in composite structures. By integrating recycled carbon fiber into composite materials, it becomes possible to monitor structural health and detect subtle damage, such as delamination, fiber breakage, or matrix cracking in real-time. This paper explores the potential of recycled carbon fiber as a dual-purpose material as both structural and damage sensing material, highlighting the opportunities it presents for enhancing safety and performance in various industries.

**Keywords** Recycled carbon fiber · Damage sensor · Smart composites

## 1 Introduction

Composite materials are widely utilized in various industries due to their exceptional mechanical properties and lightweight nature. However, one significant challenge associated with composites is the detection and monitoring of small non-critical damage that can lead to catastrophic failures if left undetected. Detecting these warning signs poses a considerable challenge due to the complex nature of composite structures. Traditional testing methods, such as tensile tests [1], bending tests [2], compression tests [3], and shear tests [4] provide fundamental information

---

T. Y. Ling

School of Electronics and Computer Science, University of Southampton, Southampton SO17 1BJ, UK

F. Zhang (✉) · K. W. Gan

Smart Manufacturing and Systems Research Group, University of Southampton Malaysia,  
Iskandar Puteri, Johor 79100, Malaysia

e-mail: [fz1y22@soton.ac.uk](mailto:fz1y22@soton.ac.uk)

about the mechanical properties of materials but may not be sufficient to identify subtle damage.

In recent years, significant advancements have been made in the field of strain sensing materials, with researchers exploring various approaches to develop sensors capable of detecting both large deformations and subtle movements. For instance, the use of conductive polyester fabric (CPF) combined with atomic layer deposition (ALD) has been shown to produce textile strain sensors with high stretchability and long-term stability [5]. These sensors have demonstrated the ability to detect joint movements and facial expressions, offering valuable applications in fields such as healthcare and human-computer interaction.

Another notable study by Ma et al. [6] focused on the development of a sensor that exhibits a fast response time of 0.4 s and a sensitivity range of 0.04–0.10 kPa<sup>-1</sup>. This sensor was created by combining PANI/Ag particle with cotton, enabling the monitoring of human movements. Additionally, researchers have explored the use of carbon nanomaterial inks [7], conductive polymers [8], and films based on graphene or reduced graphene oxide (rGO) [9], which have gained considerable attention in the field of strain sensing materials.

Interestingly, while there has been significant exploration of various materials for strain sensing applications, the potential of recycled carbon fiber has received relatively less attention. Recycled carbon fiber offers several advantages, including low density, high tensile strength up to 90% of its original state, cost-effectiveness, and favorable conductive properties. Notably, it exhibits a sheet resistance of 0.048 Ω/sq and a contact resistance of 0.293 Ω [10, 11]. Despite these promising properties, the utilization of recycled carbon fiber as a strain sensing material remains relatively underexplored.

Our work focuses on the utilization of recycled carbon fiber as a dual-purpose material for both structural reinforcement and damage sensing. Recycled carbon fiber is a waste material generated from various industries, including aerospace and automotive, yet it possesses inherent conductivity. This unique property opens opportunities to exploit recycled carbon fiber as a structural and sensing material within composite structures.

## 2 Materials and Methods

To investigate the feasibility of utilizing recycled carbon fiber as a damage sensor, composite samples were fabricated. These samples consisted of a non-woven recycled carbon fiber layer sandwiched between eight layers of commercial plain weave woven glass fibers (four layers on top and four layers on bottom), serving as electrical insulation and main structural layer. The vacuum-assisted resin infusion technique was employed to manufacture the composite samples.

## 2.1 Sample Preparation

Epoxy laminating resin (EpoxAmite 100) and epoxy curative hardener (103-Slow) were used as the matrix of the composites. The recommended ratio of resin to hardener was carefully followed during the fabrication process.

The composite lay-up was enclosed in a vacuum bagging film, and a vacuum pump was activated to facilitate resin infusion (Fig. 1a). After the infusion phase, the samples were left undisturbed for 24 h to allow for complete resin curing. After the composite panel is cured, additional glass fiber plates were bonded to the top and bottom surfaces at the ends of the samples with adhesive (ARALDITE® 2014-2) served as the tab materials for gripping in the tensile test. The plate was then cut into individual specimens using a wet diamond saw cutter. A 3.2 mm diameter solid carbide dagger drill was used to make a hole at the center of the gauge area of each specimen.

Table 1 provides an overview of the information pertaining to the glass fiber and recycled carbon fiber used in the study. Following simple approximation using weight and density of the constituent materials, the composite was found to have glass fiber 48.6%vol and recycled carbon fiber 2.3%vol.

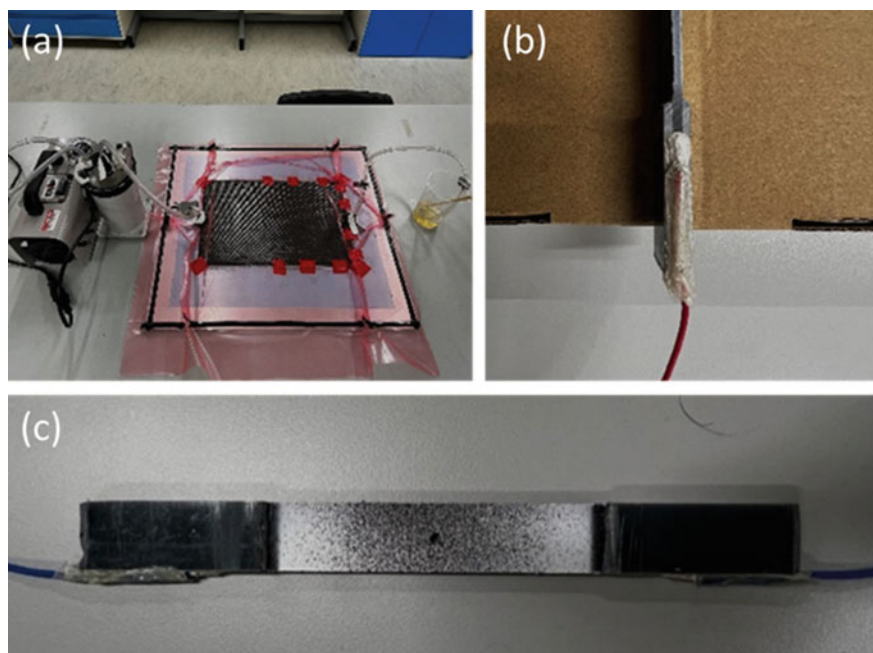


**Fig. 1** **a** Composite plate production using vacuum infusion technique, **b** Attachment of electrodes with silver conductive paste, **c** Completed test sample with speckled paint sprayed on for digital image correlation (DIC) analysis

**Table 1** Materials used for composite

Materials	GSM	Manufacturer
Non-woven recycled carbon fiber	89	ELG Carbon Fiber
Plain weave woven glass fiber	270	JUSHI

This work aims to investigate the correlation between the electrical resistance variation in the recycled carbon fiber sensing layer and the state of damage around the hole. To ensure proper electrical connections, silver conductive paste (MCN-DJ002) was employed as a reliable binder for attaching wires to both ends of the specimens as shown in Fig. 1c.

The pictures shown in Fig. 1 show the overall manufacturing process of the samples. Figure 1c shows the specimen after a spray-painting process using an air brush where black speckles are added to a white base to create a random speckle pattern for DIC analysis.

## 2.2 Mechanical Characterization

Mechanical characterization of the composite samples was conducted to assess their structural performance. The testing was carried out using a 50 kN SHIMADZU universal testing machine, equipped with a stereo digital image correlation (DIC) setup as shown in Fig. 2.

The SHIMADZU Universal Testing Machine allowed for precise control of the testing parameters, such as load, displacement, and strain rate, ensuring accurate and repeatable measurements. The DIC system provided full-field analysis of the surface deformation and strain distribution during the tests, offering valuable insights into the mechanical behavior of the composite samples. This combined approach enabled a comprehensive understanding of the mechanical properties and performance of the composite materials under different loading conditions.

## 2.3 Electrical Characterization

Resistance measurement was done with a Keithley 2600 digital multimeter. To demonstrate the electrical conductivity of the recycled carbon fiber, resistance measurement was first done on a pure recycled carbon fiber/epoxy plate to determine if the resistance is isotropic in both the weft and warp direction of the recycled carbon fiber non-woven. This was done by lasering off the surface epoxy of the plate to expose the recycled carbon fibers at multiple measurement points in the form of grid points, as shown in Fig. 3. The measurement points were filled with silver paste to facilitate resistance measurement.

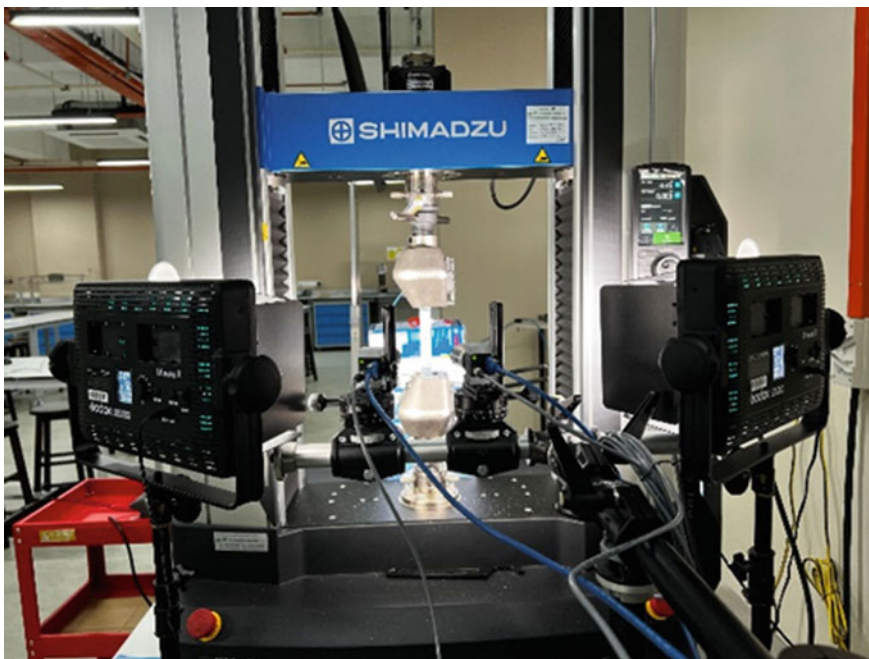


**Fig. 2** Experimental setup for tensile test

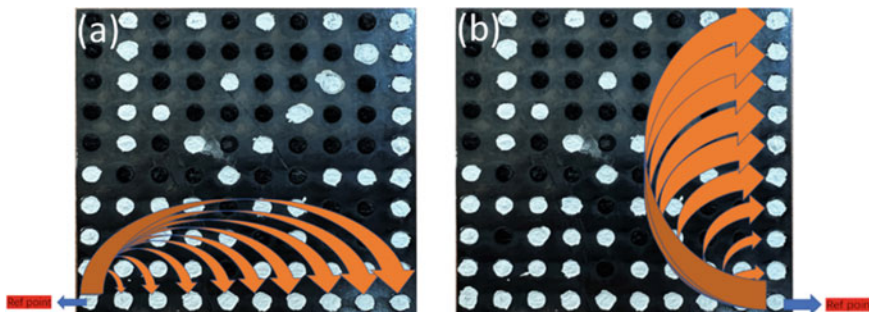


**Fig. 3** Resistance measurement in the (a)horizontal and (b) vertical directions to determine the degree of isotropy in the material. Blue arrow denotes the reference point

Similar resistance measurements were taken for the holed specimens loaded in tension at 1 mm/min. The resistance value is recorded automatically every 25 ms until material failure occurs. The results of the measurements are shown in Sect. 3.

### 3 Results and Discussion

The resistance of the samples exhibits a relatively low level of anisotropy as shown in Fig. 4. This is expected as the recycled carbon fiber non-woven was randomly orientated. Despite this, all the samples manufactured for this study are manufactured in the warp direction for consistency.

The samples fabricated from three different parts of the vacuum infusion process were tested with the SHIDMAZU Universal Testing Machine under tensile loading. The samples, labeled S1 to S3 were taken from the area close to the resin inlet (S1),

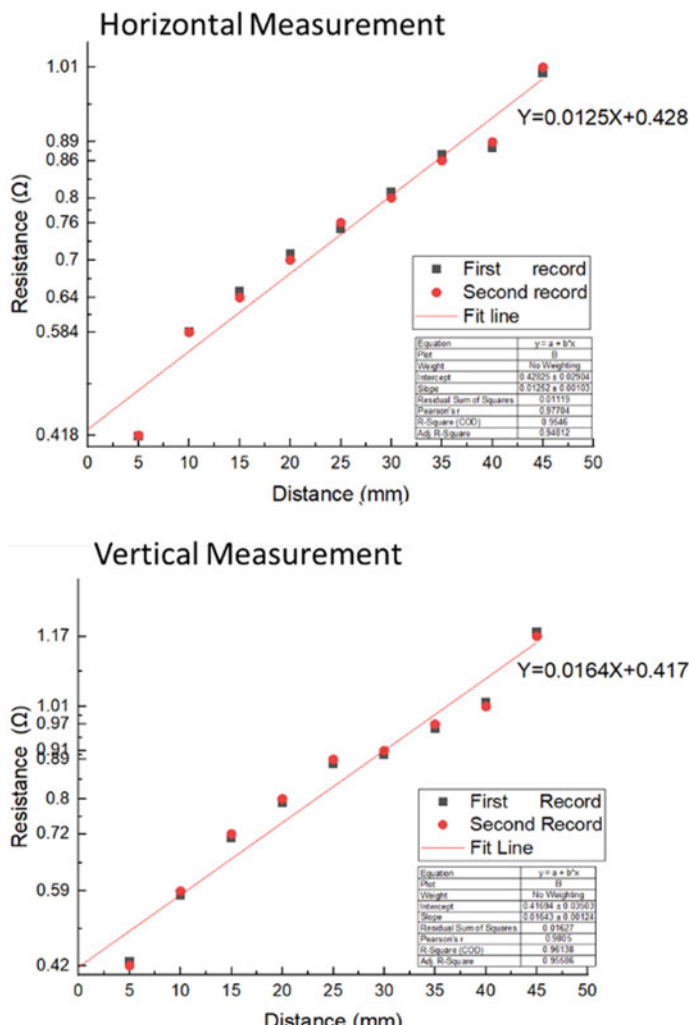


**Fig. 4** Resistance value across sample when measured horizontally (top) and vertically (bottom)

the middle of the plate (S2), and the resin outlet (S3). The result of the test was shown in Fig. 5. All three samples tested experienced slight piezo resistivity at lower load. The material then experiences an exponential change in resistance due to the damage around the hole within the recycled carbon fiber layer before catastrophic failure occurs across the entire sample.

The fluctuations experienced by sample S2 was due to the instability in electrode connection, but the data was included in this paper to show the potential problems faced by such setup. In all the three samples, the resistance gradient experienced two changes, the first peak is likely due to the irreversible damage initiation to the recycled carbon fiber (green arrow in Fig. 5). The damaged fiber relieved some stress around the hole of the composite, followed by accumulation of damage leading to catastrophic failure as the sample is pulled further by the Universal Testing Machine.

Upon failure, the samples exhibit signs of delamination (shown in Fig. 6). All the samples exhibit increase in the rate of change of resistance at approximately 9 kN. This characteristic could potentially be exploited as a method of early warning before material failure occurs.

## 4 Conclusion

In conclusion, this study investigated the potential of utilizing recycled carbon fiber as a multipurpose material enabling damage sensing capabilities in composite materials. The results obtained from testing samples fabricated using the vacuum infusion process provided valuable insights into the behavior of the material under tensile loading. The observed slight piezo resistivity at lower loads and the subsequent exponential change in resistance associated with damage within the recycled carbon fiber layer demonstrated the material's ability to sense and respond to structural changes.

By harnessing the inherent conductivity of recycled carbon fiber, composite structures can be endowed with the ability to detect and monitor subtle damage, such as delamination, fiber breakage, or matrix cracking in real-time. This innovative approach has the potential to revolutionize the field of structural health monitoring and contribute to improved safety and performance in composite applications.

Moving forward, further research and development efforts are warranted to optimize the integration of recycled carbon fiber into composite materials, exploring different fabrication techniques and sensor designs. By advancing our understanding of the behavior and capabilities of recycled carbon fiber as a sensing material, we can unlock new possibilities for enhancing the reliability, durability, and overall performance of composite structures.

**Fig. 5** Relationship between tensile force and resistance of samples. Green arrow denotes early warning point and red arrow denotes sample breaking point

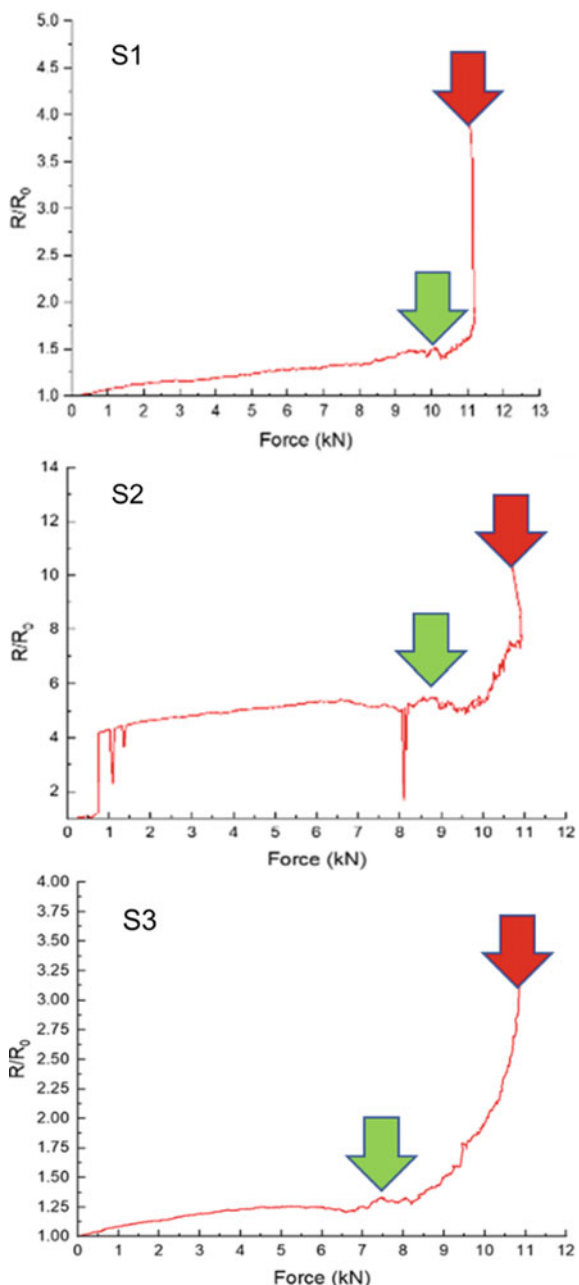




**Fig. 6** Delamination of material upon failure

**Acknowledgements** Fan Zhang would like to acknowledge the University of Southampton, Malaysia for his Ph.D. scholarship.

## References

1. Lv, S., Ma, Y., Qiu, C., Sun, T., Liu, J., Zhou, Q.: Effect of graphene oxide nanosheets of microstructure and mechanical properties of cement composites. *Constr. Build. Mater.* **49**, 121–127 (2013). <https://doi.org/10.1016/j.conbuildmat.2013.08.022>
2. Fukuda, H.: A New Bending Test Method of Advanced Composites
3. Lomov, S.V., et al.: Carbon composites based on multiaxial multiply stitched preforms. Part 3: biaxial tension, picture frame and compression tests of the preforms. *Compos. Part A Appl. Sci. Manuf.* **36**(9), 1188–1206 (2005). <https://doi.org/10.1016/j.compositesa.2005.01.015>
4. De Baere, I., Van Paepegem, W., Degrieck, J.: Design of a modified three-rail shear test for shear fatigue of composites. *Polym. Test.* **27**(3), 346–359 (2008). <https://doi.org/10.1016/j.polymertesting.2007.12.006>
5. Zhao, K., Niu, W., Zhang, S.: Highly stretchable, breathable and negative resistance variation textile strain sensor with excellent mechanical stability for wearable electronics. *J. Mater. Sci.* **55**(6), 2439–2453 (2020). <https://doi.org/10.1007/s10853-019-04189-x>
6. Ma, Z., Wang, W., Yu, D.: Assembled wearable mechanical sensor prepared based on cotton fabric. *J. Mater. Sci.* **55**(2), 796–805 (2020). <https://doi.org/10.1007/s10853-019-04035-0>
7. Qin, Y., et al.: Inkjet-printed bifunctional carbon nanotubes for pH sensing. *Mater. Lett.* **176**, 68–70 (2016). <https://doi.org/10.1016/j.matlet.2016.04.048>

8. Kitto, T., Bodart-Le Guen, C., Rossetti, N., Cicoira, F.: Processing and patterning of conducting polymers for flexible, stretchable, and biomedical electronics. In: *Handbook of Organic Materials for Electronic and Photonic Devices*, 2nd edn. Elsevier, pp. 817–842 (2018). <https://doi.org/10.1016/B978-0-08-102284-9.00025-5>
9. Seekaew, Y., Lokavee, S., Phokharatkul, D., Wisitsoraat, A., Kerdcharoen, T., Wongchoosuk, C.: Low-cost and flexible printed graphene-PEDOT:PSS gas sensor for ammonia detection. *Org. Electron.* **15**(11), 2971–2981 (2014). <https://doi.org/10.1016/j.orgel.2014.08.044>
10. Bledzki, A.K., Seidlitz, H., Goracy, K., Urbaniak, M., Rösch, J.J.: Recycling of carbon fiber reinforced composite polymers—review—part 1: VOLUME of production, recycling technologies, legislative aspects. *Polymers* **13**(2). MDPI AG, pp. 1–13 (2021). <https://doi.org/10.3390/polym13020300>
11. Bledzki, A.K., Seidlitz, H., Krenz, J., Goracy, K., Urbaniak, M., Rösch, J.J.: Recycling of carbon fiber reinforced composite polymers—review—part 2: recovery and application of recycled carbon fibers. *Polymers* **12**(12). MDPI AG, pp. 1–10 (2020). <https://doi.org/10.3390/polym12123003>